

# Low Dose Analytical Electron Microscopy of Hybrid Perovskite Photovoltaic Devices



**Felix Utama Kosasih**

*Downing College*

Department of Materials Science and Metallurgy

University of Cambridge

Supervisor: Prof. Caterina Ducati

Advisor: Prof. Paul Midgley

This thesis is submitted for the degree of

*Doctor of Philosophy*

September 2021

## **Declaration**

This thesis is the result of my own work and includes nothing which is the outcome of work done in collaboration except as declared in the Preface and specified in the text. I further state that no substantial part of my thesis has already been submitted, or, is being concurrently submitted for any such degree, diploma or other qualification at the University of Cambridge or any other University or similar institution except as declared in the Preface and specified in the text. It does not exceed the prescribed word limit for the relevant Degree Committee.

Felix Utama Kosasih

September 2021

# **Low Dose Analytical Electron Microscopy of Hybrid Perovskite Photovoltaic Devices**

*Felix Utama Kosasih*

The rapid ascent of perovskite photovoltaics over the past decade has enabled this technology to now stand on the cusp of commercialisation. However, a successful entry into the market will only be feasible if the power conversion efficiencies of perovskite solar modules can at least approach those of laboratory-scale cells. Achieving this feat requires spatially homogeneous depositions of device layers over a large area and high-quality interconnections between adjacent cells in a module. Since perovskite photovoltaic devices are nanostructured, materials characterisation with a nanometre spatial resolution can provide valuable insights to optimise the processes involved in scalable film deposition and interconnection fabrication. This thesis presents nanoscale electron microscopy investigations of perovskite photovoltaic devices made using scalable deposition methods and the cell interconnections within. A characterisation workflow consisting of cross-sectional specimen preparation, data acquisition, and multivariate statistical data analysis is developed and validated. Preparation of electron-transparent specimens is performed using focused ion beam milling, which is shown to have minimum impact on the perovskite specimen. Nanoscale compositional mapping is performed using energy-dispersive X-ray spectroscopy in a scanning transmission electron microscope, where the applied electron dose is minimised to suppress beam-induced specimen damage while still ensuring statistical significance in the data. Principal component analysis, a multivariate statistical analysis algorithm, is optimised and applied to improve the signal-to-noise ratio in the obtained datasets by an order of magnitude. This sequence allows acquisition of spatially resolved morphological and compositional data with minimum damage on the perovskite specimen, which are supported by complementary computational methods and other characterisation techniques. The optimised workflow is applied to study perovskite solar modules deposited by blade coating, where electron microscopy revealed how additives in the perovskite precursor solutions contribute towards a more homogeneous device stack and, ultimately, more efficient modules. Finally, the interconnections are studied as they are critical to ensure good electrical performance in solar modules. Compositional characterisation shows how laser pulses used in scribing the interconnection lines can decompose the perovskite layer next to those lines, and also how the decomposition is affected by the perovskite's homogeneity. Furthermore, elemental mapping reveals diffusion of sodium from the glass substrate into the active layers through the interconnection lines, even before the devices are operated. Sodium diffusion results in passivated defect sites and stronger perovskite luminescence, but also carries an inherent risk of excessive diffusion throughout the device's lifetime.

## Acknowledgements

The past four years have been an incredible experience for me, a period in which I grew not only as a researcher but also as a person. Needless to say, I owe a great deal of thanks to a great number of people, without whom my PhD could not have been as fulfilling.

I am deeply grateful to my supervisor, Prof. Caterina Ducati, who has been extremely nurturing and patient with me. Alongside a healthy dose of guidance and encouragement, Cate provided me the freedom I needed to become an independent researcher and showed me how rewarding an academic career can be. I truly appreciate the relaxed working environment she created with her ever-positive attitude, which enabled me to pursue new research directions and investigate serendipitous findings without fear of failure. Special thanks are also due to Dr. Giorgio Divitini, who went so far above and beyond his official duties to guide and support me in times of need and in ungodly hours. I shall fondly remember the odd and fun things we did together, from duct taping a leaking cooler tube in the Osiris room to sharing carbonara and tiramisu in Rome.

The research described in this thesis would not have been possible without the invaluable contributions from collaborators in Cambridge and beyond. My heartfelt gratitude goes to Jordi Ferrer Orri, Beth Tennyson, Sam Stranks, and Weiwei Li from Cambridge. To Lucija Rakocevic, Jef Poortmans, and Tom Aernouts at imec and Christof Schultz and Andreas Bartelt from HTW Berlin for their expertise in laser scribing. To Francesco di Giacomo, Fabio Matteocci, and Aldo di Carlo at CHOSE Rome Tor Vergata and Kexue Li and Katie Moore from Manchester for lending their device fabrication and characterisation capabilities. I thank Stefania Cacovich at CNRS-IPVF for her advice in the early days of my PhD and subsequent work together in the latter years.

On the technical side, I am indebted to Chris Dolan, Simon Griggs, and Mary Vickers for their endless patience in training me to use the electron microscopes and XRD equipment in Materials, and for working their magic whenever said instruments misbehaved. My sincere appreciation to all the administrators, safety officers, and cleaners in Materials who worked behind the scenes to keep the department running safely during the unprecedented times of COVID-19. I thank the Jardine Foundation and Cambridge Trust for believing in me and generously funding my doctorate. I also acknowledge financial support from the European Union through the Horizon 2020 – ESTEEM3 framework, the Engineering and Physical Sciences Research Council, and the Henry Royce Institute.

My thanks go to Farhan, Pina, Hanif, Dewi, Cindy, Dion, Zefan, Eli, Rizka, and Santi for supplying me with plenty of Indonesian food and lending their ears in moments of frustration throughout this PhD. Thank you to Peter, Cindy, and Giovani who rooted for me from afar. Finally, I thank my soon-to-be fiancée Jessica for her unwavering love, care, support, and patience, for the constant motivation and encouragement, and for trying her hardest to understand just what it is exactly I was working on.

# List of Publications

Discussed in this thesis

**Kosasih, F.U.\***, Divitini, G.\*., Ferrer Orri, J.\*., Tennyson, E.M., Kusch, G., Oliver, R.A., Stranks, S.D., Ducati, C. (2022). Optical Emission from Focused Ion Beam Milled Halide Perovskite Cross-sections. *Microscopy Research & Technique*, in press.

**Kosasih, F.U.**, Cacovich, S., Divitini, G., Ducati, C. (2020). Nanometric Chemical Analysis of Beam-sensitive Materials: A Case Study of STEM-EDX on Perovskite Solar Cells. *Small Methods*, 5(2), 2000835.

Matteocci, F., Vesce, L., **Kosasih, F.U.**, Castriotta, L. A., Cacovich, S., Palma, A. L., Divitini, G., Ducati, C., Di Carlo, A. (2019). Fabrication and Morphological Characterization of High-Efficiency Blade-Coated Perovskite Solar Modules. *ACS Applied Materials & Interfaces*, 11(28), 25195–25204.

**Kosasih, F.U.**, Rakocevic, L., Aernouts, T., Poortmans, J., Ducati, C. (2019). Electron Microscopy Characterisation of P3 Lines and Laser Scribing-induced Perovskite Decomposition in Perovskite Solar Modules. *ACS Applied Materials & Interfaces*, 11(49), 45646-45655.

Fenske, M.\*., Schultz, C.\*., Dagar, J.\*., **Kosasih, F.U.\***, Zeiser, A., Junghans, C., Bartelt, A., Ducati, C., Schlatmann, R., Unger, E., Stegemann, B. (2021). Improved Electrical Performance of Perovskite Photovoltaic Mini-Modules Through Controlled PbI<sub>2</sub> Formation Using Nanosecond Laser Pulses for P3 Patterning. *Energy Technology*, 9(4), 2000969.

**Kosasih, F.U.**, Di Giacomo, F., Ferrer Orri, J., Tennyson, E.M., Li, K., Li, W., Matteocci, F., Kusch, G., Oliver, R.A., Driscoll, J.L., Moore, K.L., Stranks, S.D., Di Carlo, A., Divitini, G., Ducati, C. Sodium Diffuses from Glass Substrates through P1 Lines and Passivates Defects in Perovskite Solar Modules. *Under review*.

\*equal contribution as lead authors

Other publications

**Kosasih, F.U.** & Ducati, C. (2018). Characterising degradation of perovskite solar cells through in-situ and operando electron microscopy. *Nano Energy*, 47, 243–256.

**Kosasih, F.U.** & Ducati, C. (2018). Attaining High Photovoltaic Efficiency and Stability with Multidimensional Perovskites. *ChemSusChem*, 11(24), 4193–4202.

Di Giacomo, F., Castriotta, L.A., Cricenti, A., Luce, M., **Kosasih, F.U.**, Ducati, C., Di Carlo, A. n-side Passivation with Insulating Nanoparticles for High Efficiency p-i-n Perovskite Solar Cells and Modules. *In preparation.*

Macdonald, T.J., **Kosasih, F.U.**, Xu, W., Righetto, M., Webb, T., Du, T., Pacalaj, R., Lin, C-T., Jiang, Z., Mohan, L., Min, G., Gasparini, N., McLachlan, M.A., Durrant, J.R., Haque, S.A., Cacialli, F., Divitini, G., Ducati, C., von Hauff, E. Guanidinium in Methylammonium Lead Triiodide Perovskites. *In preparation.*

deQuilettes, D.W., Yoo, J.J., Brenes, R., **Kosasih, F.U.**, Laitz, M., Dou, B.D., Shin, S.S., Ducati, C., Bawendi, M.G., Bulovic, V. Slowed Radiative Recombination via Surface Energy Gradient in Perovskite Solar Cells. *In preparation.*

Zanetta, A.\*, Andaji-Garmaroudi, Z.\* , Pirota, V., Pica, G., **Kosasih, F.U.**, Gouda, L., Frohma, K., Ducati, C., Doria, F., Stranks, S.D., Grancini, G. (2021). Manipulating Color Emission in Two-dimensional Hybrid Perovskites by Fine Tuning Halide Segregation: A Transparent Green Emitter. *Advanced Materials*, 34(1), 2105942.

Du, T.\* , Ratnasingham, S.R.\* , **Kosasih, F.U.**, Macdonald, T.J., Mohan, L., Augurio, A., Ahli, H., Lin, C-T., Xu, S., Xu, W., Binions, R., Ducati, C., Durrant, J., Briscoe, J., McLachlan, M. (2021). Aerosol Assisted Solvent Treatment: A Universal Method for Performance and Stability Enhancements in Perovskite Solar Cells. *Advanced Energy Materials*, 11(33), 2101420.

Di Giacomo, F., Castriotta, L.A., **Kosasih, F.U.**, Di Girolamo, D., Ducati, C., Di Carlo, A. (2020). Upscaling Inverted Perovskite Solar Cells: Optimization of Laser Scribing for Highly Efficient Mini-modules. *Micromachines*, 11(12), 1127.

Yaghoobi Nia, N., Zendehdel, M., Abdi-Jalebi, M., Castriotta, L.A., **Kosasih, F.U.**, Lamanna, E., Abolhasani, M.M., Zheng, Z., Andaji-Garmaroudi, Z., Asadi, K., Divitini, G., Ducati, C., Friend, R.H., Di Carlo, A. (2020). Beyond 17% Stable Perovskite Solar Module via Polaron Arrangement of Tuned Polymeric Hole Transport Layer. *Nano Energy*, 82, 105685.

Andaji-Garmaroudi, Z., Abdi-Jalebi, M., **Kosasih, F.U.**, Doherty, T.A.S., Macpherson, S., Bowman, A., Man, G., Cappel, U., Rensmo, H., Ducati, C., Friend, R.H., Stranks, S.D. (2020). Elucidating and Mitigating Degradation Processes in Perovskite Light-Emitting Diodes. *Advanced Energy Materials*, 10(48), 2002676.

Di Girolamo, D.\* , Phung, N.\* , **Kosasih, F.U.**, Di Giacomo, F., Matteocci, F., Turren-Cruz, S.H., Cina, L., Latini, A., Divitini, G., Ducati, C., Di Carlo, A., Dini, D., Abate, A. (2020). Ion Migration-Induced Amorphization and Phase Segregation as a Degradation Mechanism in Planar Perovskite Solar Cells. *Advanced Energy Materials*, 10(25), 2000310.

Doherty, T.A.S., Winchester, A.J., Macpherson, S., Johnstone, D.N., Pareek, V., Tennyson, E.M., Kosar, S., **Kosasih, F.U.**, Park, J-S., Jung, Y-K., Anaya, M., Abdi-Jalebi, M., Andaji-Garmaroudi, Z., Wong, E.L., Madeo, J., Parker, J., Chiang, Y-H., Petoukhoff, C.E., Quinn, P., Divitini, G., Man, M.K.L., Ducati, C., Walsh, A., Midgley, P.A., Dani, K., Stranks, S.D. (2020). Performance-limiting Nanoscale Trap Clusters at Grain Junctions in Halide Perovskites. *Nature*, 580, 360-366.

Wang, H., **Kosasih, F.U.**, Yu, H., Zheng, G., Zhang, J., Pozina, G., Liu, Y., Bao, C., Hu, Z., Liu, X., Kobera, L., Abbrent, S., Brus, J., Jin, Y., Fahlman, M., Friend, R.H., Ducati, C., Liu, X-K., Gao, F. (2020). Perovskite-Molecule Hybrid Thin Films for Efficient and Stable Solution-processed Light-emitting Diodes. *Nature Communications*, 11, 891.

Di Girolamo, D., Matteocci, F., **Kosasih, F.U.**, Chistiakova, G., Zuo, W., Divitini, G., Korte, L., Ducati, C., Di Carlo, A., Dini, D., Abate, A. (2019). Stability and Dark Hysteresis Correlate in NiO-Based Perovskite Solar Cells. *Advanced Energy Materials*, 9(31), 1901642.

Ruggeri, E., Anaya, M., Galkowski, K., Delport, G., **Kosasih, F.U.**, Abfalterer, A., Mackowski, S., Ducati, C., Stranks, S.D. (2019). Controlling the Growth Kinetics and Optoelectronic Properties of 2D/3D Lead-Tin Perovskite Heterojunctions. *Advanced Materials*, 31(51), 1905247.

Zhang, J., Futscher, M.H., Lami, V., **Kosasih, F.U.**, Cho, C., Gu, Q., Sadhanala, A., Pearson, A.J., Kan, B., Divitini, G., Wan, X., Credgington, D., Greenham, N.C., Chen, Y., Ducati, C., Ehrler, B., Vaynzof, Y., Friend, R.H., Bakulin, A.A. (2019). Sequentially Deposited versus Conventional Nonfullerene Organic Solar Cells: Interfacial Trap States, Vertical Stratification, and Exciton Dissociation. *Advanced Energy Materials*, 9(47), 1902145.

Modarres, M.H., **Kosasih, F.U.**, Ducati, C., De Volder, M. (2019). Self-Assembly of rGO Coated Nanorods into Aligned Thick Films. *Advanced Materials Interfaces*, 6(14), 1900219.

\*equal contribution as lead authors

# List of Figures

Figure 1.1   (Black line) Changes in global surface temperature relative to the 1850–1900 average. The temperature output of climate model simulations involving both human activities and natural causes are shown in brown, while those featuring only natural causes are in green. The brown and green lines represent the average of multiple models, while the shaded bands indicate the 95% confidence range. Reproduced from ref. <sup>1</sup> with permission, copyright IPCC.....	1
Figure 1.2   Sources of global primary energy consumption. Reproduced from ref. <sup>3</sup> under the Creative Commons CC-BY 4.0 License.....	2
Figure 1.3   (a) Annual net additions to the global installed capacity for solar PV, wind, and hydro power plants. (b) Global average of Si solar module prices. Panel (a) is constructed using data available in ref. <sup>4</sup> , copyright International Renewable Energy Agency. Panel (b) is reproduced from ref. <sup>3</sup> under the Creative Commons CC-BY 4.0 License. ....	3
Figure 1.4   (a) Record PCEs of various PV technologies classified according to their device area: <1 cm <sup>2</sup> (mini-cell), 1–800 cm <sup>2</sup> (standard cell), and >800 cm <sup>2</sup> (module). (b) PCE decline upon device upscaling for various PV technologies. IBC: interdigitated back contact, SHJ: Si heterojunction. PERL: passivated emitter and rear locally diffused, ABX <sub>3</sub> : perovskite, OPV: organic PV, c-Si: crystalline Si. Panel (a) is reproduced with permission from ref. <sup>27</sup> , copyright 2019 Springer Nature. Panel (b) is reproduced with permission from ref. <sup>28</sup> , copyright 2018 Springer Nature.....	5
Figure 1.5   Schematic of a PSM featuring two MI areas. The P1, P2, and P3 lines are marked. ETL: electron transport layer, HTL: hole transport layer, TCO: transparent conductive oxide. Reproduced from ref. <sup>30</sup> under the Creative Commons CC-BY 4.0 License. ....	6
Figure 2.1   (a) The cubic crystal structure of ABX <sub>3</sub> perovskite. (b) Various perovskite structures derived from the ABX <sub>3</sub> aristotype. Adapted from ref. <sup>34</sup> under the Creative Commons CC-BY 4.0 License.....	9
Figure 2.2   Goldschmidt's tolerance factor for various APbI <sub>3</sub> perovskites. Na, K, and Rb are too small to be A-cations while imidazolium (IA), ethylammonium (EA), and guanidinium (GA) are too large. Cs, methylammonium (MA), and formamidinium (FA) are of the correct size to produce photoactive perovskite. b) Top-view scanning electron micrographs of perovskite films deposited via solution processing and thermal evaporation. Panel (a) is reproduced with permission from ref. <sup>54</sup> , copyright 2017 American Association for the Advancement of Science. Panel (b) is adapted from ref. <sup>59</sup> under the Creative Commons CC-BY 4.0 License. ....	11

Figure 2.3 | (a) Calculated band structure of  $\text{MAPbI}_3$ . C and V mark the conduction band minima and valence band maxima, respectively. Blue arrow marks the direct band gap of  $\text{MAPbI}_3$ . (b) Calculated density of states for  $\text{MAPbI}_3$ ,  $\text{MAPbBr}_3$ , and  $\text{MAPbCl}_3$ . Band structure and density of states are calculated via density functional theory incorporating the GW method and spin-orbit coupling. Adapted with permission from ref.<sup>81</sup>, copyright 2016 Royal Society of Chemistry..... 13

Figure 2.4 | Band gap tunability of perovskites. (a) Photograph of colloidal  $\text{FAPbX}_3$  solution in toluene under UV light and normalised photoluminescence emission from  $\text{FAPbX}_3$  nanocrystals. (b) Photograph of PSCs with gold contacts. From left to right, the composition changes from  $\text{APbI}_3$  to  $\text{APbBr}_3$  in equal steps. From bottom to top, the composition changes from  $\text{MAPbX}_3$  to  $\text{FAPbX}_3$  in equal steps. Note that changing the halide produces a much larger band gap variation than changing the A-cation. Panel (a) is reproduced with permission from ref.<sup>96</sup>, copyright 2017 American Chemical Society. Panel (b) is reproduced with permission from ref.<sup>85</sup>, copyright 2016 Royal Society of Chemistry. .... 15

Figure 2.5 | Illustrations of (a) a perfect crystal lattice and various types of point defects: (b) vacancy, (c) interstitial, (d) antisite, (e) Frenkel pair, (f) Schottky pair, (g) substitutional impurity, and (h) interstitial impurity. Reproduced with permission from ref.<sup>97</sup>, copyright 2016 Springer Nature..... 16

Figure 2.6 | (a) Energy band schematics illustrating the formation of deep defect states in a defect intolerant material (left) and shallow or intraband defect states in a defect tolerant  $\text{APbX}_3$  (right). (b) Calculated energy levels of various point defects in  $\text{MAPbI}_3$ . Numbers in parentheses indicate the formation energies of neutral defects in eV. Panel (a) is reproduced with permission from ref.<sup>103</sup>, copyright 2017 American Association for the Advancement of Science. Panel (b) is reproduced with permission from ref.<sup>108</sup>, copyright 2014 Wiley-VCH..... 17

Figure 2.7 | Schematic of the working principle of a PSC. The red arrow marks photogeneration of EHPs ( $e^-$  and  $h^+$ ), curved arrows mark carrier transport inside the device, and straight black arrows signify electron flow in the external circuit. Cat and an stand for cathode and anode, respectively. .... 18

Figure 2.8 | Simulated J-V curves showing how series and shunt resistances affect the performance of a solar cell. The best-case curve shown in panel (a) is redrawn in red in panels (b-d) to ease comparison. The  $J_{SC}$ ,  $V_{OC}$ ,  $J_{MPP}$ , and  $V_{MPP}$  points are indicated..... 19

Figure 2.9 | The four most common PSC architectures. TCO: transparent conductive oxide. Adapted with permission from ref.<sup>122</sup>, copyright 2018 American Association for the Advancement of Science. .... 20

Figure 2.10 | Point and interfacial defect states in  $\text{MAPbI}_3$  and various passivation methods. Reproduced with permission from ref.<sup>146</sup>, copyright 2019 Royal Society of Chemistry. .... 22

Figure 2.11 | Scalable solution-based deposition methods. Reproduced with permission from ref. <sup>28</sup>, copyright 2018 Springer Nature..... 24

Figure 2.12 | (a) EPBT comparison for various PV technologies. ‘PSC’ and ‘PSC Ind’ refer to laboratory-scale and simulated industrial-scale devices, respectively. ‘Tandem’ refers to perovskite-based tandem devices with Si, CIGS, or CZTS. (b,c) LCOE estimation for four module architectures plotted as a function of (b) module lifetime and (c) module efficiency. Module A is a commercial Si cell, module B is a single-junction PSM, module C is a Si/perovskite tandem, and module D is a perovskite/perovskite tandem. Markers indicate the set of assumptions adopted for each module. Panel (a) is reproduced from ref. <sup>10</sup> under the Creative Commons CC-BY 4.0 License. Panels (b,c) are reproduced with permission from ref. <sup>14</sup>, copyright 2018 Cell Press..... 26

Figure 2.13 | (a) Schematics of a PSM with the P1, P2, and P3 lines marked. (b) Top-view optical microscope image of the MI area. (c,d) Top-view scanning electron microscopy image of a c) knife-scribed and d) laser-scribed P3 line. Scale bars represent (c) 100 µm and (d) 10 µm. Panel (a) is adapted from ref. <sup>174</sup> under the Creative Commons CC-BY 3.0 License. Panel (b) is reproduced with permission from ref. <sup>175</sup>, copyright 2017 IEEE..... 27

Figure 2.14 | (a) Typical timescales for various physical processes occurring during and after laser-material interaction. (b) Schematic of (left) defects formed in material ablation with an ns-pulse laser and (right) their absence when an fs-pulse laser is used. Panel (a) is reproduced with permission from ref. <sup>186</sup>, copyright 2008 Springer Nature. Panel (b) is reproduced with permission from ref. <sup>192</sup> under the Creative Commons CC-BY 4.0 License..... 29

Figure 2.15 | Illustration of recent trends in perovskite PV characterisation: (a) correlative multimodal characterisation with multiple probes, (b) in-situ experiments, and (c) framework for machine learning-assisted material discovery. Panel (a) is reproduced with permission from ref. <sup>196</sup>, copyright 2019 Springer Nature. Panel (b) is reproduced with permission from ref. <sup>240</sup>, copyright 2020 Wiley-VCH. Panel (c) is reproduced from ref. <sup>241</sup> under the Creative Commons CC-BY 4.0 License..... 35

Figure 3.1 | (a) Various signals generated inside a TEM by electron scattering in the specimen. (b) Schematic of elastic electron scattering by a specimen atom. The scattering angle is determined by the distance between the probe electron and the specimen nucleus. Panel (a) is reproduced from ref. <sup>242</sup> with permission, copyright 2019 Springer. Panel (b) is reproduced from ref. <sup>243</sup> with permission, copyright 2009 Springer. ..... 38

Figure 3.2 | Schematic showing beam broadening inside an EM specimen. Reproduced from ref. <sup>243</sup> with permission, copyright 2009 Springer. ..... 40

Figure 3.3   (a) Knoll and Ruska's TEM <sup>255</sup> and (b) FEI Tecnai Osiris 80-200 FEGTEM installed in the Wolfson Electron Microscopy Suite, Department of Materials Science & Metallurgy, University of Cambridge. This is the instrument used to produce all TEM data presented in this thesis. <sup>256</sup>	42
Figure 3.4   The beam-shaping portion of a TEM column when operated in parallel beam mode. Electromagnetic lenses direct the electron probe to obtain a parallel beam on the specimen plane. Reproduced from ref. <sup>243</sup> with permission, copyright 2009 Springer.....	44
Figure 3.5   (a) Bright field image of a polycrystalline aluminium film. (b) Dark field image constructed by selecting the {220} diffraction spots, showing all grains contributing to those spots. Reproduced from ref. <sup>243</sup> with permission, copyright 2009 Springer.....	45
Figure 3.6   (a) Ray diagram of a TEM operating in STEM mode. (b) Various detectors used in STEM imaging and their subtended detection angles. Reproduced from ref. <sup>243</sup> with permission, copyright 2009 Springer. ....	46
Figure 3.7   Illustration of (a) exact sampling, (b) undersampling, and (c) oversampling conditions in STEM data acquisition. Squares represent pixels while circles represent $d_{eff}$ of the electron beam.	46
Figure 3.8   (a) Calculated CTF of a FEI Tecnai F20 SuperTWIN operated in parallel beam TEM mode (dotted curve) and in STEM mode (solid curve). The CTF of a STEM is always positive, while the CTF of a TEM goes through sign reversals as the spatial frequency changes. <sup>264</sup> (b) Illustration of an SI data cube and its component images. <sup>265</sup> .....	47
Figure 3.9   Illustration of various SEM detectors: (a) an ETD, (b) a TLD, (c) a segmented BSE detector, and (d) a cross-sectional schematic of the BSE detector shown in (c). <sup>268</sup> .....	49
Figure 3.10   SE images of an Au/C samples acquired using an (a) ETD and a (b) TLD. The right side of the Au grain appears bright while the left side appears dark in panel (a) because of the ETD's directionality. Both sides appear bright in panel (b), showing their true topography. The scale bar represents 300 nm. Reproduced from ref. <sup>269</sup> with permission, copyright 2016 Microscopy Society of America. ....	50
Figure 3.11   Simulated electron scattering paths in C, Al, Cu, and Au samples. The simulated electron beam has an accelerating voltage of 20 kV. The gold arrow in each sample marks $R_{K-O}$ as calculated with Equation 3.7. Note the unique scale bar used for each sample. Reproduced from ref. <sup>267</sup> with permission, copyright 2018 Springer. ....	51
Figure 3.12   (a) Energy diagram showing generation of characteristic X-ray photons through inelastic scattering of a probe electron by a specimen electron. (b) Cross-sectional schematic of an SDD EDX detector. Reproduced from ref. <sup>243</sup> with permission, copyright 2009 Springer. ....	52

Figure 3.13   Procedure to cut an electron-transparent, cross-sectional PSC lamella with a FIB miller. Scale bars represent 10 $\mu$ m. ....	56
Figure 3.14   Cross-sectional STEM-HAADF images of the two standards used for k-factor calibration. Scale bar represents 1 $\mu$ m. ....	60
Figure 3.15   Schematics of SEM-CL instruments using (a) a photon-collecting parabolic mirror <sup>293</sup> and (b) a photon collection system integrated with an SEM. <sup>292</sup> ....	63
Figure 3.16   (a) Illustration of the PCA procedure for a generic two-dimensional data set as originally drawn by Karl Pearson, where the lines of best fit and worst fit serve as the two PCA components. (b) Illustration of dimensionality reduction through PCA, from a three-dimensional data set (left) to a two-dimensional model (right). Panel (a) is reproduced from ref. <sup>328</sup> with permission, copyright Taylor & Francis Group. Panel (b) is adapted from ref. <sup>330</sup> under the Creative Commons CC-BY 2.0 License. ....	68
Figure 3.17   (a) A scree plot of PCA components from a STEM-EDX SI. The inset shows a zoomed-in view of the first 30 components. (b-e) The result of PCA denoising on a STEM-EDX SI. (b) STEM-HAADF images of a PSC lamella with a marked pixel (red square) from which a raw spectrum (c) is taken ( $I-L_a$ SNR = 20). (d) The same spectrum as (c) after spectral rebinning by 4 ( $I-L_a$ SNR = 39). (e) A model spectrum constructed with four principal components after PCA denoising ( $I-L_a$ SNR ~296). ....	70
Figure 3.18   NMF decomposition of a hyperspectral image (a) into six components. Panels (b,c) show the (b) factors and (c) loadings of those components. <sup>336</sup> ....	72
Figure 4.1   (a) Normalised perovskite emission spectra from (red) top-view PL, (orange) top-view CL, (green) first cross-sectional CL scan, and (blue) second cross-sectional CL scan. As the SNR for the second cross-sectional CL scan is relatively low, normalisation was performed on the Gaussian fit (blue line) rather than on the data points. (b) Raw perovskite emission spectra from (green) first cross-sectional CL scan and (blue) second cross-sectional CL scan. ....	79
Figure 4.2   Perovskite emission characteristics from the (b,c) first and (d,e) second cross-sectional CL scans of a FIB milled PSC lamella. (a) SE image, (b,d) fitted peak emission energy, and (c,e) peak emission area. Dashed red lines mark the position of the perovskite layer. Scale bar represents 2 $\mu$ m and applies to all panels. ....	80
Figure 4.3   Result of Monte Carlo-based electron trajectory simulation using the CASINO software for an electron beam accelerating voltage of 5 kV and a model perovskite structure of composition $Cs_{0.05}FA_{0.81}MA_{0.14}Pb(I_{0.9}Br_{0.1})_3$ . <sup>354</sup> (a) Contours of energy deposition inside the 200 nm-thick perovskite layer, where each line marks a volume in which a certain portion of the electron beam's energy was	

dissipated. (b) Contribution of each thickness slice to the total detected CL signal (black curve) and the cumulative detected CL signal (red curve).....	81
Figure 4.4   PbI <sub>2</sub> emission characteristics from the (b,c) first and (d,e) second cross-sectional CL scans of a FIB milled PSC lamella. (a) SE image, (b,d) fitted peak emission energy, and (c,e) peak emission area. Dashed red lines mark the position of the perovskite layer. Scale bar represents 2 μm and applies to all panels.....	84
Figure 4.5   Perovskite and PbI <sub>2</sub> emission spectrum from the top-view CL scan. ....	84
Figure 4.6   A stack of four HAADF images showing where the STEM-EDX scans were performed. The top two scan areas are from the control PSC and the bottom two are from the aerosol-treated PSC. This arrangement of scan areas is used throughout this section. Dashed green lines mark the boundaries between scan areas. Dashed orange lines indicate perovskite grain boundaries. Cyan arrows mark grains of a secondary phase in the perovskite film. Dashed yellow circle mark a damaged area where the focused electron beam was unintentionally parked for a few seconds. Scale bar represents 1 μm. ....	86
Figure 4.7   Scree plot from the PCA procedure applied to the stack of STEM-EDX SIs. The inset shows a zoomed-in version where the second elbow point becomes clearly apparent. Dashed red ellipse marks the first four components appearing before the first elbow point. Dashed green ellipses mark components 5-16 appearing after the first but before the second elbow point.....	89
Figure 4.8   PCA principal components (1–4) appearing before the first elbow point in the scree plot in Figure 4.7. Dashed green lines mark the boundaries between scan areas. Scale bar represents 1 μm. 90	90
Figure 4.9   PCA principal components (8, 10, 16) appearing between the first and second elbow points in the scree plot in Figure 4.7. Dashed green lines mark the boundaries between scan areas. Scale bar represents 1 μm.....	91
Figure 4.10   PCA noise components (5–7, 9, 11–15) appearing between the first and second elbow points in the scree plot in Figure 4.7. Dashed green lines mark the boundaries between scan areas. Scale bar represents 1 μm.....	92
Figure 4.11   NMF components when $p = 4$ . Dashed green lines mark the boundaries between scan areas. Scale bar represents 1 μm. ....	94
Figure 4.12   The first 4 NMF components when $p = 16$ . Dashed green lines mark the boundaries between scan areas. Scale bar represents 1 μm. ....	95
Figure 4.13   Representative additional NMF components when $p = 16$ . Components 6, 7, 9, 11, and 12 are similar to component 5, while components 13-15 are similar to component 8. Dashed green lines mark the boundaries between scan areas. Scale bar represents 1 μm. ....	96

Figure 4.14   (a) Distributions of Pb concentration and (b-e) quantified Pb maps extracted from the (b) PCA A, (c) PCA B, (d) PCA C, (e) NMF 4, and (f) NMF 16 denoised models. Scale bar is 1 $\mu\text{m}$ ....	98
Figure 4.15   (a) Distributions of I concentration and (b-e) quantified I maps extracted from the (b) PCA A, (c) PCA B, (d) PCA C, (e) NMF 4, and (f) NMF 16 denoised models. Scale bar is 1 $\mu\text{m}$ .....	99
Figure 4.16   (a) Distributions of I/Pb ratio and (b-e) quantified I/Pb ratio maps extracted from the (b) PCA A, (c) PCA B, (d) PCA C, (e) NMF 4, and (f) NMF 16 denoised models. The I/Pb ratio maps were spatially rebinned by a factor of 2 to reduce noise. Scale bar is 1 $\mu\text{m}$ .....	100
Figure 4.17   (a) Distribution of C concentration and (b-e) C maps extracted from the (b) PCA A, (c) PCA B, (d) PCA C, (e) NMF 4, and (f) NMF 16 denoised models. Scale bar is 1 $\mu\text{m}$ .....	102
Figure 4.18   (a) Distribution of N concentration and (b-e) N maps extracted from the (b) PCA A, (c) PCA B, (d) PCA C, (e) NMF 4, and (f) NMF 16 denoised models. Scale bar is 1 $\mu\text{m}$ .....	103
Figure 4.19   (a) Distribution of N/Pb ratio and (b-e) N/Pb ratio maps extracted from the (b) PCA A, (c) PCA B, (d) PCA C, (e) NMF 4, and (f) NMF 16 denoised models. The N/Pb ratio maps were spatially rebinned by a factor of 2 to reduce noise. Scale bar is 1 $\mu\text{m}$ .....	104
Figure 4.20   Cross-sectional STEM-HAADF images acquired (a) before and (b) after STEM-EDX data acquisition. Beam damage marks are visible in the perovskite layer in (b). mp- and c-TiO <sub>2</sub> refers to mesoporous and compact TiO <sub>2</sub> layers respectively. Scale bars represent 0.5 $\mu\text{m}$ .....	107
Figure 4.21   Maps of STEM-EDX PD at a 99% CI and reference HAADF images acquired before STEM-EDX mapping. Red-shaded pixels are detectable while blue-shaded pixels are not. The red/blue shading indicates how far a pixel's $I/B$ metric is from the critical value (white) needed to achieve detectability. The maps' spatial resolution is 10 nm per pixel. Scale bar represents 400 nm and applies to all maps and images.....	109
Figure 4.22   Comparison of PD for Br-K <sub><math>\alpha</math></sub> and Br-L <sub><math>\alpha</math></sub> peaks and reference HAADF images acquired before STEM-EDX mapping. Red-shaded pixels are detectable while blue-shaded pixels are not. The red/blue shading indicates how far a pixel's $I/B$ metric is from the critical value (white) needed to achieve detectability. The Br-L <sub><math>\alpha</math></sub> peak is slightly more intense, resulting in a small improvement in statistical confidence. The maps' spatial resolution is 10 nm/pixel. Scale bar represents 400 nm and applies to all maps and images.....	110
Figure 4.23   STEM-EDX measurement errors for Pb-L <sub><math>\alpha</math></sub> , I-L <sub><math>\alpha</math></sub> , and Br-K <sub><math>\alpha</math></sub> peaks across a range of electron doses and the effect of spatial rebinning on them. a) RE on an individual pixel basis at a 95% CI and b) AE for a whole SI at a 95% CI, expressed as a percentage of MPI. Effect of spatial rebinning on RE for the SI acquired using a dose of c) 400 e <sup>-</sup> /Å <sup>2</sup> and d) 4840 e <sup>-</sup> /Å <sup>2</sup> . Symbol colour represents electron dose used in the STEM-EDX scan. ....	111

Figure 4.24 | Normalised maps of peak intensity for Br-K<sub>a</sub>, I-L<sub>a</sub>, and Pb-L<sub>a</sub> with reference HAADF images acquired before STEM-EDX mapping and average halide/Pb ratio values. The maps' spatial resolution is 10 nm/pixel. The pixel colour may be used to compare peak intensity within each map, but not across maps. Scale bar represents 400 nm and applies to all maps and images..... 112

Figure 4.25 | Effect of spatial rebinning on peak intensity maps and PD for the SIs acquired using a dose of (a) 400 e<sup>-</sup>/Å<sup>2</sup>, (b) 1200 e<sup>-</sup>/Å<sup>2</sup>, and (c) 4840 e<sup>-</sup>/Å<sup>2</sup>. Spatial rebinning lowers spatial resolution but boosts PD. A rebinning factor of (1/2/3/4) results in a spatial resolution of (10/20/30/40) nm/pixel. Scale bar represents 400 nm and applies to all maps..... 113

Figure 4.26 | Quantified elemental maps for Br-K<sub>a</sub>, I-L<sub>a</sub>, and Pb-L<sub>a</sub> with reference HAADF images acquired before STEM-EDX mapping. The maps' spatial resolution is 10 nm/pixel. Scale bar represents 400 nm and applies to all maps and images..... 114

Figure 4.27 | (a) HAADF images of the perovskite layer acquired before and after the STEM-EDX scans. Dotted rectangles in the (107 pA, 10 ms) image pair mark an area which is masked in intensity measurement. The imaged areas are of slightly different sizes due to local changes in perovskite layer thickness. (b) Intensity histograms and (c) after/before intensity ratio plot of the HAADF images shown in panel (a). Green dashed lines in panel (b) mark the positions of the 400 e<sup>-</sup>/Å<sup>2</sup> peaks. (d) Halide/Pb MPI ratio plot extracted from the STEM-EDX data. Error bars represent standard deviations across all perovskite pixels in an SI. The 'After' image frame colour in panel (a) and symbol colour in panels (c) and (d) represent electron dose used in the STEM-EDX scan. In panels (c) and (d), dashed lines highlight the exponential decline trend and do not represent measured data..... 116

Figure 4.28 | Number of lost I atoms calculated from the HAADF intensity and EDX data..... 119

Figure 4.29 | Normalised peak intensity maps of Br-K<sub>a</sub>, I-L<sub>a</sub>, and Pb-L<sub>a</sub>, showing I diffusion towards spiro-OMeTAD (blue arrows) after STEM-EDX scan using a high electron dose. Yellow dashed lines are a guide to the eye. Scale bar represents 400 nm and applies to all maps and images..... 120

Figure 5.1 | (a) Main steps of air-assisted blade coating of perovskite films: UV treatment, solution dispensing, blading, and drying. This deposition procedure was used for PbI<sub>2</sub>, PbI<sub>2</sub>:MAI, and spiro-OMeTAD depositions. (b) Schematic of the sequential deposition of MAPbI<sub>3</sub> films, showing the modifications introduced to the precursors to obtain the MAI+ and MAI+/H<sub>2</sub>O+ perovskite films.<sup>203</sup>..... 125

Figure 5.2 | (a) Photographs of the PbI<sub>2</sub> and PbI<sub>2</sub>:MAI films. (b) Absorbance spectra of the (red) PbI<sub>2</sub>, (green) PbI<sub>2</sub>:MAI, (cyan) REF perovskite, (magenta) MAI+ perovskite, and (blue) MAI+/H<sub>2</sub>O+ perovskite films. (c) PL spectra of the (red) PbI<sub>2</sub> and (green) PbI<sub>2</sub>:MAI films. (d) PL spectra of the

(cyan) REF, (magenta) MAI+, and (blue) MAI+/H <sub>2</sub> O+ perovskite films deposited on an insulating Al <sub>2</sub> O <sub>3</sub> mesoporous scaffold. <sup>203</sup>	128
Figure 5.3   XRD diffractograms of, from top to bottom, the REF, MAI+, and MAI+/H <sub>2</sub> O+ perovskite film, and a single crystal MAPbI <sub>3</sub> reference (ICSD 241477). Miller indices of the prominent perovskite peaks are marked. Blue triangles and gold squares mark the FTO and gold peaks, respectively. ....	129
Figure 5.4   Low magnification (a,d,g, scale bar = 10 μm), medium magnification (b,e,h, scale bar = 2 μm) and high magnification (c,f,i, scale bar = 1 μm) top-view SE images of the (a,b,c) REF, (d,e,f) MAI+, and (g,h,i) MAI+/H <sub>2</sub> O+ perovskite films.	129
Figure 5.5   Cross-sectional STEM-HAADF images of the (a) REF, (b) MAI+, and (c) MAI+/H <sub>2</sub> O+ devices. Cyan arrows indicate PbI <sub>2</sub> grains at the perovskite-TiO <sub>2</sub> interface. Red arrows mark incomplete TiO <sub>2</sub> pore filling by the perovskite. Green arrows point to pits in the perovskite film. Scale bars = 1 μm.	130
Figure 5.6   Cross-sectional STEM-HAADF images of STEM-EDX scan areas, quantified STEM-EDX elemental maps of Pb, I, C, and Ti, and I/Pb ratio maps of the (a) REF, (b) MAI+, and (c) MAI+/H <sub>2</sub> O+ devices. The I/Pb ratio maps were spatially rebinned by a factor of 2 to reduce noise. Yellow strips at the perovskite–spiro-OMeTAD interface in the I/Pb map indicate I diffusion caused by the STEM electron beam. The denoised STEM-EDX model SI was constructed using 7 principal components via PCA. Scale bars represent 900 nm and are applicable for all panels.	132
Figure 5.7   (a) Photograph of a PSM on a 5 × 5 cm <sup>2</sup> substrate consisting of five serially connected cells with an AA of 13.6 cm <sup>2</sup> . (b) I-V curves of the 5 × 5 cm <sup>2</sup> PSMs containing the REF, MAI+, or MAI+/H <sub>2</sub> O+ perovskite films. (c) I-V curves of four 5 × 5 cm <sup>2</sup> MAI+/H <sub>2</sub> O+ PSMs with an AA of 14 cm <sup>2</sup> . (d) I-V curve of a MAI+/H <sub>2</sub> O+ PSM on a 10 × 10 cm <sup>2</sup> substrate with a cell width of 7.05 mm. <sup>203</sup>	133
Figure 5.8   (a) Photograph of a PSM on a 10 × 10 cm <sup>2</sup> substrate consisting of 15 serially connected cells with an optimised cell width of 4.5 mm. (b) I-V curves of three MAI+/H <sub>2</sub> O+ PSMs with the optimised cell layout. The AA of the modules was 47.7 cm <sup>2</sup> and the GFF was 86.7%. (c) Normalised LBIC map of a MAI+/H <sub>2</sub> O+ PSM. (d) Histogram and Gaussian fitting of the LBIC data shown in panel (c). Mean (0.87) and standard deviation (0.057) values associated with the Gaussian fitting are also reported. <sup>203</sup>	135
Figure 5.9   MPP tracking results ( $V_{MPP}$ , steady state power output, and steady state PCE) of a 10 × 10 cm <sup>2</sup> MAI+/H <sub>2</sub> O+ PSM with the optimised cell layout. <sup>203</sup>	136
Figure 5.10   I-V curves of a 10 × 10 cm <sup>2</sup> MAI+/H <sub>2</sub> O+ PSM with the optimised cell layout acquired in (red) reverse and (green) forward scan directions. <sup>203</sup>	137

Figure 6.1 | Illustration of a PSM stack with two sets of P1-P2-P3 scribe lines. The left and right set includes a shallow and deep P3 line, respectively. The red-shaded strips mark areas cut for STEM characterisation discussed in this chapter. This schematic is not drawn to scale..... 138

Figure 6.2 | Top-view SE images of samples (a) SC, (b) SD-3.47, (c) SD-3.04, (d) SS, and (e) BS. Cyan arrows indicate the raster pattern followed by laser pulses for shallow scribe lines (1 complete line of pulses before another). Yellow lines measure each scribe line's width as summarised in the table. . 142

Figure 6.3 | (a-c) Top-view SEM images of sample SD-3.47's damaged ITO layer. (d) EDX scan area for (e-f). (e) In and (f) Si maps showing low In and high Si signal at the scratches. (g) Normalised intensity line plots of the red dashed lines in (d-f) The dips in SE Image line indicate the damage marks' locations. Scale bars in (d-f) represent 1  $\mu\text{m}$ . ..... 143

Figure 6.4 | (a,b) BSE images of sample SS, acquired with a 5 kV acceleration voltage. (c) SE image and (d) Cs map of a P3 line in sample SS. (e) and (f) are reproductions of (c) and (d) with red/yellow markers to highlight the correlation between grains and regions of high Cs intensity. Scale bars in (c) and (e) applies to (d) and (f)..... 144

Figure 6.5 | Top-view SEM-EDX mapping of samples (row 1) SC, (row 2) SD-3.47, (row 3) SD-3.04, (row 4) SS, and (row 5) BS. From left to right, each column shows the SE image of the scan area, Au, C, Pb, I, and In maps, respectively. Each scale bar applies to its respective row. ..... 145

Figure 6.6 | (a) SEM-EDX I map of sample BS. (b) Plot of horizontally averaged I intensity. Green strips mark the position of laser pulses, with darker shading indicating pulse overlaps. Sections of the plot corresponding to each pulse row are marked. (c) Plot of vertically averaged I intensity for each pulse row. (d) Schematic of heat loss through the intact gold layer surrounding a pulse crater. (e) Schematic of the perovskite surface after shallow laser scribing. ..... 146

Figure 6.7 | (a) SEM-EDX I map of sample SS. (b) Plot of horizontally averaged I intensity from (a). The green strips mark the position of the laser pulses, with darker shading indicating pulse overlaps. A section of the plot corresponding to each pulse row is marked. (c) Plot of vertically averaged I intensity for each pulse row in (a). ..... 147

Figure 6.8 | Location of the lamellae cut for STEM characterisation for samples (a) SC, (b) SD-3.47, (c) SD-3.04, (d) SS, (e) BD, (f) BS, and (g) SD-3.04. The distance between the scribe line edge and the final, thinned lamella is approximately 900 nm for those cut parallel to P3 lines (a-f). ..... 148

Figure 6.9 | (a-c) Cross-sectional STEM-HAADF images of samples (a) SC, (b) SD-3.47, and (c) SD-3.04. Cyan arrows mark non-perovskite bright grains, while red boxes mark the STEM-EDX scan areas mapped in (d). From top to bottom, the layer colour codes are: dark grey, protective Pt; gold, top Au contact; green, spiro-OMeTAD; brown, perovskite; light grey, ITO; and white, glass. The  $\text{SnO}_2$  layer

is the thin strip between perovskite and ITO. (d) Cross-sectional quantified STEM-EDX elemental maps of samples SC, SD-3.47, and SD-3.04. Thin yellow strips at the perovskite–spiro-OMeTAD interface in the I/Pb map indicate I diffusion caused by the STEM electron beam. The denoised STEM-EDX model SIs for samples SC, SD-3.47, and SD-3.04 were constructed using 14, 18, and 20 principal components via PCA, respectively. Scale bars represent (a–c) 1  $\mu\text{m}$  and (d) 600 nm..... 149

Figure 6.10 | Threshold analysis for sample SC. From top to bottom, the images are cropped HAADF image, initial thresholding result (white = spiro-OMeTAD, black = perovskite and PbI<sub>2</sub>), final thresholding result (white = perovskite, black = spiro-OMeTAD and PbI<sub>2</sub>), and PbI<sub>2</sub> grains (white = PbI<sub>2</sub>, black = perovskite and spiro-OMeTAD). At the bottom are the brightness histogram with fitted peaks and analysis results in a table. The scale bar represents 1  $\mu\text{m}$  and applies to all images. ..... 151

Figure 6.11 | Threshold analysis for sample SD-3.47. From top to bottom, the images are cropped HAADF image, initial thresholding result (white = spiro-OMeTAD, black = perovskite and PbI<sub>2</sub>), final thresholding result (white = perovskite, black = spiro-OMeTAD and PbI<sub>2</sub>), and PbI<sub>2</sub> grains (white = PbI<sub>2</sub>, black = perovskite and spiro-OMeTAD). At the bottom are the brightness histogram with fitted peaks and analysis results in a table. The scale bar represents 1  $\mu\text{m}$  and applies to all images. ..... 151

Figure 6.12 | (a) Summary of perovskite compositional changes after laser scribing, compared to control samples. (b,c) Schematics of the proposed thermal decomposition mechanisms. The dominant mechanism is determined by the presence (b) or absence (c) of pre-existing PbI<sub>2</sub> grains in the perovskite layer. If PbI<sub>2</sub> is present, most of the thermal energy flows through it (red arrows) rather than through the perovskite (yellow arrows) due to the large thermal conductivity difference. If PbI<sub>2</sub> is absent, heat flows uniformly through the perovskite (orange arrows). ..... 152

Figure 6.13 | Illustration of the heat source fronts (red lines) used to model thermal energy flow after a laser pulse. ..... 154

Figure 6.14 | Heat flux map produced by the thermal flow model. The right-side half of the heat source fronts shown in Figure 6.13 is marked by the green ellipse. Arrows indicate direction and magnitude of the heat flux (the flux in layers other than gold is so small in comparison that the arrows are not visible, see Figure 6.15). The white dashed lines delineate the position of the lamellae cut parallel to the P3 lines, ~900 nm away from the scribe line edge. Numbers on the colour bar are in 10<sup>7</sup> W/m<sup>2</sup>..... 156

Figure 6.15 | Reproduction of Figure 6.14, but numbers on the colour bar are in 10<sup>6</sup> W/m<sup>2</sup>. ..... 156

Figure 6.16 | (a–d) Cross-sectional STEM-HAADF images of samples (a) BC, (b) BD, (c) SS, and (d) BS. Red boxes mark the STEM-EDX scan areas. (e) Cross-sectional quantified STEM-EDX elemental maps of samples BC, BD, SS, and BS. Thin yellow strips at the perovskite–spiro-OMeTAD interface in the I/Pb map indicate I diffusion caused by the STEM electron beam. The denoised STEM-EDX

model SIs for samples BC, BD, and SS, and BS were constructed using 12, 9, 10, and 11 principal components via PCA, respectively. Scale bars represent (a–d) 1  $\mu\text{m}$  and (e) 600 nm..... 158

Figure 6.17 | Cross-sectional STEM-HAADF image and quantified STEM-EDX elemental maps of a perpendicular-to-P3 lamella taken from sample SD-3.04. Each red box represents a STEM-EDX scan area corresponding to maps below it. Thin yellow strips at the perovskite–spiro-OMeTAD interface in the I/Pb map indicate I diffusion caused by the STEM electron beam. The denoised STEM-EDX model SI was constructed using 14 principal components via PCA. The scale bars represent 1  $\mu\text{m}$  for the STEM-HAADF image and 600 nm for all elemental maps. ..... 160

Figure 6.18 | Top-view SE images of P3 lines scribed by a) ps and b) ns laser pulses. ..... 162

Figure 6.19 | Cross-sectional HAADF images and quantified STEM-EDX elemental maps of the reference, ps-scribed, and ns-scribed lamellae. The left end of these images and maps is located next to the P3 line edge, whereas the right end is furthest into the active area. The red dashed line marks the end of the Br-rich layer formed in the ns-scribed sample, 12  $\mu\text{m}$  from the P3 line edge. .... 163

Figure 7.1 | Cross-sectional STEM-HAADF image and STEM-EDX peak intensity maps for the NiO device. The denoised STEM-EDX model SI was constructed using 17 principal components from PCA. The Br and Na maps are spatially rebinned by a factor of 2 to reduce noise. The dashed green line marks the P1 line edge. The bottom row shows an enlarged view of the right end of the Br and Na maps as marked by the dashed blue rectangle. Green circles highlight the Na-Br correlation. Numbers in parentheses signify the range of the colour scale used for each map. Scale bar represents 2  $\mu\text{m}$ . .... 172

Figure 7.2 | Cross-sectional STEM-HAADF image and STEM-EDX peak intensity maps for the TiO<sub>2</sub> device. The denoised STEM-EDX model SI was constructed using 17 principal components from PCA. The Br and Na maps are spatially rebinned by a factor of 2 to reduce noise. Numbers in parentheses signify the range of the colour scale used for each map. Scale bar represents 2  $\mu\text{m}$ . .... 173

Figure 7.3 | (a) Schematic of the TiO<sub>2</sub> device analysed with NanoSIMS, with orientations marked as reference for panels (b-f). (b) Lateral profiles acquired from (solid line) next to and (dashed line) 100  $\mu\text{m}$  away from a P1 line. Higher slice numbers are further away from a P1 line. (c,d) Depth profiles acquired from (c) next to and (d) 100  $\mu\text{m}$  away from a P1 line. Higher slice numbers are deeper in the device stack. (e,f) 2D elemental maps (yz plane) acquired from (e) next to and (f) 100  $\mu\text{m}$  away from a P1 line. Numbers between panels (e,f) signify the range of the colour scale used for each element. Scale bars represent 5  $\mu\text{m}$  in the y direction. The slice numbers in panels (c,d) and z distance in panels (e,f) are not scaled to actual layer thicknesses. .... 175

Figure 7.4   Selected XRD peaks acquired from (blue) SLG/NiO/perovskite, (orange) Si/NiO/perovskite, (green) SLG/TiO <sub>2</sub> /perovskite, and (red) Si/TiO <sub>2</sub> /perovskite samples. Miller indices of the perovskite lattice planes are marked. ....	176
Figure 7.5   Normalised XPS spectra of (a) Pb, (b) I, (c) Br, and (d) Cs acquired from (blue) SLG/NiO/perovskite, (orange) Si/NiO/perovskite, (green) SLG/TiO <sub>2</sub> /perovskite, and (red) Si/TiO <sub>2</sub> /perovskite samples. Normalisation was performed on Gaussian fits of the raw data. ....	177
Figure 7.6   Top-view SEM images acquired from (a,b) SLG/ITO/NiO/perovskite, (c) Si/NiO/perovskite, (d,e,g-l) SLG/FTO/TiO <sub>2</sub> /perovskite, and (f) Si/TiO <sub>2</sub> /perovskite. Panels (a,d) were acquired from inside P1 lines, while panels (b,e) were taken far away from P1 lines. Panels (k) and (l) are SE and BSE images, respectively, of the same area. All other panels are SE images. Scale bars represent (a-f) 2 μm, (g,h) 200 μm, (i,j) 50 μm, or (k,l) 10 μm. ....	178
Figure 7.7   (a-e,k-o) AFM topography maps and (f-j,p-t) KPFM CPD maps acquired near to or far away from a P1 line in the NiO and TiO <sub>2</sub> devices. CPD values in panels (f-j) were multiplied by -1 to correct for the device's reversed electrical polarity. Red arrows mark the non-perovskite grains. Dotted squares in columns 1, 2, and 4 mark the areas mapped with higher magnification in columns 2, 3, and 5, respectively. Scale bars represent (column 1) 10 μm, (columns 2,4) 5 μm, or (columns 3,5) 1 μm. ..	179
Figure 7.8   (a-d) SE image of the CL scan area, (e-h) perovskite emission map, and (i-l) PbI <sub>2</sub> emission map acquired near to (Near) or far away from (Far) a P1 line in the NiO and TiO <sub>2</sub> devices. Dashed white lines mark the P1 lines. Scale bars represent (a,b,e,f,i,j) 5 μm, (c,g,k) 30 μm, or (d,h,l) 10 μm. (m,n) Average CL emission spectra for the (m) NiO and (n) TiO <sub>2</sub> devices extracted from the emission maps. Dotted lines in panels (m,n) mark the emission peak centres.....	181
Figure 7.9   Normalised (a) CL and (b) PL perovskite emission spectra acquired near to and far away from P1 lines in the NiO and TiO <sub>2</sub> devices. ....	182
Figure 7.10   Cross-sectional STEM-HAADF image and STEM-EDX peak intensity maps for the NiO device after 12 weeks of storage in a desiccator (dry air, <20% RH) at room temperature. The denoised STEM-EDX model SI was constructed using 18 principal components from PCA. The bottom row shows an enlarged view of the Br and Na maps as marked by the dashed green rectangle. The left (right) end of the lamella is ~6 (~21) μm away from a P1 line edge. Scale bar represents 2 μm.....	184

# List of Tables

Table 2.1   Spatial resolution of spatially resolved characterisation techniques. ....	32
Table 3.1   Calculations of $d_{eff}$ for the perovskite stoichiometries investigated in this thesis.....	58
Table 3.2   STEM-EDX data acquisition parameters. ....	60
Table 3.3   Calibrated k-factors. ....	61
Table 4.1   FIB milling procedure and beam parameters for cross-sectional lamella preparation. ....	77
Table 4.2   CL SI acquisition parameters. ....	78
Table 4.3   Radiation pressure calculation for PL, CL, and FIB milling. ....	83
Table 4.4   Classification of accuracy (A) and noise level (N) of the quantified elemental and ratio maps produced from the five denoised models. A is classified as either accurate (green) or not (red), while N is ranked as low noise (green), medium (yellow), and high noise (red). ....	101
Table 4.5   Electron beam parameters used to acquire 12 STEM-EDX SIs. The dose rates are calculated using a pixel size of 100 nm <sup>2</sup> . All dose rate and dose values are rounded to the nearest 10. ....	108
Table 4.6   Calculations of the $tZ_{eff}^{1.8}$ metric for pristine perovskite specimen and partially decomposed perovskite. $x$ = thickness of perovskite containing one I vacancy per unit cell, in nm. ....	117
Table 4.7   Calculations of the value of $x$ and number of lost I atoms from the measured HAADF intensity data. ....	118
Table 4.8   Calculations of number of lost I atoms from the I/Pb MPI ratio data. ....	119
Table 5.1   Precursor solution combinations used in perovskite film deposition. ....	124
Table 5.2   PV parameters of four MAI+/H <sub>2</sub> O+ PSMs on 5 × 5 cm <sup>2</sup> substrates. <sup>203</sup> ....	134
Table 5.3   PV parameters of three MAI+/H <sub>2</sub> O+ PSMs on 10 × 10 cm <sup>2</sup> substrates. <sup>203</sup> ....	134
Table 6.1   Sample codes and P3 laser scribing parameters. ....	140
Table 6.2   Properties of the Au layer used in modelling the heat source fronts. ....	153

Table 6.3 | Laser pulse parameters used in modelling the heat source fronts. ..... 153

Table 6.4 | Thermal conductivity and thickness of each device layer in the thermal flow model..... 155

## List of Abbreviations

<b>AA</b>	active area
<b>AE</b>	absolute error
<b>AFM</b>	atomic force microscope / microscopy
<b>BF</b>	bright field
<b>BOS</b>	balance of systems
<b>BSE</b>	backscattered electron
<b>CBM</b>	conduction band minimum
<b>CCD</b>	charge-coupled device
<b>CI</b>	confidence interval
<b>CL</b>	cathodoluminescence
<b>CMOS</b>	complementary metal-oxide-semiconductor
<b>CPD</b>	contact potential difference
<b>CTF</b>	contrast transfer function
<b>CTL</b>	charge transport layer
<b>DF</b>	dark field
<b>DP</b>	diffraction pattern
<b>DSSC</b>	dye-sensitised solar cell
<b>EDX</b>	energy-dispersive X-ray spectroscopy
<b>EHP</b>	electron-hole pairs
<b>EL</b>	electroluminescence
<b>EM</b>	electron microscope / microscopy
<b>EPBT</b>	energy payback time
<b>EQE</b>	external quantum efficiency
<b>ETD</b>	Everhart-Thornley detector

<b>ETL</b>	electron transport layer
<b>FEG</b>	field emission gun
<b>FF</b>	fill factor
<b>FIB</b>	focused ion beam
<b>FTO</b>	fluorine-doped tin oxide
<b>FWHM</b>	full width at half maximum
<b>GFF</b>	geometric fill factor
<b>GIS</b>	gas injection system
<b>HAADF</b>	high-angle annular dark field
<b>HAZ</b>	heat-affected zone
<b>HTL</b>	hole transport layer
<b>IR</b>	infrared
<b>ITO</b>	tin-doped indium oxide
<b>KPFM</b>	Kelvin probe force microscope / microscopy
<b>LCOE</b>	levelised cost of electricity
<b>LED</b>	light-emitting diode
<b>LIPSS</b>	laser-induced periodic surface structure
<b>LSFL</b>	low spatial frequency LIPSS
<b>MI</b>	monolithic interconnection
<b>MPI</b>	mean peak intensity
<b>MPP</b>	maximum power point
<b>MVA</b>	multivariate statistical analysis
<b>NMF</b>	non-negative matrix factorisation
<b>OIHP</b>	organic-inorganic hybrid halide perovskite
<b>PCA</b>	principal component analysis
<b>PCE</b>	power conversion efficiency

<b>PD</b>	peak detectability
<b>PL</b>	photoluminescence
<b>PSC</b>	perovskite solar cell
<b>PSM</b>	perovskite solar module
<b>PV</b>	photovoltaics
<b>RE</b>	relative error
<b>SA</b>	substrate area
<b>SDD</b>	silicon drift detector
<b>SE</b>	secondary electron
<b>SEM</b>	scanning electron microscope / microscopy
<b>SI</b>	spectrum image
<b>SIMS</b>	secondary ion mass spectrometry
<b>SLG</b>	soda lime glass
<b>SNR</b>	signal-to-noise ratio
<b>STEM</b>	scanning transmission electron microscope / microscopy
<b>TCDH</b>	triple cation, double halide
<b>TCO</b>	transparent conductive oxide
<b>TEM</b>	transmission electron microscope / microscopy
<b>TGA</b>	thermogravimetric analysis
<b>TIA</b>	TEM Imaging and Analysis (software)
<b>TLD</b>	through-the-lens detector
<b>UV</b>	ultraviolet
<b>VBM</b>	valence band maximum
<b>XPS</b>	X-ray photoelectron spectroscopy
<b>XRD</b>	X-ray diffraction

# Table of Contents

Declaration .....	i
Abstract.....	ii
Acknowledgements.....	iii
List of Publications .....	iv
List of Figures.....	vii
List of Tables .....	xx
List of Abbreviations .....	xxii
Table of Contents.....	xxv
Chapter 1: Introduction .....	1
Chapter 2: Perovskite and Perovskite Photovoltaics .....	8
2.1. Organic-Inorganic Hybrid Halide Perovskite .....	8
2.1.1. Crystal Structure and Grain Morphology .....	10
2.1.2. Band Structure and Carrier Photogeneration .....	11
2.1.3. Band Gap Tunability .....	14
2.1.4. Defect Tolerance .....	15
2.2. Perovskite Solar Cells .....	18
2.2.1. Working Principles .....	18
2.2.2. Device Architecture .....	20
2.2.3. Defect Passivation.....	21
2.2.4. Facile Synthesis and Deposition.....	22
2.3. Perovskite Solar Modules .....	23
2.3.1. Scalable, Low Cost, and Low Energy Module Fabrication .....	23
2.3.2. Monolithic Interconnection .....	27
2.3.3. Laser Scribing .....	28
2.4. Characterisation of Perovskite Photovoltaic Devices .....	30

2.5. Summary.....	35
Chapter 3: Electron Microscopy Techniques .....	37
3.1. Beam–Specimen Interaction: Electron Scattering .....	37
3.2. Transmission Electron Microscope .....	41
3.3. Scanning Transmission Electron Microscope .....	45
3.4. Scanning Electron Microscope.....	48
3.5. Energy-dispersive X-ray Spectroscopy .....	52
3.6. Focused Ion Beam Milling.....	55
3.7. STEM Data Acquisition and Analysis in this Thesis .....	57
3.8. Cathodoluminescence .....	62
3.9. Beam-induced Specimen Damage.....	64
3.10. Multivariate Statistical Analysis .....	67
3.11. Summary.....	73
Chapter 4: Optimisation of STEM-EDX and Multivariate Statistical Analysis for Characterisation of Perovskite Solar Cells .....	74
4.1. Introduction.....	74
4.2. FIB Milling-induced Modifications in PSC Lamellae.....	75
4.2.1. Introduction.....	75
4.2.2. Experimental Methods .....	76
4.2.2.1. PSC Fabrication .....	76
4.2.2.2. FIB Milling of PSC Lamella .....	76
4.2.2.3. Cathodoluminescence.....	77
4.2.2.4. Photoluminescence.....	78
4.2.3. Results and Discussion.....	79
4.3. Optimisation of PCA and NMF for STEM-EDX Analysis .....	85
4.3.1. Introduction.....	85

4.3.2. Experimental Methods .....	87
4.3.2.1. Solar Cell Fabrication.....	87
4.3.2.2. Transmission Electron Microscopy .....	88
4.3.3. Determination of Principal Components from PCA and NMF.....	88
4.3.4. Construction of Denoised Model from PCA and NMF Components .....	97
4.4. Balancing STEM-EDX Data Quality and Beam-induced Specimen Damage .....	105
4.4.1. Introduction.....	105
4.4.2. Experimental Methods .....	106
4.4.2.1. PSC Fabrication .....	106
4.4.2.2. Transmission Electron Microscopy .....	106
4.4.3. Electron Dose and STEM-EDX Data Quality .....	107
4.4.4. Electron Dose and Beam-induced Specimen Damage.....	114
4.5. Summary.....	121
Chapter 5: Solution Engineering for Homogeneous Perovskite Film Deposition over Large Areas .	122
5.1. Introduction.....	122
5.2. Experimental Methods .....	123
5.2.1. Device Fabrication .....	123
5.2.2. Optical and Optoelectronic Characterisation .....	126
5.2.3. Electron Microscopy Characterisation .....	126
5.2.4. X-ray Diffraction.....	126
5.3. Results and Discussion.....	127
5.4. Summary.....	137
Chapter 6: P3 Lines and Laser Scribing-induced Perovskite Decomposition in Their Vicinity .....	138
6.1. Introduction.....	138
6.2. Propagation of Thermal Energy from P3 Laser Scribing .....	139
6.2.1. Experimental Methods .....	139

6.2.1.1. Device Fabrication and Laser Scribing .....	139
6.2.1.2. Electron Microscopy Characterisation.....	141
6.2.2. SEM Characterisation of Laser Scribed P3 Lines.....	141
6.2.3. Laser-Induced Perovskite Decomposition in the Active Area .....	148
6.3. Comparing the Effects of Residual Heat from Nanosecond and Picosecond Laser Pulses ....	160
6.3.1. Experimental Methods .....	160
6.3.1.1. Device Fabrication and Laser Scribing.....	160
6.3.1.2. Electron Microscopy Characterisation.....	161
6.3.2. Formation of PbI <sub>2</sub> and Br-rich Perovskite .....	161
6.4. Summary.....	163
<b>Chapter 7: Sodium Diffusion from Glass through P1 Lines Passivates Perovskite Solar Modules ...</b>	<b>165</b>
7.1. Introduction.....	165
7.2. Experimental Methods .....	166
7.2.1. Film and Device Fabrication .....	166
7.2.2. Electron Microscopy Characterisation .....	168
7.2.3. NanoSIMS 3D Elemental Mapping.....	168
7.2.4. X-ray Diffraction.....	168
7.2.5. X-ray Photoelectron Spectroscopy .....	169
7.2.6. Atomic Force Microscopy and Kelvin Probe Force Microscopy.....	169
7.2.7. Cathodoluminescence .....	169
7.2.8. Photoluminescence.....	170
7.3. Na Diffusion in the Vicinity of P1 Lines.....	170
7.4. Effect of Na Diffusion on the Properties of the Perovskite .....	176
7.5. Summary.....	185
<b>Chapter 8: Conclusions and Future Work .....</b>	<b>186</b>
<b>References .....</b>	<b>189</b>

Appendix .....	233
A. EDX Analysis Code.....	233
B. CL Analysis Code .....	242

# Chapter 1

## Introduction

This introduction is written a few days after the United Nations' Intergovernmental Panel on Climate Change (IPCC) released the first part of their Sixth Assessment Report in August 2021. In it, the authors wrote that it is “indisputable” that the Earth has been warmed by human activities (Figure 1.1), thus increasing the frequency and severity of extreme climate events.<sup>1</sup> The link between human activities and warming is provided by greenhouse gases, primarily CO<sub>2</sub>, which are emitted by humans into the atmosphere and trap heat there. The authors predicted that we would fail to limit global warming to 2°C above pre-industrial temperatures, the primary target of the 2015 Paris Climate Agreement, as early as 2050 in all but the two most optimistic greenhouse gas emission scenarios.<sup>1</sup> Indeed, 1°C of warming has already been observed (Figure 1.1).<sup>1</sup> The IPCC concluded that the worst effects of global warming can only be avoided if “strong, rapid, and sustained” reductions in greenhouse gas emission, especially CO<sub>2</sub>, can be achieved.<sup>1</sup>

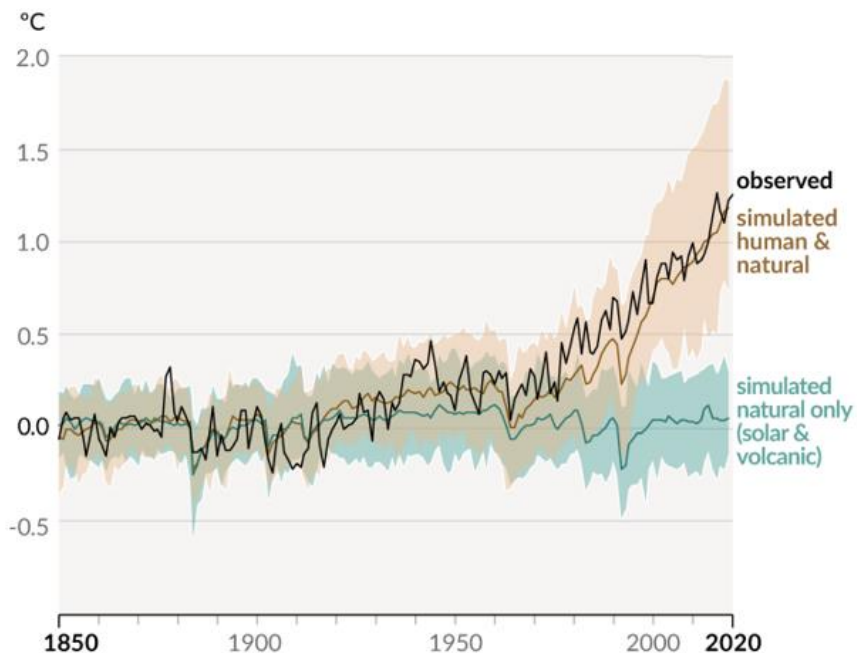


Figure 1.1 | (Black line) Changes in global surface temperature relative to the 1850–1900 average. The temperature output of climate model simulations involving both human activities and natural causes are shown in brown, while those featuring only natural causes are in green. The brown and green lines represent the average of multiple models, while the shaded bands indicate the 95% confidence range. Reproduced from ref. <sup>1</sup> with permission, copyright IPCC.

Almost three-quarters of our greenhouse gas emissions come from energy use in buildings, industry, and transport.<sup>2</sup> Therefore, decarbonising our energy generation system is essential to reduce our emissions. This can be achieved by increasing energy generation from renewable sources, such as hydropower, solar, wind, geothermal, tidal, and biomass. On the flip side, the amount of coal, oil, and gas burned to produce energy must be reduced. Although renewable energy generation has increased sharply in the past two decades, its contribution to the global energy consumption mix is still limited at about 12%.<sup>3</sup> On the other hand, fossil fuels dominate with 84% while nuclear energy contributes the remaining 4%.<sup>3</sup> Furthermore, although the *share* of energy sourced from fossil fuels is slowly declining, in absolute terms the *amount* of energy produced from them is still rapidly increasing despite the recent outpouring of global attention on fossil fuel-related emissions (Figure 1.2).<sup>3</sup> This happens because the growth in renewable and nuclear energy generation is slower than the rise in energy consumption. For any meaningful decarbonisation to occur, renewables must not only fulfil our new energy demand every year, but also replace fossil fuels in the global energy mix.

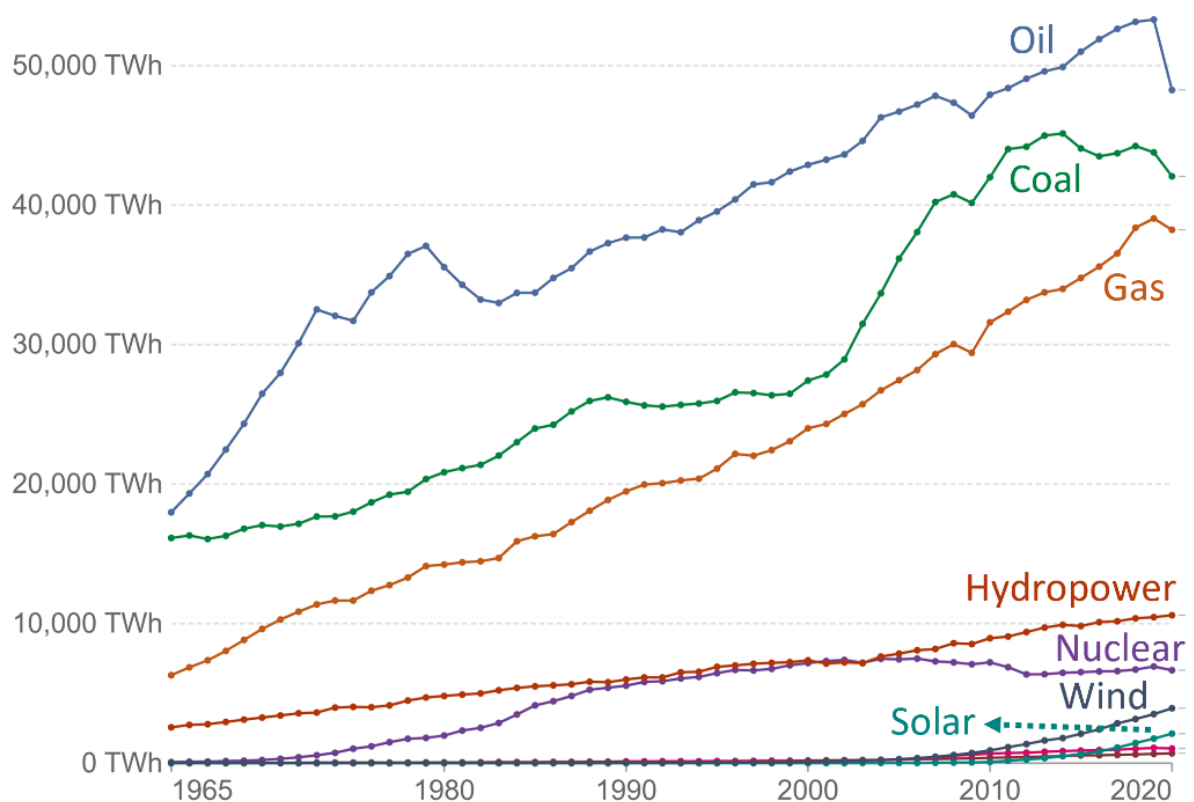


Figure 1.2 | Sources of global primary energy consumption. Reproduced from ref. <sup>3</sup> under the Creative Commons CC-BY 4.0 License.

In recent years, solar photovoltaics (PV) has been posting the fastest annual growth among all renewable technologies, albeit starting from a low base (Figure 1.3a).<sup>4</sup> This rapid advance has been enabled by a sharp decline in the cost of solar energy. From 2010 to 2020, the globally weighted average of total installation costs per generation capacity for utility-scale PV systems fell by 81%, from 4,731 to 883 US\$/kW (adjusted for inflation to 2020 US\$).<sup>5</sup> In the same period, the global levelised cost of electricity (LCOE, average net present cost of electricity generated over the lifetime of a power plant) of solar PV declined by 85%, from 38.1 to 5.7 US¢/kWh (adjusted for inflation to 2020 US\$).<sup>5</sup> This reduction has been driven largely by the declining cost of the inverter and the solar module itself, especially crystalline Si ones which account for ~95% of installed PV systems.<sup>5,6</sup> Non-module costs, such as other hardware, installation, permit application, system design, financing, margin, and others (commonly grouped together as balance of systems, BOS) have been decreasing at a slower rate.<sup>5</sup> Consequently, the share of BOS in the total installation costs has been rising. Coupled with the slowing down of (Si) module cost reductions in the last few years (Figure 1.3b), this means the total installation costs and LCOE of PV systems are likely to plateau soon, unless a new PV technology with a higher efficiency or cheaper production costs enters the market.

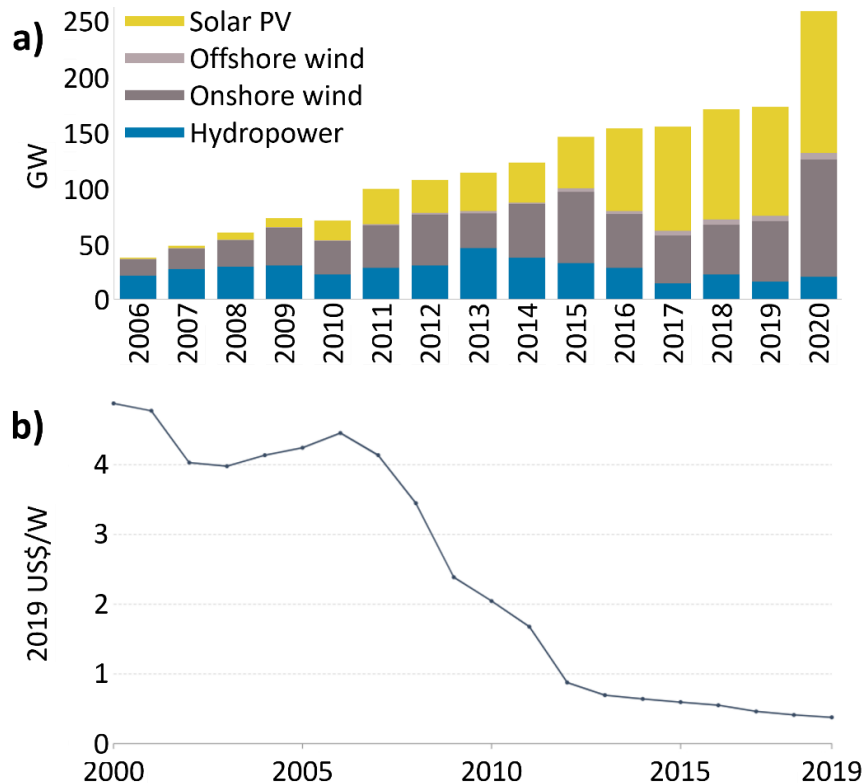


Figure 1.3 | (a) Annual net additions to the global installed capacity for solar PV, wind, and hydro power plants. (b) Global average of Si solar module prices. Panel (a) is constructed using data available in ref. <sup>4</sup>, copyright International Renewable Energy Agency. Panel (b) is reproduced from ref. <sup>3</sup> under the Creative Commons CC-BY 4.0 License.

A candidate with great potential to play this role has recently emerged in the form of perovskite solar cells (PSCs). Halide perovskites exhibit an array of material properties which make them strong contenders for a PV material, including a direct band gap with a tunable width, strong light absorption, low exciton binding energy, long carrier lifetime and diffusion length, and tolerance to point defects.<sup>7,8</sup> Since PSCs were invented in 2009, the record certified power conversion efficiency (PCE) value for research cells has soared from 3.8% to 25.5%, an unprecedented rate of increase among PV technologies.<sup>9</sup> This latest record PCE is already higher than that of multicrystalline Si and is only 0.6% lower than the record for monocrystalline Si, the two materials currently dominating the PV market.<sup>6,9</sup> Furthermore, PSCs have also passed the PCE of all other thin film and emerging PV technologies, such as organic solar cells, CuInGaS/Se (CIGS), CdTe, CuZnSnS/Se (CZTS), amorphous Si, dye-sensitised solar cells (DSSCs), and quantum dot solar cells.<sup>9</sup> Therefore, there is no doubt that the efficiency potential of PSCs is high enough to warrant a transition from laboratories to manufacturing lines.

Beyond efficiency, a PV technology must also demonstrate low production costs to be successfully commercialised. In this regard, PSC's great advantage is that it can be solution processed in a relatively simple manner and at low temperatures, as opposed to the highly controlled and energy-intensive production line used for Si solar panels.<sup>10</sup> Perovskite films can also be deposited on flexible substrates, opening the possibility of high-throughput roll-to-roll production of printed PSCs.<sup>11,12</sup> Recent technoeconomic analyses have projected LCOEs of 2.2–7.9 US¢/kWh for industrial-scale production of perovskite PV devices, on par with the current LCOE of utility-scale PV installations (5.7 US¢/kWh) and less than the LCOE of coal, oil, and gas-based power plants (5.5–14.8 US¢/kWh).<sup>5,13–17</sup> The comparability of these numbers, despite the much greater economies of scale of Si PV and fossil fuel plants, is a testament to the potential of low-cost perovskite PV technology. Moreover, flexible PSCs can enter highly lucrative niche markets which are unsuited to the rigid, brittle, and heavy Si panels, such as building-integrated PV, vehicle-integrated PV, and Internet of Things devices.<sup>10</sup>

This optimistic outlook is reliant on two major assumptions. The first is that PSCs will be sufficiently stable to reach at least a 15-year lifetime, defined as the period over which the PCE declined to 80% of its original value.<sup>18</sup> Although the lifetimes of most research devices published in the literature are still short of this benchmark, there are encouraging signs that PSCs have the potential to be as stable as Si panels (25–30 years), provided they are carefully designed. For example, a 2020 report which extrapolates published stability data has identified three device designs which could achieve a 20-year lifetime.<sup>18–21</sup> Shortly afterwards, two studies reported PSCs which successfully met the requirements of IEC 61215, a series of industry-standard accelerated degradation tests designed to assess the fitness of PV modules for long-term operation in an open-air climate.<sup>22,23</sup> Encouragingly, these works used different device architectures and fabrication methods, indicating that there are multiple paths towards highly stable PSCs. Plenty of research is being done to increase the operational stability of PSCs, and further improvements in this important facet of device performance can be expected in the near future.

The second assumption is that the high PCEs obtained in small research cells can be replicated in modules of commercially relevant sizes. This feat has proven rather challenging up until 2019, as the loss in PCE with device area enlargement has been steeper in PSCs compared to other PV technologies (Figure 1.4). However, great progress has been made since then, particularly in industrial laboratories. In early 2020, Panasonic announced a 17.9% efficient perovskite solar module (PSM) with an impressively large area of 804 cm<sup>2</sup>.<sup>24,25</sup> Less than a year later, UtmoLight exhibited a 64 cm<sup>2</sup> PSM with a PCE of 20.1%.<sup>26</sup> While these are remarkable achievements, there is still room for further improvements as even UtmoLight's PCE is still less than 80% of the record research cell PCE.

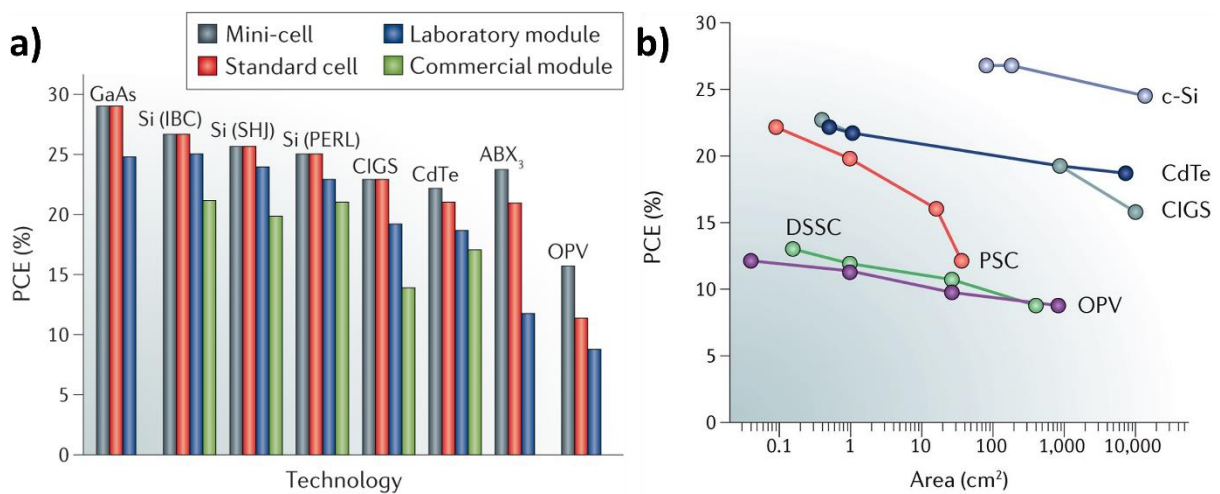


Figure 1.4 | (a) Record PCEs of various PV technologies classified according to their device area: <1 cm<sup>2</sup> (mini-cell), 1–800 cm<sup>2</sup> (standard cell), and >800 cm<sup>2</sup> (module). (b) PCE decline upon device upscaling for various PV technologies. IBC: interdigitated back contact, SHJ: Si heterojunction, PERL: passivated emitter and rear locally diffused, ABX<sub>3</sub>: perovskite, OPV: organic PV, c-Si: crystalline Si. Panel (a) is reproduced with permission from ref. <sup>27</sup>, copyright 2019 Springer Nature. Panel (b) is reproduced with permission from ref. <sup>28</sup>, copyright 2018 Springer Nature.

The key to unlock high PCEs in modules is to deposit the device layers as uniformly as possible over the large area.<sup>28,29</sup> Like other thin film PV technologies, PSMs are divided into serially connected cells to minimise power losses due to lateral current flow in the transparent contact layer. Therefore, the whole module's output current is limited by that of the weakest performing cell. Homogeneous deposition of all device layers is thus necessary to obtain a small spread in the performance of individual cells. Another important factor is the monolithic interconnection (MI) area between adjacent cells. An MI area consists of three lines (P1, P2, P3) scribed either with a knife or a pulsed laser beam, whose purpose is to partition the module into cells and serially connect those cells (Figure 1.5). MI areas do not contribute to energy conversion, but they cannot be made too narrow in order to avoid high series

resistance in the interconnection. MIs are relatively understudied as they are absent in PSCs, where a great majority of perovskite PV research has been done so far. Further research into MIs in PSMs are necessary not only to improve its design and thus the module's PCE, but also because MIs are potential starting points for module degradation.<sup>30</sup>

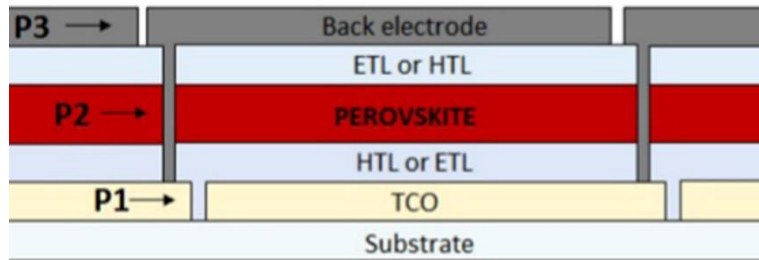


Figure 1.5 | Schematic of a PSM featuring two MI areas. The P1, P2, and P3 lines are marked. ETL: electron transport layer, HTL: hole transport layer, TCO: transparent conductive oxide. Reproduced from ref.<sup>30</sup> under the Creative Commons CC-BY 4.0 License.

The homogeneity of layer deposition and the electronic quality of the MIs are usually assessed with macroscopic techniques, such as optical microscopy, lock-in thermography, luminescence imaging, and laser-beam induced current.<sup>28</sup> While these techniques can be used to judge the overall suitability of a particular fabrication method, nanoscale characterisation is often necessary to hunt the root cause of any observed imperfections. Moreover, nanoscale characterisation may also reveal features or heterogeneities which are averaged out in macroscale observations.

In this thesis, nanoscale characterisation of PSMs is performed using a series of electron microscopy (EM) techniques, supported by other complementary methods and advanced data analysis algorithms. The aim is to obtain a deeper understanding of PSMs and their fabrication process, particularly in the context of achieving homogeneous layer deposition and optimised MI scribing as prerequisites of highly efficient PSMs. Cross-sectional scanning transmission electron microscopy (STEM) was extensively used to directly visualise the nanoscale morphology and local chemical composition of PSM stacks. Focused ion beam (FIB) milling was employed as a site-specific STEM sample preparation method, allowing a precise selection of regions of interest in a PSM from which electron-transparent specimens can be extracted for STEM characterisation.

Chapter 2 provides a review of organic-inorganic hybrid halide perovskites (OIHPs), PSCs, and PSMs. The discussion starts with the fundamental properties of OIHPs which make them such good PV materials and the basic working principles of PSCs. This is followed by an overview of the PSM

fabrication process, with special emphasis on the MI area and its scribing procedure. This chapter is ended with a brief survey of commonly used characterisation techniques in perovskite PV research.

Chapter 3 continues the literature review with a background of the EM instruments and EM-related techniques used in this thesis. It also contains a description of electron-matter interaction and the consequent electron beam-induced specimen damage, and an introduction to the multivariate statistical analysis (MVA) algorithms applied for data denoising.

In Chapter 4, the techniques and algorithms introduced in Chapter 3 are optimised and validated in the context of perovskite PV device characterisation. The suitability of FIB milling as a sample preparation method is confirmed and a STEM electron dose which best balances specimen damage and data quality for energy-dispersive X-ray spectroscopy (EDX) compositional mapping is found. Then, two MVA algorithms are carefully refined and compared to determine the best one to use in the following chapters.

Chapter 5 discusses the application of STEM imaging and STEM-EDX compositional mapping to study solution engineering in PSM fabrication via blade coating. Briefly, MAI and H<sub>2</sub>O additives introduced to the perovskite precursor solutions were found to result in spatially homogeneous perovskite films and high-efficiency modules. The nanoscale images and elemental maps of the devices obtained via STEM were key to revealing the roles played by MAI and H<sub>2</sub>O in producing the observed results.

Chapter 6 moves the region of interest from the module's constituent cells to the boundaries of the MI area. This chapter focuses on how the laser pulses used to scribe P3 lines affect the perovskite layer in the vicinity of those lines. Compositional mapping reveals perovskite decomposition close to P3 lines due to thermal energy transferred from picosecond laser pulses. Finite element method-based simulation found that secondary phases with higher thermal conductivity compared to the perovskite, such as PbI<sub>2</sub>, act as a preferred heat flow channel. Consequently, the precise effect of this energy transfer on the perovskite (de)composition was found to be dependent on the perovskite layer's initial homogeneity.

Chapter 7 shifts the investigated area from P3 lines to P1 lines. P1 lines are unique in PSMs because they are the only locations where the module's substrate is in contact with the active layers. STEM-EDX reveals Na diffusion into the cell areas in PSMs constructed on soda lime glass (SLG) substrates. Furthermore, the diffused Na was found to bond with Br from the perovskite, forming stable NaBr which passivates perovskite defects and improves the local luminescence close to P1 lines. In combination with other characterisation techniques, it is shown that the extent of Na diffusion reaches up to hundreds of microns away from the P1 line edge during module fabrication alone, with the potential for even more extensive diffusion during device operation.

Finally, Chapter 8 presents an overall summary of the results discussed in this thesis and lays out remaining challenges and possibilities for future work.

# Chapter 2

## Perovskite and Perovskite Photovoltaics

This chapter reviews the literature about the materials and devices discussed in this thesis, namely OIHPs, PSCs, and PSMs. It begins with an introduction to the OIHP family of materials before moving on to their suitability as an optoelectronic material. Then, the focus shifts to the working principles of PSCs and upscaling efforts to transform cells into large modules. Finally, this review is ended with an overview of popular spatially resolved characterisation techniques used in perovskite PV research.

### 2.1. Organic-Inorganic Hybrid Halide Perovskite

The word ‘perovskite’ originally refers specifically to the mineral  $\text{CaTiO}_3$ , thus named by its discoverer Gustavus Rose in 1839 to honour the mineralogist Lev Perovski.<sup>31</sup> From 1926, ‘perovskite’ refers more generally to all materials which adopt the crystal structure of  $\text{CaTiO}_3$ .<sup>32</sup> Each member of the perovskite family has a variation of the  $\text{ABX}_3$  general chemical formula. By combining various A-cations, B-cations, and X-anions, many perovskite compounds with a wide range of properties and applications can be synthesised. The aristotype cubic crystal structure ( $Pm\bar{3}m$ ) consists of corner-sharing  $\text{BX}_6$  octahedra with the A-cation located at the centre of the cube formed by every eight neighbouring octahedra (Figure 2.1a).<sup>33</sup> Non-ideal matching of ionic radii distorts and tilts these octahedra, resulting in orthorhombic, tetragonal, and hexagonal hettotypes. Many non- $\text{ABX}_3$  structures can also be derived. These are generally recognised as parts of the perovskite family, although they are often labelled with qualifiers such as anti-perovskites, vacant, (dis)ordered, vacancy-ordered, and low-dimensional perovskites (Figure 2.1b).<sup>34–36</sup> In this thesis, all discussions pertain only to the  $\text{ABX}_3$  perovskite.

Early investigations of perovskites were focused almost exclusively on oxide perovskites due to their natural abundance in the Earth’s mantle.<sup>37</sup> The first study on halide perovskites – then known as ‘double halides’ – was published by Félix-Polydore Boullay in 1827.<sup>38</sup> Remarkably, this article already explored double halides containing an organic ( $\text{NH}_4^+$ ) and an inorganic ( $\text{Hg}^+$ ) cation and those comprising more than one halide ( $\text{Cl}^-$  and  $\text{I}^-$ ). These concepts would, almost two centuries later, form the basis of perovskite PV. In the 1890s, the groups of Ira Remsen and H.L. Wells expanded on Boullay’s findings by synthesising many variations of double halides.<sup>39,40</sup> In 1957–8, C.K. Møller proved that  $\text{CsPbCl}_3$  and  $\text{CsPbBr}_3$  crystallise in the perovskite structure.<sup>41,42</sup> Twenty years later, Dieter Weber synthesised a set of OIHPs with methylammonium occupying the A-cation site.<sup>43,44</sup> The semiconducting nature of OIHPs was then explored by David Mitzi’s group in the 1990s, revealing its potential for PV applications.<sup>45–48</sup>

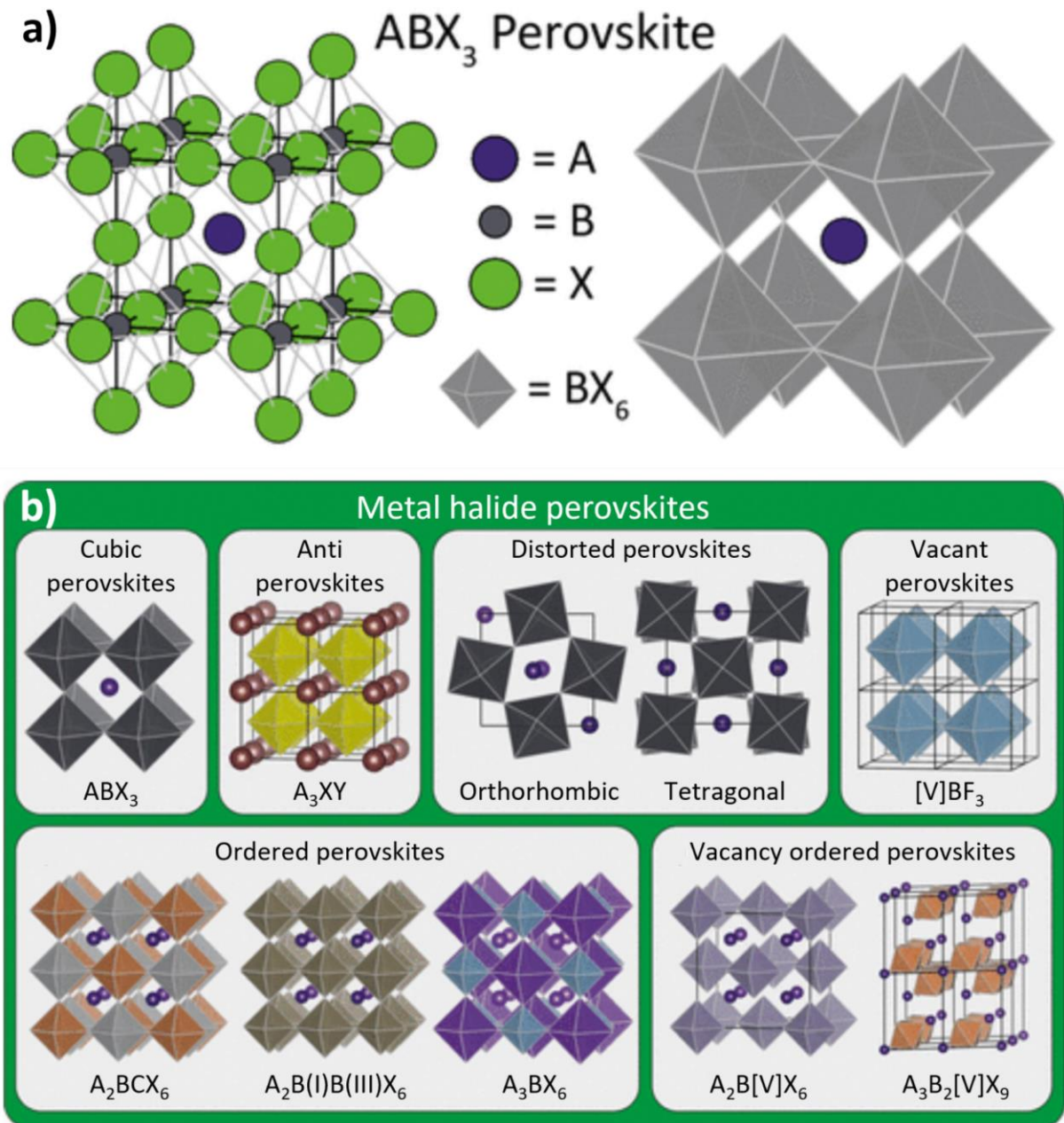


Figure 2.1 | (a) The cubic crystal structure of  $\text{ABX}_3$  perovskite. (b) Various perovskite structures derived from the  $\text{ABX}_3$  aristotype. Adapted from ref.<sup>34</sup> under the Creative Commons CC-BY 4.0 License.

OIHGs were first used as a PV absorber in 2009 by Kojima et al. in a dye-sensitised architecture.<sup>49</sup> The resulting PSC has a PCE of 3.8% but was extremely unstable due to the corrosive liquid electrolyte used. The next breakthrough happened in 2012 when Kim et al. and Lee et al. replaced the liquid electrolyte with a solid-state hole conductor, resulting in better stability and PCEs of 9.7% and 10.9%, respectively.<sup>50,51</sup> Since then, continuous research conducted by many groups has produced significant improvements in both PCE and stability. The certified record PCE currently stands at 25.5%, thanks to careful selection and optimisation of materials, device architecture, and fabrication procedure.<sup>7,52</sup> The

large amount of effort invested into perovskite PV research resulted not only in high PCEs, but also in much greater understanding of OIHP's fundamental properties which made them such a promising PV material. These properties are discussed in the following sections. From this point onwards, all uses of the term 'perovskite' refer specifically to OIHPs unless mentioned otherwise.

### 2.1.1. Crystal Structure and Grain Morphology

Perovskites crystallise in either cubic, tetragonal, orthorhombic, or hexagonal lattices. Transitions between these phases occur when perovskites are exposed to changing temperature or pressure, with different stability regimes for each specific perovskite composition. Generally, the more symmetric structure is more desirable for PV, although some less symmetric phases are also photoactive. Given a specific perovskite composition, the stable phase at room temperature and pressure can be predicted using two parameters, namely the Goldschmidt's tolerance factor  $t$  and the octahedral factor  $\mu$ .<sup>32,53</sup> They are defined as follows, where  $r_A$ ,  $r_B$ , and  $r_X$  are the radii of the ions composing  $ABX_3$ :

$$t = \frac{r_A + r_X}{\sqrt{2}(r_B + r_X)} \quad (\text{Equation 2.1})$$

$$\mu = r_B / r_X \quad (\text{Equation 2.2})$$

The value of  $t$  should be between 0.8–1 and  $\mu$  needs to be above 0.442 to achieve a stable photoactive phase.<sup>53,54</sup> Limiting ourselves to  $Pb^{2+}$  and  $Sn^{2+}$  in the B-cation site and  $Cl^-$ ,  $Br^-$ , and  $I^-$  in the X-anion site, the choices of A-cation are methylammonium ( $MA^+$ ,  $CH_3NH_3^+$ ), formamidinium ( $FA^+$ ,  $CH(NH_2)_2^+$ ), and caesium ( $Cs^+$ ) (Figure 2.2a). While photoactive perovskites can be formed with one A-cation and one X-anion (e.g.  $MAPbI_3$ ), better performance and structural robustness can be achieved by combining multiple ions.<sup>55,56</sup> Furthermore, this approach also allows using small amounts of other cations which would otherwise be too large or too small to further boost performance, such as guanidinium ( $GA^+$ ,  $C(NH_2)_3^+$ ) or rubidium ( $Rb^+$ ).<sup>57,58</sup>

In PSCs, the perovskite layer is deposited by solution processing or thermal evaporation.<sup>59</sup> When optimised, both methods can result in polycrystalline films with well-defined, highly crystalline grains with narrow size distributions. Thermal evaporation produces grains of about 100 nm or less in size, while solution processing can result in a wide range of grain sizes from hundreds of nanometres to several micrometres (Figure 2.2b).<sup>59</sup> Smooth, pinhole-free films with generally uniform composition can be reproducibly made with optimised deposition routines where a large number of parameters are

precisely tuned.<sup>60</sup> These beneficial morphological characteristics are essential to obtain high PCEs. Smooth and pinhole-free films were found to minimise shunt losses, while large grains reduce the concentration of grain boundaries which have been observed to contribute to current-voltage hysteresis and accelerate device degradation.<sup>61,62</sup>

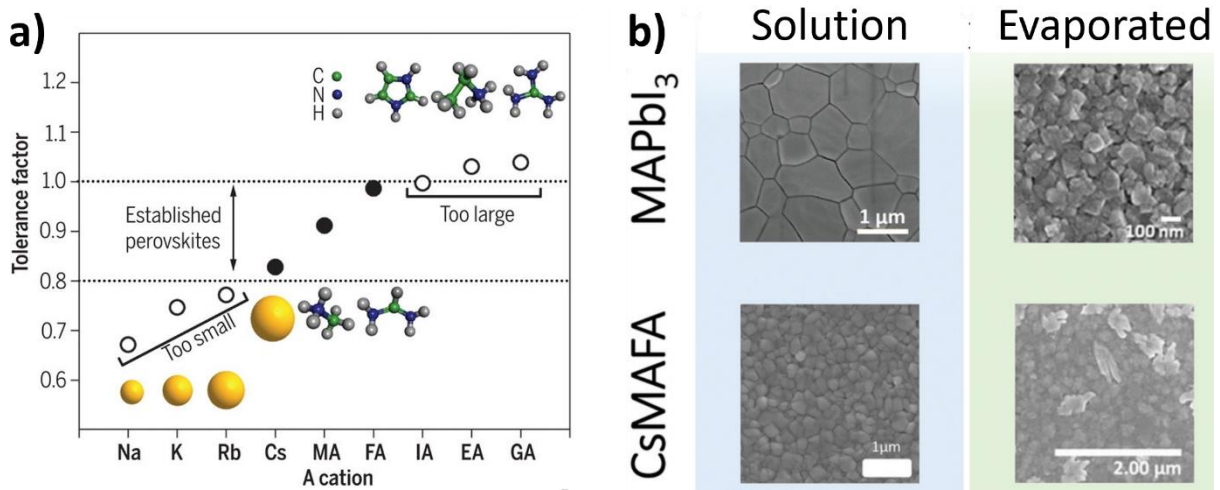


Figure 2.2 | Goldschmidt's tolerance factor for various APbI<sub>3</sub> perovskites. Na, K, and Rb are too small to be A-cations while imidazolium (IA), ethylammonium (EA), and guanidinium (GA) are too large. Cs, methylammonium (MA), and formamidinium (FA) are of the correct size to produce photoactive perovskite. b) Top-view scanning electron micrographs of perovskite films deposited via solution processing and thermal evaporation. Panel (a) is reproduced with permission from ref. <sup>54</sup>, copyright 2017 American Association for the Advancement of Science. Panel (b) is adapted from ref. <sup>59</sup> under the Creative Commons CC-BY 4.0 License.

## 2.1.2. Band Structure and Carrier Photogeneration

The first step in photogeneration of charge carriers is photon absorption. To maximise light absorption while minimising material usage, two optical properties are desirable. The first is a direct band gap at an appropriate energy ( $E_g$ , Figure 2.3a). The range of suitable  $E_g$  can be determined using the detailed balance model developed by Shockley and Queisser.<sup>63</sup> This model approximates the maximum attainable PCE of a solar cell as a function of its absorber's  $E_g$  under a series of assumptions: 1) each incoming photon with an energy  $\geq E_g$  generates one electron-hole pair (EHP) which is collectable at short circuit; 2) excited EHPs lose all energy above  $E_g$  as heat to reach thermal equilibrium with the cell; 3) all charge carrier recombination is radiative (emitting photons); and 4) each contact to the absorber is perfectly carrier-selective and has no Ohmic losses.<sup>63,64</sup> Under these conditions, when an absorber is exposed to electromagnetic radiation from a blackbody with the sun's temperature, a 30%

PCE is achievable with  $E_g = 0.91\text{--}1.65$  eV, while a maximum PCE of 33.7% is obtained at  $E_g = 1.34$  eV.<sup>63,65</sup> Although the assumptions described above are never fully attained in practical solar cells, the detailed balance model provides a starting point to evaluate the potential PCE of light absorbers. The direct  $E_g$  of many perovskite compositions can be tuned to suit the ideal range calculated by Shockley and Queisser (Section 2.1.3), fulfilling the first criterion for a good PV absorber. The second is a steep absorption onset with a high absorption coefficient at photon energies  $\geq E_g$ . This requirement is easily fulfilled by most halide perovskites thanks to their high density of states and low density of intra-gap tail states (Figure 2.3b).<sup>66,67</sup> These advantageous properties minimise the required absorber thickness and reduce the need for light trapping schemes which may complicate device fabrication. For example, the current PCE record holder (26.7%) for Si solar cells uses a 165  $\mu\text{m}$ -thick wafer with front side texturing and two dielectric anti-reflection layers to maximise light absorption.<sup>68</sup> In contrast, the PCE record holder (25.5%) for PSCs uses a 750 nm-thick perovskite film with no anti-reflection coatings.<sup>69</sup>

Energy from the absorbed photons is converted to excite bound excitons or free carriers. Because the exciton binding energy in perovskites is only a few meV at room temperature, excitons immediately dissociate into free electrons and holes.<sup>70,71</sup> To produce electrical power, the carriers must be separated and extracted before they recombine non-radiatively (producing phonons instead of photons). In terms of absorber material properties, carrier collection is maximised by low effective mass, high mobility, long lifetime, and long diffusion length. Low effective electron and hole masses ( $\sim 0.1\text{--}0.2 m_e$ ) have been found for perovskites.<sup>72</sup> These low masses enable relatively high carrier mobilities, although measurements with different techniques and perovskite compositions produce results that vary over several orders of magnitude.<sup>72,73</sup> Carrier lifetimes in excess of 6  $\mu\text{s}$  and 260  $\mu\text{s}$  and diffusion lengths of  $\sim 6 \mu\text{m}$  and  $> 175 \mu\text{m}$  have been observed in perovskite thin films and single crystals, respectively.<sup>74\text{--}76</sup> These excellent carrier transport parameters may be partially due to photon recycling (reabsorption of photons emitted through radiative recombination of charge carriers), although its overall significance is still being debated.<sup>77\text{--}80</sup>

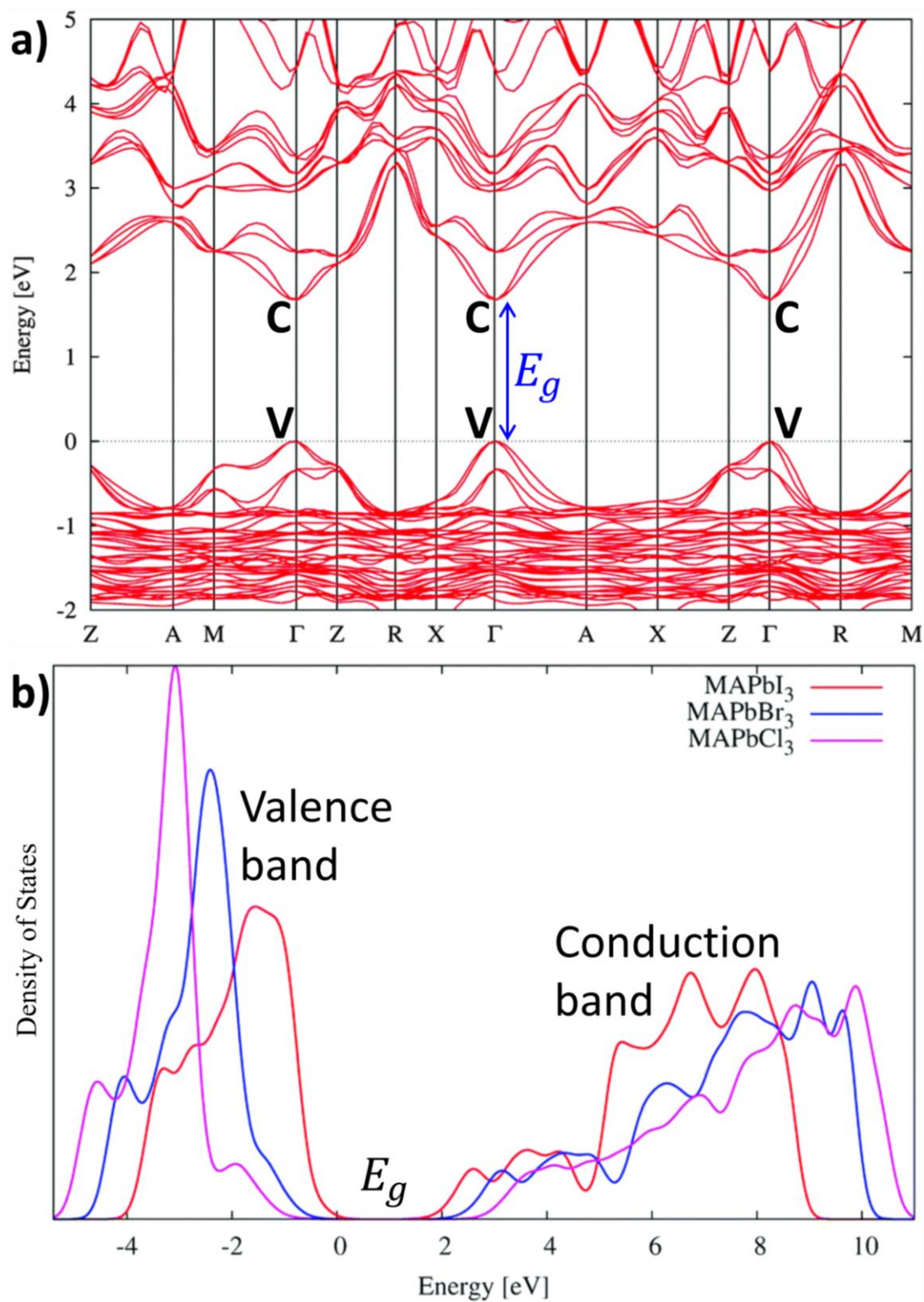


Figure 2.3 | (a) Calculated band structure of MAPbI<sub>3</sub>. C and V mark the conduction band minima and valence band maxima, respectively. Blue arrow marks the direct band gap of MAPbI<sub>3</sub>. (b) Calculated density of states for MAPbI<sub>3</sub>, MAPbBr<sub>3</sub>, and MAPbCl<sub>3</sub>. Band structure and density of states are calculated via density functional theory incorporating the GW method and spin-orbit coupling. Adapted with permission from ref. <sup>81</sup>, copyright 2016 Royal Society of Chemistry.

### 2.1.3. Band Gap Tunability

One of perovskites' strengths as a light absorber is its tunability through compositional engineering. Each of the three ion sites can be occupied by a mix of different cations or halides, providing a powerful tool to control the resulting perovskite's  $E_g$ .<sup>82</sup> This is a particularly useful feature as it allows precise tailoring of perovskite  $E_g$  for use in single-junction cells (one absorber layer) or as the top or bottom cell in tandem cells (>1 absorber layer). Because perovskites' band edges are composed of the B-cation and X-anion's orbitals, changing the ions at those sites affects  $E_g$  significantly (Figure 2.4a,b).<sup>66</sup> In contrast, the A-cation influences  $E_g$  slightly through spin-orbit coupling and inorganic octahedra tilting (Figure 2.4b).<sup>83</sup> Starting from basic  $\text{MAPbI}_3$  with an  $E_g$  of 1.55–1.60 eV,  $E_g$  can be lowered to 1.20 eV by replacing half of the  $\text{Pb}^{2+}$  cations with  $\text{Sn}^{2+}$ .<sup>84</sup> Substituting  $\text{MA}^+$  with  $\text{FA}^+$  or  $\text{Cs}^+$  changes  $E_g$  to 1.52 and 1.73 eV, respectively.<sup>85,86</sup> Switching I<sup>-</sup> with Br<sup>-</sup> or Cl<sup>-</sup> widens  $E_g$  to 2.3 and 2.9 eV, respectively.<sup>85,87</sup> While the pure-Br and pure-Cl band gaps are too wide even for the top half of tandem cells, they are promising materials for green and blue light-emitting diodes (LEDs). The ability to simultaneously alloy more than one ion site provides a wide compositional space to optimise both efficiency and stability, although efforts to alloy I<sup>-</sup> and Cl<sup>-</sup> have not been successful.<sup>88,89</sup> So far,  $\text{Cs}_{0.05}\text{FA}_{0.78}\text{MA}_{0.17}\text{Pb}(\text{I}_{0.83}\text{Br}_{0.17})_3$  (so-called triple-cation, double halide [TCDH] perovskite, nominal  $E_g = 1.62$  eV), or slight variances thereof, is broadly recognised as the best-performing composition for single-junction cells.<sup>90,91</sup> For a perovskite top cell to be paired with a Si or CIGS bottom cell ( $E_g = 1.1$  eV), the ideal  $E_g$  of ~1.7 eV can be achieved by adding a little more Br<sup>-</sup> into the TCDH perovskite formula.<sup>84</sup> For all-perovskite tandem cells, the ideal  $E_g$  values are 1.2 and 1.8 eV for the bottom and top cells, respectively.<sup>84</sup>

Other than  $E_g$  tuning, compositional engineering can impart greater structural stability to the desired photoactive phase of certain parent compositions. The best example of this is  $\text{FAPbI}_3$ . In the early days of PSC research,  $\text{FAPbI}_3$  was identified as a more suitable candidate for single-junction cells than  $\text{MAPbI}_3$  due to its lower  $E_g$  and better thermal stability.<sup>92</sup> However, the photoactive  $\alpha$ -phase of  $\text{FAPbI}_3$  is unstable at room temperature and quickly transitions to the inactive  $\delta$ -phase instead.<sup>93</sup> This is because the  $t$  of  $\text{FAPbI}_3$  is very close to the top end of the allowed tolerance factor range. Alloying  $\text{FAPbI}_3$  with  $\text{MAPbBr}_3$  lowered  $t$  and stabilised the  $\alpha$ -phase.<sup>94</sup> Later, it was found that adding a small amount of  $\text{Cs}^+$  further improved the performance and stability, resulting in the TCDH perovskite formula.<sup>55</sup> In addition to phase stabilisation, compositional engineering has also been shown to impart lower current-voltage hysteresis and slower ion migration, contributing to device robustness.<sup>56,95</sup>

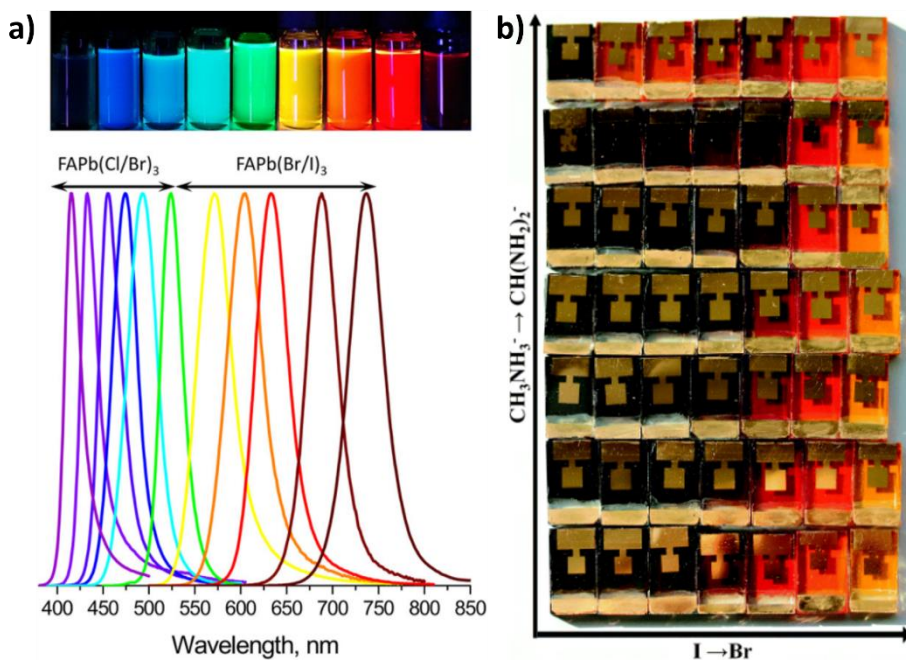


Figure 2.4 | Band gap tunability of perovskites. (a) Photograph of colloidal  $\text{FAPbX}_3$  solution in toluene under UV light and normalised photoluminescence emission from  $\text{FAPbX}_3$  nanocrystals. (b) Photograph of PSCs with gold contacts. From left to right, the composition changes from  $\text{APbI}_3$  to  $\text{APbBr}_3$  in equal steps. From bottom to top, the composition changes from  $\text{MAPbX}_3$  to  $\text{FAPbX}_3$  in equal steps. Note that changing the halide produces a much larger band gap variation than changing the A-cation. Panel (a) is reproduced with permission from ref. <sup>96</sup>, copyright 2017 American Chemical Society. Panel (b) is reproduced with permission from ref. <sup>85</sup>, copyright 2016 Royal Society of Chemistry.

## 2.1.4. Defect Tolerance

Due to entropy, it is impossible to grow a perfect crystal without any defects. Crystallographic defects range from point defects (vacancies, interstitials, antisites, impurities) and line defects (dislocations), to plane defects (stacking faults, grain boundaries, surfaces, interfaces).<sup>97</sup> Seven types of point defects are illustrated in panels b–h of Figure 2.5: vacancy (b, absence of an atom from a lattice site), interstitial (c, an atom residing between lattice sites), antisite (d, an atom occupying another atom's lattice site), Frenkel defect (e, a vacancy-interstitial pair), Schottky defect (f, a pair of anion and cation vacancies), substitutional impurity (g, a foreign atom occupying a lattice site), and interstitial impurity (h, a foreign atom residing between lattice sites). In semiconductors, these defects create electronic states in the band gap. Shallow states (a few  $kT$  away from a band edge, where  $k$  is the Boltzmann constant and  $T$  is temperature) act as trap sites for either an electron or a hole, while deep states become recombination centres which capture electrons and holes. Shallow states are relatively harmless as carriers can be

quickly detrapped before they can recombine, while defects which create deep electronic states must be suppressed to minimise non-radiative recombination.<sup>97</sup> Carrier lifetimes in established PV technologies such as Si and III-V solar cells are significantly reduced by even a low to moderate concentration of defects as these defects tend to create deep states (left side of Figure 2.6a).<sup>98,99</sup> This vulnerability necessitates extremely pure raw materials and very clean fabrication conditions. These requirements increase embodied energy and manufacturing cost, both of which are undesirable.

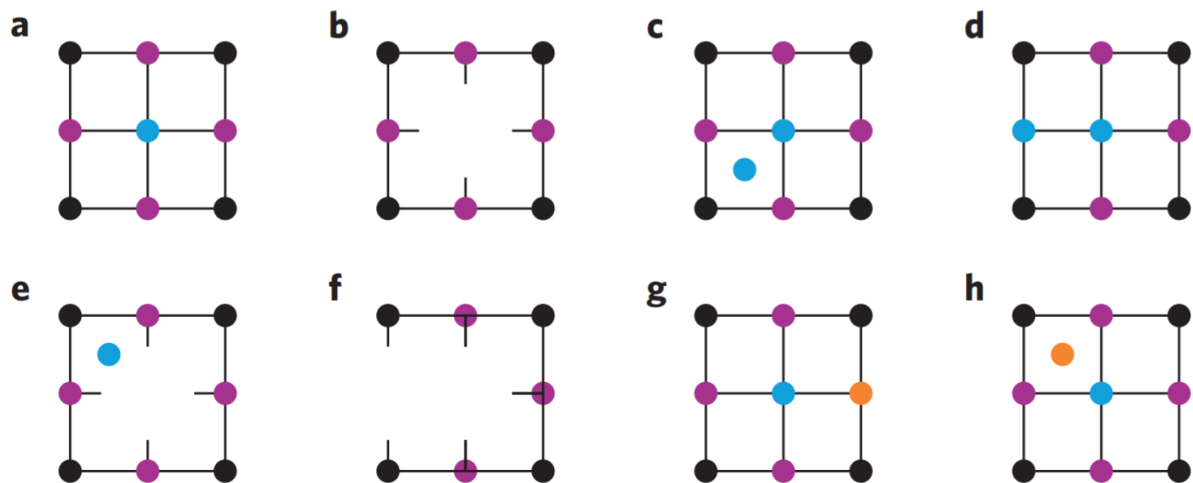


Figure 2.5 | Illustrations of (a) a perfect crystal lattice and various types of point defects: (b) vacancy, (c) interstitial, (d) antisite, (e) Frenkel pair, (f) Schottky pair, (g) substitutional impurity, and (h) interstitial impurity. Reproduced with permission from ref.<sup>97</sup>, copyright 2016 Springer Nature.

In contrast, PSCs have exhibited long carrier lifetimes and high PCEs even though their simple fabrication procedures invariably result in a high concentration of point defects ( $\sim 10^{14}$ – $10^{17} \text{ cm}^{-3}$ ).<sup>100–102</sup> This tolerance can be attributed to three electro-physical properties of perovskites.<sup>8</sup> The first is the nature of the band edges. Taking MAPbI<sub>3</sub> as an example, strong antibonding coupling between the I 5p and Pb 6s orbitals raises the valence band maximum (VBM), while negligible coupling between I 5p and Pb 6p orbitals forming the conduction band minimum (CBM) pins it close to the Pb 6p level (right side of Figure 2.6a).<sup>103</sup> Moreover, the CBM is further lowered by relativistic effects, such as spin-orbit coupling.<sup>104</sup> All these mean defect levels associated with the inorganic framework are more likely to be located close to either the VBM or CBM, or even inside the bands. The second property is the high formation energy of deep defect states, meaning defects such as I<sub>Pb</sub>, I<sub>MA</sub>, and Pb<sub>I</sub> antisites which form harmful deep states are less abundant (Figure 2.6b).<sup>105–108</sup> Finally, remaining charged defects with deep states have their influence screened by perovskites' high dielectric coefficient and strong anharmonicity.<sup>8,109</sup>

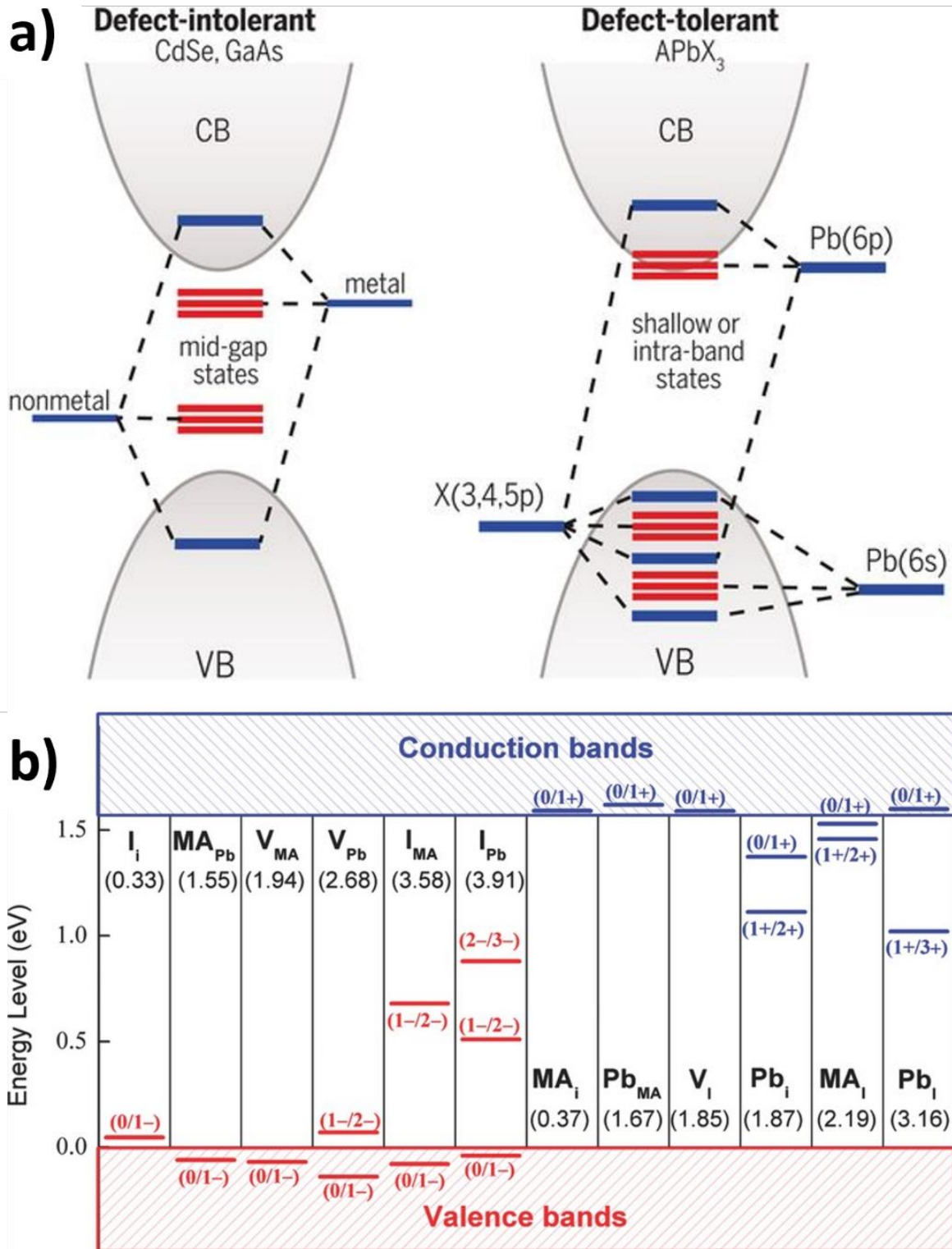


Figure 2.6 | (a) Energy band schematics illustrating the formation of deep defect states in a defect intolerant material (left) and shallow or intraband defect states in a defect tolerant APbX<sub>3</sub> (right). (b) Calculated energy levels of various point defects in MAPbI<sub>3</sub>. Numbers in parentheses indicate the formation energies of neutral defects in eV. Panel (a) is reproduced with permission from ref. <sup>103</sup>, copyright 2017 American Association for the Advancement of Science. Panel (b) is reproduced with permission from ref. <sup>108</sup>, copyright 2014 Wiley-VCH.

## 2.2. Perovskite Solar Cells

### 2.2.1. Working Principles

In PSCs, the perovskite layer acts as a light absorber material, where energy from photons is used to excite EHPs (Figure 2.7, red arrow). These charge carriers are separated by the gradients of electrical and chemical potentials in the absorber layer until they are transferred to either an electron or a hole transport layer (ETL, HTL). Then, they diffuse through the ETL/HTL to the electrodes to power an external load (Figure 2.7, black arrows). Because the carrier diffusion lengths in perovskites are generally comparable or greater than the absorber layer thickness (in the order of 1  $\mu\text{m}$  and 0.3–0.7  $\mu\text{m}$ , respectively)<sup>110</sup>, carrier separation is dominated by diffusion.<sup>111–113</sup> Efficient carrier separation via diffusion requires kinetic selectivity of carriers at the absorber interfaces, which can be established by suitable energy level matching between the absorber and the charge transport layers (CTLs).<sup>112</sup> Therefore, although the perovskite layer itself is capable of ambipolar charge transport, devices without dedicated CTLs have exhibited low PCEs.<sup>114,115</sup> Consequently, it is now standard practice to sandwich the perovskite layer between an ETL and an HTL.

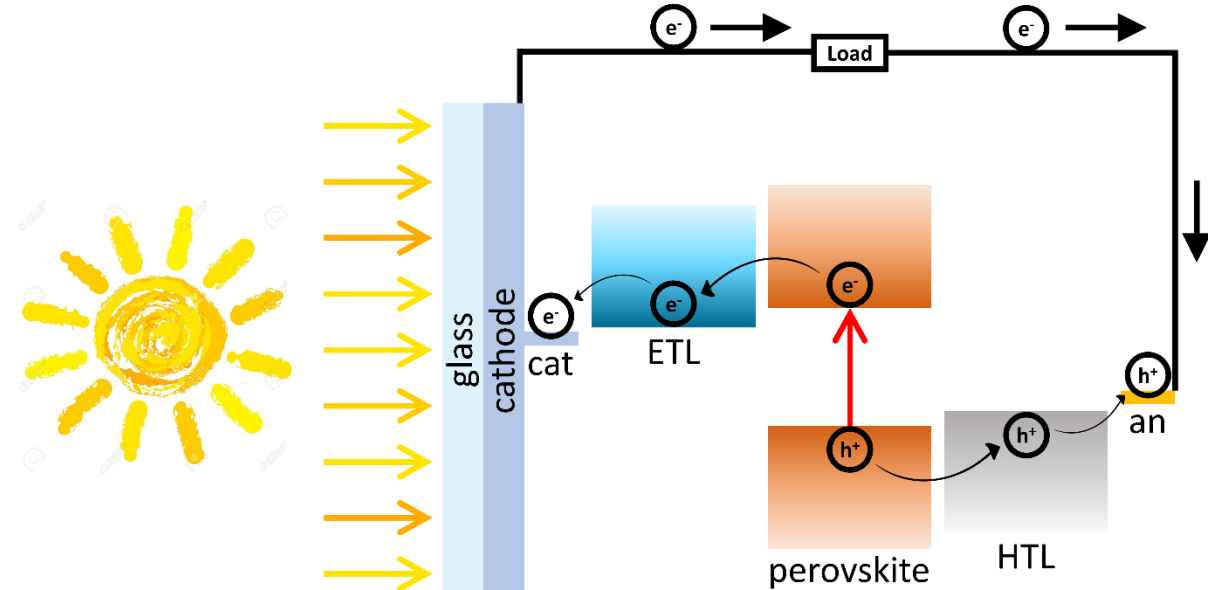


Figure 2.7 | Schematic of the working principle of a PSC. The red arrow marks photogeneration of EHPs ( $e^-$  and  $h^+$ ), curved arrows mark carrier transport inside the device, and straight black arrows signify electron flow in the external circuit. Cat and an stand for cathode and anode, respectively.

The power output of a solar cell is governed by three parameters: short circuit current density ( $J_{SC}$ ), open circuit voltage ( $V_{OC}$ ), and fill factor (FF) (Figure 2.8a). All three must be maximised to obtain as

much electrical power as possible.  $J_{SC}$  can be understood as a measure of the cell's ability to absorb incident photons and convert them to charge carriers (light management).<sup>65,116</sup> To maximise  $J_{SC}$ , the cell should have low light reflection losses, low parasitic absorption, and a long optical path length in the perovskite layer.  $V_{OC}$  is determined by how well the cell can transport and collect photogenerated carriers (carrier management).<sup>65,116</sup> To maximise  $V_{OC}$ , the cell should operate as close as possible to the radiative limit, where all charge recombination events are radiative. The key to approach this limit is to suppress non-radiative recombination by having a low density of deep defect states and well-passivated perovskite-CTL interfaces. Finally, FF is defined as the ratio between the product of  $J$  and  $V$  at the maximum power point (MPP) and the product of  $J_{SC}$  and  $V_{OC}$  (Equation 2.3, Figure 2.8d). FF shows how closely a cell behaves to an ideal diode.<sup>65</sup> FF is lowered by defect-mediated recombination, high series resistance (Ohmic resistance to current flow in the device, Figure 2.8b), and low shunt resistance (Ohmic resistance of alternative current paths which do not pass through the semiconductor junction, Figure 2.8c).

$$FF = \frac{J_{MPP} \times V_{MPP}}{J_{SC} \times V_{OC}} \quad (\text{Equation 2.3})$$

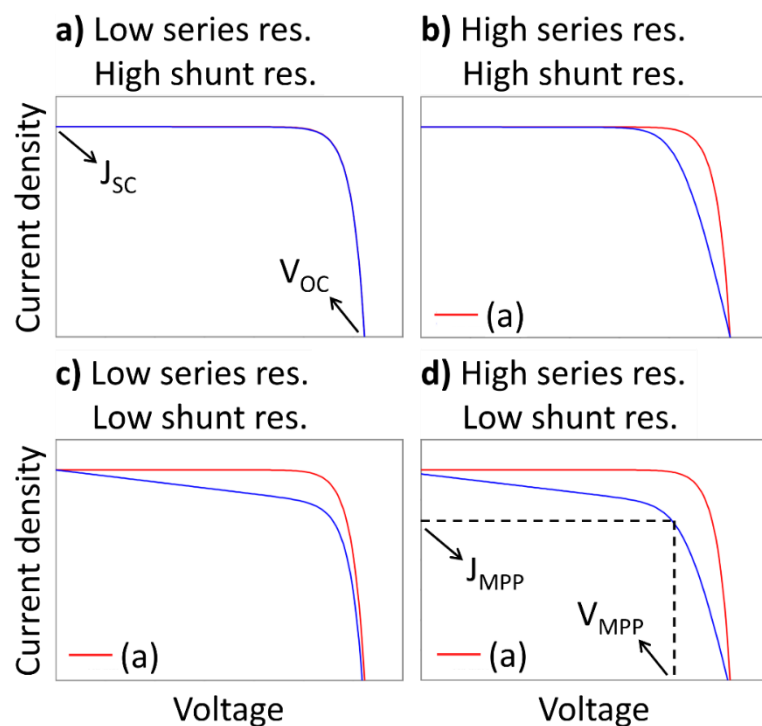


Figure 2.8 | Simulated J-V curves showing how series and shunt resistances affect the performance of a solar cell. The best-case curve shown in panel (a) is redrawn in red in panels (b-d) to ease comparison. The  $J_{SC}$ ,  $V_{OC}$ ,  $J_{MPP}$ , and  $V_{MPP}$  points are indicated.

## 2.2.2. Device Architecture

As described in Section 2.1, PSCs have their genesis in DSSCs. In their first two iterations, PSCs were made with a mesoporous network of  $\text{TiO}_2$  decorated with particles of perovskite dye a few nm in size.<sup>49,117</sup> This oxide-dye composite is in direct contact with a liquid electrolyte. Electrons excited in the perovskite dye flow into the oxide to be extracted, while a redox reaction in the liquid electrolyte replenishes those electrons. The liquid electrolyte was subsequently replaced with a solid HTL.<sup>50,51</sup> Although these pioneering publications showed extremely promising PCEs (up to 10.9%) considering the very early stage of research, it was soon realised that carrier diffusion lengths in perovskites can reach the order of micrometres.<sup>114</sup> This discovery triggered the use of a thick (0.3-0.7  $\mu\text{m}$ ) perovskite capping layer on top of the perovskite-infiltrated oxide layer, a device stack now known as the mesoporous architecture (Figure 2.9, leftmost).<sup>118-120</sup> Subsequently, perovskite's charge transport capability and the desire to further simplify device fabrication resulted in the planar architecture, where the perovskite layer is deposited on top of a planar CTL.<sup>51,121</sup>

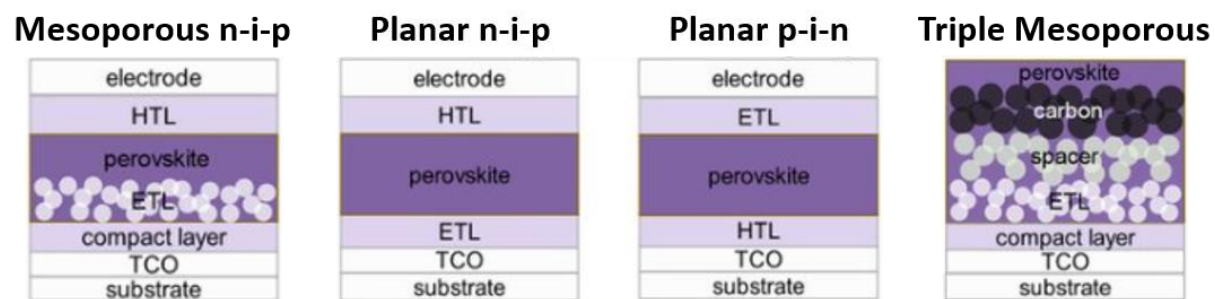


Figure 2.9 | The four most common PSC architectures. TCO: transparent conductive oxide. Adapted with permission from ref.<sup>122</sup>, copyright 2018 American Association for the Advancement of Science.

The planar design enabled another divergence in device stack. Without the mesoporous oxide ETL, the HTL can be deposited below the perovskite layer, resulting in a p-i-n (inverted) stack as opposed to an n-i-p (normal) stack (Figure 2.9, centre).<sup>123</sup> Subsequent research has revealed several interesting performance differences across these architectures. For instance, mesoporous architectures generally produce higher PCEs than planar devices, although the gap is narrowing.<sup>8,54,124</sup> Among the planar devices, the n-i-p stack exhibits higher PCEs but poorer stability than the p-i-n stack.<sup>125</sup> Beyond efficiency considerations, inverted devices are less prone to  $J-V$  hysteresis.<sup>126,127</sup> Furthermore, the mesoporous architecture is not suitable for use with flexible polymer substrates due to the high-temperature oxide sintering step.<sup>128</sup> Finally, the planar architecture, especially the inverted one, is most suitable for integration into Si/perovskite tandem cells.<sup>129</sup>

Almost all PSCs studied nowadays belong to one of the three architectures just described. However, one other cell design deserves mention. This is the HTL-free triple mesoporous stack where scaffold layers of TiO<sub>2</sub>, ZrO<sub>2</sub>, and C are printed on the substrate and then infiltrated with the perovskite (Figure 2.9, rightmost).<sup>130</sup> Photogenerated electrons flow to the TiO<sub>2</sub> while the holes go directly into the C electrode without the need of a HTL. Although the PCE obtained from this design (<15%) is not as high as the three primary architectures, its operational stability is by far the best.<sup>21,131</sup> This was demonstrated to great effect by Grancini et al., whose glass-sealed cells suffered no performance loss after 10,000 hours under UV-filtered 1 sun illumination at 55°C.<sup>21</sup>

### 2.2.3. Defect Passivation

Although the PV action of PSCs is rather tolerant to point defects as explained in Section 2.1.4, interfacial defects play a large part in *J-V* hysteresis and in preventing  $V_{OC}$  from reaching its radiative limit. This is due to the high rate of defect-assisted non-radiative surface recombination at the perovskite-CTL interfaces.<sup>132–134</sup> Furthermore, minimising overall defect density is also desirable to improve device stability as defect sites, including shallow point defects, have been identified as enablers of various degradation mechanisms.<sup>135,136</sup> For example, photoinduced halide segregation is assisted by a high concentration of halide vacancies and interstitials which facilitate hopping.<sup>137</sup> Such halide defects have lower formation energies at surfaces and interfaces as the associated lattice strain is more easily relieved.<sup>138</sup> Furthermore, the newly formed defects can also be stabilised by bonding with undercoordinated Pb at surfaces.<sup>105</sup> This explains why halide migration is accelerated at surfaces and interfaces, even though the migration activation energy there is only lower by ~0.1 eV compared to in the bulk.<sup>138,139</sup> Other than assisting ion migration, defect-rich grain boundaries provide trapped charges and ingress channels for fast and irreversible moisture- and oxygen-induced perovskite decomposition.<sup>140–142</sup> Thermal decomposition of perovskite is also influenced by defect density, with decomposition temperature increasing as defect density decreases.<sup>135,143</sup>

Considering the disadvantageous effects of defects, there is much to be gained from reducing their number and influence. In the past few years, numerous additives have been found to passivate both point and interfacial defects in PSCs. These additives range from metal ions, excess precursors, and ionic liquids, to Lewis acids, Lewis bases, and zwitterions (Figure 2.10).<sup>144</sup> Due to the ionic nature of the perovskite's inorganic sublattice, defects commonly exist as dangling bonds from undercoordinated B-cations or X-anions.<sup>144</sup> The former act as Lewis acids and can therefore be healed by Lewis bases containing electron-donating atoms or by excess halides. Conversely, the latter are Lewis bases which can be neutralised by electron-accepting additives or metal cations. Because undercoordinated cations and anions tend to be present together, zwitterions with oppositely charged ends have been used to effectively passivate both defects with one additive.<sup>145</sup> Overall, defect passivation has contributed much

to improve the performance and stability of PSCs. However, most of the explored additives so far were incorporated into small-area PSCs through spin coating. Far less work has been done on applying defect-passivating additives using scalable perovskite deposition methods, which is an important topic for future research.

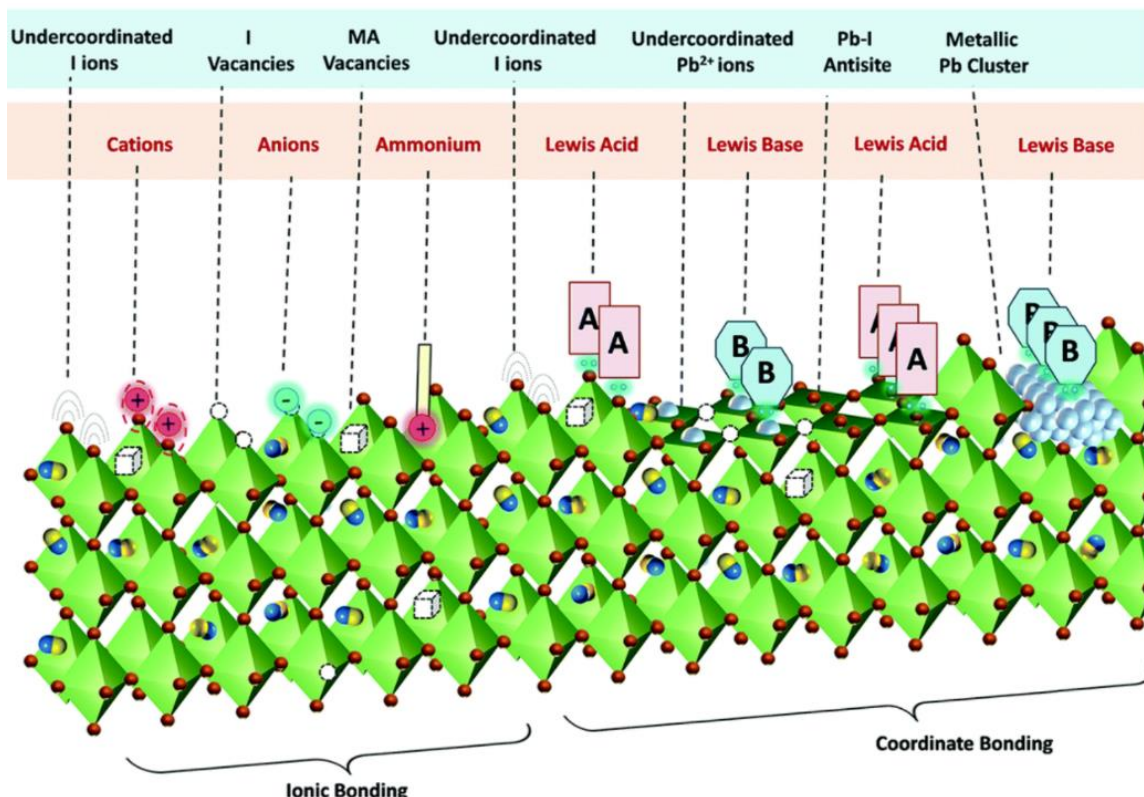


Figure 2.10 | Point and interfacial defect states in  $\text{MAPbI}_3$  and various passivation methods. Reproduced with permission from ref.<sup>146</sup>, copyright 2019 Royal Society of Chemistry.

## 2.2.4. Facile Synthesis and Deposition

Because perovskites are relatively defect tolerant, highly efficient PSCs can be fabricated using facile and inexpensive solution processing techniques or thermal evaporation.<sup>59,60</sup> In fact, this is one of the greatest advantages of PSCs compared to the market-leading Si solar cells, which require a much more complex manufacturing process. For solution processing in particular, the precursor mixture can be synthesised from relatively low purity materials and the perovskite deposition can be performed in ambient air, greatly simplifying the process.<sup>147,148</sup> Film deposition from precursor solutions proceeds through a nucleation and growth process. Nucleation is started by inducing supersaturation of the precursor solution, usually by solvent drying or by adding an antisolvent. Then, subsequent nucleation and growth are driven by thermodynamic parameters, such as temperature and changes in Gibbs free

energy.<sup>149,150</sup> Many techniques have been – and are being – developed to obtain high-quality perovskite films, such as antisolvent quenching, solution engineering, vapour-assisted solution processing, and infrared (IR) annealing.<sup>151–155</sup> In addition, the search for non-hazardous and environmentally friendly solvents has become a major research topic in perovskite PV.<sup>156</sup> All this effort has recently benefited greatly from high-throughput research enabled by robot-assisted film deposition and machine learning-based data analysis.<sup>157–162</sup>

From a commercial point of view, the PSC fabrication process is also amenable to modifications to suit various applications with different requirements. For example, flexible cells can be fabricated by replacing the glass substrate with polymers or metal foils.<sup>128</sup> Semi-transparent or even vividly colourful cells for building-integrated PV can be made by tuning the perovskite's  $E_g$  or layer thicknesses in the device stack.<sup>163,164</sup> To produce high-efficiency cells, perovskite films can be deposited directly onto Si cells to produce Si/perovskite tandem cells.<sup>129</sup> Alternatively, perovskite/perovskite tandem cells is also a viable option, offering a combination of high efficiency, flexibility, low cost, and high specific power.<sup>84</sup> Crucially, however, most real-life applications would ultimately require the ability to upscale highly efficient lab-scale cells into modules.

## 2.3. Perovskite Solar Modules

PSCs must make the transition from laboratory-scale cells ( $\sim 0.1 \text{ cm}^2$ ) to commercially relevant sizes (hundreds of  $\text{cm}^2$ ) to have a real impact on the world's energy supply. While small-area cells are almost entirely deposited using spin coating, this technique is wasteful and not scalable.<sup>28</sup> Therefore, other deposition methods must be investigated and optimised to fabricate efficient and stable large-area PSCs. Furthermore, like other thin film PV technologies, large-area PSCs need to be converted to PSMs containing series-connected cells to minimise Ohmic losses.<sup>165</sup> This conversion is often performed using the MI design, in which a series of lines are scribed using a knife or pulsed laser beam to separate neighbouring cells. All these concepts are covered in the following sections.

### 2.3.1. Scalable, Low Cost, and Low Energy Module Fabrication

Although spin coating is not suitable for PSM fabrication, there are many other potential deposition methods. These can be broadly grouped into solution processing and evaporation-based methods. The former category includes blade coating, slot-die coating, spray coating, inkjet printing, and screen printing (Figure 2.11).<sup>28</sup> The latter includes thermal (co-)evaporation, flash evaporation, close space sublimation, and chemical vapour deposition.<sup>166</sup> One technique, vapour-assisted solution processing, can be considered a hybrid of these two families. Solution processing is compatible with sheet-to-sheet

or roll-to-roll manufacturing lines, allowing high-throughput fabrication with low capital expenditure. However, many commonly used solvents are toxic or industrially irrelevant due to government regulations limiting their usage.<sup>156,166</sup> On the other hand, vapour-based techniques generally have higher capital expenditure and lower throughput, but allow greater control and reproducibility while removing the need for careful solvent handling and disposal. A major disadvantage of evaporation methods is the difficulty to incorporate additives often used in solution processing to passivate defects.<sup>59</sup>

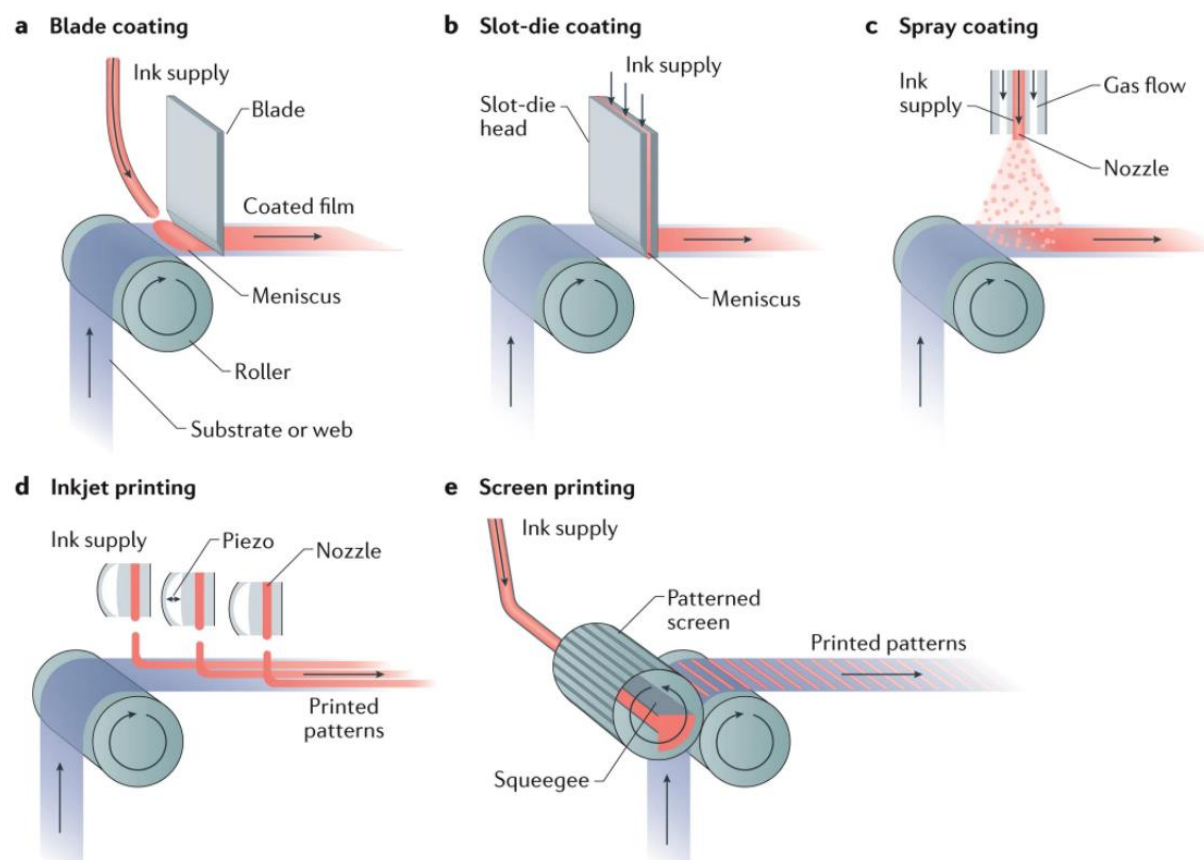


Figure 2.11 | Scalable solution-based deposition methods. Reproduced with permission from ref. <sup>28</sup>, copyright 2018 Springer Nature.

The solution-based techniques are usually enhanced by an additional step to promote supersaturation in the precursor solution and thus ensure the formation of a smooth and pinhole-free film.<sup>28</sup> This step may take the form of an antisolvent bath, heating, gas quenching, or vacuum-assisted drying. Crucially, this supersaturation-promoting step can only be performed in a limited period before a rough, dendritic perovskite film is formed.<sup>28,167</sup> Careful consideration of solvent properties is therefore necessary to prolong this window, especially boiling point, vapour pressure, viscosity, and surface tension. Once the perovskite film is formed, it may be subject to other post-growth treatments to further improve grain

morphology and crystallinity, such as annealing or gas-assisted Ostwald ripening. Regardless of the selected deposition method, the overarching goal is film uniformity over the entire substrate area.<sup>168</sup> Because the final module is composed of serially connected cells, the module's output current will be limited by the cell producing the lowest current. Therefore, it is crucial that each cell's performance is not only high, but also as similar to one another as possible. This topic is explored in Chapter 5, where a solution engineering approach is used to produce spatially homogeneous blade coated PSMs.

When manufactured at an industrial scale, solution processed PSMs can have lower cost and embedded energy compared to other PV technologies.<sup>10,16,169–171</sup> This comparison is assessed using two parameters: LCOE and energy payback time (EPBT). For a PV system, LCOE is calculated following Equation 2.4, where  $I$  is the installation cost,  $OM_t$  is the operations and maintenance expenses in year  $t$ ,  $E_t$  is the system's energy yield in year  $t$  in kWh,  $N$  is the system's (estimated) lifetime in year,  $d$  is the energy yield's annual degradation rate, and  $r$  is the discount rate. EPBT is defined as the operation period required for a power plant to generate the same amount of primary energy (energy in its original form as harvested from nature, prior to human-engineered energy conversion) that was needed to construct, operate, and dispose or recycle that plant. It is calculated according to Equation 2.5, where CED (cumulative energy demand) is the amount of energy used by the plant throughout its life cycle,  $E_g$  is the averaged amount of generated electricity per year,  $\eta$  is the conversion efficiency of electricity to primary energy, and  $E_{OM}$  is the averaged amount of energy needed for operations and maintenance of the plant per year.

$$LCOE = \frac{I + \sum_{t=0}^N \frac{OM_t}{(1+r)^t}}{\sum_{t=0}^N \frac{E_t}{(1+r)^t}} \quad (\text{Equation 2.4})$$

$$EPBT = \frac{CED}{\frac{E_g}{\eta} - E_{OM}} \quad (\text{Equation 2.5})$$

Technoeconomic analyses of single-junction PSMs and perovskite-based tandem modules have been performed using various combinations of materials and device architectures, as recently summarised in a meta-analysis by Vidal et al.<sup>10</sup> Even so, most of them are not directly comparable due to varying choices and assumptions made on material costs, module design, fabrication method, manufacturing location and capacity, module PCE and stability, and more. Consequently, LCOE projections for utility-scale PV plants using single-junction PSMs range from 2.2 to 7.9 US¢/kWh, while estimates for plants using Si/perovskite tandem cells lie between 2.3 and 5.5 US¢/kWh.<sup>13–17</sup> This range is comparable to the

global weighted average LCOE of utility-scale PV plants in 2020 (5.7 US¢/kWh) and is lower than the LCOE of fossil fuel-fired power plants in G20 countries, also in 2020 (5.5–14.8 US¢/kWh).<sup>5</sup> Furthermore, a direct comparison between harmonised EPBT data of various PV technologies (Figure 2.12a) has estimated an EPBT of 0.28 years for PSMs, 5-7x lower than crystalline Si and 2-3x lower than CdTe and CIGS.<sup>10</sup> However, it is important to recall that these LCOE and EPBT numbers are based on optimistic estimations of cost and energy instead of empirical data, as perovskite PV has not yet entered the market thus far. Therefore, the realisation of PSM's projected LCOE and EPBT is reliant on further advancements in PCE, stability, and device upscaling (Figure 2.12b,c).

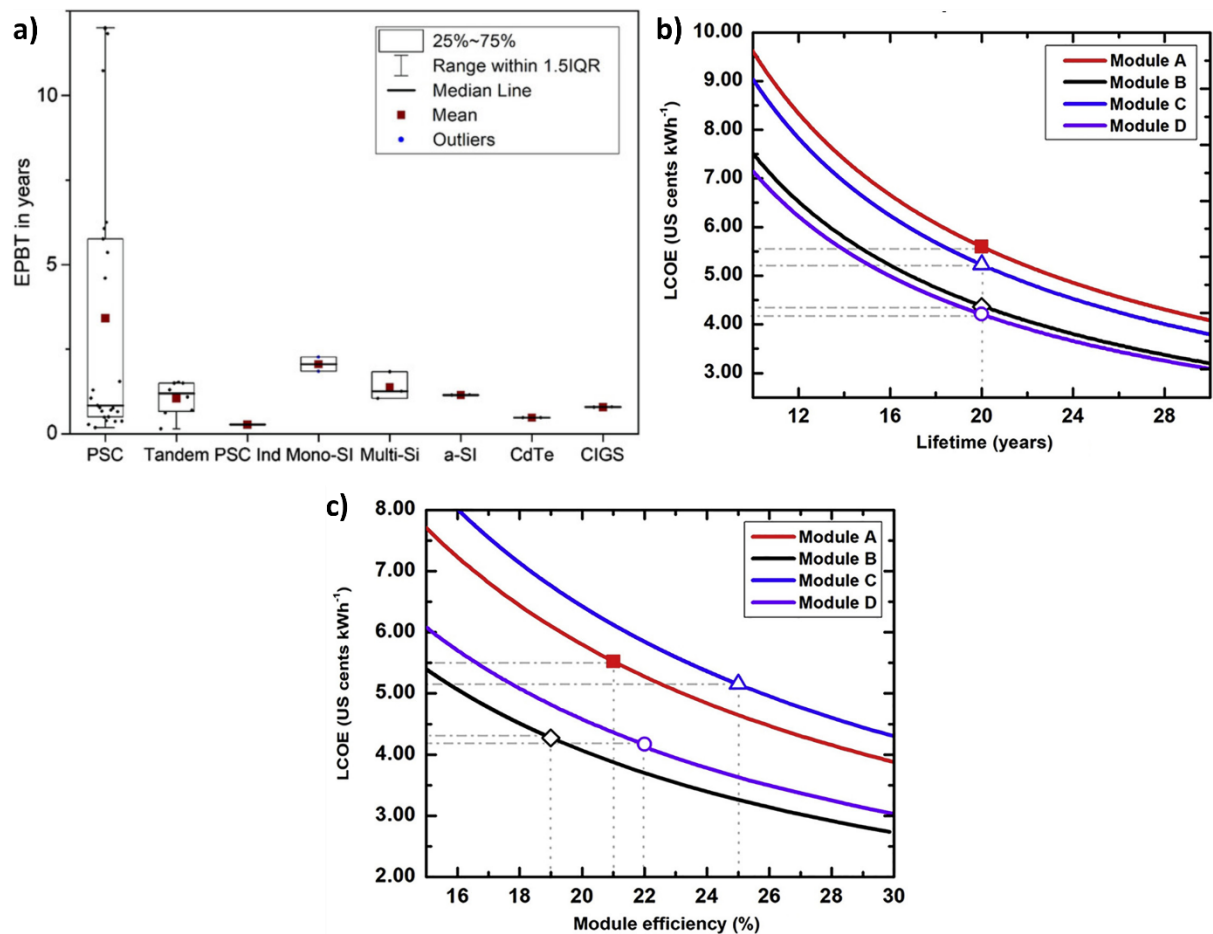


Figure 2.12 | (a) EPBT comparison for various PV technologies. ‘PSC’ and ‘PSC Ind’ refer to laboratory-scale and simulated industrial-scale devices, respectively. ‘Tandem’ refers to perovskite-based tandem devices with Si, CIGS, or CZTS. (b,c) LCOE estimation for four module architectures plotted as a function of (b) module lifetime and (c) module efficiency. Module A is a commercial Si cell, module B is a single-junction PSM, module C is a Si/perovskite tandem, and module D is a perovskite/perovskite tandem. Markers indicate the set of assumptions adopted for each module. Panel (a) is reproduced from ref. <sup>10</sup> under the Creative Commons CC-BY 4.0 License. Panels (b,c) are reproduced with permission from ref. <sup>14</sup>, copyright 2018 Cell Press.

### 2.3.2. Monolithic Interconnection

In a large-area cell, the photocurrent needs to flow over a long distance in the transparent conductive oxide (TCO) layer to reach the electrode. This layer's relatively high sheet resistance ( $7\text{-}60 \Omega/\square$ ) results in a large Ohmic loss.<sup>168</sup> This loss can be minimised by partitioning a large-area cell into several smaller series-connected cells with the MI architecture. Each pair of neighbouring cells are separated by three lines, named P1, P2, and P3 (Figure 2.13a,b).<sup>172</sup> In PSMs, P1 separates the cells' TCO contact. P2 removes layers above the TCO so that one cell's TCO can form a direct contact with the next cell's metal electrode. Finally, P3 insulates adjacent cells by separating their top metal contact and, in some cases, the layers between it and the TCO as well. The area between the P1 and P3 lines is called 'dead area' ( $W_d$ ) as it does not contribute to the module's power output. The remaining area is called 'active area' ( $W_a$ ), and the ratio between it and the total substrate area is called the geometric fill factor (GFF, Equation 2.6). The P1 and P3 lines are simple to optimise as they only need to be made as narrow as possible while still electrically isolating neighbouring cells. By carefully balancing Ohmic losses in the TCO layer, Ohmic losses in the P2 contact, and dead area losses for a given module, the ideal number of cells per module and P2 width can be modelled.<sup>173</sup>

$$GFF = \frac{W_a}{W_a + W_d} \quad (\text{Equation 2.6})$$

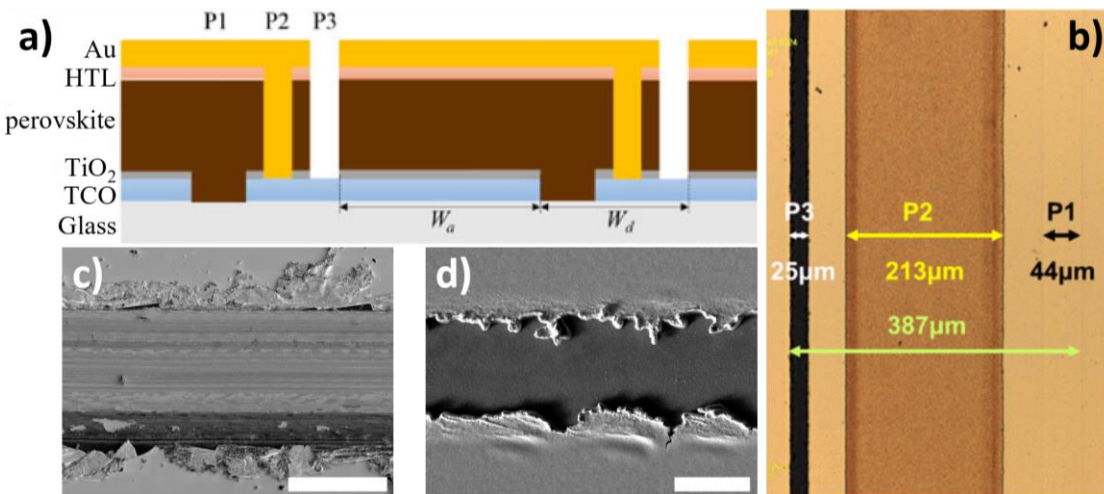


Figure 2.13 | (a) Schematics of a PSM with the P1, P2, and P3 lines marked. (b) Top-view optical microscope image of the MI area. (c,d) Top-view scanning electron microscopy image of a c) knife-scribed and d) laser-scribed P3 line. Scale bars represent (c) 100 μm and (d) 10 μm. Panel (a) is adapted from ref. <sup>174</sup> under the Creative Commons CC-BY 3.0 License. Panel (b) is reproduced with permission from ref. <sup>175</sup>, copyright 2017 IEEE.

Although it is possible to scribe these lines mechanically with a knife, laser scribing is highly preferable due to its high speed, greater accuracy and precision, minimum tool wear, higher reproducibility, potential for automation, and adaptability to various device materials.<sup>176,177</sup> Most importantly, laser scribing results in modules with much higher GFF and thus higher efficiency. While knife-scribed lines are usually about 200 µm or more in width, laser-scribed P1 and P3 lines can be as narrow as 15 µm (Figure 2.13c,d).<sup>173,178</sup> Consequently, the GFF of mechanically scribed modules is usually in the range of 70–80%, while laser-scribed modules regularly exhibit GFFs of 90–95%.<sup>175,179</sup> Very recently, a novel laser-scribed MI design with a GFF of 99% was invented.<sup>180</sup>

It has been pointed out that the MI area is a potential starting point for perovskite degradation, although so far there have been very few studies on this matter.<sup>30</sup> In the P1 line, the bottom CTL is in direct contact with the substrate, which is often soda lime glass (SLG). P1 lines may thus become an entry point for metal ions ( $\text{Na}^+$ ,  $\text{Ca}^{2+}$ ,  $\text{Mg}^{2+}$ ) from glass to diffuse into the active layers of a PSM. Chapter 7 in this thesis investigates this question and explores the effect of Na diffusion on the composition and optoelectronic properties of PSMs. In P2 lines, the metal electrode is in contact with the perovskite layer. Previous works have shown that  $\text{I}^-$  may corrode the metal electrode and metal atoms may diffuse into the perovskite film and induce degradation.<sup>181,182</sup> Therefore, this particular degradation method may be accelerated in the vicinity of P2 lines. Finally, next to P3 lines, the active layers are exposed to the environment unless the device is encapsulated. If not, the P3 line will become a fast ingress point for oxygen and moisture, leading to perovskite decomposition.

### 2.3.3. Laser Scribing

A pulsed laser beam can be used to precisely machine many kinds of materials by using its energy to remove or ablate portions of the target. Laser wavelengths ranging from IR to UV can be used, such as IR CO<sub>2</sub> lasers with  $\lambda = 10.6 \mu\text{m}$  or UV Nd:YVO<sub>4</sub> lasers with  $\lambda = 355 \text{ nm}$ . When a laser pulse hits a target material, its energy is firstly absorbed through excitation of electrons, either free or d-band electrons in metals or valence band electrons in semiconductors. Then, this energy is converted into heat through electron–phonon scattering.<sup>183</sup> The role played by thermal energy in material ablation is primarily governed by the relationship between pulse duration and electron–phonon coupling time, which is in the order of 0.1–100 ps (Figure 2.14a).<sup>184–186</sup> If the pulse duration is longer (ns-pulse), electrons have sufficient time to transfer their energy to lattice phonons, resulting in a large heat-affected zone (HAZ), material melting, and possibly vaporisation for high laser fluences (left side of Figure 2.14b). On the contrary, fs-pulse laser deposits all its energy faster than the electron–phonon coupling time, such that the solid target material is immediately converted into vapour or plasma without heat conduction to the surrounding area (right side of Figure 2.14b).<sup>185,187</sup> This process is sometimes termed cold ablation and is favoured for its small HAZ and excellent precision. However,

even for ultrashort pulses with limited heat diffusion, it has been shown that a portion of the pulse energy that was not used for ablation could remain in the bulk material.<sup>188</sup> The amount of this residual heat increases as the pulse duration lengthens and can trigger decomposition or other thermally activated processes in the remaining bulk material. Furthermore, the high cost of fs-pulse laser systems is not ideal for commercialisation of upscaled PSCs.<sup>185,187,189,190</sup> The intermediate case is ps-pulse laser, whose pulse duration is of a similar order of magnitude with the coupling time. Material removal proceeds mainly through direct solid–vapour or solid–plasma transition, but heat conduction to the bulk material may still occur to some limited, non-negligible, extent.<sup>191</sup>

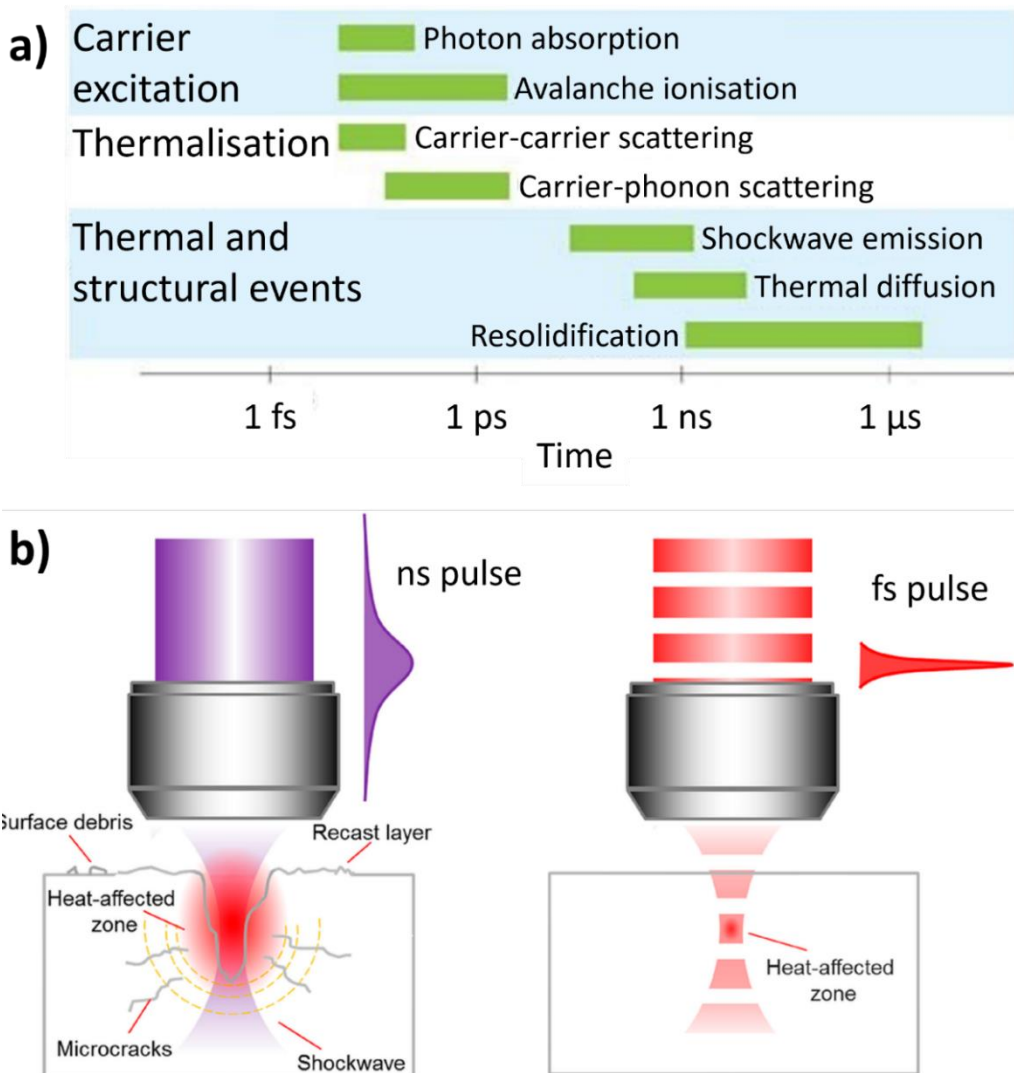


Figure 2.14 | (a) Typical timescales for various physical processes occurring during and after laser-material interaction. (b) Schematic of (left) defects formed in material ablation with an ns-pulse laser and (right) their absence when an fs-pulse laser is used. Panel (a) is reproduced with permission from ref. <sup>186</sup>, copyright 2008 Springer Nature. Panel (b) is reproduced with permission from ref. <sup>192</sup> under the Creative Commons CC-BY 4.0 License.

For PSCs specifically, studies on laser–matter interactions have focused almost exclusively on single-pulse craters or P2 lines. Bayer and co-workers have shown that depending on the irradiation direction (glass-side or metal-side), laser wavelength, and pulse duration, laser–perovskite interaction resulted in three possible removal mechanisms: ablation, delamination lift-off, or a combination of them.<sup>193</sup> Schultz et al. and Bayer et al. discovered formation of PbI<sub>2</sub>-containing residuals after scribing P2 lines with a ns-pulse laser regardless of the irradiation direction, which indicated a strong influence of thermal processes in perovskite removal.<sup>194,195</sup> This was confirmed by Turan et al., who found that perovskite removal with ns-pulse laser involves heating, melting, and evaporation irrespective of whether UV ( $\lambda = 355$  nm), green ( $\lambda = 532$  nm), or IR ( $\lambda = 1064$  nm) wavelength was used.<sup>189</sup> In contrast, using a ps-pulse laser was found to suppress PbI<sub>2</sub> formation due to reduced heat conduction.<sup>195</sup> These findings are important because it is well-known that hybrid perovskites are not stable against heating; hence, the diffused thermal energy could degrade the device stack beyond the scribe lines. This topic was investigated for a ps-pulse laser and discussed in Chapter 6 of this thesis. In addition, a comparison of residual heat propagation between an ns-pulse and a ps-pulse laser is also shown in Chapter 6.

Due to the central role played by pulse duration on material ablation and energy propagation, it is the primary parameter of importance in laser scribing. Other parameters which provide additional levers to tune the scribing process are laser wavelength, pulse frequency, patterning speed, pulse overlap, number of passes in a line, and irradiation direction.

## 2.4. Characterisation of Perovskite Photovoltaic Devices

The rapid development of perovskite PV is enabled by a wide array of characterisation techniques. They have greatly deepened our understanding of perovskite PV across complexity levels (from materials to devices), families of properties (morphological, structural, compositional, optical, electrical, optoelectronic) and length scales (from atomic to system scale). In particular, spatially resolved techniques (summarised in Table 2.1) are highly important since perovskites show considerable heterogeneity across multiple length scales, from atomic to nanoscale to tens of micrometres.<sup>196</sup> These non-uniformities manifest in the properties mentioned above, governing both device performance and stability.<sup>90,197,198</sup> This section provides a brief overview of commonly employed characterisation tools and recent trends towards high throughput, correlative, and *in situ* characterisation.

Morphological and structural properties of perovskite materials fundamentally affect the sequence of energy conversion steps happening inside PV devices, from light absorption to charge transport and collection.<sup>199,200</sup> Furthermore, the intrinsic and extrinsic stabilities of perovskite PV devices are also strongly influenced by the perovskite's morphology and structure.<sup>62,201</sup> Desirable qualities include large and strongly crystalline grains, smooth perovskite films with full substrate coverage, and conformal

contact between the perovskite and CTls.<sup>121,202–204</sup> For these reasons, morphological and structural characterisation are often used to screen perovskite films before their incorporation into devices and to help reveal the mechanism of observed changes in performance. The most common tools for morphological characterisation are scanning electron microscopy (SEM) imaging, (scanning) transmission electron microscopy (TEM/STEM) imaging, and atomic force microscopy (AFM). SEM and (S)TEM can be performed in top-view or cross-sectional manner, providing direct visualisation of grain shape and size, film thickness and uniformity, substrate coverage, presence of precipitates, scaffold pore filling, MI scribe lines, and more. SEM has a lower spatial resolution compared to (S)TEM but is simpler in terms of operation and sample preparation. AFM can provide topological information from a sample, such as film roughness and conformality. Structural information such as crystallinity, texture, and strain is obtained through diffraction, either X-ray diffraction (XRD) or electron diffraction inside an SEM/(S)TEM. In an SEM, the technique is named electron backscattered diffraction (EBSD), in a TEM it is called selected area electron diffraction (SAED), while in a STEM it is scanning electron diffraction (SED). Of the three, EBSD and SED are spatially resolved. However, highly energetic electron beams are likely to damage the perovskite sample (see Section 3.9), so advanced detectors are necessary to perform electron diffraction without excessive sample damage.<sup>90,205,206</sup> XRD can be performed in standard laboratory instruments with a tens of  $\mu\text{m}$ -wide probe beam or in synchrotrons, where the extremely bright X-ray source enables spatially resolved scanning X-ray diffraction microscopy (SXDM).<sup>207</sup> A popular variant of XRD is grazing incidence wide-angle X-ray scattering (GIWAXS), a surface technique capable of obtaining crystallographic information from thin films.<sup>208,209</sup>

Compositional heterogeneity has been getting more attention recently as the perovskite stoichiometry of state-of-the-art PSCs evolved from simple  $\text{MAPbI}_3$  to complex TCDH formulations containing various additives.<sup>8</sup> Compositional differences may occur in the lateral and vertical directions in perovskite films and may be found from the nanoscale to the microscale.<sup>196</sup> Since many other properties are influenced by the perovskite composition, a thorough understanding of compositional distribution in PSCs is desirable. Further motivation to reach this goal is provided by the desire to identify non-perovskite phases and by the discovery of photoinduced ion migration within the perovskite layer and across the device stack.<sup>182,210</sup> Compositional mapping can be performed through EDX, electron energy loss spectroscopy (EELS), secondary ion mass spectrometry (SIMS), and X-ray fluorescence (XRF).<sup>211</sup> EDX mapping is performed in an SEM/STEM while EELS mapping is done in a STEM. These techniques cover a wide range of spatial resolutions, from atomic and nanoscale (STEM-EDX, EELS, XRF, NanoSIMS) to microscale (SEM-EDX, SIMS). They have been extensively used to shed light on many aspects of PSCs, from degradation mechanisms and halide segregation to dopant distribution and trap state identification.<sup>90,207,212,213</sup> Less common compositional characterisation techniques include (hard) X-ray photoelectron spectroscopy (HAXPES/XPS), nanoscale Fourier transform infrared spectroscopy (NanoFTIR), Raman spectroscopy, and atom probe tomography (APT).<sup>214–217</sup>

Table 2.1 | Spatial resolution of spatially resolved characterisation techniques.

Property	Technique	Lateral Spatial Resolution
Morphology	SEM Imaging	1–10 nm <sup>218</sup>
	(S)TEM Imaging	Up to atomic <sup>219</sup>
	AFM	0.1–5 nm, 0.01–0.1 nm (vertical) <sup>220</sup>
Structural	EBSD	Up to 10 nm <sup>221</sup>
	SED	Sub-10 nm <sup>90</sup>
	SXDM	40 nm–1 μm <sup>207</sup>
Compositional	SEM-EDX	~1 μm <sup>220</sup>
	STEM-EDX	~10 nm (see Section 3.7)
	EELS	1–10 nm <sup>218,222</sup>
	(Nano)SIMS	50 nm–1 μm <sup>212,223</sup> , 1–10 nm (vertical) <sup>212</sup>
	XRF	40 nm–1 μm <sup>207</sup>
	HAXPES/XPS	1–400 μm <sup>214,224</sup>
	NanoFTIR	Up to 25 nm <sup>215</sup>
	Raman	~1 μm <sup>216</sup>
	APT	Sub-nm <sup>217</sup>
Optical	TAM	Sub-diffraction limit to sub-10 nm <sup>225,226</sup>
	PL	~1 μm <sup>220</sup>
	EL	Defined by the camera pixel, up to 2 μm <sup>228</sup>
	SEM-CL	The probe beam's interaction volume or the carrier diffusion length, whichever is larger <sup>207,227</sup>
	STEM-CL	
Optoelectronic	EBIC	
	XBIC	
	LBIC	1–100 μm <sup>228</sup>
	KPFM	1–100 nm <sup>229</sup>
	c-AFM	1–100 nm <sup>229</sup>
	PEEM	10–50 nm <sup>230</sup>

Since light absorption is the first step in PV energy conversion, PV materials should have high absorption for photons with energies above  $E_g$ . Furthermore, Shockley-Queisser's detailed balance model showed that maximum PV efficiency is only reachable if all carrier recombination is radiative, meaning PV absorbers must also be good light emitters.<sup>63</sup> This reciprocity was formalised by Uwe Rau, who formulated a mathematical relationship between a PV cell's external quantum efficiency (EQE, how many charge carriers are extracted per incident photon) on one side and its electroluminescence (EL, emitted photons due to an applied electrical current or field) and/or photoluminescence (PL, emitted photons due to photogenerated charge carriers) on the other, enabling a quantitative analysis of solar cells based on their emissive properties.<sup>231,232</sup> A PV material's absorption coefficient can be measured via UV-vis spectroscopy or, if a greater sensitivity is desired, with photothermal deflection spectroscopy. Other than absorption coefficient, the values of  $E_g$  and Urbach energy (a measure of energetic disorder near the band edges of a material) can also be extracted from the obtained absorption spectrum.<sup>67</sup> Another absorption-related technique is transient absorption spectroscopy, which evaluates the time-resolved carrier dynamics after an excitation event. The spatially resolved version of this technique is named transition absorption microscopy (TAM), enabling observation of excited carriers across time and space. Emission properties can be studied using EL, PL, and cathodoluminescence (CL), where the excitation source is the electron beam of an SEM/STEM. The intensity, position, and shape of the emission peaks can reveal information about carrier recombination,  $E_g$  value, material disorder, defects, and non-perovskite phases.<sup>233,234</sup> Luminescence spectra produced by EL/PL systems calibrated to measure the exact number of emitted photons can be further analysed with Rau's relations to obtain a device's EQE and  $V_{OC}$ .<sup>231,232</sup> Luminescence characterisation can be performed in a time-resolved and spatially resolved manner using a pulsed probe and a scanning or wide-field imaging system. Time-resolved PL/CL are used to measure carrier lifetimes and discern the dominant recombination mechanism. Spatially resolved EL/PL/CL produce maps of emission intensity, energy, carrier lifetime, and can also indirectly construct composition maps since the  $E_g$  of perovskite depends on its composition.<sup>235</sup> Theoretically, CL can have a much better spatial resolution compared to PL as an electron beam is not constrained by the diffraction limit, but in reality the spatial resolution is limited by either the interaction volume (space in the sample from which detected signals are generated) or by the carrier diffusion length.<sup>227</sup>

Finally, PV parameters  $J_{SC}$ ,  $V_{OC}$ , FF, and PCE are extracted from J-V curves, which are measured by stepping through a series of voltages and recording the device's output current at each voltage. With PSCs, this seemingly simple measurement is complicated by ion migration and interfacial carrier recombination.<sup>126</sup> These phenomena give rise to a capacitive current which manifests itself as hysteresis in J-V measurements.<sup>126</sup> Consequently, reverse J-V scans (from  $V = V_{OC}$  to  $V = 0$ ) tend to produce higher FF,  $V_{OC}$ , and PCE compared to forward scans. To prevent inaccuracies in PCE measurement and reporting, stabilised PCE and power output should be obtained using MPP tracking.<sup>236</sup> Briefly, an initial

$J$ - $V$  sweep is firstly performed, ideally with a slow scan rate to minimise hysteresis, to obtain an initial guess for  $V_{MPP}$ . Then, the tracker applies a small voltage oscillation around  $V_{MPP}$ , measures the new power output, and adjusts the biasing voltage. This process is iterated continuously to maintain the device at the MPP. With this so-called perturb and observe algorithm, stabilised PCE and power output can be extracted. Techniques to measure  $J$  and  $V$  in a spatially resolved manner are also available. Although they are relatively more complex to perform compared to  $J$ - $V$  curve measurements, these techniques can show quantitative parameter fluctuations across the scanned region. For example,  $V_{OC}$  heterogeneity can be mapped using AFM-based Kelvin probe force microscopy (KPFM), provided it is properly calibrated with  $J$ - $V$  and EQE measurements.<sup>229</sup> Microscopic  $J$ - $V$  measurements can be done using another AFM derivative, photoconductive AFM (pc-AFM), where the current is measured from point to point while the sample is biased and illuminated.<sup>229</sup> Current mapping is also accessible via electron/laser/X-ray beam-induced current (EBIC/LBIC/XBIC) techniques, where a device is stimulated by a scanning electron, laser, or X-ray beam and the current produced at each spot is measured.<sup>207,228</sup> Lastly, (time-resolved) photoemission electron microscopy (PEEM) has recently gained prominence as a powerful technique to map nanoscale trap states in perovskite films.<sup>230</sup>

Looking forward, there are at least three clear trends in perovskite PV characterisation. The first is correlative multimodal characterisation (Figure 2.15a). With this approach, the same region of interest is mapped with multiple spatially resolved techniques. Maps of different properties/parameters are then overlaid on one another using fiducial markers to evaluate spatial correlations among them. This versatile method has recently led to the discovery of many important relationships, such as between Br inhomogeneity and trap sites, phase impurities and degradation starting points, and between local strain and nonradiative recombination.<sup>90,197,237</sup> The second is *in situ* characterisation, where perovskite specimens are probed in real time as certain process(es) are taking place (Figure 2.15b). *In situ* characterisation can reveal the exact mechanism of those processes up to the technique's temporal resolution, as opposed to *post hoc* characterisation which can only show the end result. Plenty of instruments can be adapted to enable *in situ* work, such as laboratory XRD, SEM and (S)TEM, synchrotron beamlines, PL, and AFM.<sup>218,220,238,239</sup> The observable processes include perovskite crystallisation, phase transformation, film annealing, and various forms of degradation.<sup>218,220,238,239</sup> Both correlative multimodal and *in-situ* characterisations involve repeated scans of the same sample area, therefore utmost care must be taken to suppress probe-induced specimen damage. The third and most recent trend is high-throughput characterisation assisted by robots and machine learning algorithms (Figure 2.15c). A great number of perovskite compositions and variables can be assessed in a relatively short time using this method, enabling a faster learning process for future device improvements. Example applications include the search for new potential stoichiometries, crystallisation dynamics, antisolvent suitability, and degradation studies.<sup>157–162</sup>

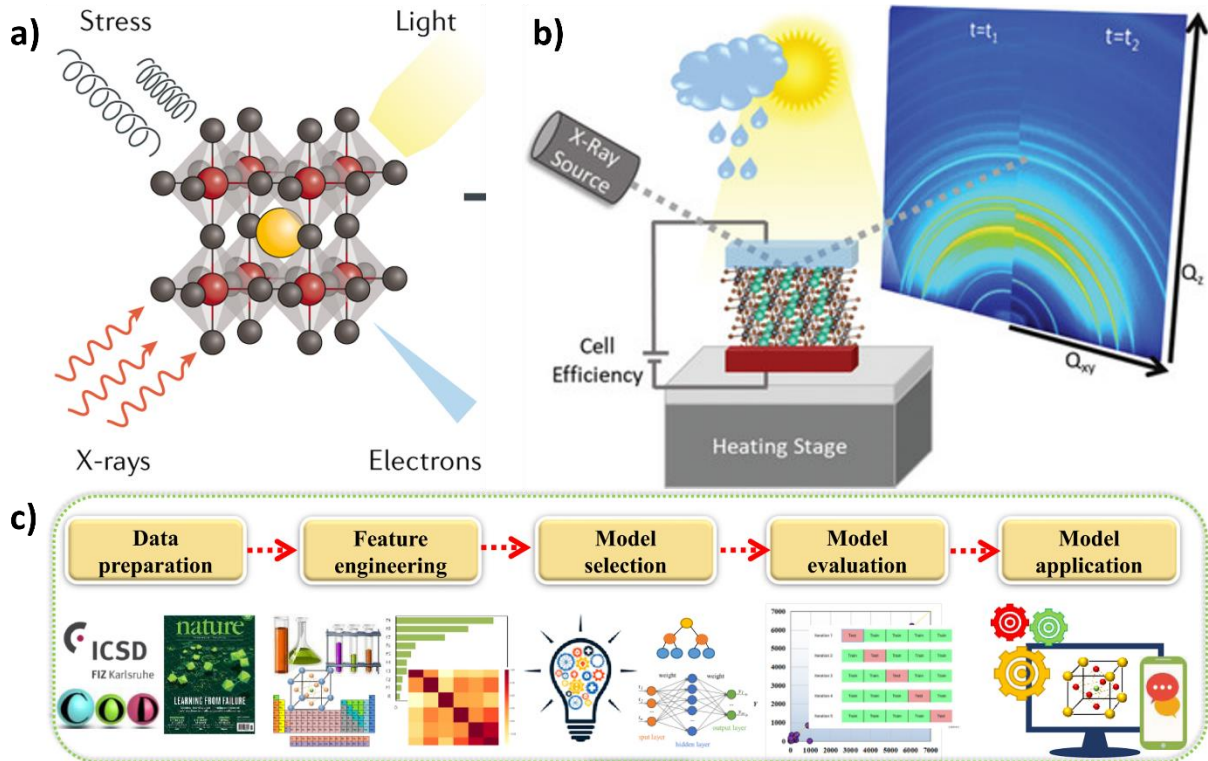


Figure 2.15 | Illustration of recent trends in perovskite PV characterisation: (a) correlative multimodal characterisation with multiple probes, (b) in-situ experiments, and (c) framework for machine learning-assisted material discovery. Panel (a) is reproduced with permission from ref. <sup>196</sup>, copyright 2019 Springer Nature. Panel (b) is reproduced with permission from ref. <sup>240</sup>, copyright 2020 Wiley-VCH. Panel (c) is reproduced from ref. <sup>241</sup> under the Creative Commons CC-BY 4.0 License.

## 2.5. Summary

Halide perovskites have matured as a PV material in a remarkably short time, enabled by its advantageous optoelectronic properties and facile, inexpensive fabrication. It is also a versatile class of materials, as illustrated by its tunability in terms of dimensionality, composition, and device architecture. Huge inroads have been made in the effort to understand and manipulate halide perovskites, resulting in rapid increases in device efficiency and stability. This great progress is made possible by the wide array of available characterisation techniques and technical advances continuously being made to come up with ever better measurement instruments and data analysis procedures.

Nonetheless, several challenges remain in perovskite PV's path from laboratories to industrial manufacturing lines. Foremost among these is the steep PCE drop upon device upscaling. More research on scalable perovskite deposition and module architecture is necessary to obtain high efficiency in large modules. Homogeneous deposition of the perovskite and contact layers is a prerequisite to achieve this goal as it ensures uniform performance across the constituent cells. The MI area is another very

important aspect of PSMs which have been relatively understudied due to its absence in lab-scale cells. It contains its own unique set of micro/nanoscale features and provides a convenient starting point for degradation mechanisms as described above. These two topics will be discussed further in Chapters 5, 6, and 7 of this thesis.

## **Chapter 3**

# **Electron Microscopy Techniques**

PSCs are multi-layered devices, with layer thicknesses ranging from tens to few hundreds of nanometres. Most layers contain nanoscale heterogeneities which dictate device performance as discussed in Chapter 2. Furthermore, the operational stability of these devices is governed by dynamic processes occurring at the micro and nanoscale, such as chemical decomposition and ion migration. EM is very useful to characterise these materials and processes with meaningful spatial resolution at those length scales. A range of EM techniques, from imaging to analytical spectroscopy, was applied to probe the interplay between morphological, chemical, and optoelectronic properties of PSCs and PSMs in this thesis. This chapter briefly summarises the signal-generating interactions that can happen between probe electrons and a specimen inside EMs, then describes the working principles behind various EM techniques used to obtain the results presented in the following chapters. The concept and mechanisms of electron beam-induced specimen damage are also introduced as it is of great relevance to beam-sensitive materials like OIHPs. Lastly, an introduction to data processing algorithms based on MVA is provided.

### **3.1. Beam–Specimen Interaction: Electron Scattering**

The working principles of all EM techniques can be described based on two kinds of interaction between probe electrons and the specimen, namely elastic and inelastic scattering. Beam-specimen interactions result in a variety of signals (Figure 3.1a) which, when collected by suitable detectors, provide contrast for EM-based imaging and mapping methods. This wide array of generated signals is what makes EM so powerful and versatile as a characterisation tool. Morphological information about the specimen is accessible through secondary, elastically scattered, and unscattered electrons. Characteristic X-rays, Auger electrons, and inelastically scattered electrons provide compositional information. Elastically scattered electrons also reveal crystallographic data through electron diffraction while electronic properties can be investigated through inelastically generated EHPs and visible light photons.

From a particle point of view, elastic scattering happens when a probe electron experiences Coulomb interaction with the (screened) nuclear potential of the specimen atoms (Rutherford scattering, Figure 3.1b). Owing to the large mass difference between the electron and the nucleus, the electron loses only a negligible amount of its kinetic energy. The scattering angle mainly depends on the distance between the electron trajectory and the specimen nucleus, with shorter distances resulting in larger deflection

angles. When the scattering angle gets larger than  $90^\circ$ , the probe electrons become backscattered electrons (BSE). From the perspective of electron as a wave, elastic scattering happens when the incoming wave experiences constructive interference due to the lattice planes of the specimen. For parallel beam illumination, diffraction from a crystalline specimen would result in patterns of either bright spots (monocrystalline) or sharp rings (polycrystalline), while an amorphous specimen would produce diffuse rings or a shapeless bright region.

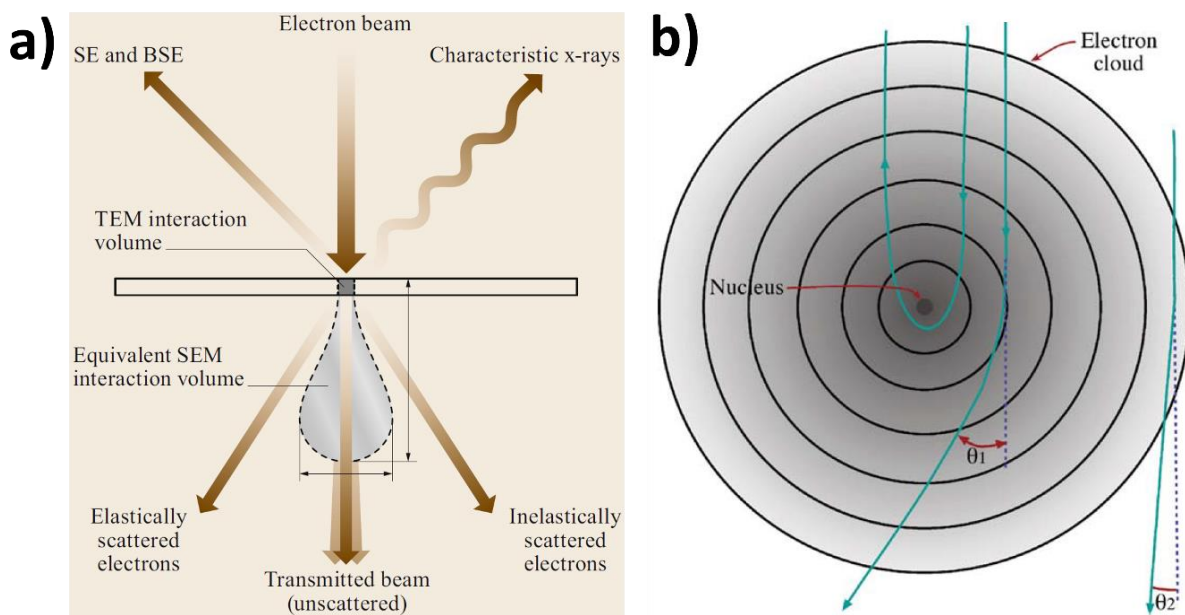


Figure 3.1 | (a) Various signals generated inside a TEM by electron scattering in the specimen. (b) Schematic of elastic electron scattering by a specimen atom. The scattering angle is determined by the distance between the probe electron and the specimen nucleus. Panel (a) is reproduced from ref.<sup>242</sup> with permission, copyright 2019 Springer. Panel (b) is reproduced from ref.<sup>243</sup> with permission, copyright 2009 Springer.

Inelastic scattering is defined as events where an incoming electron transfers a significant portion of its kinetic energy to the specimen due to electron-electron interaction. This energy can then be re-emitted as an X-ray, UV, or visible light photon, or can generate secondary electrons (SEs, ejected conduction or valance band electrons), Auger electrons (ejected outer shell electrons), plasmons (quantum of collective electron oscillations), or phonons (quantum of lattice vibrations). As it is responsible for the secondary signals shown in Figure 3.1a, inelastic scattering is the reason why analytical EM is possible at all. Unfortunately, the energy deposited on the specimen is also the cause of beam-induced specimen damage, as further explained in Section 3.9.

Another way to classify electron scattering is based on its coherence. Ideally, electrons in the probe beam are spatially coherent, meaning they are in phase with one another. Coherently scattered electrons remain so after passing through the specimen, while incoherently scattered electrons lose their phase relationship. Elastic scattering is generally coherent and forward peaked, i.e. occurring at  $<10^\circ$  ( $<175$  mrad) deflection angles.<sup>243</sup> Elastically scattered electrons become more incoherent at higher angles, meaning BSEs are always incoherent. Inelastically scattered electrons are nearly always incoherent and strongly forward peaked ( $<1^\circ$ ,  $<17.5$  mrad).<sup>243</sup> Coherent and incoherent scattering are useful in TEM, but only incoherent scattering matters in SEM as no forward scattering is possible with bulk specimens.

Each scattering type has an associated scattering cross-section ( $\sigma$ ), defined as the likelihood of that scattering type occurring.  $\sigma$  is determined by several factors, namely beam energy, specimen thickness, specimen atomic number ( $Z$ ), and the angle of the specimen with respect to the electron beam.<sup>243</sup> The  $\sigma$  for all kinds of scattering is increased with lower beam energy and thicker specimens. Consequently, there are more backscattering events and fewer forward scattering events when the beam energy is low and the specimen is thick. If the specimen is not oriented perpendicularly to the electron beam, the electron will travel through a longer distance in the specimen, thus  $\sigma$  increases. Lower  $Z$  reduces the  $\sigma$  for elastic scattering but has very little effect on inelastic scattering.<sup>243</sup> An important implication of this last point is the ability to perform  $Z$ -sensitive imaging as high- $Z$  elements generate more multiple scattering events. In practice, this is done using BSEs in SEMs and elastically scattered electrons in TEMs. Another important parameter is mean free path ( $\lambda$ ), defined as the average distance travelled by electrons between scattering events. Clearly,  $\lambda$  has a reciprocal relationship with  $\sigma$ . Following the approach of Malis et al., the value of  $\lambda$  can be approximated following Equation 3.1, where  $F$  is a relativistic factor with a value of 0.618 for a 200 kV electron beam,  $E_0$  is beam energy in keV,  $E_m$  is the average energy loss per inelastic scattering event in eV, and  $\alpha$  is the probe's convergence semi-angle.<sup>244</sup> The value of  $E_m$  was empirically found to follow Equation 3.2.<sup>244</sup> If the specimen is a compound instead of a single element, the  $Z$  parameter in Equation 3.2 must be replaced with an effective  $Z$  ( $Z_{eff}$ ). Based on the Lenz model of electron scattering, Egerton has suggested a formula to calculate  $Z_{eff}$  values for compound specimens (Equation 3.3), where  $f$  is atomic fraction.<sup>245,246</sup>  $\lambda$  is usually in the order of tens of nm for the beam voltages used in TEMs.<sup>243</sup> When the specimen thickness is significantly greater than  $\lambda$  (as is the case for the specimens investigated in this thesis, see Section 3.7), most electrons are scattered more than once. Consequently, the scattering angles increase and the beam is broadened as it travels along the specimen thickness (Figure 3.2).

$$\lambda \approx \frac{106F(\frac{E_0}{E_m})}{\ln(2\alpha\frac{E_0}{E_m})} \quad (\text{Equation 3.1})$$

$$E_m \approx 7.6Z^{0.36} \quad (\text{Equation 3.2})$$

$$Z_{eff} \approx \frac{\sum_i f_i Z_i^{1.3}}{\sum_i f_i Z_i^{0.3}} \quad (\text{Equation 3.3})$$

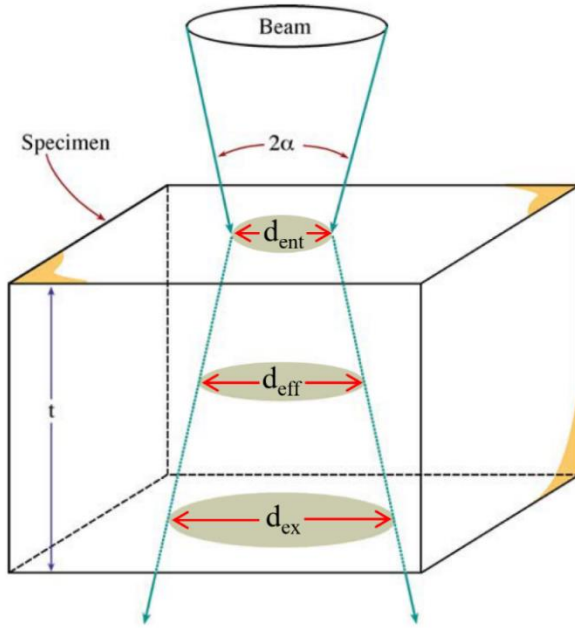


Figure 3.2 | Schematic showing beam broadening inside an EM specimen. Reproduced from ref. <sup>243</sup> with permission, copyright 2009 Springer.

Following the works of Goldstein, Jones, and Michael et al., the effect of beam broadening on spatial resolution is summarised in Equations 3.4–3.6, where  $b$  is beam broadening in nm,  $N_v$  is the specimen's number of atoms in nm<sup>-3</sup>,  $t$  is specimen thickness in nm,  $d_{ex}$  is beam diameter when it exits the specimen,  $d_{ent}$  is beam diameter when it enters the specimen, and  $d_{eff}$  is effective beam diameter.<sup>247–249</sup>  $d_{ex}$ ,  $d_{ent}$ , and  $d_{eff}$  refer to the probe area containing 90% of the electron trajectories.

$$b = 8 \times 10^{-3} \frac{Z_{eff}}{E_0} \sqrt{N_v t^3} \quad (\text{Equation 3.4})$$

$$d_{ex} = \sqrt{d_{ent}^2 + b^2} \quad (\text{Equation 3.5})$$

$$d_{eff} = \frac{1}{2} (d_{ent} + d_{ex}) \quad (\text{Equation 3.6})$$

The volume inside the specimen where electron scattering events occur is called the interaction volume. The interaction volume's shape can be approximated as a cylinder for thin TEM specimens, a cone for thicker TEM specimens, and a teardrop for bulk specimens due to beam broadening inside the specimen (Figure 3.1a and 3.2). Despite this terminology, however, it is important to remember that the various signals generated in an EM do not all come from the exact same volume. These signals have different energies and only those with enough energy to escape from the specimen can be detected. Therefore, each signal type has a typical escape depth, beyond which this signal is not detected. SEs and Auger electrons have the lowest energies at <50 eV and 50–3000 eV, respectively. Therefore, their escape depths are only about a few nm. SEs generally do not carry chemical information and they are primarily used for topography-sensitive imaging. While the energy of Auger electrons can be used to identify the emitting element, it is rarely done with an EM due to the need for an ultra-high vacuum to ensure an extremely clean specimen surface.<sup>243</sup> The energy of BSEs can be as high as the primary beam energy, so their escape depth is much greater at about 0.5 μm. Characteristic X-rays have an escape depth in the order of 1 μm as the  $\sigma$  for X-ray photons are about 4–5 orders of magnitude lower than electrons.<sup>250</sup> Finally, the escape depth for UV and visible light photons depends on the specimen's absorption coefficient at the energies of those photons. In the directions perpendicular to the electron beam path, signals are not necessarily generated only from within the beam diameter. Due to multiple scattering and beam broadening, signals with a greater escape depth tend to be emitted from a wider area. Therefore, characterisation techniques performed in EMs often do not have the same spatial resolution even when the relevant signals are collected simultaneously. This is particularly true for SEMs, while in TEMs the broadening effect is not as strong due to the limited sample thickness.

## 3.2. Transmission Electron Microscope

The invention of TEM was motivated by optical microscopy's inability to resolve things smaller than the wavelength of visible light (0.4–0.7 μm). The path towards nanoscale imaging was opened in 1924 when de Broglie hypothesised that all matter possess wave-like behaviour in accordance with the particle-wave duality.<sup>251</sup> After the first TEM (Figure 3.3a) was completed in 1932 by Knoll and Ruska<sup>252</sup>, TEMs eclipsed optical microscopes in spatial resolution in 1933 and from the 1940s onwards they have become more common in science laboratories. Modern TEMs can now reach sub-Å spatial resolution, four orders of magnitude greater than conventional optical microscopes.<sup>253,254</sup> They are better described as a comprehensive characterisation tool than merely an imaging device, capable of revealing a specimen's crystallography, 3D nanostructure, elemental distribution, chemical bonding, and various optical, electronic, and magnetic properties.

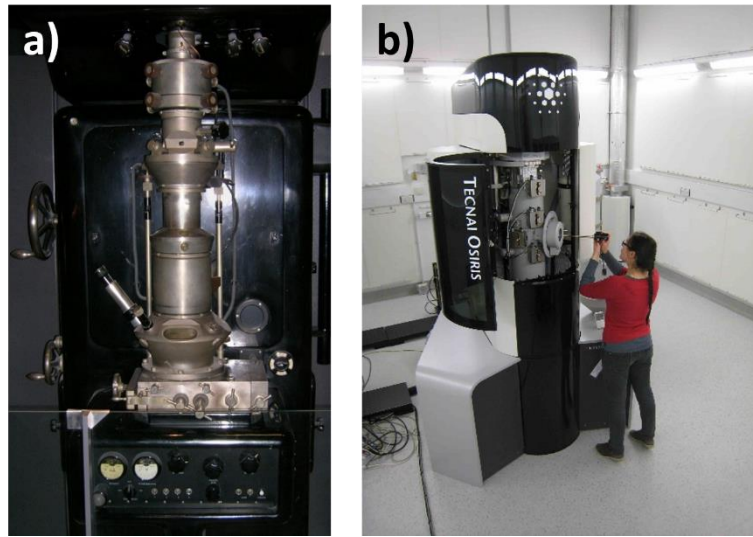


Figure 3.3 | (a) Knoll and Ruska's TEM<sup>255</sup> and (b) FEI Tecnai Osiris 80-200 FEGTEM installed in the Wolfson Electron Microscopy Suite, Department of Materials Science & Metallurgy, University of Cambridge. This is the instrument used to produce all TEM data presented in this thesis.<sup>256</sup>

These capabilities are engendered by the development of many enabling technologies: electron guns, magnetic lenses, sample holders, signal detectors, vacuum system, and other auxiliary parts. In particular, the invention of ultrabright field emission electron guns (FEGs), aberration correctors, direct electron detectors, and X-ray Si drift detectors (SDDs) have contributed much to TEM development. Most TEMs have now shifted from thermionic electron sources to FEGs with a triode system. The first anode provides the extraction voltage required to induce electron tunnelling from the cathode. These electrons are subsequently accelerated by the second anode to obtain a shorter wavelength. These two anodes focus the electron beam on a crossover point, which then becomes the virtual electron source. A FEG consists of a very sharp tip to produce higher current density and brightness ( $\beta$ ), which is defined as the emitted current density per unit solid angle of the electron source.<sup>243</sup> Depending on whether the cathode tip is heated or kept at room temperature, FEGs are classified into Schottky (thermally-assisted) FEGs and cold FEGs. Schottky FEGs are heated at about 1700 K to assist the electron emission process and keep the cathode surface pristine, making the emission more stable over time. Cold FEGs are not heated and requires a higher vacuum to keep its surface clean, but it produces a brighter, more monochromatic, and more coherent beam. The brightness of FEGs is around  $10^{12}$  and  $10^{13}$  A/m<sup>2</sup>sr for Schottky and cold FEGs, respectively, allowing the use of a tightly focused electron beam to obtain better spatial resolution while still producing sufficiently high signal.<sup>243</sup> The FEI Tecnai Osiris 80-200 FEGTEM used in this thesis (Figure 3.3b) uses a high-brightness Schottky FEG design named X-FEG by FEI, which combines a brightness level equal to cold FEGs ( $\beta = 2.6 \times 10^{13}$  A/m<sup>2</sup>sr) and the emission stability of a Schottky FEG.<sup>257</sup>

TEMs use electromagnetic lenses to shape the electron beam and to form images and diffraction patterns (DPs) (Figure 3.4). The gun crossover is firstly either demagnified or magnified by the first condenser (C1) lens, depending on the desired illumination area, into the C1 crossover. This new crossover is focused by the second condenser (C2) lens on the front focal plane of the upper objective lens (sometimes called C3 lens) to create a parallel beam on the specimen plane. The C2 lens is equipped with an associated aperture which may be used to control the beam current. After the beam has passed through the specimen, the lower objective lens forms the images and DPs and passes them on to the projector lenses to be magnified. If an image is desired, an objective aperture may be used on the back focal plane of the lower objective lens. If obtaining a DP is the goal, a selected area diffraction aperture must be inserted on the image plane of the lower objective lens. Finally, the image or DP is projected onto a screen or detector to be viewed and recorded. All the aforementioned lenses suffer from some degree of spherical aberration, chromatic aberration, and astigmatism, which lower the spatial resolution but can be ameliorated by specialised lenses called stigmators and aberration correctors. In addition, a TEM's imaging system is equipped with beam deflectors/scanning coils and drift correctors.

Several types of electron detectors are used to record images and diffraction patterns in a TEM. Older TEMs use a fluorescent screen and photographic films based on gelatin and silver halide, but these are rarely used nowadays. Most modern TEMs use charge-coupled device (CCD) or complementary metal-oxide-semiconductor (CMOS) cameras as electronic detectors. In both detector types, electrons are firstly converted into photons in a scintillator layer. These photons are then transferred to the CCD or CMOS sensor through fibre optics. The advantages of a CMOS over a CCD sensor are its faster readout speed and higher resistance to blooming, a phenomenon where the charge from an oversaturated pixel overflows into neighbouring pixels.<sup>258</sup> CCD and CMOS sensors are considered indirect detectors due to the scintillation step. This conversion reduces the detector's quantum efficiency (ratio of detected signal over emitted signal) and blurs the image due to multiple scattering in the scintillator layer. However, it is necessary as the capacitors forming the CCD/CMOS array are easily damaged by the high-energy electrons. More recently, direct electron detectors with a quantum efficiency approaching unity have been successfully used in TEMs.<sup>259</sup> These detectors use either wide and thick pixels or radiation-hardened CMOS, enabling them to withstand direct exposure to the electron beam.

In TEM imaging, a broad, parallel electron beam is incident on the sample. While passing through the sample, the probe beam is separated into a direct beam consisting of unscattered coherent electrons, and elastically scattered electrons which are either coherent or incoherent, depending on the scattering angle. Image contrast, defined as the intensity difference between two areas, is formed through one or a combination of three possible mechanisms: mass-thickness, diffraction, and phase contrasts.<sup>243</sup> In mass-thickness contrast, denser or thicker parts of the specimen deflect electrons at a greater angle due to multiple Rutherford scattering. Diffraction contrast works in crystalline samples according to Bragg's law, with electrons diffracting away from the optic axis when they scatter on crystal planes at specific

angles (Bragg angles) which depend on the electrons' energy. Both mass-thickness and diffraction contrasts may contribute to bright field (BF) or dark field (DF) images. BF images are formed by allowing only the direct beam to pass through the objective aperture. Consequently, features which are denser, thicker, or diffracting appear dark (Figure 3.5a) and, if the sample is crystalline, the final image is governed by both contrast mechanisms. In contrast, DF images can be set up such that it is dictated by one contrast mechanism only. Placing the objective aperture on a diffracted beam or part of a diffraction ring favours diffraction contrast (Figure 3.5b). On the other hand, mass-thickness contrast dominates when the objective aperture is placed anywhere else, but especially at large deflection angles where Bragg scattering is generally negligible ( $>5^\circ$ ,  $>87$  mrad).<sup>243</sup> Finally, phase contrast emerges when more than one beam is used to form an image through interference of the direct beam and one or more diffracted beams. Phase contrast is closely associated with high resolution TEM as it is capable of achieving very high spatial resolution.

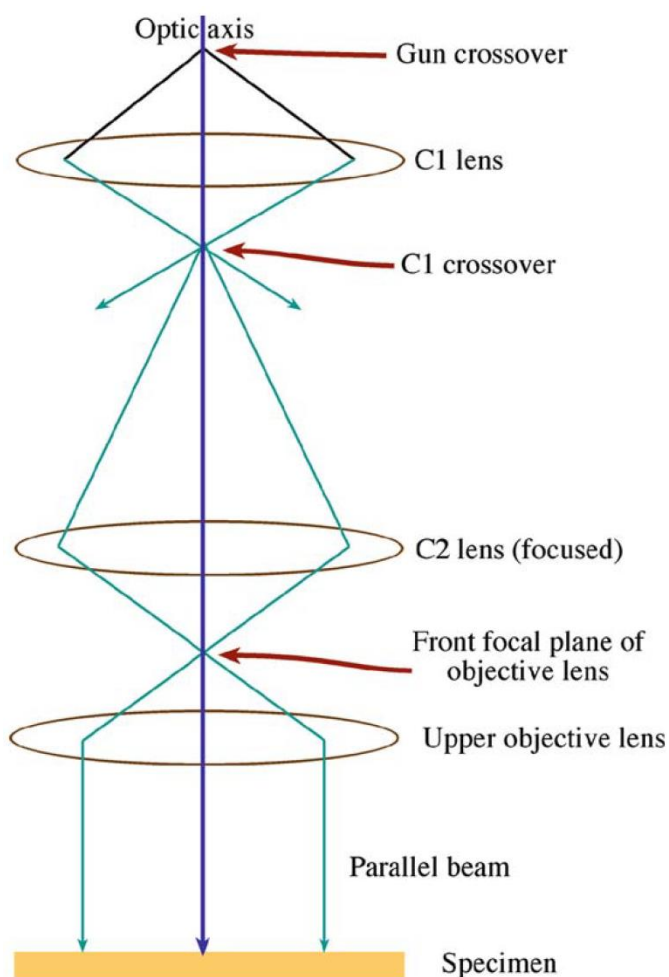


Figure 3.4 | The beam-shaping portion of a TEM column when operated in parallel beam mode. Electromagnetic lenses direct the electron probe to obtain a parallel beam on the specimen plane. Reproduced from ref.<sup>243</sup> with permission, copyright 2009 Springer.

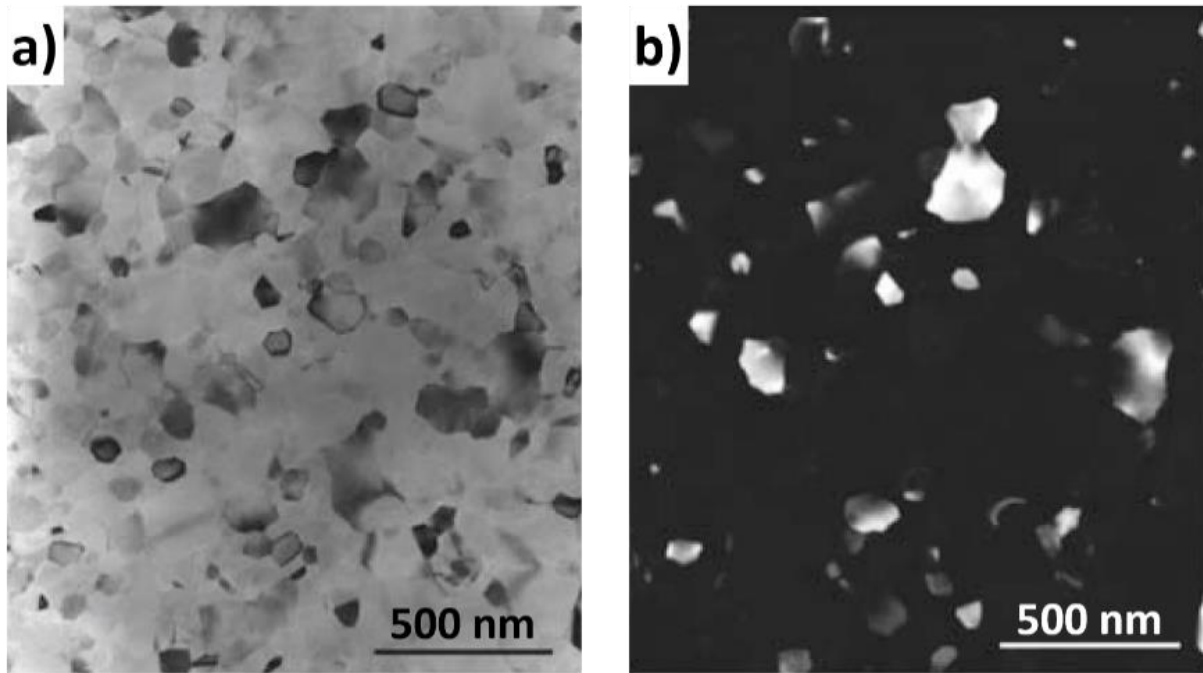


Figure 3.5 | (a) Bright field image of a polycrystalline aluminium film. (b) Dark field image constructed by selecting the {220} diffraction spots, showing all grains contributing to those spots. Reproduced from ref.<sup>243</sup> with permission, copyright 2009 Springer.

### 3.3. Scanning Transmission Electron Microscope

Whereas TEM uses an electron beam with a planar wavefront to image the specimen in a parallel manner, STEM uses the upper objective (C3) lens to focus an electron probe on the specimen plane and scanning coils to raster it across the specimen (Figure 3.6a). The electron probe spends a set amount of time at each scan position, called the dwell time, to generate signals. Signals emanating from the cylinder/cone-shaped interaction volume at each probe position are detected and mapped into a square pixel corresponding to that beam position.

The spatial resolution of images and maps acquired with STEM is determined by the larger quantity between  $d_{eff}$  and the set pixel dimension. Ideally, both parameters should have approximately the same value (Figure 3.7a). If the pixel dimension is far larger than  $d_{eff}$ , then much of the sample area is not probed by the electron beam and the representativeness of the collected data is reduced. This situation is called undersampling (Figure 3.7b). The opposite is oversampling, where  $d_{eff}$  is larger than the pixel size (Figure 3.7c). In this case, each pixel would contain some information which is also collected in the adjacent pixels (crosstalk) and some blurring will be observed in the images/maps. In particular, oversampling should be avoided when working on specimens which are easily damaged by the electron beam as it leads to parts of the specimen being scanned multiple times.

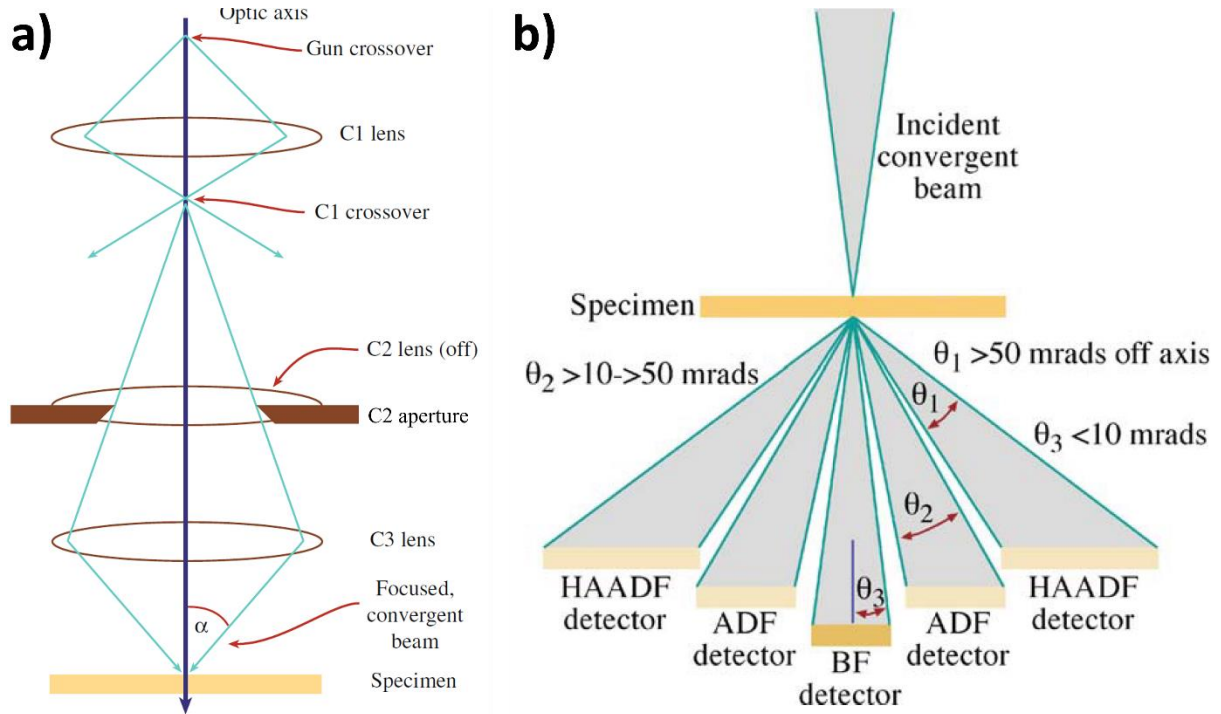


Figure 3.6 | (a) Ray diagram of a TEM operating in STEM mode. (b) Various detectors used in STEM imaging and their subtended detection angles. Reproduced from ref.<sup>243</sup> with permission, copyright 2009 Springer.

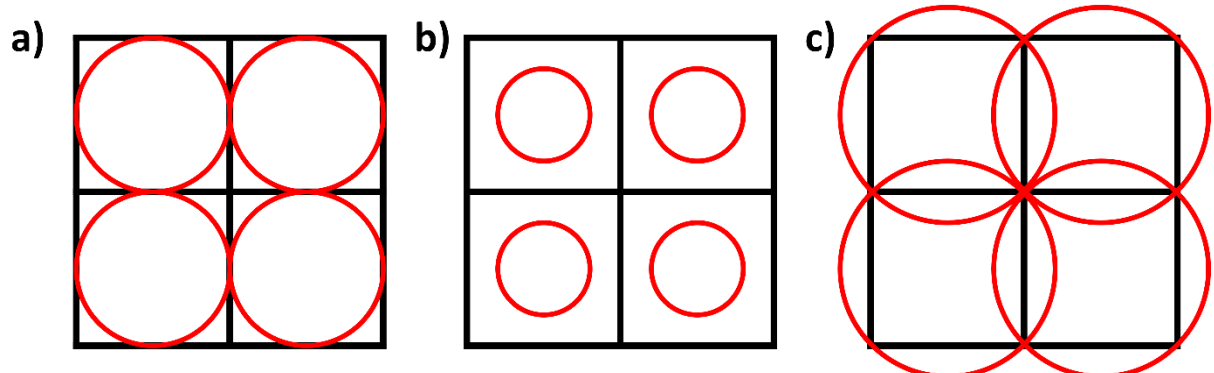


Figure 3.7 | Illustration of (a) exact sampling, (b) undersampling, and (c) oversampling conditions in STEM data acquisition. Squares represent pixels while circles represent  $d_{eff}$  of the electron beam.

STEM is also capable of forming BF and DF images, but using detectors placed at the desired detection angles rather than an objective aperture (Figure 3.6b). While the shape of an aperture is necessarily a hole, a detector can theoretically be of any shape. This advantage is exploited in high-angle annular dark field (HAADF) imaging. A HAADF detector is a large annulus around the optic axis, such that it detects electrons elastically deflected from  $\theta \sim 50$  mrad ( $\sim 3^\circ$ ) to  $\theta = 150 - 300$  mrad ( $\sim 9 - 18^\circ$ ), with the

precise subtended detection angle range determined by the microscope's camera length.<sup>243</sup> Electrons must have travelled very close to the specimen nucleus to be scattered at this angular range (Figure 3.1b), hence the detected signal is especially sensitive to Z. Consequently, heavier elements appear brighter in a HAADF image. Furthermore, many scattered wavevectors get simultaneously collected and integrated, thus any phase relationship between each wavevector is averaged out.<sup>260</sup> Owing to this phase incoherency, the contrast in HAADF images is not sensitive to diffraction contrast and crystallographic orientation of the specimen.<sup>261,262</sup> Further, incoherency also causes the monotonic dependence of STEM's contrast transfer function (CTF) on defocus (Figure 3.8a), freeing HAADF images from contrast reversals and extending the resolution to higher spatial frequencies.<sup>263,264</sup> Finally, signal incoherence means the intensity ( $I$ ) of detected signal is proportional to the number of atoms, or equivalently specimen thickness  $t$ , thus approximately  $I \propto tZ^{1.8}$ .<sup>260</sup> HAADF images' sole dependence on chemical composition and specimen thickness makes them simple to intuitively understand and interpret, an advantage compared to high resolution TEM imaging.

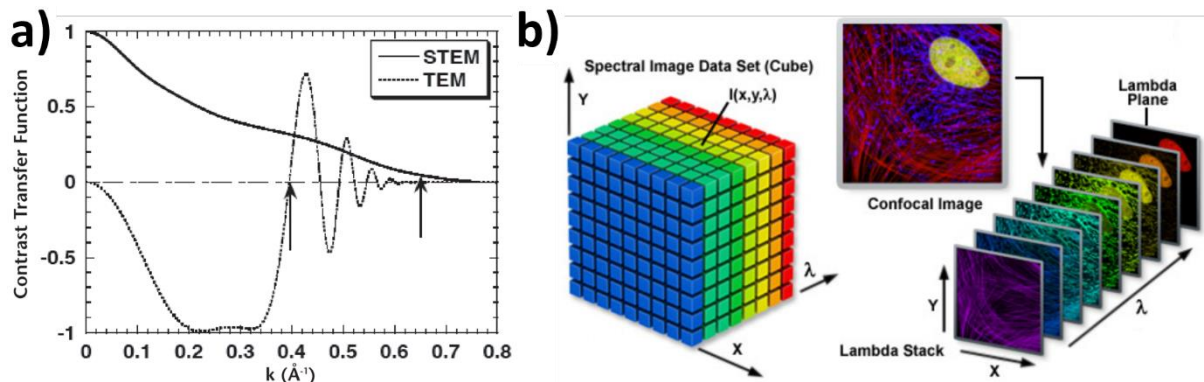


Figure 3.8 | (a) Calculated CTF of a FEI Tecnai F20 SuperTWIN operated in parallel beam TEM mode (dotted curve) and in STEM mode (solid curve). The CTF of a STEM is always positive, while the CTF of a TEM goes through sign reversals as the spatial frequency changes.<sup>264</sup> (b) Illustration of an SI data cube and its component images.<sup>265</sup>

Most importantly from an analytical perspective, STEM allows operators to obtain spectrum images (SIs). An SI is a 3D data cube where two of the axes (navigation axes) correspond to a two-dimensional region of interest on the specimen while the other (signal axis) represents an acquired data spectrum from each spot (Figure 3.8b). As the probe scans through the 2D area, an energy spectrum or other types of data is obtained and associated with a corresponding pixel. Afterwards, this data cube can be sliced according to the operator's needs, for example to look at an averaged spectrum from a particular area or to create an image formed solely by elastically scattered electrons. It can also be subjected to advanced data processing algorithms to increase the signal-to-noise ratio (SNR) and ease analysis.

Assuming the scanned area is composed of square pixels, an SI has two resolutions: a spatial resolution on the navigation axes and a spectral resolution on the signal axis. The values of these two resolutions are independent of one another and can be modified separately during data processing. For example, spatial rebinning sums the spectra from neighbouring pixels into a single spectrum associated to one pixel while spectral rebinning sums the signal counts from adjacent channels of the spectra into one channel. The former reduces spatial resolution and the latter reduces spectral resolution, but both are sometimes performed to increase signal counts and SNR.

### 3.4. Scanning Electron Microscope

An SEM is a characterisation instrument capable of specimen imaging, compositional mapping, and crystal orientation mapping using a scanned focused electron beam as a probe. In an SEM, the specimens used are bulk rather than thin and electron transparent. Therefore, only signals generated in the backward direction can be detected and these can only come, at most, from the top few  $\mu\text{m}$  of the specimen surface due to the escape depth limitations discussed in Section 3.1. The probe-forming part of an SEM is similar to that of a STEM, except in SEMs the acceleration voltages used are lower (1–30 kV). The beam is generated in a thermionic or FEG source, shaped by condenser lenses and apertures, focused by the objective lens and stigmators, and rastered along the specimen surface by scanning coils. In most SEMs, the signal detectors are placed above the specimen due to the anisotropic signal generation. However, some SEMs are fitted with a specialised sample stage and bottom-mounted detectors which allow it to perform STEM imaging with a 20–30 kV beam and thin specimens.<sup>266</sup>

SEM imaging is performed by collecting the SEs and BSEs generated at each raster position. Due to their differing generation mechanisms, the SE/BSE yield per incident electron is influenced by different specimen properties. The SE yield is highly sensitive to specimen topography due to their shallow escape depth. Furthermore, as SE generation involves stripping an electron away from the specimen, it is influenced by the specimen's work function.<sup>267</sup> Meanwhile, the BSE yield is determined by atomic number and topography as explained in Section 3.1. In addition, BSE can reveal crystallographic information when they are diffracted by lattice planes in the specimen. Therefore, the contrast in SE and BSE images carry information about the relevant properties. The key here is to selectively collect only SEs or BSEs, such that the contrast can be more accurately interpreted. This can be done using the large difference in kinetic energy between SEs (<50 eV) and BSEs (up to the primary electrons' energy).

The classic detector design used in SEMs is a scintillator surrounded by a Faraday cage, called an Everhart-Thornley detector (ETD, Figure 3.9a). An electron striking the scintillator creates a pulse of light which is directed via a light guide into a photomultiplier tube, where the light pulse is converted into an electrical charge and measured. ETDs sit to one side of the sample, so the signal collection has

a directional preference and features facing the ETD appear brighter regardless of whether they are formed by SEs or BSEs.<sup>267</sup> Thus, the image appears as if the specimen is being viewed from the direction of the electron gun while it is illuminated from the direction of the detector (Figure 3.10a), a situation sometimes called light-optical analogy.<sup>267</sup> To acquire SE images, the Faraday cage is positively biased by a few hundred volts to accelerate SEs towards the detector, even those which were emitted in the opposite direction. However, this does not fully compensate for the directional collection as the positive bias cannot be set too high to avoid any effect on the primary beam. The formed image is composed of mostly SEs and some BSEs which were emitted towards the detector's solid angle.

The interpretation of SE images can be complicated by the need to distinguish between genuine specimen topography and the artificial contrast created by the position of the ETD. This problem can be solved if the emitted electrons can be guided firstly in the direction of the gun and then towards a detector (Figure 3.9b, 3.10b). In practice, this can be done by using a strongly excited objective lens such that the magnetic field is projected into the specimen chamber. This magnetic field draws emitted SEs along the optic axis and through the objective lens, where they are then attracted sideways towards an ETD placed above the lens. This detector design is called an InLens or through-the-lens detector (TLD) depending on the SEM manufacturer (Figure 3.9b).

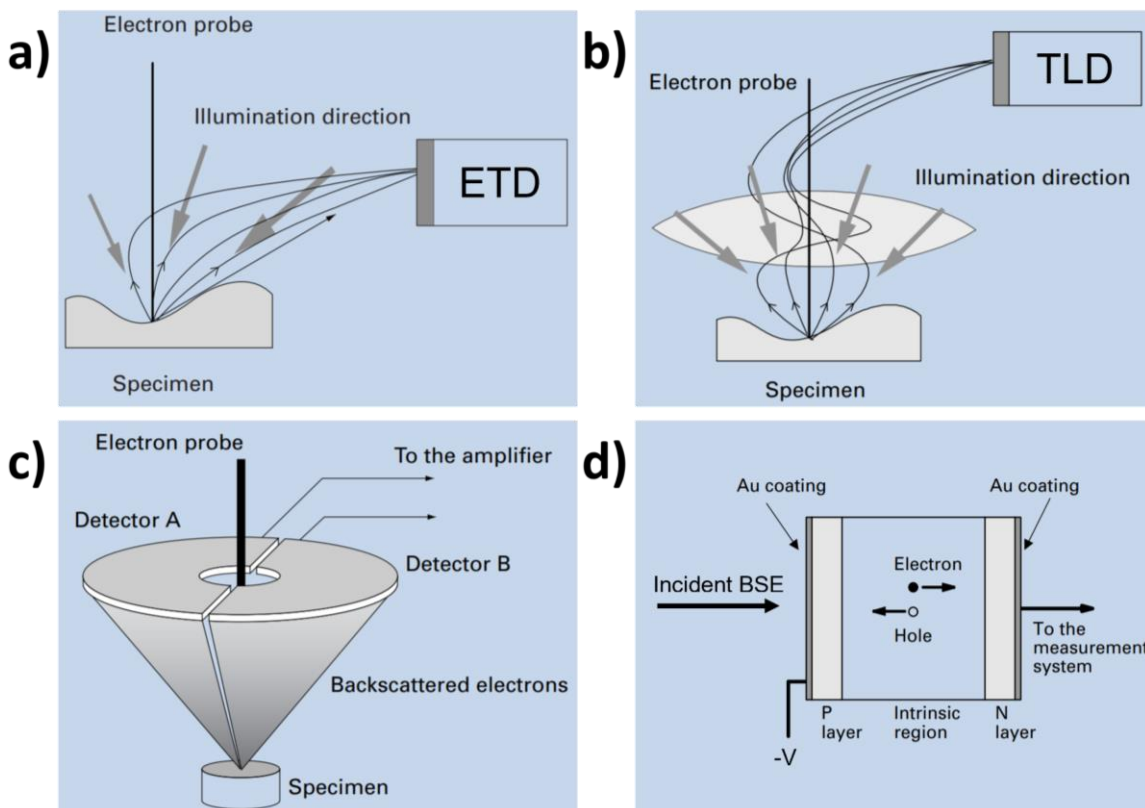


Figure 3.9 | Illustration of various SEM detectors: (a) an ETD, (b) a TLD, (c) a segmented BSE detector, and (d) a cross-sectional schematic of the BSE detector shown in (c).<sup>268</sup>

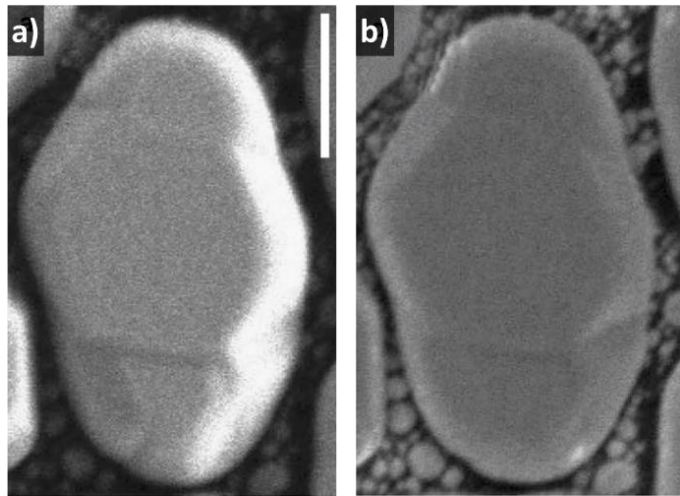


Figure 3.10 | SE images of an Au/C sample acquired using an (a) ETD and a (b) TLD. The right side of the Au grain appears bright while the left side appears dark in panel (a) because of the ETD's directionality. Both sides appear bright in panel (b), showing their true topography. The scale bar represents 300 nm. Reproduced from ref.<sup>269</sup> with permission, copyright 2016 Microscopy Society of America.

BSE images can be formed using a negatively biased ETD to deflect low-energy SEs and allow only high-energy BSEs emitted towards it to pass through. However, the negative bias also exacerbates the directional collection problem and the compositional contrast from the BSEs is mixed with the artificial topography contrast. A preferable alternative is to use a segmented, reverse-biased Si semiconductor covered by electrodes and placed just below the objective lens, with an annulus in the middle to allow the electron beam to pass through (Figure 3.9c). BSEs entering the detector uses its energy to excite EHPs which are collected by the reverse bias, converted to a voltage, amplified, and measured (Figure 3.9d). Incoming electrons need to have an energy of at least ~1 keV to penetrate through the surface electrode and be detected, so SEs are automatically excluded. Its flat and thin form allow the segments to be placed all around the optic axis rather than just to one side like an ETD. The signal recorded by each segment can be used to form images separately to obtain apparent illumination from a specific direction, summed together to suppress topographical contrast, or subtracted from the other to amplify the apparent illumination effect.<sup>267</sup>

The electron beam has a much larger interaction volume in SEMs compared to TEMs because of the bulk nature of SEM specimens and the low acceleration voltages used. Meanwhile, the beam broadening calculation shown in Equations 3.4–3.6 are invalid for cases where each electron experiences  $\gg 1$  scattering events.<sup>270</sup> Therefore, an alternative method is required to predict the interaction volume size in SEM. One such method is the Kanaya-Okayama range ( $R_{K-O}$ ), an empirical equation showing the radius of a hemisphere-shaped interaction volume containing 95% of electron trajectories in the

specimen.<sup>271</sup> The formula is shown in Equation 3.7, where  $R_{K-O}$  is in nm,  $A$  is atomic mass in g/mol, and  $\rho$  is density in g/cm<sup>3</sup>. Another option is to run Monte Carlo simulations of thousands of electron paths in solids based on theoretical scattering cross-sections and repeated random sampling (Figure 3.11). Several programs are freely available to perform such simulations. The most popular among these is CASINO, which is capable of simulating electron paths, calculating BSE yield, showing the volumes of probe energy deposition, and showing where visible light and X-ray photons are generated in the specimen. The physical models incorporated in CASINO and similar software are valid for beam acceleration voltages of 0.1–30 kV, making it a perfect match for SEM.

$$R_{K-O} = 27.6 \left( \frac{A}{Z^{0.89} \rho} \right) E_0^{1.67} \quad (\text{Equation 3.7})$$

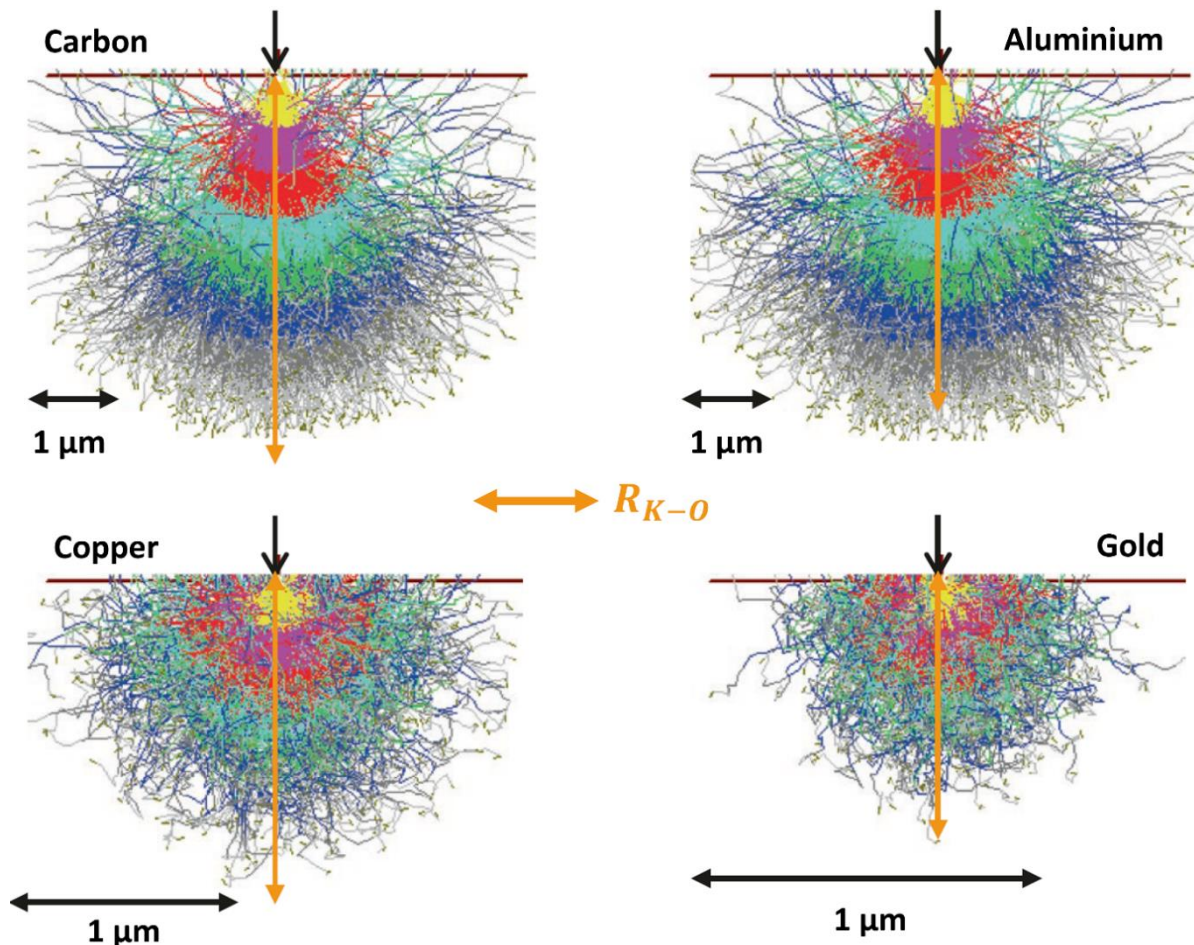


Figure 3.11 | Simulated electron scattering paths in C, Al, Cu, and Au samples. The simulated electron beam has an accelerating voltage of 20 kV. The gold arrow in each sample marks  $R_{K-O}$  as calculated with Equation 3.7. Note the unique scale bar used for each sample. Reproduced from ref. <sup>267</sup> with permission, copyright 2018 Springer.

### 3.5. Energy-dispersive X-ray Spectroscopy

When inelastic scattering occurs between a probe electron and an inner shell specimen electron, the probe electron transfers some of its energy to excite the specimen electron. The vacated low-energy state will be filled by a higher-energy electron, releasing an X-ray photon whose energy is the difference between the two states (Figure 3.12a). As each element has its own set of energy levels, the emitted photon energy is characteristic to the element as well. EDX detects these characteristic X-rays and use them for elemental identification, mapping, and quantification. EDX can be performed in an SEM, a TEM, or a STEM. It is common practice to use the microscope type as a prefix to discriminate between them (SEM-EDX, TEM-EDX, and STEM-EDX). The latter is the primary characterisation method used in all works presented in this thesis.

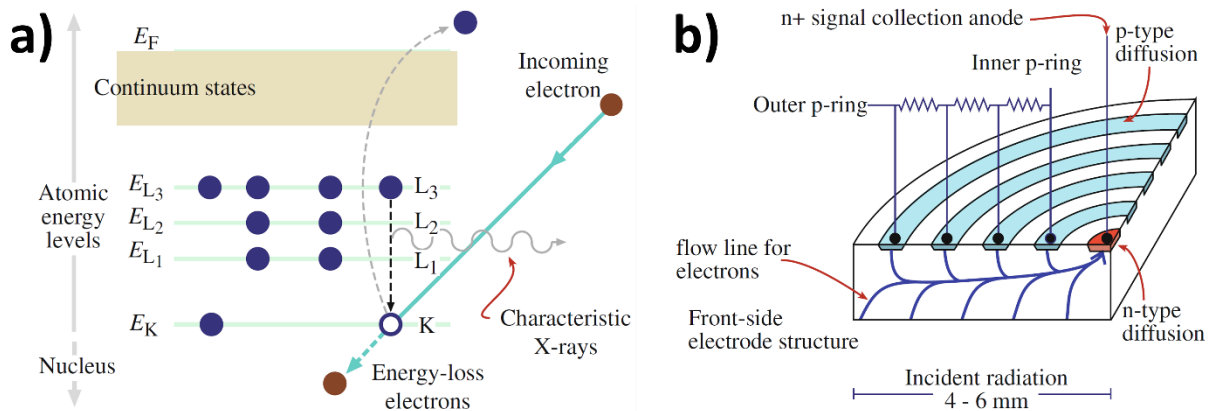


Figure 3.12 | (a) Energy diagram showing generation of characteristic X-ray photons through inelastic scattering of a probe electron by a specimen electron. (b) Cross-sectional schematic of an SDD EDX detector. Reproduced from ref.<sup>243</sup> with permission, copyright 2009 Springer.

An EDX detector works by converting incident photons into electrical current using a Si semiconductor. There are two major types of EDX detectors, Si(Li) – so-called because the primary component is Li-doped Si – and SDDs. Both types have the same working principle, namely a reverse-biased p-i-n junction containing an extended depletion region where X-rays are absorbed to generate EHPs. Compared to Si(Li) detectors, the concentric drift electrode design used in SDDs allow them to collect EHPs with a lower bias and higher throughput (Figure 3.12b). In addition, SDDs benefit from advancements in Si wafer fabrication which have largely removed the need for Li doping and liquid N<sub>2</sub> cooling. X-rays of different energies will excite different numbers of EHPs within the Si crystal, thus different amounts of charge. This charge pulse is converted to a voltage and amplified using a field effect transistor, measured, then used to discriminate the incoming X-ray photons based on their energy,

hence the name of this technique.<sup>272</sup> Regardless of the detector type used, two significant limitations of EDX are its poor spectral resolution ( $\sim 130$  eV as defined by the FWHM of the Mn-K $\alpha$  peak) and low reliability in light element detection. H and He are physically incapable of producing X-rays while elements between Li ( $Z = 3$ ) and Ne ( $Z = 10$ ) have low X-ray fluorescence yields.<sup>273</sup>

An EDX spectrum consists of characteristic elemental peaks superimposed on a continuous bremsstrahlung background. Qualitative and quantitative analysis of this spectrum needs to be carefully done as there can be artefacts in it, such as escape, sum, and internal fluorescence peaks, spurious X-rays, and system X-rays.<sup>243</sup> The first three peaks are caused by the detection system and easily identifiable. Spurious X-rays come from parts of the specimen not being probed, while system X-rays are emitted by parts of the microscope or sample holder. For example, the most prevalent system X-ray peaks are Cu-K $\alpha$ , Cu-K $\beta$ , and Cu-L $\alpha$  peaks from the TEM sample grid. In addition to these artefact peaks, the characteristic peaks may also overlap such that they must be resolved through deconvolution algorithms or careful model fitting.

In EDX, the background-corrected peak intensity ( $I$ ) for a characteristic X-ray line is assumed to be related to the number of atoms of the corresponding element present in the specimen. For an EDX peak to be detectable at a 99% confidence interval,  $I$  must be at least equal to three times the square root of the background level ( $B$ ),  $I \geq 3\sqrt{B}$ .<sup>243,274</sup>  $B$  is usually determined by fitting it to a polynomial function or by taking the average signal count from two peak-less energy windows just before and after a peak. Furthermore, because emission of X-ray photons under electron irradiation occurs randomly over time, the detected EDX signal's standard deviation ( $\sigma$ ) is given by  $\sigma = \sqrt{I}$  according to Poissonian statistics.<sup>243</sup> Therefore, the measurement uncertainty as a percentage of the detected signal can be expressed as  $100\%/\sqrt{I}$ . The conclusion from these equations is that the signal count must be maximised both to achieve detectability and to minimise uncertainty. This can be achieved through several methods. The first is to use an EDX detector that covers the largest possible collection solid angle around the specimen. Si(Li) detectors subtends only about 0.1–0.3 sr, but more advanced SDDs can cover about 0.7–0.9 sr (because X-ray photons are generated isotropically, the emission solid angle is  $4\pi$  sr). The second is to use a thicker sample to increase the number of inelastic scattering events and thus emit more X-ray photons. While this is easy to implement, it reduces spatial resolution due to beam broadening inside the specimen as discussed in Section 3.1. Furthermore, the specimen thickness cannot be increased indefinitely as eventually it will no longer be electron transparent. Finally, the third method is to increase electron dose (number of probe electrons per unit area of specimen) by prolonging dwell time or increasing beam current. However, a higher dose will aggravate beam-induced specimen damage in sensitive specimens, such as the OIHPs investigated in this thesis.

Elemental quantification based on STEM-EDX data is most commonly performed using the Cliff-Lorimer Ratio method.<sup>275</sup> Briefly, the relative abundances of elements A and B,  $C_A$  and  $C_B$ , are

proportional to their background-corrected EDX peak intensities  $I_A$  and  $I_B$  according to Equation 3.8, where  $k_{AB}$  is the Cliff-Lorimer factor or k-factor between A and B. The value of  $C_A$  and  $C_B$  can then be calculated since in a binary system, the sum of  $C_A$  and  $C_B$  is 1. This procedure is extendable to complex systems containing many elements, making it a simple and versatile method for EDX quantification. Although each pair of elements has their own k-factor, these k-factors are all related to one another (Equation 3.9). Therefore, the quantification process can be simplified by defining all k-factors against one arbitrary element. The adopted convention is to use Si, therefore the value of  $k_{Si}$  is defined as 1 and only one k-factor is needed for each of the other elements.

$$\frac{C_A}{C_B} = k_{AB} \frac{I_A}{I_B} \quad (\text{Equation 3.8})$$

$$k_{AB} = \frac{k_{AC}}{k_{BC}} \quad (\text{Equation 3.9})$$

The k-factors can be calculated based on electron-matter scattering models or calibrated using standards. To calculate the k-factors, one needs the ionisation cross-section and X-ray fluorescence yield for all elements of interest, plus the relative transition probability and detector efficiency for all X-ray peaks of interest. Many of these required variables are unknown, so it is not surprising that a comparison of calculated k-factors in literature has found significant discrepancies (generally about  $\pm 10\text{--}20\%$ , up to 60% in some cases).<sup>243</sup> Experimental determination of k-factors should theoretically provide relatively more accurate results, but published values also differ by  $\pm 10\text{--}20\%$ .<sup>243</sup> In practice, obtaining k-factors experimentally is extremely challenging as it requires standards whose compositions are already known to a high accuracy, can be thinned to electron transparency without any compositional changes, and stable under the electron beam. Furthermore, for relatively thick specimens such as the perovskite device cross-sections investigated in this thesis, a sizeable portion of the low-energy (<2 keV) X-ray photons will likely be absorbed in the specimen.<sup>276</sup> Therefore, the calibration standard should mimic the specimen of interest's scattering environment to obtain accurate k-factors with the absorption effect accounted for. Given the complex composition of multi-ion perovskites and the number of elements involved in the other device layers, this approach is not feasible.

An alternative to the Cliff-Lorimer method is the  $\zeta$ -factor method proposed by Watanabe and Williams in 2006.<sup>277</sup> The  $\zeta$ -factor method replaces the need for multielement standards with pure element standards. However, the relevant pure element standards for perovskite-forming elements are either impossible or difficult to find. At room temperature and pressure, N and Br are not solid, I is solid but spontaneously sublimates into a toxic and corrosive vapour, while Pb rapidly forms a surface oxide

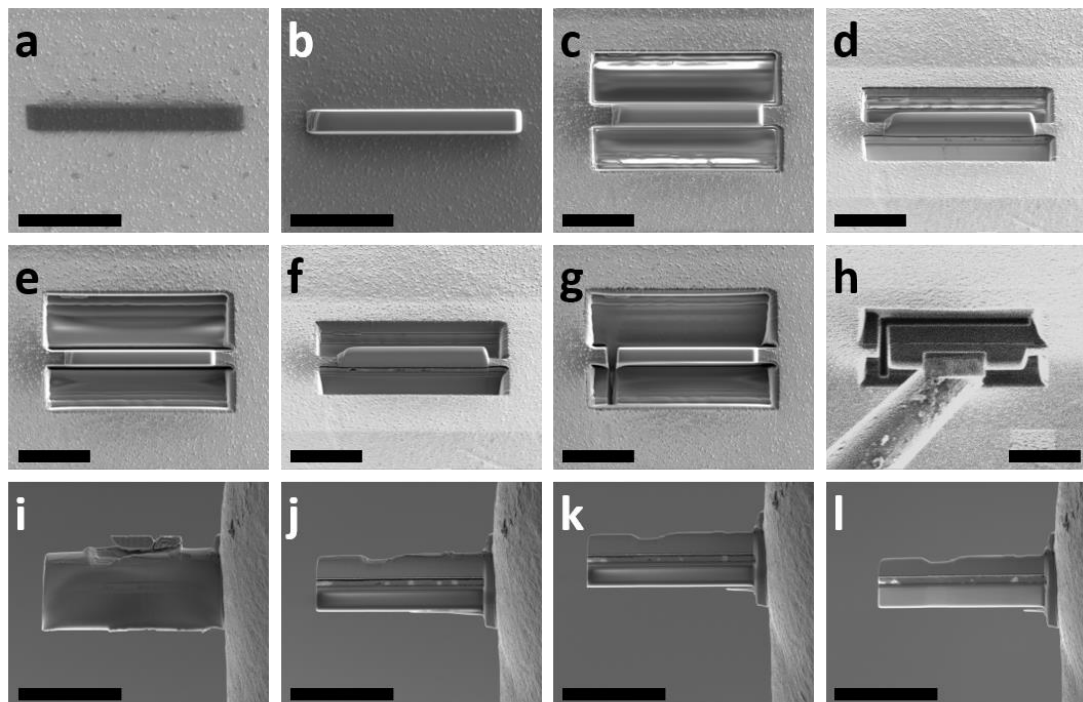
layer upon exposure to air.<sup>278–282</sup> Some calculated  $\zeta$ -factors are available in the literature, but they are limited only to the K-shell X-ray lines of elements from  $Z = 7$  (N) to  $Z = 42$  (Mo) due to the absence of a suitable standard for L-shell lines.<sup>243,277</sup> Therefore, the  $\zeta$ -factors for systems containing elements quantified based on their L-shell lines, including Pb and I, are unavailable. Because of these reasons, the Cliff-Lorimer method is still by far the more popular procedure up until the time of writing.

### 3.6. Focused Ion Beam Milling

FIB milling is the standard method used to prepare cross-sectional (S)TEM specimens from multi-layered composite structures such as PSCs. The final specimen is called a lamella, which is a thin, electron-transparent slice of the bulk sample. Conventional FIB millers use a focused  $\text{Ga}^+$  beam to mill specimens due to their relatively large atomic mass and low melting point, although recently other ion sources such as Xe, Ar, O, and Ne have been gaining prominence for faster milling and fewer sample artefacts.<sup>283</sup> Electromagnetic lenses and apertures shape the ion probe and scanning coils control its position on the specimen. The ion gun can be operated at low voltage and current for imaging (by detecting SEs or ions) or at high voltage (~5–30 keV) for material milling. In this work, the latter application is used to produce cross-sectional lamellae of PSCs. Modern FIB millers are conventionally operated in tandem with an SEM and its electron imaging system. The electron gun and the ion source are put at an angle to one another, allowing selection and visualisation of the region of interest with the less destructive electron beam as it is being milled by the  $\text{Ga}^+$  beam. FIB millers used for lamella preparation are often equipped with a gas injection system (GIS) and a micromanipulator. The GIS allows deposition of C, W, or Pt from organometallic precursors to protect the region of interest from ion-beam induced damage during milling. These layers are deposited by breaking the precursor molecules with the electron or ion beam, therefore in practice the non-C layers often contain C as well. The micromanipulator is used to transfer the milled lamella from its original position onto TEM grids, where it is welded using Pt-C from the GIS, in a technique known as *in situ* lift-out.<sup>284</sup>

Recipes for lamella preparation are often adapted from each FIB manufacturer's instructions. In this work, the procedure is based on FEI's protocol as shown in Figure 3.13.<sup>285</sup> First, two layers of Pt-C is deposited on the area of interest to protect it from the ion beam. The first layer is deposited with an electron beam to ensure minimum damage to the sample surface (Figure 3.13a) and the second with a  $\text{Ga}^+$  beam (Figure 3.13b). Then, a pair of trenches are milled surrounding the area of interest (Figure 3.13c-d). Once the trenches are deeper than all regions of interest in the lamella, the lamella surfaces are “cleaned” using line-by-line milling (Figure 3.13e-f) to remove any milled material which might have been redeposited there. The next steps are to cut the lamella from the bulk specimen on two sides (Figure 3.13g), welding it to the micromanipulator with Pt-C (Figure 3.13h), and cutting the remaining

connection between the lamella and bulk specimen. The lamella is then brought to the TEM grid, welded there (Figure 3.13i), and the lamella-micromanipulator connection is milled away. Finally, the lamella is thinned to the desired thickness with multiple rounds of milling, each round using a lower ion beam current than the previous one and performed at a specific stage tilt to minimise damage and to obtain a uniform lamella thickness (Figure 3.13j-l).



Step	Figure	Description
1	a	Platinum deposition with electron beam (200 nm thickness)
2	b	Platinum deposition with ion beam (2 µm thickness)
3	c,d	Trench milling (c = stage tilt 0°, d = stage tilt 52°)
4	e,f	Lamella surface cleaning (e = stage tilt 0°, f = stage tilt 52°)
5	g	Lamella cutting from sample bulk
6	h	Attachment to micromanipulator
7	i	Attachment to TEM sample half-grid
8	j	Thinning to 1000 nm
9	k	Thinning to 500 nm
10	l	Thinning to 200 nm

Figure 3.13 | Procedure to cut an electron-transparent, cross-sectional PSC lamella with a FIB miller. Scale bars represent 10 µm.

FIB milling can introduce several artefacts to the sample, such as preferential milling, amorphisation, redeposition of milled atoms,  $\text{Ga}^+$  ion implantation, and contamination of the sample with the protective/welding material. The latter three are generally not a problem for PSC lamellae as the cells' metal back contact layer is dense and thick enough to prevent deposition of foreign atoms in the perovskite layer. Preferential milling can be minimised by carefully following the recommended milling procedure. Some amorphisation is often observed in detailed experimental investigations, and this issue is further discussed in Chapter 4.<sup>286</sup>

### 3.7. STEM Data Acquisition and Analysis in this Thesis

Following the previous two sections, here the parameters used to acquire all STEM data presented in this thesis are summarised and justified. Firstly, PSCs are transported from their fabrication site to the EM laboratory inside bags which are either filled with  $\text{N}_2$  gas or vacuum-sealed to prevent perovskite degradation. These bags are only opened just before TEM sample preparation with FIB milling. Cross-sectional PSC lamellae are milled following the procedure described in Section 3.6, with a final thickness of  $\sim 200$  nm as measured in the FIB/SEM instrument. This value is selected based on the optimisation performed by Jeangros et al., who found that 200 nm provides the optimum balance between electron transparency, mechanical stability of the lamella on the TEM grid, high EDX signal generation, and low relative contribution from  $\text{Ga}^+$  beam-induced surface damage.<sup>287,288</sup> Furthermore, with the FEI Helios Nanolab Dualbeam FIB/SEM instrument used in this thesis, thinning the lamellae to  $<200$  nm was found to result in a high sample preparation failure rate. Once the lamella is ready (Figure 3.13l), it is immediately transferred into a TEM column, minimising air exposure to  $\sim 2$  minutes.

All STEM characterisations presented in this thesis were performed using a FEI Tecnai Osiris 80-200 FEGTEM (Figure 3.2b) operated in STEM mode with a 200 kV beam. This instrument is equipped with a high-brightness X-FEG electron source ( $\beta = 2.6 \times 10^{13}$  A/m<sup>2</sup>sr), Fischione detector for HAADF imaging, and a Bruker Super-X SDD system for EDX data collection. The Super-X is an ensemble of four SDDs arranged symmetrically around the microscope's optic axis. Each one is  $\sim 30$  mm<sup>2</sup> in size and all four together provide a total collection solid angle of  $\sim 0.9$  sr. An analytical TEM sample holder with a Be end was used to minimise system X-rays. However, as the TEM grid was made of Cu, X-ray peaks from Cu are always present in the recorded EDX spectra.

Cross-sectional STEM-HAADF imaging was performed to directly visualise the device stack, enabling immediate examination of film roughness, thickness, and conformality, grain shape, voids, pinholes, shunt paths, cracks, precipitates, scaffold pore filling, and other morphological features. Moreover, as the intensity of HAADF images is a function of  $Z_{eff}$ , they can also act as a 'sanity check' to evaluate

compositional mapping data. All HAADF images shown in this thesis were acquired with a beam current of  $\sim 250$  pA and a dwell time of 1  $\mu\text{s}/\text{pixel}$ .

To determine the appropriate spatial sampling for STEM-EDX, the effective beam diameter  $d_{eff}$  was calculated following Equations 3.3–3.6 (Table 3.1). The  $d_{eff}$  was found to be  $\sim 8$ – $10$  nm for the sets of perovskite compositions and beam parameters used in this thesis, with an average value of 9.25 nm. Based on the calculated  $d_{eff}$ , the STEM-EDX spatial sampling was set to 10 nm/pixel to reduce the possibility of crosstalk between adjacent pixels and minimise specimen damage. Additionally, using the  $Z_{eff}$  values shown in Table 3.1 and a measured  $\alpha$  value of 13 mrad, the values of  $E_m$  and  $\lambda$  were calculated using Equations 3.2 and 3.1 to be  $\sim 28$  eV and  $\sim 90$  nm, respectively.

Table 3.1 | Calculations of  $d_{eff}$  for the perovskite stoichiometries investigated in this thesis.

Chapter (Section)	4 (4.3)	4 (4.4)	5	6 (6.2)	6 (6.3)	7
Perovskite	MAPbI <sub>3</sub>	Cs <sub>0.06</sub> FA <sub>0.79</sub> MA <sub>0.15</sub> Pb (I <sub>0.85</sub> Br <sub>0.15</sub> ) <sub>3</sub>	MAPbI <sub>3</sub>	Cs <sub>0.1</sub> FA <sub>0.9</sub> Pb (I <sub>0.955</sub> Br <sub>0.045</sub> ) <sub>3</sub>	Cs <sub>0.05</sub> FA <sub>0.79</sub> MA <sub>0.16</sub> Pb (I <sub>0.83</sub> Br <sub>0.17</sub> ) <sub>3</sub>	Cs <sub>0.05</sub> FA <sub>0.81</sub> MA <sub>0.14</sub> Pb (I <sub>0.9</sub> Br <sub>0.1</sub> ) <sub>3</sub>
$Z_{eff}$	37.17	36.42	37.17	37.79	36.10	36.62
$E_0$ (kV)	200	200	200	200	200	200
$N_v$ (atoms/nm <sup>3</sup> )	12.07	16.57	12.07	16.17	16.67	16.67
$t$ (nm)	200	200	200	200	200	200
$b$ (nm)	14.61	16.77	14.61	17.19	16.68	16.91
$d_{ent}$ (nm)*	2.23	2.20**	2.20	2.20	2.23	2.23
$d_{ex}$ (nm)	14.78	16.91	14.77	17.33	16.82	17.06
$d_{eff}$ (nm)	8.50	9.56	8.49	9.77	9.53	9.65

\*The values of  $d_{ent}$  are nominal full width at tenth maximum values provided by FEI for each C1 lens, C2 lens, and C2 aperture settings. They determine the number of significant figures used for the calculation of  $d_{eff}$ .

\*\*Multiple  $d_{ent}$  values were used in Section 4.4, the largest one is used in this calculation to get the upper boundary for  $d_{eff}$ .

Cross-sectional STEM-EDX was performed using the parameters described in Table 3.2 to map the composition of perovskite PV devices. The applied electron dose can be calculated using the beam current, dwell time, and spatial sampling parameters. The research presented in Chapter 5 and Section 6.2, which were performed in the earlier part of this doctorate, used an electron dose of  $\sim 7800 \text{ e}^-/\text{\AA}^2$ . Following the dose optimisation described in Section 4.4, later works discussed in Section 4.3, Section 6.3, and Chapter 7 used a reduced dose of  $\sim 2620 \text{ e}^-/\text{\AA}^2$ , which was found to provide the best balance between suppressing specimen damage and minimising STEM-EDX measurement error. These doses are approximately 6x and 17x lower than prior applications of cross-sectional STEM-EDX on halide perovskite devices.<sup>289</sup> EDX spectra were acquired with an energy range of 0–20 keV to record all peaks emitted by the elements of interest, giving a spectral resolution of 5 eV/channel with the 4096 channels available in the detector system. The spectra were later rebinned to 20 eV/channel during data processing to increase the signal count (see also Figure 3.17c,d), thereby helping to achieve peak detectability and minimise measurement uncertainty as explained in Section 3.5. Although more extensive rebinning would result in even higher counts, it was not performed due to the presence of many pairs of X-ray peaks of interest separated by only 35–70 eV (N-K <sub>$\alpha$</sub> /Ti-L <sub>$\alpha$</sub> , Pt-M <sub>$\alpha$</sub> /Au-M <sub>$\alpha$</sub> , Sn-L <sub>$\alpha$</sub> /In-L <sub>$\beta_1$</sub> , Sn-L <sub>$\beta_2$</sub> /I-L <sub>$\alpha$</sub> , I-L <sub>$\beta_1$</sub> /Cs-L <sub>$\alpha$</sub> ). All STEM-HAADF images and STEM-EDX data were obtained using the TEM Imaging and Analysis (TIA) software. STEM-EDX data were then processed in HyperSpy as described in Sections 3.9 and 4.3.<sup>290</sup>

In this thesis, the Cliff-Lorimer method with a pseudo-standard k-factor calibration is used as a compromise between the challenges and limitations described in Section 3.5. Cross-sectional lamellae were milled from two PSCs, one using MAPbI<sub>3</sub> and one containing Cs<sub>0.05</sub>FA<sub>0.79</sub>MA<sub>0.16</sub>Pb(I<sub>0.83</sub>Br<sub>0.17</sub>)<sub>3</sub> (TCDH) perovskite. After ensuring that each specimen has a highly homogeneous perovskite layer (Figure 3.14), a STEM-EDX SI was acquired for each specimen. The acquisition parameters are as shown in the ‘Chapter 5’ column in Table 3.2. Then, sections of the EDX data corresponding to the perovskite layers were isolated, with each section containing  $\sim 4000$  spectra. These sections were firstly quantified using calculated k-factors provided by the TEM manufacturer (FEI, rightmost column in Table 3.3). The obtained  $\sim 4000$  concentration values were averaged and then used as a starting point to calibrate the k-factors for the Br-K <sub>$\alpha$</sub> , C-K <sub>$\alpha$</sub> , I-L <sub>$\alpha$</sub> , N-K <sub>$\alpha$</sub> , and Pb-L <sub>$\alpha$</sub>  X-ray lines according to the perovskite stoichiometries (Cs was not quantified due to its low concentration). The calibrated k-factors, their mean, and their difference are shown in Table 3.3. The k-factors obtained for C-K <sub>$\alpha$</sub> , I-L <sub>$\alpha$</sub> , N-K <sub>$\alpha$</sub> , and Pb-L <sub>$\alpha$</sub>  from both standards were found to be very close to one another. The k-factors shown in the ‘Mean’ column in Table 3.3 were used to generate all quantified EDX maps displayed in this thesis.

Table 3.2 | STEM-EDX data acquisition parameters.

Chapter (Section)	4 (4.3)	4 (4.4)	5	6 (6.2)	6 (6.3)	7
Perovskite	MAPbI <sub>3</sub>	Cs <sub>0.06</sub> FA <sub>0.79</sub> MA <sub>0.15</sub> Pb (I <sub>0.85</sub> Br <sub>0.15</sub> ) <sub>3</sub>	MAPbI <sub>3</sub>	Cs <sub>0.1</sub> FA <sub>0.9</sub> Pb (I <sub>0.955</sub> Br <sub>0.045</sub> ) <sub>3</sub>	Cs <sub>0.05</sub> FA <sub>0.79</sub> MA <sub>0.16</sub> Pb (I <sub>0.83</sub> Br <sub>0.17</sub> ) <sub>3</sub>	Cs <sub>0.05</sub> FA <sub>0.81</sub> MA <sub>0.14</sub> Pb (I <sub>0.9</sub> Br <sub>0.1</sub> ) <sub>3</sub>
$E_0$ (kV)	200	200	200	200	200	200
Beam current (pA)	140	Various	250	250	140	140
Dwell time (ms/pixel)	30	Various	50	50	30	30
Spatial sampling (nm/pixel)	10	10	10	10	10	10
Electron dose (e <sup>-</sup> /Å <sup>2</sup> )	2620	Various	7800	7800	2620	2620
Spectral resolution (eV/channel)	5	5	5	5	5	5
Rebinned spectral resolution (eV/channel)	20	20	20	20	20	20

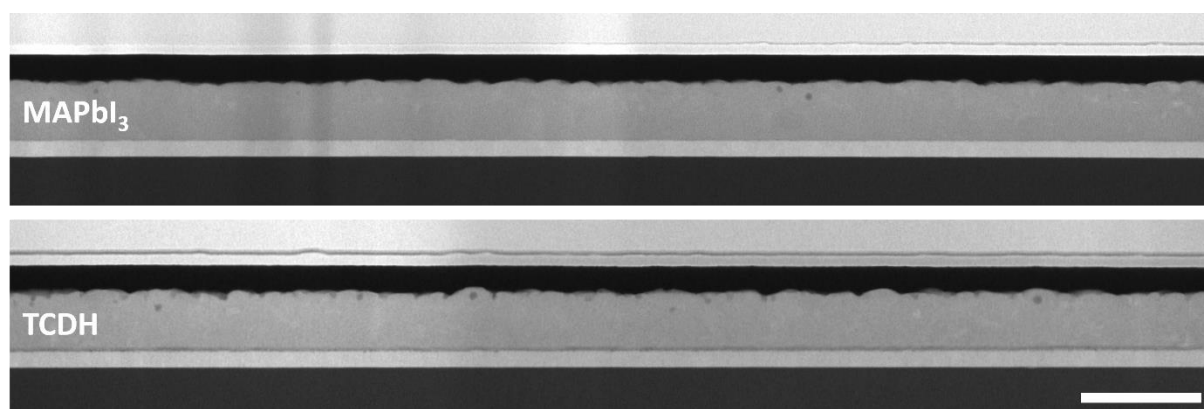


Figure 3.14 | Cross-sectional STEM-HAADF images of the two standards used for k-factor calibration.  
Scale bar represents 1 μm.

Table 3.3 | Calibrated k-factors.

X-ray Line	Calibrated k-factors					FEI k-factors
	MAPbI <sub>3</sub>	TCDH	Mean	Difference	Diff./Mean (%)	
Br-K <sub>α</sub>	N.A.	2.878	2.878	N.A.	N.A.	2.575
C-K <sub>α</sub>	2.420	2.484	2.452	0.064	2.610	3.601
I-L <sub>α</sub>	3.401	3.425	3.413	0.024	0.979	2.950
N-K <sub>α</sub>	3.957	3.755	3.856	0.202	5.239	3.466
Pb-L <sub>α</sub>	4.516	4.231	4.374	0.285	6.516	4.668

This pseudo-standard approach removes the need for complicated absorption corrections which may induce additional uncertainties.<sup>243</sup> This is because all the perovskites investigated in this thesis are also either MAPbI<sub>3</sub> or close variants of the TCDH formula, so it is reasonable to infer that the nature and extent of X-ray absorption in the specimens is mimicked by the standards. On the other hand, this calibration assumes that the standards' perovskite compositions, when averaged over the mapping area, are accurately described by their nominal stoichiometries. This is difficult to verify with certainty, especially for the small volumes probed with STEM-EDX. However, the high degree of perovskite homogeneity and lack of non-perovskite phases in the standards (Figure 3.14) lend some credence to this supposition. Further support is provided by the narrow gap between the two sets of calibrated k-factors, as they are unlikely to be so similar had the standards' compositions differed substantially from their stoichiometric formulas.

From this assumption, it follows that any changes beam damage may have imposed on the standards' perovskite compositions (see Section 3.9) are, in effect, ignored. The nature of these changes is expected to be very similar in the standards and the investigated specimens due to the unchanged beam acceleration voltage, nominal lamella thickness, and perovskite stoichiometries. The practical implication is that the calibrated k-factors have a built-in 'correction' for beam damage effects. Therefore, the absolute elemental concentrations measured by STEM-EDX must be understood in this context. Importantly, this does not affect STEM-EDX's ability to check for the presence of a certain element of interest and semi-quantitatively map nanoscale compositional heterogeneities. A comparison of STEM-EDX data across specimens also remains a valid analysis procedure provided the data acquisition parameters are exactly the same.

In the following chapters, STEM-EDX was performed on PSCs made in several laboratories using different methods (spin coating, spin coating followed by aerosol-assisted solvent treatment, blade coating, and air jet-assisted blade coating). Elemental maps produced using the calibrated k-factors

match the nominal perovskite stoichiometries closely in all cases. This agreement also supports the assumption that the standards' compositions conformed to their nominal stoichiometries. Given the complex compositions of halide perovskites, lack of suitable standards for either the Cliff-Lorimer or the  $\zeta$ -factor methods, and the unreliability associated with calculated k-factors, the pseudo-standard approach described above is considered the best compromise.

### 3.8. Cathodoluminescence

Luminescence is a semiconductor material's ability to emit a photon when a conduction band electron recombines with a valence band hole. As discussed in Chapter 2, luminescence is an important property for PV materials as strong luminescence is a sign of high EQE and  $V_{OC}$ .<sup>231,232</sup> CL, which is luminescence induced by an electron beam, can be performed in a spatially resolved manner in an SEM/STEM. In both instruments, inelastic scattering of the probe beam generates SEs, Auger electrons, and X-ray photons, which may undergo inelastic scattering as well. Because the primary beam, some of the Auger electrons, and the X-ray photons are highly energetic compared to the semiconductor  $E_g$  (<3 eV), these scattering events can lead to a very high number of excited electrons in a bulk specimen. When the excited electrons recombine radiatively across bandgap or trap states, they emit photons in the IR, visible, or UV wavelengths which can be detected. The resulting emission spectrum can reveal information about the material's  $E_g$ , disorder and heterogeneity, non-radiative recombination sites, and dopant/impurity concentrations.<sup>233,291</sup> For materials like perovskites whose  $E_g$  varies with composition, CL can also be used to indirectly map the specimen's chemistry.

The classical method to collect emitted light photons in an SEM-CL system is to place an elliptical or parabolic mirror above the sample (Figure 3.15a). Photons are reflected by this mirror into a fibre optic and then collected by a photomultiplier tube, resulting in a panchromatic image as all the emitted wavelengths are detected indiscriminately. If a monochromatic image at a known wavelength is desired, a monochromator can be inserted before the photomultiplier tube. Alternatively, hyperspectral data in the form of an SI can be acquired by dispersing photons into their component wavelengths using a diffraction grating and detecting them with a CCD camera. The SIs can subsequently be analysed to produce panchromatic or wavelength-selective maps. Recently, a more advanced design has been invented where the SEM-CL instrument essentially integrates an optical microscope and an SEM (Figure 3.15b), rather than attaching a mirror and a fibre optic into an SEM. This design allows a more efficient and spatially uniform light collection, expanding the field of view up to about 300  $\mu\text{m}$  in state-of-the-art systems, compared to  $\sim 2 \mu\text{m}$  in mirror-based instruments.<sup>292</sup>

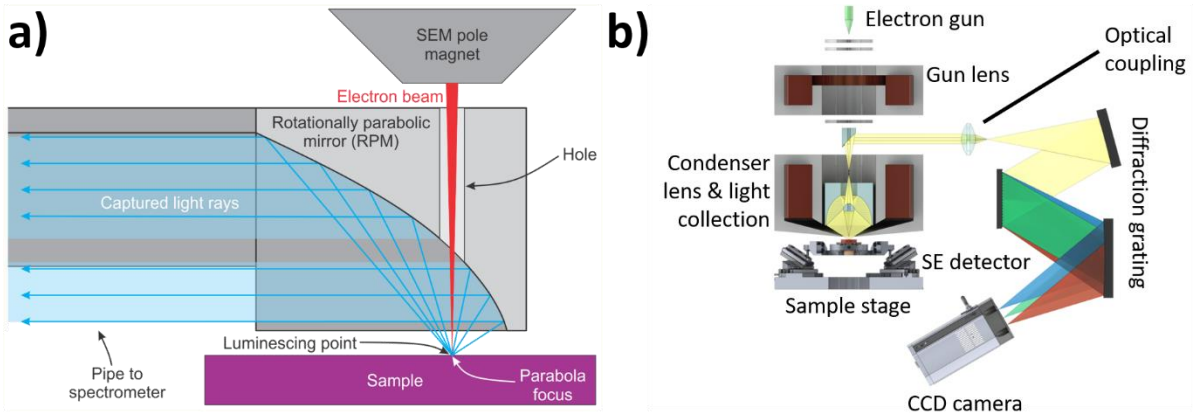


Figure 3.15 | Schematics of SEM-CL instruments using (a) a photon-collecting parabolic mirror<sup>293</sup> and (b) a photon collection system integrated with an SEM.<sup>292</sup>

Although at first glance CL looks similar to PL, a more ubiquitous technique using a laser beam to excite electrons, there are some important differences. While PL is simpler to use, its spatial resolution is usually limited by the wavelength of the probe laser beam to about 0.4–0.6  $\mu\text{m}$ , except when it is performed using a scanning near-field optical microscope. CL does not suffer from this limitation, although in practice the spatial resolution will be blurred by the electron beam interaction volume and carrier diffusion in the specimen.<sup>233</sup> The probe in CL is far more energetic compared to PL (1–10 keV vs 2–4 eV), meaning CL will likely induce a much higher excited carrier concentration and more specimen damage compared to a PL laser beam.<sup>233</sup> Furthermore, PL is a predominantly surface technique while CL can have some degree of depth information due to the tunable depth of the electron beam's interaction volume.<sup>233,234</sup> To obtain the best of both worlds, PL and CL should ideally be performed and the results compared to one another. This reduces the possibility of missing a real feature in the specimen or of basing conclusions on beam damage-induced artefacts. In this thesis, CL is used to evaluate the structural quality of FIB milled perovskite device lamellae (Chapter 4) and to map perovskite emission near a PSM's MI area (Chapter 7).

Luminescence intensity is normally distributed with respect to energy as the sharp emission line at the emitter's  $E_g$  is smeared by vibrational states around the band edges at all temperatures above 0 K.<sup>294</sup> Therefore, CL data can be analysed by fitting it to a model consisting of at least a Gaussian and a background component. One Gaussian component should be added for each emitting phase present in the specimen. The data and model can then be fitted using the desired loss function and optimisation algorithm. In this thesis, CL data fitting is performed using the Levenberg-Marquardt algorithm with a least squares loss function.<sup>295,296</sup>

### 3.9. Beam-induced Specimen Damage

When probe electrons lose energy in inelastic collisions, a part of this energy causes irreversible changes to the specimen, normally referred to as ‘damage’. There are three major variants of beam damage, namely radiolysis, knock-on or sputtering, and heating. In addition, radiation-enhanced diffusion of surface atoms and bulk vacancy migration may also be caused by elastic scattering.<sup>297</sup>

Radiolysis occurs in insulators and some semiconductors, where ejected specimen electrons cannot be replaced quickly enough before the ionised atom moves. As a result, interatomic bonds are severed and vacancies are created. It is especially harmful for polymers, ceramics, and minerals as ionisation can significantly alter the specimen’s chemistry and (crystalline) structure. Different compounds can be created if the newly formed free radicals or ions bond with each other. If the formed compounds are volatile, they will be removed by the microscope’s vacuum system and thus specimen decomposition would be driven towards completion even if the decomposition reaction were reversible in a closed environment. For polymers, the specimen’s structure can be completely changed if the main chain is broken or if crosslinking happens among side chains. The severity and spatial reach of radiolysis can be amplified by the newly formed SEs, some of which are energetic enough to impose further damage on the specimen.<sup>298</sup> The extent of radiolysis damage is usually proportional to the amount of deposited energy and thus to the electron dose.<sup>298</sup> Radiolysis can be minimised by using lower electron doses or higher beam voltages. However, reducing the number of inelastic scattering events also lowers the signal count for analytical techniques like EDX and EELS. Prior works have found that radiolysis is the dominant beam damage mechanism for halide perovskites. Observed impacts of radiolysis in perovskites include formation of vacancies through atomic/ionic displacement, disintegration of the crystal structure, and loss of volatile molecules such as MAI.<sup>299–302</sup>

Knock-on damage occurs when probe electrons transfer enough energy to a nucleus in the specimen to exceed its displacement energy threshold, knocking that atom out of the crystal lattice and creating a point defect. Sputtering is a special form of knock-on damage which happens at surface atoms, displacing them out of the specimen altogether. Knock-on damage is very important for in-situ microscopy as the created defects accelerate the kinetics of many processes, such as phase transformation, ion migration, and elemental diffusion. The only way to reduce knock-on damage is to lower the probe beam’s acceleration voltage, but this worsens radiolysis and makes the specimen less transparent to the electron beam. Comparatively, the amount of energy lost to knock-on displacement is about  $10^5$  orders of magnitude lower than that lost to radiolysis for a 200 kV electron beam.<sup>303</sup> Multiple studies have shown that knock-on damage is not a major source of damage in TEM of halide perovskites.<sup>301,302</sup>

Heating occurs when phonons are generated by the electron beam. It is generally only a problem for samples with extremely low thermal conductivity, i.e. ceramics and polymers.<sup>297</sup> These kinds of material can be heated by hundreds of Kelvins if the beam current is more than a few nA, which may trigger sublimation in some materials. In these cases, the specimen stage should be cooled with liquid N<sub>2</sub> (cryo-TEM) to prevent specimen damage. Comparative studies between room temperature TEM and cryo-TEM characterisation of perovskites are inconclusive, with conflicting observations made by different authors. Some claimed successful imaging of undamaged perovskite structure with cryo-EM, while others found that cryogenic temperatures accelerated beam-induced perovskite amorphisation.<sup>304</sup> Heating effect is usually very weak in STEM due to the relatively low beam current and small probe diameter.<sup>305</sup> The temperature rise ( $\Delta T$ ) in TEM specimens can be calculated using Equation 3.10, where  $I$  is beam current in nA,  $R_0$  is the distance from the probe position to a radial heat sink in nm,  $k$  is the specimen's thermal conductivity in W/mK, and the other variables are as previously defined.<sup>305</sup> The maximum  $\Delta T$  for the STEM-EDX works presented in this thesis can be estimated by putting the highest  $I$  value used (0.25 nA), the maximum distance between the perovskite and the metal contact layer as  $R_0$  (~800 nm), and the measured  $k$  for perovskite (~0.35 W/mK) into Equation 3.10.<sup>306-310</sup> Using these and the calculated values for  $E_m$ ,  $d_{eff}$ , and  $\lambda$ ,  $\Delta T$  is found to be 0.19 K. This low value is beneficial as substantial heating may increase a specimen's susceptibility to radiolysis.<sup>305</sup> However, some degree of error may be anticipated as Equation 3.10 assumes that a radial heat sink surrounds the illuminated area, whereas in the specimens investigated in this thesis, most of the heat would flow through the perovskite to the metal contact layer (Cu or Au) and then to the TEM grid.

$$\Delta T = \frac{IE_m \ln(\frac{2R_0}{d_{eff}})}{2\pi k \lambda} \quad (\text{Equation 3.10})$$

An important aspect of beam damage is the time scale of the physical processes involved with respect to the dwell time. If the former is longer, then there is a possibility of outrunning the damage as the collected data will, in effect, come from a pristine specimen. Approximately, SE generation and bond breaking happen in <1 fs while knock-on displacement and amorphisation occur in 1–100 fs.<sup>298</sup> It is difficult to outrun these processes due to Coulomb repulsion between primary electrons and the limited number of electrons which can be packed into a small probe.<sup>311</sup> On the other hand, diffusion-limited processes such as mass loss from the interaction volume have a much longer time scale, which may be comparable to the dwell time. In the case of halide perovskites, I<sup>-</sup> ions are generally recognised as the most mobile species.<sup>137,312,313</sup> However, measurements and calculations of I<sup>-</sup> diffusion coefficients ( $D$ ) have produced varying results, from 10<sup>-16</sup> to 10<sup>-12</sup> m<sup>2</sup>/s.<sup>137,313,314</sup> If a classical diffusion process is

assumed, the time  $\tau$  needed for a species to travel across a distance  $L$  can be approximated as  $\tau = L^2/D$ .<sup>298</sup> Using the above range of measured  $D$  and 4.6 nm as  $L$  (half of the average  $d_{eff}$  calculated in Section 3.7), a  $\tau$  range of 21  $\mu$ s to 210 ms is obtained. The high end of this range is longer than the STEM-EDX dwell times used in this thesis (30 and 50 ms/pixel), so operating in STEM mode provides a chance to outrun mass loss. In addition, the small probe size used in STEM also minimises temperature rise (Equation 3.10), thus preventing a substantial acceleration in mass diffusion and loss.<sup>315</sup> STEM can be particularly advantageous if the dwell time needed to generate enough signal is split over hundreds or thousands of frames, which are then drift-corrected and summed up. This approach, often called dose fractionation or recursive mapping, can help to reduce mass loss by providing the displaced atoms time to diffuse back to their original location while the probe is scanning the rest of the mapping area (frame time).<sup>298</sup> However, it is also possible that rather than back-diffusion, additional mass loss occurs instead during the frame time.<sup>298</sup> In this case, then a single long scan is likely to be a better option. Recursive mapping is available with more recent TEM interface software such as Velox, but it is not an option in the TIA software controlling the FEI Tecnai Osiris 80-200 FEGTEM used in this thesis.<sup>316</sup>

This discussion on beam damage is mainly written in the context of (S)TEM, but the general principles apply to SEM as well. Due to the low acceleration voltages used in SEMs, radiolysis is expected to be the dominant beam damage mechanism with the same effects as mentioned above. However, in literature, all three beam damage variants have been observed in SEM characterisation of halide perovskites.<sup>317–320</sup> Generally, SEM imaging can be performed with minimum damage as it does not require a high acceleration voltage or beam current (usually 1–2 kV and <50 pA). However, more advanced characterisation such as SEM-EDX, SEM-CL, EBIC, or EBSD are often done using far higher currents, in the order of 0.1 to 10 nA.<sup>319–323</sup> These techniques are likely to damage the perovskite specimen unless a sophisticated signal collection and detection system is used to allow a lower electron dose.<sup>205,233,317,324</sup> In addition, the perovskite specimen may undergo charging during SEM imaging due to ejection of SEs, particularly if an insulating substrate such as glass is used. Charging can be easily avoided by coating the specimen with a thin layer of C or Au. This coating can also reduce heating effects by providing a fast thermal conduction path and slow material loss due to radiolysis.<sup>325</sup>

Suppressing beam damage by minimising electron dose is important, but so is maintaining statistical significance in the collected data. Should some damage remain, the effects of said damage on the specimen must be understood to allow accurate interpretation of the acquired images and elemental distributions. In the context of this work, there is a high probability that the perovskite samples are damaged to some extent by the electron beam as shown in previous studies.<sup>299–301,304,320,326,327</sup> This scenario cannot be eliminated as high-energy electrons are necessary to probe the sample and inelastic scattering is a prerequisite of analytical microscopy. However, it can be minimised by adopting low-dose microscopy techniques. These include performing alignment and focusing work on a sacrificial area of the specimen, blanking the beam while no measurement is being made, and minimising exposure

time. Although lowering the dose results in lower SNR in the collected data, more effective detectors and data processing algorithms can help us ameliorate this problem. Finally, EM data interpretation should be supported by comparison with a control specimen, computational methods, or complementary characterisation techniques. Efforts to understand beam-induced specimen damage and to balance it against analytical data quality are further explored in Chapter 4.

### 3.10. Multivariate Statistical Analysis

All STEM-EDX data presented in this thesis were acquired in the form of SIs. This technique generates a massive amount of data which can be very time-consuming to analyse manually. Traditional EDX analysis software applies standard routines to extract elemental maps, as described in Section 3.5. However, the spatial distribution and correlation between phases are difficult to visualise by traditional methods. The development of ‘big data’ tools such as MVA and machine learning allows us to extract meaningful patterns and information from these datasets in a relatively short processing time. In this work, the relevant algorithms are principal component analysis (PCA) and non-negative matrix factorisation (NMF). Both are applied on the STEM-EDX SIs in HyperSpy, an open source Python library for multidimensional data analysis.<sup>290</sup>

PCA has been one of the most popular MVA algorithms since it was invented by Karl Pearson in 1901, widely used for dimensionality reduction of highly complex data containing lots of variables.<sup>328</sup> PCA finds correlations in a dataset by identifying a set of components (linear combinations of the data’s variables) which are orthogonal to one another and along which most of the variance lies.<sup>329</sup> The working principles of PCA are most easily illustrated by firstly considering a two-dimensional dataset (Figure 3.16a). This dataset contains  $N$  data points which can be plotted along variables  $x$  and  $y$ . By using a least-squares optimisation, a line of best fit ( $y = mx + c$ ) through the data points can be defined, such that the summation  $\sum_{i=1}^N ((mx_i + c) - y_i)^2$  is minimised. Statistically, this line represents the linear combination of  $x$  and  $y$  which accounts for as much of the dataset’s variance as possible and therefore it is the first component of this dataset. As there can only be one line which is orthogonal to the first component in a two-dimensional space, this line automatically becomes the second component. This approach can be extended to higher-dimension, multi-variable systems. The starting step is always to find the first component, one which maximally accounts for the data’s overall variance. The second component is the one which maximally accounts for the data’s remaining variance and is orthogonal to the first component. This is done iteratively until the number of components is equal to the number of original variables, or until the desired proportion of the dataset’s variance has been accounted for.

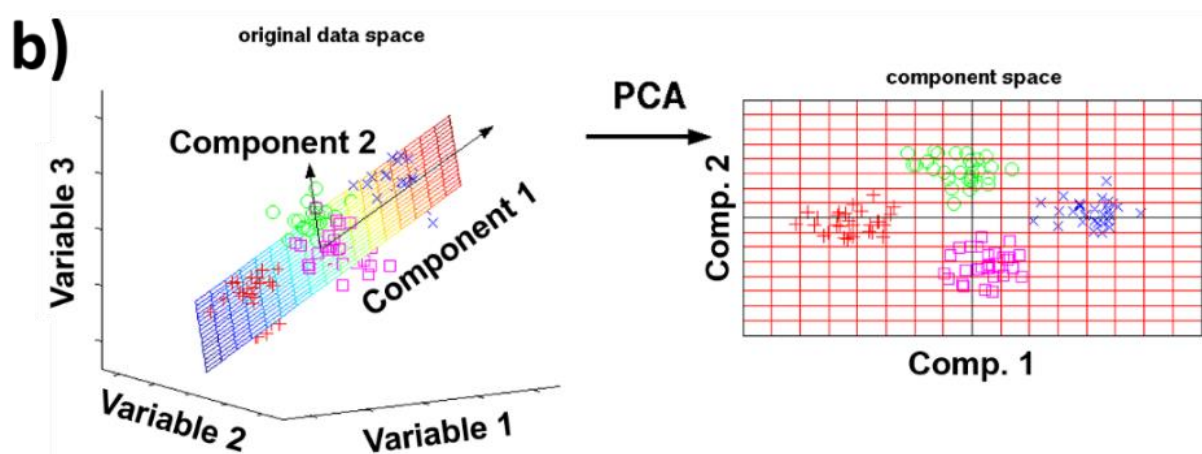
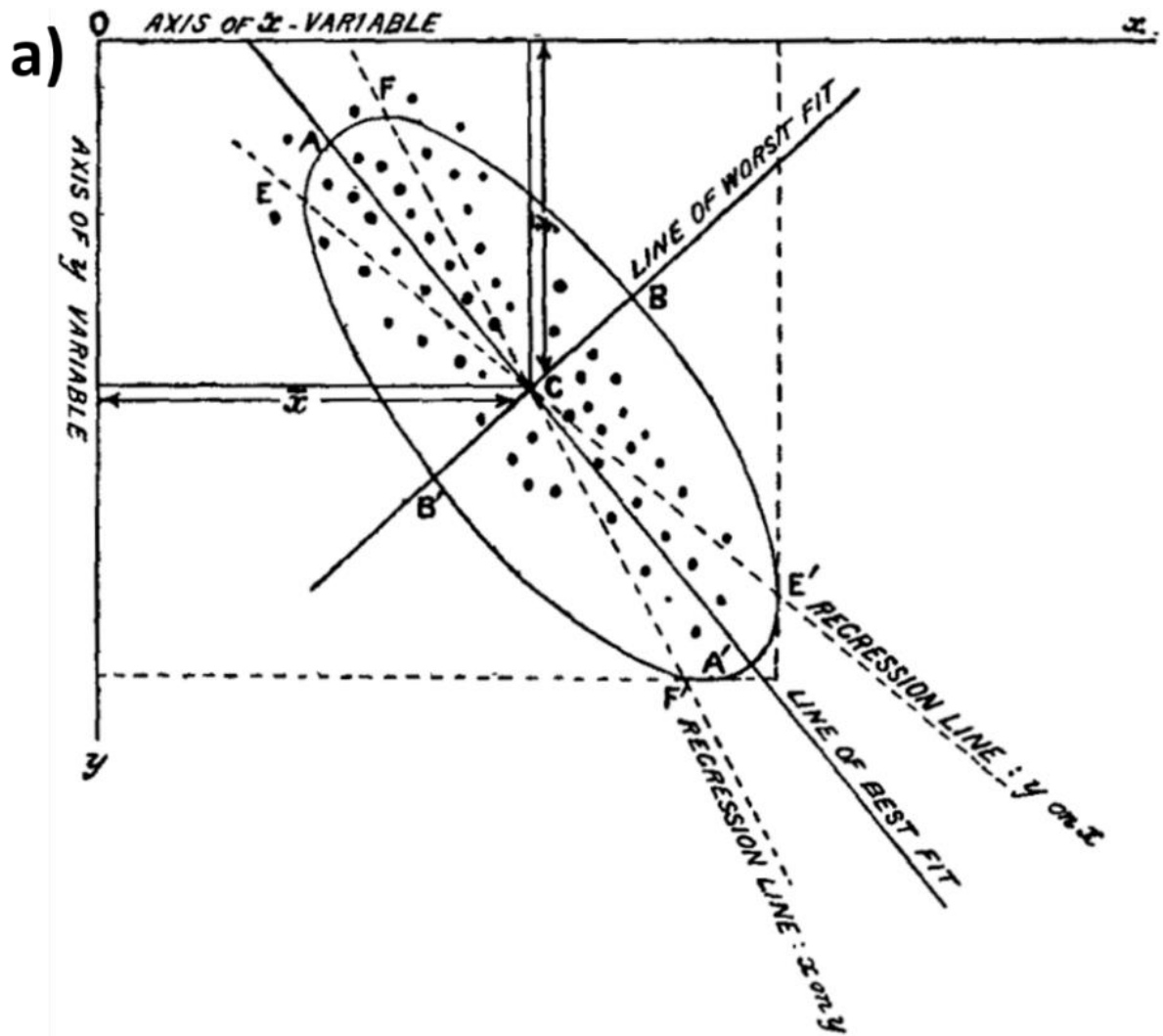


Figure 3.16 | (a) Illustration of the PCA procedure for a generic two-dimensional data set as originally drawn by Karl Pearson, where the lines of best fit and worst fit serve as the two PCA components. (b) Illustration of dimensionality reduction through PCA, from a three-dimensional data set (left) to a two-dimensional model (right). Panel (a) is reproduced from ref.<sup>328</sup> with permission, copyright Taylor & Francis Group. Panel (b) is adapted from ref.<sup>330</sup> under the Creative Commons CC-BY 2.0 License.

Once all the components have been found, the next step is to rank them in order of variance. This is done by constructing a scree plot (Figure 3.17a), a semi-logarithmic plot with variance on the  $y$ -axis and component index on the  $x$ -axis. Scree plots usually exhibit a sharp drop in the first few components, followed by a plateau of low-variance components. The former group accounts for most of the dataset's variance and are called principal components.<sup>331</sup> The dataset can be approximated by adding together only the principal components, resulting in a model that usually consists of far fewer dimensions and variables compared to the original dataset (Figure 3.16b). Because the low-variance components are often (but not always, as discussed in Chapter 4) formed of measurement noise, the model has a higher SNR than the original dataset while maintaining most of its variance. Therefore, this dimensionality reduction function is also called data denoising. Figure 3.17b-e shows the power of PCA denoising of STEM-EDX data, where the SNR for the I-L <sub>$\alpha$</sub>  peak (3.938 keV) rose from 20 in the original spectrum, to 39 after spectral rebinning by a factor of 4, and finally to ~296 in the denoised model.

The above can be described in a slightly more mathematical manner – and in the context of STEM-EDX – by representing the original data set as an  $m \times n$  matrix  $D$ . It includes all the acquired spectral data, in which  $m$  is the number of energy channels in each spectrum and  $n$  is the number of individual spectrum (equivalently, the number of scanned pixels). Within this matrix, PCA finds one component which maximally accounts for the data's overall variance. This process is continued iteratively, with each new orthogonal component maximally accounting for the variance left undescribed by previous components. At the end of the process, the principal components are normally sufficient to represent the specimen's features of interest. If there are  $p$  principal components, then the remaining  $n - p$  components are the measurement noise.  $D$  can then be approximated as  $D'$ , which is defined as:

$$D' = FL^T \quad (\text{Equation 3.11})$$

where  $F$  is the  $m \times p$  factor matrix,  $L$  is the  $n \times p$  loading matrix, and the superscript  $T$  is the matrix command for transpose. In line with the definition of components as linear combinations of variables, the factor matrix contains the variables while the loading matrix contains the coefficients of those variables in the linear combinations. It is important to note that the loading and factor matrices are often not directly interpretable in a physically meaningful manner. For example, a STEM-EDX spectrum cannot contain a negative intensity count. However, PCA components obtained from STEM-EDX data can and do have negative values. Therefore, the principal components must firstly be added together into a denoised model of the original dataset. This model can then be treated just like the original EDX dataset and subjected to typical EDX analysis procedures, such as peak assignment to specific elements based on an X-ray line database, background correction, peak intensity extraction, and quantification.

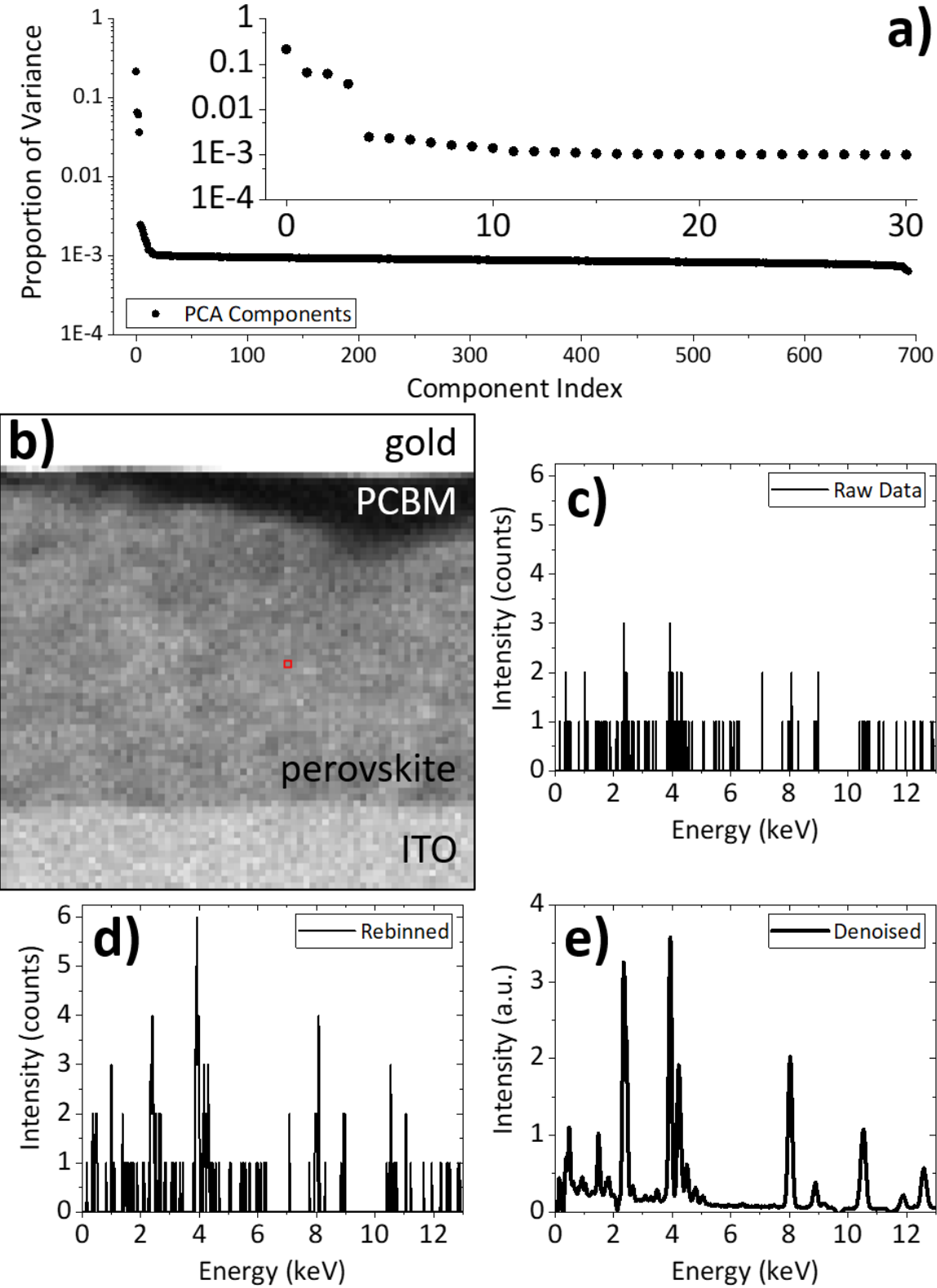


Figure 3.17 | (a) A scree plot of PCA components from a STEM-EDX SI. The inset shows a zoomed-in view of the first 30 components. (b-e) The result of PCA denoising on a STEM-EDX SI. (b) STEM-HAADF images of a PSC lamella with a marked pixel (red square) from which a raw spectrum (c) is taken ( $I-L_\alpha$  SNR = 20). (d) The same spectrum as (c) after spectral rebinning by 4 ( $I-L_\alpha$  SNR = 39). (e) A model spectrum constructed with four principal components after PCA denoising ( $I-L_\alpha$  SNR  $\sim$ 296).

The abstract nature of its components is the primary limitation of PCA. Each component is separated solely on the basis of statistical variance, so it does not necessarily correspond to different chemical phases or other physically meaningful distinctions.<sup>332</sup> NMF is a decomposition algorithm which seeks to solve this problem by replacing the constraint of orthogonality by non-negativity, meaning the  $F$  and  $L$  matrices in Equation 3.11 can only contain zero or positive numbers.<sup>333,334</sup> NMF is more intuitive to the typical human thinking of adding parts into a whole (Figure 3.18), and also potentially more relevant for EDX, where negative signal counts or elemental concentrations make no physical sense. Therefore, direct interpretation of NMF components is usually more straightforward compared to PCA.<sup>335</sup> However, NMF requires the user to know the desired number of output components ( $p$  value for the  $F$  and  $L$  matrices in Equation 3.11) beforehand.<sup>336</sup> NMF looks for  $p$  components which together most closely approximate the original data and discards everything else as noise. When  $p$  is set too low, NMF does not properly separate distinct phases in the specimen into different components. In fact, for original datasets containing no negative values such as STEM-EDX SIs, the component produced by NMF with  $p = 1$  will be exactly the same as the first component produced by PCA, which is simply a multidimensional version of the data's 'line of best fit' as described above. On the other hand, when  $p$  is too high, signals which belong to the same chemical phase may get sorted into separate components. For example, the peaks of elements A and B may appear in different components even though they exist only as compound  $A_xB_y$  in the specimen. From a denoising point of view, a low  $p$  value may result in some genuine signals wrongfully discarded as noise, while too much noise may be included in components produced with a high  $p$ . The number of principal components identified by PCA is usually a good starting guess for  $p$ , as will be shown in Chapter 4.<sup>336</sup> This approach is more efficient compared to iteratively running NMF with blind guesses of  $p$ , since NMF is about 10-100x more demanding in terms of computational time compared to PCA. A more in-depth study on the suitability of PCA and NMF for STEM-EDX data and the necessary adaptation to both procedures is presented in Chapter 4.

As EDX involves the counting of uncorrelated events, the measurement noise is Poissonian in nature.<sup>337</sup> A feature of Poisson distribution is the non-uniformity of uncertainty across the dataset, meaning noise components do not originally possess constant variance as implied by the plateau previously mentioned. Consequently, components representing genuine signal from scarce elements may be overwhelmed by noise associated with the more abundant elements.<sup>338</sup> Therefore, the standard PCA and NMF algorithms must be modified by incorporating the error covariance information. This approach provides a more interpretable and accurate representation of the data.<sup>337</sup> In this thesis, all MVA were done in this manner.

These automated procedures help us sieve through data produced by spectrum imaging through dimensionality reduction and decomposition, while maintaining most of the original dataset's variance. After denoising, spectral characteristics of the elemental components can be extracted from the simplified data ( $D'$  in Equation 3.11) to obtain the spatial distribution of relevant chemical phases. Finally, the concentration of each element can be quantified using the Cliff-Lorimer ratio method

previously described.<sup>275</sup> Most importantly in the context of beam-sensitive perovskites, PCA enables STEM-EDX data acquisition using far lower electron doses than what would have been required otherwise. This reduces specimen damage and is invaluable for the characterisation of soft materials.

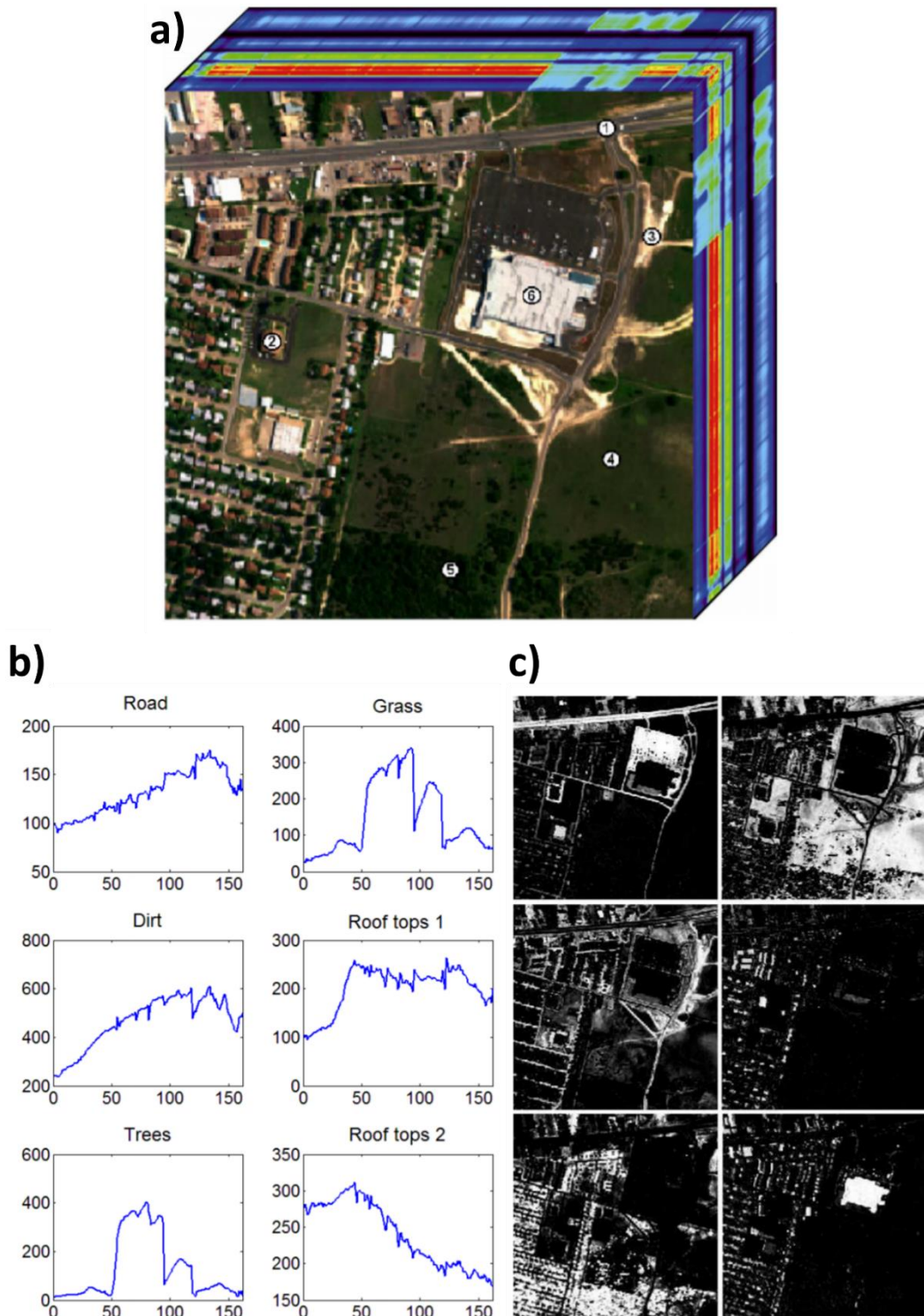


Figure 3.18 | NMF decomposition of a hyperspectral image (a) into six components. Panels (b,c) show the (b) factors and (c) loadings of those components.<sup>336</sup>

### **3.11. Summary**

EM is a powerful and versatile platform for nanoscale characterisation of materials. Bulk specimens can be investigated in an SEM while thin, electron-transparent specimens are probed at higher magnifications in a (S)TEM. Due to the large variety of signals generated by elastic and inelastic electron-matter scattering, the properties accessible via EM range from morphology (imaging) and crystallography (electron diffraction) to composition (EDX, EELS) and even functional (EBIC, CL). In this thesis, SEM imaging, SEM-EDX, SEM-CL, STEM-HAADF imaging, and STEM-EDX are used to study perovskite PV devices, specifically PSMs and the MI area contained therein.

Inelastic scattering is very useful in EM to generate many of the signals used to characterise the specimen. However, inelastic scattering necessarily involves energy transfer from the probe electron to the specimen. When the electron dose is too high or the specimen is particularly prone to degradation, energy deposition can damage the specimen. Radiolysis, knock-on displacement, and heating are the most common forms of damage. With the exception of electron dose reduction, often a step taken to reduce one form of damage also exacerbates the other. Therefore, a good understanding of the dominant beam damage mechanism in a particular specimen and electron dose minimisation are essential when working on easily damaged specimens. At the same time, obtaining sufficient signal counts is also important to lower measurement uncertainty. Advanced data analysis algorithms based on MVA is a tremendous help in this regard, enabling acquisition of quality data with minimum specimen damage.

## **Chapter 4**

# **Optimisation of STEM-EDX and Multivariate Statistical Analysis for Characterisation of Perovskite Solar Cells**

### **4.1. Introduction**

As described in Chapter 2, perovskites contain nanoscale heterogeneities which control their optoelectronic properties.<sup>196</sup> Compositional non-uniformity in the perovskite film is arguably the most important form of heterogeneity as it results in  $E_g$  fluctuations, thereby strongly affecting carrier generation, recombination, and collection.<sup>339,340</sup> Furthermore, interfaces between domains of different perovskite compositions are likely to host non-radiative recombination sites and provide energetically preferred locations for perovskite degradation.<sup>90,135</sup> The recent advent of multi-ion perovskites containing up to four A cations and two X anions, combined with the ease of ion migration in OIHPs, provide a strong motivation to understand the compositional landscape of PSCs.<sup>58,137,341,342</sup>

Chapter 3 introduces STEM-EDX as a technique capable of nanoscale elemental mapping, making it a powerful tool to study the chemical make-up of PSCs. When performed on a cross-sectional slice of a full PSC stack, STEM-EDX can reveal the presence of non-perovskite phases, interlayer atomic diffusion, and degradation products in addition to the perovskite composition itself. Cross-sectional lamellae of multi-layered devices such as PSCs can be prepared through FIB milling with Ga<sup>+</sup> ions. However, both FIB milling and STEM-EDX use highly energetic particles which are likely to damage a beam-sensitive material like OIHPs.<sup>206,327</sup> Therefore, it is necessary to understand the effects of beam-induced specimen damage and explore practical methods of suppressing them.

This chapter firstly describes the effect of FIB milling on the perovskite film in a PSC lamella as investigated through CL. The results delineate areas of study where FIB milled lamellae can be appropriately used to investigate PSCs and others where they are not representative of their parent devices. Then, the MVA algorithms introduced in Chapter 3 are optimised in the specific context of cross-sectional STEM-EDX of PSC specimens in order to obtain the most accurate elemental maps. The stages of optimisation include a) proper discrimination between significant and noise PCA components, b) choosing the right number of output components for NMF, and c) comparison between denoised models constructed from PCA or NMF components. Finally, the specimen damage induced by STEM-EDX is studied in detail and balanced with the need to produce statistically significant X-ray signal counts. The principles outlined in this chapter form the basis for STEM-EDX data acquisition and analysis performed in the works described in Chapters 5 to 7.

## 4.2. FIB Milling-induced Modifications in PSC Lamellae

### 4.2.1. Introduction

Despite its widespread use in the literature, the suitability of FIB milling for specimen preparation of beam-sensitive OIHPs has been questioned due to the expected  $\text{Ga}^+$  beam-induced irreversible surface amorphisation through accumulation of defects created by ion collision cascades.<sup>206,286,327,343</sup> Therefore, FIB-induced modifications to OIHP lamellae need to be understood to guide future characterisation work performed on them and critically assess the validity of results reported in the literature. Previously, several groups have shown that gradual amorphisation in various OIHPs can be induced by compressing them in a diamond anvil cell.<sup>344–348</sup> Amorphisation causes a continuous reduction in PL intensity and a  $E_g$  widening of ~0.2 eV, until luminescence is eventually eliminated by strong non-radiative recombination when the perovskite is fully amorphised.<sup>344–348</sup> The  $E_g$  widening was found to be caused by suppression of atomic orbital overlap due to pressure-induced breaking of long-range order in the perovskite lattice.<sup>344,346</sup> Interestingly, the original crystallinity and luminescence were largely recovered when the pressure was relaxed.<sup>344–348</sup>

The observed relationship between perovskite structure and luminescence means the latter can be used as a proxy to examine the former. This link between the two properties is valuable to assess the suitability of FIB milling since amorphisation is the primary form of damage suspected in FIB-milled perovskite lamellae, even though in this case amorphisation is caused by ion collisions rather than hydrostatic pressure. More precisely, if a lamella produces an emission peak that is centred at the same energy as its parent device's emission, then this similarity can be taken as a sign that the perovskite's crystalline structure in the lamella is not amorphised by FIB milling. A lamella with a partially amorphised perovskite layer is expected to exhibit a blue-shifted (and likely broadened) luminescence peak relative to its parent device. Finally, an absence of emission is considered a manifestation of complete perovskite amorphisation.

In this section, the well-established relationship between crystallinity and luminescence as described above is assumed to hold, such that the luminescence measured with hyperspectral CL mapping is taken to evaluate the structural quality of the perovskite layer in a FIB-milled PSC lamella. Top-view PL and CL spectra were also acquired from a perovskite half-cell specimen as reference points to evaluate the lamella emission. This study is used to validate the FIB sample preparation protocol described in this thesis, and it is also the first demonstration of optical activity in FIB-milled PSC lamellae. The PSC devices used in this study have a nominal perovskite stoichiometry of  $\text{Cs}_{0.05}\text{FA}_{0.81}\text{MA}_{0.14}\text{Pb}(\text{I}_{0.9}\text{Br}_{0.1})_3$ , a variant of the state-of-the-art TCDH perovskite formula. The emission characteristics of a perovskite film with this exact formulation has previously been investigated with PL and published in ref. <sup>349</sup>, showing an emission peak centred at 1.59 eV (780 nm).

## 4.2.2. Experimental Methods

### 4.2.2.1. PSC Fabrication

The PSCs were fabricated by Dr. Francesco di Giacomo (University of Rome Tor Vergata).

Two devices were used in this study, a half-cell consisting of glass/tin-doped indium oxide (ITO)/NiO/perovskite and a full PSC consisting of glass/ITO/NiO/perovskite/PCBM/BCP/Au. The perovskite stoichiometry is  $\text{Cs}_{0.05}\text{FA}_{0.81}\text{MA}_{0.14}\text{Pb}(\text{I}_{0.9}\text{Br}_{0.1})_3$ .

The NiO ink was prepared by adding 35.5 mg of  $\text{NiCl}\cdot\text{6H}_2\text{O}$  to 1 ml of 2-methoxyethanol. After adding 20  $\mu\text{l}$  of nitric acid, the solution was heated at 75°C for 2 h. The ink was aged for at least 2 days before use. The perovskite ink was prepared by adding 1521.8 mg of  $\text{PbI}_2$ , 104.3 mg of  $\text{PbBr}_2$ , 44.8 mg of CsI, 479.1 mg of FAI and 55.0 mg of MABr to 1.899 ml of N,N-dimethylformamide (DMF) and 0.601 ml of dimethyl sulfoxide (DMSO). The formulation contains a 4% excess of Pb salts. 50  $\mu\text{l}$  of 1-butyl-3-methylimidazolium tetrafluoroborate (BMITFB) ionic liquid were added to 1 ml of DMF, and 20  $\mu\text{l}$  of this solution was added to 1 ml of the perovskite ink. ETL solution was prepared by adding 27 mg of phenyl-C<sub>61</sub>-butyricacid methylester (PCBM) to 750  $\mu\text{l}$  of chlorobenzene and 250  $\mu\text{l}$  of dichlorobenzene, and by adding 5 mg of bathocuproine (BCP) to 10 ml of isopropanol.

Glass/ITO substrates were scrubbed with water and soap solution (Hellmanex 2% in deionised water) and cleaned with three stages of ultrasonic bath: first in water and soap, then in ultrapure water, and finally in isopropanol. After drying, they were treated for 15 min in a UV/O<sub>3</sub> tool. The NiO ink was spun at 4000 RPM for 30 s and annealed for 5 min at 75°C, 10 min at 120°C, and 1 h at 300°C. After cooling down, the samples were transferred into an N<sub>2</sub>-filled glovebox. The perovskite ink was spun at 4000 RPM for 35 s, and 180  $\mu\text{l}$  of chlorobenzene were dropped at 20 s. The film was annealed for 10 min at 100°C. For the full device sample, PCBM was spun at 1700 RPM for 30 s and annealed at 100°C for 5 min. BCP was spun at 4000 RPM. Finally, a 100 nm-thick Au layer was thermally evaporated.

### 4.2.2.2. FIB Milling of PSC Lamella

The cross-sectional PSC lamella was FIB milled using an FEI Helios Nanolab Dualbeam FIB/SEM. Milling was performed using a Ga<sup>+</sup> beam, following the steps and parameters detailed in Figure 3.13 and Table 4.1. This lamella was immediately transferred into an Attolight SEM-CL, minimising air exposure to ~2 min. After thinning, the lamella was not imaged using an electron or ion beam to prevent any additional specimen damage.

Table 4.1 | FIB milling procedure and beam parameters for cross-sectional lamella preparation.

Step	Description	Beam	Voltage (kV)	Current (pA)
1	Pt-C deposition with electron beam	Electron	5	1400
2	Pt-C deposition with ion beam	Ga <sup>+</sup>	30	280
3	Trench milling	Ga <sup>+</sup>	30	2800
4	Lamella surface cleaning	Ga <sup>+</sup>	30	2800
5	Lamella cutting	Ga <sup>+</sup>	30	920
6	Attachment to micromanipulator	Ga <sup>+</sup>	30	280
7	Attachment to sample grid	Ga <sup>+</sup>	30	28
8	Thinning to 1 µm	Ga <sup>+</sup>	8	110
9	Thinning to 500 nm	Ga <sup>+</sup>	8	62
10	Thinning to 200 nm	Ga <sup>+</sup>	8	21

#### 4.2.2.3. Cathodoluminescence

CL data was acquired by Mr. Jordi Ferrer Orri (University of Cambridge) and analysed primarily by the author, who benefited from discussions with Mr. Ferrer Orri and Dr. Giorgio Divitini (University of Cambridge).

Top-view CL on half-cell: CL SI was acquired using an Attolight Allalin 4027 Chronos SEM-CL with the sample oriented perpendicular to the electron beam path. The SIs were recorded with an iHR320 spectrometer (320 mm focal length, 150 gratings/mm blazed at 500 nm, 7000 µm entrance slit) and an Andor 1024 pixel CCD (4x horizontal binning, 1x signal amplification). CL data was obtained in continuous wave mode at 5 kV acceleration voltage, 62.5 pA beam current, and 48.8 ms/px dwell time. All measurements were performed at room temperature under high vacuum. Beam focusing was performed away from the sample areas used for the measurements to prevent specimen damage.

Cross-sectional CL on lamella: CL SIs were acquired on the same SEM-CL system. Due to its far higher specific surface area, the lamella is expected to be more prone to specimen damage compared to the half-cell sample. Therefore, a pulsed electron beam was used to acquire both CL SIs at a beam current of 23.0 pA, as this condition was previously found by Mr. Ferrer Orri to minimise detrimental beam damage-related effects in the perovskite emission.<sup>317</sup> To maintain a similar electron dose to the top-view CL (Table 4.2), a dwell time of 124.1 ms/pixel was used. The beam acceleration voltage was maintained at 5 kV. The pulsed beam was obtained by pulsing an electron gun with the third harmonic

of an Nd:YAG laser ( $\lambda = 355$  nm) at a pulse width of 7 ps and a frequency of 80.6 MHz. All measurements were performed at room temperature under high vacuum. Beam focusing was performed away from the sample areas used for the measurements to prevent specimen damage.

Luminescence spectra acquired from similar TCDH perovskite films through continuous wave and pulsed mode CL were previously found to be comparable to one another in terms of emission energy.<sup>317</sup>

Table 4.2 | CL SI acquisition parameters.

Parameter	Cross-sectional lamella	Top-view
Mode	Pulsed beam	Continuous wave
Acceleration voltage (kV)	5	5
Beam current (pA)	23.0	62.5
Dwell time (ms/pixel)	124.1	48.8
Pixel size (nm)	277	284
Electron dose (e <sup>-</sup> /Å <sup>2</sup> )	2.32	2.36

CL SIs were analysed in LumiSpy 0.1.<sup>350</sup> Artefacts caused by cosmic rays saturating the spectrometer were removed, and the edges of each map were cropped out as they tend to show edge effects. An initial survey of the SIs found that all CL spectra contain two emission peaks, identifiable by their energies to be perovskite and PbI<sub>2</sub>. Therefore, the panchromatic CL spectrum ( $s$ ) in each pixel ( $x$ ) was fitted to a linear summation of two Gaussian distributions ( $g$ ) and a constant background offset ( $k_{bkg}$ ):

$$s(x) = k_{bkg}(x) + g_{\text{perovskite}}(x) + g_{\text{PbI}_2}(x) \quad (\text{Equation 4.1})$$

One Gaussian represents the perovskite's emission and the other represents the emission of PbI<sub>2</sub>. Fitting was performed using least-squares optimisation with the Levenberg-Marquardt algorithm.<sup>295,296</sup>

#### 4.2.2.4. Photoluminescence

PL data was acquired by Dr. Elizabeth Tennyson (University of Cambridge).

The PL data was acquired with a Photon Etc IMA microscope with a diffraction-limited spatial resolution ( $\sim 500$  nm with a  $100\times$  objective lens of numerical aperture = 0.9). A volume Bragg grating was placed before the camera to detect only specific wavelengths with a spectral resolution of 2.5 nm. A 405 nm laser was normally incident on the sample, with a spot size of  $\sim 150$   $\mu\text{m}$  in diameter. The sample stage was immobile during data acquisition while the collection wavelength was swept (integration time/wavelength = 3 s). The incident photon flux was equivalent to 1 sun illumination.

#### 4.2.3. Results and Discussion

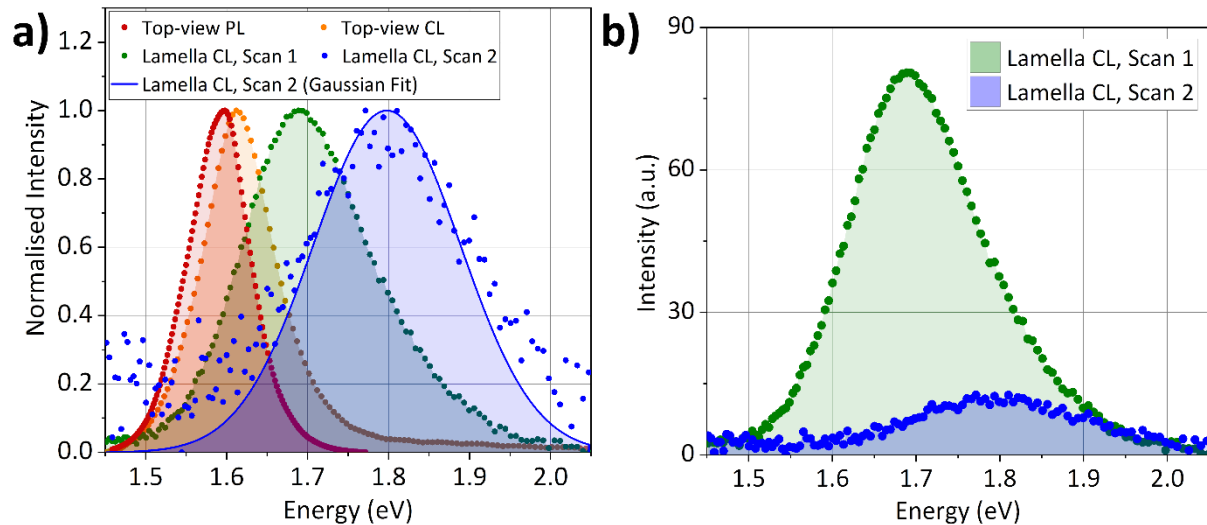


Figure 4.1 | (a) Normalised perovskite emission spectra from (red) top-view PL, (orange) top-view CL, (green) first cross-sectional CL scan, and (blue) second cross-sectional CL scan. As the SNR for the second cross-sectional CL scan is relatively low, normalisation was performed on the Gaussian fit (blue line) rather than on the data points. (b) Raw perovskite emission spectra from (green) first cross-sectional CL scan and (blue) second cross-sectional CL scan.

Top-view PL and CL data were firstly acquired from the half-cell as reference points for perovskite luminescence energy. A peak emission at  $1.596 \pm 0.002$  eV (777 nm) and  $1.612 \pm 0.004$  eV (769 nm) was observed for PL and CL respectively (Figure 4.1a, red and orange curves). The small blue-shift from PL to CL and the high-energy tail seen in the CL spectrum are often observed in literature, with both usually attributed to the filling of higher energy states by the higher concentration of excited carriers in CL.<sup>351-353</sup> A lamella with a nominal thickness of 200 nm was then cut from the full cell sample using a  $\text{Ga}^+$  FIB miller as described above. Figure 4.2a shows an SE image of the lamella, which was acquired at the same time as the CL SI. The perovskite layer is luminescent as shown in Figure 4.2b and c, which display the fitted peak centre energy and integrated peak area of the perovskite

emission, respectively. The interaction volume generated by the 5 kV electron beam is likely to span the entire 200 nm thickness of the perovskite layer in the lamella, as indicated by the Monte Carlo-based electron trajectory simulations (Figure 4.3a).<sup>354</sup> Based on the output of the simulation shown in Figure 4.3b, it appears that the CL emission emerges from the entire lamella thickness, with the top half contributing approximately two-thirds of the total intensity.

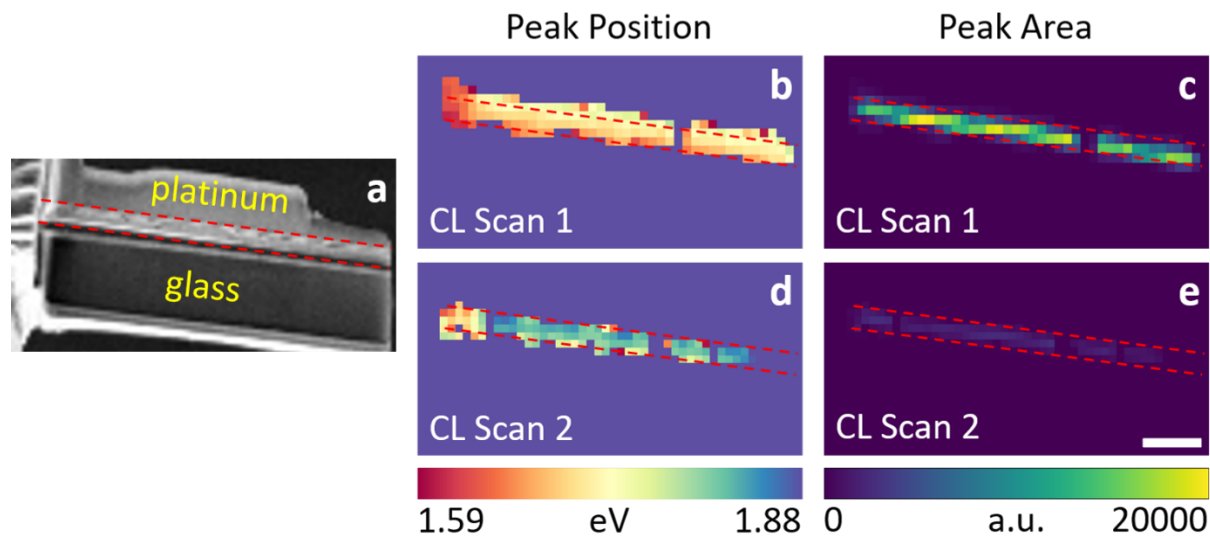


Figure 4.2 | Perovskite emission characteristics from the (b,c) first and (d,e) second cross-sectional CL scans of a FIB milled PSC lamella. (a) SE image, (b,d) fitted peak emission energy, and (c,e) peak emission area. Dashed red lines mark the position of the perovskite layer. Scale bar represents 2  $\mu\text{m}$  and applies to all panels.

Figure 4.1a,b (green curve) and 4.2b show that the emission of the perovskite lamella is centred at  $1.688 \pm 0.004$  eV (734 nm) with a full width at half maximum (FWHM) of  $0.185 \pm 0.006$  eV. This emission peak is blue-shifted by  $0.076 \pm 0.006$  eV (35 nm) and broadened by  $0.078 \pm 0.008$  eV compared to the top-view CL spectrum (FWHM =  $0.107 \pm 0.006$  eV, orange curve in Figure 4.1a). The blue-shifted and broadened emission indicates that only a fraction of the perovskite, most likely the closest to the lamella's top and bottom surfaces, is damaged by the Ga<sup>+</sup> beam. The exact form of damage cannot be divulged from the emission data but is likely to be amorphisation as it is a) the most common type of specimen damage in Ga<sup>+</sup> FIB milling, especially for semiconductors,<sup>286,355–359</sup> and b) consistent with the observation of blue-shifted emission from amorphised perovskite described in the introduction to this section.<sup>344–348</sup> This amorphisation is due to defect accumulation, thus it and the observed blue-shift are likely to be irreversible, in contrast to the reversible pressure-induced amorphisation.<sup>286,343–348</sup>

While it is well-known that a  $\text{Ga}^+$  beam induces amorphisation, even a low-energy electron beam (4.5–60 eV) can also cause specimen damage in perovskites.<sup>360</sup> Therefore, CL emission is also used to investigate whether the observed changes in emission are caused by the CL electron beam as well. In this study, the effect of the CL electron beam on lamellae cannot be properly assessed by comparing the PL and top-view CL spectra because of the different nature of bulk specimens and thin lamellae. For example, the higher specific surface area of a lamella likely accelerates the loss of volatile molecules, a known beam damage mechanism in OIHPs.<sup>299,300,327</sup>

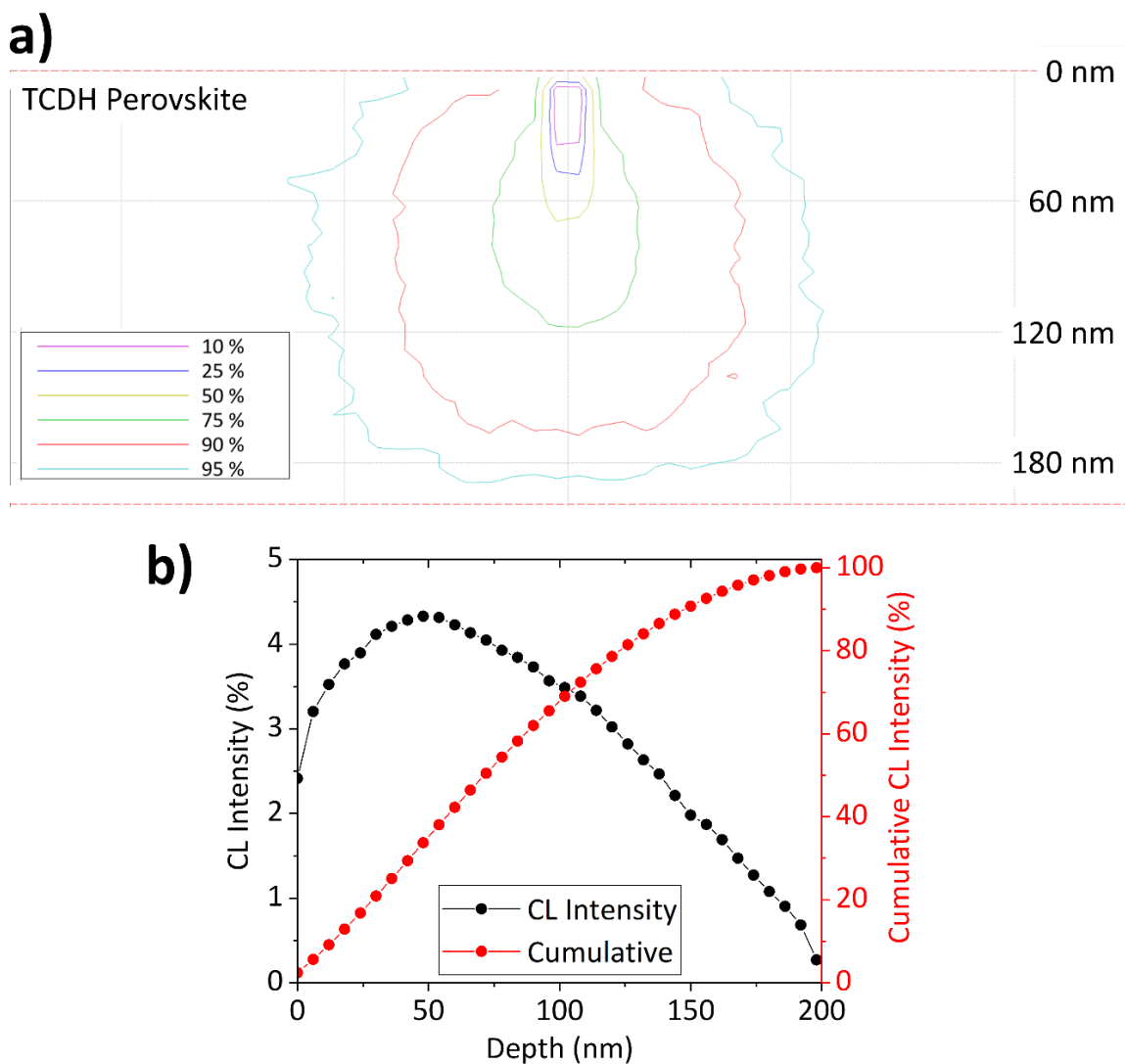


Figure 4.3 | Result of Monte Carlo-based electron trajectory simulation using the CASINO software for an electron beam accelerating voltage of 5 kV and a model perovskite structure of composition  $\text{Cs}_{0.05}\text{FA}_{0.81}\text{MA}_{0.14}\text{Pb}(\text{I}_{0.9}\text{Br}_{0.1})_3$ .<sup>354</sup> (a) Contours of energy deposition inside the 200 nm-thick perovskite layer, where each line marks a volume in which a certain portion of the electron beam's energy was dissipated. (b) Contribution of each thickness slice to the total detected CL signal (black curve) and the cumulative detected CL signal (red curve).

To obtain an estimate of the CL electron beam's effect on lamellae, another CL scan was run on the same lamella. Its fitted emission parameters are shown in Figure 4.2d,e, and the average spectrum is plotted in Figure 4.1a,b (blue dots). The perovskite layer was barely optically active after this second scan, with the emission weakened by a factor of 8, broadened ( $\text{FWHM} = 0.213 \pm 0.006 \text{ eV}$ ), and further blue-shifted by  $0.110 \pm 0.006 \text{ eV}$  (44 nm) compared to the first scan (Figure 4.1b). These results suggest that the CL electron beam contributes to perovskite amorphisation. This agrees well with previous studies which observed CL emission darkening and blue-shifting by 0.10–0.25 eV after exposure to an electron beam.<sup>320,326,361</sup> Therefore, the  $0.076 \pm 0.006 \text{ eV}$  blue-shift observed between the top-view CL and first cross-sectional CL spectra was likely caused by both the  $\text{Ga}^+$  beam and the CL electron beam.

The relative contributions of the CL electron beam and the FIB  $\text{Ga}^+$  beam on the specimen amorphisation can be approximated by comparing the magnitude of the radiation pressure ( $P$ ) they exerted on the specimen.  $P$  is defined as the pressure imposed on a surface due to momentum transfer from an incident electromagnetic wave. It is calculated according to Equation 4.2, where  $P$  is in Pa,  $I$  is the incident wave's intensity in  $\text{W/m}^2$ ,  $c$  is the speed of light, and  $\theta$  is the angle between the incident wave and the surface's normal. An analogue of Equation 4.2 for a beam of electrically charged particles can be derived by calculating the beam's intensity (Equation 4.3) and replacing  $c$  with  $v$ , the particle velocity in m/s (Equation 4.4). In Equations 4.3 and 4.4,  $i$  is the beam current in A,  $V$  is the beam's acceleration voltage in V,  $d$  is the beam diameter in m,  $v$  is the particle velocity in m/s,  $q$  is the particle's charge in C, and  $m$  is the particle's mass in kg. Furthermore, since the  $\text{Ga}^+$  beam is always brought back to focus every time the stage tilt is changed, the beam area is constant at all values of  $\theta$ . Consequently, only one  $\cos(\theta)$  term is required in the formula for  $P$ , to represent the component of the incident ion's momentum that is perpendicular to the lamella surface. The final formula is shown in Equation 4.5.

$$P = \frac{I \cos^2 \theta}{c} \quad (\text{Equation 4.2})$$

$$I = \frac{\text{Beam Power}}{\text{Beam Area}} = \frac{iV}{\pi(d/2)^2} \quad (\text{Equation 4.3})$$

$$v = \sqrt{\frac{2qV}{m}} \quad (\text{Equation 4.4})$$

$$P = \frac{4i \cos(\theta) \sqrt{Vm}}{\pi d^2 \sqrt{2q}} \quad (\text{Equation 4.5})$$

$P$  for the cross-sectional CL scans and the final lamella thinning step of FIB milling (step 10 in Table 4.1) were calculated using the parameters shown in Table 4.3. For the sake of completeness, the  $P$  exerted by the laser beam used in PL and the electron beam in top-view CL was also calculated. As shown in the last row of Table 4.3,  $P$  for the lamella thinning step is 5x lower than the  $P$  for cross-sectional CL scans due to the greater beam diameter and glancing angle used in lamella thinning. This comparison suggests that the role of the CL electron beam in causing the observed emission blue-shift is significant, though not necessarily 5x greater than that of the  $\text{Ga}^+$  beam. The  $P$  values obtained in Table 4.3 are far lower than the hydrostatic pressures used to amorphise perovskite in refs. <sup>344-348</sup>, which are in the order of GPa. However, this does not mean the relationship between perovskite structure and luminescence observed in those studies cannot be applied in this study. Rather, it is simply the amorphisation mechanism that is different. Instead of relying on a very high pressure to trigger a transition into an amorphous phase, the amorphisation in FIB milling is caused by accumulation of defects created by radiolysis and atomic displacement.<sup>286,297,298,343</sup>

Table 4.3 | Radiation pressure calculation for PL, CL, and FIB milling.

Known Parameters	PL (laser beam)	Top-view CL ( $e^-$ beam)	Cross-sectional CL ( $e^-$ beam)	FIB Milling ( $\text{Ga}^+$ beam)
$i$ (A)	N.A.	$6.25 \times 10^{-11}$	$2.30 \times 10^{-11}$	$2.1 \times 10^{-11}$
$V$ (V)	N.A.	$5.00 \times 10^3$	$5.00 \times 10^3$	$8.00 \times 10^3$
$m$ (kg)	N.A.	$9.11 \times 10^{-31}$	$9.11 \times 10^{-31}$	$1.16 \times 10^{-25}$
$d$ (m)	N.A.	$5.00 \times 10^{-9}$	$5.00 \times 10^{-9}$	$3.00 \times 10^{-8}$
$ q $ (C)	N.A.	$1.60 \times 10^{-19}$	$1.60 \times 10^{-19}$	$1.60 \times 10^{-19}$
$\theta$ (°)	0	0	0	89
$c$ (m/s)	$3.00 \times 10^8$	N.A.	N.A.	N.A.
$I$ (W/m <sup>2</sup> )	$1 \times 10^3$	N.A.	N.A.	N.A.
Calculated Parameters	PL (laser beam)	Top-view CL ( $e^-$ beam)	Cross-sectional CL ( $e^-$ beam)	FIB Milling ( $\text{Ga}^+$ beam)
$I$ (W/m <sup>2</sup> )	N.A.	$1.59 \times 10^{10}$	$5.86 \times 10^9$	$2.38 \times 10^8$
$v$ (m/s)	N.A.	$4.19 \times 10^7$	$4.19 \times 10^7$	$1.49 \times 10^5$
$P$ (Pa)	$3.33 \times 10^{-6}$	$3.79 \times 10^2$	$1.40 \times 10^2$	$2.79 \times 10^1$

In addition to perovskite emission,  $\text{PbI}_2$  emission (2.41–2.46 eV) was observed only from a small number of isolated areas in the perovskite layer in both cross-sectional CL scans (Figure 4.4).  $\text{PbI}_2$  has previously been identified as a product of beam damage-induced perovskite decomposition.<sup>320</sup> However, the presence of a  $\text{PbI}_2$  peak in the top-view CL spectrum (Figure 4.5) suggests that the 4% excess Pb salts in the perovskite precursor solution is the most likely source of the  $\text{PbI}_2$  emission observed in Figure 4.4b,c, as opposed to beam-induced perovskite decomposition.

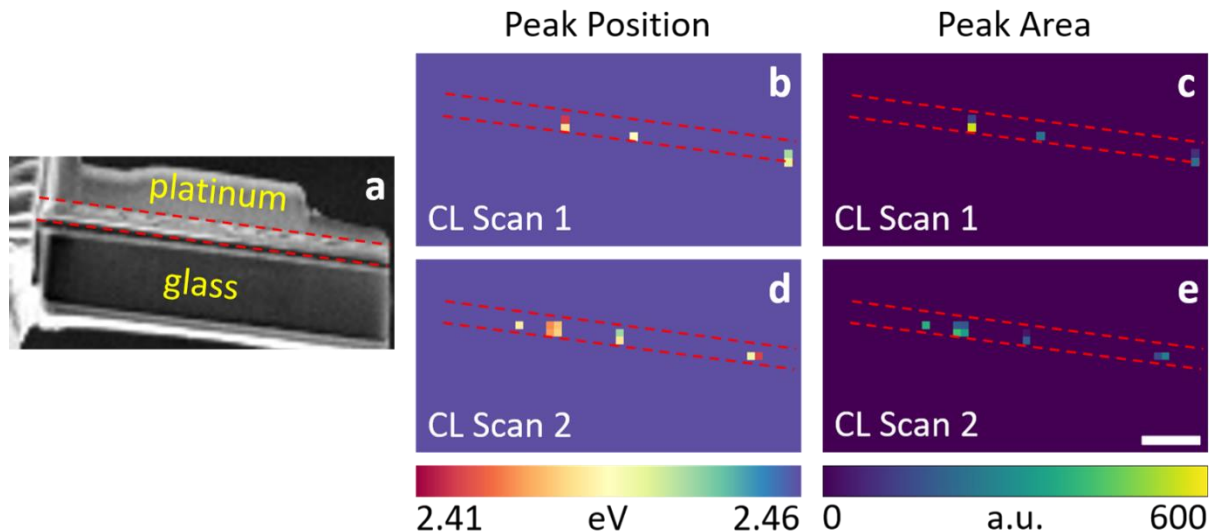


Figure 4.4 |  $\text{PbI}_2$  emission characteristics from the (b,c) first and (d,e) second cross-sectional CL scans of a FIB milled PSC lamella. (a) SE image, (b,d) fitted peak emission energy, and (c,e) peak emission area. Dashed red lines mark the position of the perovskite layer. Scale bar represents 2  $\mu\text{m}$  and applies to all panels.

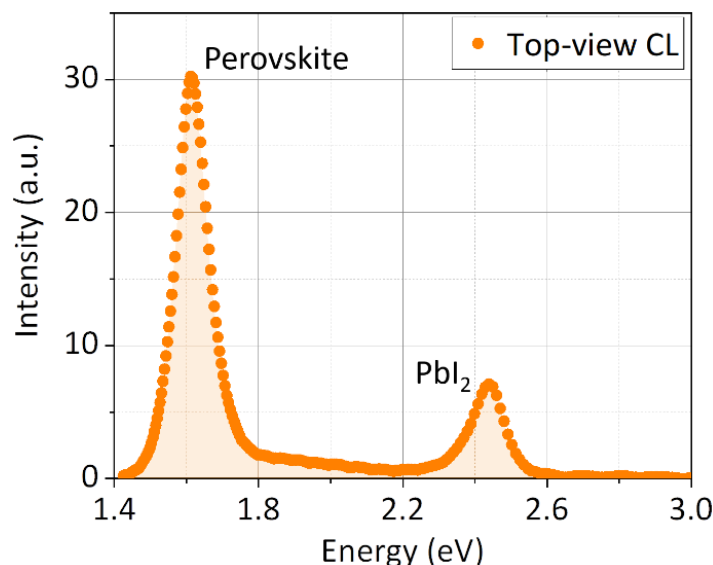


Figure 4.5 | Perovskite and  $\text{PbI}_2$  emission spectrum from the top-view CL scan.

In conclusion, FIB-milled PSC lamellae have been shown to remain optically active, albeit with a slightly blue-shifted luminescence compared to its top-view CL emission. This blue-shift suggests that PSC lamellae do not accurately represent their parent device in terms of radiative emission. However, the extant luminescence and limited  $\text{PbI}_2$  emission indicate that the perovskite crystal structure and composition are in large part preserved. This means useful information can be obtained from EM studies of FIB-prepared PSC lamellae. For example, investigations of device morphology or compositional heterogeneity, and comparative studies of multiple lamellae prepared with identical FIB milling parameters are fruitful methods of PSC characterisation by TEM.<sup>178,362</sup>

## 4.3. Optimisation of PCA and NMF for STEM-EDX Analysis

### 4.3.1. Introduction

PCA and NMF were introduced in Section 3.10 as two MVA algorithms which can be used to decompose STEM-EDX SIs into components, each one containing a signal and an associated spatial distribution map. While the general principles of PCA and NMF are applicable to many different types of (multidimensional) datasets, there are several subtle nuances involved in their specific application to STEM-EDX data which deserve further refinement. For example, while the principle of choosing significant components using the elbow point in a scree plot is straightforward, it may not necessarily be easy or accurate in practice. Then, if the elbow point approach is indeed non-ideal, another method may be needed to more accurately discriminate between principal and noise components. Furthermore, the suitability of the elbow point to choose the number of output NMF components should also be assessed. Finally, for the purpose of denoising, it is not immediately clear whether the denoised dataset should be constructed using PCA or NMF components to model the original SI most closely and obtain accurate elemental maps. This section explores these topics using a stack of four STEM-EDX SIs acquired from two PSC lamellae as a case study, in order to find out how PCA and NMF can be best applied to STEM-EDX data analysis. The first lamella was cut from a spin coated  $\text{MAPbI}_3$  PSC (control) and the second was taken from a spin coated  $\text{MAPbI}_3$  PSC which had been subsequently exposed to aerosolised DMF (aerosol-treated) as described in the Experimental Methods section. The scan areas mapped in this stack are shown in Figure 4.6, with the boundaries between scan areas marked by dashed green lines. The top two areas are from the control specimen, while the bottom two come from an aerosol-treated specimen. Each scan area contains four major layers, namely ITO, perovskite, PCBM, and Cu.

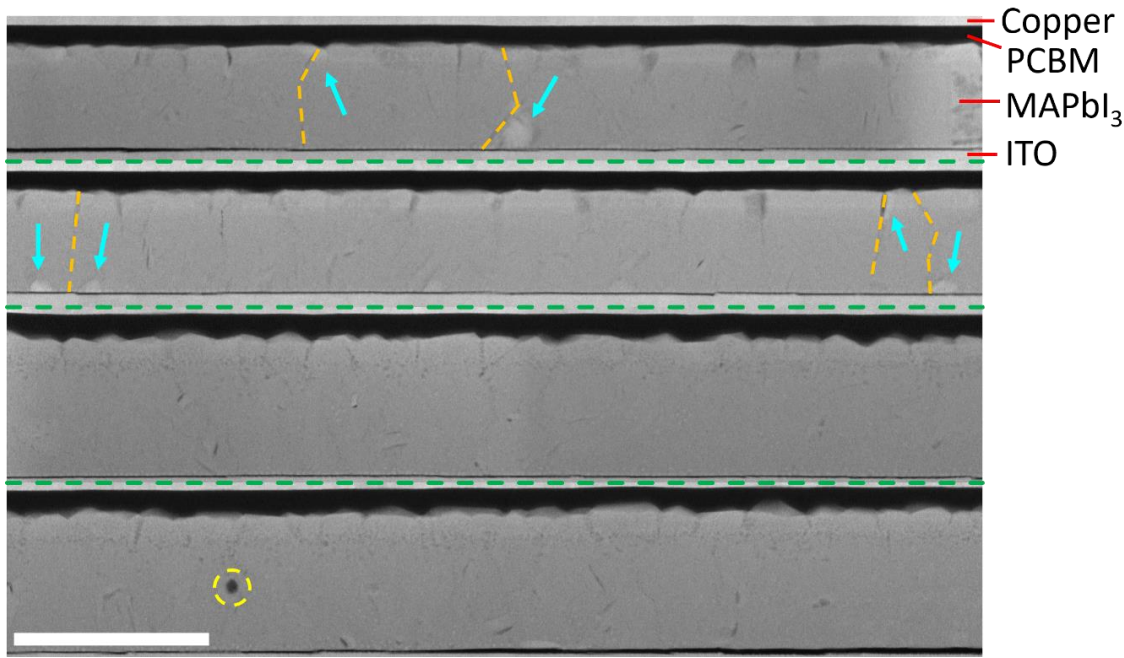


Figure 4.6 | A stack of four HAADF images showing where the STEM-EDX scans were performed. The top two scan areas are from the control PSC and the bottom two are from the aerosol-treated PSC. This arrangement of scan areas is used throughout this section. Dashed green lines mark the boundaries between scan areas. Dashed orange lines indicate perovskite grain boundaries. Cyan arrows mark grains of a secondary phase in the perovskite film. Dashed yellow circle mark a damaged area where the focused electron beam was unintentionally parked for a few seconds. Scale bar represents 1  $\mu\text{m}$ .

The spin coating step was performed in exactly the same manner for both devices. Importantly, an annealing step was performed after spin coating for the control device, but it was delayed until after the aerosol treatment for the aerosol-treated device.<sup>363</sup> Previous research has shown that an annealing step of the same duration and temperature leads to MAI loss through the perovskite grain boundaries, resulting in  $\text{PbI}_2$  formation in the vicinity of those grain boundaries.<sup>364</sup> This also happened in the control device examined here, as indicated by the presence of bright grains next to the perovskite grain boundaries (cyan arrows and dashed orange lines in the top half of Figure 4.6). These bright grains are shown below to be  $\text{PbI}_2$ . On the other hand, those grains are absent in the aerosol-treated device (bottom half of Figure 4.6). This is because the aerosol treatment fostered further perovskite grain growth through solvent vapour-assisted Ostwald ripening, leading to a lower concentration of grain boundaries.<sup>363</sup> MAI loss and  $\text{PbI}_2$  formation were thus suppressed. Consequently, the aerosol-treated device exhibits a thicker perovskite film and should be richer in C and N relative to the control sample due to the inhibited MAI loss. If properly constructed (using either PCA or NMF), a denoised STEM-EDX model should show the presence of  $\text{PbI}_2$  in the control device and the difference in C and N concentrations between both devices. Therefore, these two features can be used to evaluate the suitability of a denoising procedure for production of accurate STEM-EDX elemental maps.

## 4.3.2. Experimental Methods

### 4.3.2.1. Solar Cell Fabrication

The PSCs were fabricated by Dr. Tian Du and Dr. Sinclair Ryley Ratnasingham (Imperial College London).

The precursor solution for  $\text{MAPbI}_3$  devices was prepared by dissolving equimolar concentrations (1.5 mol/dm<sup>3</sup>) of  $\text{PbI}_2$  and MAI in a mixed solvent of DMF and DMSO (9:1.1, volume ratio). The solution was stirred at 60°C for 1 h and was passed through a 0.45 µm polytetrafluoroethylene filter before use. 40 µl precursor solution was dropped onto each substrate and spun at 4000 RPM for 30 s. At the 7th second, 0.5 ml diethyl ether was dripped onto the spinning substrate. The control  $\text{MAPbI}_3$  films were then annealed on a hot plate at 100°C for 20 min. The aerosol-treated  $\text{MAPbI}_3$  films were pre-annealed at 100°C for 2 min to dry most of the solvent prior to aerosol treatment. Films were then placed within the pre-heated reactor, with the temperature set at 100°C. The treatment was carried out by flowing aerosolised DMF into the reactor at 0.5 dm<sup>3</sup>/min for 5 min. The aerosol was generated using a piezoelectric generator. The substrates were placed in the central section of the reactor, approximately 4 cm from the aerosol inlet. After 5 min have elapsed, the aerosol flow was switched to  $\text{N}_2$  and the samples were left on the heated graphite block for a further 5 min at the same temperature to sweep out the remaining DMF in the chamber. Samples were left to cool, then placed into a glovebox for thermal annealing at 100°C for 20 min.

All devices were fabricated on ITO-coated glass substrates sequentially cleaned in acetone, isopropanol and deionised water (using ultrasonics) for 10 min followed by a  $\text{N}_2$  dry. Prior to deposition, the substrates were treated by oxygen plasma for 10 min. Poly(*N,N'*-bis-4-butylphenyl-*N,N'*-bisphenyl)benzidine (PolyTPD, 0.25 wt% in chlorobenzene) was spin coated onto the ITO at 5000 RPM for 20 s as the HTL. After drying for 1 min, Poly[(9,9-bis(3'-(*N,N*-dimethyl)-*N*-ethylammonium)-propyl)-2,7-fluorene]-alt-2,7-(9,9-dioctylfluorene)] (PFN-Br, 0.05 wt% in methanol) was spin coated onto the HTL at 5000 RPM for 15 s as an interfacial modifier to reduce surface hydrophobicity. Solutions of the ETL were prepared by dissolving 30 mg/ml PCBM in chlorobenzene. The solution was stirred at 40°C for 1 h and filtered through a 0.45 µm polytetrafluoroethylene filter before use. The PCBM solution was spin coated on to  $\text{MAPbI}_3$  films at 2000 RPM for 45 s. An ultra-thin interfacial dipole layer was prepared by spin coating a BCP solution (0.5 mg/ml in methanol) on top of the PCBM layer at 4000 RPM for 30 s. Finally, the devices were completed by thermally evaporating 100 nm of Cu at a rate of 1 Å/s and a base pressure of  $5 \times 10^{-6}$  mbar.

#### **4.3.2.2. Transmission Electron Microscopy**

Cross-sectional TEM lamellae were prepared with an FEI Helios Nanolab Dualbeam FIB/SEM. The lamellae were immediately transferred into an FEI Tecnai Osiris 80-200 FEGTEM, minimising air exposure to ~2 min. STEM-HAADF images and STEM-EDX SIs were obtained using the beam parameters described in Section 3.7 and Table 3.2. MVA of STEM-EDX SIs was performed in HyperSpy.<sup>290</sup>

#### **4.3.3. Determination of Principal Components from PCA and NMF**

The most critical step in PCA denoising is the selection of components used to build the denoised model. The conventional approach is to use a scree plot as described in Section 3.10, with components appearing before the elbow point considered as principal components and included in the model while the rest are considered noise and discarded.<sup>331,365</sup> The primary advantage of this approach is the removal of bias or subjectivity in component choice, as a scree plot ranks components solely based on statistical variance. However, this method is also more of an empirical guidance than an exact rule. While the scree plot method has been found to work well for STEM-EDX datasets of relatively homogeneous specimens<sup>335</sup>, it is reasonable to suspect that the elbow point method will eventually fail as specimens get more heterogeneous. This is because genuine spectral features which are only present in a few pixels may have lower variance compared to spectral noise which appear in many pixels, or which is related to very intense X-ray peaks. To provide an example in the context of PSCs, the component which represents small, localised inclusions such as PbI<sub>2</sub> grains is likely to be ranked lower in the scree plot than components showing noise from the organic transport layer's C peak or the metal electrode's metal peaks. Therefore, it is of great interest to investigate whether the elbow point approach can be used to accurately identify components containing real features for cross-sectional STEM-EDX data of PSCs.

PCA was performed on the stack of STEM-EDX SIs described in the introduction to this section, and the resulting components were ranked in the scree plot shown in Figure 4.7. At first glance, selecting the principal components seems straightforward as the first four components (marked by a dashed red ellipse in Figure 4.7) clearly have far higher variances than the rest. Furthermore, it looks like the variance quickly plateaus after component 4. Therefore, the standard elbow point method identifies four principal components and discards the rest as noise. However, zooming in on the scree plot (inset in Figure 4.7) reveals a secondary elbow point where components 5–16, marked by the dashed green ellipses, also show somewhat high variances.

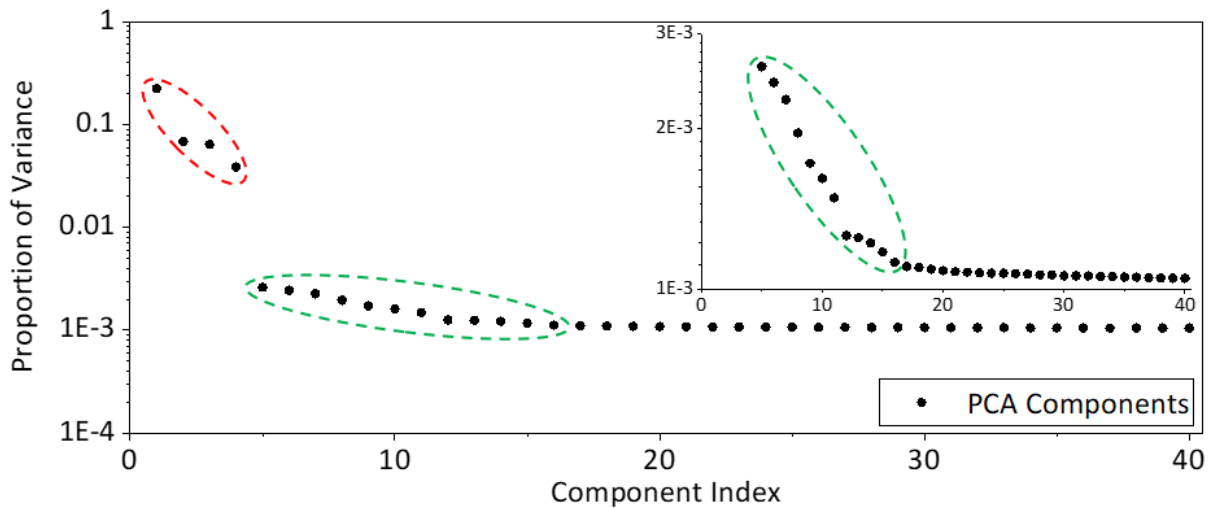


Figure 4.7 | Scree plot from the PCA procedure applied to the stack of STEM-EDX SIs. The inset shows a zoomed-in version where the second elbow point becomes clearly apparent. Dashed red ellipse marks the first four components appearing before the first elbow point. Dashed green ellipses mark components 5–16 appearing after the first but before the second elbow point.

The distribution maps and spectra of components 1–4 are displayed in Figure 4.8. As expected from their very high variance, they show genuine physical features from the specimen and are indeed principal components. On the other hand, components 5–16 are a mix of real features and noise. Components 8 and 10 (Figure 4.9) appear to correlate with a compositional difference between the control and aerosol-treated specimens. This is exactly the kind of useful information one would wish to find out by performing STEM-EDX on these specimens. Component 16 (Figure 4.9) contains information on nanoscale heterogeneity as it shows small areas in the perovskite layer which are Pb-rich and I-poor compared to their surroundings. Components 8, 10, and 16 are considered principal components as their loadings clearly have a non-random distribution of values and their factors feature peaks and valleys whose energies correspond to X-ray lines of relevant elements. In contrast, the loadings of components 5–7, 9, and 11–15 only show random distributions and their factors are dominated by spikes instead of peaks and valleys (Figure 4.10). Therefore, these components can be considered noise. Importantly, principal components 8, 10, and 16 are interspersed with noise components 5–7, 9, and 11–15 in the scree plot. This shows that principal component selection should not be based entirely on variance ranking.

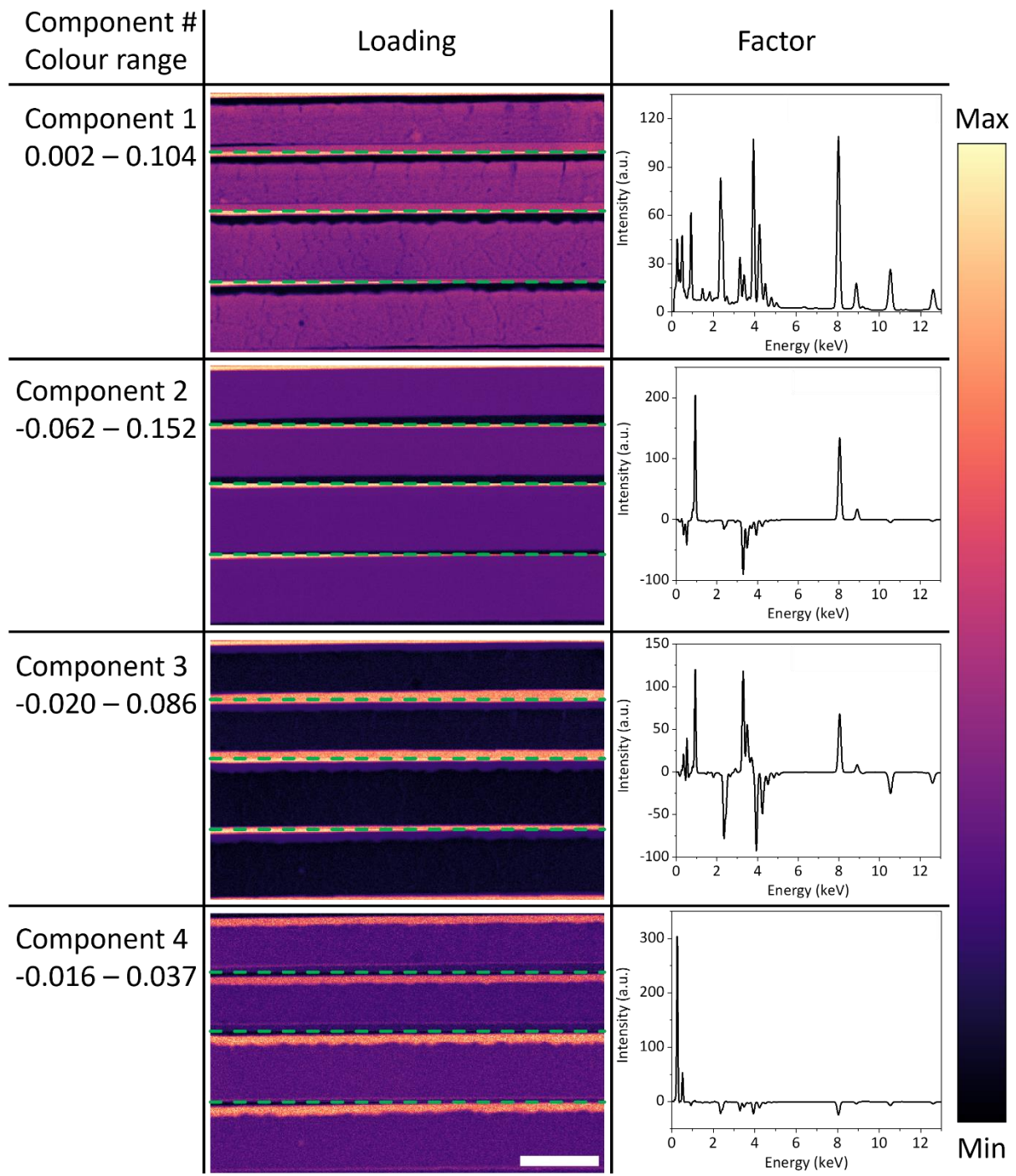


Figure 4.8 | PCA principal components (1–4) appearing before the first elbow point in the scree plot in Figure 4.7. Dashed green lines mark the boundaries between scan areas. Scale bar represents 1  $\mu\text{m}$ .

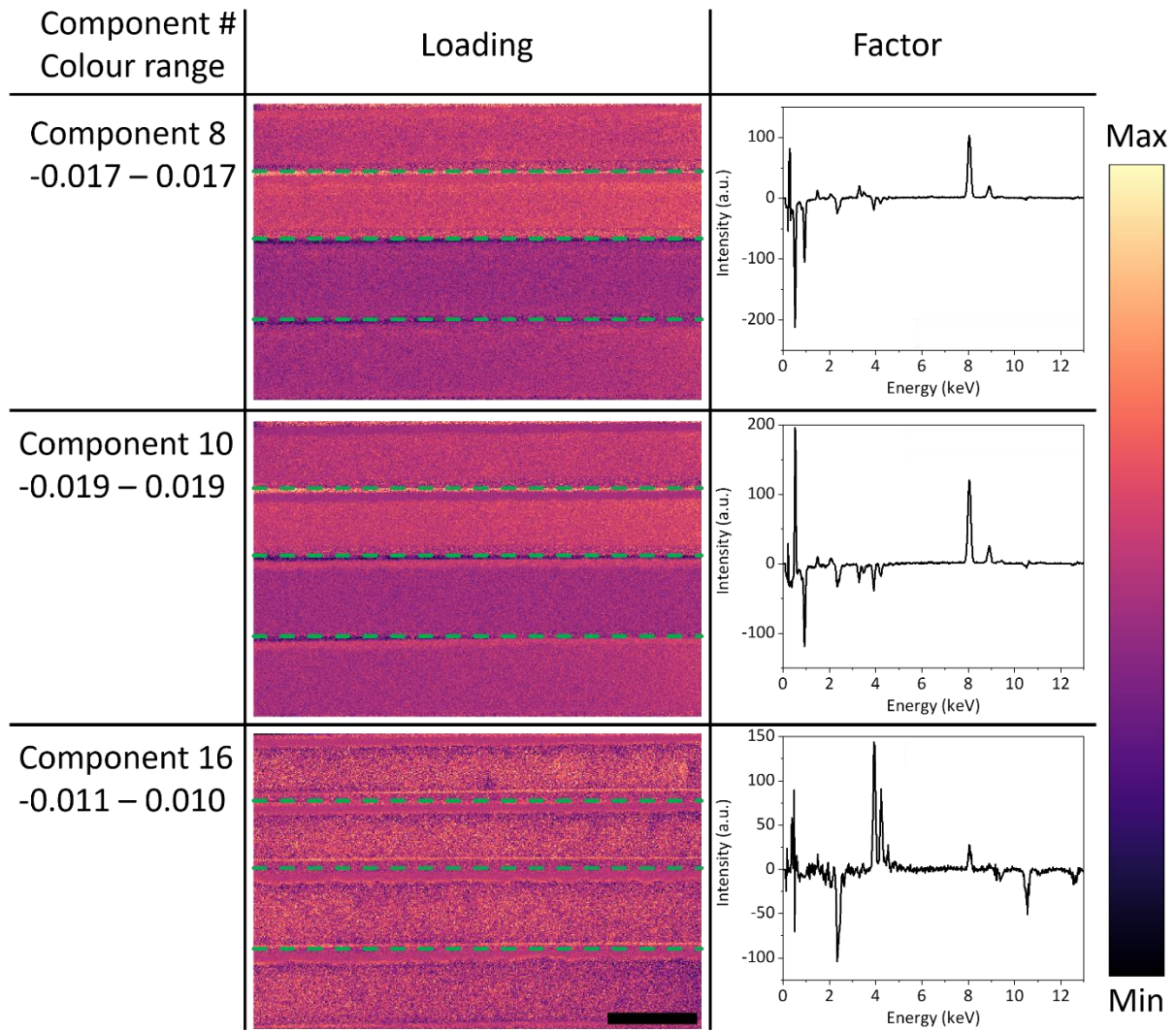


Figure 4.9 | PCA principal components (8, 10, 16) appearing between the first and second elbow points in the scree plot in Figure 4.7. Dashed green lines mark the boundaries between scan areas. Scale bar represents 1  $\mu\text{m}$ .

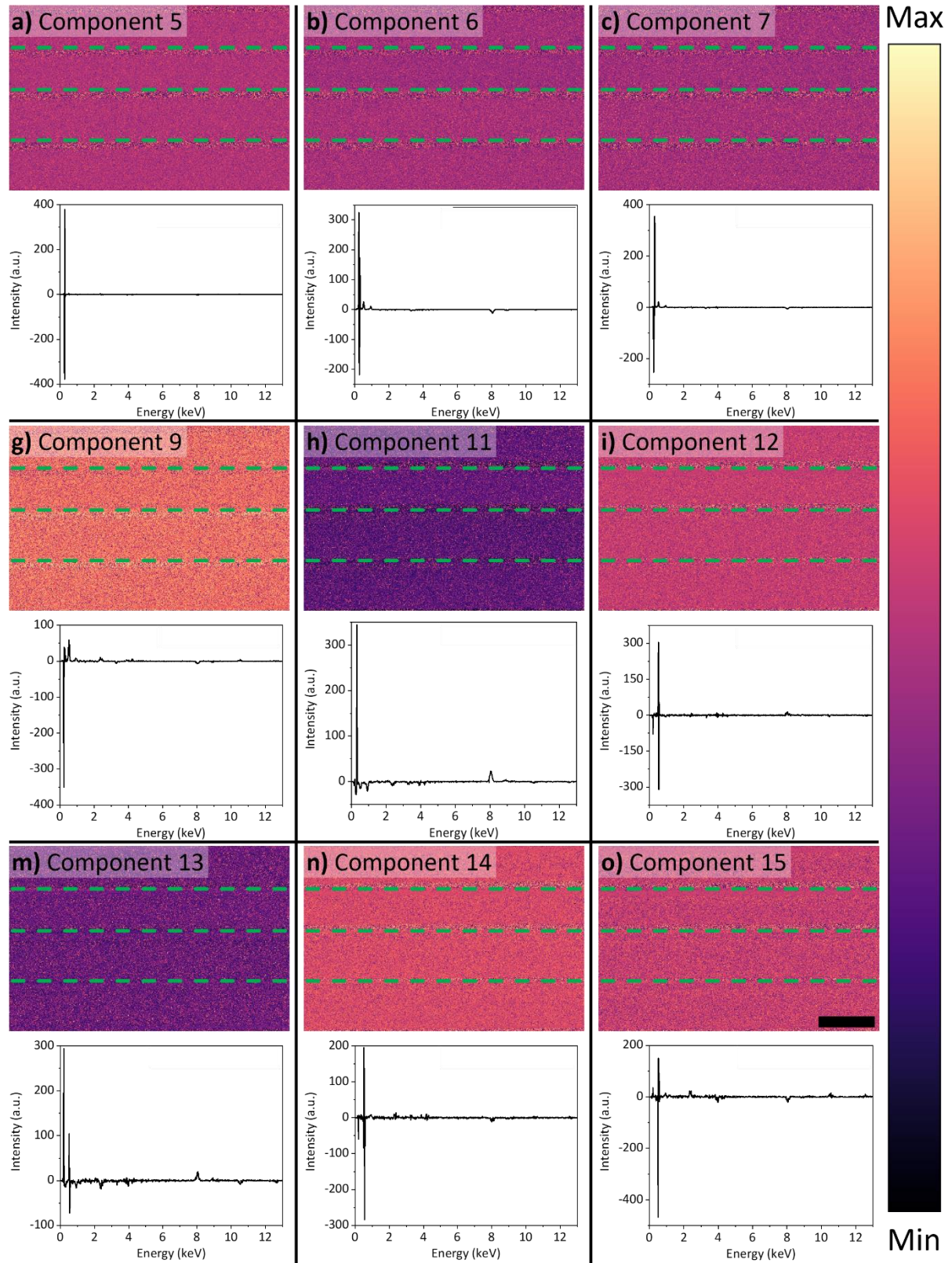


Figure 4.10 | PCA noise components (5–7, 9, 11–15) appearing between the first and second elbow points in the scree plot in Figure 4.7. Dashed green lines mark the boundaries between scan areas. Scale bar represents 1  $\mu\text{m}$ .

NMF is another MVA algorithm capable of decomposing STEM-EDX SIs into components. It requires the desired number of output components ( $p$ ) as an input parameter. Normally, PCA is run first, and then the number of principal components identified by the elbow point method (4 in this case) is fed into the NMF algorithm as  $p$ . However, the preceding discussion has shown that a) there may be a secondary elbow point in the scree plot and b) principal and noise components may be mixed between the first and second elbow points. Therefore, the next step is to examine the product of the NMF procedure while varying  $p$  from 4 to 16. Figure 4.11 shows the resulting four components when  $p = 4$ . All 4 components show real features of the specimens, with loadings that correlate well with the STEM-HAADF images and factors showing peaks attributable to X-ray lines. Components 1 to 4 show the perovskite layer (including the heterogeneities within), the Cu electrode, the ITO layer, and the PCBM layer, respectively. Components 1 and 3 also show Cu peaks which come from the Cu TEM sample half-grid. It is immediately clear that NMF factors are more directly comparable to the raw EDX data than PCA components. Both peak positions and peak intensities can be readily interpreted and assigned to specific X-ray lines.

When  $p$  is set to 16, only the first 4 components show physical features while the rest consist of mostly noise. These 4 components (Figure 4.12) appear similar to those shown in Figure 4.11, but there are some important differences. Most notably, the peaks attributable to Cu-K $\alpha$  (8.04 keV) and K $\beta$  (8.90 keV) in components 1–3 are greatly diminished, the O-K $\alpha$  peaks (0.53 keV) disappear from the ITO and PCBM components, and the C-K $\alpha$  signal (0.27 keV) in component 4 changed from a typical EDX peak into a very narrow spike. These changes occur because the signal corresponding to those peaks were assigned to the other 12 components instead, which can be grouped into three types as shown in Figure 4.13. The first type (component 10, Figure 4.13) includes the Cu-K $\alpha$  and K $\beta$  signal missing from components 1–3. The second (components 5–7, 9, 11, 12, Figure 4.13) are very sharp C-K $\alpha$  spikes at energies surrounding 0.27 keV, suggesting that the C-K $\alpha$  peak's signal count was split into several components. Finally, the third type (components 8, 13–15, Figure 4.13) contain the O-K $\alpha$  signal which should have been present in the ITO and PCBM components. Comparing the components produced by  $p = 4$  and  $p = 16$ , the former produces the more physically meaningful set of results because of the differences described above. For example, there is no physical basis for the separation of the O-K $\alpha$  peak from the ITO and PCBM components. Indeed, its absence from those components when  $p = 16$  (Figure 4.12) means the factors of those components no longer accurately represent ITO and PCBM, both of which are known to contain O. Therefore, it can be concluded that the standard elbow point method is still useful to infer the most appropriate  $p$  for NMF from a PCA scree plot.

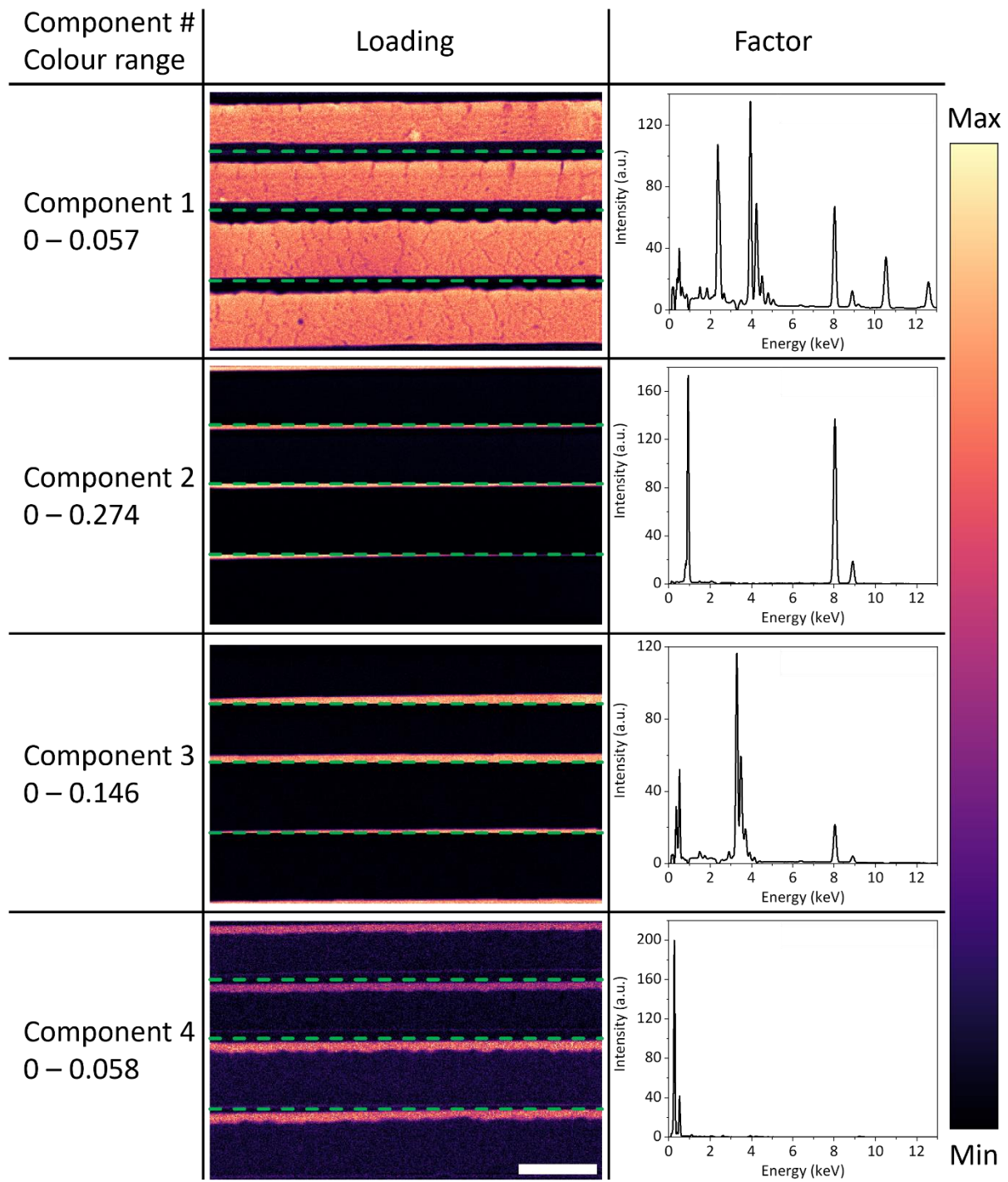


Figure 4.11 | NMF components when  $p = 4$ . Dashed green lines mark the boundaries between scan areas. Scale bar represents  $1 \mu\text{m}$ .

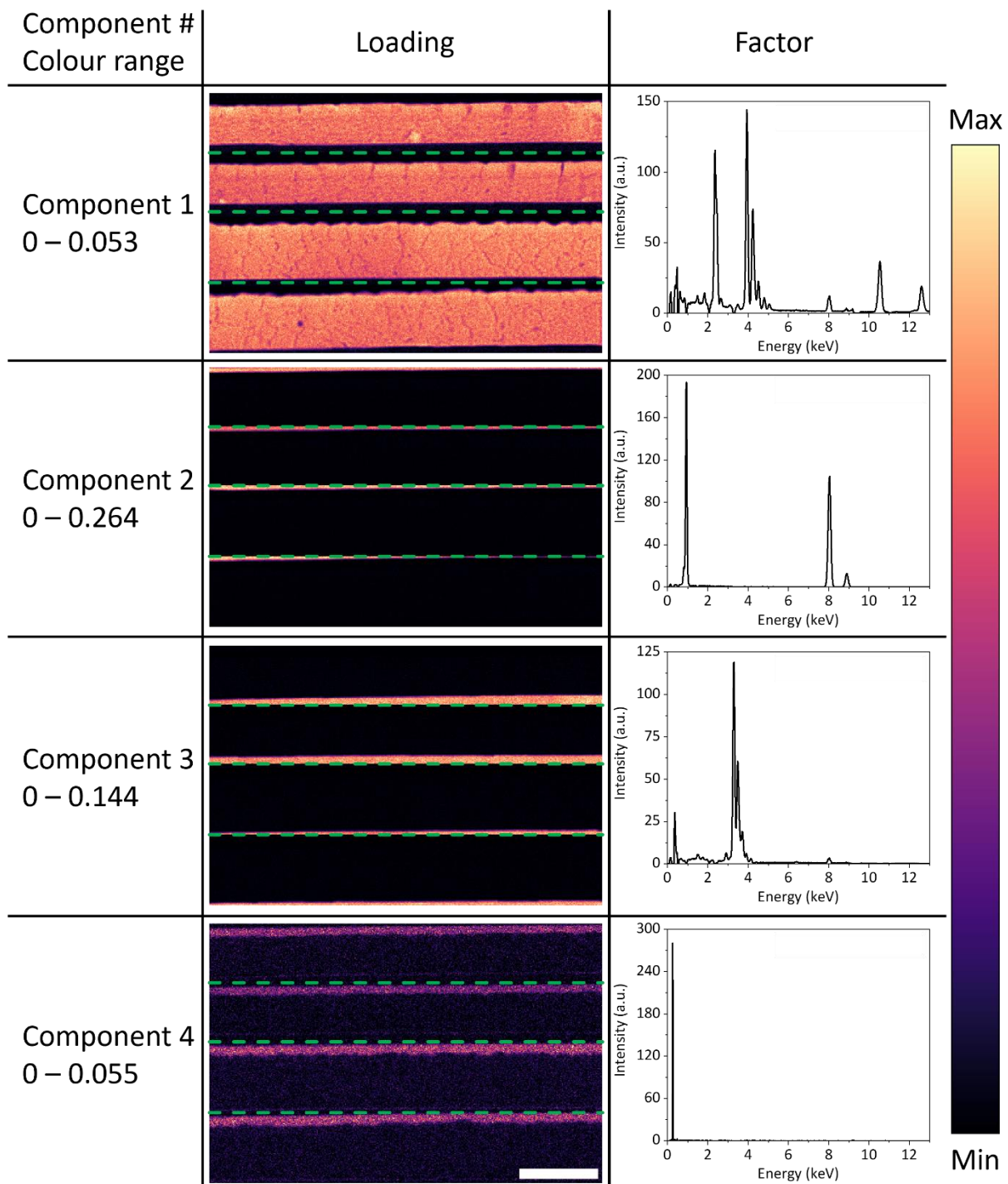


Figure 4.12 | The first 4 NMF components when  $p = 16$ . Dashed green lines mark the boundaries between scan areas. Scale bar represents 1  $\mu\text{m}$ .

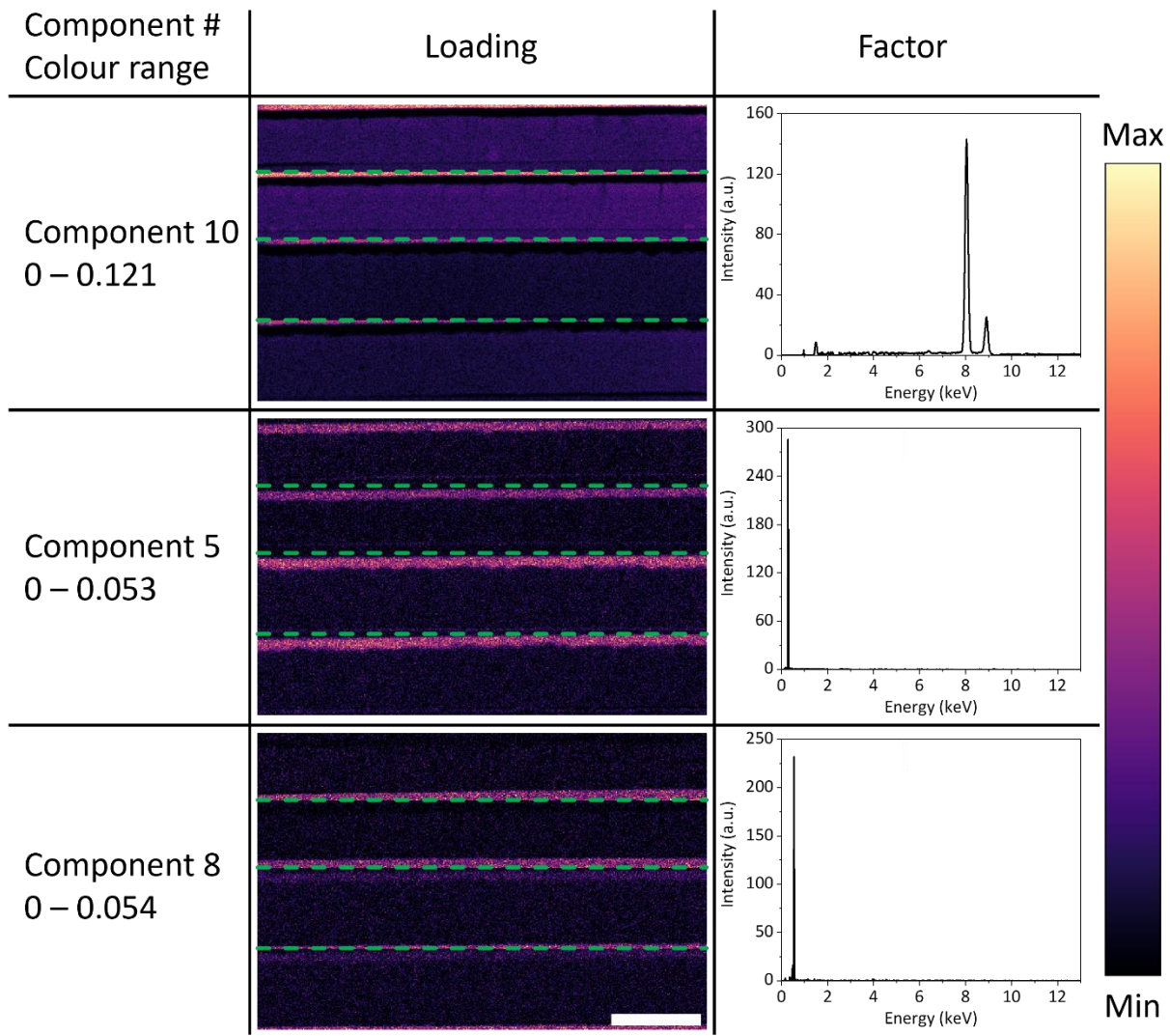


Figure 4.13 | Representative additional NMF components when  $p = 16$ . Components 6, 7, 9, 11, and 12 are similar to component 5, while components 13-15 are similar to component 8. Dashed green lines mark the boundaries between scan areas. Scale bar represents 1  $\mu\text{m}$ .

#### 4.3.4. Construction of Denoised Model from PCA and NMF Components

The previous section has shown that the elbow point method is not necessarily the best way to sort out the principal and noise components in PCA of STEM-EDX data. While this is a useful finding, identification of the principal components is usually not the final goal of STEM-EDX. Rather, it is merely an intermediate step required to construct a denoised model of the raw data, from which elemental maps can be extracted. Therefore, it is important to investigate how the choice of principal components affect the elemental maps retrieved from this process.

Five denoised SIs were constructed to model the raw dataset introduced in the previous section. These are named PCA A, PCA B, PCA C, NMF 4, and NMF 16. The PCA A model was built using principal components identified by the standard elbow point method, namely PCA components 1–4. The PCA B model includes 16 PCA components located before the secondary elbow point. Manual selection of principal components was used to build the PCA C model, which includes components 1–4, 8, 10, and 16. Finally, the NMF 4 and NMF 16 models were built with all components produced via NMF run with  $p = 4$  and  $p = 16$ , respectively. Each denoised model is then subjected to peak intensity extraction and Cliff-Lorimer quantification to obtain quantified elemental maps. The relevant X-ray peaks here are Pb-L<sub>α</sub> (10.5 keV), I-L<sub>α</sub> (3.94 keV), C-K<sub>α</sub> (0.27 keV), and N-K<sub>α</sub> (0.39 keV).

The chemical maps and distribution profiles are shown in Figure 4.14–4.19 for Pb, I, I/Pb ratio, C, N, and N/Pb ratio, respectively. The distribution profiles were produced by grouping all pixels in each map into bins based on their value, and then counting the number of pixels in each bin. The bin widths are 1 at% for the elemental maps and 0.05 for the ratio maps. All five models indicate slightly lower concentrations of the inorganic elements Pb (Figure 4.14) and I (Figure 4.15) in the aerosol-treated sample. For both elements, the PCA A and NMF 4 models have the least amount of noise as expected from their low number of components, with their distribution profiles dropping sharply at the high concentration end. PCA B has the noisiest maps as indicated by its wide distribution profiles. PCA C model results in visibly less noisy maps and narrower distribution profiles compared to PCA B. Importantly, the control sample maps produced from PCA B and C show Pb-rich areas which are attributable to PCA component 16 (Figure 4.9). The effect of including this component is most obvious in the I/Pb ratio maps (Figure 4.16). The PCA A and both NMF models produce very sharp distribution profiles with perfectly uniform perovskite layers where every single pixel has practically the same I/Pb ratio, even where the perovskite was damaged in the bottom scan area. However, this is not an accurate portrayal of the specimens. The PCA B and C maps clearly show areas where the local I/Pb ratio is lower. The shape and location of these areas can be matched to features visible in the HAADF images (Figure 4.6) and in PCA component 16 (Figure 4.9), proving that they are real features rather than noise. The NMF 16 model seems to be the worst option based on the Pb, I, and I/Pb maps, having roughly the same level of noise as PCA B but failing to show the heterogeneities in the perovskite layer.

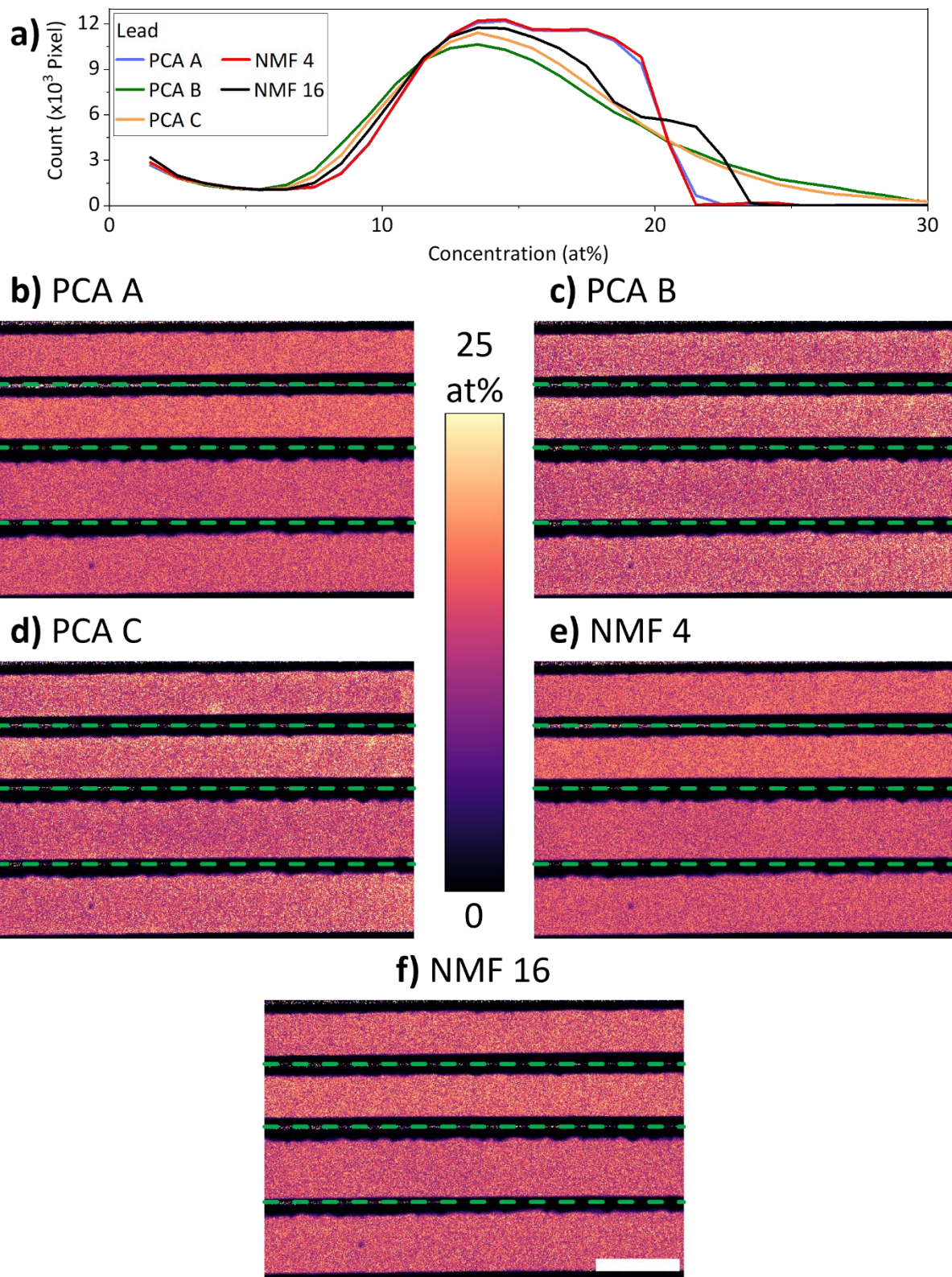


Figure 4.14 | (a) Distributions of Pb concentration and (b-e) quantified Pb maps extracted from the (b) PCA A, (c) PCA B, (d) PCA C, (e) NMF 4, and (f) NMF 16 denoised models. Scale bar is 1  $\mu\text{m}$ .

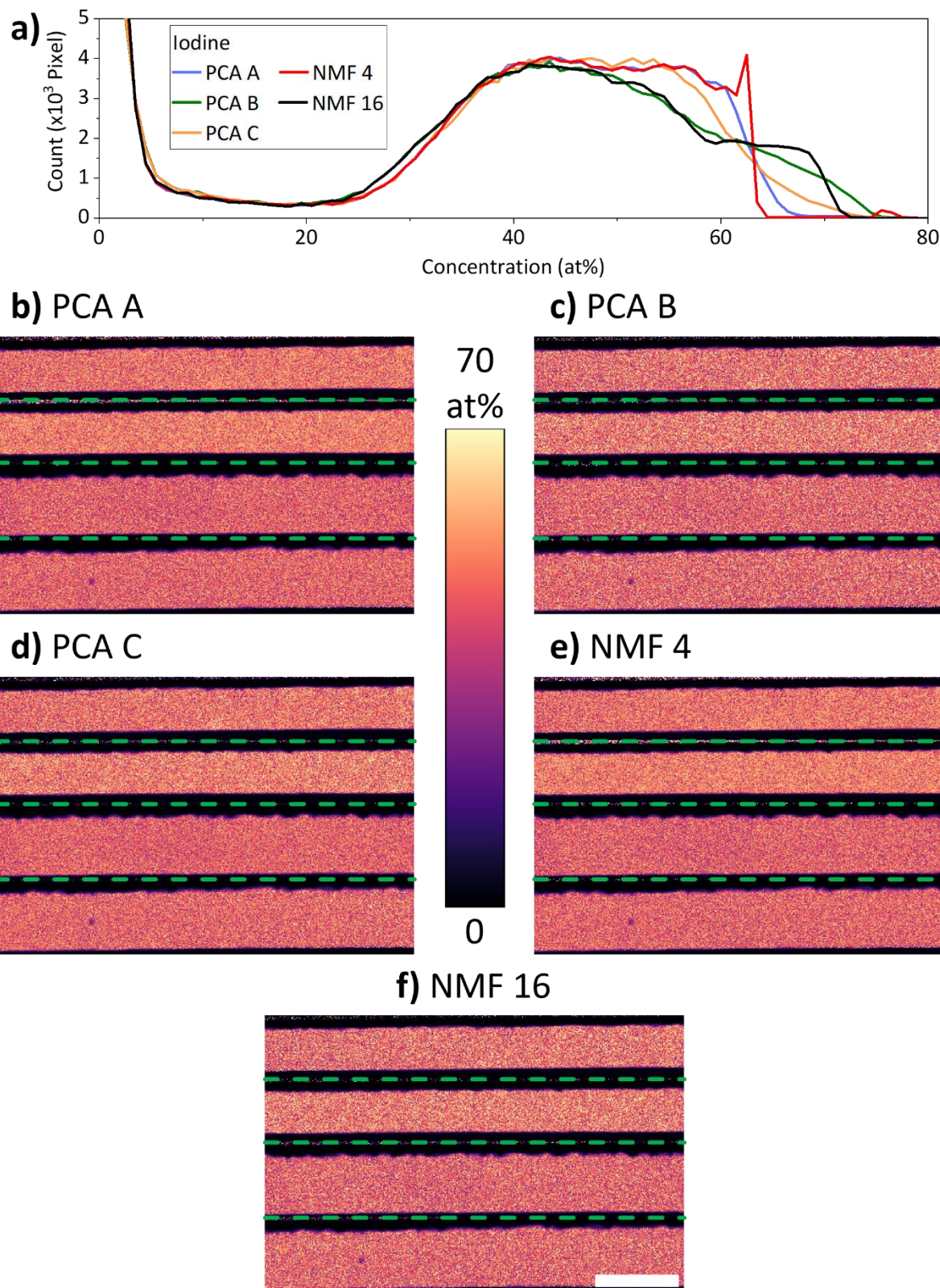


Figure 4.15 | (a) Distributions of I concentration and (b-e) quantified I maps extracted from the (b) PCA A, (c) PCA B, (d) PCA C, (e) NMF 4, and (f) NMF 16 denoised models. Scale bar is 1  $\mu$ m.

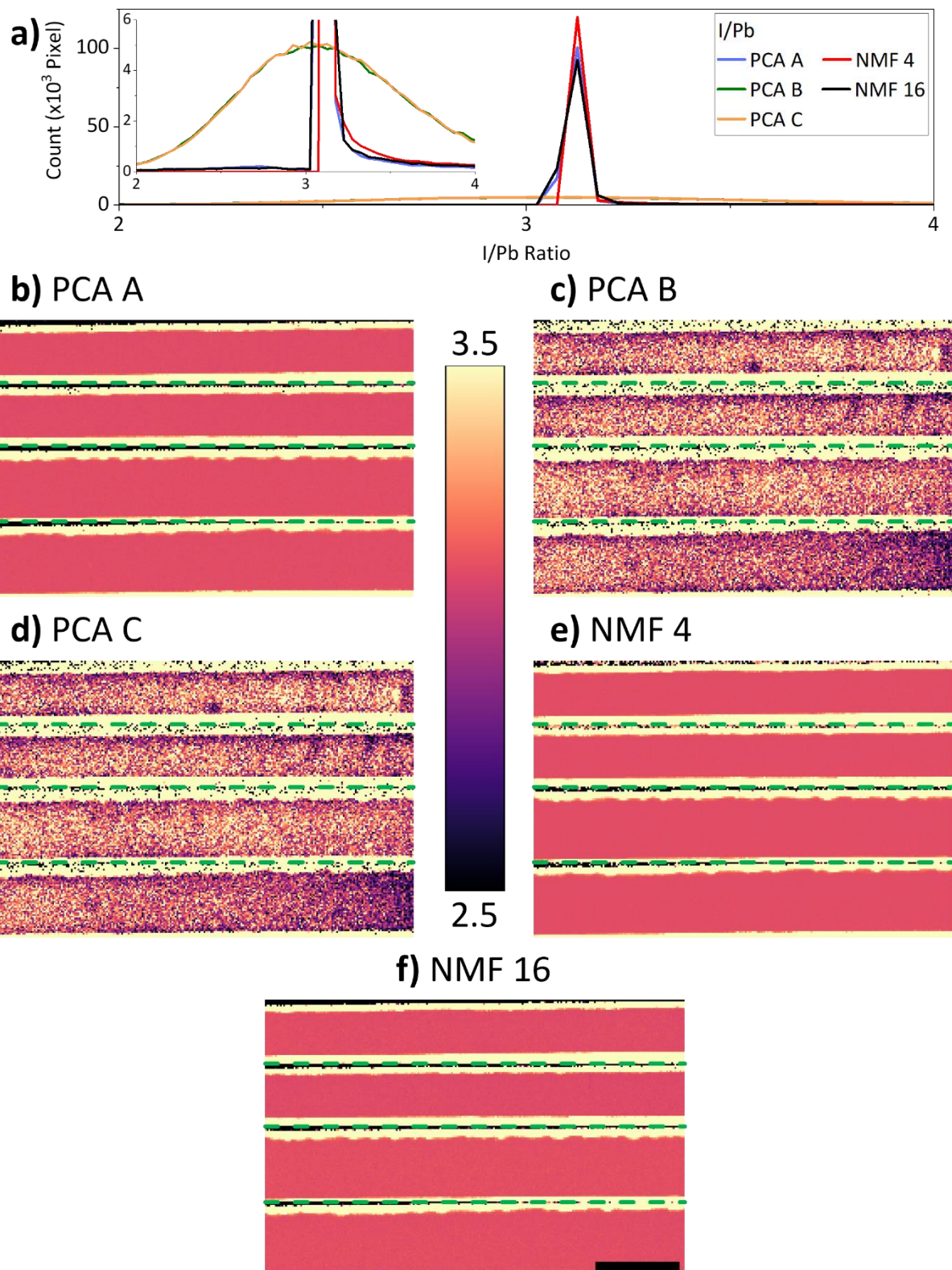


Figure 4.16 | (a) Distributions of I/Pb ratio and (b-e) quantified I/Pb ratio maps extracted from the (b) PCA A, (c) PCA B, (d) PCA C, (e) NMF 4, and (f) NMF 16 denoised models. The I/Pb ratio maps were spatially rebinned by a factor of 2 to reduce noise. Scale bar is  $1 \mu\text{m}$ .

As for the organic elements, the C maps and distribution profiles (Figure 4.17) are largely similar for the five models. The higher C concentration in the aerosol-treated sample is visible in all cases, as is the high C content in the damaged perovskite area, which is expected due to perovskite vaporisation and C deposition by prolonged exposure (a few seconds) to the focused electron beam. On the other hand, the N (Figure 4.18) and N/Pb ratio (Figure 4.19) distributions illustrate the differences between the five denoised models very well. The PCA A and both NMF models do not show higher N content and N/Pb ratio in the aerosol-treated sample as PCA B and C do. Furthermore, PCA A, NMF 4, and NMF 16 also suggest that both the N and N/Pb distributions are uniform throughout the perovskite layer. Meanwhile, the PCA B and C maps show a thin strip at the top of the perovskite layer (near the perovskite-PCBM interface) where the N concentration and N/Pb ratio is lower than the rest of the perovskite. This is in excellent agreement with the HAADF images (Figure 4.6) which appear brighter at the same locations, indicating that there are fewer light atoms or more heavy atoms there. These differences are attributable to PCA components 8, 10, and 16 in the denoised model. Comparing the PCA B and C maps, the high noise in the B maps obscures features with low N content to the point that they are hardly visible. PCA C produces the most accurate N and N/Pb maps, correctly showing higher N content in the aerosol-treated sample, lower N content at the perovskite/PCBM interface in the control sample, and the N-poor features distributed in the perovskite layer.

Differences in the accuracy and noise level of elemental maps produced from the five denoised models are summarised in Table 4.4. Overall, it is concluded that PCA with manual selection of the principal components is the best approach to construct the denoised model of the original dataset. This method accurately reproduces the existence of small heterogeneities in the specimen without including excessive noise. All STEM-EDX data presented in this thesis are therefore processed in this manner.

Table 4.4 | Classification of accuracy (A) and noise level (N) of the quantified elemental and ratio maps produced from the five denoised models. A is classified as either accurate (green) or not (red), while N is ranked as low noise (green), medium (yellow), and high noise (red).

Element / Ratio	PCA A		PCA B		PCA C		NMF 4		NMF 16	
	A	N	A	N	A	N	A	N	A	N
Pb	Red	Green	Green	Red	Green	Yellow	Red	Green	Red	Green
I	Green	Green	Green	Red	Green	Yellow	Green	Green	Green	Red
I/Pb	Red	Green	Green	Yellow	Green	Yellow	Red	Green	Red	Green
C	Green	Green	Green	Yellow	Green	Yellow	Green	Green	Green	Yellow
N	Red	Green	Green	Red	Green	Yellow	Red	Green	Red	Red
N/Pb	Red	Green	Green	Red	Green	Yellow	Red	Green	Red	Red

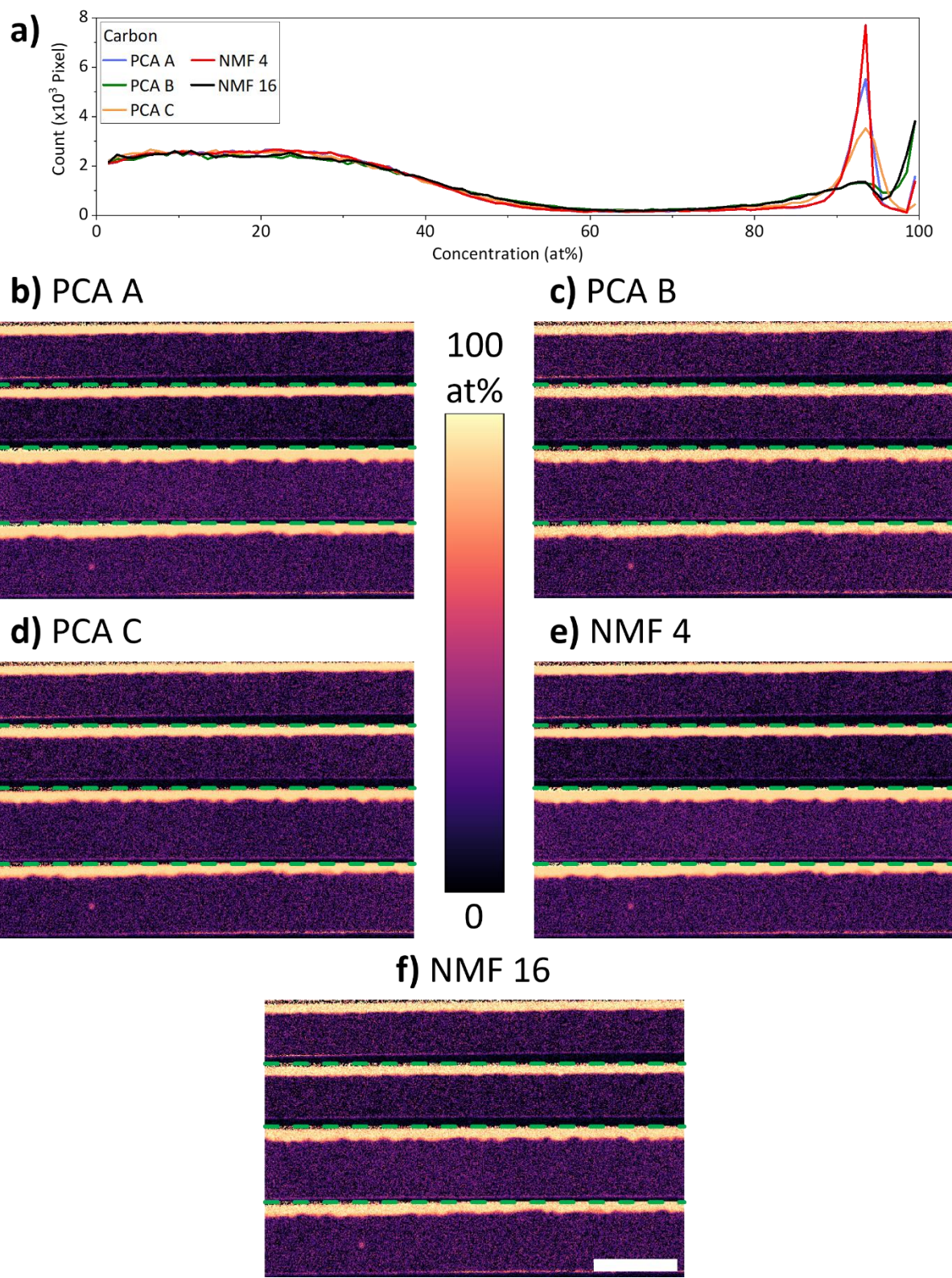


Figure 4.17 | (a) Distribution of C concentration and (b-e) C maps extracted from the (b) PCA A, (c) PCA B, (d) PCA C, (e) NMF 4, and (f) NMF 16 denoised models. Scale bar is 1  $\mu\text{m}$ .

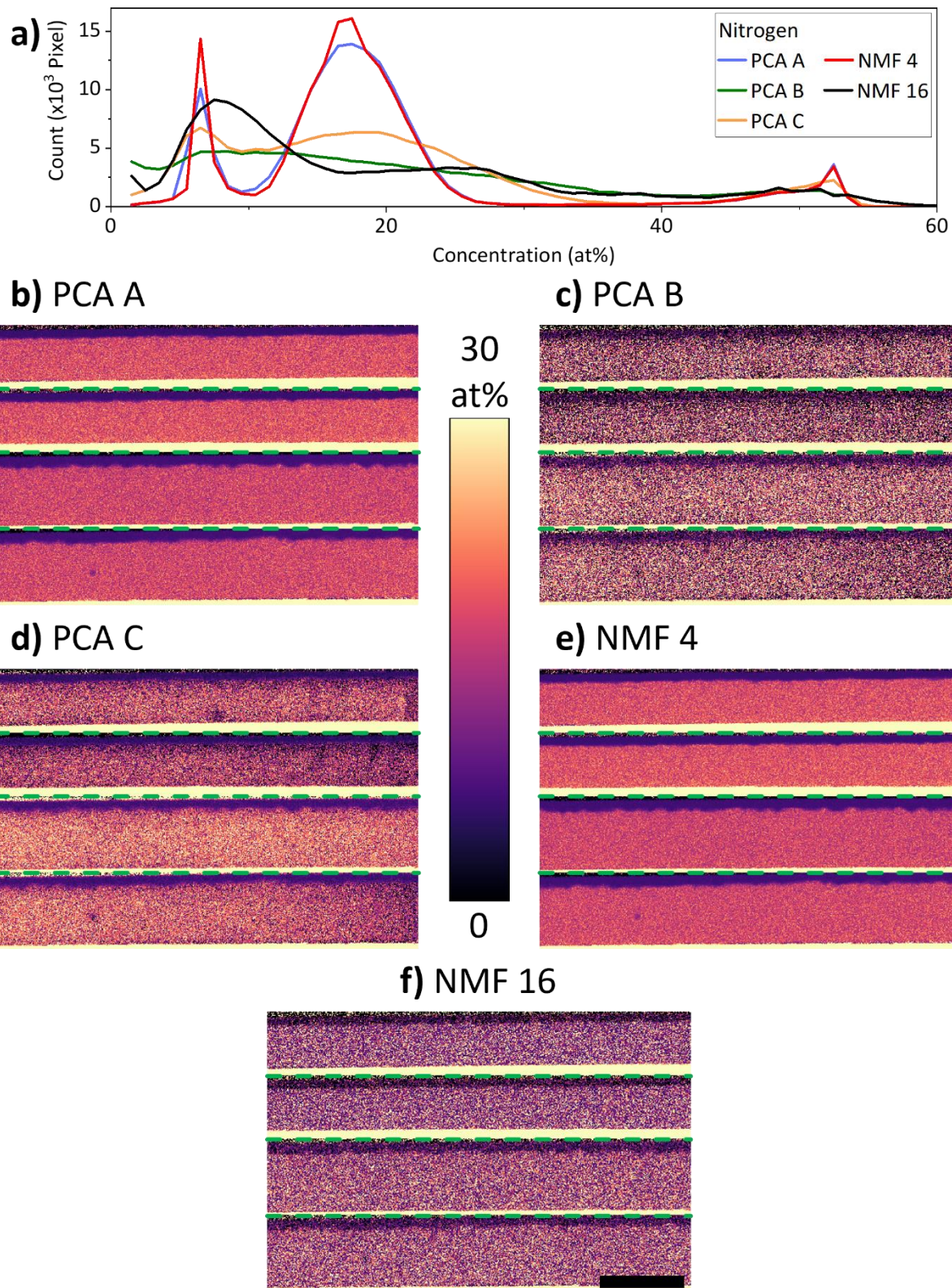


Figure 4.18 | (a) Distribution of N concentration and (b-e) N maps extracted from the (b) PCA A, (c) PCA B, (d) PCA C, (e) NMF 4, and (f) NMF 16 denoised models. Scale bar is 1  $\mu\text{m}$ .

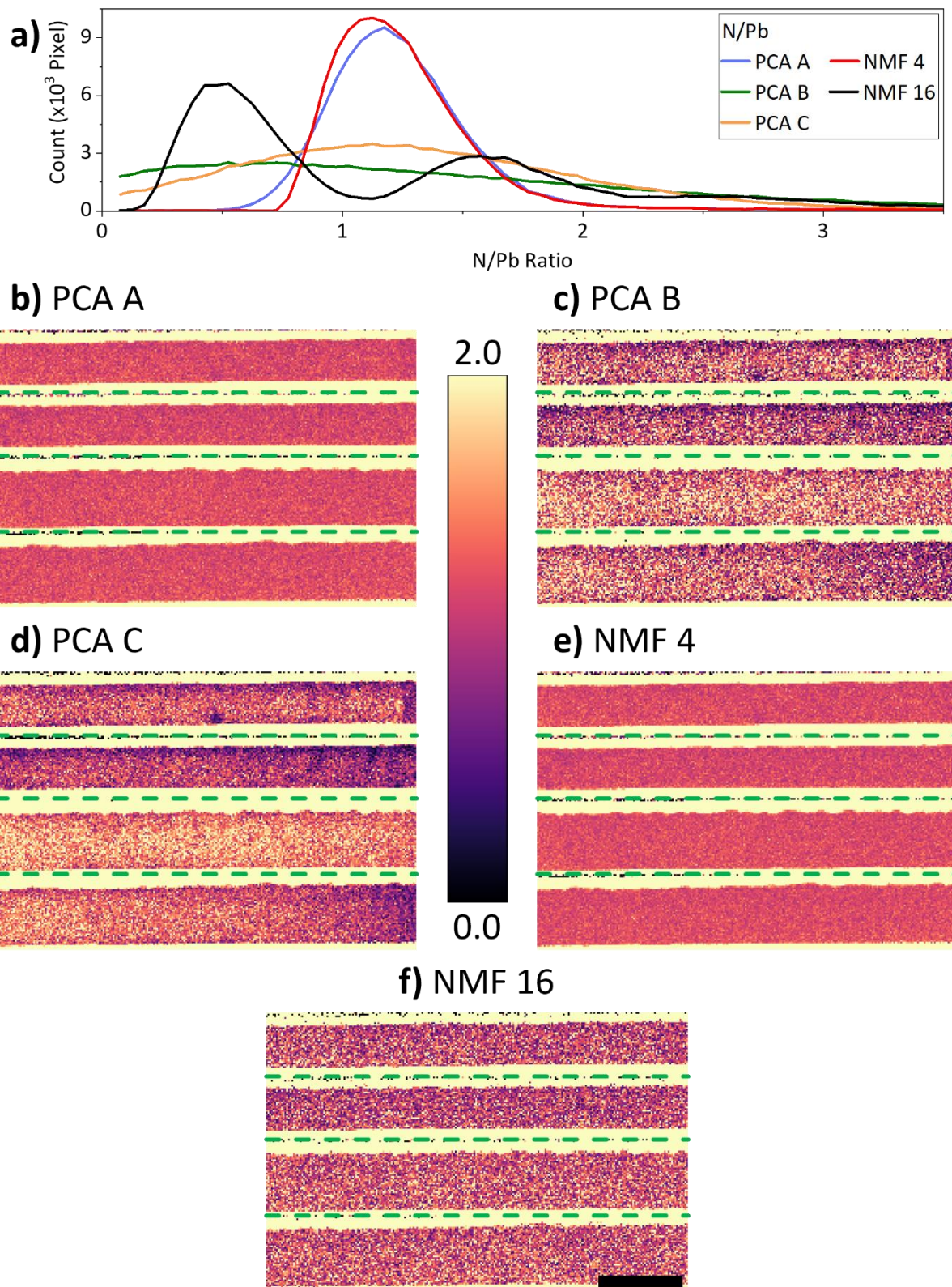


Figure 4.19 | (a) Distribution of N/Pb ratio and (b-e) N/Pb ratio maps extracted from the (b) PCA A, (c) PCA B, (d) PCA C, (e) NMF 4, and (f) NMF 16 denoised models. The N/Pb ratio maps were spatially rebinned by a factor of 2 to reduce noise. Scale bar is 1  $\mu\text{m}$ .

## 4.4. Balancing STEM-EDX Data Quality and Beam-induced Specimen Damage

The contents of this section have been published in ref.<sup>366</sup> and are reproduced here with minor alterations where necessary for flow and clarity.

### 4.4.1. Introduction

The reliability of quantitative EDX analysis is strongly dependent on the SNR across the energy spectrum, which in turn depends on the number of characteristic and bremsstrahlung X-rays emitted by the sample and on the detector's collection efficiency. The latter is generally limited by the small solid angle accessible by EDX detectors in a (S)TEM column (usually 0.2–0.9 sr) to 2–7% of the generated X-rays. The former, for a given specimen thickness, depends on the electron dose and hence can be increased to obtain characteristic X-ray peaks which are quantifiable with higher accuracy by increasing either the beam current or the dwell time. It follows that for elements present in small concentrations, or those with lower X-ray generation rates, precise quantification would require high electron doses. However, this is very challenging when dealing with OIHPs which are prone to beam damage when subjected to high-intensity electron bombardment.<sup>206,213,324,327</sup> Previous research has shown that the primary beam damage mechanism for hybrid perovskites is radiolysis or ionisation damage, which causes bond breaking and disintegration of the perovskite crystal structure.<sup>301,302</sup> Possible results of radiolysis include formation of vacancies through atomic/ionic displacement and loss of volatile molecules.<sup>299,300</sup> Both types of damage affect the accuracy of elemental quantification in STEM-EDX, with the latter being more detrimental as it is usually accompanied by a transformation of the pristine specimen into another chemical phase. In OIHPs, it is well known that I diffuses easily due to its low migration activation energy, making I loss a likely manifestation of beam damage.<sup>137,341,342</sup> Indeed, TEM-EDX and SAED have been shown to cause decomposition of  $\text{MAPbI}_3$  into hexagonal  $\text{PbI}_2$  through formation of I vacancies and loss of volatile gases.<sup>299,327</sup> Other than electron dose, an influential parameter in TEM characterisation of beam sensitive materials is dose rate (dose per unit time). Low dose rates, achieved by using low beam currents or a broad parallel beam, are expected to cause minimal beam damage. On the other hand, STEM-EDX normally involves high dose rates, whose effect is not as clear due to the complex pathways and timescales of damage mechanisms.<sup>298</sup>

In this section, several metrics to quantify STEM-EDX data quality and beam damage are outlined and tested by systematic variation of data acquisition conditions on a well-studied PSC architecture. These robust metrics are used to estimate quantification errors and demonstrate spatial rebinning as a powerful

method to reduce such errors. It is further shown that minimising electron dose for the acquisition of STEM-EDX SIs of OIHPs is of utmost importance. Finally, Pb, I, and Br elemental maps with minimised statistical uncertainty are produced.

## 4.4.2. Experimental Methods

### 4.4.2.1. PSC Fabrication

The PSC device was fabricated by Dr. Mojtaba Abdi-Jalebi (University College London).

A glass substrate coated with fluorine-doped tin oxide (FTO) was cleaned sequentially in 2% Hellmanex detergent, 2-propanol, and ethanol, and then treated with a UV/O<sub>3</sub> cleaner for 15 min. A compact TiO<sub>2</sub> layer was deposited by spray pyrolysis using a precursor solution of 0.6 ml titanium diisopropoxide bis(acetylacetone) in 8 ml ethanol on a hot plate at 450°C. The titanium acetylacetone was prepared by pouring acetylacetone into titanium isopropoxide with a mole ratio of 2:1. For the preparation of mesoporous TiO<sub>2</sub> scaffold, a commercial TiO<sub>2</sub> paste and two synthesised TiO<sub>2</sub> pastes were diluted with ethanol (2:7 weight ratio) and then spin coated at 5000 RPM for 30 s. After drying at 125°C, the TiO<sub>2</sub> film was gradually heated to 500°C and annealed at this temperature for 20 min.

The Cs<sub>0.06</sub>FA<sub>0.79</sub>MA<sub>0.15</sub>Pb(I<sub>0.85</sub>Br<sub>0.15</sub>)<sub>3</sub> perovskite ink was prepared by dissolving PbI<sub>2</sub> (1.2 M), FAI (1.11 M), MABr (0.21 M) and PbBr<sub>2</sub> (0.21 M) in a mixture of anhydrous DMF:DMSO (4:1 v:v), followed by addition of 5 vol% from CsI stock solution (1.5 M in DMSO). The perovskite solution was spin coated using a two-step program at 2000 and 6000 RPM for 10 and 30 s, respectively, adding a 150 µl drop of chlorobenzene 30 s after the start of the spinning routine. The film was then annealed at 100 °C for 1 h. All the film preparations were performed in an N<sub>2</sub>-filled glove box.

After infiltration of TiO<sub>2</sub> scaffold with perovskite, the HTL was spin coated at 4000 RPM for 30 s. The HTL was prepared by dissolving 72.3 mg 2,2',7,7'-Tetrakis[N,N-di(4-methoxyphenyl)amino]-9,9'-spirobifluorene (spiro-OMeTAD), 28.8 ml 4-tert-butylpyridine (4-TBP), 17.5 ml of a solution of 520 mg/ml Li-bis(trifluoromethylsulphonyl)imide (Li-TFSI) in acetonitrile and 29 ml of a solution of 300 mg/ml tris(2-(1H-pyrazol-1-yl)-4-tert-butylpyridine) cobalt(III) tri[bis(trifluoromethane)sulfonimide] (FK 209 Co(III)TFSI) in acetonitrile in 1 ml chlorobenzene. Finally, 70 nm of Au was thermally evaporated on top of the device to form the back contact. The device fabrication was carried out under controlled atmospheric conditions with a humidity of <1%.

### 4.4.2.2. Transmission Electron Microscopy

A cross-sectional TEM lamella was prepared with an FEI Helios Nanolab Dualbeam FIB/SEM. This lamella was immediately transferred into an FEI Tecnai Osiris 80-200 FEGTEM, minimising air

exposure to ~2 min. STEM-HAADF images were acquired using a Fischione detector with a dwell time of 1  $\mu$ s/pixel. STEM-EDX SIs were obtained with 12 combinations of electron beam current (64, 107, 155, 242 pA) and dwell time (10, 30, 50 ms/pixel) to achieve a series of electron doses, ranging from 400 to 7560 e $^-$ /Å $^2$ . STEM-EDX SIs were denoised with PCA and processed in HyperSpy following the procedure explained in Section 4.3.<sup>290</sup>

#### 4.4.3. Electron Dose and STEM-EDX Data Quality

First, the effect of electron dose on the quality of STEM-EDX data is explored. The specimen is a FIB milled PSC lamella consisting of glass/FTO/compact TiO<sub>2</sub>/mesoporous TiO<sub>2</sub>/perovskite/spiro-OMeTAD/Au (Figure 4.20a). The perovskite has a nominal stoichiometry of Cs<sub>0.06</sub>FA<sub>0.79</sub>MA<sub>0.15</sub>Pb(I<sub>0.85</sub>Br<sub>0.15</sub>)<sub>3</sub>. This TCDH composition, or slight variations thereof, is commonly used in highly efficient PSCs.<sup>[20]</sup> 12 STEM-EDX SIs were acquired on a PSC lamella using combinations of four beam current and three dwell time values (Table 4.4). A pair of STEM-HAADF images were also acquired, one taken before and another after the STEM-EDX scans (Figure 4.20). As the dwell time per pixel for HAADF imaging is 1  $\mu$ s, and no change is detectable after single imaging scans, their contribution to specimen damage is negligible in comparison to STEM-EDX mapping.

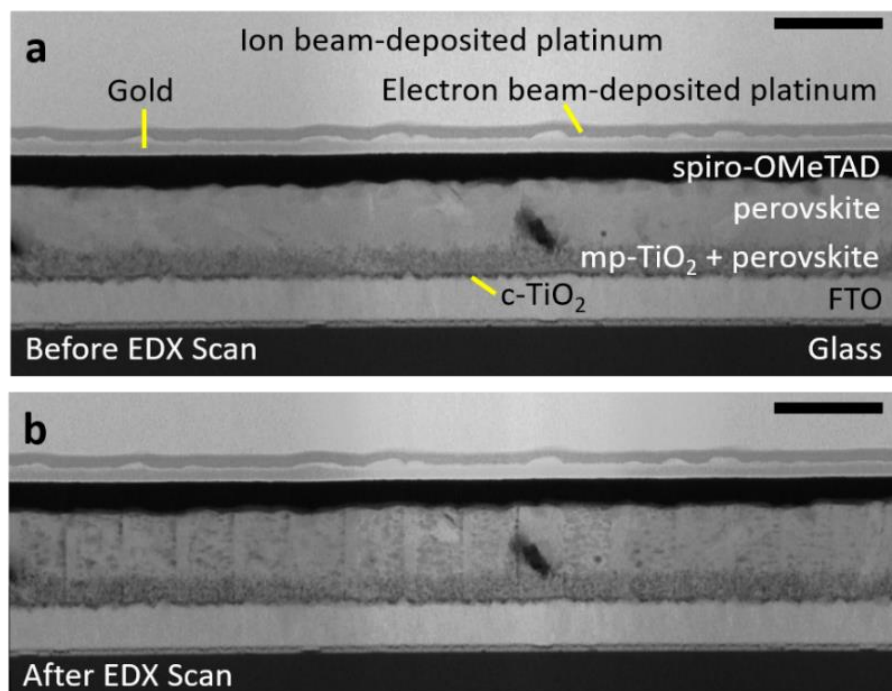


Figure 4.20 | Cross-sectional STEM-HAADF images acquired (a) before and (b) after STEM-EDX data acquisition. Beam damage marks are visible in the perovskite layer in (b). mp- and c-TiO<sub>2</sub> refers to mesoporous and compact TiO<sub>2</sub> layers respectively. Scale bars represent 0.5  $\mu$ m.

Table 4.5 | Electron beam parameters used to acquire 12 STEM-EDX SIs. The dose rates are calculated using a pixel size of  $100\text{ nm}^2$ . All dose rate and dose values are rounded to the nearest 10.

Beam current (pA)	Dose rate ( $\text{e}^-/\text{\AA}^2\text{s}$ )	Dwell time (ms)	Dose ( $\text{e}^-/\text{\AA}^2$ )
64	39950	10	400
		30	1200
		50	2000
107	66780	10	670
		30	2010
		50	3340
155	96740	10	970
		30	2910
		50	4840
242	151050	10	1510
		30	4540
		50	7560

STEM-EDX data quality for different electron doses must be determined to understand the quantification accuracy achievable while using minimum electron doses. For all dose values used in this work, the raw X-ray counts per energy channel is too low to perform further pixel-by-pixel analysis with statistical confidence. Therefore, the SIs were spectrally rebinned by a factor of 4, reducing spectral resolution from 5 eV/channel to 20 eV/channel. Then, PCA was performed to denoise the data as described in Section 4.3. From this denoised SI, peak intensity data were extracted to evaluate chemical composition.

The PCA-treated EDX data were first examined to check for peak detectability (PD) of the Pb-L<sub>a</sub>, I-L<sub>a</sub>, and Br-K<sub>a</sub> peaks, the elemental lines of highest interest for TCDH perovskite. A peak is considered detectable at a 99% confidence interval (CI) if  $I/\sqrt{B} > 3$ , where  $I$  is the background-corrected peak intensity and  $B$  is the background level.<sup>243,274</sup> Maps of PD at 99% CI are shown in Figure 4.21, where the red/blue shading indicates the difference between the measured  $I/\sqrt{B}$  and the critical value required to achieve PD. The I-L<sub>a</sub> and Pb-L<sub>a</sub> peaks are easily detectable even with the lowest dose, but for this specific perovskite formulation, the Br-K<sub>a</sub> peak only becomes consistently detectable with a dose of  $2910\text{ e}^-/\text{\AA}^2$  due to the relatively low Br content compared to I or Pb. The slightly more intense Br-

$L_\alpha$  peak may be used instead, but the signal count increase is marginal (Figure 4.22) and  $\text{Br}-L_\alpha$  has a higher chance of overlapping with other peaks due to its much lower energy ( $\text{Al}-K_\alpha$  being the most probable overlapping peak for optoelectronic device specimens).

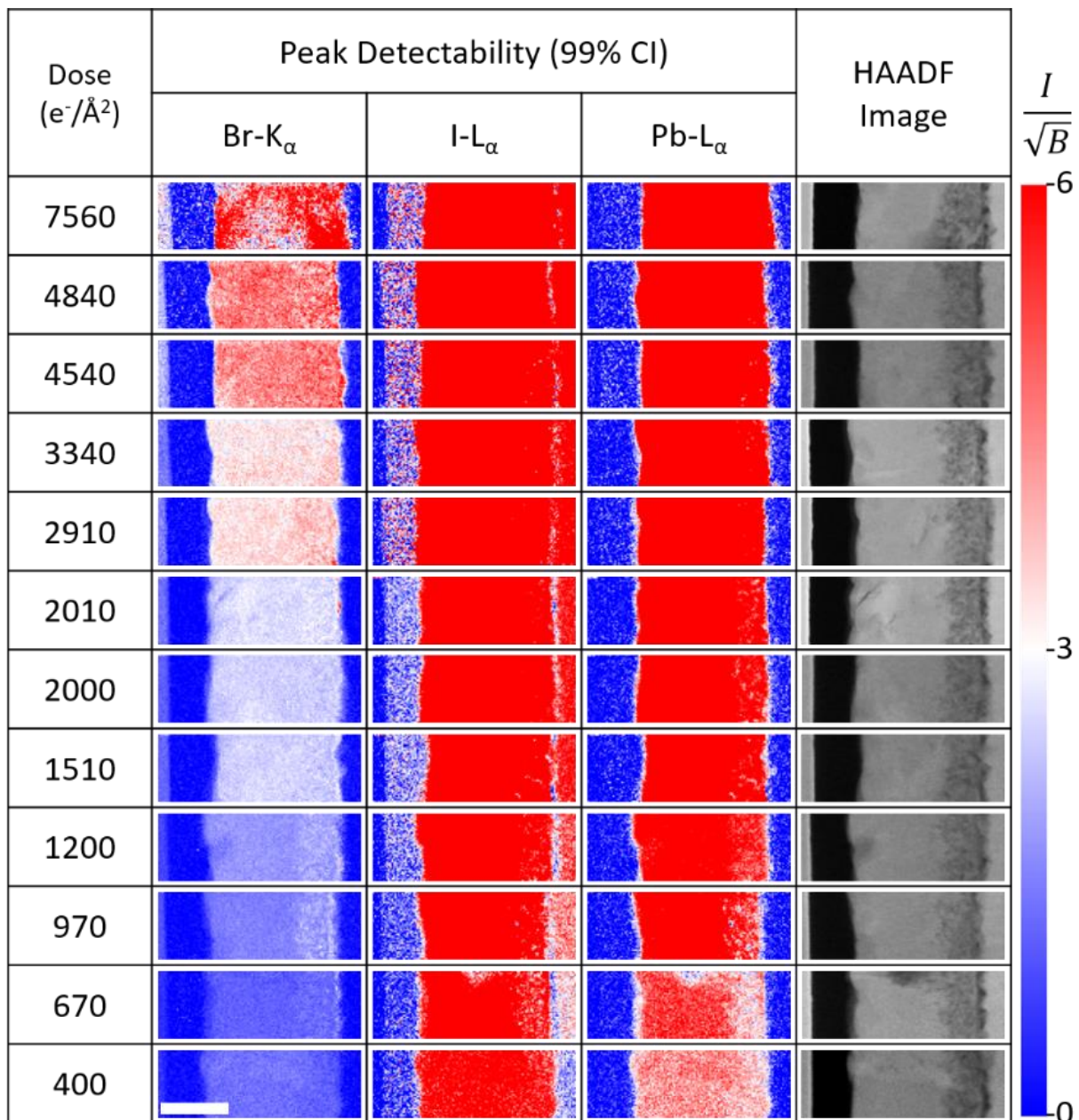


Figure 4.21 | Maps of STEM-EDX PD at a 99% CI and reference HAADF images acquired before STEM-EDX mapping. Red-shaded pixels are detectable while blue-shaded pixels are not. The red/blue shading indicates how far a pixel's  $I/\sqrt{B}$  metric is from the critical value (white) needed to achieve detectability. The maps' spatial resolution is 10 nm per pixel. Scale bar represents 400 nm and applies to all maps and images.

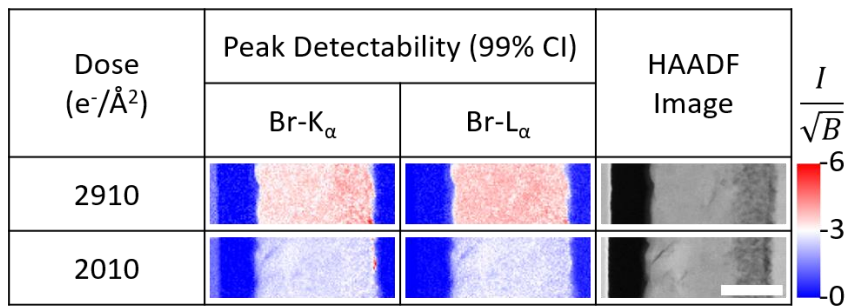


Figure 4.22 | Comparison of PD for Br-K<sub>α</sub> and Br-L<sub>α</sub> peaks and reference HAADF images acquired before STEM-EDX mapping. Red-shaded pixels are detectable while blue-shaded pixels are not. The red/blue shading indicates how far a pixel's  $I/\sqrt{B}$  metric is from the critical value (white) needed to achieve detectability. The Br-L<sub>α</sub> peak is slightly more intense, resulting in a small improvement in statistical confidence. The maps' spatial resolution is 10 nm/pixel. Scale bar represents 400 nm and applies to all maps and images.

Once PD has been established, two parameters are chosen to evaluate the quality of PCA-treated EDX data corresponding to the main characteristic peaks. The first is relative error (RE) at a 95% CI, here taken as the error in the measurement of background-corrected peak intensity  $I$  at each pixel, averaged across  $n$  pixels identified as a specific compound, in this case perovskite. As X-ray counts follow Gaussian statistics, RE can be calculated as<sup>243</sup>

$$RE = \frac{100\%}{n} \sum_1^n \frac{1.96}{\sqrt{I}} \quad (\text{Equation 4.4})$$

The RE remains high even at the highest dose, with values of 33%, 24%, and 74% for Pb, I, and Br, respectively (Figure 4.23a). Because RE is proportional to  $I^{-0.5}$ , there is limited benefit in further increasing the electron dose as shown by the plateaus in Figure 4.23a. Although this high degree of error precludes accurate quantification, the data contains useful qualitative information on spatial heterogeneity. A more accurate assessment of composition can be made on a many-pixel basis by examining a large number of pixels contained in the SI. The appropriate error metric for this approach is no longer RE but absolute error (AE), which is chosen as the second EDX data quality parameter. AE at a 95% CI, expressed as a percentage of the mean peak intensity (MPI), is calculated according to Equation 4.5, where MPI ( $\sigma$ ) is the mean (standard deviation) of  $I$  calculated from  $n$  pixels of the chemical species of interest, in this case perovskite.

$$AE = \frac{1.96\sigma}{\sqrt{n}} \times \frac{100\%}{MPI} \quad (\text{Equation 4.5})$$

In this experiment,  $n$  is  $\sim 2080$  for each SI, with slight variations (up to  $\pm 6\%$ ) from one SI to another due to the roughness of the films. This high  $n$  results in low AE values of 0.5–1.6% of MPI across the dose range (Figure 4.23b). The AE for Br-K $_{\alpha}$  is unexpectedly high for the highest electron dose, most likely due to the abnormally heterogeneous Br distribution in the corresponding scan area (see Figure 4.24) rather than the electron dose itself, as the AEs for Pb-L $_{\alpha}$  and I-L $_{\alpha}$  at this dose agree well with the trend established by other data points. There are common acquisition conditions where  $n$  may be far lower or higher than 2080. For low magnification ( $\sim 20\text{kX}$  or less) STEM-EDX scans of a typical PSC lamella,  $n$  for the bulk perovskite can easily reach 50000, whereas in high magnification experiments, a small-area scan over  $\sim 100$  pixels might be desirable to establish the composition of small inclusions or precipitates. Even with an  $n$  value as low as 100, the AE would still only be in the range of 2.4–5.4%, 2.5–5.0%, and 2.5–7.0% for Pb-L $_{\alpha}$ , I-L $_{\alpha}$ , and Br-K $_{\alpha}$ , respectively, assuming similar  $\sigma$  values. This means that even in highly heterogeneous specimens (many precipitates or segregation of certain elements), small volumes of such heterogeneities are sufficient to accurately obtain their compositions.

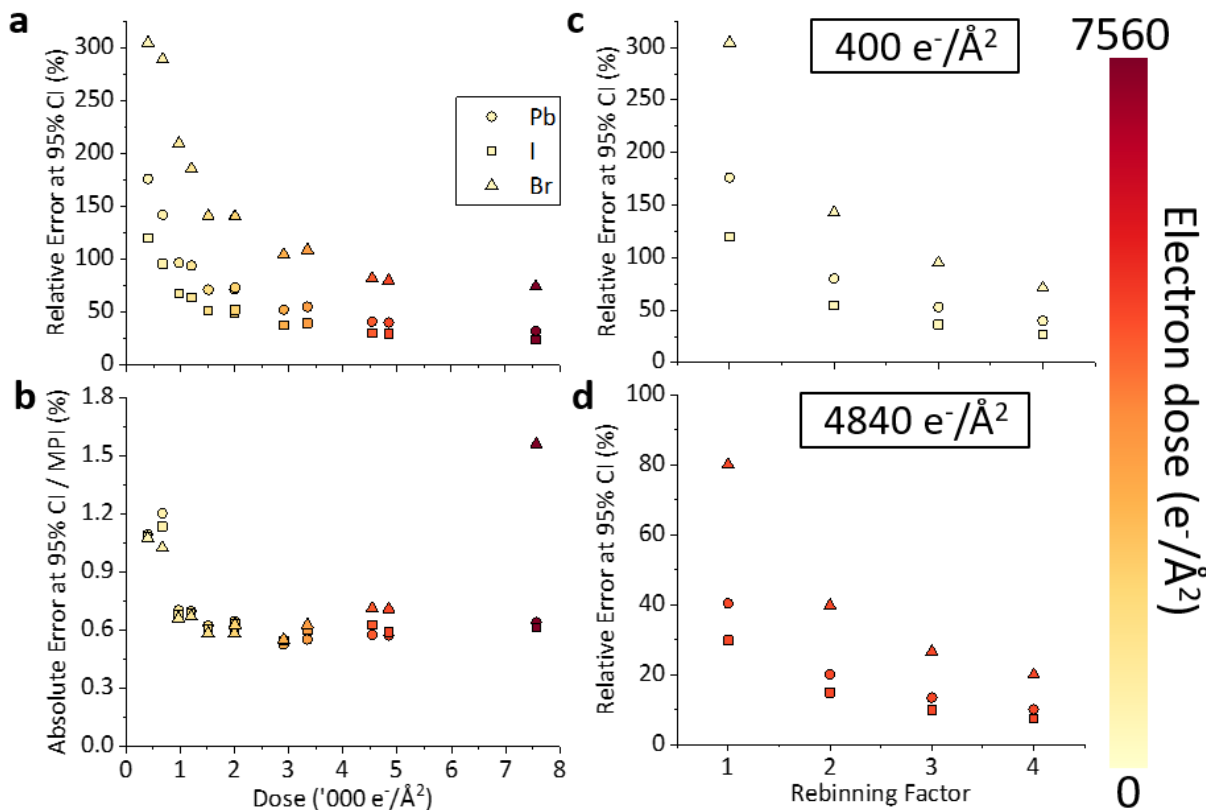


Figure 4.23 | STEM-EDX measurement errors for Pb-L $_{\alpha}$ , I-L $_{\alpha}$ , and Br-K $_{\alpha}$  peaks across a range of electron doses and the effect of spatial rebinnning on them. a) RE on an individual pixel basis at a 95% CI and b) AE for a whole SI at a 95% CI, expressed as a percentage of MPI. Effect of spatial rebinnning on RE for the SI acquired using a dose of c)  $400 \text{ e}^{-}/\text{\AA}^2$  and d)  $4840 \text{ e}^{-}/\text{\AA}^2$ . Symbol colour represents electron dose used in the STEM-EDX scan.

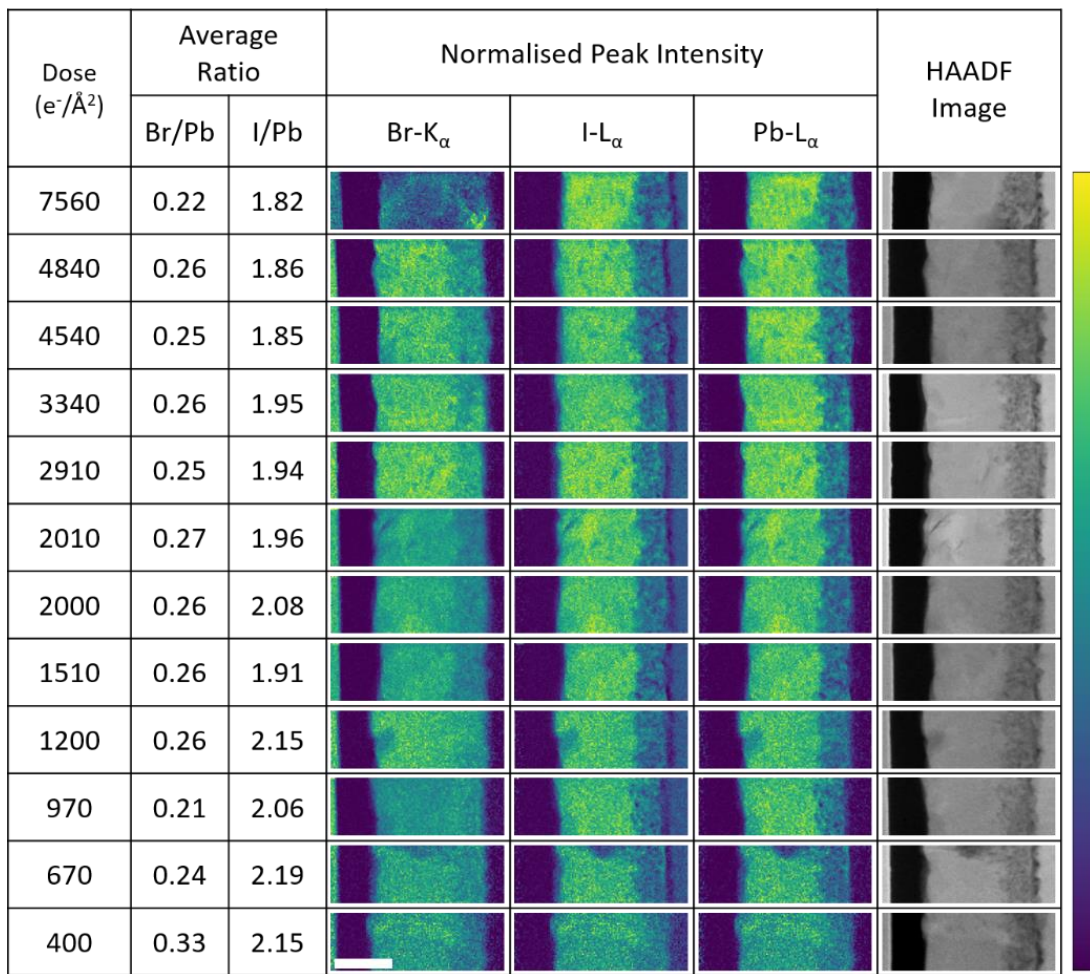


Figure 4.24 | Normalised maps of peak intensity for Br-K<sub>α</sub>, I-L<sub>α</sub>, and Pb-L<sub>α</sub> with reference HAADF images acquired before STEM-EDX mapping and average halide/Pb ratio values. The maps' spatial resolution is 10 nm/pixel. The pixel colour may be used to compare peak intensity within each map, but not across maps. Scale bar represents 400 nm and applies to all maps and images.

In practice, this many-pixel approach can be done by performing spatial rebinning. This step transforms (a portion of) the original SI into a new one with fewer pixels, where a rebinning factor of  $m$  means the data from  $m^2$  neighbouring pixels in the original SI are summed into one pixel in the new SI. Spatial rebinning thereby increases  $I$ , reduces RE, and enables a more accurate quantification at the cost of lower spatial resolution (Figure 4.23c,d, 4.25). One may also perform spectral rebinning to a greater extent than the one used in this work (from 5 to 20 eV/channel) to further reduce RE at the expense of lower spectral resolution. Importantly, rebinning is also a powerful approach to achieve PD without resorting to high doses. For example, spatially rebinning the 400 (1200) e<sup>-</sup>/Å<sup>2</sup> SI by a factor of 3 (2) allows the Br-K<sub>α</sub> peak to achieve PD (Figure 4.25). However, one should not acquire an SI with low dose and very high spatial resolution, with a plan to spatially rebin it later, without first considering beam broadening, possible oversampling, and the consequent compounded beam damage. This is

especially true when working on a thick specimen such as the lamellae used in the works discussed in this thesis. In summary, the data displayed in Figure 4.23 shows that pixel-by-pixel quantification at a 10 nm/pixel spatial resolution suffers from a large error at the dose range examined. However, data from many pixels in an SI can be gathered through spatial rebinning to achieve sufficient statistical confidence for quantification of the elements of interest. Depending on the level of precision and resolution desired, information may be obtained from both the original and rebinned SIs. The original SI provides qualitative elemental maps showing compositional heterogeneity at high spatial resolution, while the rebinned SI supplies accurate quantitative compositions for specific areas of interest.

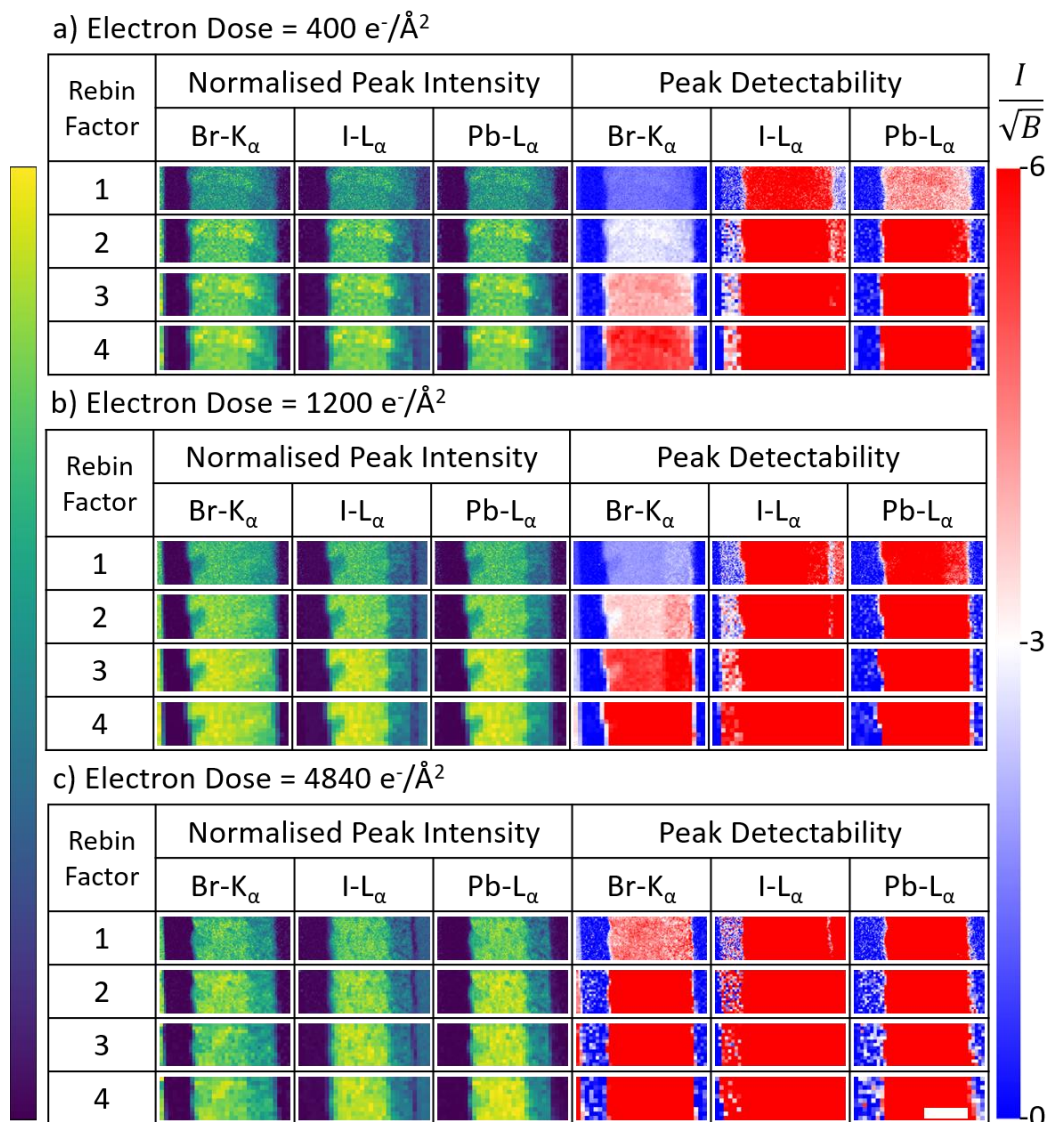


Figure 4.25 | Effect of spatial rebinning on peak intensity maps and PD for the SIs acquired using a dose of (a) 400 e<sup>-</sup>/Å<sup>2</sup>, (b) 1200 e<sup>-</sup>/Å<sup>2</sup>, and (c) 4840 e<sup>-</sup>/Å<sup>2</sup>. Spatial rebinning lowers spatial resolution but boosts PD. A rebinning factor of (1/2/3/4) results in a spatial resolution of (10/20/30/40) nm/pixel. Scale bar represents 400 nm and applies to all maps.

Once the PD of important elemental peaks has been confirmed and measurement errors have been estimated at the desired spatial resolution, the background-corrected intensity data may be converted into quantitative maps via Cliff-Lorimer quantification.<sup>275</sup> Importantly, each EDX analysis software may have its own threshold of minimum peak intensity required for quantification. For example, the analysis platform used in this thesis, HyperSpy, cannot quantify SIs acquired with the two lowest doses used here. Quantitative maps extracted from the remaining 10 SIs are displayed in Figure 4.26.

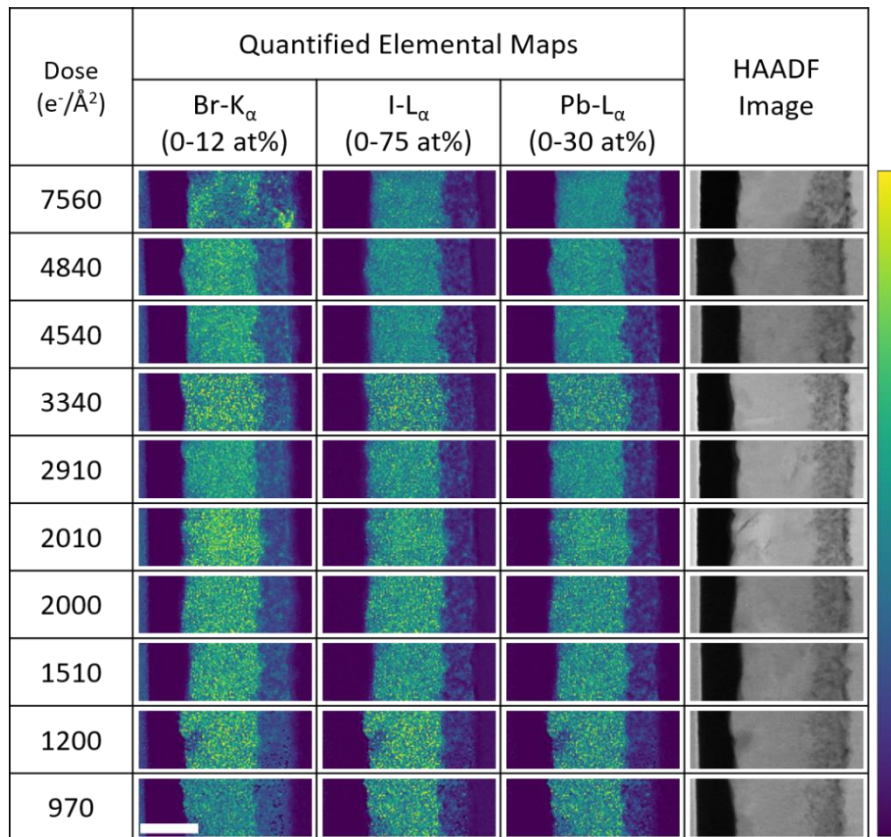


Figure 4.26 | Quantified elemental maps for Br-K<sub>α</sub>, I-L<sub>α</sub>, and Pb-L<sub>α</sub> with reference HAADF images acquired before STEM-EDX mapping. The maps' spatial resolution is 10 nm/pixel. Scale bar represents 400 nm and applies to all maps and images.

#### 4.4.4. Electron Dose and Beam-induced Specimen Damage

To obtain a quantitative measure of beam damage, changes in X/Pb (X = I, Br) STEM-EDX peak intensity ratios and after/before HAADF intensity ratio are monitored as the dose is increased. The intensity ( $I$ ) of a HAADF image is proportional to specimen thickness ( $t$ ) and its effective atomic number ( $Z_{eff}$ ) as in Equation 4.6.<sup>243,260</sup> HAADF intensity changes can thus be used as a proxy to gauge the extent of mass loss due to vacancy formation and volatilisation.

$$I \propto tZ_{eff}^{1.8} \quad (\text{Equation 4.6})$$

Comparing the ‘before’ and ‘after’ HAADF images in Figure 4.27a, STEM-EDX clearly affects the perovskite layer. Histograms of HAADF intensity acquired before STEM-EDX mapping (Figure 4.27b, left column), show similar distributions for the different scan areas. Peak heights and FWHM values are comparable, indicating that the thickness and composition of the lamella are initially uniform. With rising electron doses used for STEM-EDX mapping, the corresponding HAADF intensity distributions broaden, with the maximum gradually shifting towards lower counts for the ‘after’ scans. The peaks also become more asymmetric as the low-intensity tails grow, corresponding to the larger, darker speckles visible in the ‘after’ images of higher dose STEM-EDX scans (Figure 4.27a). These trends are also captured by taking an after/before average intensity ratio, which declines exponentially as electron dose increases (Figure 4.27c).

Interpreting HAADF intensity using Equation 4.6, given the composition and thickness of the lamella, a 6% decline could be explained by:

- A 6% loss of the number of TCDH perovskite unit cells in the region under the beam (complete volatilisation);
- A 3.4% reduction of  $Z_{eff}$ ;
- A combination of the above.

A simple model is devised to relate the decline of average HAADF intensity after STEM-EDX scan and perovskite decomposition. In this model, the electron beam passes through two distinct materials, namely pristine TCDH perovskite and the decomposition product. Following Equation 4.6, the contribution of each material’s  $tZ_{eff}^{1.8}$  metric is linearly summed and then divided by the equivalent parameter for a fresh perovskite specimen. The ratio calculated from this model is compared to the measured HAADF intensity ratio to obtain the extent of degradation. The procedure is as follows:

1. Calculate  $Z_{eff}$  for the fresh perovskite and the decomposition products with Equation 3.3.
2. Calculate the decomposition product/fresh perovskite  $t$  ratio using their unit cell parameters.
3. Calculate the  $tZ_{eff}^{1.8}$  metric for all materials and their ratio.
4. Compare the  $tZ_{eff}^{1.8}$  ratio from step 3 with measured HAADF intensity ratio to get the extent of decomposition.

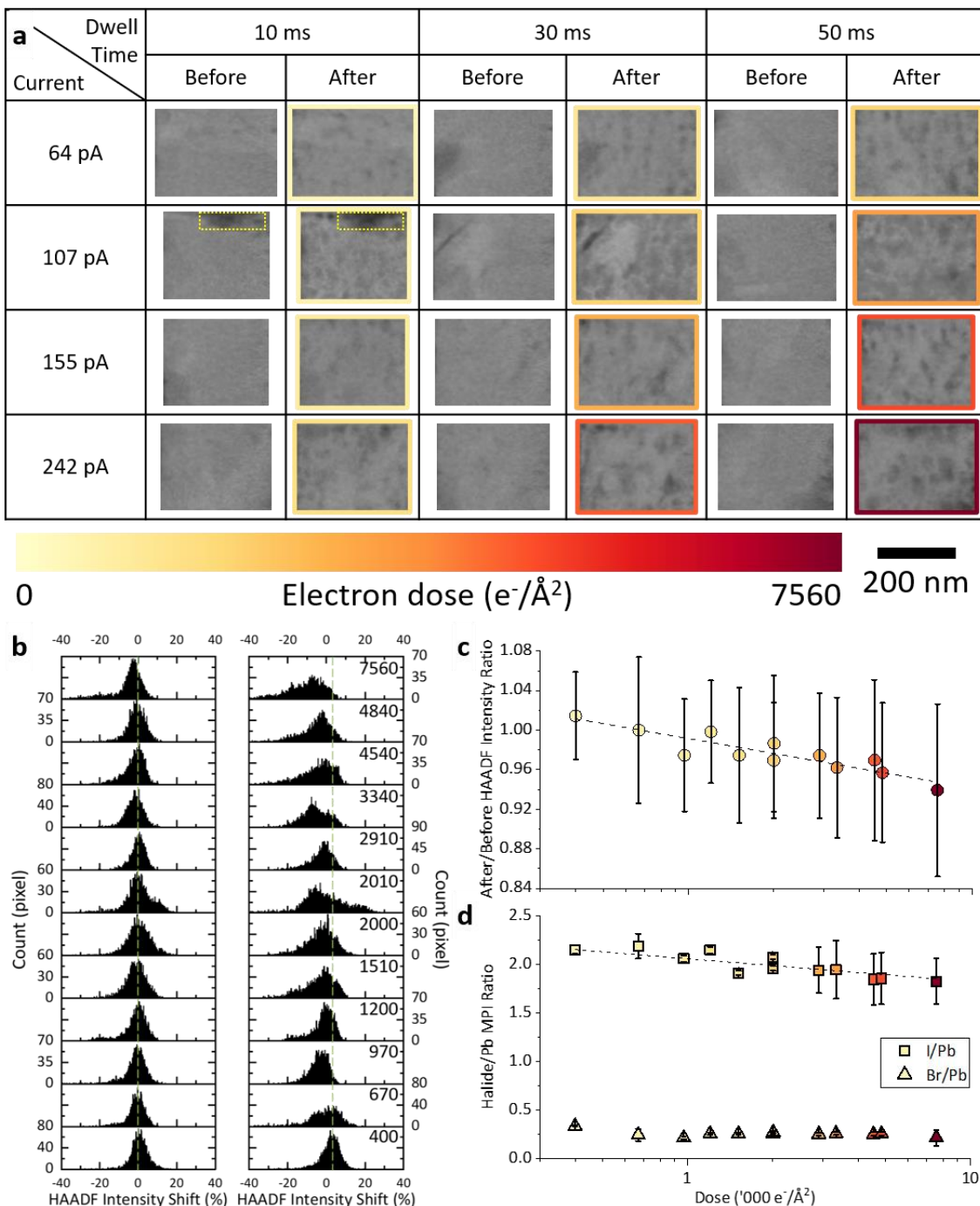


Figure 4.27 | (a) HAADF images of the perovskite layer acquired before and after the STEM-EDX scans. Dotted rectangles in the (107 pA, 10 ms) image pair mark an area which is masked in intensity measurement. The imaged areas are of slightly different sizes due to local changes in perovskite layer thickness. (b) Intensity histograms and (c) after/before intensity ratio plot of the HAADF images shown in panel (a). Green dashed lines in panel (b) mark the positions of the  $400 \text{ e}^-/\text{\AA}^2$  peaks. (d) Halide/Pb MPI ratio plot extracted from the STEM-EDX data. Error bars represent standard deviations across all perovskite pixels in an SI. The ‘After’ image frame colour in panel (a) and symbol colour in panels (c) and (d) represent electron dose used in the STEM-EDX scan. In panels (c) and (d), dashed lines highlight the exponential decline trend and do not represent measured data.

These steps are firstly used to predict the change in HAADF intensity if TCDH perovskite transformed into PbI<sub>2</sub>. The PbI<sub>2</sub>/fresh perovskite  $Z_{eff}^{1.8}$  ratio is calculated to be 2.72. Using unit cell parameters for TCDH perovskite from ref. <sup>91</sup> and for hexagonal PbI<sub>2</sub> from ref. <sup>367</sup>, a PbI<sub>2</sub>/fresh perovskite  $t$  ratio of 0.605 is obtained. Multiplying these two numbers, a  $tZ_{eff}^{1.8}$  ratio of 1.65 is found. Since this ratio is larger than 1, any transformation of TCDH perovskite into PbI<sub>2</sub> will result in an increase of HAADF intensity. This is not observed in the HAADF images, so it can be concluded that TCDH perovskite does not decompose to PbI<sub>2</sub> under electron beam irradiation at the dose range explored. This calculation is then repeated using TCDH perovskite with one I vacancy ( $Cs_{0.06}FA_{0.79}MA_{0.15}PbI_{1.55}Br_{0.45}$ ) as the decomposition product. The  $Z_{eff}^{1.8}$  ratio is calculated to be 0.87. As the unit cell parameters do not change, the  $t$  ratio is 1. As the product of these two ratios is smaller than 1, formation of I vacancies will result in a decrease of HAADF intensity which is observed in the experimental data. The extent of I vacancy formation can then be found. The calculations done in step 3 and 4 of this procedure are shown in Table 4.6 and 4.7, respectively.

Table 4.6 | Calculations of the  $tZ_{eff}^{1.8}$  metric for pristine perovskite specimen and partially decomposed perovskite.  $x$  = thickness of perovskite containing one I vacancy per unit cell, in nm.

	Material	$t$	$Z_{eff}^{1.8}$	$tZ_{eff}^{1.8}$
Original sample	Pristine TCDH perovskite	200	646.22	129244
Decomposed sample	Remaining pristine perovskite	200– $x$	646.22	129244–646.22 $x$
	Perovskite with one I vacancy per unit cell	$x$	561.38	561.38 $x$
	Total	200		129244–84.85 $x$

From Table 4.6, a  $tZ_{eff}^{1.8}$  ratio of  $(129244–84.85x) / 129244$  is obtained. This ratio can be compared to the measured HAADF intensity to obtain the values of  $x$ . These values, in turn, can be used to calculate the number of lost I atoms using the nominal lamella thickness (200 nm) and perovskite unit cell parameters (Table 4.7). In the pristine sample, along the lamella thickness, there are approximately 575 I atoms in one column of unit cells.

Table 4.7 | Calculations of the value of  $x$  and number of lost I atoms from the measured HAADF intensity data.

Dose ( $e^-/\text{\AA}^2$ )	Measured after/before HAADF intensity ratio	$x$ (nm)	% of lost I atoms	Number of lost I atoms
400	1.01448	N.A.	N.A.	N.A.
670	0.99991	0.14	0.03	0.15
970	0.97459	38.71	7.59	43.61
1200	0.99840	2.44	0.48	2.75
1510	0.97455	38.77	7.60	43.68
2000	0.96939	46.63	9.14	52.54
2010	0.98647	20.61	4.04	23.22
2910	0.97421	39.29	7.70	44.27
3340	0.96205	57.81	11.34	65.14
4540	0.96951	46.45	9.11	52.33
4840	0.95698	65.53	12.85	73.84
7560	0.93923	92.57	18.15	104.31

Finally, the percentage of lost I atoms in Table 4.7 can be compared with those measured through STEM-EDX (Table 4.8). The I/Pb MPI ratio from the  $400 \text{ e}^-/\text{\AA}^2$  SI was selected as a base value to calculate the percentage and number of lost I atoms. The number of lost I atoms calculated from HAADF intensity and STEM-EDX data are plotted in Figure 4.28, which shows a good agreement in the general trend between both sets of values.

The absence of a Br vacancy in the decomposition product is justified by the halide/Pb MPI ratios, as shown in Figure 4.27d. While the Br/Pb ratio stays approximately constant before dropping only at the highest dose, the I/Pb ratio declines exponentially, decreasing by 15% from the lowest dose to the highest. This finding is expected as prior studies have shown that Br are more stable compared to I.<sup>368,369</sup> Indeed, electron beam-induced Br desorption has only been observed in  $\text{CsPbBr}_3$  nanocrystals whose dimensions are orders of magnitude lower than a typical PSC lamella.<sup>302,370</sup> This 15% drop in I/Pb ratio is in very good agreement with the 3.4% reduction in  $Z_{eff}$  inferred from the HAADF intensity data, which corresponds to a 18% I loss (Figure 4.28). This similarity confirms that the main damage mechanism is through formation of I vacancies rather than complete evaporation, as the latter would result in no changes to the I/Pb ratio. I vacancies could have been formed through I diffusion into spiro-OMeTAD, which is found to occur to a greater extent with higher electron doses (Figure 4.29).

Table 4.8 | Calculations of number of lost I atoms from the I/Pb MPI ratio data.

Dose ( $e^-/\text{\AA}^2$ )	Measured I/Pb MPI ratio	% of lost I atoms	Number of lost I atoms
400	2.15	0.00	0.00
670	2.19	N.A.	N.A.
970	2.06	4.16	23.93
1200	2.15	0.09	0.51
1510	1.91	11.11	63.82
2000	2.08	3.51	20.20
2010	1.96	8.87	50.97
2910	1.94	9.81	56.39
3340	1.95	9.52	54.69
4540	1.85	14.20	81.59
4840	1.86	13.73	78.88
7560	1.82	15.15	87.08

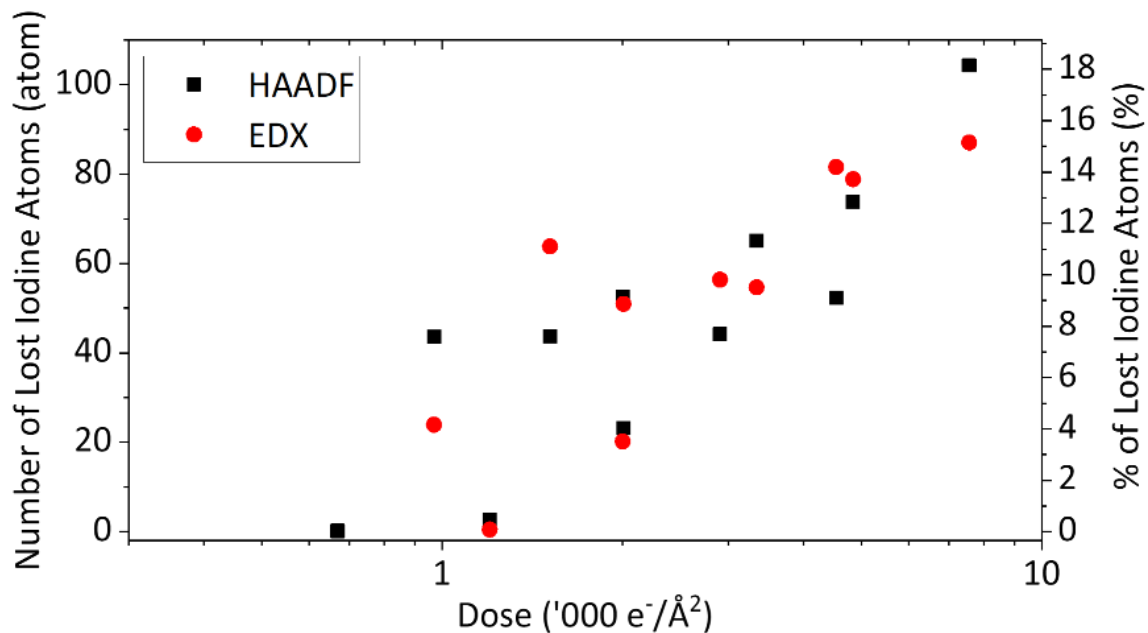


Figure 4.28 | Number of lost I atoms calculated from the HAADF intensity and EDX data.

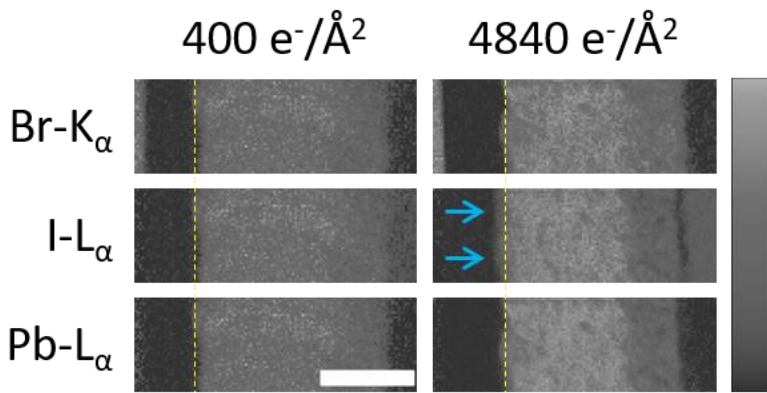


Figure 4.29 | Normalised peak intensity maps of  $\text{Br-K}_\alpha$ ,  $\text{I-L}_\alpha$ , and  $\text{Pb-L}_\alpha$ , showing I diffusion towards spiro-OMeTAD (blue arrows) after STEM-EDX scan using a high electron dose. Yellow dashed lines are a guide to the eye. Scale bar represents 400 nm and applies to all maps and images.

The exponential decline in both HAADF intensity and I/Pb ratio highlight the necessity of minimising electron dose, even in the absence of  $\text{PbI}_2$  formation. The observed trend suggests radiolysis as the dominant beam damage mechanism as it has been shown to exhibit an exponential dependence on total dose.<sup>298</sup> Furthermore, it indicates that dose rate has minimum impact on beam damage, as previous works conducted with parallel beam TEM-EDX also observed a similar decline of I/Pb ratio in  $\text{MAPbI}_3$ .<sup>213,299,327</sup> Factors other than total dose may affect the extent of radiolysis, such as electron beam energy or sample thickness (or surface/volume ratio).<sup>301</sup> Here both are nominally constant, so have been disregarded from the analysis. Furthermore, precautionary measures such as C coating may be used to reduce beam damage by reducing the loss of volatile species formed during irradiation.<sup>297,298,300</sup> However, this would not necessarily preserve crystallographic structure, but just overall composition.

In summary, the relationship between electron dose, quality of STEM-EDX signal, and beam damage is investigated for quantitative analysis of a TCDH perovskite as a model beam-sensitive material with a complex chemistry. In particular, five parameters are outlined which may be used to quantify STEM-EDX data quality and beam-induced chemical changes: PD, RE on a pixel-by pixel-basis, AE for multiple pixels, HAADF intensity ratio, and EDX peak intensity ratio. PD at a spatial resolution of (10/20/30) nm/pixel is achieved for  $\text{Br-K}_\alpha$ ,  $\text{I-L}_\alpha$ , and  $\text{Pb-L}_\alpha$  peaks with a dose of  $(2910/1200/400) \text{ e}^-/\text{\AA}^2$ . Highly accurate quantification on a pixel-by-pixel basis is not possible at the dose range and spatial resolution used here, but can be done at a lower spatial resolution by gathering data from multiple pixels through spatial rebinning. Beam damage is quantified across an electron dose range of 400–7560  $\text{e}^-/\text{\AA}^2$  for a lamella of ~200 nm nominal thickness, and both HAADF intensity and I/Pb peak intensity ratios are seen to decline exponentially with dose. This underline the necessity of minimising electron dose while maintaining statistical confidence in the characterisation results, even though perovskite decomposition into  $\text{PbI}_2$  is not observed. The ideal electron dose for STEM-EDX of OIHPs appear to

lie between 2000 and 2910 e<sup>-</sup>/Å<sup>2</sup>. Within this range, PD of Br-K<sub>a</sub> is achieved at a spatial resolution of 10 nm/pixel (Figure 4.21), the RE and AE parameters start to plateau (Figure 4.23a,b), and I loss is limited to 10% (Figure 4.28). The delicate balancing act between data quality and beam damage calls for the use of advanced hardware and post-processing techniques, such as large-area EDX detectors, spatial and spectral rebinning, and data denoising.

## 4.5. Summary

Cross-sectional STEM-EDX is an invaluable tool for PSC characterisation, but it is not without its limitations. The electron-transparent lamellae are prepared via FIB milling, in which the Ga<sup>+</sup> beam may amorphise and decompose the perovskite close to the lamella surfaces. Subsequently, the high-energy TEM electron beam can very quickly induce specimen damage in OIHPs. Therefore, it is crucial that these potential artefacts are understood, minimised, and carefully taken into account before valid conclusions can be drawn from STEM-EDX data.

In this chapter, CL mapping was used to show that the Ga<sup>+</sup> beam-induced damage in FIB milling is minimal. The perovskite in the produced PSC lamellae is only partially amorphised as proven by the extant – albeit blue-shifted – luminescence. Furthermore, it is minimally decomposed at most as indicated by the weak and spatially isolated PbI<sub>2</sub> emission. Therefore, meticulous TEM studies of PSC lamellae can produce useful information, such as device morphology or compositional heterogeneity. Another method is to prepare lamellae from multiple samples using identical FIB milling parameters, allowing a comparative study with minimal interference from the FIB milling step.

In STEM-EDX, electron beam-induced damage can generally be suppressed by reducing the electron dose. Doing so would also reduce the signal count and hence measurement accuracy, but this disadvantageous effect can be ameliorated using MVA algorithms such as PCA and NMF. Both algorithms were optimised for their application to STEM-EDX data in this chapter, resulting in a PCA workflow which best balances the necessity of recognising all real physical features and the goal of maximising SNR. This optimised workflow was then applied to show that creation of I vacancies through radiolysis is the primary form of beam damage in STEM-EDX of OIHPs. The choice of electron dose is therefore a balance between the two goals of minimising beam damage on one hand and maximising statistical confidence and measurement accuracy on the other hand. Even with the assistance of MVA, the identified ideal dose of between 2000-2910 e<sup>-</sup>/Å<sup>2</sup> will likely still induce a measurable specimen damage. Therefore, the need to carefully consider beam-induced damage in the interpretation of STEM-EDX data is again stressed. Conclusions should only be drawn when comparison with an identically prepared and characterised control specimen can be made, or when observations are supported by other characterisation techniques.

## **Chapter 5**

# **Solution Engineering for Homogeneous Perovskite Film Deposition over Large Areas**

The contents of this chapter have been published in ref.<sup>203</sup> (copyright 2018 American Chemical Society) and are reproduced here except for the STEM-EDX maps, which are replaced with those of larger scan areas in this thesis. In addition, minor alterations are made where necessary for flow and clarity. This study was led by Dr. Fabio Matteocci (University of Rome Tor Vergata) but included in this thesis as the EM component of the study was pivotal in explaining the results of the macroscale characterisation performed in Rome. In addition, the topic investigated in this chapter complements the studies on PSM discussed in Chapters 6 and 7 very well. Specific details about the division of work between Dr. Matteocci's team and the author is provided in the Experimental Methods section.

### **5.1. Introduction**

Since the invention of PSCs in 2009, their certified PCE records have been broken many times up to the most recent value of 25.5%.<sup>52</sup> However, these high PCEs are generally obtained in cells with an active area (AA) of the order of 0.1 cm<sup>2</sup> and achieving them in large modules has proven challenging. This is partially because high-PCE cells are often fabricated using an antisolvent or additives to obtain uniform perovskite films composed of large, highly crystalline grains. The most prominent examples of this approach include Jeon et al.'s pioneering antisolvent-assisted deposition work and the use of SCN<sup>-</sup> ions as a pseudo-halide.<sup>151,371</sup> While many such recipes have been honed to perfection for spin coated films, they are not directly applicable to the scalable deposition methods described in Chapter 2 due to differences in solvent evaporation and crystallisation kinetics.<sup>28,167</sup> The need for analogous solution engineering approaches suitable for large-area deposition is augmented by the fact that thin film solar modules are divided into connected cells. Since the module's overall output current or voltage is limited by that of the weakest-performing cell, the produced power is maximised when every single cell is working similarly well. Therefore, obtaining a spatially homogeneous and high-quality perovskite film over a large area (tens to hundreds of cm<sup>2</sup>) is of utmost importance. One of the most promising potential strategies to achieve this goal is to learn from solution engineering techniques which work well in spin coating and adapt them for use with scalable deposition methods.

In this chapter, the fabrication of efficient  $\text{MAPbI}_3$  PSMs with an AA of  $47.7 \text{ cm}^2$  and an average PCE of  $(11.97 \pm 0.83)\%$  is reported. A simple sequential deposition method consisting of  $\text{PbI}_2$  blade coating followed by MAI dipping was developed, with both steps performed in ambient air to maximise module processability and lower production cost. The use of an automated air-jet-assisted blade coater avoids typical problems encountered by large-area spin coating deposition, such as material waste, poor substrate coverage, and significant heterogeneity of the perovskite films.<sup>372</sup> To improve both the spatial uniformity and performance of the module, the perovskite precursor solutions were modified using two additives: MAI additive in the  $\text{PbI}_2$  solution for the blade coating step and  $\text{H}_2\text{O}$  additive in the MAI solution for the dipping step. Previous research performed on small spin coated cells found that the morphology of the  $\text{PbI}_2$  layer determines the quality of sequentially deposited perovskite films. More specifically, MAI addition formed less crystalline and nanoporous  $\text{PbI}_2$  films with smaller grains, ultimately enabling higher quality perovskite layers.<sup>373–375</sup>  $\text{H}_2\text{O}$  addition into the MAI precursor solution resulted in larger perovskite grains and increased crystallinity.<sup>376</sup> Here, these two approaches were adapted for large-area deposition and combined, resulting in completely formed, spatially homogeneous perovskite films which were further developed into efficient PSMs. A combination of optical spectroscopy, optoelectronic characterisation, XRD, and EM was used to extensively characterise the perovskite films and full devices. In particular, cross-sectional STEM-HAADF imaging and STEM-EDX directly visualised the effect of MAI and  $\text{H}_2\text{O}$  additions on the perovskite film and helped to explain the improved PSM performance. It was found that the additives enabled a complete perovskite formation reaction, significantly improved perovskite infiltration into the mesoporous scaffold layer, and led to perovskite films with a narrower distribution of morphological grain size and fewer pinholes.

## 5.2. Experimental Methods

The PSM fabrication, UV-vis absorption spectroscopy, PL, *I-V* curve measurement, and MPP tracking were performed by Dr. Fabio Matteocci and his colleagues at University of Rome Tor Vergata. SEM, STEM, and XRD data was acquired, analysed, and interpreted by the author, who also wrote the parts of the published article corresponding to these techniques.

### 5.2.1. Device Fabrication

Four precursor solutions were used to deposit the perovskite films in this study: a reference  $\text{PbI}_2$  solution ( $\text{PbI}_2$ ), a  $\text{PbI}_2$  solution containing a MAI additive ( $\text{PbI}_2:\text{MAI}$ ), a reference MAI solution (MAI), and a MAI solution containing an  $\text{H}_2\text{O}$  additive (MAI: $\text{H}_2\text{O}$ ). The  $\text{PbI}_2$  precursor solution was prepared by dissolving 400 mg/ml  $\text{PbI}_2$  in anhydrous DMF. The  $\text{PbI}_2:\text{MAI}$  solution was obtained by adding 17 mg MAI for every 1 ml of the reference  $\text{PbI}_2$  solution. The MAI solution was prepared by dissolving 10

mg/ml MAI in anhydrous 2-propanol. The MAI:H<sub>2</sub>O solution was made by adding 1 ml deionised water to 19 ml MAI/2-propanol solution (1:20 v/v).

5 × 5 or 10 × 10 cm<sup>2</sup> FTO-coated glass substrates were scribed with P1 lines using an IR ( $\lambda = 1064$  nm) pulsed Nd:YVO<sub>4</sub> laser, with a fluence of 11.5 J/cm<sup>2</sup> and a pulse length of 15 ns. The P1-patterned substrates were cleaned with three stages of ultrasonic bath: first in deionised water and detergent, then in acetone, and finally in isopropanol. After drying, a 30 nm compact TiO<sub>2</sub> layer was prepared by spray pyrolysis of a solution of diisopropoxytitanium bis(acetylacetone) (0.16 M) and acetylacetone (0.4 M) in ethanol. The substrates were preheated to 450°C and kept at that temperature for 10 min to complete the deposition, then cooled down to room temperature in about 1 h. For the mesoporous TiO<sub>2</sub> layer, a Greatcell 30-NRD paste was diluted in ethanol (1:9 w/w), then blade coated on the compact TiO<sub>2</sub> layer (blade height 30 μm, plate speed 10 mm/s, room temperature) and sintered at 450 °C for 30 min. The final thickness was measured by a profilometer to be 200 ± 20 nm. Then, the samples were soaked under UV light for 30 min prior to deposition of the perovskite layer (Figure 5.1a). Three combinations of perovskite precursor solutions were used as detailed in Table 5.1 and Figure 5.1b.

Table 5.1 | Precursor solution combinations used in perovskite film deposition.

Sample Code	PbI <sub>2</sub> Precursor Solution	MAI Precursor Solution
REF	PbI <sub>2</sub>	MAI
MAI+	PbI <sub>2</sub> :MAI	MAI
MAI+/H <sub>2</sub> O+	PbI <sub>2</sub> :MAI	MAI:H <sub>2</sub> O

Both PbI<sub>2</sub> precursor solutions (PbI<sub>2</sub> or PbI<sub>2</sub>:MAI) were blade coated in ambient air (Figure 5.1a). 100 μl of the precursor solution was injected on the substrate with an automated syringe, then the plate was placed 110 μm below the blade and moved at a fixed speed of 10 mm/s under the blade. After the substrate crossed the blade, it passed below an air gun which was used to dry the deposited film with hot air (temperature 50°C, flow rate 125 l/min). No annealing step was performed on the deposited PbI<sub>2</sub> layer. Afterwards, the samples were dipped in MAI-containing solutions (MAI or MAI:H<sub>2</sub>O) for 20 min. The perovskite surface was then washed with anhydrous 2-propanol and dried with an N<sub>2</sub> flow. After that, the samples were annealed at 100°C for 10 min prior to deposition of the spiro-OMeTAD layer. The doped spiro-OMeTAD solution in chlorobenzene (60 mM) was blade coated in ambient air. 150 μL of the precursor solution was injected on the substrate, then the plate was placed 90 μm below the blade moved at a fixed speed of 20 mm/s under the blade. After the substrate crossed the blade, it passed below an air gun which was used to dry the deposited film with room temperature air (flow rate 125 l/min). The molar ratio between the dopants and the spiro-OMeTAD was 0.5, 3.3, and 0.03 for Li-TFSI, 4-TBP, and FK209 cobalt additives, respectively.

To complete the MI between cells, P2 lines were scribed using a green ( $\lambda = 532$  nm) pulsed Nd:YVO<sub>4</sub> laser, with a fluence of 0.115 J/cm<sup>2</sup> and a pulse length of 15 ns. A 100 nm-thick Au layer was then deposited by thermal evaporation. Finally, P3 scribing was performed using the same laser system and parameters employed in the P2 step.

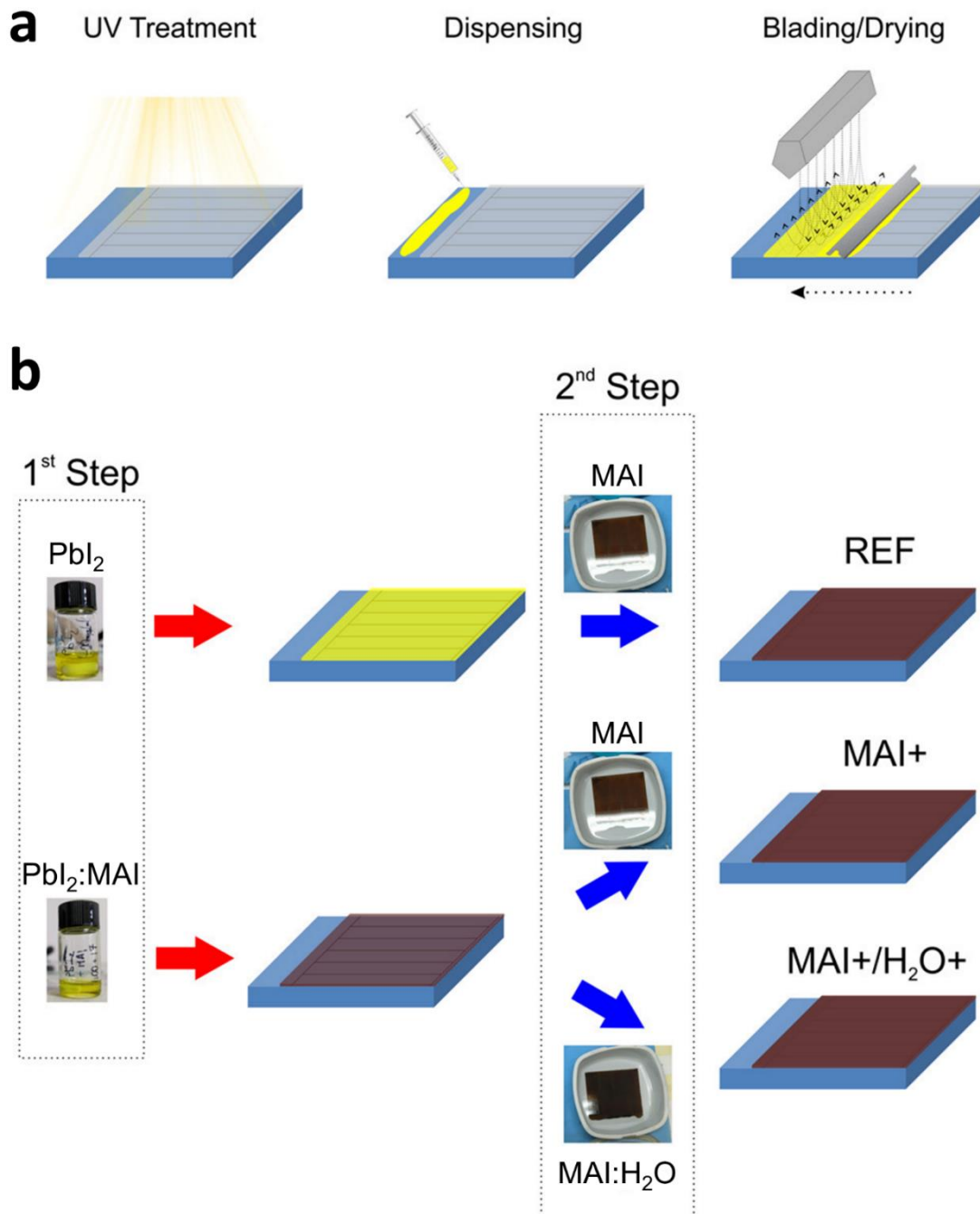


Figure 5.1 | (a) Main steps of air-assisted blade coating of perovskite films: UV treatment, solution dispensing, blading, and drying. This deposition procedure was used for PbI<sub>2</sub>, PbI<sub>2</sub>:MAI, and spiro-OMeTAD depositions. (b) Schematic of the sequential deposition of MAPbI<sub>3</sub> films, showing the modifications introduced to the precursors to obtain the MAI+ and MAI+/H<sub>2</sub>O+ perovskite films.<sup>203</sup>

### **5.2.2. Optical and Optoelectronic Characterisation**

*I-V* curves were obtained with a calibrated ABET Class A solar simulator under AM1.5G 1 sun illumination. Except where indicated otherwise, *I-V* scans were performed in the reverse direction (from  $V_{OC}$  to  $J_{SC}$ ) with a scan rate of 33 mV/s. MPP tracking was performed by firstly running a *I-V* scan in the forward direction to find the MPP condition. Then, the device was maintained in the MPP condition by applying a small perturbation of  $V$  and  $I$  to obtain the dynamic MPP values for 300 s. Two types of PCE are reported in this chapter: active area PCE (AA PCE) and substrate area PCE (SA PCE). AA PCE is calculated only over the module's AA while SA PCE includes the intercell MI areas as well. These quantities are related through Equation 5.1, where GFF is as defined in Equation 2.6.

$$SA\ PCE = AA\ PCE \times GFF \quad (\text{Equation 5.1})$$

Absorbance spectra were obtained using a Shimadzu UV-2550 UV-vis spectrophotometer equipped with an integrating sphere. Steady-state PL and EL measurements were performed with an Arkeo-Cicci Research spectrometer. The samples were excited with a green ( $\lambda = 532$  nm) laser at a  $45^\circ$  incidence angle with a spot diameter of 1 mm. PL signal was acquired with an integration time of 100 ms.

Light beam-induced current (LBIC) mapping were performed using a Leica DMI 5000 inverted microscope coupled with a monochromator and illuminated by a 200 W xenon lamp. The wavelength was fixed to 530 nm ( $\pm 2$  nm). A long working distance objective lens with a  $100\times$  magnification yielded a  $50 \times 50 \mu\text{m}$  spot area. The device area was scanned in steps of  $500 \mu\text{m}$  with an x-y motorised stage.

### **5.2.3. Electron Microscopy Characterisation**

Top-view SEM images were acquired in SE mode using an ETD on a Zeiss Crossbeam 540 operated at 2 kV. For STEM characterisation, cross-sectional lamellae were prepared with an FEI Helios Nanolab Dualbeam FIB/SEM. The lamellae were immediately transferred into an FEI Tecnai Osiris 80-200 FEGTEM, minimising air exposure to  $\sim 2$  min. STEM-HAADF images and STEM-EDX SIs were obtained using the beam parameters described in Section 3.7 and Table 3.2. STEM-EDX SIs were denoised with PCA and processed in HyperSpy following the procedure explained in Section 4.3.<sup>290</sup>

### **5.2.4. X-ray Diffraction**

XRD was performed with a Bruker D8 DAVINCI fitted with a LYNXEYE-XE detector, Ni-K $\beta$  filter, and a Cu-K $\alpha$  X-ray source ( $\lambda = 1.5418 \text{ \AA}$ ) operated at 40 kV, 40 mA. The acquisition parameters were

$10^\circ$ - $60^\circ$   $2\theta$  range,  $0.025^\circ$  step size, and  $0.1$  s dwell time. The spectra were processed using PANalytical HighScore 4.8 software.

## 5.3. Results and Discussion

The blade coated  $\text{PbI}_2$  and  $\text{PbI}_2:\text{MAI}$  films were firstly optically characterised to evaluate their absorption and emission properties. By comparing their colour under room lighting (Figure 5.2a), absorption spectra (red and green curves in Figure 5.2b), and PL emission (Figure 5.2c), it is clear that MAI addition into the  $\text{PbI}_2$  solution led to early, partial formation of  $\text{MAPbI}_3$ . The absorbance spectrum of the  $\text{PbI}_2:\text{MAI}$  film contains the characteristic absorption onset of  $\text{MAPbI}_3$  at  $780$  nm and weak but detectable absorption from there to about  $515$  nm, the absorption onset of  $\text{PbI}_2$  (Figure 5.2b). A comparison of the PL spectra of both films echoes this finding. While PL emission was detected in the range of  $750$ – $850$  nm for the  $\text{PbI}_2:\text{MAI}$  film, the  $\text{PbI}_2$  film's PL spectrum shows only noise in that range (Figure 5.2c). This confirms partial conversion of  $\text{PbI}_2$  into  $\text{MAPbI}_3$  in the  $\text{PbI}_2:\text{MAI}$  film. Optical spectroscopy was performed again after the  $\text{PbI}_2$  and  $\text{PbI}_2:\text{MAI}$  films were fully converted into  $\text{MAPbI}_3$  with MAI dipping and annealing. The absorbance spectra of the REF, MAI+, and MAI+/ $\text{H}_2\text{O}^+$  perovskite films are displayed by the cyan, magenta, and blue curves in Figure 5.2b, respectively. An increase of absorbance for the MAI+/ $\text{H}_2\text{O}^+$  film with respect to the REF and MAI+ films was observed in the entire absorption range. PL emission spectra of the three perovskite films are shown in Figure 5.2d. To replicate the mesoporous device architecture while minimising carrier transport out of the perovskite layer, an insulating  $\text{Al}_2\text{O}_3$  scaffold was used in place of the  $\text{TiO}_2$  layer for PL spectroscopy only. The MAI+/ $\text{H}_2\text{O}^+$  film shows the brightest PL emission intensity, followed by the MAI+ and REF films. Overall, the optical characterisation data shows that the MAI+/ $\text{H}_2\text{O}^+$  film has the most desirable optical properties, with the highest absorbance and the lowest non-radiative recombination.

The crystallographic quality of the perovskite films was evaluated through XRD. The diffractograms of the three perovskite films and for a single crystal  $\text{MAPbI}_3$  reference (Inorganic Crystal Structure Database collection code: 241477) are shown in Figure 5.3. All films show a marked preference for the  $(hh0)$  family of planes, which evidences orientated grain growth during perovskite formation. Previous theoretical work has predicted a textured growth of  $\text{MAPbI}_3$   $(110)$  planes on  $\text{TiO}_2$  due to strong compatibility between the perovskite's surface I atoms and undercoordinated Ti atoms.<sup>377</sup> Oriented perovskite grains, in particular of the  $(hh0)$  family, have been shown to lower charge recombination and accelerate hole transport to spiro-OMeTAD because of the prevalence of low-angle grain boundaries and stronger orbital overlap, resulting in higher  $V_{OC}$  and  $J_{SC}$ .<sup>378,379</sup> Figure 5.3 also shows that the  $\text{MAPbI}_3$  peaks are very sharp in all films, with low FWHM values of the  $(110)$  peak ( $0.11^\circ$ – $0.16^\circ$ ). This demonstrates excellent crystallinity of the perovskite grains as is also visible in the top-view SEM images (Figure 5.4), thus facilitating more efficient and stable modules.<sup>202,380</sup>

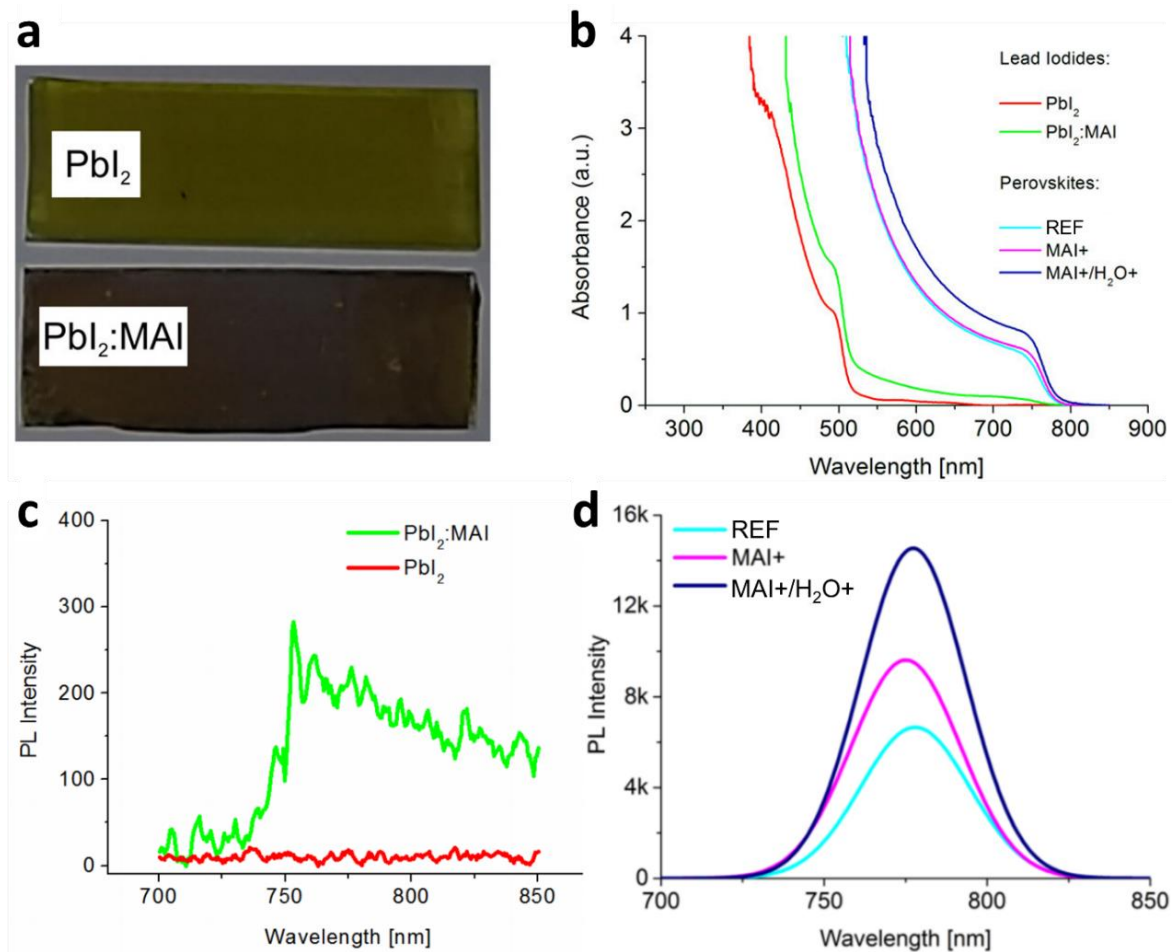


Figure 5.2 | (a) Photographs of the PbI<sub>2</sub> and PbI<sub>2</sub>:MAI films. (b) Absorbance spectra of the (red) PbI<sub>2</sub>, (green) PbI<sub>2</sub>:MAI, (cyan) REF perovskite, (magenta) MAI+ perovskite, and (blue) MAI+/H<sub>2</sub>O+ perovskite films. (c) PL spectra of the (red) PbI<sub>2</sub> and (green) PbI<sub>2</sub>:MAI films. (d) PL spectra of the (cyan) REF, (magenta) MAI+, and (blue) MAI+/H<sub>2</sub>O+ perovskite films deposited on an insulating Al<sub>2</sub>O<sub>3</sub> mesoporous scaffold.<sup>203</sup>

Top-view SEM imaging was performed in topography-sensitive SE mode to assess the effect of MAI and H<sub>2</sub>O additives on the perovskite grain morphology (Figure 5.4). All low-magnification SEM images (Figure 5.4a,d,g) show continuous perovskite films without any microscale pinholes. However, a closer examination reveals some irregularities in the REF and MAI+ films. The REF film contains some large grains of up to 1 μm in size which appear to jut out of the film (Figure 5.4b,c). MAI addition reduced the number of these out-of-plane grains, yielding more homogenous crystal sizes and shapes (Figure 5.4f,i). However, the MAI+ film appears to also contain small pits (Figure 5.4e,f). With the addition of H<sub>2</sub>O, the grain morphology becomes more cuboid and uniform, with a narrower size distribution centred around  $438 \pm 74$  nm (Figure 5.4h,i). Due to the roughness of the MAI+/H<sub>2</sub>O+ film, it is not clear from Figure 5.4i whether the pits seen in the MAI+ film are eliminated by H<sub>2</sub>O addition. This information, along with the depth of the pits, was instead obtained through cross-sectional imaging as shown below.

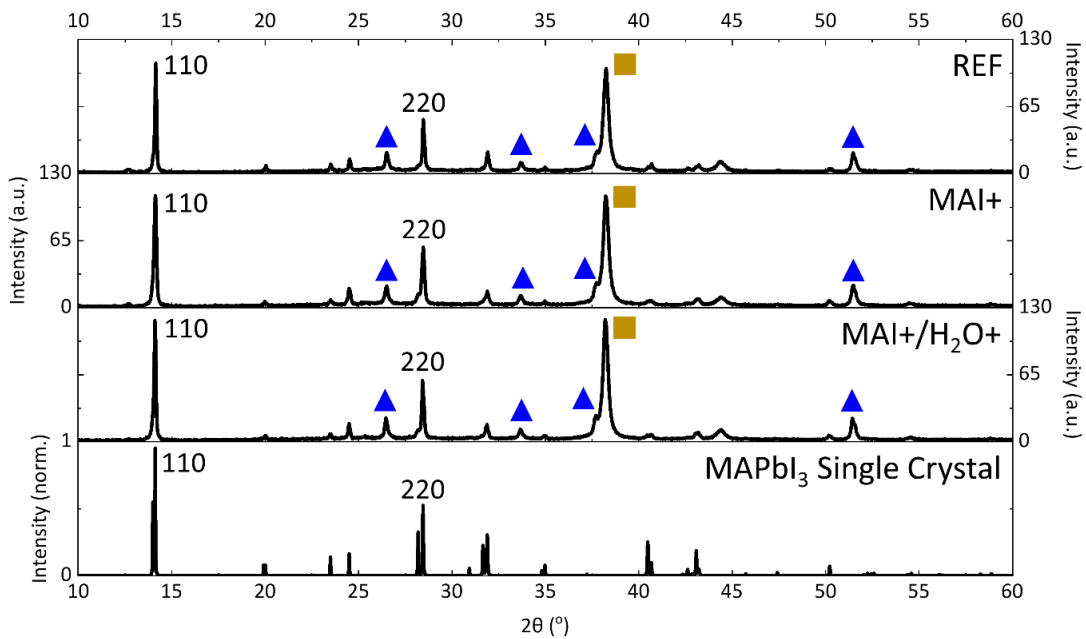


Figure 5.3 | XRD diffractograms of, from top to bottom, the REF, MAI+, and MAI+/H<sub>2</sub>O+ perovskite film, and a single crystal MAPbI<sub>3</sub> reference (ICSD 241477). Miller indices of the prominent perovskite peaks are marked. Blue triangles and gold squares mark the FTO and gold peaks, respectively.

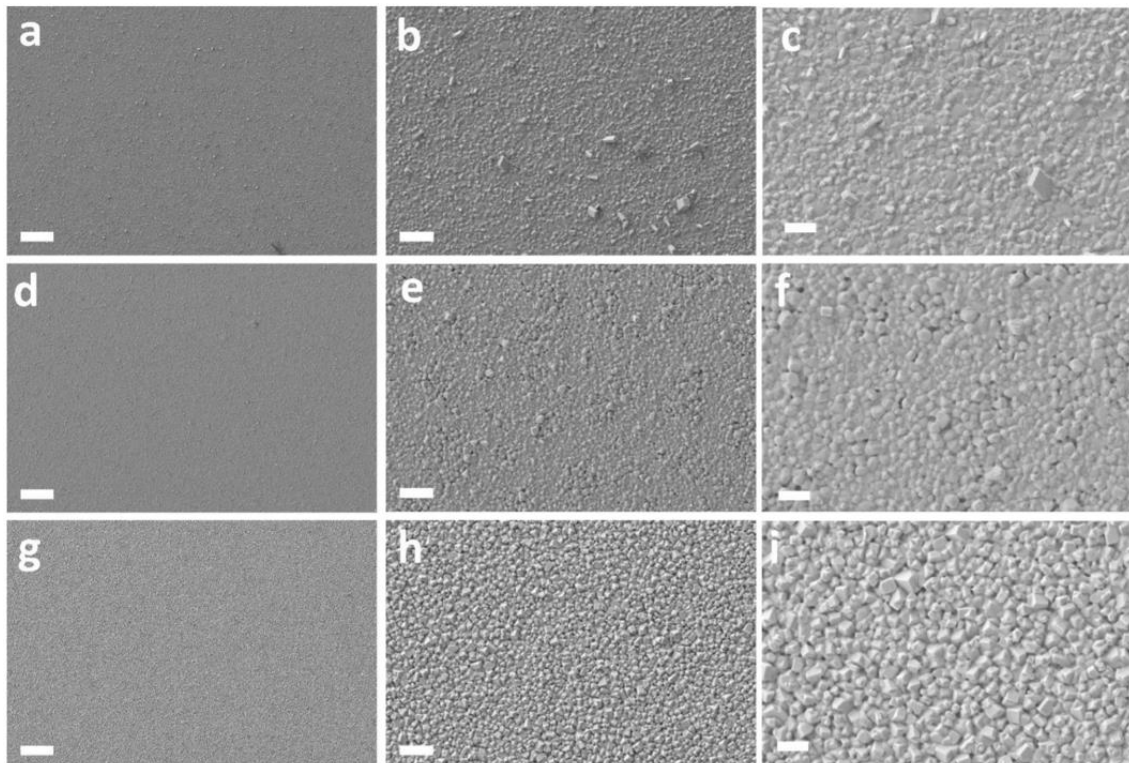


Figure 5.4 | Low magnification (a,d,g, scale bar = 10  $\mu$ m), medium magnification (b,e,h, scale bar = 2  $\mu$ m) and high magnification (c,f,i, scale bar = 1  $\mu$ m) top-view SE images of the (a,b,c) REF, (d,e,f) MAI+, and (g,h,i) MAI+/H<sub>2</sub>O+ perovskite films.

Further evidence of improved perovskite morphology due to MAI and H<sub>2</sub>O additions was obtained with cross-sectional STEM-HAADF imaging of full devices (Figure 5.5). The REF device (Figure 5.5a) contained plenty of non-perovskite bright grains (cyan arrow) and voids in the mp-TiO<sub>2</sub> layer (red arrow) spread throughout the length of the lamella. As the intensity of HAADF images increases with higher  $Z_{eff}$ , the bright grains are provisionally assigned to unreacted PbI<sub>2</sub> and the voids appear black presumably due to a lack of perovskite infiltration into the mp-TiO<sub>2</sub> pores (both proven in Figure 5.6). This high prevalence of PbI<sub>2</sub> evidences a severely incomplete perovskite formation reaction in the REF film. Furthermore, most of the mp-TiO<sub>2</sub> voids are located below the PbI<sub>2</sub> grains, suggesting that the unreacted PbI<sub>2</sub> blocked the perovskite from percolating through the TiO<sub>2</sub> network. This could be a significant drawback to module performance as a large perovskite-TiO<sub>2</sub> interfacial surface area is essential for fast collection of photogenerated electrons. The MAI+ and MAI+/H<sub>2</sub>O+ films (Figure 5.5b,c) have far less unreacted PbI<sub>2</sub> and no voids in the mp-TiO<sub>2</sub> layer, but also show some pits in the perovskite layer (green arrows). None of the pits were deep enough to reach the TiO<sub>2</sub> layer, indicating a low probability of shunt formation. Figure 5.5c shows that H<sub>2</sub>O addition reduced the number of pits and formed more cuboid perovskite grains, in agreement with the top-view SEM images (Figure 5.4).

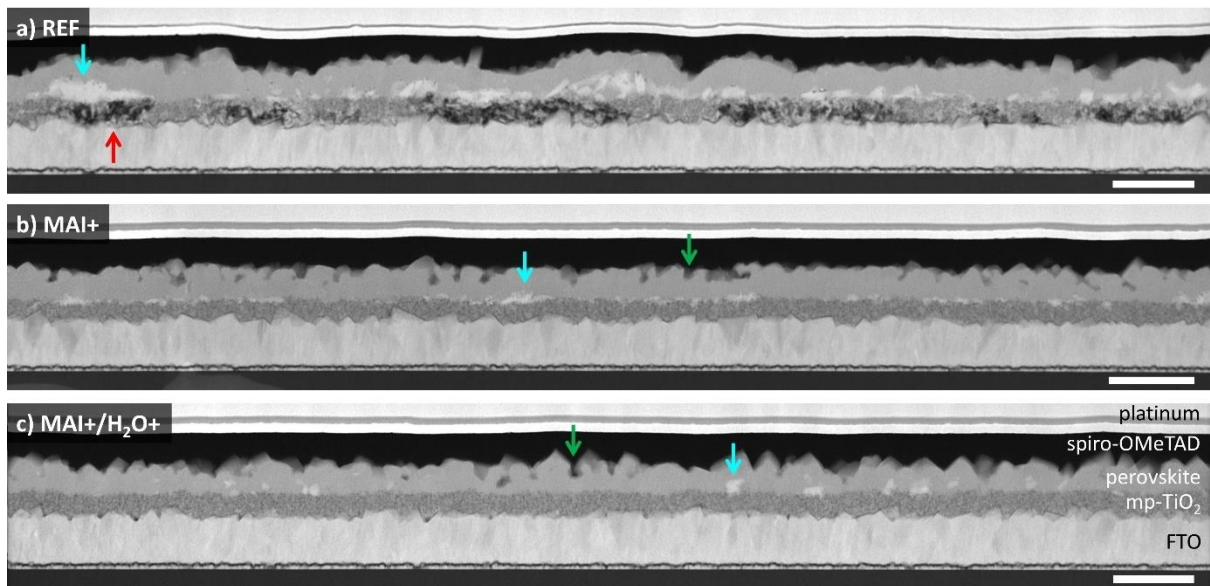


Figure 5.5 | Cross-sectional STEM-HAADF images of the (a) REF, (b) MAI+, and (c) MAI+/H<sub>2</sub>O+ devices. Cyan arrows indicate PbI<sub>2</sub> grains at the perovskite-TiO<sub>2</sub> interface. Red arrows mark incomplete TiO<sub>2</sub> pore filling by the perovskite. Green arrows point to pits in the perovskite film. Scale bars = 1 μm.

These additive-induced morphological improvements can be rationalised by recalling what others have discovered regarding the effects of MAI and H<sub>2</sub>O additives in perovskite crystallisation. In literature,

optical microscopy and XRD have shown that adding MAI into  $\text{PbI}_2$  solution slowed down  $\text{PbI}_2$  crystal growth upon deposition, resulting in smaller  $\text{PbI}_2$  grains.<sup>375</sup> Slower grain growth can improve mp- $\text{TiO}_2$  pore filling as it allows more  $\text{PbI}_2$  to percolate into the nanoscale pores of the mp- $\text{TiO}_2$  layer before they grow too large to enter the pore network (cyan arrow in Figure 5.5a). Then, during the MAI dipping step, perovskite formation progresses from the surfaces of  $\text{PbI}_2$  grains inwards.<sup>381</sup> This process occurs more slowly when the  $\text{PbI}_2$  film is thick and dense. Previously, others have found that blade coated  $\text{PbI}_2$  films are more compact compared to spin coated ones.<sup>372</sup> Consequently, a longer dipping time is required to produce devices with comparable PCEs if the  $\text{PbI}_2$  layer is blade coated. MAI addition can increase the specific surface area of  $\text{PbI}_2$  films through formation of nanopores and reduction in  $\text{PbI}_2$  grain size, thus accelerating its reaction with MAI and allowing complete perovskite formation with a shorter dipping time.<sup>373–375</sup>  $\text{H}_2\text{O}$  accelerates the perovskite formation further by increasing the mobility of water-soluble  $\text{MA}^+$  and  $\text{I}^-$  ions.<sup>376</sup> In short, the additions of MAI and  $\text{H}_2\text{O}$  are demonstrated to be highly beneficial for the blade coating of large-area perovskite films, bequeathing near-complete perovskite formation reaction, high spatial homogeneity, complete scaffold pore filling, and larger morphological grain size. Indeed, the higher light absorbance and emission of the MAI+/ $\text{H}_2\text{O}^+$  film (Figure 5.2b,d) can be attributed to these improvements in perovskite morphology.

Cross-sectional STEM-EDX was performed to map the composition of full devices made with the three types of perovskite films. Figure 5.6 shows STEM-HAADF images of the mapped areas, quantified elemental maps for Pb, I, C, and Ti, and I/Pb ratio maps acquired from the REF, MAI+, and MAI+/ $\text{H}_2\text{O}^+$  devices. The C maps show that spiro-OMeTAD fills the pits in the MAI+ and MAI+/ $\text{H}_2\text{O}^+$  perovskite films (Figure 5.6b,c). No pits were observed to be deep enough to reach the  $\text{TiO}_2$  layer. Although the sample volume probed by STEM is necessarily small, this suggests that the pits are shallow and unlikely to form shunt paths. The Ti maps show that the mesoporous  $\text{TiO}_2$  layer is well-formed in all devices. Importantly, the Ti map of the REF sample (Figure 5.6a) appears identical both inside and outside the voids identified by the red arrow in Figure 5.5. This confirms that those voids are caused by a lack of perovskite infiltration rather than imperfections of the  $\text{TiO}_2$  scaffold, as further evidenced by the low Pb and I signals in those voids (Figure 5.6a). The Pb maps for all devices show high concentrations of Pb at the bright grains identified by cyan arrows in Figure 5.5, confirming that they are unreacted  $\text{PbI}_2$ . Their high I concentration is not as apparent due to the I maps' wider colour range compared to the Pb maps. Final confirmation of the  $\text{PbI}_2$  grains' identity is provided by the I/Pb ratio maps, which show low I/Pb ratio at the bright grains' locations (Figure 5.6a-c). The REF and MAI+/ $\text{H}_2\text{O}^+$  devices demonstrate uniform I/Pb ratio throughout their perovskite films except for the  $\text{TiO}_2$  voids and  $\text{PbI}_2$  grains (Figure 5.6a,c). The MAI+ device shows a slightly higher I/Pb ratio compared to the other devices due to the MAI additive (Figure 5.6b). The I/Pb ratio is particularly high in the titania network, suggesting that the excess I might have an affinity with  $\text{TiO}_2$ . The mechanism behind this I enrichment could not be divulged from the STEM-EDX data, but is possibly related to the propensity of I to bond

with undercoordinated Ti atoms on the surfaces of  $\text{TiO}_2$  as mentioned above.<sup>382</sup> This increased I/Pb ratio is not observed in the MAI+/H<sub>2</sub>O+ device, likely because H<sub>2</sub>O, through its ability to dissolve MA<sup>+</sup> and I<sup>-</sup> ions, helped to remove excess MAI in the drying and annealing steps.<sup>376</sup>

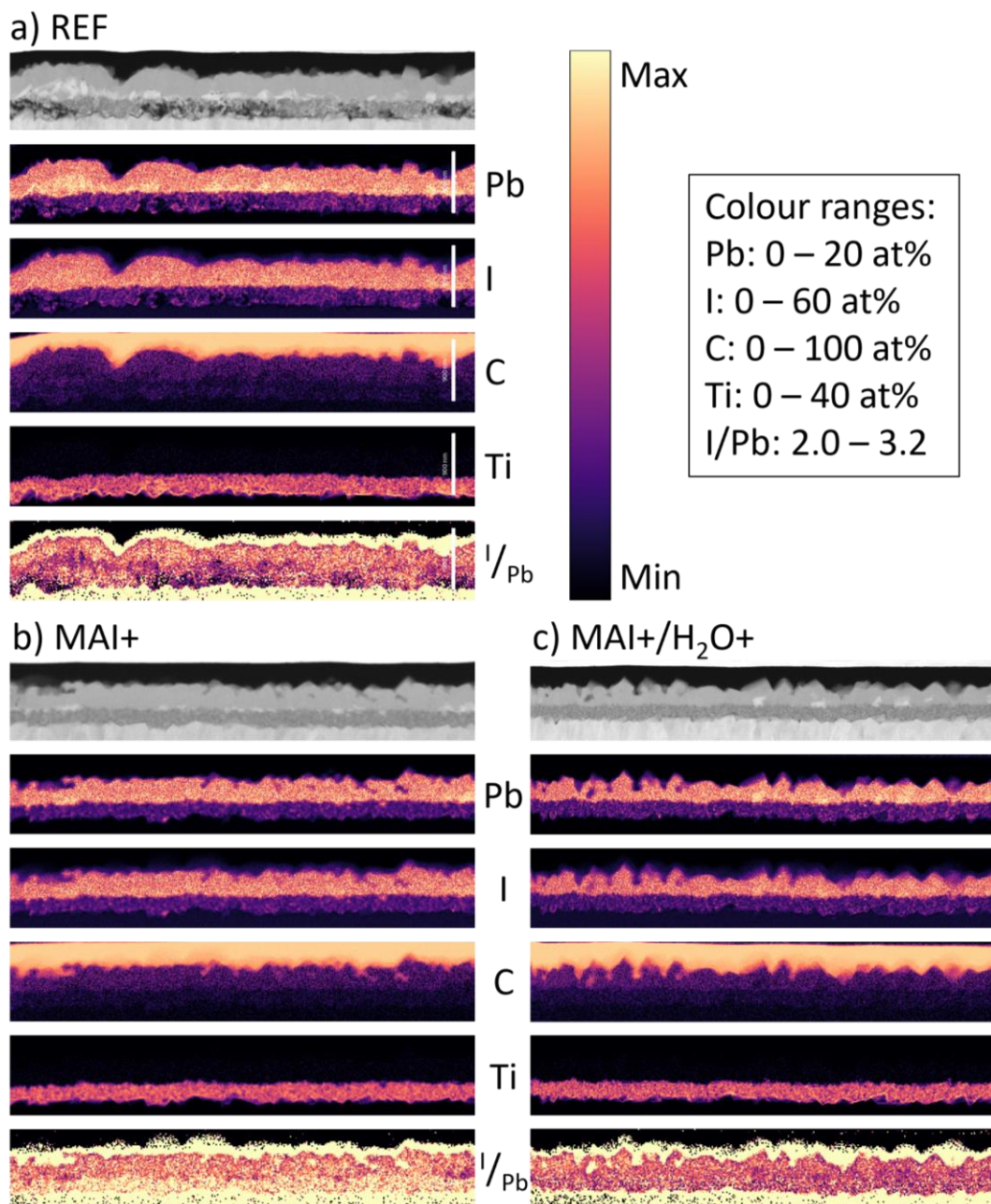


Figure 5.6 | Cross-sectional STEM-HAADF images of STEM-EDX scan areas, quantified STEM-EDX elemental maps of Pb, I, C, and Ti, and I/Pb ratio maps of the (a) REF, (b) MAI+, and (c) MAI+/H<sub>2</sub>O+ devices. The I/Pb ratio maps were spatially rebinned by a factor of 2 to reduce noise. Yellow strips at the perovskite–spiro-OMeTAD interface in the I/Pb map indicate I diffusion caused by the STEM electron beam. The denoised STEM-EDX model SI was constructed using 7 principal components via PCA. Scale bars represent 900 nm and are applicable for all panels.

The perovskite films were then used to fabricate  $5 \times 5 \text{ cm}^2$  PSMs composed of 5 serially connected cells with a cell width of 7.05 mm (Figure 5.7a). Their *I-V* curves were measured and displayed in Figure 5.7b. The REF, MAI+, and MAI+/H<sub>2</sub>O+ modules produce AA PCEs of 9.1, 11.7, and 13.2%, respectively, corresponding to SA PCEs of 8.2, 10.6, and 11.9% with a GFF of 90.5%. The REF module has a markedly low  $V_{OC}$  (4.42 V) compared to that of the MAI+ (5.05 V) and MAI+/H<sub>2</sub>O+ (5.14 V) modules. The low  $V_{OC}$  can be ascribed to the smaller perovskite grain size and poor scaffold pore filling, leading to strong bulk and interfacial non-radiative recombination.<sup>383</sup>

Based on the *I-V* curves shown in Figure 5.7b and other characterisations described above, the MAI+/H<sub>2</sub>O+ formulation was selected for further module optimisation and upscaling. In Figure 5.7c, the *I-V* characteristics of four  $5 \times 5 \text{ cm}^2$  PSMs processed with the MAI+/H<sub>2</sub>O+ recipe are reported. An average AA PCE of  $(12.63 \pm 0.26)\%$  was demonstrated on an AA of  $14.21 \text{ cm}^2$ . The module GFF was 90.5%, leading to an average SA PCE of  $(11.43 \pm 0.23)\%$ . The PV parameters of these modules are summarised in Table 5.2. The low standard deviations of the PV parameters demonstrate the good reproducibility of the deposition process.

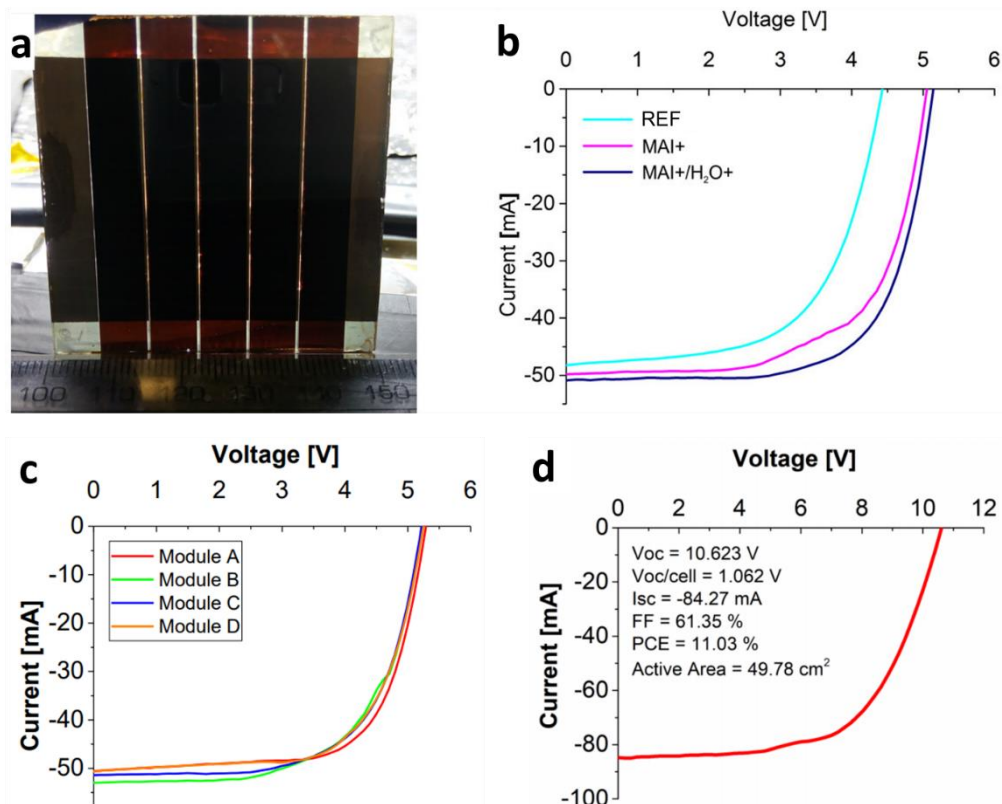


Figure 5.7 | (a) Photograph of a PSM on a  $5 \times 5 \text{ cm}^2$  substrate consisting of five serially connected cells with an AA of  $13.6 \text{ cm}^2$ . (b) *I-V* curves of the  $5 \times 5 \text{ cm}^2$  PSMs containing the REF, MAI+, or MAI+/H<sub>2</sub>O+ perovskite films. (c) *I-V* curves of four  $5 \times 5 \text{ cm}^2$  MAI+/H<sub>2</sub>O+ PSMs with an AA of  $14 \text{ cm}^2$ . (d) *I-V* curve of a MAI+/H<sub>2</sub>O+ PSM on a  $10 \times 10 \text{ cm}^2$  substrate with a cell width of 7.05 mm.<sup>203</sup>

Table 5.2 | PV parameters of four MAI+/H<sub>2</sub>O+ PSMs on 5 × 5 cm<sup>2</sup> substrates.<sup>203</sup>

Module	V <sub>oc</sub> (V)	Mean V <sub>oc</sub> per cell (V)	I <sub>sc</sub> (mA)	FF (%)	AA PCE (%)	SA PCE (%)
A	5.30	1.060	50.17	68.60	12.82	11.60
B	5.21	1.042	52.56	63.59	12.64	11.44
C	5.19	1.038	51.04	66.11	12.86	11.64
D	5.26	1.052	50.06	66.43	12.21	11.05
Mean	5.24 ± 0.04	1.048 ± 0.009	50.96 ± 1.00	66.18 ± 1.78	12.63 ± 0.26	11.43 ± 0.23

Further upscaling to a 10 × 10 cm<sup>2</sup> substrate area was firstly performed using the same cell width as for the 5 × 5 cm<sup>2</sup> module. This large module showed an AA PCE of 11.03% (Figure 5.7d), a 13% drop compared to the 5 × 5 cm<sup>2</sup> modules. This efficiency reduction can be assigned to higher Ohmic losses, as indicated by the large drop in FF from 66.18% to 61.35%. To ameliorate this PCE decline, the cell width was reduced to 4.5 mm following the optimisation approach described by Galagan et al.<sup>165</sup> This resulted in modules containing 15 serially connected cells with an AA of 47.7 cm<sup>2</sup>. Due to the higher number of MI areas required, the GFF decreased from 90.5% to 86.7%. A photograph of a typical 10 × 10 cm<sup>2</sup> module with the optimised cell layout is shown in Figure 5.8a. I-V curves of three such modules are displayed in Figure 5.8b, producing an average AA PCE of (13.81 ± 0.96)% and an average SA PCE of (11.97 ± 0.83)%. The PV parameters of these modules are summarised in Table 5.3. Remarkably, the average AA and SA PCEs of the 10 × 10 cm<sup>2</sup> modules are higher than those of the 5 × 5 cm<sup>2</sup> modules. The MPP tracking data and hysteresis behaviour of module 2 are reported in Figure 5.9 and 5.10, respectively. These plots point the way for further improvements to the module fabrication and design processes, namely device stability enhancement and hysteresis reduction.

Table 5.3 | PV parameters of three MAI+/H<sub>2</sub>O+ PSMs on 10 × 10 cm<sup>2</sup> substrates.<sup>203</sup>

Module	V <sub>oc</sub> (V)	Mean V <sub>oc</sub> per cell (V)	I <sub>sc</sub> (mA)	FF (%)	AA PCE (%)	SA PCE (%)
1	16.36	1.091	60.88	67.77	14.26	12.36
2	16.63	1.109	63.51	65.53	14.70	12.74
3	15.81	1.054	58.57	63.64	12.48	10.82
Mean	16.27 ± 0.34	1.085 ± 0.023	60.99 ± 2.02	65.65 ± 1.69	13.81 ± 0.96	11.97 ± 0.83

Finally, the spatial uniformity of the  $10 \times 10 \text{ cm}^2$  PSM was macroscopically evaluated using LBIC measurement. The produced  $I$  map is shown in Figure 5.8c and the associated statistical distribution is plotted in Figure 5.8d. The  $I$  map and distribution evidence uniform deposition of the module's constituent layers, showing a standard deviation of less than 6% in the AA. This intra-module uniformity is essential to achieve the high batch-to-batch reproducibility shown by the low standard deviation of PV parameters in Table 5.3.

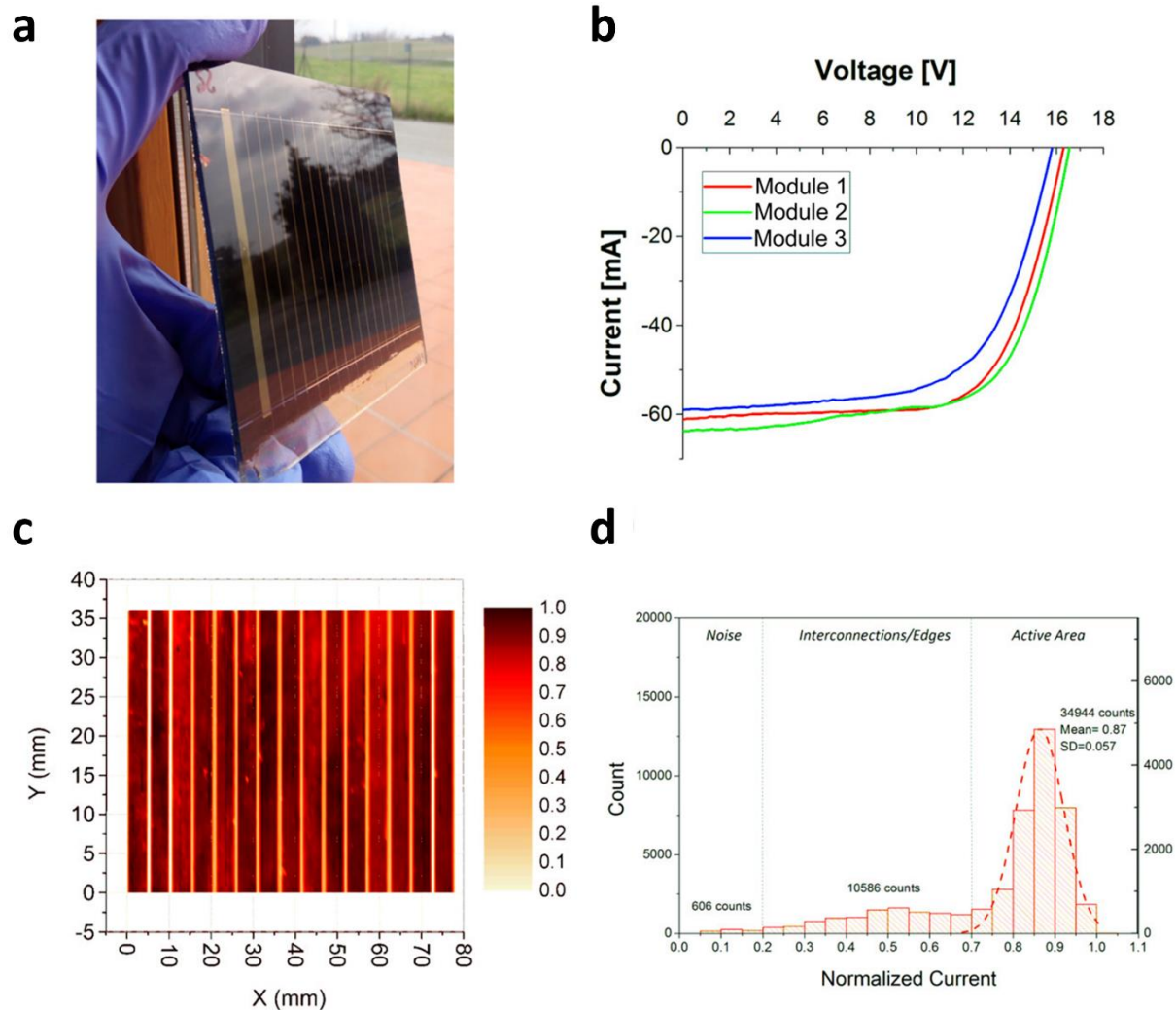


Figure 5.8 | (a) Photograph of a PSM on a  $10 \times 10 \text{ cm}^2$  substrate consisting of 15 serially connected cells with an optimised cell width of 4.5 mm. (b)  $I$ - $V$  curves of three MAI $+$ /H $_2$ O $^{+}$  PSMs with the optimised cell layout. The AA of the modules was  $47.7 \text{ cm}^2$  and the GFF was 86.7%. (c) Normalised LBIC map of a MAI $+$ /H $_2$ O $^{+}$  PSM. (d) Histogram and Gaussian fitting of the LBIC data shown in panel (c). Mean (0.87) and standard deviation (0.057) values associated with the Gaussian fitting are also reported.<sup>203</sup>

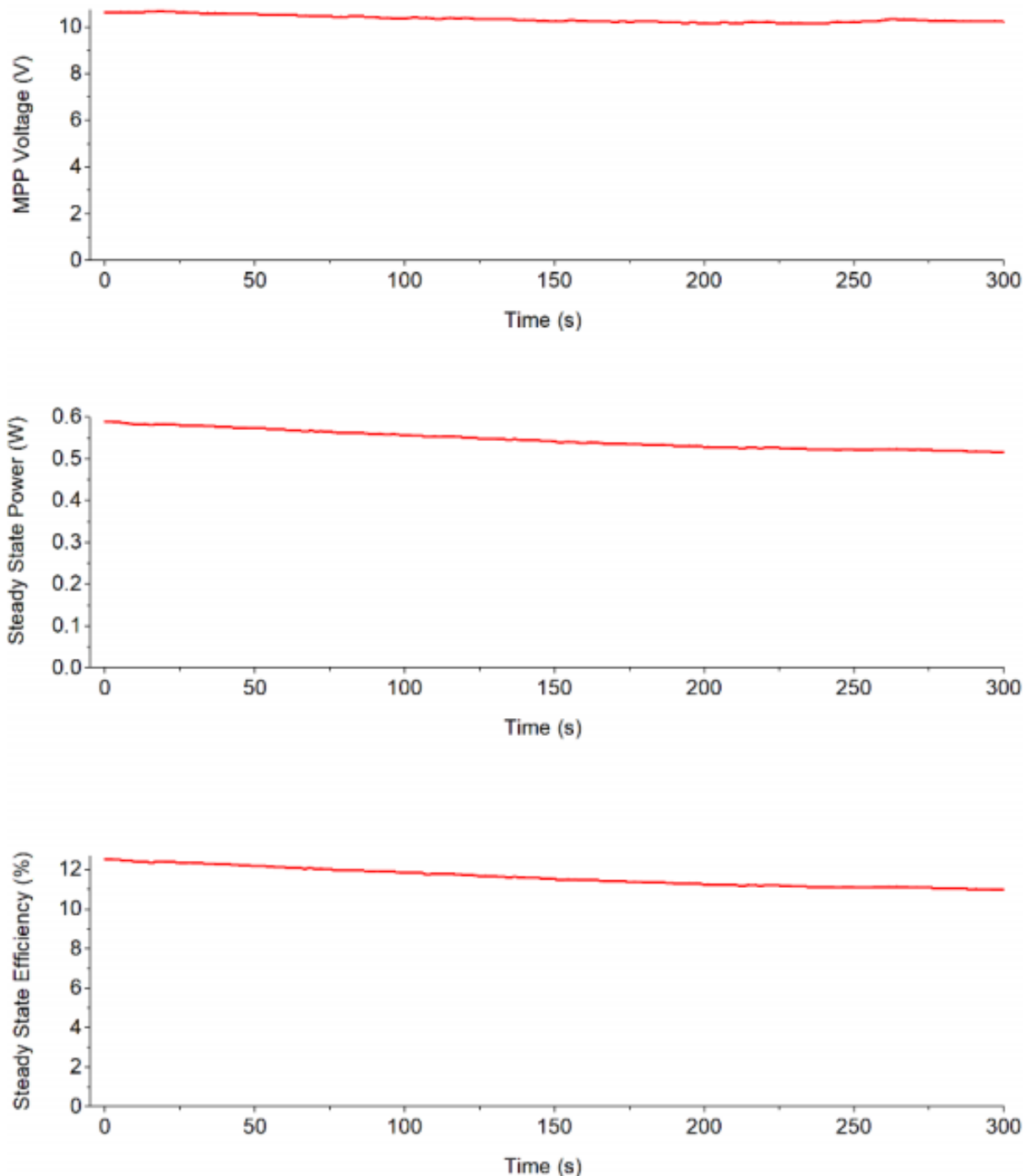


Figure 5.9 | MPP tracking results ( $V_{MPP}$ , steady state power output, and steady state PCE) of a  $10 \times 10$  cm $^2$  MAI+/H $_2$ O+ PSM with the optimised cell layout.<sup>203</sup>

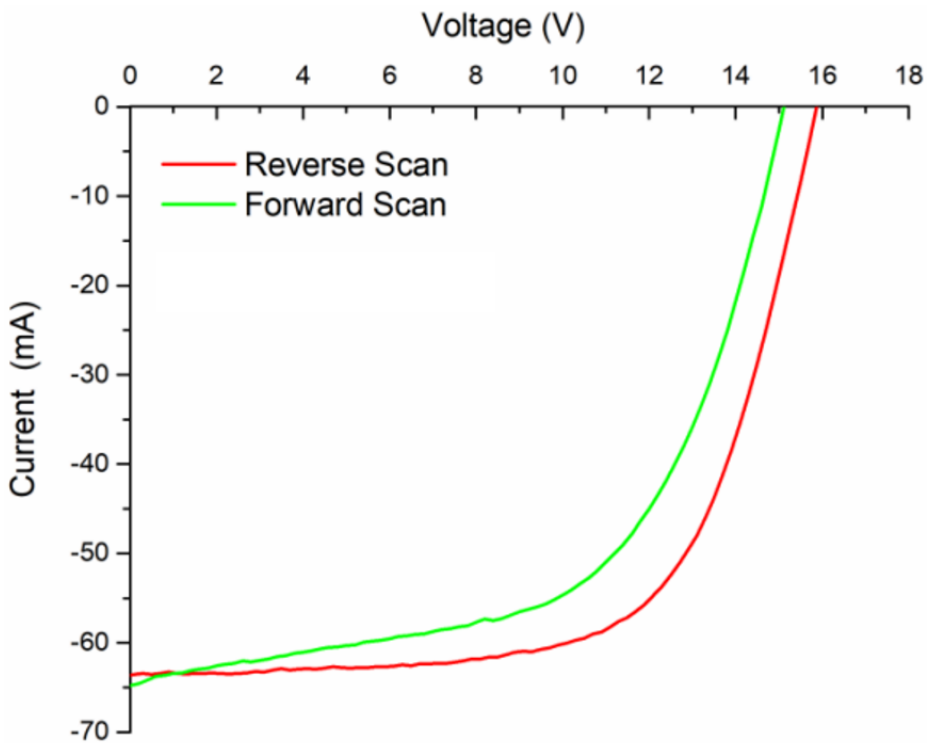


Figure 5.10 |  $I$ - $V$  curves of a  $10 \times 10 \text{ cm}^2$   $\text{MAI}^+/\text{H}_2\text{O}^+$  PSM with the optimised cell layout acquired in (red) reverse and (green) forward scan directions.<sup>203</sup>

## 5.4. Summary

In this chapter, an optimised material processing strategy is demonstrated for the deposition of large PSMs (up to  $47.7 \text{ cm}^2$  AA). An air-jet-assisted blade coating technique was used due to its easy scalability and low material waste. The sequential deposition process of the perovskite films is refined by a combination of MAI and  $\text{H}_2\text{O}$  additives in the precursor ink formulation, which proved essential to obtain high-quality  $\text{MAPbI}_3$  films in a mesoscopic device architecture. Cross-sectional STEM-HAADF imaging and STEM-EDX elemental mapping were used to understand how the additives affected the perovskite formation process, showing clear improvements in perovskite morphology, homogeneity, and scaffold pore filling. Based on the observed morphological improvements and prior findings from literature, a mechanism can thus be proposed. MAI addition into the  $\text{PbI}_2$  solution created more porous  $\text{PbI}_2$  grains and assisted their penetration into the mp- $\text{TiO}_2$  layer before they grow too large. Meanwhile,  $\text{H}_2\text{O}$  addition into the MAI solution increased the mobility of  $\text{MA}^+$  and  $\text{I}^-$  ions, thus easing MAI penetration into  $\text{PbI}_2$  and enabling a more complete perovskite formation. Optimised precursor formulation and module layout resulted in an average AA PCE of  $(13.81 \pm 0.96)\%$  for a PSM with an AA of  $47.7 \text{ cm}^2$  and a GFF of 86.7%, resulting in an average SA PCE of  $(11.97 \pm 0.83)\%$ . Future process developments should focus on upscaling to even larger substrates,  $I$ - $V$  hysteresis suppression, and device stability improvements.

# Chapter 6

## P3 Lines and Laser Scribing-induced Perovskite Decomposition in Their Vicinity

The contents of this chapter have been published in refs. <sup>178</sup> (copyright 2019 American Chemical Society) and <sup>384</sup> (copyright 2021 Wiley-VCH), and are reproduced here with minor alterations where necessary for flow and clarity.

### 6.1. Introduction

Obtaining a homogeneous perovskite film over a large area is a necessary step towards efficient PSMs, but it is not the only requirement. A large cell has to be converted into a module by dividing the active area into multiple cells connected by MI areas. In the MI scheme used in thin film PV modules, P3 lines separate neighbouring cells by removing the top metal contact and CTL (shallow scribing, Figure 6.1). In practice, however, often the perovskite and bottom CTL are also deliberately removed, such that only the TCO layer remains to ensure electrical insulation (deep scribing, Figure 6.1).<sup>172</sup> As discussed in Chapter 2, laser scribing is the preferred method to scribe MI lines, including the P3 lines. However, thermal energy deposited by the laser pulses may propagate away from the ablation volume and degrade the surrounding material.

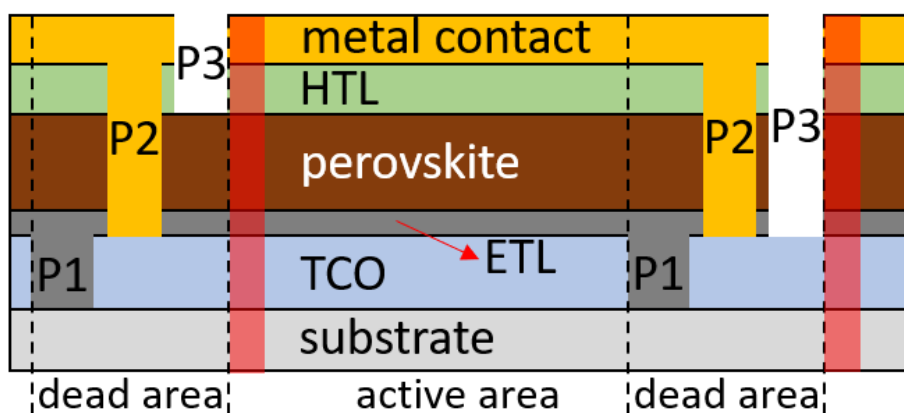


Figure 6.1 | Illustration of a PSM stack with two sets of P1-P2-P3 scribe lines. The left and right set includes a shallow and deep P3 line, respectively. The red-shaded strips mark areas cut for STEM characterisation discussed in this chapter. This schematic is not drawn to scale.

It is well-known that OIHPs are generally prone to thermal degradation. Dualeh et al. used thermogravimetric analysis (TGA) to show that  $\text{MAPbI}_3$  decomposes into  $\text{PbI}_2$  when heated by first losing HI and, at a higher temperature, methylamine ( $\text{CH}_3\text{NH}_2$ ).<sup>385</sup> The latter requires more energy to vaporise due to hydrogen bonds formed between methylamine and the perovskite matrix, which have to be broken before vaporisation.<sup>385</sup> Frost et al. proposed a mechanism through which this decomposition reaction is enabled and accelerated by the presence of  $\text{H}_2\text{O}$ .<sup>386</sup> Water triggers a Lewis acid–base reaction and dissolves the produced HI and methylamine molecules, pushing the decomposition reaction to completion.<sup>386</sup> The HI-methylamine pathway has also been confirmed by other groups in  $\text{MAPbI}_3$  and  $\text{FAPbI}_3$ , with formamidine ( $\text{HN}=\text{CHNH}_2$ ) replacing methylamine in the latter case.<sup>143,387</sup> Formamidine needs a larger amount of energy to vaporise compared to methylamine as the former is less acidic, heavier, and capable of forming two hydrogen bonds per molecule.<sup>388,389</sup> It is difficult to predict the precise effect of laser-induced perovskite decomposition into  $\text{PbI}_2$  on PSC performance as the exact roles  $\text{PbI}_2$  plays in PSCs are still being debated. However, the consensus is that small amounts of  $\text{PbI}_2$  passivate non-radiative recombination sites at grain boundaries and interfaces while too much of it slows down charge carrier transport and collection.<sup>390–395</sup>

There has not been an investigation on whether the perovskite layer next to scribe lines is indeed thermally degraded by laser pulses. This consideration is not necessary for P1 lines as the TCO is scribed before other layers are deposited. Any extra-scribe damage caused by P2 scribing can be neglected because the region between each set of P1 and P3 lines does not contribute photocurrent regardless. However, the other side of a P3 line is considered an active area of the next cell. Rakocevic et al. have previously shown scribing damage at the edges of a P3 line in the form of Au and spiro-OMeTAD delamination. However, decomposition of the perovskite layer itself has not been studied, even though it is essential not only to accurately define a module's AA, but also to gain a deeper understanding of the effect of laser scribing on the device stack.<sup>396</sup>

## 6.2. Propagation of Thermal Energy from P3 Laser Scribing

### 6.2.1. Experimental Methods

#### 6.2.1.1. Device Fabrication and Laser Scribing

The PSMs were fabricated by Dr. Lucija Rakocevic (imec and Katholieke Universiteit Leuven).

Samples were prepared on 9 cm<sup>2</sup> glass substrates covered with 150 nm-thick ITO. These substrates were sequentially cleaned using soap, deionised water, acetone, and isopropanol for 10 min each, then exposed to UV light for 15 min before  $\text{SnO}_2$  deposition. The  $\text{SnO}_2$  colloidal nanoparticle water-based solution was spin coated and annealed in air to form a 20 nm-thick  $\text{SnO}_2$  layer. Perovskite and the spiro-

OMeTAD layer were deposited in an N<sub>2</sub>-filled glovebox. The spin coated perovskite layer was deposited following a two-step procedure to form the Cs<sub>0.1</sub>FA<sub>0.9</sub>Pb(I<sub>0.955</sub>Br<sub>0.045</sub>)<sub>3</sub> photoactive layer.<sup>397</sup> 0.12 mmol CsI and 1.2 mmol PbI<sub>2</sub> were dissolved in a mixture of 0.876 ml DMF and 86.4 µl DMSO. This solution was spin coated onto the substrate at 3000 RPM for 30 s. Then, a mixed FAI and FABr solution in isopropanol (0.422 mmol/ml) was spin coated at 3000 RPM for 30 s. The molar fraction of FABr in the mixed solution was 15%. After that, the substrate was annealed on the hotplate at 100 °C for 30 min. The perovskite layer was followed by deposition of an 80 mg/ml spiro-OMeTAD solution doped with 17.5 µl/ml Li-TFSI (520 mg/ml in acetonitrile) and 28.5 µl/ml 4-TBP. Samples with the spiro-OMeTAD top layer were exposed to dry air in the dark for 12 h to dope the spiro-OMeTAD layer. Finally, cell fabrication was completed by thermal evaporation of 80 nm of gold. For one-step blade coating, a single perovskite precursor solution was prepared with the DMF/N-methyl-2-pyrrolidone (NMP) solvent mixture. The other device fabrication steps were the same as with the spin coated devices. Perovskite layer thickness was measured to be ~480 nm for spin coating and ~300 nm for blade coating.

Laser scribing was performed using an M-Solv MSV 500 advanced diode-pumped solid-state laser processing tool integrated into a glovebox with an N<sub>2</sub> atmosphere. The laser  $\lambda$  was set at 355 nm (UV) to scribe P3 lines after all layers have been deposited. The scribing parameters were set at 10 ps pulse duration, 200 kHz pulse frequency, and 100 mm/s patterning speed. All scribing was performed on the Au contact side. Sample-specific scribing parameters were set as detailed in Table 6.1.

Table 6.1 | Sample codes and P3 laser scribing parameters.

Sample Code	Perovskite Deposition	Pulse Spot Diameter (µm)	Effective Fluence (J/cm <sup>2</sup> )	Scribe Type
SC	Spin coating	N.A.	N.A.	Knife scribe
SD-3.47	Spin coating	11	3.47	Laser, deep
SD-3.04	Spin coating	18	3.04	Laser, deep
BC	Blade coating	N.A.	N.A.	Not scribed
BD	Blade coating	18	3.04	Laser, deep
SS	Spin coating	18	0.47	Laser, shallow
BS	Blade coating	18	0.47	Laser, shallow

### **6.2.1.2. Electron Microscopy Characterisation**

SEM images and SEM-EDX elemental maps were acquired with an FEI Nova NanoSEM fitted with a Bruker XFlash EDX detector. The acceleration voltage was set at 2 kV for imaging and at 10 kV for EDX mapping, while the beam current was 27 pA for imaging and 790 pA for EDX mapping. Low-magnification SE imaging (Figure 6.2,6.3a,6.4c,d,6.5,6.8) was done using an ETD while high-magnification SE imaging (Figure 6.3b,c) used a TLD. BSE imaging was performed using a segmented semiconductor detector with all the segments activated. The BSE images were formed by summing the detected signals from all segments to form compositional contrast. SEM-EDX maps were acquired and processed in Bruker Esprit 1.9. For STEM characterisation, cross-sectional sample lamellae were prepared with an FEI Helios Nanolab Dualbeam FIB/SEM. The lamellae were immediately transferred into an FEI Tecnai Osiris 80-200 FEGTEM, minimising air exposure to ~2 min. STEM-HAADF images and STEM-EDX SIs were obtained using the beam parameters described in Section 3.7 and Table 3.2. STEM-EDX SIs were spatially rebinned by a factor of 2, denoised with PCA, and processed in HyperSpy following the procedure explained in Section 4.3.<sup>290</sup>

### **6.2.2. SEM Characterisation of Laser Scribed P3 Lines**

A set of samples composed of glass/ITO/SnO<sub>2</sub>/Cs<sub>0.1</sub>FA<sub>0.9</sub>PbI<sub>2.865</sub>Br<sub>0.135</sub>/spiro-OMeTAD/Au were fabricated with either a two-step spin coating or a one-step blade coating process. The P3 lines were scribed while varying laser fluence and scribing depth compared to reference samples (Table 6.1). Each sample is coded according to the perovskite deposition method (first letter, S = spin coated; B = blade coated) and scribe type (second letter, C = control; D = deep laser; S = shallow laser).

Since the purpose of P3 lines is to separate the back contact of neighbouring cells, they are first examined with top-view SEM imaging and SEM-EDX mapping to ensure proper cell isolation. SEM images of P3 lines are shown in Figure 6.2. There are major morphological differences among a knife scribe line (Figure 6.2a), deep laser scribe lines (Figure 6.2b,c), and shallow laser scribe lines (Figure 6.2d,e). While the deep scribes were ablated by one row of laser pulses, shallow scribing used a three-row configuration with the laser beam moving in a raster pattern as indicated by the cyan arrows in Figure 6.2e. This three-row arrangement was adopted to ensure complete separation of neighbouring cells' back contact layer, as the low pulse overlap necessary to limit the scribe lines' depth may result in incomplete Au removal if only one row of laser pulses is used.<sup>189</sup> Although wider than the deep P3 lines, the width of the shallow P3 lines (~40 µm) is still comparable to current best practice.<sup>174,175,398</sup>

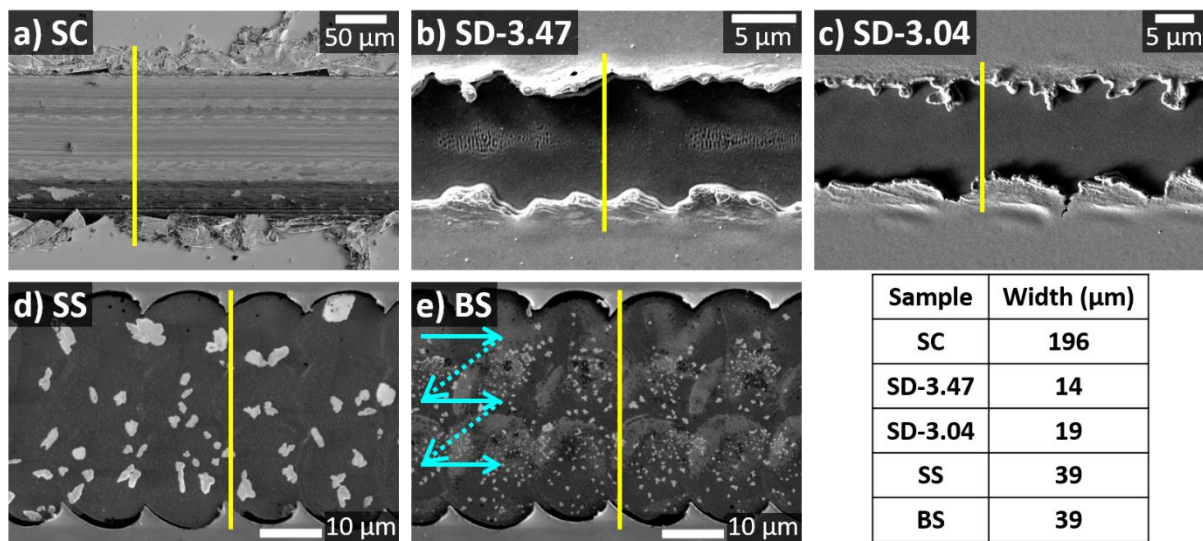


Figure 6.2 | Top-view SE images of samples (a) SC, (b) SD-3.47, (c) SD-3.04, (d) SS, and (e) BS. Cyan arrows indicate the raster pattern followed by laser pulses for shallow scribe lines (1 complete line of pulses before another). Yellow lines measure each scribe line's width as summarised in the table.

The mechanical scribing process produces plenty of debris next to the scribe line, whereas laser scribing exfoliated the Au and spiro-OMeTAD layers, similar to a previous observation.<sup>396</sup> Layer delamination was caused by the steep temperature gradient during the pulse duration. This gradient created a high thermal stress, which can induce bending of thin films by stripping them from their substrate if the stress is stronger than the films' adhesion force.<sup>399,400</sup> Spiro-OMeTAD in particular has a very low fracture resistance, especially after it crystallises at about 85°C.<sup>401</sup> Taking the piled-up debris and delaminated layers into account, the knife scribe line is about 12 and 5 times wider than the deep and shallow laser scribe lines, respectively, corresponding to an increase of approximately 180 and 160 μm in  $W_d$ .

In sample SD-3.47, the ITO layer suffered from periodic damage marks where the glass substrate is exposed (Figure 6.2b, 6.3). This would result in reduced lateral conductivity in ITO as its cross-sectional area is reduced. Importantly, sample SD-3.04 did not show ITO damage, meaning its lower laser fluence was more suitable for P3 scribing. The periodic nature of these damage marks suggests that they are a form of laser-induced periodic surface structures (LIPSS). The ratio between their periodicity ( $265 \pm 46$  nm, Figure 6.3g) and the laser pulse's wavelength (355 nm) indicates that these damage marks belong to the low spatial frequency LIPSS – type 1 (LSFL-I) category according to Bonse et al.'s LIPSS classification.<sup>402</sup> LSFL-I is caused by interference between the incident laser pulses and reflected or scattered waves at a rough surface.<sup>187,402</sup> These scattered waves can be either the laser pulse itself or, in the case of fs-pulse laser, surface plasmon polaritons (SPPs) generated in the material.<sup>403–406</sup> This requirement for an fs-pulse laser is important because it allows transient changes of the material's permittivity, allowing excitation of SPPs even in dielectrics and semiconductors. Therefore, SPPs are

not involved in this case since a ps-pulse laser was used and thus the interference was only between the incident and scattered laser waves. Another theory suggests that even in cases where the laser energy arriving at a rough surface is not enough for material ablation, it is still possible to form LSFL-I through rapid local melting and subsequent re-solidification as long as the interference requirement is satisfied.<sup>407,408</sup> Regardless of the active mechanism, laser fluence and pulse overlap have a large effect on LIPSS formation. Sufficiently high fluence is needed to excite SPPs and/or melt the material. Meanwhile, a high overlap ratio assists LIPSS formation because the rough material surface created by an earlier pulse amplifies wave scattering of subsequent pulses.<sup>402</sup> These two parameters explain why LIPSS was only observed in sample SD-3.47 in this work.

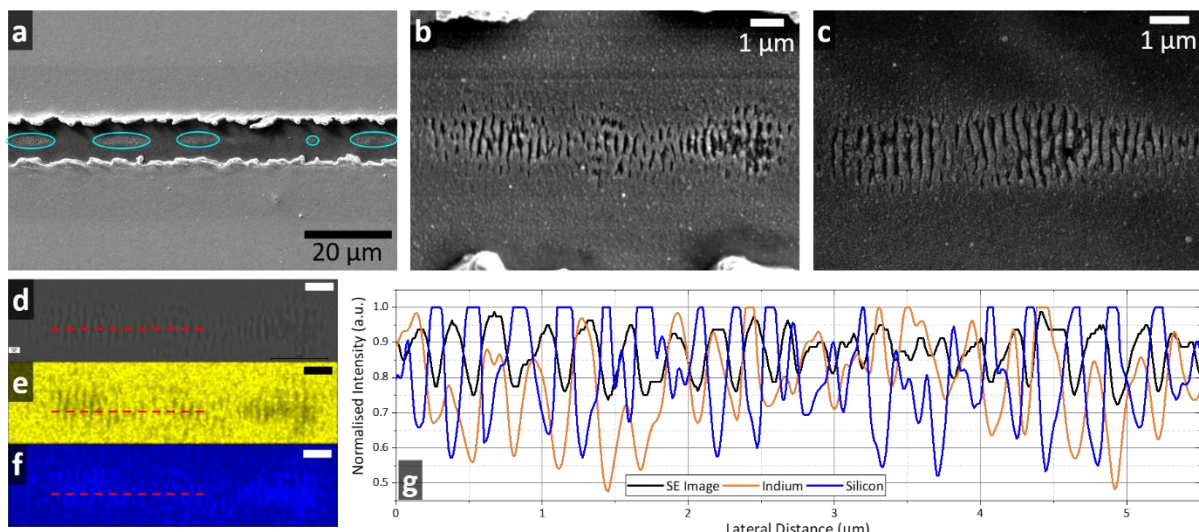


Figure 6.3 | (a-c) Top-view SEM images of sample SD-3.47's damaged ITO layer. (d) EDX scan area for (e-f). (e) In and (f) Si maps showing low In and high Si signal at the scratches. (g) Normalised intensity line plots of the red dashed lines in (d-f). The dips in SE Image line indicate the damage marks' locations. Scale bars in (d-f) represent 1 μm.

Another interesting feature in Figure 6.2 is the grains apparent on the perovskite surface of shallow scribed samples (Figure 6.2d,e). These grains appear brighter than the perovskite surface in SE images (Figure 6.2d,e, 6.4c). However, this intensity difference disappears in BSE images (Figure 6.4a,b). SE images are sensitive to the sample's topography while the contrast in BSE images is dominated by high-Z elements.<sup>267</sup> The BSE images therefore show that these grains have the same heavy elements as the perovskite layer underneath them, namely Cs, Pb, and I. Figure 6.4c-f further show that these grains are relatively Cs-rich. They are likely to be remnants of the perovskite that was melted but not vaporised by the laser pulse. Since the organic FA cation is the most susceptible to heat, the resolidified grains are richer in Cs compared to the bulk perovskite.

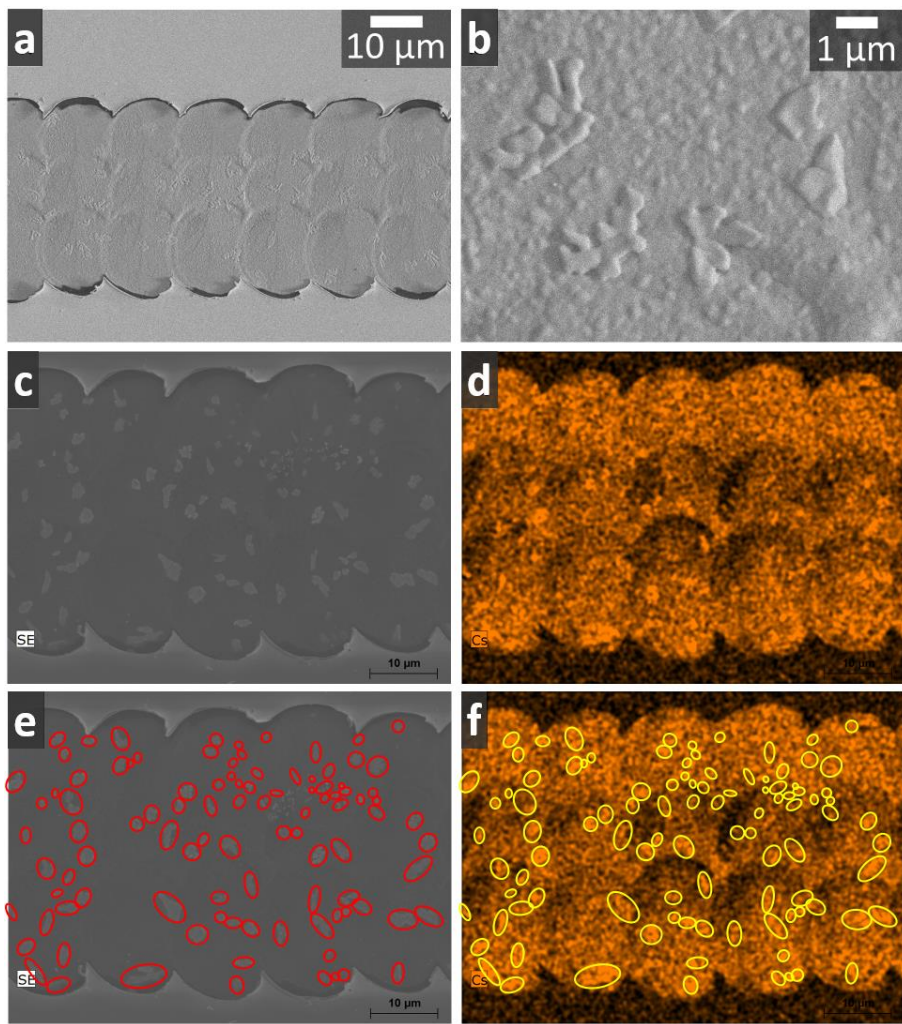


Figure 6.4 | (a,b) BSE images of sample SS, acquired with a 5 kV acceleration voltage. (c) SE image and (d) Cs map of a P3 line in sample SS. (e) and (f) are reproductions of (c) and (d) with red/yellow markers to highlight the correlation between grains and regions of high Cs intensity. Scale bars in (c) and (e) applies to (d) and (f).

Elemental maps of P3 lines evidence no Au redeposition in all scribe line types, proving the suitability of the P3 scribing parameters used (Figure 6.5). Inside the knife scribe line (Figure 6.5, row 1), there is a band covering the bottom third of the line where Au and spiro-OMeTAD layers were removed, but perovskite was not, as shown by high Pb and I signals and low In signals. This demonstrates the low uniformity of mechanical scribing, likely caused by some scribed material sticking to the knife edge or knife wear. Pb, I, and In maps of shallow scribed samples (Figure 6.5, rows 4,5) show uneven material removal in their scribe lines due to low pulse overlap. At the pulse overlap areas, Pb and I maps appear darker, while In map looks brighter, indicating that a larger fraction of the perovskite layer was ablated there. Pb and I maps of sample BS (Figure 6.5, row 5) are darker and less uniform than those of sample SS (Figure 6.5, row 4) because the blade coated perovskite layer is thinner (~300 vs ~480 nm).

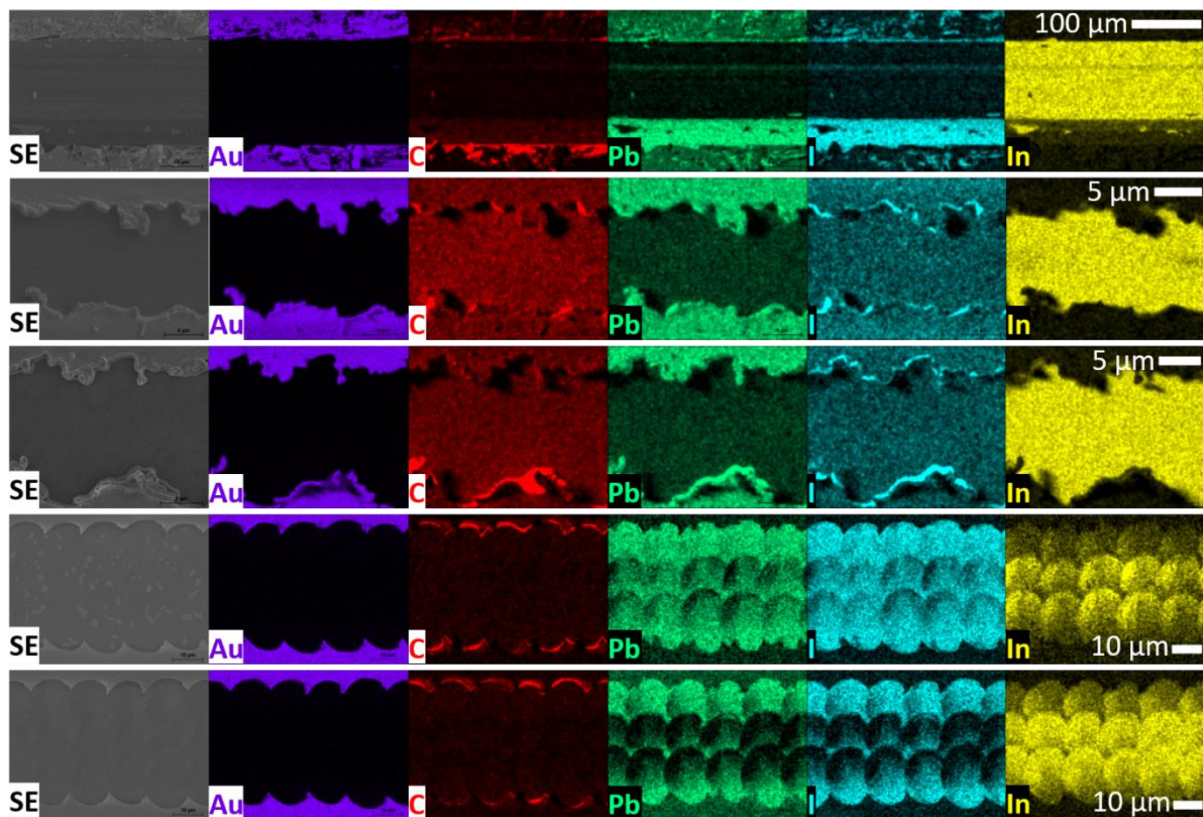


Figure 6.5 | Top-view SEM-EDX mapping of samples (row 1) SC, (row 2) SD-3.47, (row 3) SD-3.04, (row 4) SS, and (row 5) BS. From left to right, each column shows the SE image of the scan area, Au, C, Pb, I, and In maps, respectively. Each scale bar applies to its respective row.

To reveal the cause of shallow scribe lines' low uniformity, line plots of I signal intensity are extracted from sample BS's I map (Figure 6.6a-c). To produce Figure 6.6b, each pixel's I intensity is averaged horizontally and then plotted vertically. Green strips on the sides mark the position of laser pulses, with darker shading showing where adjacent pulses overlap. Figure 6.6c shows the horizontal variation of I intensity within each pulse row. Here, each pixel's I intensity is vertically averaged over its respective row's width (excluding the portion that overlaps with the adjacent pulse row) and then plotted horizontally. Figure 6.6b,c and all green strips are scaled to conform with the I map shown in Figure 6.6a. As expected, the I intensity is lowest at the pulse overlaps, both within each row and across rows. The top pulse row, which was scribed first, has a markedly higher I intensity than the other two rows (Figure 6.6c), meaning its ablation craters are shallower. If the pulse duration was short enough to prevent energy loss from excited electrons inside the laser pulse's absorption volume to the lattice of the surrounding material, the ablation crater's depth is dictated only by the absorption volume and thus should be very similar for all craters.<sup>409</sup> Therefore, the discrepancy in I intensity across rows is a clear indication that a fraction of the laser pulses' thermal energy is dissipated from the absorption volume into the rest of the target material, affecting the depth of the ablation craters.

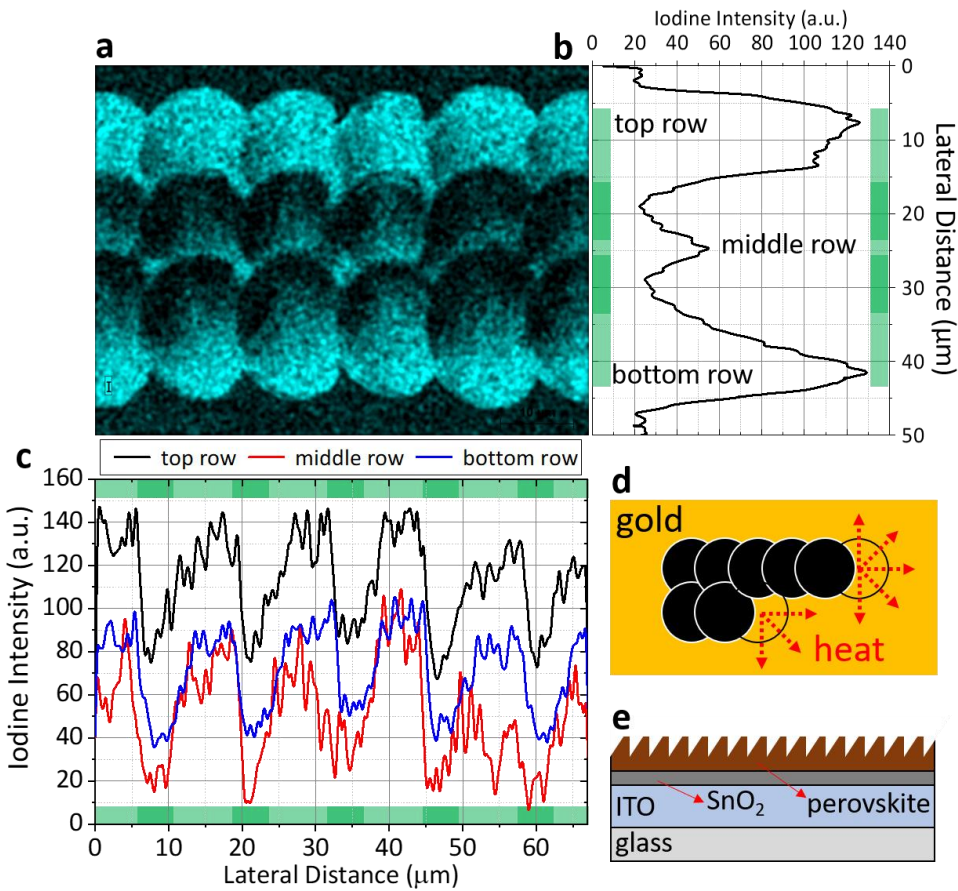


Figure 6.6 | (a) SEM-EDX I map of sample BS. (b) Plot of horizontally averaged I intensity. Green strips mark the position of laser pulses, with darker shading indicating pulse overlaps. Sections of the plot corresponding to each pulse row are marked. (c) Plot of vertically averaged I intensity for each pulse row. (d) Schematic of heat loss through the intact gold layer surrounding a pulse crater. (e) Schematic of the perovskite surface after shallow laser scribing.

Thermal energy dissipation can occur through lateral heat flow into the intact material beyond the pulse diameter, especially into the Au layer whose thermal conductivity is the highest.<sup>409,410</sup> When a top row pulse hits a target, a higher fraction of its crater perimeter is composed of the intact material as it only has one neighbouring crater, compared to a middle or bottom row pulse which has 2 (Figure 6.6d). Consequently, more heat was lost through the Au layer at the top row and less perovskite was ablated there. Moreover, heat loss at the top row is also vertically symmetric, unlike for the middle and bottom row pulses. This is why in Figure 6.6b, the I intensity immediately falls sharply from the bottom P3 line edge inwards, as there was no Au heat sink in that direction when the bottom row pulses were applied. On the other hand, the I intensity decreases slowly from the top edge inwards since Au was still present in that direction when the top row pulses were scribed. The cause of this slow decline, rather than a flat profile expected from symmetric heat loss, is the Gaussian tail of the middle row pulses. Comparing the middle and bottom pulse rows, the middle row has a slightly lower I intensity (Figure 6.6c). This

difference cannot be explained by considering lateral heat flows. Rather, this is due to the Gaussian nature of the laser pulses. The bottom row was only exposed to the middle row pulses' Gaussian tail, while the scribe line's centre area was affected by pulse tails from both the top and bottom rows; hence, the ablation craters there are slightly deeper. Another possible explanation for the roughness of the shallow scribe lines' surface is accumulation of laser-induced damage in the perovskite layer over multiple pulses. However, this is far less likely as Au is much more thermally conductive than all other layers, so lateral heat loss through Au will occur faster than vertical heat diffusion into perovskite.

Based on the above discussion, heat diffusion from the ps-pulse laser into the target material clearly cannot be ignored. If heat diffusion is negligible, then there would be neither heat loss nor damage accumulation in perovskite. In this case, the target material would not be affected beyond the laser pulses' absorption volume. All three rows of pulses should then exhibit about the same crater depths, which is not the case (Figure 6.6c). The same consideration holds for sample SS as well (Figure 6.7) except for smaller intensity variations and differences due to its thicker perovskite layer.

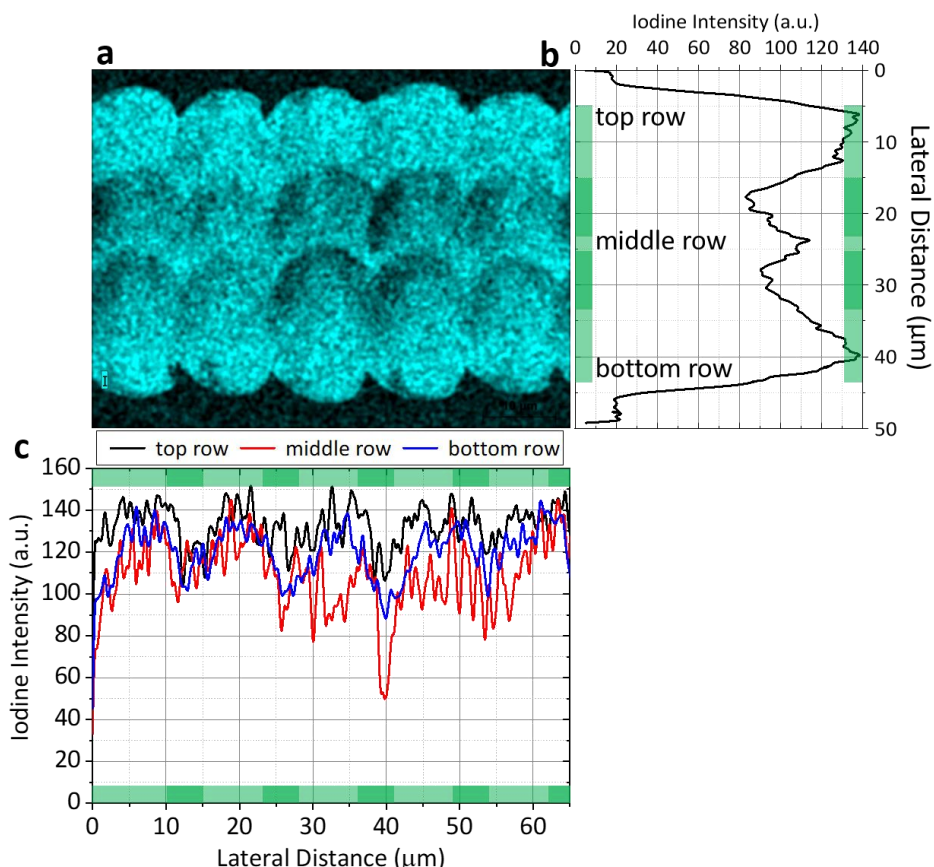


Figure 6.7 | (a) SEM-EDX I map of sample SS. (b) Plot of horizontally averaged I intensity from (a). The green strips mark the position of the laser pulses, with darker shading indicating pulse overlaps. A section of the plot corresponding to each pulse row is marked. (c) Plot of vertically averaged I intensity for each pulse row in (a).

### 6.2.3. Laser-Induced Perovskite Decomposition in the Active Area

After looking at the P3 lines themselves, the adjacent perovskite layer's integrity is then examined by cross-sectional STEM-HAADF imaging and STEM-EDX elemental mapping. Device lamellae were cut parallel to P3 lines (except for sample BC, which had no scribe line), ~900 nm away from P3 line edges (Figure 6.8). STEM-EDX SIs of the lamellae were acquired and denoised with PCA as described in Chapter 4. First, samples SC, SD-3.47, and SD-3.04 are compared to investigate the effect of laser scribing generally and laser fluence specifically. Figure 6.9a–c displays the HAADF images of these samples. Layers in the device stack are denoted by coloured strips at the right edge of Figure 6.9a and identified in the figure caption. Figure 6.9a–c display highly heterogeneous perovskite layers in all three samples, with bright needle-like features and large grains (marked with cyan arrows). The laser-scribed samples have more needles than sample SC, with increasing mean needle thickness from  $(57 \pm 17)$  nm in SC to  $(103 \pm 52)$  nm in SD-3.47 and  $(94 \pm 41)$  nm in SD-3.04. There is no difference in the number or size of the bright large grains, indicating that they were not caused or affected by laser scribing. Rather, these large grains are most likely unreacted precursors resulting from non-optimal two-step perovskite film formation.

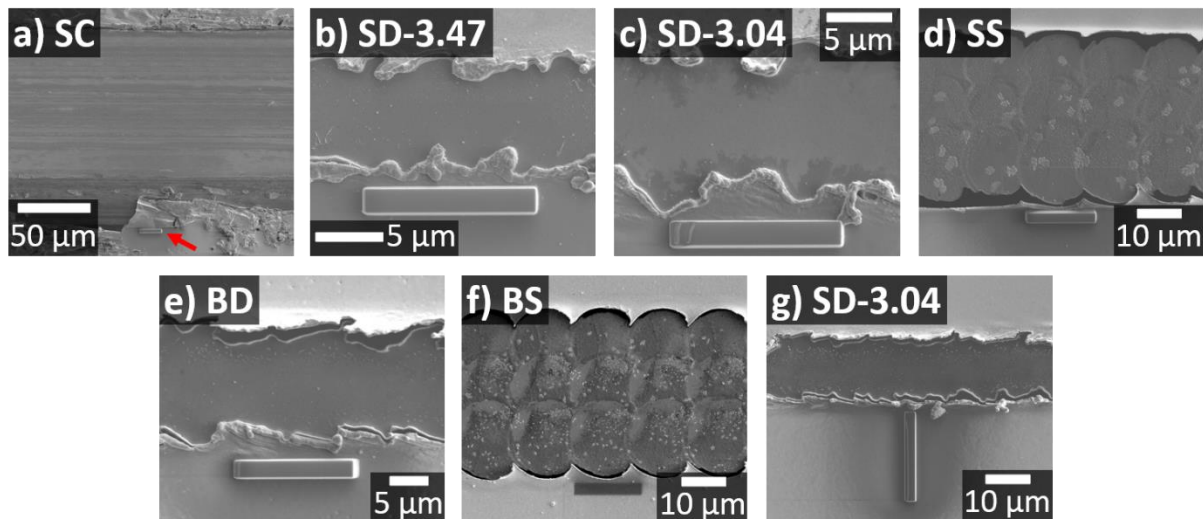


Figure 6.8 | Location of the lamellae cut for STEM characterisation for samples (a) SC, (b) SD-3.47, (c) SD-3.04, (d) SS, (e) BD, (f) BS, and (g) SD-3.04. The distance between the scribe line edge and the final, thinned lamella is approximately 900 nm for those cut parallel to P3 lines (a-f).

Figure 6.9d displays quantified elemental maps (I, Pb, C, and N) and an I/Pb ratio map acquired from areas marked with red boxes in Figure 6.9a–c. These maps illustrate the effect of laser fluence on perovskite's elemental constituents in the stack next to a P3 line edge. Figure 6.9d shows that the

needles in SD-3.47 and SD-3.04 have high concentrations of Pb and I and very low N concentration. Furthermore, their grain shape is also consistent with the needle-like crystal morphology of  $\text{PbI}_2$  observed by others, leading to the conclusion that they are  $\text{PbI}_2$ .<sup>364</sup> These  $\text{PbI}_2$  needles are not visible in the Pb and I maps of sample SC because they are much thinner than the lamella thickness ( $\sim 200$  nm), meaning that their high Pb and I signals were moderated by the surrounding perovskite. Identification of these needles as  $\text{PbI}_2$  suggests that non-perovskite phases in sample SC are unreacted precursors. However, the higher number and thickness of these needles in samples SD-3.47 and SD-3.04 compared to sample SC prove that laser pulses induced further growth of  $\text{PbI}_2$  close to a scribe line edge, most likely as a product of thermal degradation of perovskite.

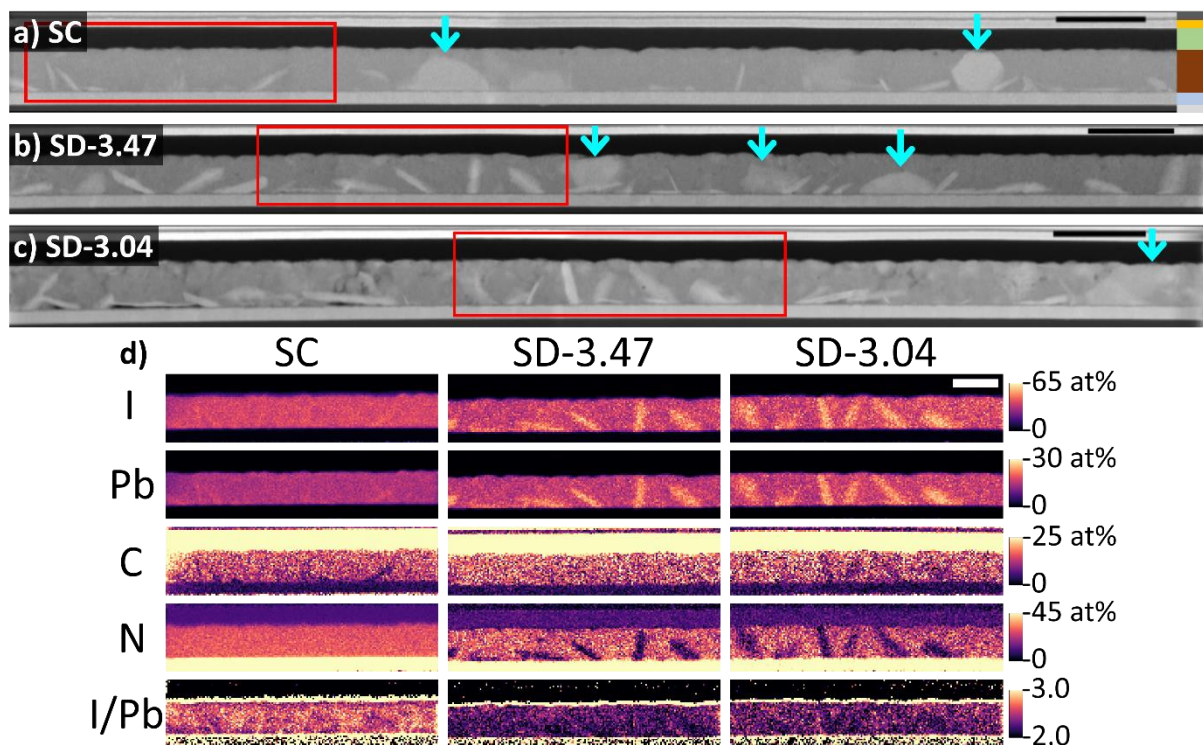


Figure 6.9 | (a–c) Cross-sectional STEM-HAADF images of samples (a) SC, (b) SD-3.47, and (c) SD-3.04. Cyan arrows mark non-perovskite bright grains, while red boxes mark the STEM-EDX scan areas mapped in (d). From top to bottom, the layer colour codes are: dark grey, protective Pt; gold, top Au contact; green, spiro-OMeTAD; brown, perovskite; light grey, ITO; and white, glass. The  $\text{SnO}_2$  layer is the thin strip between perovskite and ITO. (d) Cross-sectional quantified STEM-EDX elemental maps of samples SC, SD-3.47, and SD-3.04. Thin yellow strips at the perovskite–spiro-OMeTAD interface in the I/Pb map indicate I diffusion caused by the STEM electron beam. The denoised STEM-EDX model SIs for samples SC, SD-3.47, and SD-3.04 were constructed using 14, 18, and 20 principal components via PCA, respectively. Scale bars represent (a–c) 1  $\mu\text{m}$  and (d) 600 nm.

Interestingly, Barbé et al. recently devised a novel method to controllably decompose perovskite into PbI<sub>2</sub> with a continuous wave laser.<sup>411</sup> They found that if the effective thickness of the PbI<sub>2</sub> film is less than 20 nm, then the net effect is beneficial; otherwise, high series resistance dramatically lowers the output current. Implied in Barbé et al.'s conclusion is an assumption that PbI<sub>2</sub> was created in the form of a thin film. Figure 6.9 shows that the PbI<sub>2</sub> needles in fact vary in size and do not lie flat on the perovskite–SnO<sub>2</sub> interface to form a thin film. Rather, they are interspersed within the perovskite layer and tilted at a wide range of angles. Therefore, slower charge transport should be expected close to P3 lines due to the high PbI<sub>2</sub> content.<sup>390–395</sup>

An intensity threshold analysis on the cross-sectional STEM-HAADF images of samples SC and SD-3.47 was conducted to measure the volume fraction occupied by PbI<sub>2</sub> in the perovskite layer. This fraction was found to increase significantly from 6.65% in sample SC to 15.84% in sample SD-3.47 (Figure 6.10, 6.11). The steps in this analysis are as follows:

1. Crop the HAADF images such that only the perovskite layer remains. Further, sections of the image containing bright grains marked with cyan arrows in Figure 6.9 are also cropped out to remove their influence on the thresholding.
2. Extract a histogram of brightness values. Remove the lowest-intensity peak which belongs to spiro-OMeTAD pixels. Fit the remaining two peaks (perovskite, red and PbI<sub>2</sub>, green) with Gaussian fitting.
3. Run an initial thresholding to isolate the remaining spiro-OMeTAD pixels. The threshold limits used here are from 0 to X. The value of X can be easily determined by eye as the intensity of spiro-OMeTAD pixels is far below other pixels.
4. Run the final thresholding to separate bulk perovskite and PbI<sub>2</sub>. The threshold limits here are X to Y for perovskite and Y to 65535 for PbI<sub>2</sub>, with Y being the crossover point of the two fitted peaks.
5. After both thresholding rounds, note the percentage of pixels occupied by spiro-OMeTAD, perovskite, and PbI<sub>2</sub>

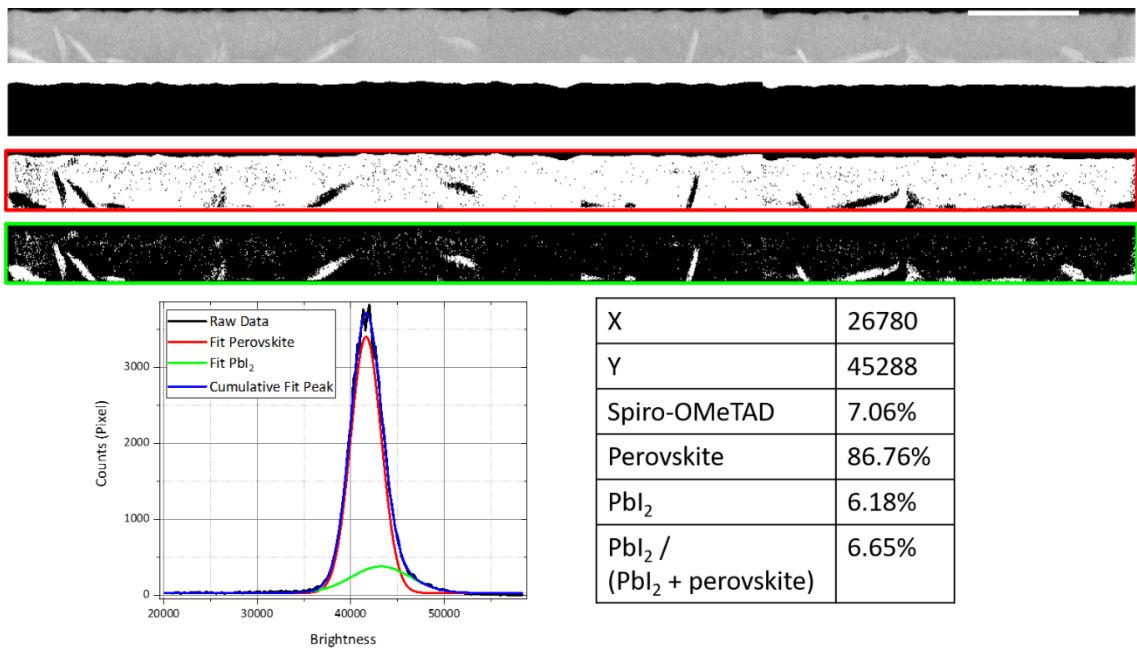


Figure 6.10 | Threshold analysis for sample SC. From top to bottom, the images are cropped HAADF image, initial thresholding result (white = spiro-OMeTAD, black = perovskite and PbI<sub>2</sub>), final thresholding result (white = perovskite, black = spiro-OMeTAD and PbI<sub>2</sub>), and PbI<sub>2</sub> grains (white = PbI<sub>2</sub>, black = perovskite and spiro-OMeTAD). At the bottom are the brightness histogram with fitted peaks and analysis results in a table. The scale bar represents 1 μm and applies to all images.

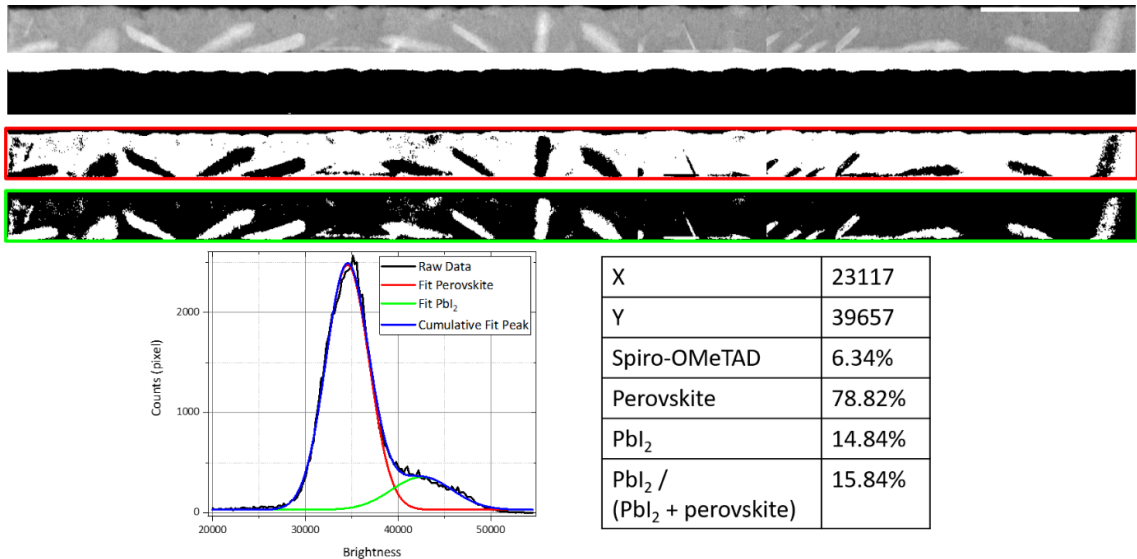


Figure 6.11 | Threshold analysis for sample SD-3.47. From top to bottom, the images are cropped HAADF image, initial thresholding result (white = spiro-OMeTAD, black = perovskite and PbI<sub>2</sub>), final thresholding result (white = perovskite, black = spiro-OMeTAD and PbI<sub>2</sub>), and PbI<sub>2</sub> grains (white = PbI<sub>2</sub>, black = perovskite and spiro-OMeTAD). At the bottom are the brightness histogram with fitted peaks and analysis results in a table. The scale bar represents 1 μm and applies to all images.

Beyond  $\text{PbI}_2$  needles, lower concentration of I and higher levels of Pb, C, and N are measured in the perovskite layer of samples SD-3.47 and SD-3.04 compared to sample SC (Figure 6.12, “SD vs SC” column). At first glance, these findings do not conform to the decomposition mechanism proposed by Dualeh et al. and Frost et al.<sup>385,386</sup> Although their TGA experiments were performed on  $\text{MAPbI}_3$ , a later study has shown that  $\text{FAPbI}_3$  also decomposes by initial evaporation of HI followed by formamidine.<sup>387</sup> It is reasonable to expect that the  $\text{Cs}_{0.1}\text{FA}_{0.9}\text{PbI}_{2.865}\text{Br}_{0.135}$  perovskite used here will degrade in a similar manner as the percentage of the inorganic cation is small. If this is the case, a drop in C and N concentrations and an increase in Pb and I levels would be expected after laser scribing. The I concentration would still increase despite HI vaporisation because each vaporised pair of formamidine and HI molecules removes one C and two N atoms but only one I atom (H cannot be detected by EDX and thus is not accounted for in this discussion).

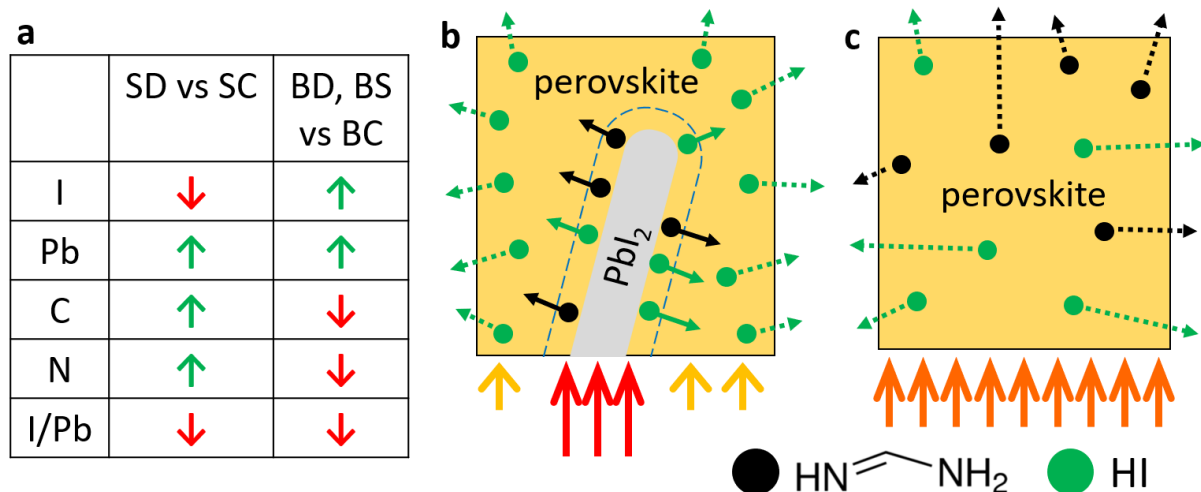


Figure 6.12 | (a) Summary of perovskite compositional changes after laser scribing, compared to control samples. (b,c) Schematics of the proposed thermal decomposition mechanisms. The dominant mechanism is determined by the presence (b) or absence (c) of pre-existing  $\text{PbI}_2$  grains in the perovskite layer. If  $\text{PbI}_2$  is present, most of the thermal energy flows through it (red arrows) rather than through the perovskite (yellow arrows) due to the large thermal conductivity difference. If  $\text{PbI}_2$  is absent, heat flows uniformly through the perovskite (orange arrows).

These unexpected compositional changes can be rationalised by considering the imbalance of thermal conductivities between perovskite and  $\text{PbI}_2$ . Halide perovskites have an exceptionally low thermal conductivity of about 0.3–0.4 W/mK for room temperature and above.<sup>306–310</sup> Most of these published values are for  $\text{MAPbI}_3$ , but Kovalsky et al. have demonstrated that the A-site cation’s nature (organic MA vs inorganic Cs) has very little effect on thermal conductivity at room temperature and above as Umklapp scattering is the dominant phonon scattering mechanism in both cases, a finding later

confirmed by Lee et al.<sup>308,412</sup> In contrast, PbI<sub>2</sub>'s thermal conductivity is almost an order of magnitude higher at approximately 2.7 W/mK.<sup>413</sup> Consequently, in the perovskite layer, a large share of the laser pulses' deposited thermal energy will flow through existing PbI<sub>2</sub> grains.

This mechanism is supported by a finite element analysis-based modelling of thermal flow inside a laser scribed PSM sample just after a laser pulse ends. The steady-state heat transfer module in QuickField software is used to qualitatively capture a snapshot of the heat flux of the residual thermal energy to see where it flows in the device stack. First, two essential parameters to delineate the heat sources are calculated, namely optical penetration depth ( $l_\alpha$ ) and heat diffusion length ( $l_T$ ). Both values are calculated for the Au contact as the first layer hit by the laser pulse. Relevant physical properties of the Au layer are summarised in Table 6.2 and the laser parameters in Table 6.3.

Table 6.2 | Properties of the Au layer used in modelling the heat source fronts.

Physical Property	Value
Thickness ( $t$ )	80 nm
Absorption coefficient at 355 nm ( $\alpha$ )	67.623/ $\mu\text{m}$ <sup>414</sup>
Thermal diffusivity ( $D$ )	1.2 cm <sup>2</sup> /s <sup>415</sup>

Table 6.3 | Laser pulse parameters used in modelling the heat source fronts.

Laser Parameter	Value
Pulse spot diameter ( $d$ )	18 $\mu\text{m}$
Pulse duration ( $\tau$ )	10 ps

Optical penetration depth can be calculated as  $l_\alpha = 1/\alpha = 15$  nm. As  $l_\alpha < t$ , all laser photons were absorbed in the Au layer. Heat diffusion length is calculated as  $l_T = 2\sqrt{D\tau} = 70$  nm.  $l_T$  gives the average distance over which heat propagates in time  $\tau$ . In the context of laser ablation and with  $\tau$  = pulse duration,  $l_T$  provides a measure of thermal energy spread in the target material during laser irradiation due to thermal conduction.<sup>409,416</sup> This energy will then propagate further into the bulk material.<sup>188</sup> With these two characteristic distances, the model's heat sources are illustrated (not to scale) in Figure 6.13. The nature of these heat source fronts is subject to the following approximations and simplifications:

1. The shape of the heat source fronts should have followed the laser beam's Gaussian nature. However, both  $l_\alpha$  and  $l_T$  are very small compared to the pulse spot radius (9  $\mu\text{m}$ ), so both the horizontal and vertical heat source fronts can be approximated as straight lines.
2. As  $l_\alpha + l_T > t$ , the deepest heat source front should have been located outside the gold layer. However, spiro-OMeTAD's thermal diffusivity is expected to be at least three orders of magnitude lower than gold. Therefore, the value of  $l_T$  approaches 0 in spiro-OMeTAD and the heat source front was placed at the gold–spiro-OMeTAD interface instead.
3. The heat source fronts were estimated to have a temperature of 700 K (427°C). It is not possible to accurately approximate the actual temperature just as the laser pulse ends due to the high complexity of laser-material interactions. This estimation is based on the work of Schultz and colleagues, who calculated that an ns-pulse laser with a fluence of 1.36 J/cm<sup>2</sup> can induce a local temperature of approximately 650–700 K at a distance of ~9  $\mu\text{m}$  away the scribe line centre, which is where the P3 line edge is located in this study.<sup>384</sup> As a ps-pulse laser with less residual heat is used here, the heat front temperature is likely lower than Schultz et al's approximation. Nonetheless, the 700 K value is used as it is the best available approximation and since this model is more concerned with the direction of heat flow rather than its exact magnitude. Decomposition of perovskite into PbI<sub>2</sub> has been observed at temperatures as low as 85°C, so the PbI<sub>2</sub> growth observed through STEM is not incompatible with the temperature estimation used here.<sup>417</sup> Furthermore, since the STEM electron beam-induced heating is estimated to cause a temperature rise of only 0.19 K (Section 3.9), this effect is ignored.

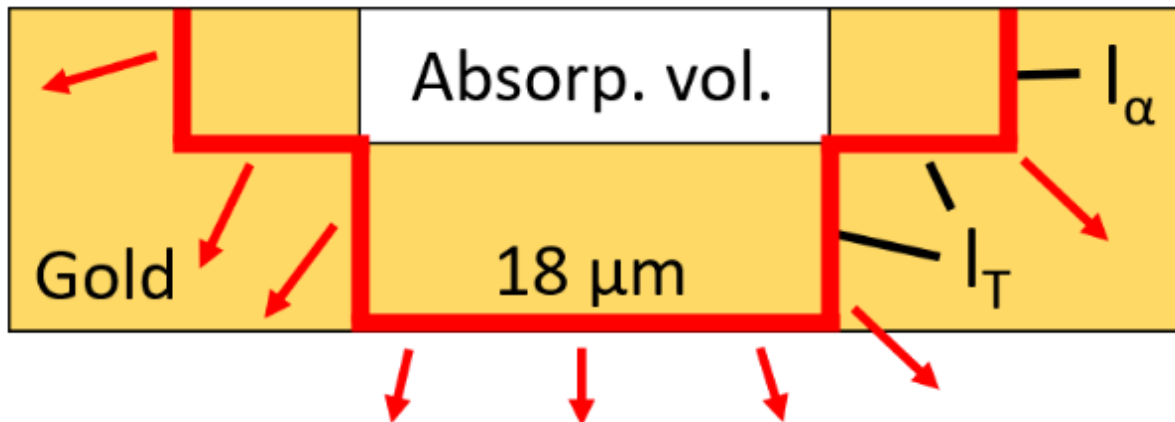


Figure 6.13 | Illustration of the heat source fronts (red lines) used to model thermal energy flow after a laser pulse.

Other than the heat source fronts, other important details of the model are:

1. The side edges of all layers and the bottom edge of the glass substrate layer are modelled as heat sinks with a temperature of 298 K (25°C).
2. Heat loss at the gold layer's top surface (gold-N<sub>2</sub> interface) is modelled as natural convection of heat in a N<sub>2</sub> atmosphere. The convection coefficient was calculated in QuickField to be 126 W/m<sup>2</sup>K.<sup>418</sup>
3. Thermal conductivities and thicknesses of the material layers are described in Table 6.4. Thermal conductivity values were measured at temperatures lower than the relevant range for this model. Regardless, they are used here due to lack of experimental data at the appropriate temperatures.
4. PbI<sub>2</sub> needles occupied ~6.7% of the perovskite layer's volume, as measured in Figure 6.10.

Table 6.4 | Thermal conductivity and thickness of each device layer in the thermal flow model.

Material	Thermal Conductivity (W/mK)	Modelled Thickness (nm)
Au	310 <sup>415</sup>	80
Spiro-OMeTAD	0.1 (estimated)	250
Perovskite	0.3 <sup>306–309</sup>	500
PbI <sub>2</sub>	2.7 <sup>413</sup>	N.A.
SnO <sub>2</sub>	40 <sup>419</sup>	20
ITO	5.6 <sup>420</sup>	150
Glass	0.8 <sup>421</sup>	1000

The result of this modelling shows that heat flows through the Au layer much faster than through the other layers, as expected from its high thermal conductivity (Figure 6.14). As the thermal energy propagates laterally through Au, some of it travels into the other layers. Within the perovskite layer, there is a funnelling effect as heat passes through PbI<sub>2</sub> needles about 8–9x faster than through the perovskite (Figure 6.15). This model thus shows that during laser scribing, a significant portion of the residual thermal energy which flows through the perovskite layer will travel through PbI<sub>2</sub> if it is present. This conclusion validates the proposed thermal flow mechanism.

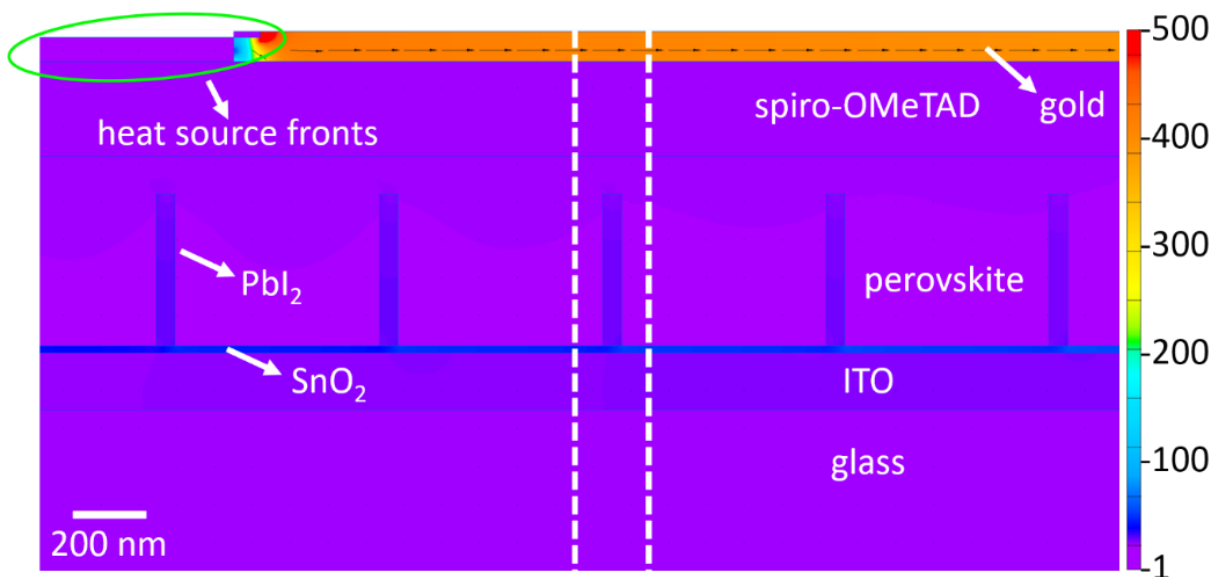


Figure 6.14 | Heat flux map produced by the thermal flow model. The right-side half of the heat source fronts shown in Figure 6.13 is marked by the green ellipse. Arrows indicate direction and magnitude of the heat flux (the flux in layers other than gold is so small in comparison that the arrows are not visible, see Figure 6.15). The white dashed lines delineate the position of the lamellae cut parallel to the P3 lines, ~900 nm away from the scribe line edge. Numbers on the colour bar are in  $10^7 \text{ W/m}^2$ .

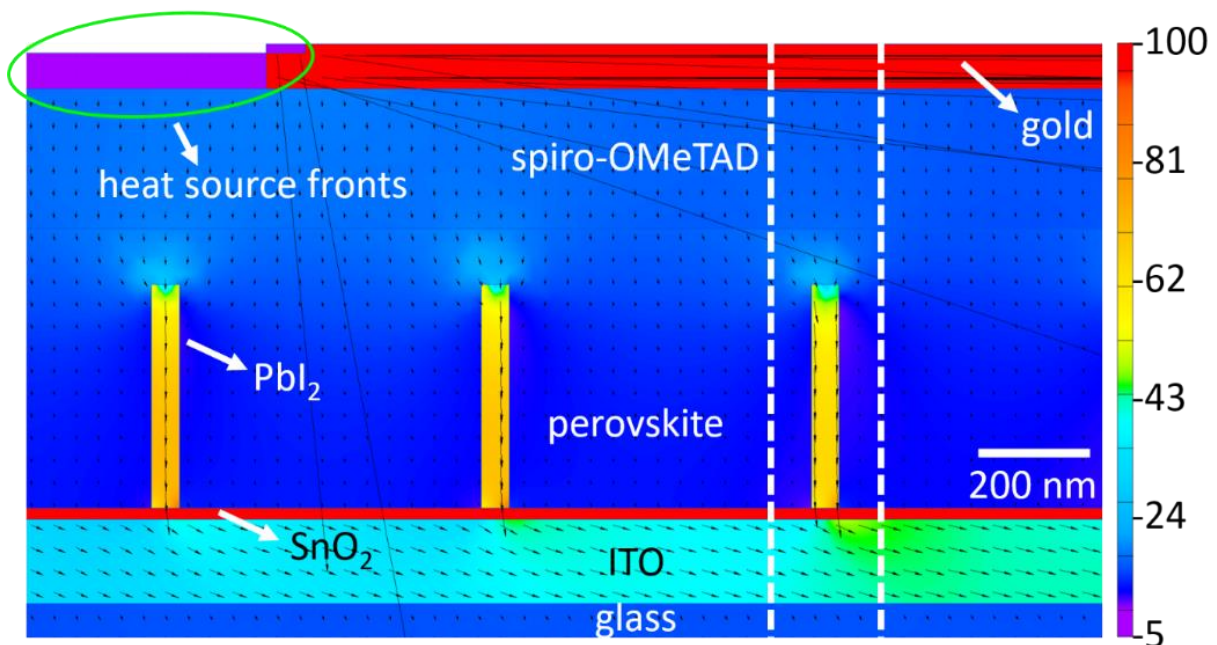


Figure 6.15 | Reproduction of Figure 6.14, but numbers on the colour bar are in  $10^6 \text{ W/m}^2$ .

Due to the high thermal energy density in the existing  $\text{PbI}_2$  grains, the surrounding perovskite is decomposed into more  $\text{PbI}_2$ , thus allowing existing  $\text{PbI}_2$  grains to thicken. Elemental maps suggest that the relatively low thermal energy density in the perovskite layer (away from  $\text{PbI}_2$  grains) was sufficient to vaporise HI but not to break the hydrogen bonds tethering formamidine molecules to the perovskite matrix (Figure 6.9d, 6.12b). This would result in higher C, N, and Pb contents and lower I concentration as reflected in the elemental maps. The consequence of changes in I and Pb concentrations is best illustrated by I/Pb ratio maps in Figure 6.9d. In samples SD-3.47 and SD-3.04, the I/Pb ratio is far lower than its stoichiometric value of 2.865. As perovskite's  $E_g$  and other optoelectronic properties are sensitive to changes in halide composition, these affected regions are unlikely to contribute much to the overall device performance.<sup>94,235</sup> To sum up, these maps evidence perovskite decomposition next to a P3 line upon deep laser scribing with a ps-pulse laser. These changes in perovskite composition mean that the lateral flow of thermal energy discussed in the previous section for shallow scribed samples must also be present in deep-scribed samples. However, the deep scribe lines did not exhibit poor surface uniformity like the shallow scribe lines (Figure 6.2, 6.6) due to their single-row design and high overlap ratio.

The proposed thermal flow mechanism can be experimentally verified by comparing control and laser-scribed samples whose perovskite layer is homogeneous, that is, containing no unreacted precursors acting as preferential heat flow channels. To obtain such a layer requires a complete perovskite formation reaction, so one-step blade coating is used to deposit the perovskite. Blade coating was selected as it is one of the most popular scalable fabrication methods used to produce PSMs.<sup>28,203</sup> HAADF images of samples BC and BD are shown in Figure 6.16a,b, while their STEM-EDX maps are displayed in the left half of Figure 6.16e. HAADF images prove that samples BC and BD have a very homogeneous perovskite layer although they feature several voids on the perovskite– $\text{SnO}_2$  interface, which range in size from about 50 to 400 nm. The largest void (inside the red box in Figure 6.16a) even spanned the entire perovskite layer's thickness, forming a shunt path since it is filled by spiro-OMeTAD (Figure 6.16e, column BC).<sup>422</sup> These voids were most likely caused by imperfections in the blade coating process rather than laser scribing as they appear in all blade coated samples, albeit with different sizes. The vastly improved perovskite homogeneity in the blade coated samples can be rationalised by considering that the spin coating procedure used here is a two-step method that relies on interdiffusion of (FAI/FABr)-isopropanol and ( $\text{CsI}/\text{PbI}_2$ )-DMF/DMSO solutions.<sup>397</sup> Meanwhile, the blade coating procedure is a one-step method with only one solution containing all the precursors.

Elemental maps of samples BC and BD (Figure 6.16e) show a small increase in Pb and I concentrations after laser scribing while C and N levels dropped slightly (Figure 6.12a, “BD, BS vs BC” column), as expected if the thermal decomposition followed Dualeh et al.'s mechanism.<sup>385</sup> In this case, there is no  $\text{PbI}_2$  to act as a preferential thermal flow channel. The laser pulses' thermal energy flowed uniformly

through the perovskite layer, supplying enough energy to vapourise HI and formamidine (Figure 6.12c). The absence of  $\text{PbI}_2$  needles even after scribing suggests that the decomposition process was very uniformly dispersed throughout the perovskite layer, such that the formed  $\text{PbI}_2$  grains were too small to be detected either by HAADF imaging or by EDX mapping. This is supported by the I/Pb ratio maps. They show that although there is still an overall decrease from sample BC to BD, the change is much less severe compared to the spin coated samples (Figure 6.9d).

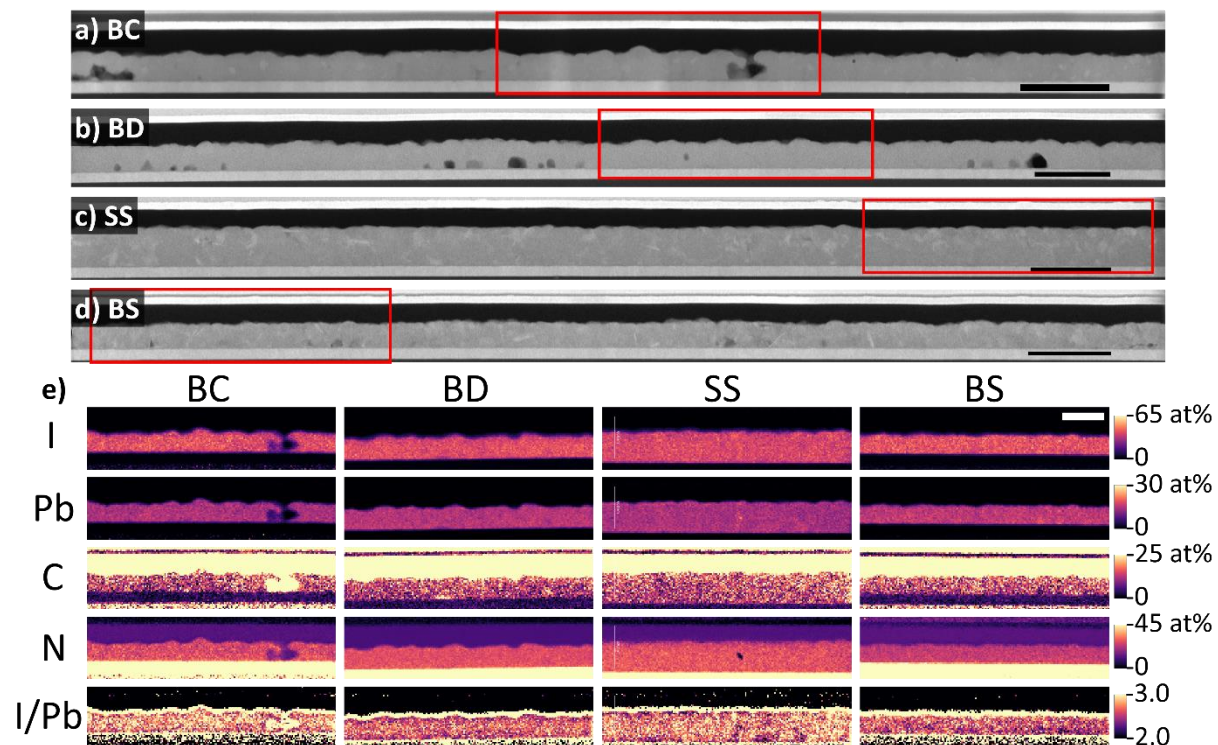


Figure 6.16 | (a–d) Cross-sectional STEM-HAADF images of samples (a) BC, (b) BD, (c) SS, and (d) BS. Red boxes mark the STEM-EDX scan areas. (e) Cross-sectional quantified STEM-EDX elemental maps of samples BC, BD, SS, and BS. Thin yellow strips at the perovskite–spiro-OMeTAD interface in the I/Pb map indicate I diffusion caused by the STEM electron beam. The denoised STEM-EDX model SIs for samples BC, BD, and SS, and BS were constructed using 12, 9, 10, and 11 principal components via PCA, respectively. Scale bars represent (a–d) 1  $\mu\text{m}$  and (e) 600 nm.

Finally, the effect of ablation depth on perovskite decomposition is examined. Figure 6.16c,d and the right half of Figure 6.16e illustrate the effect of shallow scribing for both spin- and blade coated samples. Rather than large needles and grains, samples SS and BS display nm-scale HAADF intensity variations throughout the perovskite layer. Assuming that the thickness of the lamella is constant, this indicates local variation in the chemical composition, which is likely a form of perovskite damage

induced by the shallow scribing process as these bright flecks only appear in these samples. They are concentrated in the perovskite layer's top half in sample SS and more uniformly distributed in sample BS, as expected since the blade coated perovskite is thinner. Compared to their respective control samples, Pb and I levels rose slightly, while C and N concentrations dropped a little in both cases, again in good agreement with Dualeh et al.'s perovskite decomposition mechanism.<sup>385</sup> This supports the proposed thermal flow mechanism as outlined above because unlike other spin coated samples, sample SS did not have unreacted  $\text{PbI}_2$  needles. Therefore, its composition changes follow that of samples BD and BS. Due to this lack of existing  $\text{PbI}_2$ , however, samples SD-3.04 and SS cannot be fairly compared to evaluate whether shallow scribing is less damaging compared to deep scribing. Samples BS and BD demonstrated largely similar compositions, hinting that shallow and deep scribing resulted in comparable effects. Indeed, HAADF images show that sample BD has a more homogeneous perovskite layer than sample BS. The tiny bright flecks seen in the HAADF images of samples SS and BS are not visible in their elemental maps as they are very small compared to the lamella thickness, just like the  $\text{PbI}_2$  needles in sample SC.

After it has been established that ps-pulse laser causes thermal decomposition of perovskite in the device stack adjacent to a P3 line, a lamella is cut perpendicular to a P3 line from sample SD-3.04 to measure the spatial extent of this damage. This sample was selected rather than the blade coated samples to get a worst-case estimate of the decomposition extent. A cross-sectional STEM-HAADF image of this lamella is shown in Figure 6.17, where the left end is the closest to the P3 line and the right end is the furthest into the device's AA. This image shows a consistent number and thickness of  $\text{PbI}_2$  needles along the lamella's length, indicating that  $\text{PbI}_2$  growth observed in Figure 6.9b,c is limited to a very short distance from a P3 line edge. EDX data was acquired as a set of four scan areas instead of one large area to minimise the effect of thermal drift during scanning. The elemental maps (Figure 6.17) show a slight I increase and significant rise in Pb concentration at box 1 (closest to P3 line), while both C and N levels decreased slightly. This high-Pb area extends to the right end of box 1 but does not continue at the left end of box 2, indicating that laser-induced compositional change ended between these two scan areas ( $\sim 4 \mu\text{m}$  from the P3 line edge). Scanning parameters for all boxes were identical and all four EDX SIs were analysed simultaneously in HyperSpy, so this difference in perovskite composition is not an artefact of the measurement or analysis. This set of compositional changes in box 1 indicates that thermal energy flowed into the AA through the perovskite layer homogeneously, volatilising both HI and formamidine. Therefore, deep laser scribing altered the perovskite composition up to  $\sim 4 \mu\text{m}$  away from a P3 line edge, potentially leading to changes in  $E_g$  and charge collection efficiency. Importantly, this affected volume will very likely be larger if an ns-pulse laser is used, as a longer pulse allows for more significant thermal diffusion.<sup>187,409,416</sup> Furthermore, decomposition may also become more severe if MA cations are present as the FA/Cs system used in this work has been recognised as one of the most thermally stable among 3D perovskites.<sup>388</sup>

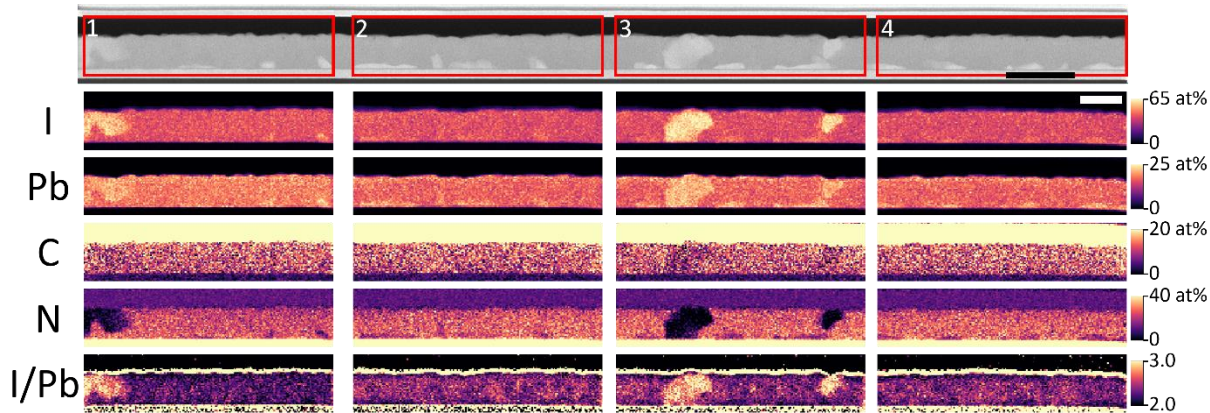


Figure 6.17 | Cross-sectional STEM-HAADF image and quantified STEM-EDX elemental maps of a perpendicular-to-P3 lamella taken from sample SD-3.04. Each red box represents a STEM-EDX scan area corresponding to maps below it. Thin yellow strips at the perovskite–spiro-OMeTAD interface in the I/Pb map indicate I diffusion caused by the STEM electron beam. The denoised STEM-EDX model SI was constructed using 14 principal components via PCA. The scale bars represent 1  $\mu\text{m}$  for the STEM-HAADF image and 600 nm for all elemental maps.

## 6.3. Comparing the Effects of Residual Heat from Nanosecond and Picosecond Laser Pulses

### 6.3.1. Experimental Methods

#### 6.3.1.1. Device Fabrication and Laser Scribing

The PSMs were fabricated by Dr. Christof Schultz (Hochschule für Technik und Wirtschaft Berlin).

Glass substrates with an area of  $2.5 \times 2.5 \text{ cm}^2$  were coated with 120 nm-thick ITO ( $R_{\text{sq}} \sim 15 \Omega/\text{cm}^2$ ). Subsequently, the ITO layer was P1 patterned. Afterwards, the substrates were cleaned in an ultrasonic bath, first in a soap solution, deionised water, acetone and then in isopropanol for 15 min each. After drying with  $\text{N}_2$ , the substrates were UV/O<sub>3</sub> treated for 15 min. The SnO<sub>2</sub> solution was prepared by dissolving  $\text{SnCl}_2 \cdot 2\text{H}_2\text{O}$  in ethanol and stirring it overnight at room temperature. In the next step, the SnO<sub>2</sub> ETL was deposited by spin-coating; first at a speed of 1500 RPM for 30 s and then ramped to 2500 RPM for another 30 s. The ETL was cured at 180°C in ambient atmosphere. The  $\text{Cs}_{0.05}\text{FA}_{0.79}\text{MA}_{0.16}\text{Pb}(\text{I}_{0.83}\text{Br}_{0.17})_3$  perovskite ink was prepared by dissolving  $\text{PbI}_2$  (1.1 M), FAI (1 M), MABr (0.2 M) and  $\text{PbBr}_2$  (0.2 M) in a mixture of anhydrous DMF:DMSO (4:1 v:v), followed by addition of 5 vol% CsI stock solution (1.5 M in DMSO).<sup>55</sup> The perovskite solution was spin coated using a two-step program at 1000 and 6000 RPM for 10 and 20 s, respectively, adding a 100  $\mu\text{l}$  drop of

chlorobenzene 25 s after the start of the spinning routine. The film was then annealed at 100 °C for 1 h. For the HTL preparation, a 36.2 mg/ml solution of spiro-OMeTAD precursor was dissolved in chlorobenzene and then finally doped with 4-TBP (14.4 µl/ml), Li-TFSI (8.8 µl/ml), and Co(III) complex (14.5 µl/ml) dopants. The spiro-OMeTAD solution was spin-coated over the perovskite film at 1800 RPM for 30 s. After that, the sample was P2 patterned. A 100 nm Au layer was evaporated under low pressure as the back contact and subsequently P3 patterned to complete the MI of the PSMs. All the film preparations were performed in an N<sub>2</sub>-filled glove box.

Laser scribing was carried out using a Rofin Baasel Lasertech system equipped with an ns laser source ( $\lambda = 532$  nm, pulse duration = 20 ns). The beam diameter was  $28.1\text{ }\mu\text{m} \pm 10\%$  at its focal plane and the laser fluence was  $1.36\text{ J/cm}^2$ . A ps laser source was also used, with  $\lambda = 532$  nm and pulse duration = 10 ps. The beam diameter was  $26.7\text{ }\mu\text{m} \pm 10\%$  at its focal plane and the fluence was  $2.31\text{ J/cm}^2$ . The beam diameters were determined following the method of Liu.<sup>423</sup> The sample was translated using an x–y motion system with a scribing speed of 500 mm/s and a positioning accuracy of <5 µm. The laser beam was guided via fixed optics to the sample surface. To avoid material degradation and to collect debris, the samples were patterned in a chamber with a continuous N<sub>2</sub> flow. The pulse-to-pulse overlap was about 11% (7%) for the ns-pulse (ps-pulse) laser. Scribing was performed from the Au side.

### 6.3.1.2. Electron Microscopy Characterisation

SEM images were acquired in an FEI Nova NanoSEM with a 2 kV beam acceleration voltage and a 110 pA beam current. For STEM characterisation, cross-sectional sample lamellae were prepared with an FEI Helios Nanolab Dualbeam FIB/SEM. The lamellae were immediately transferred into an FEI Tecnai Osiris 80-200 FEGTEM, minimising air exposure to ~2 min. STEM-HAADF images and STEM-EDX SIs were obtained using the beam parameters described in Section 3.7 and Table 3.2. STEM-EDX SIs were denoised with PCA and processed in HyperSpy following the procedure explained in Section 4.3.<sup>290</sup>

### 6.3.2. Formation of PbI<sub>2</sub> and Br-rich Perovskite

The surface morphology of P3 lines was firstly investigated by top-view SEM imaging. Figure 6.18 shows some residual material appearing as grains and debris on the trench surface. Notably, only a few needle-shaped grains appear in the ps-scribed P3 line (Figure 6.18a), while many of them are present in the ns-scribed P3 line (Figure 6.18b). As mentioned previously, these needles can be assigned to PbI<sub>2</sub>.<sup>364</sup> It is a common product of thermal decomposition of perovskite, so Figure 6.18 suggests that the ns pulses dissipate even more thermal energy to the target material compared to ps pulses, as expected from the theory of laser-material interaction discussed in Chapter 2.<sup>415,417,424</sup>

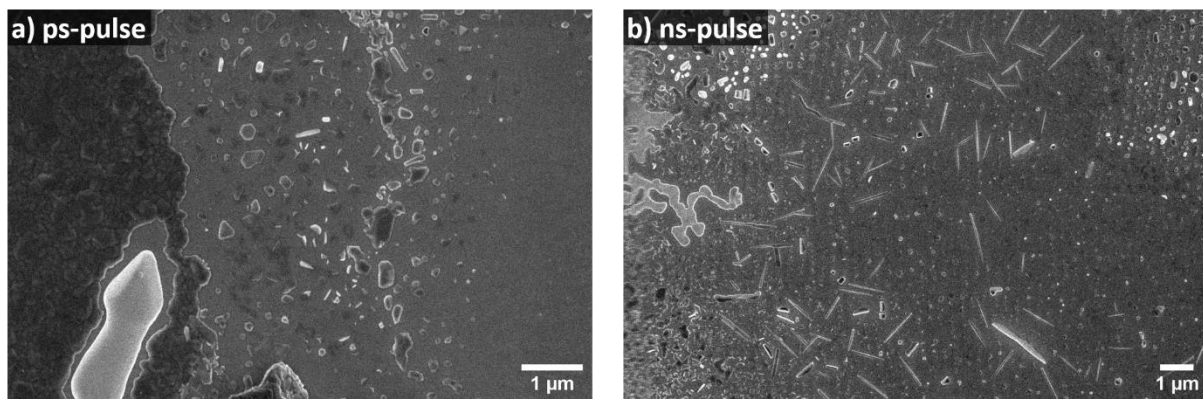


Figure 6.18 | Top-view SE images of P3 lines scribed by a) ps and b) ns laser pulses.

Cross-sectional lamellae were prepared for STEM imaging and STEM-EDX analysis to investigate whether and how the perovskite composition is modified by the P3 scribing process. Figure 6.19 shows cross-sectional HAADF images and quantified STEM-EDX elemental maps of three lamellae: a reference lamella cut far from any scribe line and one each from next to an ns- or ps-scribed P3 line, cut perpendicularly with respect to the P3 lines. For these lamellae, the left edge of the images and maps are closest to the P3 line edge. The images and maps of the reference and ps-scribed lamellae look largely similar. In both samples, the perovskite layer contains grains which are Br- and (slightly) Pb-rich while the I distribution is homogeneous throughout. Only the number of these grains differ, with more of them appearing in the ps-scribed sample than in the reference. On the other hand, the elemental maps of the ns-scribed sample reveal the presence of a thin Br-rich, I-poor layer at the perovskite/HTL interface. This layer extends for about  $12\text{ }\mu\text{m}$  into the AA, as marked by the red dashed line in Figure 6.19. The Br-rich grains found in the reference and the ps-scribed sample do not exist within this distance but reappear again beyond the  $12\text{ }\mu\text{m}$  mark. These maps suggest a remixing of Br and Pb close to the edge of ns-scribed P3 lines, which appears to convert the morphology of the Br- and Pb-rich area from distinctively shaped grains to a thin layer. The presence of such a Br-rich layer at the perovskite/HTL interface has previously been shown to improve charge carrier collection by acting as a hole-blocking layer, a role made possible by its wider  $E_g$  compared to that of the original perovskite stoichiometry.<sup>425,426</sup> The STEM analysis shows that the thermal impact of the ns laser pulse promotes local changes in perovskite composition in the vicinity of laser-scribed P3 lines. In comparison, minimal compositional changes are observed next to ps-scribed P3 lines relative to the reference sample.

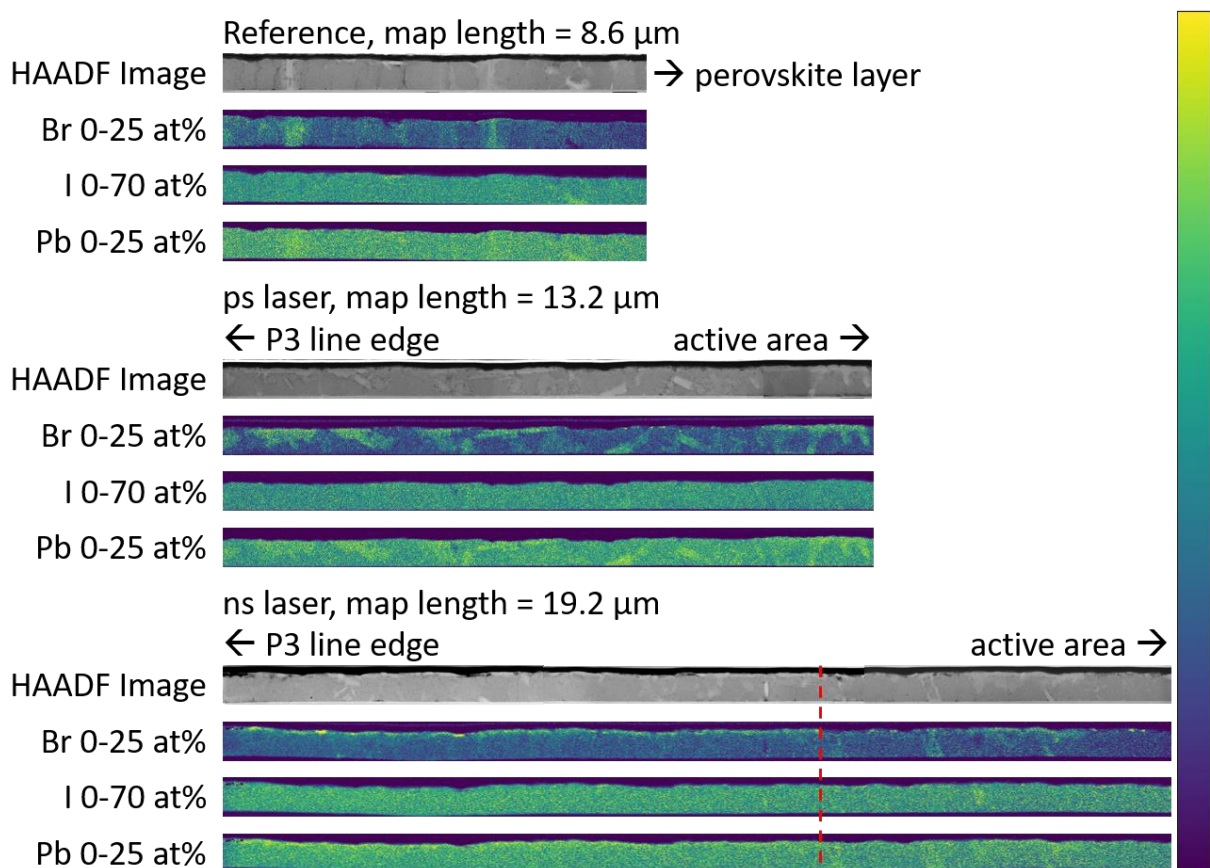


Figure 6.19 | Cross-sectional HAADF images and quantified STEM-EDX elemental maps of the reference, ps-scribed, and ns-scribed lamellae. The left end of these images and maps is located next to the P3 line edge, whereas the right end is furthest into the active area. The red dashed line marks the end of the Br-rich layer formed in the ns-scribed sample, 12  $\mu\text{m}$  from the P3 line edge.

## 6.4. Summary

Material ablation with a pulsed laser beam is a very useful technique to machine various materials, including to fabricate cell-to-cell MI in PSMs. However, depending on the pulse duration used, some of the deposited energy is converted to heat which may then propagate further into the target material. In the case of OIHPs, this residual heat can trigger thermal decomposition, thus potentially reducing a module's power output and shortening its operational lifetime.

In this chapter, a combination of SEM and STEM is applied to evaluate how various laser parameters affect the scribing of P3 lines and perovskite decomposition in their vicinity. Deep laser scribing with a ps-pulse and ns-pulse laser is found to trigger perovskite decomposition next to a P3 line edge. The longer pulse duration results in more extensive compositional changes as more time is available for heat propagation away from the ablated volume. This undesirable side effect can be minimised by reducing the laser fluence. However, this carries an increased risk of intercell shunting, which can only be

lowered by widening the scribe line and hence lowering GFF. Another option is to use an fs-pulse laser to suppress HAZ, but its relatively high cost will increase the production cost of PSMs.

Rather unexpectedly, perovskite homogeneity is also found to affect the mechanism of perovskite decomposition. When non-perovskite phases with relatively high thermal conductivities are present in the perovskite layer, they become preferred heat flow channels. Consequently, perovskite decomposition is concentrated around those phases and the perovskite far away from them is less affected. If the perovskite layer is homogeneous, on the other hand, thermal energy flows uniformly throughout. The nature and eventual extent of perovskite decomposition will be determined by a complex interplay of laser parameters and properties of the materials forming the PSMs. Careful optimisation of all these factors is an essential step towards maximising the performance of PSMs.

# Chapter 7

## Sodium Diffusion from Glass through P1 Lines Passivates Perovskite Solar Modules

### 7.1. Introduction

The fast rise of PSCs over the past several years has been enabled largely by careful selection and optimisation of the perovskite absorber and the CTls.<sup>7</sup> However, very little attention has been paid to the substrate material. Almost all non-flexible thin film PV rely on SLG as a substrate material due to its low cost, high optical transparency, and suitability as a support for TCOs such as ITO and FTO. While SLG is primarily composed of SiO<sub>2</sub>, it also contains several alkali oxides added to reduce its melting temperature and viscosity. The most plentiful of these are Na<sub>2</sub>O, CaO, and MgO, whose abundances are approximately 13–16, 7–12, and 2–5 wt%, respectively.<sup>427</sup> In SLG, the alkali cations are separated from the O anions such that they can diffuse through the silica network. Due to its low charge and small radius, the diffusivity of Na<sup>+</sup> is much higher compared to Ca<sup>2+</sup> and Mg<sup>2+</sup>.<sup>427</sup>

Owing to its high diffusivity and relatively high concentration, the possibility of Na intrusion into a solar cell's active layers must be considered. Indeed, this phenomenon has long been known and harnessed to improve the performance of CIGS and CZTS solar cells. With these absorbers, Na diffusion from SLG was found to increase PCE through improvements in film morphology, grain crystallinity, and defect passivation.<sup>428–432</sup> Similar effects have been observed in PSCs deliberately doped with Na, although a mechanistic explanation for those beneficial outcomes is still lacking. In these studies, various Na-containing additives were either added into the perovskite precursor solution<sup>433–441</sup> or deposited as a thin interlayer between a CTL and the perovskite layer<sup>442–445</sup>. Notably, while these additives have beneficial effects when added at the optimum quantities, significant performance and stability deterioration was observed when the amount of Na is >1–2 mol%.<sup>433,435,436,445</sup> As for inadvertent Na diffusion from SLG, Bi et al. attributed a temporary PCE increase in their PSCs after 2–3 days of storage to perovskite defect passivation by Na.<sup>446</sup> Unfortunately, here a mechanism for the defect passivation was again absent. Notably, Bi et al. claimed that Na diffused through both ITO and 80 nm-thick poly[bis(4-phenyl)(2,4,6-trimethylphenyl)amine] (PTAA) layers even though the highest temperature reached in their device fabrication procedure was only 100°C. This observation suggests that Na diffusion could reach a greater extent in devices using metal oxide CTls such as TiO<sub>2</sub>, which needs to be annealed at 400–500°C. Na diffusion from SLG is also an important topic from a device upscaling and commercialisation point of view. In PSMs with a P1-P2-P3 MI, the TCO layer is

removed at the P1 lines. The substrate-side CTL is thus in direct contact with SLG, providing a pathway for vertical (from SLG into CTL and perovskite inside the P1 lines) and lateral (from P1 lines into the AA) Na diffusion.

In this chapter, Na diffusion in the vicinity of P1 lines and its effects on PSMs' optoelectronic performance are examined. To maximise the generality of this study, PSMs of n-i-p and p-i-n architectures are investigated. The n-i-p stack consists of SLG/FTO/TiO<sub>2</sub>/perovskite/PTAA/Au while the p-i-n stack is composed of SLG/ITO/NiO/perovskite/PCBM/BCP/Au. In both cases, a state-of-the-art TCDH perovskite with a nominal stoichiometry of Cs<sub>0.05</sub>MA<sub>0.14</sub>FA<sub>0.81</sub>PbI<sub>2.7</sub>Br<sub>0.3</sub> is used. Importantly, NiO and TiO<sub>2</sub> have different sintering routines, which permit a look on how annealing duration and temperature affect the extent of Na diffusion. Na diffusion for up to 360 μm from P1 line edges was observed, corresponding to ~7% of typical cell widths in a PSM.<sup>173</sup> This diffusion is most likely enabled by thermal energy provided during CTL and perovskite annealing. A series of microscopy and spectroscopy techniques show that where Na is present, the perovskite luminescence is boosted by ~5x due to defect passivation through formation of NaBr. The resulting Br deficiency in the perovskite induced formation of Br-poor, I-rich perovskite with a red-shifted emission close to the P1 line. Furthermore, NaBr is shown to be stable in the perovskite layer for at least 12 weeks of storage. These findings reveal an untapped lever to boost the performance of perovskite PV at the module level, but also a potential source of degradation over the long term due to the uncontrollable nature of Na diffusion from SLG.

## 7.2. Experimental Methods

### 7.2.1. Film and Device Fabrication

The perovskite films, half devices, and full-stack PSCs were fabricated by Dr. Francesco di Giacomo and Dr. Fabio Matteocci (University of Rome Tor Vergata).

The perovskite ink (Cs<sub>0.05</sub>MA<sub>0.14</sub>FA<sub>0.81</sub>PbI<sub>2.7</sub>Br<sub>0.3</sub>) was prepared by adding 1521.8 mg PbI<sub>2</sub>, 104.3 mg PbBr<sub>2</sub>, 44.8 mg CsI, 479.1 mg FAI and 55.0 mg MABr to 1.899 ml DMF and 0.601 ml DMSO. The formulation contains a 4% excess of Pb salts and a DMF:DMSO volume ratio of 3.16:1.

For the p-i-n device with NiO (called NiO device onwards), the NiO ink was formulated by adding 35.5 mg NiCl·6H<sub>2</sub>O to 1 ml 2-methoxyethanol. The solution was heated at 75°C for 2 h after adding 20 μl nitric acid. The ink was used at least 2 days after preparation. The ETL solutions were prepared by adding 27 mg PCBM to 750 μl chlorobenzene and 250 μl dichlorobenzene, and by adding 5 mg BCP to 10 ml isopropanol. 2.5 × 2.5 cm<sup>2</sup> SLG/ITO substrates were diced with a glass cutter and P1 lines were scribed with an ns pulsed UV laser ( $\lambda = 355$  nm). The fluence per pulse was 0.30 J/cm<sup>2</sup>. The

ablations were carried out from the ITO side at a repetition rate of 80 kHz and a scanning speed of 195 mm/s. Substrates were scrubbed with water and soap solution (Hellmanex 2% in deionised water) and cleaned with three stages of ultrasonic bath: first in water and soap, then in ultrapure water, and finally in isopropanol. After drying, they were treated for 15 minutes in a UV/O<sub>3</sub> tool. The NiO ink was spun on the substrates at 4000 RPM for 30 s and annealed for 5 min at 75°C, 10 minutes at 120°C and 1 h at 300°C. After cooling down in air, the samples were transferred into an N<sub>2</sub>-filled glovebox. The perovskite ink was spun at 4000 RPM for 35 s and 180 µl of chlorobenzene were dropped after 20 s. The film was then annealed for 10 minutes at 100°C. After the perovskite deposition, PCBM was spin coated at 1700 RPM for 30 s and annealed at 100°C for 5 min. BCP was spin coated at 4000 RPM. Finally, a 100 nm-thick Au layer was deposited by thermal evaporation.

For the n-i-p device with TiO<sub>2</sub> (called TiO<sub>2</sub> device onwards), the HTL solution was prepared by dissolving PTAA in toluene at a concentration of 10 mg/ml. Then, 5 µl Li-TFSI solution and 10 µl TBP were added for each ml of PTAA solution. Li-TFSI solution was prepared by adding 170 mg Li-TFSI powder in 1 ml acetonitrile. 2.5 × 2.5 cm<sup>2</sup> SLG/FTO substrates were diced with a glass cutter and P1 lines were scribed with an ns pulsed UV laser ( $\lambda = 355$  nm). The fluence per pulse was 0.44 J/cm<sup>2</sup>. The ablations were carried out from the ITO side at a repetition rate of 80 kHz and a scanning speed of 195 mm/s. The fluence was higher than that used for the NiO device as FTO is thicker than ITO. Substrates were cleaned as described above. After drying, they were treated for 15 minutes in a UV/O<sub>3</sub> tool. The compact TiO<sub>2</sub> layer was prepared by spray pyrolysis of a solution of diisopropoxytitanium bis(acetylacetone) (0.16 M) and acetylacetone (0.4 M) in ethanol. The substrates were preheated to 450°C and kept at that temperature for 10 min to complete the deposition, then cooled down to room temperature in about 1 h. For the mesoporous TiO<sub>2</sub> layer, a Greatcell 30-NRD paste was diluted 1:5 in ethanol, spin coated at 3000 RPM for 30 s, and then sintered using the following annealing program: 5 min ramp from room temperature to 120°C, 5 min at 120°C, 15 min ramp from 120°C to 325°C, 5 min at 325°C, 5 min ramp to 375°C, 5 min at 375°C, 5 min ramp to 480°C, and 30 min at 480°C. After cooling down in air, the samples were transferred into an N<sub>2</sub>-filled glovebox. The perovskite ink was spun at 4000 RPM for 35 s and 180 µl of chlorobenzene were dropped after 20 s. The film was then annealed for 10 minutes at 100°C. After the perovskite deposition, doped PTAA was spin coated at 4000 RPM for 20 s. Finally, an 80 nm-thick Au layer was deposited by thermal evaporation.

In addition to full devices, perovskite films and half devices were also fabricated. The film samples are SLG/NiO/perovskite, Si/NiO/perovskite, SLG/TiO<sub>2</sub>/perovskite, and Si/TiO<sub>2</sub>/perovskite. The half devices are SLG/ITO/NiO/perovskite and SLG/FTO/TiO<sub>2</sub>/perovskite, both of which were P1 patterned. The deposition of each layer contained in these samples and the P1 line scribing were done following the same procedure as described above.

## 7.2.2. Electron Microscopy Characterisation

SEM images were acquired in an FEI Nova NanoSEM with a 2 kV beam acceleration voltage and a 27 pA beam current. SE images were obtained using a TLD to form topography contrast. BSE imaging was performed using a segmented semiconductor detector with all the segments activated. The BSE images were formed by summing the detected signals from all segments to form compositional contrast. For STEM characterisation, cross-sectional sample lamellae were prepared with an FEI Helios Nanolab Dualbeam FIB/SEM. The lamellae were immediately transferred into an FEI Tecnai Osiris 80-200 FEGTEM, minimising air exposure to ~2 min. STEM-HAADF images and STEM-EDX SIs were obtained using the beam parameters described in Section 3.7 and Table 3.2. STEM-EDX SIs were denoised with PCA and processed in HyperSpy following the procedure explained in Section 4.3.<sup>290</sup>

## 7.2.3. NanoSIMS 3D Elemental Mapping

NanoSIMS data was acquired by Dr. Kexue Li (University of Manchester) and analysed primarily by the author, who benefited from discussions with Dr. Li and Dr. Katie Moore (University of Manchester).

High resolution SIMS analysis was performed using a CAMECA NanoSIMS 50L with a 16 keV O<sup>-</sup> primary beam with a beam current of 8.6 pA. Six secondary ions were collected simultaneously using a double focusing mass spectrometer: <sup>12</sup>C<sup>+</sup>, <sup>23</sup>Na<sup>+</sup>, <sup>28</sup>Si<sup>+</sup>, <sup>48</sup>Ti<sup>+</sup>, <sup>120</sup>Sn<sup>+</sup>, and <sup>208</sup>Pb<sup>+</sup>. Ti, Sn, and Pb metal standards were used to align the detectors. Each dataset is 350 slices deep with each slice containing 256 × 256 pixels, representing a scan area of 10 × 10 μm. The D1 slit was set to D1-3 (200 μm in diameter), entrance slit was set to ES-1 (30 × 180 μm), opened aperture slit AS-0, and opened energy slit ES-0. Data analysis was performed in HyperSpy<sup>290</sup> with the help of Dr. Thomas Aarholt (University of Oslo) who provided a function to read NanoSIMS datasets in Python. The outermost 32–51 pixels (1.25–2 μm) of each dataset were cropped out to remove edge-related artefacts in the data.

## 7.2.4. X-ray Diffraction

XRD was performed using a Bruker D8 DAVINCI fitted with a LYNXEYE-XE detector, Ni-K<sub>β</sub> filter, and a Cu-K<sub>α</sub> X-ray source ( $\lambda = 1.5418 \text{ \AA}$ ) operated at 40 kV, 40 mA. The acquisition parameters were 10°–60° 2θ range, 0.025° step size, and 0.1 s dwell time. The spectra were processed using PANalytical HighScore 4.8 software.

### **7.2.5. X-ray Photoelectron Spectroscopy**

XPS data was acquired by Dr. Weiwei Li (University of Cambridge).

XPS was performed using a monochromatic Al-K<sub>α</sub> X-ray source ( $h\nu = 1486.6$  eV) in a SPECS PHOIBOS 150 electron energy analyser with a total energy resolution of 0.5 eV. Conductive Ag paint was used to connect the sample surface to the holder to avoid charge accumulation during measurement.

### **7.2.6. Atomic Force Microscopy and Kelvin Probe Force Microscopy**

AFM and KPFM data was acquired and analysed by Dr. Elizabeth Tennyson (University of Cambridge).

AFM and KPFM were performed on a wafer-scale Bruker's Dimension Icon AFM. The lowest magnification set of AFM and KPFM maps contain  $256 \times 256$  pixels while the maps with higher magnifications were acquired with  $512 \times 512$  pixels using frequency modulated KPFM. Pt-Ir coated Si probes (model: SCM-PIT) with an average resonant frequency of 75 kHz and a spring constant of 2.8 N/m were used. All measurements were performed in the dark and in ambient atmospheric conditions.

### **7.2.7. Cathodoluminescence**

CL data was acquired by Mr. Jordi Ferrer Orri (University of Cambridge) and analysed by the author and Mr. Ferrer Orri.

CL SIs were acquired using an Attolight Allalin 4027 Chronos SEM-CL with the sample oriented perpendicular to the electron beam path. The SIs were recorded with an iHR320 spectrometer (320 mm focal length, 150 gratings/mm blazed at 500 nm, 7000  $\mu\text{m}$  entrance slit) and an Andor 1024 pixel CCD (4x horizontal binning, 1x signal amplification). CL data was obtained in continuous wave mode at 5 kV acceleration voltage, 62.5 pA beam current, and 48.8 ms/px acquisition time. All measurements were performed at room temperature under high vacuum. Beam focusing was performed away from the sample areas used for the measurements to prevent specimen damage. CL SIs were analysed in LumiSpy 0.1.<sup>350</sup> Artefacts caused by cosmic rays saturating the spectrometer were removed, and the edges of each map were cropped out as they tend to show edge effects. An initial survey of the SIs found that all CL spectra contain two emission peaks, identifiable by their wavelengths to be perovskite and PbI<sub>2</sub>. Therefore, the panchromatic CL spectrum ( $s$ ) in each pixel ( $x$ ) was fitted to a linear summation of two Gaussian distributions ( $g$ ) and a constant background offset ( $k_{bg}$ ) (Equation 7.1). One Gaussian represents the perovskite's emission and the other represents the emission of PbI<sub>2</sub>. Fitting was performed using least-squares optimisation with the Levenberg-Marquardt algorithm.<sup>295,296</sup>

$$s(x) = k_{bkg}(x) + g_{perovskite}(x) + g_{PbI_2}(x) \quad (\text{Equation 7.1})$$

## 7.2.8. Photoluminescence

PL data was acquired by Dr. Elizabeth Tennyson (University of Cambridge).

The PL spectra were acquired with a Photon Etc IMA microscope with a diffraction-limited spatial resolution (~500 nm with a 100× objective lens of numerical aperture = 0.9). A volume Bragg grating was placed before the camera in order to detect only specific wavelengths, the spectral resolution is 2.5 nm. A 405 nm laser was normally incident on the sample, with a spot size of ~150 μm in diameter. The sample stage was immobile during data acquisition while the collection wavelength was swept (integration time/wavelength = 3 s). The incident photon flux was equivalent to 1 sun illumination.

## 7.3. Na Diffusion in the Vicinity of P1 Lines

The first question to be answered is whether Na diffusion from glass occurs through P1 lines. This was investigated by performing cross-sectional STEM-EDX of lamellae extracted from next to P1 lines. STEM-HAADF images and elemental maps from the NiO and TiO<sub>2</sub> devices are shown in Figure 7.1 and 7.2, respectively. Three important observations can be made from the STEM-EDX data. First, the Na maps clearly show the presence of Na in the AA of NiO and TiO<sub>2</sub> devices, both in the perovskite film and the bottom CTL. Second, in the AA, the Na signal intensity is higher in the perovskite layer than in the TCO layer. This suggests that Na diffusion occurs vertically only inside the P1 lines, as shown by the high Na signal in the perovskite film and bottom CTL inside the P1 line, and not in the AA as it appears to be blocked by the TCO there. Vertical diffusion seems to be followed by lateral diffusion in the perovskite and NiO or TiO<sub>2</sub> layers, from the P1 line into the AA. In the TiO<sub>2</sub> device, the restriction of vertical Na diffusion to the P1 lines can be explained by the presence of a thin SiO<sub>2</sub> diffusion barrier inside the FTO layer (cyan arrow in Figure 7.2). However, the absence of vertical Na diffusion in the AA of the NiO device is contrary to Bi et al.'s claim of spontaneous Na diffusion through ITO and PTAA.<sup>446</sup> Finally, the third and most interesting finding is the strong correlation between the Br and Na maps for both devices. In the NiO device, Na and Br form nm-sized inclusions in the perovskite film (green circles in Figure 7.1). Many of these inclusions are located at the perovskite/NiO interface. In the TiO<sub>2</sub> device, the Na and Br signal intensities are highest in the mesoporous titania layer, all the way from the P1 line edge to the right end of the lamella.

Comparing the Na maps in Figure 7.1 and 7.2, more Na diffused in the TiO<sub>2</sub> device compared to the NiO device. This can be explained by the longer time and higher temperature needed to anneal the

compact and mesoporous TiO<sub>2</sub> layers compared to the NiO layer. Na diffusion in the TiO<sub>2</sub> device may also have been assisted by redeposition of ablated glass at the P1 line edge, since the higher laser fluence used to scribe P1 lines in the TiO<sub>2</sub> device likely resulted in more glass being ablated. Indeed, a low Si signal is detected at the TiO<sub>2</sub>-FTO interface up to 6 μm from the P1 line edge of the TiO<sub>2</sub> device (green arrows in Figure 7.2), but not in the NiO device (Figure 7.1). Finally, like other diffusion processes, the extent of Na diffusion might also have been affected by differences in crystal structure and in the concentration and type of defects which may have been present in the NiO and TiO<sub>2</sub> lattices. Research on TiO<sub>2</sub> as a Na ion battery electrode has shown that Na has a relatively high diffusivity in crystalline TiO<sub>2</sub>, providing another possible explanation for the higher amount of Na in the TiO<sub>2</sub> device.<sup>447,448</sup>

The Na-Br correlation indicates that Na is not uniformly dispersed through the perovskite film, as it would be if it were incorporated into the perovskite lattice in the A-cation or interstitial sites. Rather, the similarity in spatial distribution strongly suggests formation of NaBr clusters. This is in excellent agreement with the work of Kubicki et al., who used solid state nuclear magnetic resonance to observe NaBr formation over time after NaI addition to TCDH perovskite.<sup>449</sup> In addition, Abdi-Jalebi et al. and Andaji-Garmaroudi et al. also found KBr formation through STEM-EDX after adding KI into TCDH PSCs and perovskite LEDs.<sup>91,450</sup> Taken together, these observations conclusively show that formation of alkali bromides are preferred over their iodide counterparts in TCDH perovskites.

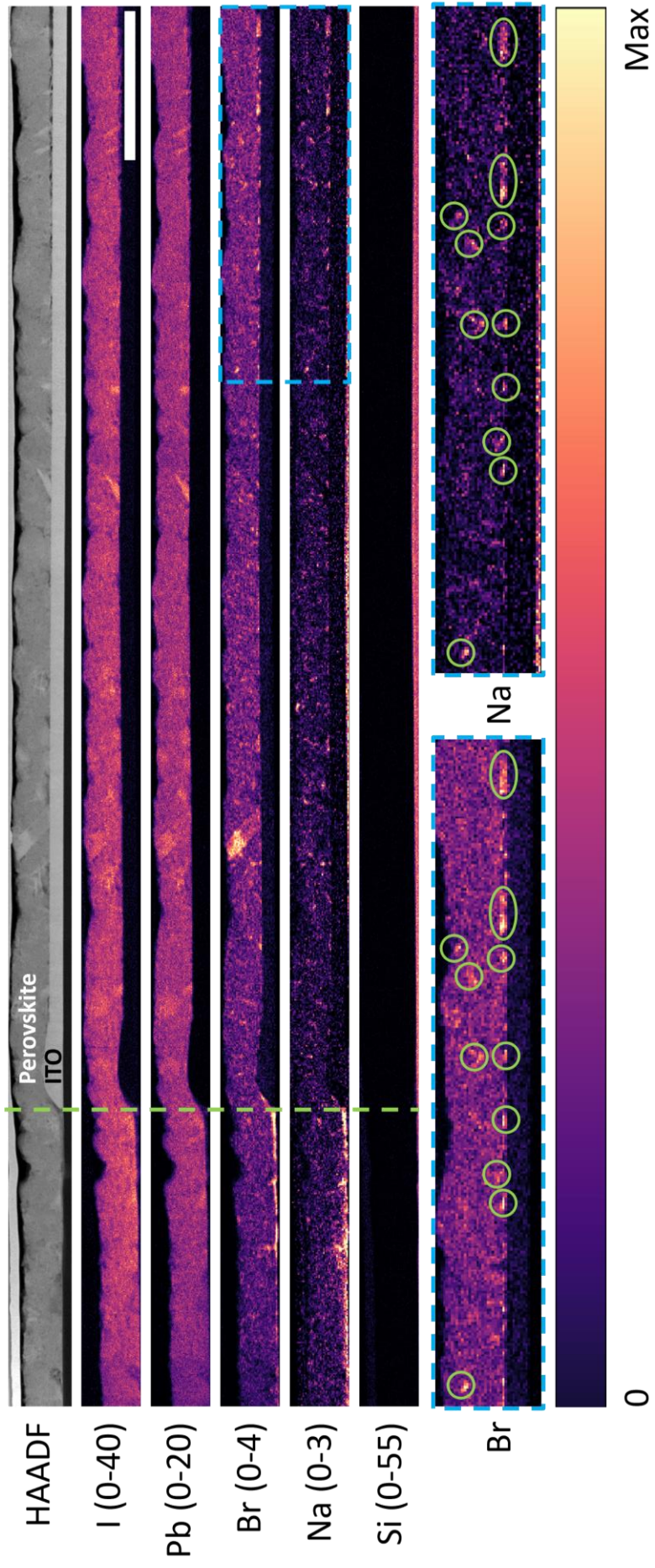


Figure 7.1 | Cross-sectional STEM-HAADF image and STEM-EDX peak intensity maps for the NiO device. The denoised STEM-EDX model SI was constructed using 17 principal components from PCA. The Br and Na maps are spatially rebinned by a factor of 2 to reduce noise. The dashed green line marks the P1 line edge. The bottom row shows an enlarged view of the right end of the Br and Na maps as marked by the dashed blue rectangle. Green circles highlight the Na-Br correlation. Numbers in parentheses signify the range of the colour scale used for each map. Scale bar represents 2  $\mu\text{m}$ .

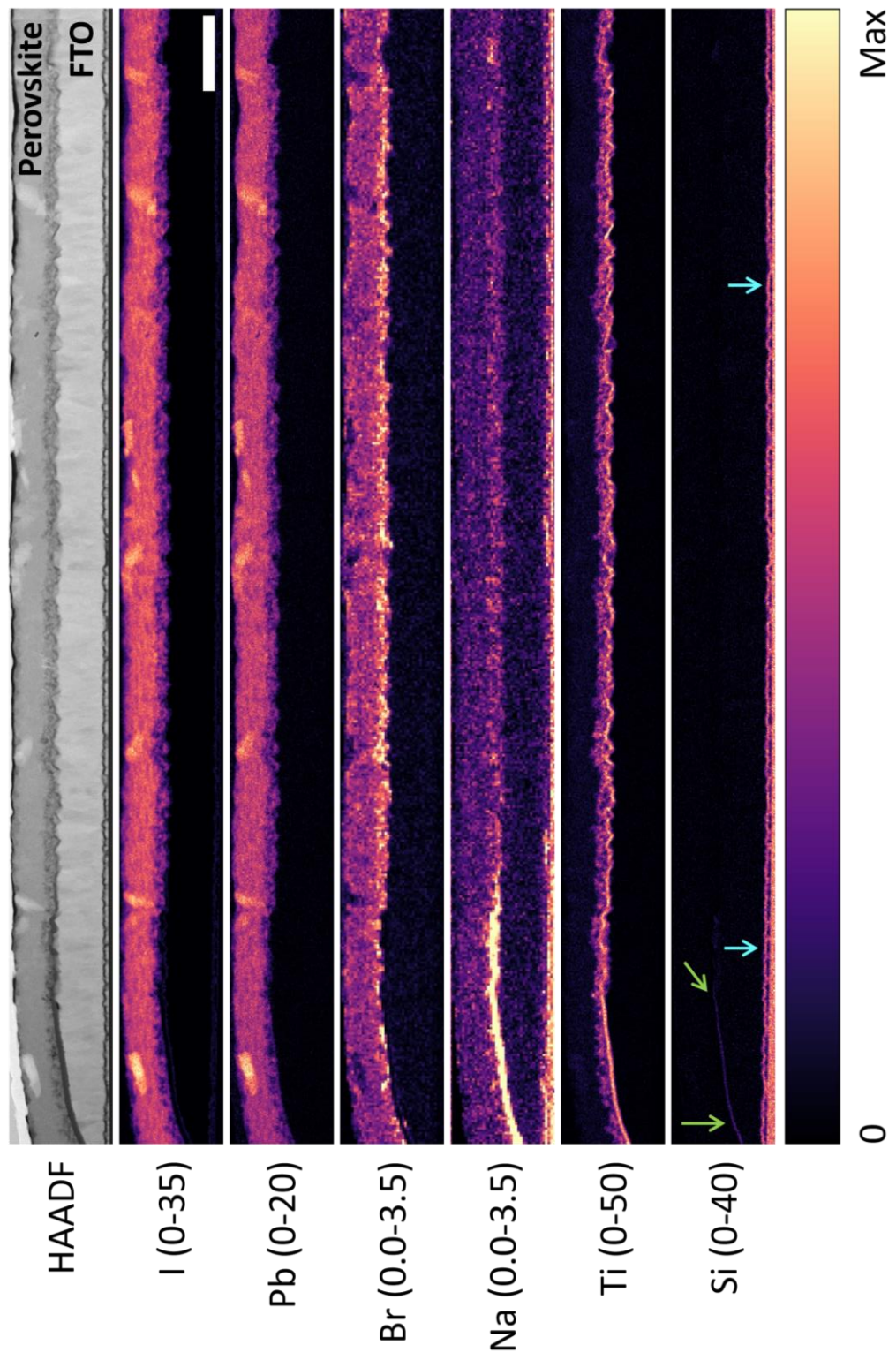


Figure 7.2 | Cross-sectional STEM-HAADF image and STEM-EDX peak intensity maps for the  $\text{TiO}_2$  device. The denoised STEM-EDX model SI was constructed using 17 principal components from PCA. The Br and Na maps are spatially rebinned by a factor of 2 to reduce noise. Numbers in parentheses signify the range of the colour scale used for each map. Scale bar represents 2  $\mu\text{m}$ .

In Figure 7.1 and 7.2, Na is still detected in the perovskite film or bottom CTL at the right end of the lamella, which is furthest away (15–16  $\mu\text{m}$ ) from the P1 line edge. Therefore, the STEM-EDX data do not reveal the full extent of Na diffusion. To confirm the STEM-EDX findings and characterise Na diffusion over a greater distance, NanoSIMS was performed at two locations on the  $\text{TiO}_2$  device: right next to a P1 line (0  $\mu\text{m}$ ) and 100  $\mu\text{m}$  into the active area (100  $\mu\text{m}$ ). The elemental abundance profiles and maps are displayed in Figure 7.3, where panel (a) shows a schematic of the device layers and the orientational frame of reference used in the rest of the figure. Figure 7.3b shows a lateral profile of Na, Ti, Sn, and Pb signal intensities, integrated across the y and z directions and plotted in the x direction from the side that is closest to the P1 line to the opposite side. The Au and SLG layers were excluded to avoid distortions of the data, particularly of Na which is abundant in the SLG. Within each dataset, the Na concentration does not change much along the x direction (Figure 7.3b). However, when the Na signal intensities at the two locations are compared to one another (Figure 7.3b-d), there is a clear decline from the 0  $\mu\text{m}$  dataset ( $184 \pm 6$ ) to the 100  $\mu\text{m}$  one ( $118 \pm 3$ ). This lateral gradient conclusively proves that Na diffuses from the P1 line into the AA. Despite the decline, the Na signal intensity at the 100  $\mu\text{m}$  location is only reduced by 36% from the 0  $\mu\text{m}$  location. This suggests that the full extent of Na diffusion could reach at least a few hundreds of  $\mu\text{m}$  into the AA. Figure 7.3c-f shows the depth profiles and maps of the elements. The profiles (Figure 7.3c,d) are integrated across the x and y directions and plotted in the z direction from the Au side to the substrate. The maps (Figure 7.3e,f) are displayed in the yz plane, summed across all slices in the x direction. Note that in the vertical (z) direction, the slice numbers do not correspond to actual layer thicknesses. The maps give another view of the decrease in Na concentration from the 0  $\mu\text{m}$  location to the 100  $\mu\text{m}$  one. Moreover, the depth profiles and maps also show far lower Na signal in the FTO layer. This proves that vertical diffusion of Na occurs only inside the P1 lines, confirming the STEM-EDX observations.

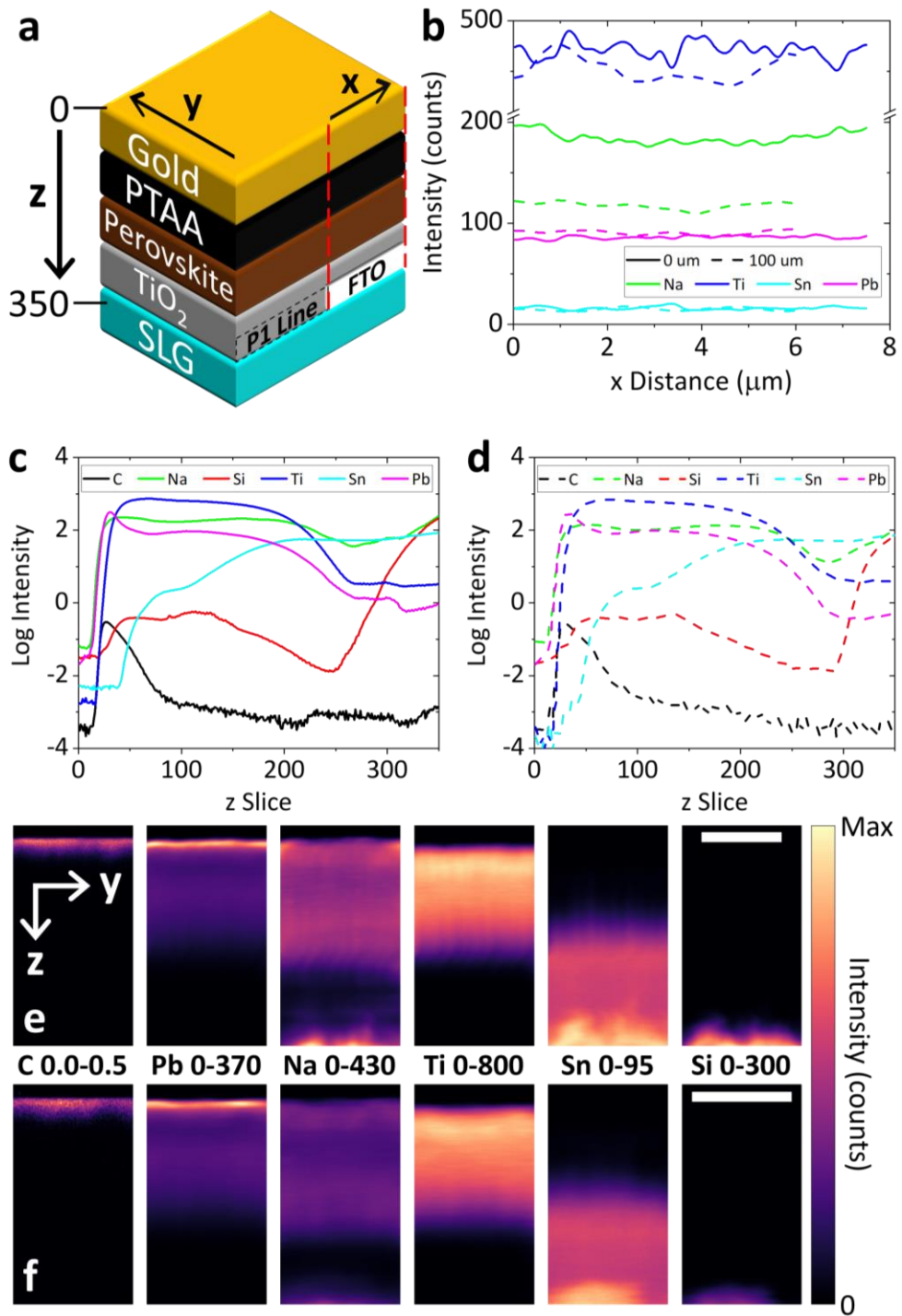


Figure 7.3 | (a) Schematic of the TiO<sub>2</sub> device analysed with NanoSIMS, with orientations marked as reference for panels (b-f). (b) Lateral profiles acquired from (solid line) next to and (dashed line) 100 μm away from a P1 line. Higher slice numbers are further away from a P1 line. (c,d) Depth profiles acquired from (c) next to and (d) 100 μm away from a P1 line. Higher slice numbers are deeper in the device stack. (e,f) 2D elemental maps (yz plane) acquired from (e) next to and (f) 100 μm away from a P1 line. Numbers between panels (e,f) signify the range of the colour scale used for each element. Scale bars represent 5 μm in the y direction. The slice numbers in panels (c,d) and z distance in panels (e,f) are not scaled to actual layer thicknesses.

## 7.4. Effect of Na Diffusion on the Properties of the Perovskite

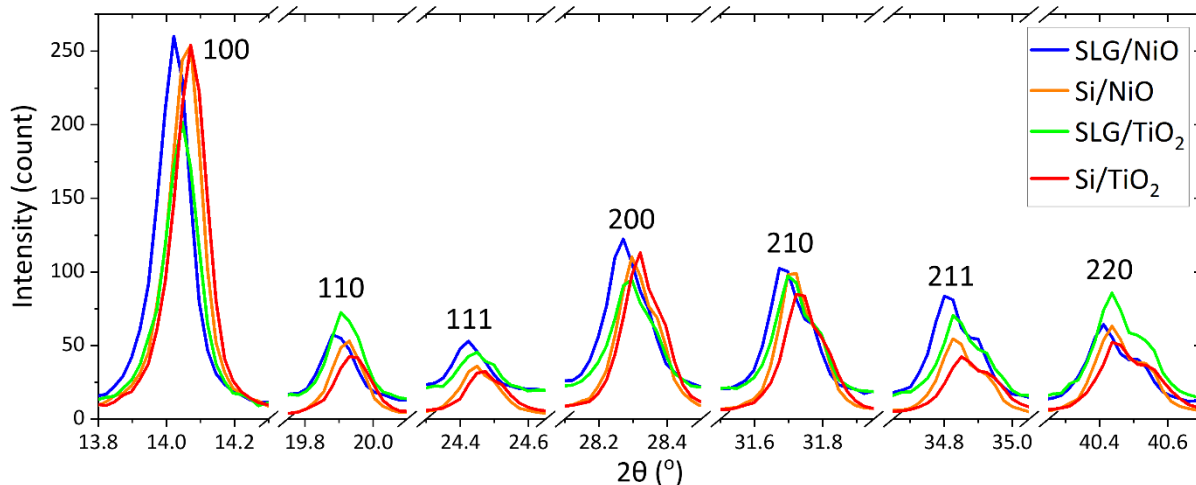


Figure 7.4 | Selected XRD peaks acquired from (blue) SLG/NiO/perovskite, (orange) Si/NiO/perovskite, (green) SLG/TiO<sub>2</sub>/perovskite, and (red) Si/TiO<sub>2</sub>/perovskite samples. Miller indices of the perovskite lattice planes are marked.

After Na diffusion from P1 lines into the AA has been confirmed with STEM-EDX and NanoSIMS, the next question to be investigated is how Na affects the perovskite film and its optoelectronic properties. First, the effect of Na on the perovskite crystallography is studied by performing XRD on perovskite films deposited on four substrate types: SLG/NiO, Si/NiO, SLG/TiO<sub>2</sub>, and Si/TiO<sub>2</sub>. Both NiO and TiO<sub>2</sub> were used as perovskite structure is influenced by the type of substrate (planar or mesoporous) it is deposited on.<sup>451</sup> No TCO was put on top of SLG to enable Na diffusion throughout the film area. The XRD peaks of perovskite films deposited on SLG are shifted to lower angles by 0.02–0.07° compared to the Si-based reference films, indicating wider interplanar spacings in the perovskite lattice (Figure 7.4). A possible explanation for this shift is that Na diffuses from SLG and resides in the perovskite lattice's interstitial sites. However, this is unlikely as the STEM-EDX data shows that Na is not homogeneously distributed in the perovskite layer. Furthermore, Kubicki et al. have shown that Na does not get incorporated into the lattice of TCDH perovskite at all.<sup>449</sup> The shift to lower angles suggests that Na does not occupy the A-cation site either, as in that case, the lattice would have shrunk instead of expanded. This agrees well with the Goldschmidt tolerance factor, which predicts that the ionic radius of Na<sup>+</sup> (116 pm) is too small to sustain the PbI<sub>x</sub>Br<sub>y</sub> octahedra.<sup>32</sup> The absence of Na in the A-cation site, at least in the top few nm of the perovskite film, is supported by XPS spectra acquired from a sister set of samples. No binding energy shift was observed for the Pb, I, Br, and Cs characteristic peaks, indicating that there is no bonding between Na and those elements in the perovskite. (Figure 7.5). Instead, a more probable explanation for the XRD peak shift is that it is caused by a deviation in the

perovskite's halide composition. If perovskite films deposited on SLG are Br-poor and I-rich relative to those on Si, they would have wider lattice plane spacings due to the I<sup>-</sup> anions' larger radius. Consequently, the perovskite XRD peaks would shift to slightly lower angles as observed.

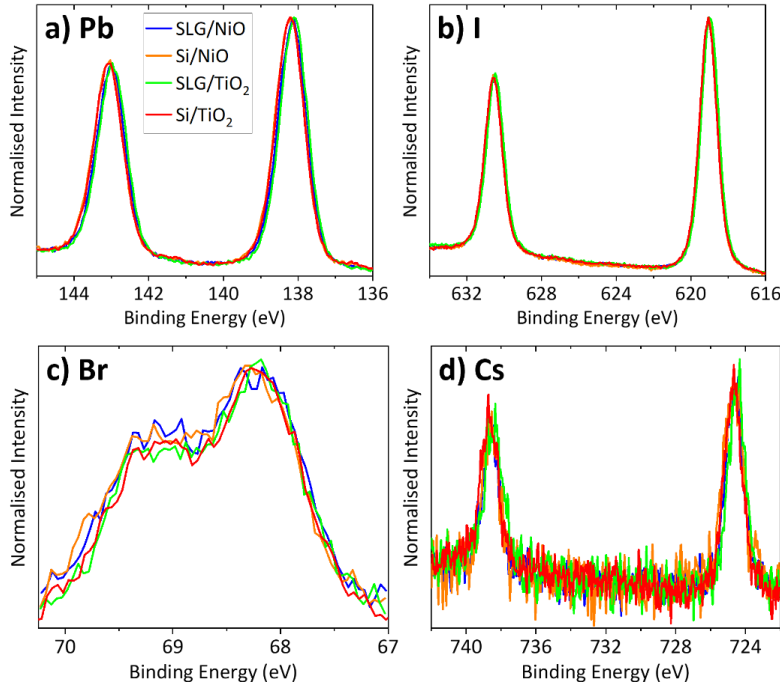


Figure 7.5 | Normalised XPS spectra of (a) Pb, (b) I, (c) Br, and (d) Cs acquired from (blue) SLG/NiO/perovskite, (orange) Si/NiO/perovskite, (green) SLG/TiO<sub>2</sub>/perovskite, and (red) Si/TiO<sub>2</sub>/perovskite samples. Normalisation was performed on Gaussian fits of the raw data.

SEM imaging was used to check if Na diffusion altered the perovskite grain and film morphology. Here four types of half devices were examined: SLG/ITO/NiO/perovskite, Si/NiO/perovskite, SLG/FTO/TiO<sub>2</sub>/perovskite, and Si/TiO<sub>2</sub>/perovskite. For the samples based on SLG, the ITO and FTO layers were P1-patterned to enable comparison of grain/film morphology inside and outside P1 lines. Figure 7.6 displays SEM images of all four half devices, acquired in SE (Figure 7.6a-k) or BSE (Figure 7.6l) mode. There is no difference in the perovskite grain shape or size regardless of the CTL, substrate, or location with respect to a P1 line (Figure 7.6a-f). However, inside a P1 line, there are either slightly fewer (NiO device, Figure 7.6a) or no bright grains (TiO<sub>2</sub> device, Figure 7.6d) compared to outside a P1 line (Figure 7.6b,e) or on the Si-based film (Figure 7.6c,f). Bright grains such as these have previously been attributed to PbI<sub>2</sub>, although without direct evidence.<sup>452-454</sup> Lower magnification images of the SLG/FTO/TiO<sub>2</sub>/perovskite half device (Figure 7.6g-j) reveal that the bright grains are missing not only in the P1 lines, but also inside Brownian tree-shaped areas which grow perpendicularly from P1 line edges and extend for up to 360 μm into the AA. Brownian trees are often formed by diffusion-

limited processes and their appearance here strongly indicates that they were formed by Na diffusion from the P1 line.<sup>455</sup> It is plausible that the reach of these Brownian trees may be used to infer the furthest extent of Na diffusion. Figure 7.6k,l were acquired at the same edge of one of the tree's branches. These images show that the contrast in the SE image (Figure 7.6k) is far less pronounced in the BSE image (Figure 7.6l). This means the difference in signal intensity is due to grain topography or work function ( $\phi$ ) difference instead of compositional differences. More specifically, the bright grains likely have the same heavy elements as the perovskite (predominantly Pb and I).

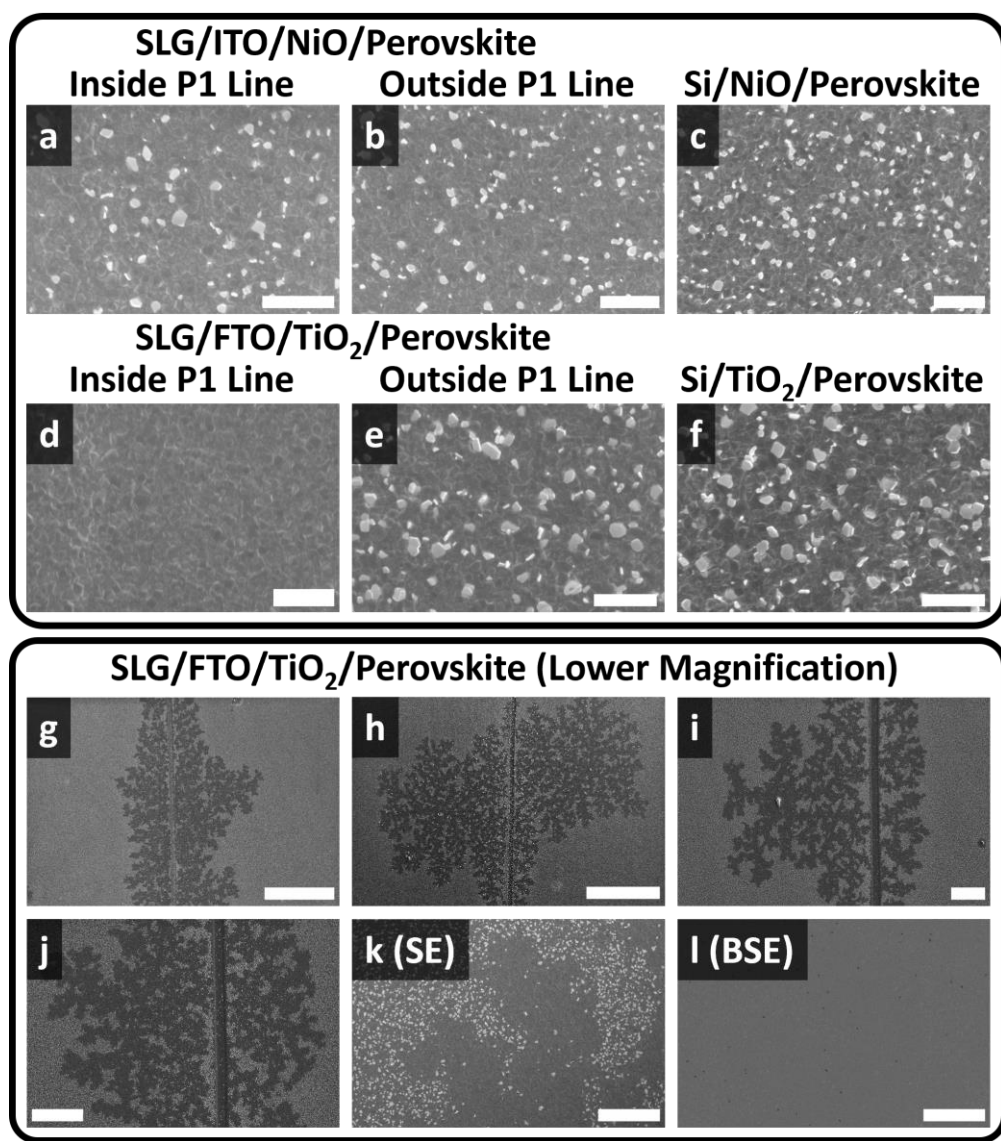


Figure 7.6 | Top-view SEM images acquired from (a,b) SLG/ITO/NiO/perovskite, (c) Si/NiO/perovskite, (d,e,g-l) SLG/FTO/TiO<sub>2</sub>/perovskite, and (f) Si/TiO<sub>2</sub>/perovskite. Panels (a,d) were acquired from inside P1 lines, while panels (b,e) were taken far away from P1 lines. Panels (k) and (l) are SE and BSE images, respectively, of the same area. All other panels are SE images. Scale bars represent (a-f) 2  $\mu$ m, (g,h) 200  $\mu$ m, (i,j) 50  $\mu$ m, or (k,l) 10  $\mu$ m.

The SEM observations are confirmed by AFM and KPFM mapping performed on the same specimens. AFM topography maps (Figure 7.7a-e,k-o) show that NiO and TiO<sub>2</sub> samples contain platelike grains jutting out of the perovskite film. KPFM (Figure 7.7f-j,p-t) produced maps of contact potential difference (CPD) on the same areas. CPD is defined as the difference in  $\phi$  between the specimen surface and the Pt-Ir probe tip, divided by the electron charge. In the KPFM maps (Figure 7.7f-j,p-t), darker colours correspond to lower  $\phi$  compared to the brighter colours. KPFM maps show that the plates seen in AFM are not perovskite, as they exhibit markedly lower  $\phi$  compared to the rest of the film (red arrows in Figure 7.7). Both the non-flat topography and the low  $\phi$  of the non-perovskite phase increases its SE yield during SEM imaging, explaining why it appears bright in Figure 7.6a-k. In both samples, fewer of these non-perovskite plates appear close to the P1 lines. SEM, AFM, and KPFM suggest that Na diffusion is responsible for the absence of the non-perovskite species close to P1 lines and inside the Brownian trees. The outline of a Brownian tree can be seen in Figure 7.7p, supporting this deduction.

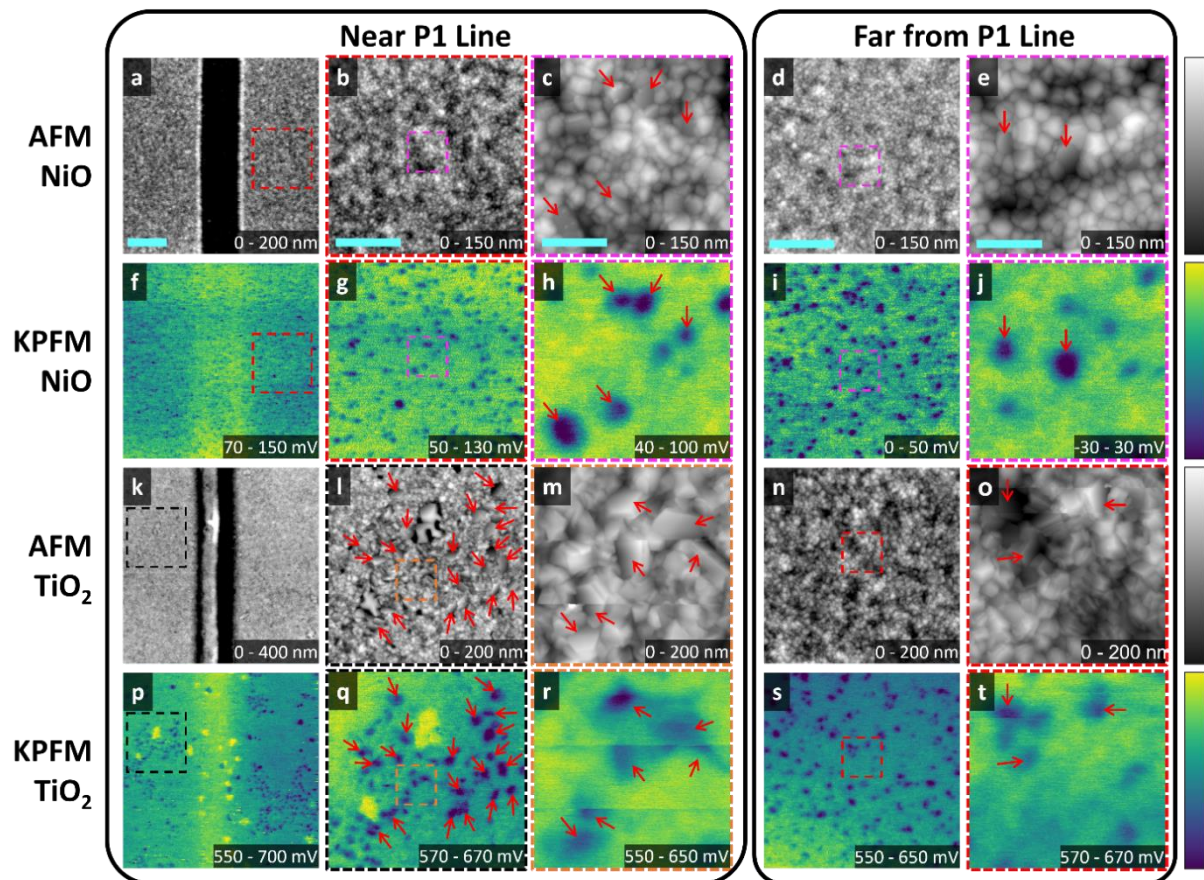


Figure 7.7 | (a-e,k-o) AFM topography maps and (f-j,p-t) KPFM CPD maps acquired near to or far away from a P1 line in the NiO and TiO<sub>2</sub> devices. CPD values in panels (f-j) were multiplied by -1 to correct for the device's reversed electrical polarity. Red arrows mark the non-perovskite grains. Dotted squares in columns 1, 2, and 4 mark the areas mapped with higher magnification in columns 2, 3, and 5, respectively. Scale bars represent (column 1) 10  $\mu\text{m}$ , (columns 2,4) 5  $\mu\text{m}$ , or (columns 3,5) 1  $\mu\text{m}$ .

Hyperspectral CL mapping was performed on the half device samples to evaluate how Na affects radiative recombination in the perovskite. Panels a-d in Figure 7.8 show SE images of the CL scan area, while panels e-h and i-l show the luminescence maps for perovskite and PbI<sub>2</sub>, respectively. Averaged perovskite luminescence spectra extracted from the CL SIs are shown in Figure 7.8m,n. The perovskite luminescence maps and spectra show that in both samples, the perovskite emission close to P1 lines is stronger by ~5x than that away from P1 lines. Interestingly, for the TiO<sub>2</sub> sample, the emission peak close to P1 is red-shifted by  $18 \pm 6$  meV ( $1.603 \pm 0.004$  eV vs  $1.621 \pm 0.004$  eV, Figure 7.8n) while for the NiO sample the emission peak energy is unchanged ( $1.616 \pm 0.004$  eV and  $1.612 \pm 0.004$  eV, Figure 7.8m). A  $17 \pm 3$  meV red-shift close to P1 lines in the TiO<sub>2</sub> sample was also observed with PL spectroscopy (Figure 7.9), confirming that the red-shift was not caused by specimen damage from the CL electron beam (which would be expected to be broadly equal for all SIs). In literature, weak or quenched steady state luminescence from samples which include a CTL is often desired as it is taken as a sign of efficient charge transport and low non-radiative recombination at the perovskite/CTL interface.<sup>444</sup> However, Kirchartz et al. have shown that this is only true when luminescence spectroscopy is conducted on a biased device with an applied  $V$  significantly below  $V_{OC}$ .<sup>234</sup> This condition is rarely fulfilled as luminescence measurements are often performed without any external circuit, as was done here. If the sample is at open circuit, strong luminescence intensity is desirable even when a CTL is used, as it signifies low non-radiative recombination and high quasi-Fermi level splitting.

The Brownian trees previously observed in SEM and KPFM are also visible in SEM-CL. Inside these trees, the perovskite emission is brighter (Figure 7.8g) and the PbI<sub>2</sub> emission is not present (Figure 7.8k). This unambiguously identifies the non-perovskite plates as PbI<sub>2</sub>. The lack of PbI<sub>2</sub> inside the Brownian trees and the observed red-shift in perovskite emission suggest that the perovskite close to P1 is I-rich and Br-poor compared to that deeper in the AA. Taken together with the XRD peak shift towards smaller angles for perovskite films deposited on SLG, the Brownian trees indicate that lateral Na diffusion is responsible for the change in halide proportion. Although these trees are not visible in the NiO samples, PbI<sub>2</sub> emission in this sample is also weaker close to the P1 lines (Figure 7.8i,j). This agrees well with the SEM images and KPFM maps, which show only a slight reduction in the number of bright grains or dark spots, respectively, inside or close to P1 lines of the NiO sample (Figure 7.6a-c, 7.7g,i). This discrepancy between the NiO and TiO<sub>2</sub> devices is likely caused by less Na diffusing in the NiO device, as also observed with STEM-EDX (Figure 7.1).

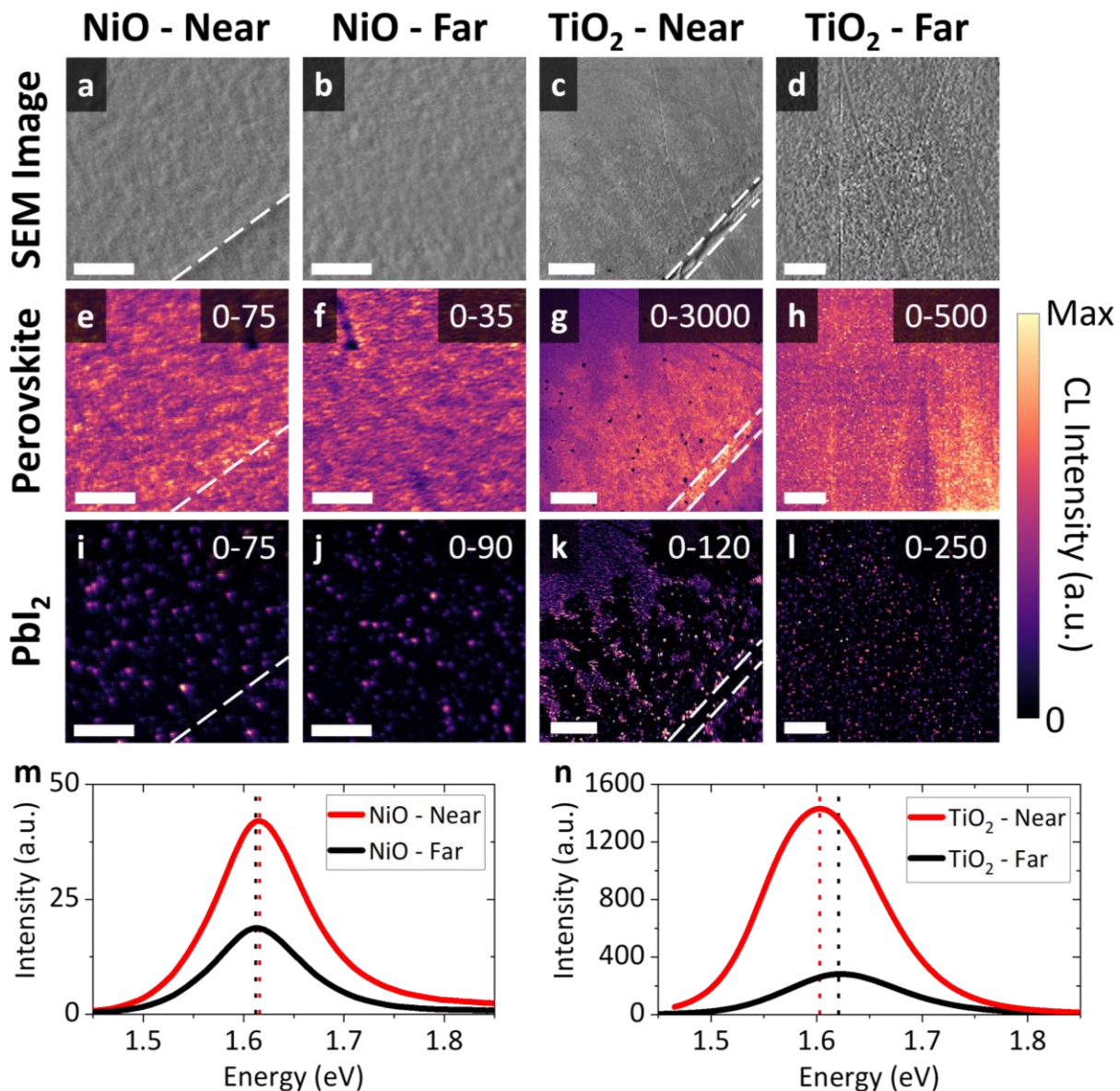


Figure 7.8 | (a-d) SE image of the CL scan area, (e-h) perovskite emission map, and (i-l)  $\text{PbI}_2$  emission map acquired near to (Near) or far away from (Far) a P1 line in the NiO and  $\text{TiO}_2$  devices. Dashed white lines mark the P1 lines. Scale bars represent (a,b,e,f,i,j) 5  $\mu\text{m}$ , (c,g,k) 30  $\mu\text{m}$ , or (d,h,l) 10  $\mu\text{m}$ . (m,n) Average CL emission spectra for the (m) NiO and (n)  $\text{TiO}_2$  devices extracted from the emission maps. Dotted lines in panels (m,n) mark the emission peak centres.

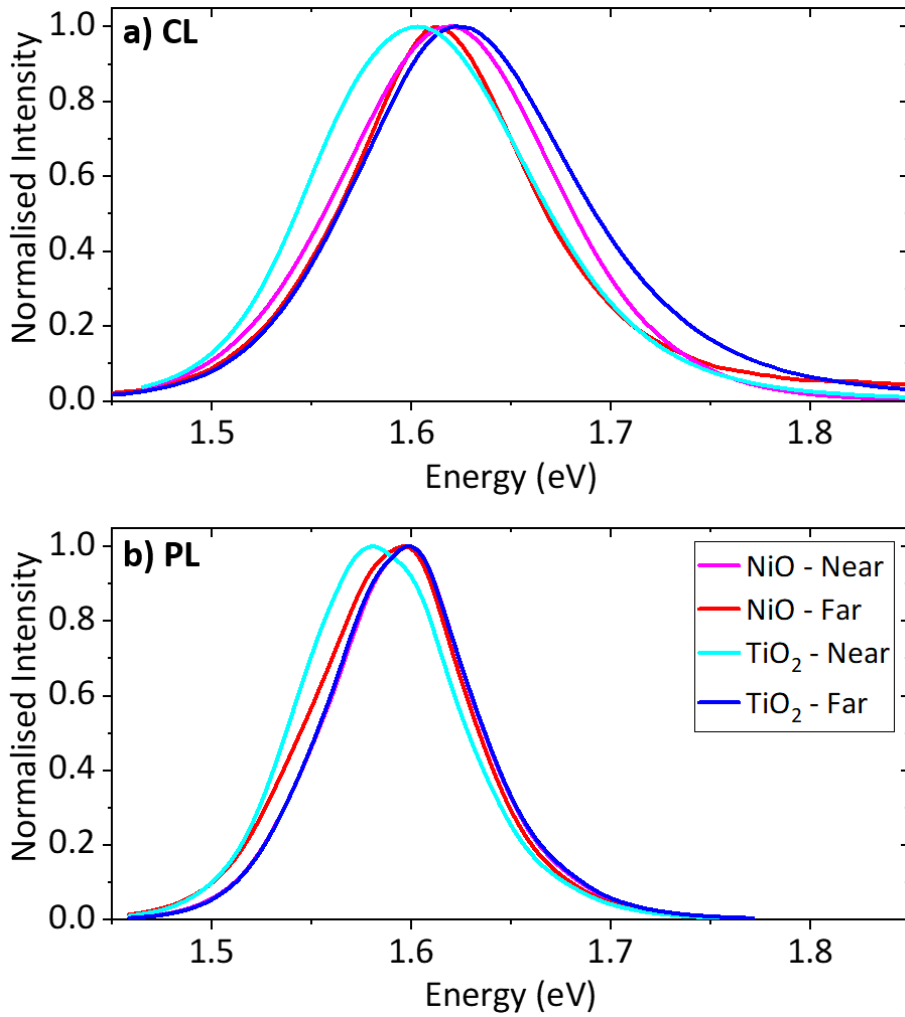


Figure 7.9 | Normalised (a) CL and (b) PL perovskite emission spectra acquired near to and far away from P1 lines in the NiO and TiO<sub>2</sub> devices.

A coherent mechanism explaining how Na diffusion results in the described observations can now be formed. Due to its concentration gradient, Na diffuses from glass into the device's active layers, first vertically inside P1 lines and then laterally towards the AA (Figure 7.1-7.3). Since the kinetics of solid-state diffusion is determined by the diffusant's ability to overcome the energy barrier for lattice site hopping, it is accelerated by the thermal energy supplied during CTL and perovskite annealing.<sup>456</sup> Therefore, more Na diffused in the TiO<sub>2</sub> device compared to the NiO one (Figure 7.1,7.2) due to the longer and higher temperature annealing used for TiO<sub>2</sub>, likely further assisted by the ease of Na diffusion in the TiO<sub>2</sub> lattice.<sup>447,448</sup> The diffused Na preferentially binds with Br (Figure 7.1,7.2), drawing it out of the perovskite precursor solution and the formed perovskite. To compensate for the resulting halide deficiency, more I (from the excess PbI<sub>2</sub> precursor) reacts to form the perovskite. This results in less residual PbI<sub>2</sub> (Figure 7.6,7.8i-l) and the formation of Br-poor, I-rich perovskite close to P1 lines, causing the luminescence peak shift and in agreement with the XRD peak shifts (Figure 7.4,7.8,7.9).

The higher amount of diffused Na in the TiO<sub>2</sub> sample means that some of the effects of Na diffusion are only visible there, such as the Brownian trees and the luminescence red-shift (Figure 7.6,7.8,7.9). Finally, NaBr appears to boost the perovskite luminescence through defect passivation (Figure 7.8m,n). As previously described for K passivation, NaBr immobilises excess halides, thus suppressing the concentration of halide interstitials.<sup>91</sup> It is probable that this defect passivation mechanism will only translate into better PV parameters when excess halide is available in the perovskite precursor to make up for the scavenged Br atoms during a moderate annealing treatment (which aids diffusion and healing of high energy defects). Otherwise, the perovskite lattice will contain halide vacancies which are likely to facilitate ion migration and phase segregation.<sup>457</sup> In addition, other researchers have used Na doping to passivate interfacial defects.<sup>443–445</sup> Since much of the formed NaBr in this study is located near the perovskite/NiO interface or within the mesoporous TiO<sub>2</sub> layer (Figure 7.1,7.2), it is quite likely that reduction of interfacial non-radiative recombination could also have taken place.

All the characterisation results presented so far were obtained from fresh samples. Therefore, most of the observed Na diffusion, if not all, occurred during device fabrication. However, since OIHPs tend to exhibit quite high ionic diffusivity and conductivity, it is plausible that Na diffusion will proceed further into a PSM's AA during its operational lifetime.<sup>312,458</sup> External stimuli such as elevated temperatures, electrical bias, and light may also accelerate Na movement. Given this possibility, it is of interest to know whether the formed NaBr is stable in the perovskite layer. To answer this question, a NiO device was stored in a desiccator at room temperature for 12 weeks. Inside the desiccator, this device was exposed to an atmosphere of dry air with <20% relative humidity. A TEM lamella was then cut approximately 6 µm away from a P1 line edge in this device. The cross-sectional STEM-HAADF image and STEM-EDX peak intensity maps acquired from this lamella are shown in Figure 7.10. The Na-Br correlation becomes more obvious and more spatially concentrated compared to Figure 7.1, suggesting that the formed NaBr, and therefore the effects of Na diffusion, is long-lasting. While continued defect passivation is advantageous, too much Na inside the perovskite layer was found to deteriorate PV performance.<sup>433,435,436,441,445</sup> Therefore, if PSMs are to be used for long periods of time, Na diffusion from SLG should be prevented or at least slowed down, as otherwise it will be continuously driven to a greater extent by the Na concentration gradient and electric field.

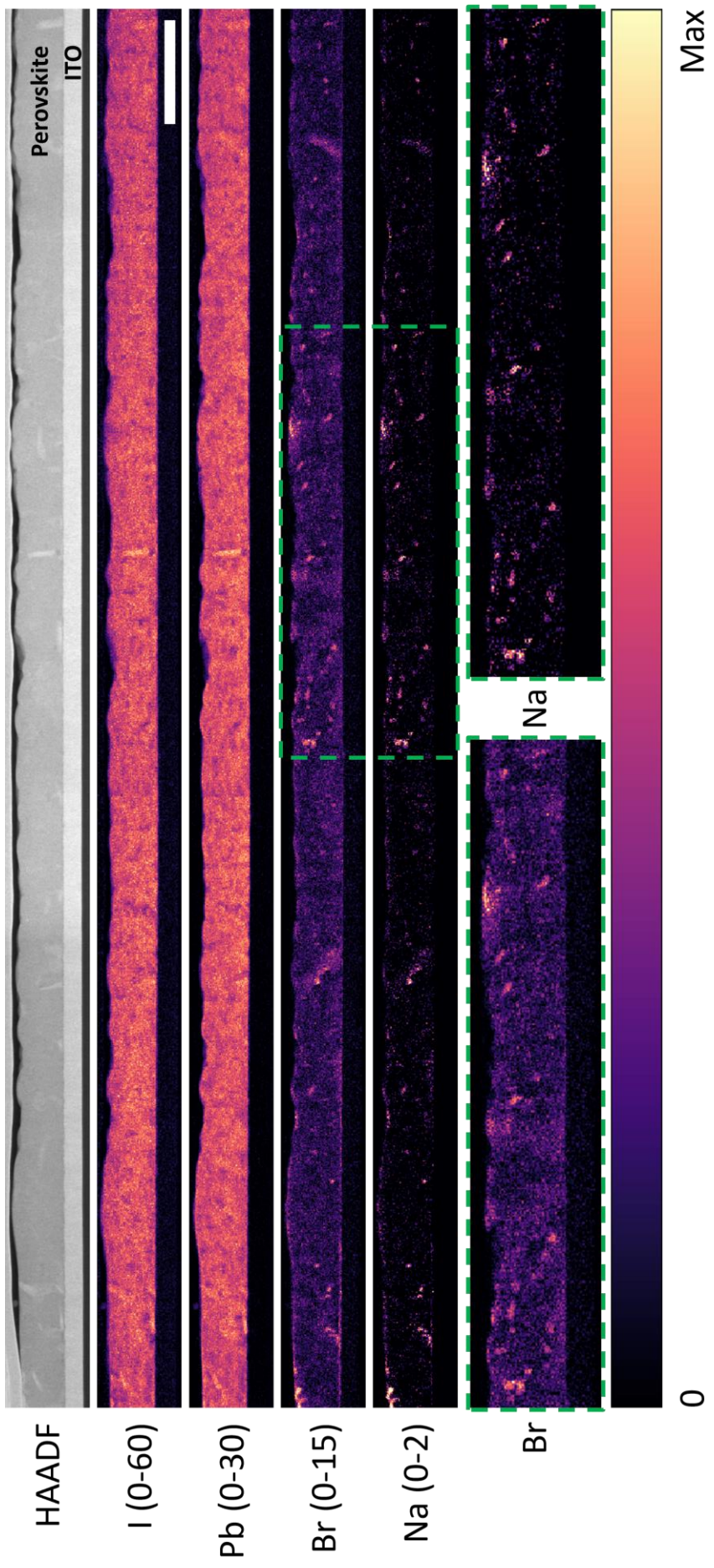


Figure 7.10 | Cross-sectional STEM-HAADF image and STEM-EDX peak intensity maps for the NiO device after 12 weeks of storage in a desiccator (dry air, <20% RH) at room temperature. The denoised STEM-EDX model SI was constructed using 18 principal components from PCA. The bottom row shows an enlarged view of the Br and Na maps as marked by the dashed green rectangle. The left (right) end of the lamella is ~6 (~21)  $\mu\text{m}$  away from a P1 line edge. Scale bar represents 2  $\mu\text{m}$ .

## 7.5. Summary

In this chapter, Na diffusion from SLG substrates is shown to occur through P1 lines in PSMs. This phenomenon and its effects were studied with several complementary characterisation techniques. The experimental evidence supports the following mechanism: CTL and perovskite annealing steps during device fabrication provide sufficient energy for Na to diffuse vertically inside P1 lines and then laterally for up to 360 µm into the AA. The diffusing Na extracts Br from the perovskite and forms NaBr, leaving Br-poor, I-rich perovskite in the vicinity of P1 lines. NaBr passivates defect sites in the perovskite layer, reducing non-radiative recombination and strengthening perovskite luminescence. Importantly, Na diffusion and NaBr formation continue in the device's lifetime, even at room temperature, and its effects seem to be long-lasting.

Although a more intense luminescence leads to higher  $V_{OC}$  and is thus desirable, sustained or uncontrolled Na diffusion will result in a high Na concentration in the perovskite layer. Studies of deliberate Na doping have shown that this results in a decreased power output from the module. Therefore, it will likely be necessary to prevent or at least suppress Na diffusion from SLG. This can be done by, for example, using substrates which feature a diffusion barrier layer and making sure this layer is not scribed away in the P1 lines. Other possibilities include using low-Na glass substrates, replacing TiO<sub>2</sub> with other CTLs which do not require high-temperature annealing, or developing low-temperature CTL deposition methods.

Na intrusion from SLG into the active layers of a PSM is a topic little investigated, especially when compared to other thin film PV devices. To cite just an example, Na migration from SLG has been identified as the primary mechanism of potential-induced degradation in CIGS solar cells.<sup>459–461</sup> In light of the results presented in this chapter, looking into how electrical bias and other external stimuli affect Na diffusion in PSMs is a very interesting research topic, which will provide useful insights towards the commercialisation of PSMs.

## **Chapter 8**

### **Conclusions and Future Work**

Perovskite PV has advanced rapidly over the past decade, maturing from a newfound curiosity to a technology standing on the cusp of commercialisation in a very short period. This progress was enabled in no small part by extensive characterisation works performed on perovskite materials and devices, which have greatly deepened our understanding of their structure-property-processing-performance relationship. This comprehension, combined with the empirical know-how collected over years of gradual improvements in device-making, has resulted in ever more efficient and stable solar cells. Perovskite PV now offers a tantalising combination of high PCE and low fabrication cost, complemented with the promise of a much lower capital expenditure compared to Si PV manufacturing. The all-important goal of affordable LCOE is thus now closer than ever.

Several challenges remain on perovskite PV's path to the market. Chief among these is replicating the performance of  $<1\text{ cm}^2$ -sized cells to modules capable of large-scale power production. Attaining this feat requires a spatially homogeneous deposition of all device layers over a large area and an optimised MI design with due consideration for any effects the scribing process may have on the AA. Just like with other nanostructured devices, the material and engineering challenges related to PSM development can only be solved through insights obtained with nanoscale characterisation. However, materials characterisation at the nanoscale often involves probing the specimen with a high-energy probe which may introduce some beam-induced damage. This problem is particularly complex for photoactive perovskites, whose structure comprises both organic and inorganic components. Therefore, such characterisation methods should firstly be optimised and validated before they are applied in the study of perovskite PV.

In this thesis, a workflow for STEM characterisation of perovskite PV devices is developed and applied to study the PSM fabrication process. The procedure consists of cross-sectional specimen preparation with FIB milling, Z-sensitive STEM-HAADF imaging, STEM-EDX compositional mapping, and data analysis using PCA. The optimisation and validation of this sequence is described in Chapter 4. First, a FIB milled perovskite device lamella is shown to be luminescent, indicating that the perovskite structure is largely preserved after the milling process. Then, the effect of electron dose on the EDX data quality is considered and carefully weighed against specimen damage caused by the electron beam to obtain a dose which minimises measurement uncertainty without excessive damage. Finally, two MVA algorithms, PCA and NMF, are optimised, used to construct denoised models of the EDX data, and

compared to one another. PCA was found to produce more accurate compositional maps and was therefore used for subsequent data analysis.

Chapter 5 discusses a solution engineering approach for homogeneous perovskite blade coating. MAI and H<sub>2</sub>O additions to the perovskite precursor solutions were found to result in >12% efficient PSMs with an AA of 47.7 cm<sup>2</sup>. The described STEM procedure was key to revealing the roles played by MAI and H<sub>2</sub>O in achieving those improvements. Specifically, they fostered a more complete perovskite formation reaction which produces a homogeneous perovskite film with minimum secondary phases, more uniform grains, and complete scaffold pore filling. Based on the STEM findings and observations made in prior research, a mechanism can be proposed to describe how MAI and H<sub>2</sub>O modified the reaction kinetics. During the PbI<sub>2</sub> blade coating step, the MAI additive slowed down PbI<sub>2</sub> grain growth, which allows PbI<sub>2</sub> to percolate through the TiO<sub>2</sub> network's nanosized pores before the grains grow too large. Moreover, MAI also formed porous PbI<sub>2</sub> grains which are easier to convert into perovskite in the MAI dipping step, especially with H<sub>2</sub>O increasing the mobility of MA<sup>+</sup> and I<sup>-</sup> ions. The perovskite formation is thus assisted and can proceed to completion.

The MI area of PSMs and its vicinity are investigated in Chapters 6 and 7. Chapter 6 discusses the laser scribing process of P3 lines and how it damages the perovskite layer next to those lines. STEM-EDX elemental maps and heat flow simulation revealed that the nature of laser-induced perovskite decomposition is determined by the presence or absence of non-perovskite phases acting as fast thermal flow channels. If such a phase is present, such as PbI<sub>2</sub> grains, most of the thermal energy deposited by the laser pulses flows through them and the perovskite surrounding those grains is decomposed, thus growing the PbI<sub>2</sub> grains. Without a relatively thermally conductive phase present, the thermal energy flows through the perovskite layer uniformly and the induced compositional changes are more subtle. In addition, the nature of ITO damage in the P3 lines due to excessive laser fluences and the effect of laser pulse duration on the extent of perovskite decomposition are also discussed in Chapter 6.

Finally, Chapter 7 details an investigation of Na diffusion around P1 lines in PSMs. As the substrate-side CTL is in contact with the SLG substrate in P1 lines, a direct path exists for Na diffusion from SLG into the active layers. Together with NanoSIMS, STEM-EDX was instrumental in verifying that even in fresh devices, Na diffusion reached hundreds of μm from the P1 line edge. The diffused Na was found to bond preferentially with Br in the perovskite layer and at the perovskite/CTL interface. This reduced the Br content of the perovskite and forced the excess PbI<sub>2</sub> precursor to react, thus forming I-rich, Br-poor perovskite close to P1 lines. Luminescence measurements showed that NaBr passivated perovskite defect sites and boosted its emission by a factor of 5 around P1 lines. Furthermore, the formed NaBr was shown to be stable for 12 weeks in storage, suggesting that Na diffusion can be far more extensive once the device is operated and exposed to illumination, elevated temperatures, and electrical bias.

In summary, this thesis describes the development and application of analytical STEM as a powerful tool to study PSMs at the nanoscale. Undesirable beam-induced specimen damage is suppressed by a judicious selection of electron dose and the use of PCA to denoise the acquired STEM-EDX data. Observations made and discussed herein have contributed to a deeper understanding of large-area homogeneous perovskite deposition and the MI area in PSMs, both important aspects of the journey towards high performance PSMs.

In the future, STEM-EDX of halide perovskites with no or low beam damage can be expected due to the rising adoption of recursive mapping and development of ever more efficient EDX detectors. For example, the state-of-the-art Bruker Ultra-X detector employed in the new ThermoFisher Spectra Ultra (S)TEM boasts a collection solid angle of up to 4.54 sr, five times greater than the Super-X detector used in this thesis.<sup>462</sup> This is a very important development for EM of beam-sensitive materials such as the halide perovskites investigated in this thesis. In particular, highly efficient detectors may allow repeated scans of the same area of the specimen without excessive damage, thus enabling *in situ* STEM-EDX in which the PSC specimen is heated, biased, illuminated, or otherwise stimulated inside the STEM column while EDX is performed. This powerful experimental approach can reveal the mechanism(s) behind device degradation, a step forward from post-mortem examinations which could only show the end result of degradation.

In a similar vein, the recent increasing availability of direct electron detectors has made low dose SED more accessible, paving the way for simultaneous and correlative compositional and crystallographic mapping at the nanoscale.<sup>463</sup> To fully exploit the advantages provided by these technological advancements, more research should be directed towards an accurate calculation or experimental calibration of Cliff-Lorimer k-factors or  $\zeta$ -factors, so that EDX quantification can be performed with fewer assumptions. With continuous developments of ever more powerful hardware and data analysis software, the importance of EM for in-depth characterisation of perovskite PV devices will only increase. It promises precious nanoscale insights towards further advancements in material and device design, ultimately leading to more efficient, more stable, and more affordable solar cells.

## References

- [1] IPCC, Climate Change 2021: The Physical Science Basis. Contribution of Working Group I to the Sixth Assessment Report of the Intergovernmental Panel on Climate Change, Cambridge University Press, Cambridge, 2021.
- [2] H. Ritchie, M. Roser, CO<sub>2</sub> and Greenhouse Gas Emissions, OurWorldInData.Org. (2020). <https://ourworldindata.org/co2-and-other-greenhouse-gas-emissions> (accessed August 19, 2021).
- [3] H. Ritchie, M. Roser, Energy, OurWorldInData.Org. (2020). <https://ourworldindata.org/energy> (accessed August 19, 2021).
- [4] IRENA, Statistics Time Series: Trends in Renewable Energy, (2021). <https://www.irena.org/Statistics/View-Data-by-Topic/Capacity-and-Generation/Statistics-Time-Series> (accessed August 19, 2021).
- [5] IRENA, Renewable Power Generation Costs in 2020, Abu Dhabi, 2021.
- [6] Fraunhofer ISE, Photovoltaics Report, Freiburg, 2021.
- [7] A.K. Jena, A. Kulkarni, T. Miyasaka, Halide Perovskite Photovoltaics: Background, Status, and Future Prospects, Chem. Rev. 119 (2019) 3036–3103. doi:10.1021/acs.chemrev.8b00539.
- [8] J.Y. Kim, J.-W. Lee, H.S. Jung, H. Shin, N.-G. Park, High-Efficiency Perovskite Solar Cells, Chem. Rev. 120 (2020) 7867–7918. doi:10.1021/acs.chemrev.0c00107.
- [9] NREL, Best Research-Cell Efficiencies, (2021).
- [10] R. Vidal, J. Alberola-Borràs, N. Sánchez-Pantoja, I. Mora-Seró, Comparison of Perovskite Solar Cells with other Photovoltaics Technologies from the Point of View of Life Cycle Assessment, Adv. Energy Sustain. Res. 2 (2021) 2000088. doi:10.1002/aesr.202000088.
- [11] Y.-S. Jung, K. Hwang, Y.-J. Heo, J.-E. Kim, D. Vak, D.-Y. Kim, Progress in Scalable Coating and Roll-to-Roll Compatible Printing Processes of Perovskite Solar Cells toward Realization of Commercialization, Adv. Opt. Mater. 6 (2018) 1701182. doi:10.1002/adom.201701182.
- [12] B. Dou, J.B. Whitaker, K. Bruening, D.T. Moore, L.M. Wheeler, J. Ryter, N.J. Breslin, J.J. Berry, S.M. Garner, F.S. Barnes, S.E. Shaheen, C.J. Tassone, K. Zhu, M.F.A.M. van Hest, Roll-to-Roll Printing of Perovskite Solar Cells, ACS Energy Lett. 3 (2018) 2558–2565. doi:10.1021/acsenergylett.8b01556.

- [13] L.A. Zafoschnig, S. Nold, J.C. Goldschmidt, The Race for Lowest Costs of Electricity Production: Techno-Economic Analysis of Silicon, Perovskite and Tandem Solar Cells, *IEEE J. Photovoltaics.* 10 (2020) 1632–1641. doi:10.1109/JPHOTOV.2020.3024739.
- [14] Z. Li, Y. Zhao, X. Wang, Y. Sun, Z. Zhao, Y. Li, H. Zhou, Q. Chen, Cost Analysis of Perovskite Tandem Photovoltaics, *Joule.* 2 (2018) 1559–1572. doi:10.1016/j.joule.2018.05.001.
- [15] S.E. Sofia, H. Wang, A. Bruno, J.L. Cruz-Campa, T. Buonassisi, I.M. Peters, Roadmap for cost-effective, commercially-viable perovskite silicon tandems for the current and future PV market, *Sustain. Energy Fuels.* 4 (2020) 852–862. doi:10.1039/c9se00948e.
- [16] Z. Song, A. Abate, S.C. Watthage, G.K. Liyanage, A.B. Phillips, U. Steiner, M. Graetzel, M.J. Heben, Perovskite Solar Cell Stability in Humid Air: Partially Reversible Phase Transitions in the PbI<sub>2</sub>-CH<sub>3</sub>NH<sub>3</sub>I-H<sub>2</sub>O System, *Adv. Energy Mater.* 6 (2016) 1600846. doi:10.1002/aenm.201600846.
- [17] J. Qian, M. Ernst, N. Wu, A. Blakers, Impact of perovskite solar cell degradation on the lifetime energy yield and economic viability of perovskite/silicon tandem modules, *Sustain. Energy Fuels.* 3 (2019) 1439–1447. doi:10.1039/C9SE00143C.
- [18] S. He, L. Qiu, L.K. Ono, Y. Qi, How far are we from attaining 10-year lifetime for metal halide perovskite solar cells?, *Mater. Sci. Eng. R Reports.* 140 (2020) 100545. doi:10.1016/j.mser.2020.100545.
- [19] S.-H. Turren-Cruz, A. Hagfeldt, M. Saliba, Methylammonium-free, high-performance, and stable perovskite solar cells on a planar architecture, *Science.* 362 (2018) 449–453. doi:10.1126/science.aat3583.
- [20] T. Leijtens, G.E. Eperon, S. Pathak, A. Abate, M.M. Lee, H.J. Snaith, Overcoming ultraviolet light instability of sensitized TiO<sub>2</sub> with meso-superstructured organometal tri-halide perovskite solar cells, *Nat. Commun.* 4 (2013) 1–8. doi:10.1038/ncomms3885.
- [21] G. Grancini, C. Roldán-Carmona, I. Zimmermann, E. Mosconi, X. Lee, D. Martineau, S. Narbey, F. Oswald, F. De Angelis, M. Graetzel, M.K. Nazeeruddin, One-Year stable perovskite solar cells by 2D/3D interface engineering, *Nat. Commun.* 8 (2017) 15684. doi:10.1038/ncomms15684.
- [22] A. Mei, Y. Sheng, Y. Ming, Y. Hu, Y. Rong, W. Zhang, S. Luo, G. Na, C. Tian, X. Hou, Y. Xiong, Z. Zhang, S. Liu, S. Uchida, T.-W. Kim, Y. Yuan, L. Zhang, Y. Zhou, H. Han, Stabilizing Perovskite Solar Cells to IEC61215:2016 Standards with over 9,000-h Operational Tracking, *Joule.* 4 (2020) 2646–2660. doi:10.1016/j.joule.2020.09.010.

- [23] L. Shi, M.P. Bucknall, T.L. Young, M. Zhang, L. Hu, J. Bing, D.S. Lee, J. Kim, T. Wu, N. Takamure, D.R. McKenzie, S. Huang, M.A. Green, A.W.Y. Ho-Baillie, Gas chromatography–mass spectrometry analyses of encapsulated stable perovskite solar cells, *Science*. 368 (2020) eaba2412. doi:10.1126/science.aba2412.
- [24] Panasonic, Japan’s NEDO and Panasonic Achieve the World’s Highest Conversion Efficiency of 16.09% for Largest-area Perovskite Solar Cell Module, (2020). <https://news.panasonic.com/global/press/data/2020/02/en200207-2/en200207-2.html> (accessed August 20, 2021).
- [25] T. Negami, H. Higuchi, T. Nishihara, R. Uchida, T. Yamamoto, T. Matsui, Y. Kaneko, Perovskite Photovoltaic Modules Fabricated by Ink Jet Printing, in: Proc. 4th Asia-Pacific Int. Conf. Perovskite, Org. Photovoltaics Optoelectron., Fundació Scito, València, 2019. doi:10.29363/nanoge.iperop.2020.047.
- [26] A. Bhamhani, Chinese Perovskite Tech Firm Wuxi Utmost Light Claims 20.5% ‘World Record’ Efficiency For Perovskite Solar Mini-Module, Certified By Japan’s JET; Plans To Build Large-Area Perovskite Solar Module Production Lines, TaiyangNews. (2020). <http://taiyangnews.info/technology/20-5-world-record-efficiency-for-perovskite-solar-module/> (accessed August 20, 2021).
- [27] P.K. Nayak, S. Mahesh, H.J. Snaith, D. Cahen, Photovoltaic solar cell technologies: analysing the state of the art, *Nat. Rev. Mater.* 4 (2019) 269–285. doi:10.1038/s41578-019-0097-0.
- [28] Z. Li, T.R. Klein, D.H. Kim, M. Yang, J.J. Berry, M.F.A.M. van Hest, K. Zhu, Scalable fabrication of perovskite solar cells, *Nat. Rev. Mater.* 3 (2018) 18017. doi:10.1038/natrevmats.2018.17.
- [29] N.-G. Park, K. Zhu, Scalable fabrication and coating methods for perovskite solar cells and solar modules, *Nat. Rev. Mater.* (2020). doi:10.1038/s41578-019-0176-2.
- [30] Y. Galagan, Stability of perovskite PV modules, *J. Phys. Energy.* 2 (2020) 021004. doi:10.1088/2515-7655/ab7077.
- [31] A. von Humboldt, C.G. Ehrenberg, G. Rose, Theil 1: Mineralogisch-geognostische Reise nach dem Ural, dem Altai und dem Kaspischen Meere. Band 2: Reise nach dem südlichen Ural und dem Kaspischen Meere, Uebersicht der Mineralien und Gebirgsarten des Ural, Humboldt-Universität zu Berlin, 1842. doi:<http://dx.doi.org/10.18452/440>.
- [32] V.M. Goldschmidt, Die Gesetze der Krystallochemie, *Naturwissenschaften*. 14 (1926) 477–485. doi:10.1007/BF01507527.

- [33] H.D. Megaw, Crystal Structure of Barium Titanate, *Nature*. 155 (1945) 484–485. doi:10.1038/155484b0.
- [34] Q.A. Akkerman, L. Manna, What Defines a Halide Perovskite?, *ACS Energy Lett.* 5 (2020) 604–610. doi:10.1021/acsenergylett.0c00039.
- [35] F.U. Kosasih, C. Ducati, Attaining High Photovoltaic Efficiency and Stability with Multidimensional Perovskites, *ChemSusChem*. 11 (2018) 4193–4202. doi:10.1002/cssc.201801905.
- [36] E. Ruggeri, M. Anaya, K. Gałkowski, G. Delport, F.U. Kosasih, A. Abfalterer, S. Mackowski, C. Ducati, S.D. Stranks, Controlling the Growth Kinetics and Optoelectronic Properties of 2D/3D Lead–Tin Perovskite Heterojunctions, *Adv. Mater.* 31 (2019) 1905247. doi:10.1002/adma.201905247.
- [37] P. Szuromi, B. Grocholski, Natural and engineered perovskites, *Science*. 358 (2017) 732–733. doi:10.1126/science.358.6364.732.
- [38] F.-P. Boullay, Mémoire sur les Iodures doubles, *Ann. Chim. Phys.* 34 (1827) 337–380.
- [39] I. Remsen, G.M. Richardson, C.H. Herty, C.E. Saunders, C. Pliny Brigham, J.E. Gilpin, Researches on the Double Halides, *Am. Chem. J.* 14 (1892) 81–184.
- [40] H.L. Wells, On the caesium- and the potassium-lead halides, *Am. J. Sci.* s3-45 (1893) 121–134. doi:10.2475/ajs.s3-45.266.121.
- [41] C.K. Møller, A Phase Transition in Cæsium Plumbochloride, *Nature*. 180 (1957) 981–982. doi:10.1038/180981a0.
- [42] C.K. Møller, Crystal Structure and Photoconductivity of Caesium Plumbohalides, *Nature*. 182 (1958) 1436–1436. doi:10.1038/1821436a0.
- [43] D. Weber,  $\text{CH}_3\text{NH}_3\text{PbX}_3$ , ein Pb(II)-System mit kubischer Perowskitstruktur /  $\text{CH}_3\text{NH}_3\text{PbX}_3$ , a Pb(II)-System with Cubic Perovskite Structure, *Zeitschrift Für Naturforsch. B*. 33 (1978) 1443–1445. doi:10.1515/znb-1978-1214.
- [44] D. Weber,  $\text{CH}_3\text{NH}_3\text{SnBr}_x\text{I}_{3-x}$  ( $x = 0\text{--}3$ ), ein Sn(II)-System mit kubischer Perowskitstruktur /  $\text{CH}_3\text{NH}_3\text{SnBr}_x\text{I}_{3-x}$  ( $x = 0\text{--}3$ ), a Sn(II)-System with Cubic Perovskite Structure, *Zeitschrift Für Naturforsch. B*. 33 (1978) 862–865. doi:10.1515/znb-1978-0809.
- [45] D.B. Mitzi, C.A. Feild, Z. Schlesinger, R.B. Laibowitz, Transport, Optical, and Magnetic Properties of the Conducting Halide Perovskite  $\text{CH}_3\text{NH}_3\text{SnI}_3$ , *J. Solid State Chem.* 114 (1995) 159–163. doi:10.1006/jssc.1995.1023.

- [46] D.B. Mitzi, S. Wang, C.A. Feild, C.A. Chess, A.M. Guloy, Conducting Layered Organic-inorganic Halides Containing <110>-Oriented Perovskite Sheets, *Science*. 267 (1995) 1473–1476. doi:10.1126/science.267.5203.1473.
- [47] D.B. Mitzi, K. Liang, Synthesis, Resistivity, and Thermal Properties of the Cubic Perovskite  $\text{NH}_2\text{CH}=\text{NH}_2\text{SnI}_3$  and Related Systems, *J. Solid State Chem.* 134 (1997) 376–381. doi:10.1006/jssc.1997.7593.
- [48] D.B. Mitzi, Synthesis, Structure, and Properties of Organic-Inorganic Perovskites and Related Materials, in: K.D. Karlin (Ed.), *Prog. Inorg. Chem.*, Volume 48, John Wiley & Sons, 2007: pp. 1–121. doi:10.1002/9780470166499.ch1.
- [49] A. Kojima, K. Teshima, Y. Shirai, T. Miyasaka, Organometal Halide Perovskites as Visible-Light Sensitizers for Photovoltaic Cells, *J Am Chem Soc.* 131 (2009) 6050–6051. doi:10.1021/ja809598r.
- [50] H.S. Kim, C.R. Lee, J.H. Im, K.B. Lee, T. Moehl, A. Marchioro, S.J. Moon, R. Humphry-Baker, J.H. Yum, J.E. Moser, M. Grätzel, N.G. Park, Lead iodide perovskite sensitized all-solid-state submicron thin film mesoscopic solar cell with efficiency exceeding 9%, *Sci. Rep.* 2 (2012) 1–7. doi:10.1038/srep00591.
- [51] M.M. Lee, J. Teuscher, T. Miyasaka, T.N. Murakami, H.J. Snaith, Efficient Hybrid Solar Cells Based on Meso-Superstructured Organometal Halide Perovskites, *Science*. 338 (2012) 643–647. doi:10.1126/science.1228604.
- [52] M.A. Green, E.D. Dunlop, J. Hohl-Ebinger, M. Yoshita, N. Kopidakis, X. Hao, Solar cell efficiency tables (Version 58), *Prog. Photovoltaics Res. Appl.* 29 (2021) 657–667. doi:10.1002/pip.3444.
- [53] C. Li, X. Lu, W. Ding, L. Feng, Y. Gao, Z. Guo, Formability of  $\text{ABX}_3$  ( $\text{X} = \text{F}, \text{Cl}, \text{Br}, \text{I}$ ) halide perovskites, *Acta Crystallogr. Sect. B Struct. Sci.* 64 (2008) 702–707. doi:10.1107/S0108768108032734.
- [54] J.-P. Correa-Baena, M. Saliba, T. Buonassisi, M. Grätzel, A. Abate, W. Tress, A. Hagfeldt, Promises and challenges of perovskite solar cells, *Science*. 358 (2017) 739–744. doi:10.1126/science.aam6323.
- [55] M. Saliba, T. Matsui, J.-Y. Seo, K. Domanski, J.-P. Correa-Baena, M.K. Nazeeruddin, S.M. Zakeeruddin, W. Tress, A. Abate, A. Hagfeldt, M. Grätzel, Cesium-containing triple cation perovskite solar cells: improved stability, reproducibility and high efficiency, *Energy Environ. Sci.* 9 (2016) 1989–1997. doi:10.1039/C5EE03874J.

- [56] D.P. McMeekin, G. Sadoughi, W. Rehman, G.E. Eperon, M. Saliba, M.T. Horantner, A. Haghhighirad, N. Sakai, L. Korte, B. Rech, M.B. Johnston, L.M. Herz, H.J. Snaith, A mixed-cation lead mixed-halide perovskite absorber for tandem solar cells, *Science*. 351 (2016) 151–155. doi:10.1126/science.aad5845.
- [57] D.W. Ferdani, S.R. Pering, D. Ghosh, P. Kubiak, A.B. Walker, S.E. Lewis, A.L. Johnson, P.J. Baker, M.S. Islam, P.J. Cameron, Partial cation substitution reduces iodide ion transport in lead iodide perovskite solar cells, *Energy Environ. Sci.* 12 (2019) 2264–2272. doi:10.1039/C9EE00476A.
- [58] M. Saliba, T. Matsui, K. Domanski, J.-Y. Seo, A. Ummadisingu, S.M. Zakeeruddin, J.-P. Correa-Baena, W.R. Tress, A. Abate, A. Hagfeldt, M. Gratzel, Incorporation of rubidium cations into perovskite solar cells improves photovoltaic performance, *Science*. 354 (2016) 206–209. doi:10.1126/science.aah5557.
- [59] Y. Vaynzof, The Future of Perovskite Photovoltaics—Thermal Evaporation or Solution Processing?, *Adv. Energy Mater.* 10 (2020) 2003073. doi:10.1002/aenm.202003073.
- [60] M. Saliba, J.-P. Correa-Baena, C.M. Wolff, M. Stolterfoht, N. Phung, S. Albrecht, D. Neher, A. Abate, How to Make over 20% Efficient Perovskite Solar Cells in Regular (n–i–p) and Inverted (p–i–n) Architectures, *Chem. Mater.* 30 (2018) 4193–4201. doi:10.1021/acs.chemmater.8b00136.
- [61] P. Kaienburg, P. Hartnagel, B.E. Pieters, J. Yu, D. Grabowski, Z. Liu, J. Haddad, U. Rau, T. Kirchartz, How Contact Layers Control Shunting Losses from Pinholes in Thin-Film Solar Cells, *J. Phys. Chem. C*. 122 (2018) 27263–27272. doi:10.1021/acs.jpcc.8b09400.
- [62] A. Castro-Méndez, J. Hidalgo, J. Correa-Baena, The Role of Grain Boundaries in Perovskite Solar Cells, *Adv. Energy Mater.* 9 (2019) 1901489. doi:10.1002/aenm.201901489.
- [63] W. Shockley, H.J. Queisser, Detailed Balance Limit of Efficiency of p-n Junction Solar Cells, *J. Appl. Phys.* 32 (1961) 510–519. doi:10.1063/1.1736034.
- [64] J.-F. Guillemoles, T. Kirchartz, D. Cahen, U. Rau, Guide for the perplexed to the Shockley–Queisser model for solar cells, *Nat. Photonics*. 13 (2019) 501–505. doi:10.1038/s41566-019-0479-2.
- [65] A. Polman, M. Knight, E.C. Garnett, B. Ehrler, W.C. Sinke, Photovoltaic materials: Present efficiencies and future challenges, *Science*. 352 (2016) aad4424–aad4424. doi:10.1126/science.aad4424.

- [66] W.-J. Yin, T. Shi, Y. Yan, Superior Photovoltaic Properties of Lead Halide Perovskites: Insights from First-Principles Theory, *J. Phys. Chem. C.* 119 (2015) 5253–5264. doi:10.1021/jp512077m.
- [67] S. De Wolf, J. Holovsky, S.J. Moon, P. Löper, B. Niesen, M. Ledinsky, F.J. Haug, J.H. Yum, C. Ballif, Organometallic halide perovskites: Sharp optical absorption edge and its relation to photovoltaic performance, *J. Phys. Chem. Lett.* 5 (2014) 1035–1039. doi:10.1021/jz500279b.
- [68] K. Yoshikawa, H. Kawasaki, W. Yoshida, T. Irie, K. Konishi, K. Nakano, T. Uto, D. Adachi, M. Kanematsu, H. Uzu, K. Yamamoto, Silicon heterojunction solar cell with interdigitated back contacts for a photoconversion efficiency over 26%, *Nat. Energy.* 2 (2017) 17032. doi:10.1038/nenergy.2017.32.
- [69] M. Jeong, I.W. Choi, E.M. Go, Y. Cho, M. Kim, B. Lee, S. Jeong, Y. Jo, H.W. Choi, J. Lee, J.-H. Bae, S.K. Kwak, D.S. Kim, C. Yang, Stable perovskite solar cells with efficiency exceeding 24.8% and 0.3-V voltage loss, *Science.* 369 (2020) 1615–1620. doi:10.1126/science.abb7167.
- [70] A. Miyata, A. Mitioglu, P. Plochocka, O. Portugall, J.T.W. Wang, S.D. Stranks, H.J. Snaith, R.J. Nicholas, Direct measurement of the exciton binding energy and effective masses for charge carriers in organic-inorganic tri-halide perovskites, *Nat. Phys.* 11 (2015) 582–587. doi:10.1038/nphys3357.
- [71] Q. Lin, A. Armin, R.C.R. Nagiri, P.L. Burn, P. Meredith, Electro-optics of perovskite solar cells, *Nat. Photonics.* 9 (2015) 106–112. doi:10.1038/nphoton.2014.284.
- [72] L.M. Herz, Charge-Carrier Mobilities in Metal Halide Perovskites: Fundamental Mechanisms and Limits, *ACS Energy Lett.* 2 (2017) 1539–1548. doi:10.1021/acsenergylett.7b00276.
- [73] J. Peng, Y. Chen, K. Zheng, T. Pullerits, Z. Liang, Insights into charge carrier dynamics in organo-metal halide perovskites: from neat films to solar cells, *Chem. Soc. Rev.* 46 (2017) 5714–5729. doi:10.1039/C6CS00942E.
- [74] X. Yang, Y. Fu, R. Su, Y. Zheng, Y. Zhang, W. Yang, M. Yu, P. Chen, Y. Wang, J. Wu, D. Luo, Y. Tu, L. Zhao, Q. Gong, R. Zhu, Superior Carrier Lifetimes Exceeding 6  $\mu$ s in Polycrystalline Halide Perovskites, *Adv. Mater.* 32 (2020) 2002585. doi:10.1002/adma.202002585.
- [75] F. Zhang, B. Yang, X. Mao, R. Yang, L. Jiang, Y. Li, J. Xiong, Y. Yang, R. He, W. Deng, K. Han, Perovskite  $\text{CH}_3\text{NH}_3\text{PbI}_{3-x}\text{Br}_x$  Single Crystals with Charge-Carrier Lifetimes Exceeding 260  $\mu$ s, *ACS Appl. Mater. Interfaces.* 9 (2017) 14827–14832. doi:10.1021/acsami.7b01696.

- [76] Q. Dong, Y. Fang, Y. Shao, P. Mulligan, J. Qiu, L. Cao, J. Huang, Electron-hole diffusion lengths > 175  $\mu$ m in solution-grown  $\text{CH}_3\text{NH}_3\text{PbI}_3$  single crystals, *Science*. 347 (2015) 967–970. doi:10.1126/science.aaa5760.
- [77] L.M. Pazos-Outon, M. Szumilo, R. Lamboll, J.M. Richter, M. Crespo-Quesada, M. Abdi-Jalebi, H.J. Beeson, M. Vrini, M. Alsari, H.J. Snaith, B. Ehrler, R.H. Friend, F. Deschler, Photon recycling in lead iodide perovskite solar cells, *Science*. 351 (2016) 1430–1433. doi:10.1126/science.aaf1168.
- [78] R. Brenes, M. Laitz, J. Jean, D.W. DeQuilettes, V. Bulović, Benefit from Photon Recycling at the Maximum-Power Point of State-of-the-Art Perovskite Solar Cells, *Phys. Rev. Appl.* 12 (2019) 014017. doi:10.1103/PhysRevApplied.12.014017.
- [79] F. Staub, I. Anusca, D.C. Lupascu, U. Rau, T. Kirchartz, Effect of reabsorption and photon recycling on photoluminescence spectra and transients in lead-halide perovskite crystals, *J. Phys. Mater.* 3 (2020) 025003. doi:10.1088/2515-7639/ab6fd0.
- [80] S. Lee, K. Choi, C.H. Min, M.Y. Woo, J.H. Noh, Photon recycling in halide perovskite solar cells for higher efficiencies, *MRS Bull.* 45 (2020) 439–448. doi:10.1557/mrs.2020.145.
- [81] E. Mosconi, P. Umari, F. De Angelis, Electronic and optical properties of  $\text{MAPbX}_3$  perovskites ( $X = \text{I}, \text{Br}, \text{Cl}$ ): a unified DFT and GW theoretical analysis, *Phys. Chem. Chem. Phys.* 18 (2016) 27158–27164. doi:10.1039/C6CP03969C.
- [82] M. Saliba, Polyelemental, Multicomponent Perovskite Semiconductor Libraries through Combinatorial Screening, *Adv. Energy Mater.* 9 (2019) 1803754. doi:10.1002/aenm.201803754.
- [83] A. Amat, E. Mosconi, E. Ronca, C. Quarti, P. Umari, M.K. Nazeeruddin, M. Grätzel, F. De Angelis, Cation-Induced Band-Gap Tuning in Organohalide Perovskites: Interplay of Spin–Orbit Coupling and Octahedra Tilting, *Nano Lett.* 14 (2014) 3608–3616. doi:10.1021/nl5012992.
- [84] X. Zheng, A.Y. Alsalloum, Y. Hou, E.H. Sargent, O.M. Bakr, All-Perovskite Tandem Solar Cells: A Roadmap to Uniting High Efficiency with High Stability, *Accounts Mater. Res.* 1 (2020) 63–76. doi:10.1021/accountsmr.0c00017.
- [85] T. Jesper Jacobsson, J.-P. Correa-Baena, M. Pazoki, M. Saliba, K. Schenk, M. Grätzel, A. Hagfeldt, Exploration of the compositional space for mixed lead halogen perovskites for high efficiency solar cells, *Energy Environ. Sci.* 9 (2016) 1706–1724. doi:10.1039/C6EE00030D.

- [86] A. Swarnkar, A.R. Marshall, E.M. Sanehira, B.D. Chernomordik, D.T. Moore, J.A. Christians, T. Chakrabarti, J.M. Luther, Quantum dot-induced phase stabilization of  $\text{CsPbI}_3$  perovskite for high-efficiency photovoltaics, *Science*. 354 (2016) 92–95. doi:10.1126/science.aag2700.
- [87] M. Caputo, N. Cefarin, A. Radivo, N. Demitri, L. Gigli, J.R. Plaisier, M. Panighel, G. Di Santo, S. Moretti, A. Giglia, M. Polentarutti, F. De Angelis, E. Mosconi, P. Umari, M. Tormen, A. Goldoni, Electronic structure of  $\text{MAPbI}_3$  and  $\text{MAPbCl}_3$ : importance of band alignment, *Sci. Rep.* 9 (2019) 15159. doi:10.1038/s41598-019-50108-0.
- [88] H. Yu, F. Wang, F. Xie, W. Li, J. Chen, N. Zhao, The Role of Chlorine in the Formation Process of “ $\text{CH}_3\text{NH}_3\text{PbI}_{3-x}\text{Cl}_x$ ” Perovskite, *Adv. Funct. Mater.* 24 (2014) 7102–7108. doi:10.1002/adfm.201401872.
- [89] S. Colella, E. Mosconi, P. Fedeli, A. Listorti, F. Gazza, F. Orlandi, P. Ferro, T. Besagni, A. Rizzo, G. Calestani, G. Gigli, F. De Angelis, R. Mosca,  $\text{MAPbI}_{3-x}\text{Cl}_x$  Mixed Halide Perovskite for Hybrid Solar Cells: The Role of Chloride as Dopant on the Transport and Structural Properties, *Chem. Mater.* 25 (2013) 4613–4618. doi:10.1021/cm402919x.
- [90] T.A.S. Doherty, A.J. Winchester, S. Macpherson, D.N. Johnstone, V. Pareek, E.M. Tennyson, S. Kosar, F.U. Kosasih, M. Anaya, M. Abdi-Jalebi, Z. Andaji-Garmaroudi, E.L. Wong, J. Madeo, Y.-H. Chiang, J.-S. Park, Y.-K. Jung, C.E. Petoukhoff, G. Divitini, M.K.L. Man, C. Ducati, A. Walsh, P.A. Midgley, K.M. Dani, S.D. Stranks, Performance-limiting nanoscale trap clusters at grain junctions in halide perovskites, *Nature*. 580 (2020). doi:10.1038/s41586-020-2184-1.
- [91] M. Abdi-Jalebi, Z. Andaji-Garmaroudi, S. Cacovich, C. Stavrakas, B. Philippe, J.M. Richter, M. Alsari, E.P. Booker, E.M. Hutter, A.J. Pearson, S. Lilliu, T.J. Savenije, H. Rensmo, G. Divitini, C. Ducati, R.H. Friend, S.D. Stranks, Maximizing and stabilizing luminescence from halide perovskites with potassium passivation, *Nature*. 555 (2018) 497–501. doi:10.1038/nature25989.
- [92] G.E. Eperon, S.D. Stranks, C. Menelaou, M.B. Johnston, L.M. Herz, H.J. Snaith, Formamidinium lead trihalide: a broadly tunable perovskite for efficient planar heterojunction solar cells, *Energy Environ. Sci.* 7 (2014) 982. doi:10.1039/c3ee43822h.
- [93] T.M. Koh, K. Fu, Y. Fang, S. Chen, T.C. Sum, N. Mathews, S.G. Mhaisalkar, P.P. Boix, T. Baikie, Formamidinium-containing metal-halide: An alternative material for near-IR absorption perovskite solar cells, *J. Phys. Chem. C*. 118 (2014) 16458–16462. doi:10.1021/jp411112k.
- [94] N.J. Jeon, J.H. Noh, W.S. Yang, Y.C. Kim, S. Ryu, J. Seo, S. Il Seok, Compositional engineering of perovskite materials for high-performance solar cells, *Nature*. 517 (2015) 476–480. doi:10.1038/nature14133.

- [95] P. Liu, W. Wang, S. Liu, H. Yang, Z. Shao, Fundamental Understanding of Photocurrent Hysteresis in Perovskite Solar Cells, *Adv. Energy Mater.* 9 (2019) 1803017. doi:10.1002/aenm.201803017.
- [96] I. Levchuk, A. Osvet, X. Tang, M. Brandl, J.D. Perea, F. Hoegl, G.J. Matt, R. Hock, M. Batentschuk, C.J. Brabec, Brightly Luminescent and Color-Tunable Formamidinium Lead Halide Perovskite  $\text{FAPbX}_3$  ( $X = \text{Cl}, \text{Br}, \text{I}$ ) Colloidal Nanocrystals, *Nano Lett.* 17 (2017) 2765–2770. doi:10.1021/acs.nanolett.6b04781.
- [97] J.M. Ball, A. Petrozza, Defects in perovskite-halides and their effects in solar cells, *Nat. Energy*. 1 (2016) 16149. doi:10.1038/nenergy.2016.149.
- [98] C. Battaglia, A. Cuevas, S. De Wolf, High-efficiency crystalline silicon solar cells: status and perspectives, *Energy Environ. Sci.* 9 (2016) 1552–1576. doi:10.1039/C5EE03380B.
- [99] C.L. Andre, D.M. Wilt, A.J. Pitera, M.L. Lee, E.A. Fitzgerald, S.A. Ringel, Impact of dislocation densities on n+/p and p+/n junction GaAs diodes and solar cells on SiGe virtual substrates, *J. Appl. Phys.* 98 (2005) 014502. doi:10.1063/1.1946194.
- [100] W.S. Yang, B. Park, E.H. Jung, N.J. Jeon, Iodide management in formamidinium-lead-halide – based perovskite layers for efficient solar cells, *Science*. 356 (2017) 1376–1379. doi:10.1126/science.aan2301.
- [101] S.D. Stranks, V.M. Burlakov, T. Leijtens, J.M. Ball, A. Goriely, H.J. Snaith, Recombination Kinetics in Organic-Inorganic Perovskites: Excitons, Free Charge, and Subgap States, *Phys. Rev. Appl.* 2 (2014) 034007. doi:10.1103/PhysRevApplied.2.034007.
- [102] L.K. Ono, S. (Frank) Liu, Y. Qi, Reducing Detrimental Defects for High-Performance Metal Halide Perovskite Solar Cells, *Angew. Chemie Int. Ed.* 59 (2020) 6676–6698. doi:10.1002/anie.201905521.
- [103] M. V. Kovalenko, L. Protesescu, M.I. Bodnarchuk, Properties and potential optoelectronic applications of lead halide perovskite nanocrystals, *Science*. 358 (2017) 745–750. doi:10.1126/science.aam7093.
- [104] P. Umari, E. Mosconi, F. De Angelis, Relativistic GW calculations on  $\text{CH}_3\text{NH}_3\text{PbI}_3$  and  $\text{CH}_3\text{NH}_3\text{SnI}_3$  Perovskites for Solar Cell Applications, *Sci. Rep.* 4 (2014) 1–7. doi:10.1038/srep04467.
- [105] D. Meggiolaro, S.G. Motti, E. Mosconi, A.J. Barker, J. Ball, C. Andrea Riccardo Perini, F. Deschler, A. Petrozza, F. De Angelis, Iodine chemistry determines the defect tolerance of lead-halide perovskites, *Energy Environ. Sci.* 11 (2018) 702–713. doi:10.1039/C8EE00124C.

- [106] S.G. Motti, D. Meggiolaro, S. Martani, R. Sorrentino, A.J. Barker, F. De Angelis, A. Petrozza, Defect Activity in Lead Halide Perovskites, *Adv. Mater.* 31 (2019) 1901183. doi:10.1002/adma.201901183.
- [107] D. Shi, V. Adinolfi, R. Comin, M. Yuan, E. Alarousu, A. Buin, Y. Chen, S. Hoogland, A. Rothenberger, K. Katsiev, Y. Losovyj, X. Zhang, P.A. Dowben, O.F. Mohammed, E.H. Sargent, O.M. Bakr, Low trap-state density and long carrier diffusion in organolead trihalide perovskite single crystals, *Science*. 347 (2015) 519–522. doi:10.1126/science.aaa2725.
- [108] W.-J. Yin, T. Shi, Y. Yan, Unique Properties of Halide Perovskites as Possible Origins of the Superior Solar Cell Performance, *Adv. Mater.* 26 (2014) 4653–4658. doi:10.1002/adma.201306281.
- [109] X. Zhang, M.E. Turiansky, C.G. Van de Walle, Correctly Assessing Defect Tolerance in Halide Perovskites, *J. Phys. Chem. C*. 124 (2020) 6022–6027. doi:10.1021/acs.jpcc.0c01324.
- [110] O. Gunawan, S.R. Pae, D.M. Bishop, Y. Virgus, J.H. Noh, N.J. Jeon, Y.S. Lee, X. Shao, T. Todorov, D.B. Mitzi, Carrier-resolved photo-Hall effect, *Nature*. 575 (2019). doi:10.1038/s41586-019-1632-2.
- [111] O.J. Sandberg, J. Kurpiers, M. Stolterfoht, D. Neher, P. Meredith, S. Shoae, A. Armin, On the Question of the Need for a Built-In Potential in Perovskite Solar Cells, *Adv. Mater. Interfaces*. 7 (2020) 2000041. doi:10.1002/admi.202000041.
- [112] T. Kirchartz, J. Bisquert, I. Mora-Sero, G. Garcia-Belmonte, Classification of solar cells according to mechanisms of charge separation and charge collection, *Phys. Chem. Chem. Phys.* 17 (2015) 4007–4014. doi:10.1039/C4CP05174B.
- [113] S. Ravishankar, S. Gharibzadeh, C. Roldán-Carmona, G. Grancini, Y. Lee, M. Ralaiarisoa, A.M. Asiri, N. Koch, J. Bisquert, M.K. Nazeeruddin, Influence of Charge Transport Layers on Open-Circuit Voltage and Hysteresis in Perovskite Solar Cells, *Joule*. (2018). doi:10.1016/j.joule.2018.02.013.
- [114] S.D. Stranks, G.E. Eperon, G. Grancini, C. Menelaou, M.J.P. Alcocer, T. Leijtens, L.M. Herz, A. Petrozza, H.J. Snaith, Electron-Hole Diffusion Lengths Exceeding 1 Micrometer in an Organometal Trihalide Perovskite Absorber, *Science*. 342 (2014) 341–344. doi:10.1126/science.1243982.
- [115] C. Zuo, H.J. Bolink, H. Han, J. Huang, D. Cahen, L. Ding, Advances in Perovskite Solar Cells, *Adv. Sci.* 3 (2016) 1500324. doi:10.1002/advs.201500324.

- [116] B. Ehrler, E. Alarcón-Lladó, S.W. Tabernig, T. Veeken, E.C. Garnett, A. Polman, Photovoltaics Reaching for the Shockley–Queisser Limit, *ACS Energy Lett.* 5 (2020) 3029–3033. doi:10.1021/acsenergylett.0c01790.
- [117] J.-H. Im, C.-R. Lee, J.-W. Lee, S.-W. Park, N.-G. Park, 6.5% efficient perovskite quantum-dot-sensitized solar cell, *Nanoscale*. 3 (2011) 4088. doi:10.1039/c1nr10867k.
- [118] J.-H. Im, I.-H. Jang, N. Pellet, M. Grätzel, N.-G. Park, Growth of  $\text{CH}_3\text{NH}_3\text{PbI}_3$  cuboids with controlled size for high-efficiency perovskite solar cells, *Nat. Nanotechnol.* 9 (2014) 927–932. doi:10.1038/nnano.2014.181.
- [119] J.-W. Lee, D.-J. Seol, A.-N. Cho, N.-G. Park, High-Efficiency Perovskite Solar Cells Based on the Black Polymorph of  $\text{HC}(\text{NH}_2)_2\text{PbI}_3$ , *Adv. Mater.* 26 (2014) 4991–4998. doi:10.1002/adma.201401137.
- [120] J.H. Heo, S.H. Im, J.H. Noh, T.N. Mandal, C.-S. Lim, J.A. Chang, Y.H. Lee, H. Kim, A. Sarkar, M.K. Nazeeruddin, M. Grätzel, S. Il Seok, Efficient inorganic–organic hybrid heterojunction solar cells containing perovskite compound and polymeric hole conductors, *Nat. Photonics*. 7 (2013) 486–491. doi:10.1038/nphoton.2013.80.
- [121] G.E. Eperon, V.M. Burlakov, P. Docampo, A. Goriely, H.J. Snaith, Morphological Control for High Performance, Solution-Processed Planar Heterojunction Perovskite Solar Cells, *Adv. Funct. Mater.* 24 (2014) 151–157. doi:10.1002/adfm.201302090.
- [122] Y. Rong, Y. Hu, A. Mei, H. Tan, M.I. Saidaminov, S. Il Seok, M.D. McGehee, E.H. Sargent, H. Han, Challenges for commercializing perovskite solar cells, *Science*. 361 (2018) eaat8235. doi:10.1126/science.aat8235.
- [123] J.-Y.Y. Jeng, Y.-F.F. Chiang, M.-H.H. Lee, S.-R.R. Peng, T.-F.F. Guo, P. Chen, T.-C.C. Wen,  $\text{CH}_3\text{NH}_3\text{PbI}_3$  Perovskite/Fullerene Planar-Heterojunction Hybrid Solar Cells, *Adv. Mater.* 25 (2013) 3727–3732. doi:10.1002/adma.201301327.
- [124] J.J. Yoo, G. Seo, M.R. Chua, T.G. Park, Y. Lu, F. Rotermund, Y.-K. Kim, C.S. Moon, N.J. Jeon, J.-P. Correa-Baena, V. Bulović, S.S. Shin, M.G. Bawendi, J. Seo, Efficient perovskite solar cells via improved carrier management, *Nature*. 590 (2021) 587–593. doi:10.1038/s41586-021-03285-w.
- [125] X. Zheng, Y. Hou, C. Bao, J. Yin, F. Yuan, Z. Huang, K. Song, J. Liu, J. Troughton, N. Gasparini, C. Zhou, Y. Lin, D.J. Xue, B. Chen, A.K. Johnston, N. Wei, M.N. Hedhili, M. Wei, A.Y. Alsalloum, P. Maity, B. Turedi, C. Yang, D. Baran, T.D. Anthopoulos, Y. Han, Z.H. Lu, O.F. Mohammed, F. Gao, E.H. Sargent, O.M. Bakr, Managing grains and interfaces via ligand anchoring enables 22.3%-efficiency inverted perovskite solar cells, *Nat. Energy*. 5 (2020) 131–

140. doi:10.1038/s41560-019-0538-4.

- [126] D. Kang, N. Park, On the Current–Voltage Hysteresis in Perovskite Solar Cells: Dependence on Perovskite Composition and Methods to Remove Hysteresis, *Adv. Mater.* 31 (2019) 1805214. doi:10.1002/adma.201805214.
- [127] L. Meng, J. You, T.-F. Guo, Y. Yang, Recent Advances in the Inverted Planar Structure of Perovskite Solar Cells, *Acc. Chem. Res.* 49 (2016) 155–165. doi:10.1021/acs.accounts.5b00404.
- [128] J. Zhang, W. Zhang, H.-M. Cheng, S.R.P. Silva, Critical review of recent progress of flexible perovskite solar cells, *Mater. Today* 39 (2020) 66–88. doi:10.1016/j.mattod.2020.05.002.
- [129] J. Werner, B. Niesen, C. Ballif, Perovskite/Silicon Tandem Solar Cells: Marriage of Convenience or True Love Story? – An Overview, *Adv. Mater. Interfaces* 5 (2018) 1700731. doi:10.1002/admi.201700731.
- [130] A. Mei, X. Li, L. Liu, Z. Ku, T. Liu, Y. Rong, M. Xu, M. Hu, J. Chen, Y. Yang, M. Gratzel, H. Han, A hole-conductor-free, fully printable mesoscopic perovskite solar cell with high stability, *Science*. 345 (2014) 295–298. doi:10.1126/science.1254763.
- [131] I. Zimmermann, P. Gratia, D. Martineau, G. Grancini, J.-N. Audinot, T. Wirtz, M.K. Nazeeruddin, Improved efficiency and reduced hysteresis in ultra-stable fully printable mesoscopic perovskite solar cells through incorporation of CuSCN into the perovskite layer, *J. Mater. Chem. A*. 7 (2019) 8073–8077. doi:10.1039/C9TA00669A.
- [132] T.S. Sherkar, C. Momblona, L. Gil-Escríg, J. Ávila, M. Sessolo, H.J. Bolink, L.J.A. Koster, Recombination in Perovskite Solar Cells: Significance of Grain Boundaries, Interface Traps, and Defect Ions, *ACS Energy Lett.* 2 (2017) 1214–1222. doi:10.1021/acsenergylett.7b00236.
- [133] D. Głowienka, D. Zhang, F. Di Giacomo, M. Najafi, S. Veenstra, J. Szmytkowski, Y. Galagan, Role of surface recombination in perovskite solar cells at the interface of HTL/CH<sub>3</sub>NH<sub>3</sub>PbI<sub>3</sub>, *Nano Energy*. 67 (2020) 104186. doi:10.1016/j.nanoen.2019.104186.
- [134] D. Di Girolamo, F. Matteocci, F.U. Kosasih, G. Chistiakova, W. Zuo, G. Divitini, L. Korte, C. Ducati, A. Di Carlo, D. Dini, A. Abate, Stability and Dark Hysteresis Correlate in NiO-Based Perovskite Solar Cells, *Adv. Energy Mater.* 9 (2019) 1901642. doi:10.1002/aenm.201901642.
- [135] Y. Chen, H. Zhou, Defects chemistry in high-efficiency and stable perovskite solar cells, *J. Appl. Phys.* 128 (2020) 060903. doi:10.1063/5.0012384.
- [136] H. Xie, Z. Wang, Z. Chen, C. Pereyra, M. Pols, K. Galkowski, M. Anaya, S. Fu, X. Jia, P. Tang, D.J. Kubicki, A. Agarwalla, H.-S. Kim, D. Prochowicz, X. Borrisé, M. Bonn, C. Bao, X. Sun, S.M. Zakeeruddin, L. Emsley, J. Arbiol, F. Gao, F. Fu, H.I. Wang, K.-J. Tielrooij, S.D. Stranks,

- S. Tao, M. Grätzel, A. Hagfeldt, M. Lira-Cantu, Decoupling the effects of defects on efficiency and stability through phosphonates in stable halide perovskite solar cells, Joule. 5 (2021) 1246–1266. doi:10.1016/j.joule.2021.04.003.
- [137] C. Eames, J.M. Frost, P.R.F. Barnes, B.C. O'Regan, A. Walsh, M.S. Islam, Ionic transport in hybrid lead iodide perovskite solar cells, Nat. Commun. 6 (2015) 7497. doi:10.1038/ncomms8497.
- [138] D. Meggiolaro, E. Mosconi, F. De Angelis, Formation of Surface Defects Dominates Ion Migration in Lead-Halide Perovskites, ACS Energy Lett. 4 (2019) 779–785. doi:10.1021/acsenergylett.9b00247.
- [139] Y. Shao, Y. Fang, T. Li, Q. Wang, Q. Dong, Y. Deng, Y. Yuan, H. Wei, M. Wang, A. Gruverman, J. Shield, J. Huang, Grain boundary dominated ion migration in polycrystalline organic-inorganic halide perovskite films, Energy Environ. Sci. 9 (2016) 1752–1759. doi:10.1039/C6EE00413J.
- [140] N. Ahn, K. Kwak, M.S. Jang, H. Yoon, B.Y. Lee, J.-K. Lee, P. V. Pikhitsa, J. Byun, M. Choi, Trapped charge-driven degradation of perovskite solar cells, Nat. Commun. 7 (2016) 13422. doi:10.1038/ncomms13422.
- [141] Q. Wang, B. Chen, Y. Liu, Y. Deng, Y. Bai, Q. Dong, J. Huang, Scaling behavior of moisture-induced grain degradation in polycrystalline hybrid perovskite thin films, Energy Environ. Sci. 10 (2017) 516–522. doi:10.1039/C6EE02941H.
- [142] N. Aristidou, C. Eames, I. Sanchez-Molina, X. Bu, J. Kosco, M.S. Islam, S.A. Haque, Fast oxygen diffusion and iodide defects mediate oxygen-induced degradation of perovskite solar cells, Nat. Commun. 8 (2017) 15218. doi:10.1038/ncomms15218.
- [143] Y. Liu, Z. Yang, D. Cui, X. Ren, J. Sun, X. Liu, J. Zhang, Q. Wei, H. Fan, F. Yu, X. Zhang, C. Zhao, S.F. Liu, Two-Inch-Sized Perovskite  $\text{CH}_3\text{NH}_3\text{PbX}_3$  ( $\text{X} = \text{Cl}, \text{Br}, \text{I}$ ) Crystals: Growth and Characterization, Adv. Mater. 27 (2015) 5176–5183. doi:10.1002/adma.201502597.
- [144] L. Fu, H. Li, L. Wang, R. Yin, B. Li, L. Yin, Defect passivation strategies in perovskites for an enhanced photovoltaic performance, Energy Environ. Sci. 13 (2020) 4017–4056. doi:10.1039/D0EE01767A.
- [145] X. Zheng, B. Chen, J. Dai, Y. Fang, Y. Bai, Y. Lin, H. Wei, X.C. Zeng, J. Huang, Defect passivation in hybrid perovskite solar cells using quaternary ammonium halide anions and cations, Nat. Energy. 2 (2017) 17102. doi:10.1038/nenergy.2017.102.

- [146] B. Chen, P.N. Rudd, S. Yang, Y. Yuan, J. Huang, Imperfections and their passivation in halide perovskite solar cells, *Chem. Soc. Rev.* 48 (2019) 3842–3867. doi:10.1039/C8CS00853A.
- [147] I.M. Asuo, D. Gedamu, N.Y. Doumon, I. Ka, A. Pignolet, S.G. Cloutier, R. Nechache, Ambient condition-processing strategy for improved air-stability and efficiency in mixed-cation perovskite solar cells, *Mater. Adv.* 1 (2020) 1866–1876. doi:10.1039/D0MA00528B.
- [148] N. Guo, T. Zhang, G. Li, F. Xu, X. Qian, Y. Zhao, A simple fabrication of  $\text{CH}_3\text{NH}_3\text{PbI}_3$  perovskite for solar cells using low-purity  $\text{PbI}_2$ , *J. Semicond.* 38 (2017) 014004. doi:10.1088/1674-4926/38/1/014004.
- [149] N. Ahn, S.M. Kang, J.-W. Lee, M. Choi, N.-G. Park, Thermodynamic regulation of  $\text{CH}_3\text{NH}_3\text{PbI}_3$  crystal growth and its effect on photovoltaic performance of perovskite solar cells, *J. Mater. Chem. A.* 3 (2015) 19901–19906. doi:10.1039/C5TA03990H.
- [150] C. Liu, Y.-B. Cheng, Z. Ge, Understanding of perovskite crystal growth and film formation in scalable deposition processes, *Chem. Soc. Rev.* 49 (2020) 1653–1687. doi:10.1039/C9CS00711C.
- [151] N.J. Jeon, J.H. Noh, Y.C. Kim, W.S. Yang, S. Ryu, S. Il Seok, Solvent engineering for high-performance inorganic–organic hybrid perovskite solar cells, *Nat. Mater.* 13 (2014) 897–903. doi:10.1038/nmat4014.
- [152] H. Yu, X. Liu, Y. Xia, Q. Dong, K. Zhang, Z. Wang, Y. Zhou, B. Song, Y. Li, Room-temperature mixed-solvent-vapor annealing for high performance perovskite solar cells, *J. Mater. Chem. A.* 4 (2016) 321–326. doi:10.1039/C5TA08565A.
- [153] M. Jung, S.-G. Ji, G. Kim, S. Il Seok, Perovskite precursor solution chemistry: from fundamentals to photovoltaic applications, *Chem. Soc. Rev.* 48 (2019) 2011–2038. doi:10.1039/C8CS00656C.
- [154] S. Sánchez, J. Jerónimo-Rendon, M. Saliba, A. Hagfeldt, Highly efficient and rapid manufactured perovskite solar cells via Flash InfraRed Annealing, *Mater. Today.* 35 (2020) 9–15. doi:10.1016/j.mattod.2019.11.003.
- [155] H. Wang, F.U. Kosasih, H. Yu, G. Zheng, J. Zhang, G. Pozina, Y. Liu, C. Bao, Z. Hu, X. Liu, L. Kobera, S. Abbrent, J. Brus, Y. Jin, M. Fahlman, R.H. Friend, C. Ducati, X.-K. Liu, F. Gao, Perovskite-molecule composite thin films for efficient and stable light-emitting diodes, *Nat. Commun.* 11 (2020) 891. doi:10.1038/s41467-020-14747-6.
- [156] R. Vidal, J.-A. Alberola-Borràs, S.N. Habisreutinger, J.-L. Gimeno-Molina, D.T. Moore, T.H. Schloemer, I. Mora-Seró, J.J. Berry, J.M. Luther, Assessing health and environmental impacts

- of solvents for producing perovskite solar cells, *Nat. Sustain.* 4 (2021) 277–285. doi:10.1038/s41893-020-00645-8.
- [157] K. Higgins, M. Ziatdinov, S. V. Kalinin, M. Ahmadi, High-Throughput Study of Antisolvents on the Stability of Multicomponent Metal Halide Perovskites through Robotics-Based Synthesis and Machine Learning Approaches, *ArXiv*. (2021).
- [158] K. Higgins, S.M. Valletti, M. Ziatdinov, S. V. Kalinin, M. Ahmadi, Chemical Robotics Enabled Exploration of Stability in Multicomponent Lead Halide Perovskites via Machine Learning, *ACS Energy Lett.* 5 (2020) 3426–3436. doi:10.1021/acsenergylett.0c01749.
- [159] J. Kirman, A. Johnston, D.A. Kuntz, M. Askerka, Y. Gao, P. Todorović, D. Ma, G.G. Privé, E.H. Sargent, Machine-Learning-Accelerated Perovskite Crystallization, *Matter.* 2 (2020) 938–947. doi:10.1016/j.matt.2020.02.012.
- [160] E. Gu, X. Tang, S. Langner, P. Duchstein, Y. Zhao, I. Levchuk, V. Kalancha, T. Stubhan, J. Hauch, H.J. Egelhaaf, D. Zahn, A. Osvet, C.J. Brabec, Robot-Based High-Throughput Screening of Antisolvents for Lead Halide Perovskites, *Joule.* 4 (2020) 1806–1822. doi:10.1016/j.joule.2020.06.013.
- [161] Z. Li, M.A. Najeeb, L. Alves, A.Z. Sherman, V. Shekar, P. Cruz Parrilla, I.M. Pendleton, W. Wang, P.W. Nega, M. Zeller, J. Schrier, A.J. Norquist, E.M. Chan, Robot-Accelerated Perovskite Investigation and Discovery, *Chem. Mater.* 32 (2020) 5650–5663. doi:10.1021/acs.chemmater.0c01153.
- [162] Y. Zhao, J. Zhang, Z. Xu, S. Sun, S. Langner, N.T.P. Hartono, T. Heumueller, Y. Hou, J. Elia, N. Li, G.J. Matt, X. Du, W. Meng, A. Osvet, K. Zhang, T. Stubhan, Y. Feng, J. Hauch, E.H. Sargent, T. Buonassisi, C.J. Brabec, Discovery of temperature-induced stability reversal in perovskites using high-throughput robotic learning, *Nat. Commun.* 12 (2021) 2191. doi:10.1038/s41467-021-22472-x.
- [163] S. Rahmany, L. Etgar, Semitransparent Perovskite Solar Cells, *ACS Energy Lett.* 5 (2020) 1519–1531. doi:10.1021/acsenergylett.0c00417.
- [164] H. Wang, J. Li, H.A. Dewi, N. Mathews, S. Mhaisalkar, A. Bruno, Colorful Perovskite Solar Cells: Progress, Strategies, and Potentials, *J. Phys. Chem. Lett.* (2021) 1321–1329. doi:10.1021/acs.jpclett.0c03445.
- [165] Y. Galagan, E.W.C. Coenen, W.J.H. Verhees, R. Andriessen, Towards the scaling up of perovskite solar cells and modules, *J. Mater. Chem. A.* 4 (2016) 5700–5705. doi:10.1039/C6TA01134A.

- [166] R. Swartwout, M.T. Hoerantner, V. Bulović, Scalable Deposition Methods for Large-area Production of Perovskite Thin Films, *ENERGY Environ. Mater.* 2 (2019) 119–145. doi:10.1002/eem2.12043.
- [167] M. Yang, Z. Li, M.O. Reese, O.G. Reid, D.H. Kim, S. Siol, T.R. Klein, Y. Yan, J.J. Berry, M.F.A.M. van Hest, K. Zhu, Perovskite ink with wide processing window for scalable high-efficiency solar cells, *Nat. Energy*. 2 (2017) 17038. doi:10.1038/nenergy.2017.38.
- [168] Y. Galagan, Perovskite Solar Cells: Toward Industrial-Scale Methods, *J. Phys. Chem. Lett.* (2018) 4326–4335. doi:10.1021/acs.jpclett.8b01356.
- [169] J. Gong, S.B. Darling, F. You, Perovskite photovoltaics: life-cycle assessment of energy and environmental impacts, *Energy Environ. Sci.* 8 (2015) 1953–1968. doi:10.1039/C5EE00615E.
- [170] T. Ibn-Mohammed, S.C.L. Koh, I.M. Reaney, A. Acquaye, G. Schileo, K.B. Mustapha, R. Greenough, Perovskite solar cells: An integrated hybrid lifecycle assessment and review in comparison with other photovoltaic technologies, *Renew. Sustain. Energy Rev.* 80 (2017) 1321–1344. doi:10.1016/j.rser.2017.05.095.
- [171] H. Sarialtin, R. Geyer, C. Zafer, Life cycle assessment of hole transport free planar–mesoscopic perovskite solar cells, *J. Renew. Sustain. Energy*. 12 (2020) 023502. doi:10.1063/1.5129784.
- [172] G. Mincuzzi, A.L. Palma, A. Di Carlo, T.M. Brown, Laser Processing in the Manufacture of Dye-Sensitized and Perovskite Solar Cell Technologies, *ChemElectroChem*. 3 (2016) 9–30. doi:10.1002/celc.201500389.
- [173] F. Di Giacomo, L.A. Castriotta, F.U. Kosasih, D. Di Girolamo, C. Ducati, A. Di Carlo, Upscaling Inverted Perovskite Solar Cells: Optimization of Laser Scribing for Highly Efficient Mini-Modules, *Micromachines*. 11 (2020) 1127. doi:10.3390/mi11121127.
- [174] A. Walter, S.-J. Moon, B.A. Kamino, L. Lofgren, D. Sacchetto, F. Matteucci, B. Taheri, J. Bailat, A. Di Carlo, C. Ballif, S. Nicolay, Closing the Cell-to-Module Efficiency Gap: A Fully Laser Scribed Perovskite Minimodule With 16% Steady-State Aperture Area Efficiency, *IEEE J. Photovoltaics*. 8 (2018) 151–155. doi:10.1109/JPHOTOV.2017.2765082.
- [175] A.L. Palma, F. Matteucci, A. Agresti, S. Pescetelli, E. Calabro, L. Vesce, S. Christiansen, M. Schmidt, A. Di Carlo, Laser-Patterning Engineering for Perovskite Solar Modules With 95% Aperture Ratio, *IEEE J. Photovoltaics*. 7 (2017) 1674–1680. doi:10.1109/JPHOTOV.2017.2732223.
- [176] H. Booth, Laser Processing in Industrial Solar Module Manufacturing, *JLMN-Journal of Laser Micro/Nanoengineering*. 5 (2010). doi:10.2961/jlmn.2010.03.0001.

- [177] L. Rakocevic, R. Gehlhaar, T. Merckx, W. Qiu, U.W. Paetzold, H. Fledderus, J. Poortmans, Interconnection Optimization for Highly Efficient Perovskite Modules, *IEEE J. Photovoltaics*. 7 (2017) 404–408. doi:10.1109/JPHOTOV.2016.2626144.
- [178] F.U. Kosasih, L. Rakocevic, T. Aernouts, J. Poortmans, C. Ducati, Electron Microscopy Characterization of P3 Lines and Laser Scribing-Induced Perovskite Decomposition in Perovskite Solar Modules, *ACS Appl. Mater. Interfaces*. 11 (2019) 45646–45655. doi:10.1021/acsami.9b15520.
- [179] J. Li, H.A. Dewi, H. Wang, J.H. Lew, N. Mathews, S. Mhaisalkar, A. Bruno, Design of Perovskite Thermally Co-Evaporated Highly Efficient Mini-Modules with High Geometrical Fill Factors, *Sol. RRL*. 4 (2020). doi:10.1002/solr.202000473.
- [180] L. Rakocevic, G. Schöpe, B. Turan, J. Genoe, T. Aernouts, S. Haas, R. Gehlhaar, J. Poortmans, Perovskite modules with 99% geometrical fill factor using point contact interconnections design, *Prog. Photovoltaics Res. Appl.* 28 (2020) 1120–1127. doi:10.1002/pip.3312.
- [181] K. Domanski, J.P. Correa-Baena, N. Mine, M.K. Nazeeruddin, A. Abate, M. Saliba, W. Tress, A. Hagfeldt, M. Grätzel, Not All That Glitters Is Gold: Metal-Migration-Induced Degradation in Perovskite Solar Cells, *ACS Nano*. 10 (2016) 6306–6314. doi:10.1021/acsnano.6b02613.
- [182] S. Cacovich, L. Ciná, F. Matteocci, G. Divitini, P.A. Midgley, A. Di Carlo, C. Ducati, Gold and iodine diffusion in large area perovskite solar cells under illumination, *Nanoscale*. 9 (2017) 4700–4706. doi:10.1039/C7NR00784A.
- [183] E. Carpene, D. Hoche, P. Schaaf, Fundamentals of Laser-Material Interactions, in: P. Schaaf (Ed.), *Laser Process. Mater.*, Springer, Berlin, 2010: pp. 21–47. doi:10.1007/978-3-642-13281-0\_3.
- [184] D. Bäuerle, Thermal, Photophysical, and Photochemical Processes, in: *Laser Process. Chem.*, Springer Berlin Heidelberg, Berlin, Heidelberg, 2011: pp. 13–38. doi:10.1007/978-3-642-17613-5\_2.
- [185] Y.L. Yao, H. Chen, W. Zhang, Time scale effects in laser material removal: a review, *Int. J. Adv. Manuf. Technol.* 26 (2005) 598–608. doi:10.1007/s00170-003-2026-y.
- [186] R.R. Gattass, E. Mazur, Femtosecond laser micromachining in transparent materials, *Nat. Photonics*. 2 (2008) 219–225. doi:10.1038/nphoton.2008.47.
- [187] K. Sugioka, Y. Cheng, Ultrafast lasers—reliable tools for advanced materials processing, *Light Sci. Appl.* 3 (2014) e149–e149. doi:10.1038/lsa.2014.30.

- [188] Y. Hirayama, M. Obara, Heat effects of metals ablated with femtosecond laser pulses, *Appl. Surf. Sci.* 197–198 (2002) 741–745. doi:10.1016/S0169-4332(02)00403-8.
- [189] B. Turan, A. Huuskonen, I. Kühn, T. Kirchartz, S. Haas, Cost-Effective Absorber Patterning of Perovskite Solar Cells by Nanosecond Laser Processing, *Sol. RRL*. 1 (2017) 1700003. doi:10.1002/solr.201700003.
- [190] S. Röttinger, B. Schwarz, S. Schäfer, R. Gauch, B. Zimmermann, U. Würfel, Laser patterning of vacuum processed small molecular weight organic photovoltaics, *Sol. Energy Mater. Sol. Cells.* 154 (2016) 35–41. doi:10.1016/j.solmat.2016.04.032.
- [191] B.N. Chichkov, C. Momma, S. Nolte, F. Yon Alvensleben, A. Tunnermann, Femtosecond, picosecond and nanosecond laser ablation of solids, *Appl. Phys. A*. 63 (1996) 109–115.
- [192] F. He, Y. Liao, J. Lin, J. Song, L. Qiao, Y. Cheng, K. Sugioka, Femtosecond Laser Fabrication of Monolithically Integrated Microfluidic Sensors in Glass, *Sensors*. 14 (2014) 19402–19440. doi:10.3390/s141019402.
- [193] L. Bayer, X. Ye, P. Lorenz, K. Zimmer, Studies on perovskite film ablation and scribing with ns-, ps- and fs-laser pulses, *Appl. Phys. A*. 123 (2017) 619. doi:10.1007/s00339-017-1234-5.
- [194] C. Schultz, F. Schneider, A. Neubauer, A. Bartelt, M. Jost, B. Rech, R. Schlatmann, S. Albrecht, B. Stegemann, Evidence of PbI<sub>2</sub>-Containing Debris Upon P2 Nanosecond Laser Patterning of Perovskite Solar Cells, *IEEE J. Photovoltaics*. 8 (2018) 1244–1251. doi:10.1109/JPHOTOV.2018.2858934.
- [195] L. Bayer, M. Ehrhardt, P. Lorenz, S. Pisoni, S. Buecheler, A.N. Tiwari, K. Zimmer, Morphology and topography of perovskite solar cell films ablated and scribed with short and ultrashort laser pulses, *Appl. Surf. Sci.* 416 (2017) 112–117. doi:10.1016/j.apsusc.2017.04.058.
- [196] E.M. Tennyson, T.A.S. Doherty, S.D. Stranks, Heterogeneity at multiple length scales in halide perovskite semiconductors, *Nat. Rev. Mater.* (2019) 1. doi:10.1038/s41578-019-0125-0.
- [197] S. Macpherson, T.A.S. Doherty, A.J. Winchester, S. Kosar, D.N. Johnstone, Y.-H. Chiang, K. Galkowski, M. Anaya, K. Frohma, A.N. Iqbal, B. Roose, Z. Andaji-Garmaroudi, P.A. Midgley, K.M. Dani, S.D. Stranks, Local Nanoscale Defective Phase Impurities Are the Sites of Degradation in Halide Perovskite Devices, ArXiv. (2021).
- [198] K. Frohma, M. Anaya, S. Macpherson, J. Sung, T.A.S. Doherty, Y.-H. Chiang, A.J. Winchester, K.M. Dani, A. Rao, S.D. Stranks, Nanoscale Chemical Heterogeneity Dominates the Optoelectronic Response over Local Electronic Disorder and Strain in Alloyed Perovskite Solar Cells, ArXiv. (2021).

- [199] T. Salim, S. Sun, Y. Abe, A. Krishna, A.C. Grimsdale, Y.M. Lam, Perovskite-based solar cells: impact of morphology and device architecture on device performance, *J. Mater. Chem. A*. 3 (2015) 8943–8969. doi:10.1039/C4TA05226A.
- [200] Y. Li, L. Ji, R. Liu, C. Zhang, C.H. Mak, X. Zou, H.-H. Shen, S.-Y. Leu, H.-Y. Hsu, A review on morphology engineering for highly efficient and stable hybrid perovskite solar cells, *J. Mater. Chem. A*. 6 (2018) 12842–12875. doi:10.1039/C8TA04120B.
- [201] N. Phung, A. Abate, The Impact of Nano- and Microstructure on the Stability of Perovskite Solar Cells, *Small*. 1802573 (2018) 1802573. doi:10.1002/smll.201802573.
- [202] W. Nie, H. Tsai, J.C. Blancon, F. Liu, C.C. Stoumpos, B. Traore, M. Kepenekian, O. Durand, C. Katan, S. Tretiak, J. Crochet, P.M. Ajayan, M. Kanatzidis, J. Even, A.D. Mohite, Critical Role of Interface and Crystallinity on the Performance and Photostability of Perovskite Solar Cell on Nickel Oxide, *Adv. Mater.* 30 (2018) 1–9. doi:10.1002/adma.201703879.
- [203] F. Matteocci, L. Vesce, F.U. Kosasih, L.A. Castriotta, S. Cacovich, A.L. Palma, G. Divitini, C. Ducati, A. Di Carlo, Fabrication and Morphological Characterization of High-Efficiency Blade-Coated Perovskite Solar Modules, *ACS Appl. Mater. Interfaces*. 11 (2019) 25195–25204. doi:10.1021/acsami.9b05730.
- [204] A. Sharenko, M.F. Toney, Relationships between Lead Halide Perovskite Thin-Film Fabrication, Morphology, and Performance in Solar Cells, *J. Am. Chem. Soc.* 138 (2016) 463–470. doi:10.1021/jacs.5b10723.
- [205] H. Sun, G.W.P. Adhyaksa, E.C. Garnett, The Application of Electron Backscatter Diffraction on Halide Perovskite Materials, *Adv. Energy Mater.* 10 (2020) 2000364. doi:10.1002/aenm.202000364.
- [206] M.U. Rothmann, W. Li, J. Etheridge, Y.-B. Cheng, Microstructural Characterisations of Perovskite Solar Cells – From Grains to Interfaces: Techniques, Features, and Challenges, *Adv. Energy Mater.* 7 (2017) 1700912. doi:10.1002/aenm.201700912.
- [207] M. Kodur, R.E. Kumar, Y. Luo, D.N. Cakan, X. Li, M. Stuckelberger, D.P. Fenning, X-Ray Microscopy of Halide Perovskites: Techniques, Applications, and Prospects, *Adv. Energy Mater.* 10 (2020) 1903170. doi:10.1002/aenm.201903170.
- [208] J. Schlipf, P. Müller-Buschbaum, Structure of Organometal Halide Perovskite Films as Determined with Grazing-Incidence X-Ray Scattering Methods, *Adv. Energy Mater.* 7 (2017) 1700131. doi:10.1002/aenm.201700131.

- [209] C. Wang, C. Zuo, Q. Chen, L. Ding, GIWAXS: A powerful tool for perovskite photovoltaics, *J. Semicond.* 42 (2021) 060201. doi:10.1088/1674-4926/42/6/060201.
- [210] I.C. Smith, E.T. Hoke, D. Solis-Ibarra, M.D. McGehee, H.I. Karunadasa, A Layered Hybrid Perovskite Solar-Cell Absorber with Enhanced Moisture Stability, *Angew. Chemie - Int. Ed.* 53 (2014) 11232–11235. doi:10.1002/anie.201406466.
- [211] T.L. Burnett, P.J. Withers, Completing the picture through correlative characterization, *Nat. Mater.* 18 (2019) 1041–1049. doi:10.1038/s41563-019-0402-8.
- [212] S.P. Harvey, J. Messinger, K. Zhu, J.M. Luther, J.J. Berry, Investigating the Effects of Chemical Gradients on Performance and Reliability within Perovskite Solar Cells with TOF-SIMS, *Adv. Energy Mater.* 10 (2020) 1903674. doi:10.1002/aenm.201903674.
- [213] J. Ran, O. Dyck, X. Wang, B. Yang, D.B. Geohegan, K. Xiao, Electron-Beam-Related Studies of Halide Perovskites: Challenges and Opportunities, *Adv. Energy Mater.* 10 (2020) 1903191. doi:10.1002/aenm.201903191.
- [214] Q. Sun, P. Fassl, Y. Vaynzof, Large-Scale Compositional and Electronic Inhomogeneities in  $\text{CH}_3\text{NH}_3\text{PbI}_3$ Perovskites and Their Effect on Device Performance, *ACS Appl. Energy Mater.* 1 (2018) 2410–2416. doi:10.1021/acsaem.8b00509.
- [215] R. Szostak, J.C. Silva, S.-H. Turren-Cruz, M.M. Soares, R.O. Freitas, A. Hagfeldt, H.C.N. Tolentino, A.F. Nogueira, Nanoscale mapping of chemical composition in organic-inorganic hybrid perovskite films, *Sci. Adv.* 5 (2019) eaaw6619. doi:10.1126/sciadv.aaw6619.
- [216] M. Ledinský, P. Löper, B. Niesen, J. Holovský, S.-J. Moon, J.-H. Yum, S. De Wolf, A. Fejfar, C. Ballif, Raman Spectroscopy of Organic–Inorganic Halide Perovskites, *J. Phys. Chem. Lett.* 6 (2015) 401–406. doi:10.1021/jz5026323.
- [217] N.A. Rivas, A. Babayigit, B. Conings, T. Schwarz, A. Sturm, A. Garzón Manjón, O. Cojocaru-Mirédin, B. Gault, F.U. Renner, Cryo-focused ion beam preparation of perovskite based solar cells for atom probe tomography, *PLoS One.* 15 (2020) e0227920. doi:10.1371/journal.pone.0227920.
- [218] J. Hidalgo, A. Castro-Méndez, J. Correa-Baena, Imaging and Mapping Characterization Tools for Perovskite Solar Cells, *Adv. Energy Mater.* 9 (2019) 1900444. doi:10.1002/aenm.201900444.
- [219] K. Song, L. Liu, D. Zhang, M.P. Hautzinger, S. Jin, Y. Han, Atomic-Resolution Imaging of Halide Perovskites Using Electron Microscopy, *Adv. Energy Mater.* 10 (2020) 1904006. doi:10.1002/aenm.201904006.

- [220] M. Kim, S. Ham, D. Cheng, T.A. Wynn, H.S. Jung, Y.S. Meng, Advanced Characterization Techniques for Overcoming Challenges of Perovskite Solar Cell Materials, *Adv. Energy Mater.* 11 (2021) 2001753. doi:10.1002/aenm.202001753.
- [221] L.A. Muscarella, E.M. Hutter, S. Sanchez, C.D. Dieleman, T.J. Savenije, A. Hagfeldt, M. Saliba, B. Ehrler, Crystal Orientation and Grain Size: Do They Determine Optoelectronic Properties of  $\text{MAPbI}_3$  Perovskite?, *J. Phys. Chem. Lett.* 10 (2019) 6010–6018. doi:10.1021/acs.jpclett.9b02757.
- [222] B. Yang, O. Dyck, W. Ming, M.-H. Du, S. Das, C.M. Rouleau, G. Duscher, D.B. Geohegan, K. Xiao, Observation of Nanoscale Morphological and Structural Degradation in Perovskite Solar Cells by in Situ TEM, *ACS Appl. Mater. Interfaces.* 8 (2016) 32333–32340. doi:10.1021/acsami.6b11341.
- [223] K. Li, J. Liu, C.R.M. Grovenor, K.L. Moore, NanoSIMS Imaging and Analysis in Materials Science, *Annu. Rev. Anal. Chem.* 13 (2020) 273–292. doi:10.1146/annurev-anchem-092019-032524.
- [224] S. Béchu, M. Ralaiarisoa, A. Etcheberry, P. Schulz, Photoemission Spectroscopy Characterization of Halide Perovskites, *Adv. Energy Mater.* 10 (2020) 1904007. doi:10.1002/aenm.201904007.
- [225] S. Deng, D.D. Blach, L. Jin, L. Huang, Imaging Carrier Dynamics and Transport in Hybrid Perovskites with Transient Absorption Microscopy, *Adv. Energy Mater.* 10 (2020) 1903781. doi:10.1002/aenm.201903781.
- [226] C. Schnedermann, J. Sung, R. Pandya, S.D. Verma, R.Y.S. Chen, N. Gauriot, H.M. Bretscher, P. Kukura, A. Rao, Ultrafast Tracking of Exciton and Charge Carrier Transport in Optoelectronic Materials on the Nanometer Scale, *J. Phys. Chem. Lett.* 10 (2019) 6727–6733. doi:10.1021/acs.jpclett.9b02437.
- [227] M. Kociak, L.F. Zagonel, Cathodoluminescence in the scanning transmission electron microscope, *Ultramicroscopy* 176 (2017) 112–131. doi:10.1016/j.ultramic.2017.03.014.
- [228] M.C. Schubert, L.E. Mundt, D. Walter, A. Fell, S.W. Glunz, Spatially Resolved Performance Analysis for Perovskite Solar Cells, *Adv. Energy Mater.* 10 (2020) 1904001. doi:10.1002/aenm.201904001.
- [229] J.M. Howard, R. Lahoti, M.S. Leite, Imaging Metal Halide Perovskites Material and Properties at the Nanoscale, *Adv. Energy Mater.* 10 (2020) 1903161. doi:10.1002/aenm.201903161.

- [230] A.J. Winchester, C. Petoukhoff, M. Abdi-Jalebi, Z. Andaji-Garmaroudi, V. Pareek, E.L. Wong, J. Madéo, M.K.L. Man, S.D. Stranks, K. Dani, Investigation of Trap States and Their Dynamics in Hybrid Organic-inorganic Mixed Cation Perovskite Films Using Time Resolved Photoemission Electron Microscopy, in: Conf. Lasers Electro-Optics, OSA, Washington, D.C., 2018: p. FM4F.2. doi:10.1364/CLEO\_QELS.2018.FM4F.2.
- [231] U. Rau, Reciprocity relation between photovoltaic quantum efficiency and electroluminescent emission of solar cells, *Phys. Rev. B.* 76 (2007) 085303. doi:10.1103/PhysRevB.76.085303.
- [232] U. Rau, Superposition and Reciprocity in the Electroluminescence and Photoluminescence of Solar Cells, *IEEE J. Photovoltaics.* 2 (2012) 169–172. doi:10.1109/JPHOTOV.2011.2179018.
- [233] H. Guthrey, J. Moseley, A Review and Perspective on Cathodoluminescence Analysis of Halide Perovskites, *Adv. Energy Mater.* 10 (2020) 1903840. doi:10.1002/aenm.201903840.
- [234] T. Kirchartz, J.A. Márquez, M. Stolterfoht, T. Unold, Photoluminescence-Based Characterization of Halide Perovskites for Photovoltaics, *Adv. Energy Mater.* 10 (2020) 1904134. doi:10.1002/aenm.201904134.
- [235] J.H. Noh, S.H. Im, J.H. Heo, T.N. Mandal, S. Il Seok, Chemical management for colorful, efficient, and stable inorganic-organic hybrid nanostructured solar cells, *Nano Lett.* 13 (2013) 1764–1769. doi:10.1021/nl400349b.
- [236] L. Rakocevic, F. Ernst, N.T. Yimga, S. Vashishtha, T. Aernouts, T. Heumueller, C.J. Brabec, R. Gehlhaar, J. Poortmans, Reliable Performance Comparison of Perovskite Solar Cells Using Optimized Maximum Power Point Tracking, *Sol. RRL.* 3 (2019) 1800287. doi:10.1002/solr.201800287.
- [237] T.W. Jones, A. Osherov, M. Alsari, M. Sponseller, B.C. Duck, Y.-K. Jung, C. Settens, F. Niroui, R. Brenes, C. V. Stan, Y. Li, M. Abdi-Jalebi, N. Tamura, J.E. Macdonald, M. Burghammer, R.H. Friend, V. Bulović, A. Walsh, G.J. Wilson, S. Lilliu, S.D. Stranks, Lattice strain causes non-radiative losses in halide perovskites, *Energy Environ. Sci.* 12 (2019) 596–606. doi:10.1039/C8EE02751J.
- [238] F.U. Kosasih, C. Ducati, Characterising degradation of perovskite solar cells through in-situ and operando electron microscopy, *Nano Energy.* 47 (2018) 243–256. doi:10.1016/j.nanoen.2018.02.055.
- [239] D. Di Girolamo, N. Phung, F.U. Kosasih, F. Di Giacomo, F. Matteocci, J.A. Smith, M.A. Flatken, H. Köbler, S.H. Turren Cruz, A. Mattoni, L. Cinà, B. Rech, A. Latini, G. Divitini, C. Ducati, A. Di Carlo, D. Dini, A. Abate, Ion Migration-Induced Amorphization and Phase Segregation as a Degradation Mechanism in Planar Perovskite Solar Cells, *Adv. Energy Mater.*

10 (2020) 2000310. doi:10.1002/aenm.202000310.

- [240] L.E. Mundt, L.T. Schelhas, Structural Evolution During Perovskite Crystal Formation and Degradation: In Situ and Operando X-Ray Diffraction Studies, *Adv. Energy Mater.* 10 (2020) 1903074. doi:10.1002/aenm.201903074.
- [241] Q. Tao, P. Xu, M. Li, W. Lu, Machine learning for perovskite materials design and discovery, *Npj Comput. Mater.* 7 (2021) 23. doi:10.1038/s41524-021-00495-8.
- [242] J. McKinley, Electron and Ion Beam Characterization of Glass, in: J.D. Musgraves, J. Hu, L. Calvez (Eds.), *Springer Handb. Glas.*, 1st ed., Springer Nature, Cham, 2019: pp. 931–954. doi:10.1007/978-3-319-93728-1\_27.
- [243] D.B. Williams, C.B. Carter, *Transmission Electron Microscopy*, Springer US, Boston, MA, 1996. doi:10.1007/978-1-4757-2519-3.
- [244] T. Malis, S.C. Cheng, R.F. Egerton, EELS log-ratio technique for specimen-thickness measurement in the TEM, *J. Electron Microsc. Tech.* 8 (1988) 193–200. doi:10.1002/jemt.1060080206.
- [245] R.F. Egerton, *Electron Energy-Loss Spectroscopy in the Electron Microscope*, 3rd ed., Springer US, 2011. doi:10.1007/978-1-4419-9583-4.
- [246] F. Lenz, Zur Streuung mittelschneller Elektronen in kleinste Winkel, *Zeitschrift Fur Naturforsch.* (1954) 185–204.
- [247] J.I. Goldstein, D.B. Williams, G. Cliff, Quantitative X-Ray Analysis, in: D.C. Joy, A.D. Romig, J.I. Goldstein (Eds.), *Princ. Anal. Electron Microsc.*, Springer US, Boston, MA, 1986: pp. 155–217. doi:10.1007/978-1-4899-2037-9\_5.
- [248] I.P. Jones, *Chemical microanalysis: using electron beams*, Institute of Materials, London, 1992.
- [249] J.R. Michael, D.B. Williams, C.F. Klein, R. Ayer, The measurement and calculation of the X-ray spatial resolution obtained in the analytical electron microscope, *J. Microsc.* 160 (1990) 41–53. doi:10.1111/j.1365-2818.1990.tb03046.x.
- [250] R. Henderson, The potential and limitations of neutrons, electrons and X-rays for atomic resolution microscopy of unstained biological molecules, *Q. Rev. Biophys.* 28 (1995) 171. doi:10.1017/S003358350000305X.
- [251] L.-V.-P.-R. de Broglie, *Research on the Theory of Quanta*, University of Paris, 1924.
- [252] M. Knoll, E. Ruska, Das Elektronenmikroskop, *Zeitschrift Fur Phys.* 78 (1932) 318–339. doi:10.1007/BF01342199.

- [253] P.E. Batson, N. Dellby, O.L. Krivanek, Sub-ångstrom resolution using aberration corrected electron optics, *Nature*. 418 (2002) 617–620. doi:10.1038/nature00972.
- [254] R. Erni, M.D. Rossell, C. Kisielowski, U. Dahmen, Atomic-resolution imaging with a sub-50-pm electron probe, *Phys. Rev. Lett.* 102 (2009) 1–4. doi:10.1103/PhysRevLett.102.096101.
- [255] S.A. Edwards, The development of the electron microscope, (2012). <https://www.aaas.org/blog/scientia/development-electron-microscope> (accessed March 12, 2021).
- [256] FEI Tecnai Osiris, (n.d.). <http://www.wems.msm.cam.ac.uk/pages/osiris.html> (accessed March 12, 2021).
- [257] FEI Company, FEI's New X-FEG Electron Source Further Extends Lead In Scanning/Transmission Electron Microscope Imaging And Analysis, *Lab. Netw.* (2008). <https://www.laboratorynetwork.com/doc/feis-new-x-feg-electron-source-further-0001> (accessed August 12, 2021).
- [258] M. Bigas, E. Cabruja, J. Forest, J. Salvi, Review of CMOS image sensors, *Microelectronics J.* 37 (2006) 433–451. doi:10.1016/j.mejo.2005.07.002.
- [259] I. MacLaren, T.A. Macgregor, C.S. Allen, A.I. Kirkland, Detectors—The ongoing revolution in scanning transmission electron microscopy and why this important to material characterization, *APL Mater.* 8 (2020) 110901. doi:10.1063/5.0026992.
- [260] P. Hartel, H. Rose, C. Dinges, Conditions and reasons for incoherent imaging in STEM, *Ultramicroscopy*. 63 (1996) 93–114. doi:10.1016/0304-3991(96)00020-4.
- [261] M.M.J. Treacy, A. Howie, C.J. Wilson, Z contrast of platinum and palladium catalysts, *Philos. Mag. A.* 38 (1978) 569–585. doi:10.1080/01418617808239255.
- [262] A. Howie, Image Contrast And Localized Signal Selection Techniques, *J. Microsc.* 117 (1979) 11–23. doi:10.1111/j.1365-2818.1979.tb00228.x.
- [263] A. Engel, J.W. Wiggins, D.C. Woodruff, A comparison of calculated images generated by six modes of transmission electron microscopy, *J. Appl. Phys.* 45 (1974) 2739–2747. doi:10.1063/1.1663659.
- [264] M. Weyland, D.A. Muller, Tuning the convergence angle for optimum STEM performance, *ArXiv.* (2020).
- [265] M.E. Dickinson, M.W. Davidson, Spectral Imaging, (n.d.). <http://zeiss-campus.magnet.fsu.edu/articles/spectralimaging/introduction.html> (accessed March 12, 2021).

- [266] D.J. Stokes, Principles and Practice of Variable Pressure/Environmental Scanning Electron Microscopy (VP-ESEM), John Wiley & Sons, Ltd, Chichester, UK, 2008. doi:10.1002/9780470758731.
- [267] J.I. Goldstein, D.E. Newbury, J.R. Michael, N.W.M. Ritchie, J.H.J. Scott, D.C. Joy, Scanning Electron Microscopy and X-Ray Microanalysis, Springer New York, New York, NY, 2018. doi:10.1007/978-1-4939-6676-9.
- [268] JEOL, Scanning Electron Microscope A to Z: Basic Knowledge for Using the SEM, (n.d.).
- [269] X. Zhang, X. Cen, R. Ravichandran, L.A. Hughes, K. van Benthem, Simultaneous Scanning Electron Microscope Imaging of Topographical and Chemical Contrast Using In-Lens, In-Column, and Everhart–Thornley Detector Systems, *Microsc. Microanal.* 22 (2016) 565–575. doi:10.1017/S1431927616000751.
- [270] D.B. Williams, J.R. Michael, J.I. Goldstein, A.D. Romig, Definition of the spatial resolution of X-ray microanalysis in thin foils, *Ultramicroscopy*. 47 (1992) 121–132. doi:10.1016/0304-3991(92)90189-Q.
- [271] K. Kanaya, S. Okayama, Penetration and energy-loss theory of electrons in solid targets, *J. Phys. D. Appl. Phys.* 5 (1972) 308. doi:10.1088/0022-3727/5/1/308.
- [272] J. Thomas, T. Gemming, Analytical Transmission Electron Microscopy, 2014. doi:10.2138/rmg.2014.78.6.
- [273] M.O. Krause, J.H. Oliver, Natural widths of atomic K and L levels,  $K_{\alpha}$  X-ray lines and several KLL Auger lines, *J. Phys. Chem. Ref. Data.* 8 (1979) 329–338. doi:10.1063/1.555595.
- [274] H.A. Liebhafsky, H.G. Pfeiffer, E.H. Winslow, P.D. Zemany, X-rays, Electrons and Analytical Chemistry, John Wiley & Sons, New York, 1972.
- [275] G. Cliff, G.W. Lorimer, The quantitative analysis of thin specimens, *J. Microsc.* 103 (1975) 203–207. doi:10.1111/j.1365-2818.1975.tb03895.x.
- [276] M. Watanabe, Practical Aspects and Advanced Applications of XEDS, in: C.B. Carter, D.B. Williams (Eds.), *Transm. Electron Microsc. Diffraction, Imaging, Spectrom.*, 1st ed., Springer International Publishing, Cham, 2016: pp. 467–503. doi:10.1007/978-3-319-26651-0.
- [277] M. Watanabe, D.B. Williams, The quantitative analysis of thin specimens: a review of progress from the Cliff-Lorimer to the new zeta-factor methods, *J. Microsc.* 221 (2006) 89–109. doi:10.1111/j.1365-2818.2006.01549.x.
- [278] M. Stojanovska, V.M. Petruševski, B. Šoptrajanov, The concept of sublimation – iodine as an example, *Educ. Química.* 23 (2012) 171–175. doi:10.1016/S0187-893X(17)30149-0.

- [279] I.A. Leenson, Sublimination of Iodine at Various Pressures: Mutlipurpose Experiments in Inorganic and Physical Chemistry, *J. Chem. Educ.* 82 (2005) 241. doi:10.1021/ed082p241.
- [280] M.J. O'Neil, ed., *The Merck Index - An Encyclopedia of Chemicals, Drugs, and Biologicals*, 13th ed., Merck and Co., Inc., Whitehouse Station, 2001.
- [281] K. Thurmer, Autocatalytic Oxidation of Lead Crystallite Surfaces, *Science*. 297 (2002) 2033–2035. doi:10.1126/science.297.5589.2033.
- [282] S. Acharya, Lead between the lines, *Nat. Chem.* 5 (2013) 894–894. doi:10.1038/nchem.1761.
- [283] P.J.W. Moll, Focused Ion Beam Microstructuring of Quantum Matter, *Annu. Rev. Condens. Matter Phys.* 9 (2018) 147–162. doi:10.1146/annurev-conmatphys-033117-054021.
- [284] R.. Langford, C. Clinton, In situ lift-out using a FIB-SEM system, *Micron*. 35 (2004) 607–611. doi:10.1016/j.micron.2004.03.002.
- [285] FEI Company, TEM Preparation Notes, (n.d.).
- [286] Y. Huh, K.J. Hong, K.S. Shin, Amorphization Induced by Focused Ion Beam Milling in Metallic and Electronic Materials, *Microsc. Microanal.* 19 (2013) 33–37. doi:10.1017/S1431927613012282.
- [287] Q. Jeangros, M. Duchamp, J. Werner, M. Kruth, R.E. Dunin-Borkowski, B. Niesen, C. Ballif, A. Hessler-Wyser, In Situ TEM Analysis of Organic-Inorganic Metal-Halide Perovskite Solar Cells under Electrical Bias, *Nano Lett.* 16 (2016) 7013–7018. doi:10.1021/acs.nanolett.6b03158.
- [288] J.R. Fryer, Radiation damage in organic crystalline films, *Ultramicroscopy*. 14 (1984) 227–236. doi:10.1016/0304-3991(84)90091-3.
- [289] S. Cacovich, Electron Microscopy Studies of Hybrid Perovskite Solar Cells, University of Cambridge, 2018. doi:10.17863/CAM.24048.
- [290] F. de la Peña, E. Prestat, V.T. Fauske, P. Burdet, T. Furnival, P. Jokubauskas, M. Nord, T. Ostasevicius, K.E. MacArthur, D.N. Johnstone, M. Sarahan, J. Lahnemann, J. Taillon, T. Aarholt, V. Migunov, A. Eljarrat, J. Caron, S. Mazzucco, B. Martineau, S. Somnath, T. Poon, M. Walls, T. Slater, N. Tappy, N. Cautaerts, F. Winkler, G. Donval, J.C. Myers, HyperSpy 1.6.1, (2020). doi:10.5281/zenodo.4294676.
- [291] C. Trager-Cowan, A. Alasmari, W. Avis, J. Bruckbauer, P.R. Edwards, G. Ferenczi, B. Hourahine, A. Kotzai, S. Kraeusel, G. Kusch, R.W. Martin, R. McDermott, G. Naresh-Kumar, M. Nouf-Allehiani, E. Pascal, D. Thomson, S. Vespucci, M.D. Smith, P.J. Parbrook, J. Enslin, F. Mehnke, C. Kuhn, T. Wernicke, M. Kneissl, S. Hagedorn, A. Knauer, S. Walde, M. Weyers,

- P.-M. Coulon, P.A. Shields, J. Bai, Y. Gong, L. Jiu, Y. Zhang, R.M. Smith, T. Wang, A. Winkelmann, Structural and luminescence imaging and characterisation of semiconductors in the scanning electron microscope, *Semicond. Sci. Technol.* 35 (2020) 054001. doi:10.1088/1361-6641/ab75a5.
- [292] Attolight, Allalin, (n.d.). <https://attolight.com/allalin/> (accessed March 12, 2021).
- [293] K. Hollocher, Centering the RPM (rotationally-parabolic mirror), (n.d.). [http://minerva.union.edu/hollochk/sem/cl\\_center\\_mirror.html](http://minerva.union.edu/hollochk/sem/cl_center_mirror.html) (accessed March 12, 2021).
- [294] A. Alkauskas, M.D. McCluskey, C.G. Van de Walle, Tutorial: Defects in semiconductors—Combining experiment and theory, *J. Appl. Phys.* 119 (2016) 181101. doi:10.1063/1.4948245.
- [295] K. Levenberg, A method for the solution of certain non-linear problems in least squares, *Q. Appl. Math.* 2 (1944) 164–168. doi:10.1090/qam/10666.
- [296] D.W. Marquardt, An Algorithm for Least-Squares Estimation of Nonlinear Parameters, *J. Soc. Ind. Appl. Math.* 11 (1963) 431–441. doi:10.1137/0111030.
- [297] R.F. Egerton, P. Li, M. Malac, Radiation damage in the TEM and SEM, *Micron*. 35 (2004) 399–409. doi:10.1016/j.micron.2004.02.003.
- [298] R.F. Egerton, Radiation damage to organic and inorganic specimens in the TEM, *Micron*. 119 (2019) 72–87. doi:10.1016/j.micron.2019.01.005.
- [299] S. Chen, X. Zhang, J. Zhao, Y. Zhang, G. Kong, Q. Li, N. Li, Y. Yu, N. Xu, J. Zhang, K. Liu, Q. Zhao, J. Cao, J. Feng, X. Li, J. Qi, D. Yu, J. Li, P. Gao, Atomic scale insights into structure instability and decomposition pathway of methylammonium lead iodide perovskite, *Nat. Commun.* 9 (2018) 4807. doi:10.1038/s41467-018-07177-y.
- [300] S. Chen, Y. Zhang, X. Zhang, J. Zhao, Z. Zhao, X. Su, Z. Hua, J. Zhang, J. Cao, J. Feng, X. Wang, X. Li, J. Qi, J. Li, P. Gao, General Decomposition Pathway of Organic–Inorganic Hybrid Perovskites through an Intermediate Superstructure and its Suppression Mechanism, *Adv. Mater.* 32 (2020) 2001107. doi:10.1002/adma.202001107.
- [301] S. Chen, Y. Zhang, J. Zhao, Z. Mi, J. Zhang, J. Cao, J. Feng, G. Zhang, J. Qi, J. Li, P. Gao, Transmission electron microscopy of organic-inorganic hybrid perovskites: myths and truths, *Sci. Bull.* (2020) 2004.12262v1. doi:10.1016/j.scib.2020.05.020.
- [302] Z. Dang, J. Shamsi, F. Palazon, M. Imran, Q.A. Akkerman, S. Park, G. Bertoni, M. Prato, R. Brescia, L. Manna, In Situ Transmission Electron Microscopy Study of Electron Beam-Induced Transformations in Colloidal Cesium Lead Halide Perovskite Nanocrystals, *ACS Nano*. 11 (2017) 2124–2132. doi:10.1021/acsnano.6b08324.

- [303] R.F. Egerton, Mechanisms of radiation damage in beam-sensitive specimens, for TEM accelerating voltages between 10 and 300 kV, *Microsc. Res. Tech.* 75 (2012) 1550–1556. doi:10.1002/jemt.22099.
- [304] S. Chen, P. Gao, Challenges, myths, and opportunities of electron microscopy on halide perovskites, *J. Appl. Phys.* 128 (2020) 010901. doi:10.1063/5.0012310.
- [305] R. Egerton, Radiation Damage and Nanofabrication in TEM and STEM, *Micros. Today.* 29 (2021) 56–59. doi:10.1017/S1551929521000663.
- [306] A. Pisoni, J. Jaćimović, O.S. Barišić, M. Spina, R. Gaál, L. Forró, E. Horváth, Ultra-Low Thermal Conductivity in Organic–Inorganic Hybrid Perovskite  $\text{CH}_3\text{NH}_3\text{PbI}_3$ , *J. Phys. Chem. Lett.* 5 (2014) 2488–2492. doi:10.1021/jz5012109.
- [307] Z. Guo, S.J. Yoon, J.S. Manser, P. V. Kamat, T. Luo, Structural Phase- and Degradation-Dependent Thermal Conductivity of  $\text{CH}_3\text{NH}_3\text{PbI}_3$  Perovskite Thin Films, *J. Phys. Chem. C.* 120 (2016) 6394–6401. doi:10.1021/acs.jpcc.6b00513.
- [308] A. Kovalsky, L. Wang, G.T. Marek, C. Burda, J.S. Dyck, Thermal Conductivity of  $\text{CH}_3\text{NH}_3\text{PbI}_3$  and  $\text{CsPbI}_3$ : Measuring the Effect of the Methylammonium Ion on Phonon Scattering, *J. Phys. Chem. C.* 121 (2017) 3228–3233. doi:10.1021/acs.jpcc.6b12231.
- [309] M. Wang, S. Lin, Anisotropic and Ultralow Phonon Thermal Transport in Organic-Inorganic Hybrid Perovskites: Atomistic Insights into Solar Cell Thermal Management and Thermoelectric Energy Conversion Efficiency, *Adv. Funct. Mater.* 26 (2016) 5297–5306. doi:10.1002/adfm.201600284.
- [310] T. Ye, X. Wang, X. Li, A.Q. Yan, S. Ramakrishna, J. Xu, Ultra-high Seebeck coefficient and low thermal conductivity of a centimeter-sized perovskite single crystal acquired by a modified fast growth method, *J. Mater. Chem. C.* 5 (2017) 1255–1260. doi:10.1039/C6TC04594D.
- [311] J.C.H. Spence, Outrunning damage: Electrons vs X-rays—timescales and mechanisms, *Struct. Dyn.* 4 (2017) 044027. doi:10.1063/1.4984606.
- [312] M.H. Futscher, J. V. Milić, Mixed Conductivity of Hybrid Halide Perovskites: Emerging Opportunities and Challenges, *Front. Energy Res.* 9 (2021). doi:10.3389/fenrg.2021.629074.
- [313] M.H. Futscher, J.M. Lee, L. McGovern, L.A. Muscarella, T. Wang, M.I. Haider, A. Fakharuddin, L. Schmidt-Mende, B. Ehrler, Quantification of ion migration in  $\text{CH}_3\text{NH}_3\text{PbI}_3$  perovskite solar cells by transient capacitance measurements, *Mater. Horizons.* 6 (2019) 1497–1503. doi:10.1039/C9MH00445A.

- [314] M. Sajedi Alvar, P.W.M. Blom, G.A.H. Wetzelaer, Device Model for Methylammonium Lead Iodide Perovskite With Experimentally Validated Ion Dynamics, *Adv. Electron. Mater.* 6 (2020) 1900935. doi:10.1002/aelm.201900935.
- [315] R.F. Egerton, H. Qian, Exploiting the Dose-Rate Dependence of Radiolysis – a Future for Cryo-STEM ?, *Microsc. Microanal.* 25 (2019) 992–993. doi:10.1017/S1431927619005695.
- [316] ThermoFisher Scientific, Velox, (2018). <https://assets.thermofisher.com/TFS-Assets/MSD/Datasheets/velox-datasheet.pdf> (accessed August 26, 2021).
- [317] J. Ferrer Orri, E.M. Tennyson, G. Kusch, G. Divitini, S. Macpherson, R. Oliver, C. Ducati, S. Stranks, Using pulsed mode scanning electron microscopy for cathodoluminescence studies on hybrid perovskite films, *Nano Express.* (2021). doi:10.1088/2632-959X/abfe3c.
- [318] B. Jin, D. Zhao, F. Liang, L. Liu, D. Liu, P. Wang, M. Qiu, Electron-Beam Irradiation Induced Regulation of Surface Defects in Lead Halide Perovskite Thin Films, *Research. 2021* (2021) 1–11. doi:10.34133/2021/9797058.
- [319] Y. Tian, M. Peter, E. Unger, M. Abdellah, K. Zheng, T. Pullerits, A. Yartsev, V. Sundström, I.G. Scheblykin, Mechanistic insights into perovskite photoluminescence enhancement: light curing with oxygen can boost yield thousandfold, *Phys. Chem. Chem. Phys.* 17 (2015) 24978–24987. doi:10.1039/C5CP04410C.
- [320] C. Xiao, Z. Li, H. Guthrey, J. Moseley, Y. Yang, S. Wozny, H. Moutinho, B. To, J.J. Berry, B. Gorman, Y. Yan, K. Zhu, M. Al-Jassim, Mechanisms of Electron-Beam-Induced Damage in Perovskite Thin Films Revealed by Cathodoluminescence Spectroscopy, *J. Phys. Chem. C.* 119 (2015) 26904–26911. doi:10.1021/acs.jpcc.5b09698.
- [321] C.G. Bischak, E.M. Sanehira, J.T. Precht, J.M. Luther, N.S. Ginsberg, Heterogeneous Charge Carrier Dynamics in Organic–Inorganic Hybrid Materials: Nanoscale Lateral and Depth-Dependent Variation of Recombination Rates in Methylammonium Lead Halide Perovskite Thin Films, *Nano Lett.* 15 (2015) 4799–4807. doi:10.1021/acs.nanolett.5b01917.
- [322] E. Edri, S. Kirmayer, S. Mukhopadhyay, K. Gartsman, G. Hodes, D. Cahen, Elucidating the charge carrier separation and working mechanism of  $\text{CH}_3\text{NH}_3\text{PbI}_3-\text{xCl}_x$  perovskite solar cells, *Nat. Commun.* 5 (2014) 3461. doi:10.1038/ncomms4461.
- [323] G.W.P. Adhyaksa, S. Brittman, H. Ābolinš, A. Lof, X. Li, J.D. Keelor, Y. Luo, T. Duevski, R.M.A. Heeren, S.R. Ellis, D.P. Fenning, E.C. Garnett, Understanding Detrimental and Beneficial Grain Boundary Effects in Halide Perovskites, *Adv. Mater.* 30 (2018) 1804792. doi:10.1002/adma.201804792.

- [324] N. Klein-Kedem, D. Cahen, G. Hodes, Effects of Light and Electron Beam Irradiation on Halide Perovskites and Their Solar Cells, *Acc. Chem. Res.* 49 (2016) 347–354. doi:10.1021/acs.accounts.5b00469.
- [325] J.I. Goldstein, D.E. Newbury, P. Echlin, D.C. Joy, A.D. Romig, C.E. Lyman, C. Fiori, E. Lifshin, Coating and Conductivity Techniques for SEM and Microanalysis, in: *Scanning Electron Microsc. X-Ray Microanal.*, Springer US, Boston, MA, 1992: pp. 671–740. doi:10.1007/978-1-4613-0491-3\_13.
- [326] H. Yuan, E. Debroye, K. Janssen, H. Naiki, C. Steuwe, G. Lu, M. Moris, E. Orgiu, H. Uji-I, F. De Schryver, P. Samorì, J. Hofkens, M. Roeffaers, Degradation of Methylammonium Lead Iodide Perovskite Structures through Light and Electron Beam Driven Ion Migration, *J. Phys. Chem. Lett.* 7 (2016) 561–566. doi:10.1021/acs.jpclett.5b02828.
- [327] M.U. Rothmann, W. Li, Y. Zhu, A. Liu, Z. Ku, U. Bach, J. Etheridge, Y.-B. Cheng, Structural and Chemical Changes to  $\text{CH}_3\text{NH}_3\text{PbI}_3$  Induced by Electron and Gallium Ion Beams, *Adv. Mater.* 30 (2018) 1800629. doi:10.1002/adma.201800629.
- [328] K. Pearson, On lines and planes of closest fit to systems of points in space, London, Edinburgh, Dublin Philos. Mag. J. Sci. 2 (1901) 559–572. doi:10.1080/14786440109462720.
- [329] P. Geladi, H. Grahn, *Multivariate image analysis*, Wiley, 1996.
- [330] M. Scholz, *Approaches to analyse and interpret biological profile data*, Universität Potsdam, 2006.
- [331] R.B. Cattell, The Scree Test For The Number Of Factors, *Multivariate Behav. Res.* 1 (1966) 245–276. doi:10.1207/s15327906mbr0102\_10.
- [332] N. Bonnet, N. Bonnet, N. Brun, N. Brun, C. Colliex, C. Colliex, Extracting information from sequences of spatially resolved EELS spectra using multivariate statistical analysis, *Ultramicroscopy*. 77 (1999) 97–112. doi:10.1016/S0304-3991(99)00042-X.
- [333] P. Paatero, U. Tapper, Positive matrix factorization: A non-negative factor model with optimal utilization of error estimates of data values, *Environmetrics*. 5 (1994) 111–126. doi:10.1002/env.3170050203.
- [334] D.D. Lee, H.S. Seung, Learning the parts of objects by non-negative matrix factorization, *Nature*. 401 (1999) 788–791. doi:10.1038/44565.
- [335] S. Cacovich, F. Matteocci, M. Abdi-Jalebi, S.D. Stranks, A. Di Carlo, C. Ducati, G. Divitini, Unveiling the Chemical Composition of Halide Perovskite Films Using Multivariate Statistical Analyses, *ACS Appl. Energy Mater.* 1 (2018) 7174–7181. doi:10.1021/acsaelm.8b01622.

- [336] N. Gillis, The Why and How of Nonnegative Matrix Factorization, ArXiv. (2014).
- [337] M.R. Keenan, P.G. Kotula, Accounting for Poisson noise in the multivariate analysis of ToF-SIMS spectrum images, *Surf. Interface Anal.* 36 (2004) 203–212. doi:10.1002/sia.1657.
- [338] P.D. Wentzell, D.T. Andrews, D.C. Hamilton, K. Faber, B.R. Kowalski, Maximum Likelihood Principal Component Analysis, *J. Chemom.* 11 (1997) 339–366.
- [339] E.T. Hoke, D.J. Slotcavage, E.R. Dohner, A.R. Bowring, H.I. Karunadasa, M.D. McGehee, Reversible photo-induced trap formation in mixed-halide hybrid perovskites for photovoltaics, *Chem. Sci.* 6 (2015) 613–617. doi:10.1039/C4SC03141E.
- [340] S. Feldmann, S. Macpherson, S.P. Senanayak, M. Abdi-Jalebi, J.P.H. Rivett, G. Nan, G.D. Tainter, T.A.S. Doherty, K. Frohma, E. Ringe, R.H. Friend, H. Sirringhaus, M. Saliba, D. Beljonne, S.D. Stranks, F. Deschler, Photodoping through local charge carrier accumulation in alloyed hybrid perovskites for highly efficient luminescence, *Nat. Photonics.* 14 (2020) 123–128. doi:10.1038/s41566-019-0546-8.
- [341] J.M. Azpiroz, E. Mosconi, J. Bisquert, F. De Angelis, Defect migration in methylammonium lead iodide and its role in perovskite solar cell operation, *Energy Environ. Sci.* 8 (2015) 2118–2127. doi:10.1039/C5EE01265A.
- [342] J. Haruyama, K. Sodeyama, L. Han, Y. Tateyama, First-principles study of ion diffusion in perovskite solar cell sensitizers, *J. Am. Chem. Soc.* 137 (2015) 10048–10051. doi:10.1021/jacs.5b03615.
- [343] A. Baba, D. Bai, T. Sadoh, A. Kenjo, H. Nakashima, H. Mori, T. Tsurushima, Behavior of radiation-induced defects and amorphization in silicon crystal, *Nucl. Instruments Methods Phys. Res. Sect. B Beam Interact. with Mater. Atoms.* 121 (1997) 299–301. doi:10.1016/S0168-583X(96)00392-8.
- [344] Y. Wang, X. Lü, W. Yang, T. Wen, L. Yang, X. Ren, L. Wang, Z. Lin, Y. Zhao, Pressure-Induced Phase Transformation, Reversible Amorphization, and Anomalous Visible Light Response in Organolead Bromide Perovskite, *J. Am. Chem. Soc.* 137 (2015) 11144–11149. doi:10.1021/jacs.5b06346.
- [345] P. Wang, J. Guan, D.T.K. Galeschuk, Y. Yao, C.F. He, S. Jiang, S. Zhang, Y. Liu, M. Jin, C. Jin, Y. Song, Pressure-Induced Polymorphic, Optical, and Electronic Transitions of Formamidinium Lead Iodide Perovskite, *J. Phys. Chem. Lett.* 8 (2017) 2119–2125. doi:10.1021/acs.jpcllett.7b00665.

- [346] H. Zhu, T. Cai, M. Que, J.P. Song, B.M. Rubenstein, Z. Wang, O. Chen, Pressure-Induced Phase Transformation and Band-Gap Engineering of Formamidinium Lead Iodide Perovskite Nanocrystals, *J. Phys. Chem. Lett.* 9 (2018) 4199–4205. doi:10.1021/acs.jpclett.8b01852.
- [347] L. Wang, K. Wang, B. Zou, Pressure-Induced Structural and Optical Properties of Organometal Halide Perovskite-Based Formamidinium Lead Bromide, *J. Phys. Chem. Lett.* 7 (2016) 2556–2562. doi:10.1021/acs.jpclett.6b00999.
- [348] L. Zhang, Q. Zeng, K. Wang, Pressure-Induced Structural and Optical Properties of Inorganic Halide Perovskite  $\text{CsPbBr}_3$ , *J. Phys. Chem. Lett.* 8 (2017) 3752–3758. doi:10.1021/acs.jpclett.7b01577.
- [349] Y. Kuang, V. Zardetto, R. van Gils, S. Karwal, D. Koushik, M.A. Verheijen, L.E. Black, C. Weijtens, S. Veenstra, R. Andriessen, W.M.M. Kessels, M. Creatore, Low-Temperature Plasma-Assisted Atomic-Layer-Deposited  $\text{SnO}_2$  as an Electron Transport Layer in Planar Perovskite Solar Cells, *ACS Appl. Mater. Interfaces.* 10 (2018) 30367–30378. doi:10.1021/acsami.8b09515.
- [350] J. Ferrer Orri, J. Lähnemann, E. Prestat, D.N. Johnstone, N. Tappy, LumiSpy, (2021). doi:10.5281/zenodo.4640446.
- [351] M.I. Dar, G. Jacopin, M. Hezam, N. Arora, S.M. Zakeeruddin, B. Deveaud, M.K. Nazeeruddin, M. Grätzel, Asymmetric Cathodoluminescence Emission in  $\text{CH}_3\text{NH}_3\text{PbI}_{3-x}\text{Br}_x$  Perovskite Single Crystals, *ACS Photonics.* 3 (2016) 947–952. doi:10.1021/acsphotonics.6b00290.
- [352] D. Cortecchia, K.C. Lew, J.-K. So, A. Bruno, C. Soci, Cathodoluminescence of Self-Organized Heterogeneous Phases in Multidimensional Perovskite Thin Films, *Chem. Mater.* 29 (2017) 10088–10094. doi:10.1021/acs.chemmater.7b03851.
- [353] N. Riesen, M. Lockrey, K. Badek, H. Riesen, On the origins of the green luminescence in the “zero-dimensional perovskite”  $\text{Cs}_4\text{PbBr}_6$ : conclusive results from cathodoluminescence imaging, *Nanoscale.* 11 (2019) 3925–3932. doi:10.1039/C8NR09255A.
- [354] D. Drouin, A.R. Couture, D. Joly, X. Tastet, V. Aimez, R. Gauvin, CASINO V2.42—A Fast and Easy-to-use Modeling Tool for Scanning Electron Microscopy and Microanalysis Users, *Scanning.* 29 (2007) 92–101. doi:10.1002/sca.20000.
- [355] E. Salvati, L.R. Brandt, C. Papadaki, H. Zhang, S.M. Mousavi, D. Wermeille, A.M. Korsunsky, Nanoscale structural damage due to focused ion beam milling of silicon with Ga ions, *Mater. Lett.* 213 (2018) 346–349. doi:10.1016/j.matlet.2017.11.043.

- [356] L.A. Giannuzzi, R. Geurts, J. Ringnalda, 2 keV Ga<sup>+</sup> FIB Milling for Reducing Amorphous Damage in Silicon, *Microsc. Microanal.* 11 (2005). doi:10.1017/S1431927605507797.
- [357] L. Pastewka, R. Salzer, A. Graff, F. Altmann, M. Moseler, Surface amorphization, sputter rate, and intrinsic stresses of silicon during low energy Ga<sup>+</sup> focused-ion beam milling, *Nucl. Instruments Methods Phys. Res. Sect. B Beam Interact. with Mater. Atoms.* 267 (2009) 3072–3075. doi:10.1016/j.nimb.2009.06.094.
- [358] J. Liu, R. Niu, J. Gu, M. Cabral, M. Song, X. Liao, Effect of Ion Irradiation Introduced by Focused Ion-Beam Milling on the Mechanical Behaviour of Sub-Micron-Sized Samples, *Sci. Rep.* 10 (2020) 10324. doi:10.1038/s41598-020-66564-y.
- [359] J. Mayer, L.A. Giannuzzi, T. Kamino, J. Michael, TEM Sample Preparation and FIB-Induced Damage, *MRS Bull.* 32 (2007) 400–407. doi:10.1557/mrs2007.63.
- [360] A.R. Milosavljević, W. Huang, S. Sadhu, S. Ptasińska, Low-Energy Electron-Induced Transformations in Organolead Halide Perovskite, *Angew. Chemie Int. Ed.* 55 (2016) 10083–10087. doi:10.1002/anie.201605013.
- [361] O. Hentz, Z. Zhao, S. Gradečak, Impacts of Ion Segregation on Local Optical Properties in Mixed Halide Perovskite Films, *Nano Lett.* 16 (2016) 1485–1490. doi:10.1021/acs.nanolett.5b05181.
- [362] G. Divitini, S. Cacovich, F. Matteocci, L. Cinà, A. Di Carlo, C. Ducati, In situ observation of heat-induced degradation of perovskite solar cells, *Nat. Energy.* 1 (2016) 15012. doi:10.1038/nenergy.2015.12.
- [363] T. Du, S.R. Ratnasingham, F.U. Kosasih, T.J. Macdonald, L. Mohan, A. Augurio, H. Ahli, C. Lin, S. Xu, W. Xu, R. Binions, C. Ducati, J.R. Durrant, J. Briscoe, M.A. McLachlan, Aerosol Assisted Solvent Treatment: A Universal Method for Performance and Stability Enhancements in Perovskite Solar Cells, *Adv. Energy Mater.* (2021) 2101420. doi:10.1002/aenm.202101420.
- [364] T. Du, C.H. Burgess, J. Kim, J. Zhang, J.R. Durrant, M.A. McLachlan, Formation, location and beneficial role of PbI<sub>2</sub> in lead halide perovskite solar cells, *Sustain. Energy Fuels.* 1 (2017) 119–126. doi:10.1039/C6SE00029K.
- [365] M. Zhu, A. Ghodsi, Automatic dimensionality selection from the scree plot via the use of profile likelihood, *Comput. Stat. Data Anal.* 51 (2006) 918–930. doi:10.1016/j.csda.2005.09.010.
- [366] F.U. Kosasih, S. Cacovich, G. Divitini, C. Ducati, Nanometric Chemical Analysis of Beam-Sensitive Materials: A Case Study of STEM-EDX on Perovskite Solar Cells, *Small Methods.* (2020) 2000835. doi:10.1002/smtd.202000835.

- [367] R.S. Mitchell, Structural polytypism of lead iodide and its relationship to screw dislocations, *Zeitschrift Für Krist. - Cryst. Mater.* 111 (1959) 372–384. doi:10.1524/zkri.1959.111.16.372.
- [368] J. Yang, X. Liu, Y. Zhang, X. Zheng, X. He, H. Wang, F. Yue, S. Braun, J. Chen, J. Xu, Y. Li, Y. Jin, J. Tang, C. Duan, M. Fahlman, Q. Bao, Comprehensive understanding of heat-induced degradation of triple-cation mixed halide perovskite for a robust solar cell, *Nano Energy*. 54 (2018) 218–226. doi:10.1016/j.nanoen.2018.10.011.
- [369] W. Tan, A.R. Bowring, A.C. Meng, M.D. McGehee, P.C. McIntyre, Thermal Stability of Mixed Cation Metal Halide Perovskites in Air, *ACS Appl. Mater. Interfaces*. 10 (2018) 5485–5491. doi:10.1021/acsami.7b15263.
- [370] Z. Dang, J. Shamsi, Q.A. Akkerman, M. Imran, G. Bertoni, R. Brescia, L. Manna, Low-Temperature Electron Beam-Induced Transformations of Cesium Lead Halide Perovskite Nanocrystals, *ACS Omega*. 2 (2017) 5660–5665. doi:10.1021/acsomega.7b01009.
- [371] M.K. Kim, T. Jeon, H. Il Park, J.M. Lee, S.A. Nam, S.O. Kim, Effective control of crystal grain size in  $\text{CH}_3\text{NH}_3\text{PbI}_3$  perovskite solar cells with a pseudohalide  $\text{Pb}(\text{SCN})_2$  additive, *CrystEngComm*. 18 (2016) 6090–6095. doi:10.1039/C6CE00842A.
- [372] S. Razza, F. Di Giacomo, F. Matteocci, L. Cinà, A.L. Palma, S. Casaluci, P. Cameron, A. D'Epifanio, S. Licoccia, A. Reale, T.M. Brown, A. Di Carlo, Perovskite solar cells and large area modules (100 cm<sup>2</sup>) based on an air flow-assisted  $\text{PbI}_2$  blade coating deposition process, *J. Power Sources*. 277 (2015) 286–291. doi:10.1016/J.JPOWSOUR.2014.12.008.
- [373] T. Zhang, M. Yang, Y. Zhao, K. Zhu, Controllable Sequential Deposition of Planar  $\text{CH}_3\text{NH}_3\text{PbI}_3$  Perovskite Films via Adjustable Volume Expansion, *Nano Lett.* 15 (2015) 3959–3963. doi:10.1021/acs.nanolett.5b00843.
- [374] J. Cao, F. Wang, H. Yu, Y. Zhou, H. Lu, N. Zhao, C.-P. Wong, Porous  $\text{PbI}_2$  films for the fabrication of efficient, stable perovskite solar cells via sequential deposition, *J. Mater. Chem. A*. 4 (2016) 10223–10230. doi:10.1039/C6TA03121H.
- [375] Y.-J. Heo, J.-E. Kim, H. Weerasinghe, D. Angmo, T. Qin, K. Sears, K. Hwang, Y.-S. Jung, J. Subbiah, D.J. Jones, M. Gao, D.-Y. Kim, D. Vak, Printing-friendly sequential deposition via intra-additive approach for roll-to-roll process of perovskite solar cells, *Nano Energy*. 41 (2017) 443–451. doi:10.1016/J.NANOEN.2017.09.051.
- [376] N. Adhikari, A. Dubey, E.A. Gaml, B. Vaagensmith, K.M. Reza, S.A.A. Mabrouk, S. Gu, J. Zai, X. Qian, Q. Qiao, Crystallization of a perovskite film for higher performance solar cells by controlling water concentration in methyl ammonium iodide precursor solution, *Nanoscale*. 8 (2016) 2693–2703. doi:10.1039/C5NR06687E.

- [377] E. Mosconi, E. Ronca, F. De Angelis, First-Principles Investigation of the TiO<sub>2</sub>/Organohalide Perovskites Interface: The Role of Interfacial Chlorine, *J. Phys. Chem. Lett.* 5 (2014) 2619–2625. doi:10.1021/jz501127k.
- [378] S. Bae, J.-S. Park, I.K. Han, T.J. Shin, W.H. Jo, CH<sub>3</sub>NH<sub>3</sub>PbI<sub>3</sub> crystal orientation and photovoltaic performance of planar heterojunction perovskite solar cells, *Sol. Energy Mater. Sol. Cells.* 160 (2017) 77–84. doi:10.1016/j.solmat.2016.10.019.
- [379] C. Jiang, Y. Xie, R.R. Lunt, T.W. Hamann, P. Zhang, Elucidating the Impact of Thin Film Texture on Charge Transport and Collection in Perovskite Solar Cells, *ACS Omega*. 3 (2018) 3522–3529. doi:10.1021/acsomega.8b00026.
- [380] H. Tsai, W. Nie, Y. Lin, J.C. Blancon, S. Tretiak, J. Even, G. Gupta, P.M. Ajayan, A.D. Mohite, Effect of Precursor Solution Aging on the Crystallinity and Photovoltaic Performance of Perovskite Solar Cells, *Adv. Energy Mater.* 7 (2017) 1602159. doi:10.1002/aenm.201602159.
- [381] Y. Wu, A. Islam, X. Yang, C. Qin, J. Liu, K. Zhang, W. Peng, L. Han, Retarding the crystallization of PbI<sub>2</sub> for highly reproducible planar-structured perovskite solar cells via sequential deposition, *Energy Environ. Sci.* 7 (2014) 2934–2938. doi:10.1039/C4EE01624F.
- [382] V. Roiati, E. Mosconi, A. Listorti, S. Colella, G. Gigli, F. De Angelis, Stark Effect in Perovskite/TiO<sub>2</sub> Solar Cells: Evidence of Local Interfacial Order, *Nano Lett.* 14 (2014) 2168–2174. doi:10.1021/nl500544c.
- [383] T. Leijtens, B. Lauber, G.E. Eperon, S.D. Stranks, H.J. Snaith, The Importance of Perovskite Pore Filling in Organometal Mixed Halide Sensitized TiO<sub>2</sub>-Based Solar Cells, *J. Phys. Chem. Lett.* 5 (2014) 1096–1102. doi:10.1021/jz500209g.
- [384] M. Fenske, C. Schultz, J. Dagar, F.U. Kosasih, A. Zeiser, C. Junghans, A. Bartelt, C. Ducati, R. Schlatmann, E. Unger, B. Stegemann, Improved Electrical Performance of Perovskite Photovoltaic Mini-Modules through Controlled PbI<sub>2</sub> Formation Using Nanosecond Laser Pulses for P3 Patterning, *Energy Technol.* 9 (2021) 2000969. doi:10.1002/ente.202000969.
- [385] A. Dualeh, P. Gao, S. Il Seok, M.K. Nazeeruddin, M. Grätzel, Thermal behavior of methylammonium lead-trihalide perovskite photovoltaic light harvesters, *Chem. Mater.* 26 (2014) 6160–6164. doi:10.1021/cm502468k.
- [386] J.M. Frost, K.T. Butler, F. Brivio, C.H. Hendon, M. van Schilfgaarde, A. Walsh, Atomistic Origins of High-Performance in Hybrid Halide Perovskite Solar Cells, *Nano Lett.* 14 (2014) 2584–2590. doi:10.1021/nl500390f.

- [387] Q. Han, S.-H. Bae, P. Sun, Y.-T. Hsieh, Y.M. Yang, Y.S. Rim, H. Zhao, Q. Chen, W. Shi, G. Li, Y. Yang, Single Crystal Formamidinium Lead Iodide ( $\text{FAPbI}_3$ ): Insight into the Structural, Optical, and Electrical Properties, *Adv. Mater.* 28 (2016) 2253–2258. doi:10.1002/adma.201505002.
- [388] T. Leijtens, K. Bush, R. Cheacharoen, R. Beal, A. Bowring, M.D. McGehee, Towards enabling stable lead halide perovskite solar cells; interplay between structural, environmental, and thermal stability, *J. Mater. Chem. A* 5 (2017) 11483–11500. doi:10.1039/C7TA00434F.
- [389] F.C. Hanusch, E. Wiesenmayer, E. Mankel, A. Binek, P. Angloher, C. Fraunhofer, N. Giesbrecht, J.M. Feckl, W. Jaegermann, D. Johrendt, T. Bein, P. Docampo, Efficient Planar Heterojunction Perovskite Solar Cells Based on Formamidinium Lead Bromide, *J. Phys. Chem. Lett.* 5 (2014) 2791–2795. doi:10.1021/jz501237m.
- [390] D. Bi, W. Tress, M.I. Dar, P. Gao, J. Luo, C. Renevier, K. Schenk, A. Abate, F. Giordano, J.-P. Correa Baena, J.-D. Decoppet, S.M. Zakeeruddin, M.K. Nazeeruddin, M. Grätzel, A. Hagfeldt, Efficient luminescent solar cells based on tailored mixed-cation perovskites, *Sci. Adv.* 2 (2016) e1501170. doi:10.1126/sciadv.1501170.
- [391] D.H. Cao, C.C. Stoumpos, C.D. Malliakas, M.J. Katz, O.K. Farha, J.T. Hupp, M.G. Kanatzidis, Remnant  $\text{PbI}_2$ , an unforeseen necessity in high-efficiency hybrid perovskite-based solar cells?, *APL Mater.* 2 (2014) 091101. doi:10.1063/1.4895038.
- [392] C. Roldán-Carmona, P. Gratia, I. Zimmermann, G. Grancini, P. Gao, M. Graetzel, M.K. Nazeeruddin, High efficiency methylammonium lead triiodide perovskite solar cells: the relevance of non-stoichiometric precursors, *Energy Environ. Sci.* 8 (2015) 3550–3556. doi:10.1039/C5EE02555A.
- [393] Y.C. Kim, N.J. Jeon, J.H. Noh, W.S. Yang, J. Seo, J.S. Yun, A. Ho-Baillie, S. Huang, M.A. Green, J. Seidel, T.K. Ahn, S. Il Seok, Beneficial Effects of  $\text{PbI}_2$  Incorporated in Organo-Lead Halide Perovskite Solar Cells, *Adv. Energy Mater.* 6 (2016) 1502104. doi:10.1002/aenm.201502104.
- [394] Y.H. Lee, J. Luo, R. Humphry-Baker, P. Gao, M. Grätzel, M.K. Nazeeruddin, Unraveling the Reasons for Efficiency Loss in Perovskite Solar Cells, *Adv. Funct. Mater.* 25 (2015) 3925–3933. doi:10.1002/adfm.201501024.
- [395] T.J. Jacobsson, J.-P. Correa-Baena, E. Halvani Anarakı, B. Philippe, S.D. Stranks, M.E.F. Bouduban, W. Tress, K. Schenk, J. Teuscher, J.-E. Moser, H. Rensmo, A. Hagfeldt, Unreacted  $\text{PbI}_2$  as a Double-Edged Sword for Enhancing the Performance of Perovskite Solar Cells, *J. Am. Chem. Soc.* 138 (2016) 10331–10343. doi:10.1021/jacs.6b06320.

- [396] L. Rakocevic, R. Gehlhaar, M. Jaysankar, W. Song, T. Aernouts, H. Fledderus, J. Poortmans, Translucent, color-neutral and efficient perovskite thin film solar modules, *J. Mater. Chem. C.* 6 (2018) 3034–3041. doi:10.1039/C7TC05863B.
- [397] W. Qiu, A. Ray, M. Jaysankar, T. Merckx, J.P. Bastos, D. Cheyns, R. Gehlhaar, J. Poortmans, P. Heremans, An Interdiffusion Method for Highly Performing Cesium/Formamidinium Double Cation Perovskites, *Adv. Funct. Mater.* 27 (2017) 1–9. doi:10.1002/adfm.201700920.
- [398] S.-J. Moon, J.-H. Yum, L. Lofgren, A. Walter, L. Sansonnens, M. Benkhaira, S. Nicolay, J. Bailat, C. Ballif, Laser-Scribing Patterning for the Production of Organometallic Halide Perovskite Solar Modules, *IEEE J. Photovoltaics.* 5 (2015) 1087–1092. doi:10.1109/JPHOTOV.2015.2416913.
- [399] X. Zhao, Y. Cao, Q. Nian, Y.C. Shin, G. Cheng, Precise selective scribing of thin-film solar cells by a picosecond laser, *Appl. Phys. A.* 116 (2014) 671–681. doi:10.1007/s00339-014-8330-6.
- [400] Z. Toth, B. Hopp, T. Szoerenyi, Z. Bor, E.A. Shakhno, V.P. Veiko, Pulsed laser ablation mechanisms of thin metal films, in: V.P. Veiko, T. Szoerenyi (Eds.), *Proc. SPIE*, International Society for Optics and Photonics, 1999: pp. 18–26. doi:10.1117/12.364228.
- [401] N. Rolston, B.L. Watson, C.D. Bailie, M.D. McGehee, J.P. Bastos, R. Gehlhaar, J.-E. Kim, D. Vak, A.T. Mallajosyula, G. Gupta, A.D. Mohite, R.H. Dauskardt, Mechanical integrity of solution-processed perovskite solar cells, *Extrem. Mech. Lett.* 9 (2016) 353–358. doi:10.1016/j.eml.2016.06.006.
- [402] J. Bonse, S. Hohm, S. V. Kirner, A. Rosenfeld, J. Kruger, Laser-Induced Periodic Surface Structures— A Scientific Evergreen, *IEEE J. Sel. Top. Quantum Electron.* 23 (2017). doi:10.1109/JSTQE.2016.2614183.
- [403] J. Bonse, A. Rosenfeld, J. Krüger, On the role of surface plasmon polaritons in the formation of laser-induced periodic surface structures upon irradiation of silicon by femtosecond-laser pulses, *J. Appl. Phys.* 106 (2009) 104910. doi:10.1063/1.3261734.
- [404] M. Huang, F. Zhao, Y. Cheng, N. Xu, Z. Xu, Origin of Laser-Induced Near-Subwavelength Ripples: Interference between Surface Plasmons and Incident Laser, *ACS Nano.* 3 (2009) 4062–4070. doi:10.1021/nm900654v.
- [405] G. Miyaji, K. Miyazaki, Origin of periodicity in nanostructuring on thin film surfaces ablated with femtosecond laser pulses, *Opt. Express.* 16 (2008) 16265. doi:10.1364/OE.16.016265.

- [406] F. Garrelie, J.-P. Colombier, F. Pigeon, S. Tonchev, N. Faure, M. Bounhalli, S. Reynaud, O. Parriaux, Evidence of surface plasmon resonance in ultrafast laser-induced ripples, *Opt. Express.* 19 (2011) 9035. doi:10.1364/OE.19.009035.
- [407] Y. Katsumata, T. Morita, Y. Morimoto, T. Shintani, T. Saiki, Self-organization of a periodic structure between amorphous and crystalline phases in a GeTe thin film induced by femtosecond laser pulse amorphization, *Appl. Phys. Lett.* 105 (2014) 031907. doi:10.1063/1.4890862.
- [408] D. Puerto, M. Garcia-Lechuga, J. Hernandez-Rueda, A. Garcia-Leis, S. Sanchez-Cortes, J. Solis, J. Siegel, Femtosecond laser-controlled self-assembly of amorphous-crystalline nanogratings in silicon, *Nanotechnology*. 27 (2016) 265602. doi:10.1088/0957-4484/27/26/265602.
- [409] X. Liu, D. Du, G. Mourou, Laser ablation and micromachining with ultrashort laser pulses, *IEEE J. Quantum Electron.* 33 (1997) 1706–1716. doi:10.1109/3.631270.
- [410] G.K. White, Thermal Conductivity of Pure Metals and Alloys · Ac - Fe, in: O. Madelung, G.K. White (Eds.), *Therm. Conduct. Pure Met. Alloy.*, 15C ed., Springer-Verlag, Berlin/Heidelberg, 1991: pp. 10–23. doi:10.1007/10031435\_4.
- [411] J. Barbé, M. Newman, S. Lilliu, V. Kumar, H.K.H. Lee, C. Charbonneau, C. Rodenburg, D. Lidzey, W.C. Tsoi, Localized effect of PbI<sub>2</sub> excess in perovskite solar cells probed by high-resolution chemical-optoelectronic mapping, *J. Mater. Chem. A.* 6 (2018) 23010–23018. doi:10.1039/C8TA09536A.
- [412] W. Lee, H. Li, A.B. Wong, D. Zhang, M. Lai, Y. Yu, Q. Kong, E. Lin, J.J. Urban, J.C. Grossman, P. Yang, Ultralow thermal conductivity in all-inorganic halide perovskites, *Proc. Natl. Acad. Sci.* 114 (2017) 8693–8697. doi:10.1073/pnas.1711744114.
- [413] T.S. Silva, A.S. Alves, I. Pepe, H. Tsuzuki, O. Nakamura, M.M.F. d’Aguiar Neto, A.F. da Silva, N. Veissid, C.Y. An, Thermal diffusivity of lead iodide, *J. Appl. Phys.* 83 (1998) 6193–6195. doi:10.1063/1.367492.
- [414] D.I. Yakubovsky, A. V. Arsenin, Y. V. Stebunov, D.Y. Fedyanin, V.S. Volkov, Optical constants and structural properties of thin gold films, *Opt. Express.* 25 (2017) 25574. doi:10.1364/OE.25.025574.
- [415] D. Bäuerle, *Laser Processing and Chemistry*, Springer Berlin Heidelberg, Berlin, Heidelberg, 2011. doi:10.1007/978-3-642-17613-5.
- [416] M.S. Brown, C.B. Arnold, Fundamentals of Laser-Material Interaction and Application to Multiscale Surface Modification, in: K. Sugioka, M. Meunier, A. Pique (Eds.), *Laser Precis. Microfabr.*, Springer, 2010: pp. 91–120. doi:10.1007/978-3-642-10523-4\_4.

- [417] B. Conings, J. Drijkonigen, N. Gauquelin, A. Babayigit, J. D'Haen, L. D'Olieslaeger, A. Ethirajan, J. Verbeeck, J. Manca, E. Mosconi, F. De Angelis, H.G. Boyen, Intrinsic Thermal Instability of Methylammonium Lead Trihalide Perovskite, *Adv. Energy Mater.* 5 (2015) 1–8. doi:10.1002/aenm.201500477.
- [418] Tera Analysis Ltd., Natural convection coefficient calculator, (n.d.). [https://quickfield.com/natural\\_convection.htm](https://quickfield.com/natural_convection.htm) (accessed June 18, 2019).
- [419] L. Gmelin, *Handbuch der Anorganischen Chemie*, 8th ed., 1967.
- [420] T. Ashida, A. Miyamura, N. Oka, Y. Sato, T. Yagi, N. Taketoshi, T. Baba, Y. Shigesato, Thermal transport properties of polycrystalline tin-doped indium oxide films, *J. Appl. Phys.* 105 (2009) 073709. doi:10.1063/1.3093684.
- [421] H.D. Young, R.A. Freedman, *University Physics with Modern Physics*, 14th ed., Pearson, 2014.
- [422] M.T. Hörantner, P.K. Nayak, S. Mukhopadhyay, K. Wojciechowski, C. Beck, D. McMeekin, B. Kamino, G.E. Eperon, H.J. Snaith, Shunt-Blocking Layers for Semitransparent Perovskite Solar Cells, *Adv. Mater. Interfaces*. 3 (2016) 1–7. doi:10.1002/admi.201500837.
- [423] J.M. Liu, Simple technique for measurements of pulsed Gaussian-beam spot sizes, *Opt. Lett.* 7 (1982) 196. doi:10.1364/OL.7.000196.
- [424] E.J. Juarez-Perez, L.K. Ono, M. Maeda, Y. Jiang, Z. Hawash, Y. Qi, Photodecomposition and thermal decomposition in methylammonium halide lead perovskites and inferred design principles to increase photovoltaic device stability, *J. Mater. Chem. A*. 6 (2018) 9604–9612. doi:10.1039/C8TA03501F.
- [425] K.T. Cho, S. Paek, G. Grancini, C. Roldán-Carmona, P. Gao, Y. Lee, M.K. Nazeeruddin, Highly efficient perovskite solar cells with a compositionally engineered perovskite/hole transporting material interface, *Energy Environ. Sci.* 10 (2017) 621–627. doi:10.1039/C6EE03182J.
- [426] N. Yaghoobi Nia, M. Zendehdel, M. Abdi-Jalebi, L.A. Castriotta, F.U. Kosasih, E. Lamanna, M.M. Abolhasani, Z. Zheng, Z. Andaji-Garmaroudi, K. Asadi, G. Divitini, C. Ducati, R.H. Friend, A. Di Carlo, Beyond 17% Stable Perovskite Solar Module via Polaron Arrangement of Tuned Polymeric Hole Transport Layer, *Nano Energy*. 82 (2020) 105685. doi:10.1016/j.nanoen.2020.105685.
- [427] E. Le Bourhis, *Glass: Mechanics and Technology*, 2nd ed., Wiley-VCH Verlag, 2014.
- [428] T. Prabhakar, N. Jampana, Effect of sodium diffusion on the structural and electrical properties of Cu<sub>2</sub>ZnSnS<sub>4</sub> thin films, *Sol. Energy Mater. Sol. Cells.* 95 (2011) 1001–1004. doi:10.1016/j.solmat.2010.12.012.

- [429] D. Braunger, D. Hariskos, G. Bilger, U. Rau, H.W. Schock, Influence of sodium on the growth of polycrystalline Cu(In,Ga)Se<sub>2</sub> thin films, *Thin Solid Films.* 361–362 (2000) 161–166. doi:10.1016/S0040-6090(99)00777-4.
- [430] P.T. Erslev, J.W. Lee, W.N. Shafarman, J.D. Cohen, The influence of Na on metastable defect kinetics in CIGS materials, *Thin Solid Films.* 517 (2009) 2277–2281. doi:10.1016/j.tsf.2008.10.140.
- [431] D. Rudmann, A.F. da Cunha, M. Kaelin, F. Kurdesau, H. Zogg, A.N. Tiwari, G. Bilger, Efficiency enhancement of Cu(In,Ga)Se<sub>2</sub> solar cells due to post-deposition Na incorporation, *Appl. Phys. Lett.* 84 (2004) 1129–1131. doi:10.1063/1.1646758.
- [432] S.-H. Wei, S.B. Zhang, A. Zunger, Effects of Na on the electrical and structural properties of CuInSe<sub>2</sub>, *J. Appl. Phys.* 85 (1999) 7214–7218. doi:10.1063/1.370534.
- [433] K.M. Boopathi, R. Mohan, T.-Y. Huang, W. Budiawan, M.-Y. Lin, C.-H. Lee, K.-C. Ho, C.-W. Chu, Synergistic improvements in stability and performance of lead iodide perovskite solar cells incorporating salt additives, *J. Mater. Chem. A.* 4 (2016) 1591–1597. doi:10.1039/C5TA10288J.
- [434] H. Lee, A. Kim, H.-C. Kwon, W. Yang, Y. Oh, D. Lee, J. Moon, Retarding Crystallization during Facile Single Coating of NaCl-Incorporated Precursor Solution for Efficient Large-Area Uniform Perovskite Solar Cells, *ACS Appl. Mater. Interfaces.* 8 (2016) 29419–29426. doi:10.1021/acsami.6b08783.
- [435] S. Bag, M.F. Durstock, Large Perovskite Grain Growth in Low-Temperature Solution-Processed Planar p-i-n Solar Cells by Sodium Addition, *ACS Appl. Mater. Interfaces.* 8 (2016) 5053–5057. doi:10.1021/acsami.5b11494.
- [436] J. Chang, Z. Lin, H. Zhu, F.H. Isikgor, Q.-H. Xu, C. Zhang, Y. Hao, J. Ouyang, Enhancing the photovoltaic performance of planar heterojunction perovskite solar cells by doping the perovskite layer with alkali metal ions, *J. Mater. Chem. A.* 4 (2016) 16546–16552. doi:10.1039/C6TA06851K.
- [437] Z. Tang, S. Uchida, T. Bessho, T. Kinoshita, H. Wang, F. Awai, R. Jono, M.M. Maitani, J. Nakazaki, T. Kubo, H. Segawa, Modulations of various alkali metal cations on organometal halide perovskites and their influence on photovoltaic performance, *Nano Energy.* 45 (2018) 184–192. doi:10.1016/j.nanoen.2017.12.047.
- [438] Y. Yang, X. Zou, Y. Pei, X. Bai, W. Jin, D. Chen, Effect of doping of NaI monovalent cation halide on the structural, morphological, optical and optoelectronic properties of MAPbI<sub>3</sub> perovskite, *J. Mater. Sci. Mater. Electron.* 29 (2018) 205–210. doi:10.1007/s10854-017-7905-3.

- [439] M. Abdi-Jalebi, M.I. Dar, A. Sadhanala, S.P. Senanayak, M. Franckevičius, N. Arora, Y. Hu, M.K. Nazeeruddin, S.M. Zakeeruddin, M. Grätzel, R.H. Friend, Impact of Monovalent Cation Halide Additives on the Structural and Optoelectronic Properties of  $\text{CH}_3\text{NH}_3\text{PbI}_3$  Perovskite, *Adv. Energy Mater.* 6 (2016) 1502472. doi:10.1002/aenm.201502472.
- [440] M. Abdi-Jalebi, M. Pazoki, B. Philippe, M.I. Dar, M. Alsari, A. Sadhanala, G. Divitini, R. Imani, S. Lilliu, J. Kullgren, H. Rensmo, M. Grätzel, R.H. Friend, Dedoping of Lead Halide Perovskites Incorporating Monovalent Cations, *ACS Nano.* 12 (2018) 7301–7311. doi:10.1021/acsnano.8b03586.
- [441] S. Xiang, W. Li, Y. Wei, J. Liu, H. Liu, L. Zhu, S. Yang, H. Chen, Natrium Doping Pushes the Efficiency of Carbon-Based  $\text{CsPbI}_3$  Perovskite Solar Cells to 10.7%, *IScience.* 15 (2019) 156–164. doi:10.1016/j.isci.2019.04.025.
- [442] L. Wang, D. Moghe, S. Hafezian, P. Chen, M. Young, M. Elinski, L. Martinu, S. Kéna-Cohen, R.R. Lunt, Alkali Metal Halide Salts as Interface Additives to Fabricate Hysteresis-Free Hybrid Perovskite-Based Photovoltaic Devices, *ACS Appl. Mater. Interfaces.* 8 (2016) 23086–23094. doi:10.1021/acsami.6b07368.
- [443] J. Ma, X. Guo, L. Zhou, Z. Lin, C. Zhang, Z. Yang, G. Lu, J. Chang, Y. Hao, Enhanced Planar Perovskite Solar Cell Performance via Contact Passivation of  $\text{TiO}_2$ /Perovskite Interface with  $\text{NaCl}$  Doping Approach, *ACS Appl. Energy Mater.* 1 (2018) 3826–3834. doi:10.1021/acsaelm.8b00602.
- [444] S. You, H. Wang, S. Bi, J. Zhou, L. Qin, X. Qiu, Z. Zhao, Y. Xu, Y. Zhang, X. Shi, H. Zhou, Z. Tang, A Biopolymer Heparin Sodium Interlayer Anchoring  $\text{TiO}_2$  and  $\text{MAPbI}_3$  Enhances Trap Passivation and Device Stability in Perovskite Solar Cells, *Adv. Mater.* 30 (2018) 1706924. doi:10.1002/adma.201706924.
- [445] D. Di Girolamo, N. Phung, M. Jošt, A. Al-Ashouri, G. Chistiakova, J. Li, J.A. Márquez, T. Unold, L. Korte, S. Albrecht, A. Di Carlo, D. Dini, A. Abate, From Bulk to Surface: Sodium Treatment Reduces Recombination at the Nickel Oxide/Perovskite Interface, *Adv. Mater. Interfaces.* 6 (2019) 1900789. doi:10.1002/admi.201900789.
- [446] C. Bi, X. Zheng, B. Chen, H. Wei, J. Huang, Spontaneous Passivation of Hybrid Perovskite by Sodium Ions from Glass Substrates: Mysterious Enhancement of Device Efficiency Revealed, *ACS Energy Lett.* 2 (2017) 1400–1406. doi:10.1021/acsenergylett.7b00356.
- [447] D. Su, S. Dou, G. Wang, Anatase  $\text{TiO}_2$ : Better Anode Material Than Amorphous and Rutile Phases of  $\text{TiO}_2$  for Na-Ion Batteries, *Chem. Mater.* 27 (2015) 6022–6029. doi:10.1021/acs.chemmater.5b02348.

- [448] W. Wang, Y. Liu, X. Wu, J. Wang, L. Fu, Y. Zhu, Y. Wu, X. Liu, Advances of TiO<sub>2</sub> as Negative Electrode Materials for Sodium-Ion Batteries, *Adv. Mater. Technol.* 3 (2018) 1800004. doi:10.1002/admt.201800004.
- [449] D.J. Kubicki, D. Prochowicz, J. Wiktor, C. Grey, S.D. Stranks, The microscopic mechanism of sodium doping in hybrid and all-inorganic halide perovskites, in: Proc. 13th Conf. Hybrid Org. Photovoltaics, Fundacio Scito, 2021: p. 65.
- [450] Z. Andaji-Garmaroudi, M. Abdi-Jalebi, F.U. Kosasih, T. Doherty, S. Macpherson, A.R. Bowman, G.J. Man, U.B. Cappel, H. Rensmo, C. Ducati, R.H. Friend, S.D. Stranks, Elucidating and Mitigating Degradation Processes in Perovskite Light-Emitting Diodes, *Adv. Energy Mater.* 10 (2020) 2002676. doi:10.1002/aenm.202002676.
- [451] A. Listorti, E.J. Juarez-Perez, C. Frontera, V. Roiati, L. Garcia-Andrade, S. Colella, A. Rizzo, P. Ortiz, I. Mora-Sero, Effect of Mesostructured Layer upon Crystalline Properties and Device Performance on Perovskite Solar Cells, *J. Phys. Chem. Lett.* 6 (2015) 1628–1637. doi:10.1021/acs.jpclett.5b00483.
- [452] G. Tumen-Ulzii, C. Qin, D. Klotz, M.R. Leyden, P. Wang, M. Auffray, T. Fujihara, T. Matsushima, J. Lee, S. Lee, Y. Yang, C. Adachi, Detrimental Effect of Unreacted PbI<sub>2</sub> on the Long-Term Stability of Perovskite Solar Cells, *Adv. Mater.* 32 (2020) 1905035. doi:10.1002/adma.201905035.
- [453] Q. Jiang, Z. Chu, P. Wang, X. Yang, H. Liu, Y. Wang, Z. Yin, J. Wu, X. Zhang, J. You, Planar-Structure Perovskite Solar Cells with Efficiency beyond 21%, *Adv. Mater.* 29 (2017) 1703852. doi:10.1002/adma.201703852.
- [454] O.S. Game, J.A. Smith, T.I. Alanazi, M. Wong-Stringer, V. Kumar, C. Rodenburg, N.J. Terrill, D.G. Lidzey, Solvent vapour annealing of methylammonium lead halide perovskite: what's the catch?, *J. Mater. Chem. A.* 8 (2020) 10943–10956. doi:10.1039/D0TA03023F.
- [455] T.A. Witten, L.M. Sander, Diffusion-Limited Aggregation, a Kinetic Critical Phenomenon, *Phys. Rev. Lett.* 47 (1981) 1400–1403. doi:10.1103/PhysRevLett.47.1400.
- [456] R. O'Hayre, Transport Kinetics (Diffusion), in: *Mater. Kinet. Fundam.*, 1st ed., John Wiley & Sons, Hoboken, 2015: pp. 84–147.
- [457] A.J. Barker, A. Sadhanala, F. Deschler, M. Gandini, S.P. Senanayak, P.M. Pearce, E. Mosconi, A.J. Pearson, Y. Wu, A.R. Srimath Kandada, T. Leijtens, F. De Angelis, S.E. Dutton, A. Petrozza, R.H. Friend, Defect-Assisted Photoinduced Halide Segregation in Mixed-Halide Perovskite Thin Films, *ACS Energy Lett.* 2 (2017) 1416–1424. doi:10.1021/acsenergylett.7b00282.

- [458] N. Vicente, G. Garcia-Belmonte, Organohalide Perovskites are Fast Ionic Conductors, *Adv. Energy Mater.* 7 (2017) 1700710. doi:10.1002/aenm.201700710.
- [459] V. Fjallstrom, P.M.P. Salome, A. Hultqvist, M. Edoff, T. Jarmar, B.G. Aitken, K. Zhang, K. Fuller, C.K. Williams, Potential-Induced Degradation of  $\text{CuIn}_{1-x}\text{Ga}_x\text{Se}_2$  Thin Film Solar Cells, *IEEE J. Photovoltaics.* 3 (2013) 1090–1094. doi:10.1109/JPHOTOV.2013.2253833.
- [460] V. Fjallstrom, P. Szaniawski, B. Vermang, P.M.P. Salome, F. Rostvall, U. Zimmermann, M. Edoff, Recovery After Potential-Induced Degradation of  $\text{CuIn}_{1-x}\text{Ga}_x\text{Se}_2$ , *IEEE J. Photovoltaics.* 5 (2015) 664–669. doi:10.1109/JPHOTOV.2014.2384839.
- [461] C.P. Muzzillo, S. Glynn, P. Hacke, H.R. Moutinho, M.R. Young, G. Teeter, I.L. Repins, L.M. Mansfield, Potential-Induced Degradation of  $\text{Cu}(\text{In},\text{Ga})\text{Se}_2$  Solar Cells: Alkali Metal Drift and Diffusion Effects, *IEEE J. Photovoltaics.* 8 (2018) 1337–1342. doi:10.1109/JPHOTOV.2018.2858549.
- [462] ThermoFisher Scientific, Spectra Ultra S/TEM, (2021). <https://www.thermofisher.com/uk/en/home/electron-microscopy/products/transmission-electron-microscopes/spectra-ultra-tem.html> (accessed August 22, 2021).
- [463] B.D.A. Levin, Direct detectors and their applications in electron microscopy for materials science, *J. Phys. Mater.* 4 (2021) 042005. doi:10.1088/2515-7639/ac0ff9.

# Appendix

## A. EDX Analysis Code

```
#load HyperSpy and Python libraries, set colour map
%matplotlib qt

import hyperspy.api as hs
import numpy as np
import matplotlib.pyplot as plt
plt.set_cmap("magma")

#load SIs
s1 = hs.load("14.34.18 Spectrum image.emi")
s2 = hs.load("15.39.09 Spectrum image.emi")
s3 = hs.load("16.39.24 Spectrum image.emi")

#cut energy axis at 14 keV
s1.crop(axis = 2, end = 2800)
s2.crop(axis = 2, end = 2800)
s3.crop(axis = 2, end = 2800)

#stack all SIs into 1
s = hs.stack([s1,s2,s3], axis = 0)

#rebin energy axis by 4
s = s.rebin([450,700,700])

#set title
s.metadata.set_item("General.title", 'PSC Elemental Mapping')

s.change_dtype('float32')

#PCA step
s.decomposition(normalize_poissonian_noise = True)
```

```

#show scree plots
s.plot_explained_variance_ratio(n = 20)
s.plot_explained_variance_ratio(n = 50)

#show PCA components
s.plot_decomposition_results()

#put PCA factors and loadings into variables
PCA_factors = s.get_decomposition_factors()
PCA_loadings = s.get_decomposition_loadings()

#save PCA factors as .tif
for i in [0,1,2,3,11,12]:
    PCA_factors.inav[i].plot()
    fig = plt.gcf()
    fig.savefig('PCA_factor_%i.tif' %i)

#save PCA loadings as .tif
for i in [0,1,2,3,11,12]:
    PCA_loadings.inav[i].plot()
    fig = plt.gcf()
    fig.savefig('PCA_loading_%i.tif' %i)

#save PCA factors as .txt for plotting
PCA_factors.inav[0].data.tofile(file="PCA_factor_0", sep=",", format="%f")
PCA_factors.inav[1].data.tofile(file="PCA_factor_1", sep=",", format="%f")
PCA_factors.inav[2].data.tofile(file="PCA_factor_2", sep=",", format="%f")
PCA_factors.inav[3].data.tofile(file="PCA_factor_3", sep=",", format="%f")
PCA_factors.inav[11].data.tofile(file="PCA_factor_11", sep=",", format="%f")
PCA_factors.inav[12].data.tofile(file="PCA_factor_12", sep=",", format="%f")

#NMF step
s.decomposition(normalize_poissonian_noise = True, algorithm = "nmf",
tol=1e-10, max_iter = 1000, output_dimension = 4)

```

```

#show NMF components
s.plot_decomposition_results()

#put NMF factors and loadings into variables
NMF_factors=s.get_decomposition_factors()
NMF_loadings=s.get_decomposition_loadings()

#save NMF factors as .tif
for i in [0,1,2,3]:
    NMF_factors.inav[i].plot()
    fig = plt.gcf()
    fig.savefig('NMF_factor_%i.tif'%i)

#save NMF loadings as .tif
for i in [0,1,2,3]:
    NMF_loadings.inav[i].plot()
    fig = plt.gcf()
    fig.savefig('NMF_loading_%i.tif'%i)

#save NMF factors as .txt for plotting
NMF_factors.inav[0].data.tofile(file="NMF_factor_0", sep=",", format="%f")
NMF_factors.inav[1].data.tofile(file="NMF_factor_1", sep=",", format="%f")
NMF_factors.inav[2].data.tofile(file="NMF_factor_2", sep=",", format="%f")
NMF_factors.inav[3].data.tofile(file="NMF_factor_3", sep=",", format="%f")

#elemental mapping step with PCA components (not NMF)
#build denoised model
sm = s.get_decomposition_model([0,1,2,3,11,12])
sm.set_signal_type("EDS_TEM")

#add X-ray lines of interest
sm.set_elements(['Au', 'Br', 'C', 'I', 'N', 'Pb', 'Sn', 'Ti'])

```

```

sm.set_lines(["Au_La", "Br_Ka", "C_Ka", "I_La", "N_Ka", "Pb_La", "Sn_La",
"Ti_Ka"])

#construct background windows
bw = sm.estimate_background_windows(line_width = [2.0, 2.0])

#set position of background windows
#BG window widths = peak FWHM

#Au_La
bw[0,0]= 9127.4
bw[0,1] = 9290
bw[0,2] = 10055
bw[0,3] = 10217.6

#Br_Ka
bw[1,0] = 10811.2
bw[1,1] = 10990
bw[1,2] = 12935
bw[1,3] = 13113.8

#C_Ka
bw[2,0] = 147.3
bw[2,1] = 200.6
bw[2,2] = 612.6
bw[2,3] = 665.9

#I_La
bw[3,0] = 2815.5
bw[3,1] = 2925
bw[3,2] = 5272
bw[3,3] = 5381.5

#N_Ka
bw[4,0] = 147.3

```

```

bw[4,1] = 200.6
bw[4,2] = 612.6
bw[4,3] = 665.9

#Pb_La
bw[5,0] = 10045.2
bw[5,1] = 10224
bw[5,2] = 10820
bw[5,3] = 10988.9

#Sn_La
bw[6,0] = 2815.5
bw[6,1] = 2925
bw[6,2] = 5272
bw[6,3] = 5381.5

#Ti_Ka
bw[7,0] = 2809.1
bw[7,1] = 2925
bw[7,2] = 5272
bw[7,3] = 5387.9

#check that BG windows do not overlap with peaks
sm.plot(background_windows = bw)

#extract BG-corrected line intensities
intensities = sm.get_lines_intensity(background_windows = bw, plot_result = False)

#remove unphysical negative intensity
intensities[0].data[intensities[0].data < 0] = 0
intensities[1].data[intensities[1].data < 0] = 0
intensities[2].data[intensities[2].data < 0] = 0
intensities[3].data[intensities[3].data < 0] = 0

```

```

intensities[4].data[intensities[4].data < 0] = 0
intensities[5].data[intensities[5].data < 0] = 0
intensities[6].data[intensities[6].data < 0] = 0
intensities[7].data[intensities[7].data < 0] = 0

#save line intensities maps as .tif
intensities_img0 = intensities[0].as_signal2D((0,1))
intensities_img0.plot(vmin = 0)
fig = plt.gcf()
fig.savefig('Au_La_int.tif')

intensities_img1 = intensities[1].as_signal2D((0,1))
intensities_img1.plot(vmin = 0)
fig = plt.gcf()
fig.savefig('Br_Ka_int.tif')

intensities_img2 = intensities[2].as_signal2D((0,1))
intensities_img2.plot(vmin = 0)
fig = plt.gcf()
fig.savefig('C_Ka_int.tif')

intensities_img3 = intensities[3].as_signal2D((0,1))
intensities_img3.plot(vmin = 0)
fig = plt.gcf()
fig.savefig('I_La_int.tif')

intensities_img4 = intensities[4].as_signal2D((0,1))
intensities_img4.plot(vmin = 0)
fig = plt.gcf()
fig.savefig('N_Ka_int.tif')

intensities_img5 = intensities[5].as_signal2D((0,1))
intensities_img5.plot(vmin = 0)

```

```

fig = plt.gcf()
fig.savefig('Pb_La_int.tif')

intensities_img6 = intensities[6].as_signal2D((0,1))
intensities_img6.plot(vmin = 0)
fig = plt.gcf()
fig.savefig('Sn_La_int.tif')

intensities_img7 = intensities[7].as_signal2D((0,1))
intensities_img7.plot(vmin = 0)
fig = plt.gcf()
fig.savefig('Ti_Ka_int.tif')

#input k-factors for quantification
kfactors=[4.256, #Au_La
           2.878, #Br_Ka
           2.452, #C_Ka
           3.413, #I_La
           3.856, #N_Ka
           4.374, #Pb_La
           2.653, #Sn_La
           1.227] #Ti_Ka

#Cliff-Lorimer quantification step
maps = sm.quantification(intensities, method = 'CL', factors = kfactors,
composition_units = 'atomic', plot_result = False)

#save quantified maps as .tif
maps_img0 = maps[0].as_signal2D((0,1))
maps_img0.plot(vmin = 0, vmax = 100)
fig = plt.gcf()
fig.savefig('Au_La_map.tif')
maps_img1 = maps[1].as_signal2D((0,1))
maps_img1.plot(vmin = 0,vmax = 10)

```

```
fig = plt.gcf()
fig.savefig('Br_Ka_map.tif')

maps_img2 = maps[2].as_signal2D((0,1))
maps_img2.plot(vmin = 0,vmax = 100)
fig = plt.gcf()
fig.savefig('C_Ka_map.tif')

maps_img3 = maps[3].as_signal2D((0,1))
maps_img3.plot(vmin = 0,vmax = 70)
fig = plt.gcf()
fig.savefig('I_La_map.tif')

maps_img4 = maps[4].as_signal2D((0,1))
maps_img4.plot(vmin = 0,vmax = 40)
fig = plt.gcf()
fig.savefig('N_Ka_map.tif')

maps_img5 = maps[5].as_signal2D((0,1))
maps_img5.plot(vmin = 0,vmax = 25)
fig = plt.gcf()
fig.savefig('Pb_La_map.tif')

maps_img6 = maps[6].as_signal2D((0,1))
maps_img6.plot(vmin = 0,vmax = 35)
fig = plt.gcf()
fig.savefig('Sn_La_map.tif')

maps_img7 = maps[7].as_signal2D((0,1))
maps_img7.plot(vmin = 0,vmax = 35)
```

```

fig = plt.gcf()
fig.savefig('Ti_Ka_map.tif')

Au = maps[0]
Br = maps[1]
C = maps[2]
I = maps[3]
N = maps[4]
Pb = maps[5]
Sn = maps[6]
Ti = maps[7]

#construct ratio maps
#mask pixels where I or Pb is less than 0.1 at%
mask_I = I > 0.1
mask_Pb = Pb > 0.1
maskI = I * mask_I
maskPb = Pb * mask_Pb

I_Pb = maskI / maskPb
I_Pb.data = np.nan_to_num(I_Pb.data)
I_Pb.data[I_Pb.data < 0] = 0
I_Pb.data[I_Pb.data > 1000000] = 1000000

I_Pb.metadata.set_item("General.title",'2.5 < I/Pb < 3.5')
I_Pbimage = I_Pb.as_signal2D((0,1))
I_Pbimage.plot(vmin = 2.5, vmax = 3.5)
fig = plt.gcf()
fig.savefig('I_Pb_ratio_map.tif')

```

## B. CL Analysis Code

```
#load Lumispy, HyperSpy, and Python libraries, set colour map
%matplotlib qt
import hyperspy.api as hs
import lumispy as lum
import numpy as np
import matplotlib.pyplot as plt
plt.set_cmap("magma")

#load CL SI
path = "MAP1_processed.hspy"
cl_sem = lum.load(path)

#plot panchromatic image and average CL spectrum
cl_sem.T.mean().plot()
cl_sem.mean().plot()

#gaussian fitting
#define model for fitting
m = cl_sem.create_model()

gpvk = hs.model.components1D.Gaussian()
gpbi2 = hs.model.components1D.Gaussian()
bkg = hs.model.components1D.Offset()
m.extend([gpvk, gpbi2, bkg])

#calculate average background level
sum_over_pixels = cl_sem.sum(axis=0).sum(axis=0)
background_sum = sum_over_pixels.data[0:30].sum() +
sum_over_pixels.data[476:506].sum()
background_estimate = background_sum/(60 * cl_sem.data.shape[0] *
cl_sem.data.shape[1])
background_estimate
```

```

#define Gaussian fitting initial values and boundaries

gpvk.centre.value = 735      #based on average spectrum
gpvk.centre.bmin = 685       #min boundary
gpvk.centre.bmax = 785       #max boundary

gpvk.sigma.value = 40        #guess for FWHM
gpvk.sigma.bmin = 1
gpvk.sigma.bmax = 100

gpvk.A.value = 500           #guess for integrated intensity
gpvk.A.bmin = 1
gpvk.A.bmax = 10000

gpbi2.centre.value = 520
gpbi2.centre.bmin = 500
gpbi2.centre.bmax = 540

gpbi2.sigma.value = 40
gpbi2.sigma.bmin = 1
gpbi2.sigma.bmax = 100

gpbi2.A.value = 500
gpbi2.A.bmin = 0
gpbi2.A.bmax = 1000

bkg.offset.value = background_estimate
bkg.offset.bmin = background_estimate - 5
bkg.offset.bmax = background_estimate + 5

m.set_signal_range(330,870) #fitting range

#model fitting
m.multifit(bounded = True)

```

```

gpvk.centre.plot(vmin = 660, vmax = 780)
gpvk.A.plot(vmin = 0, vmax = 20000)

gpbi2.centre.plot(vmin = 500, vmax = 540)
gpbi2.A.plot(vmin = 0, vmax = 600)

#masked centre wavelength map
peakpvk = gpvk.centre.as_signal()
heightpvk = gpvk.A.as_signal()
maskpvk = np.zeros((25,45))

for i in range(0,25):
    for j in range(0,45):
        if(heightpvk.isig[i,j].data >20 and peakpvk.isig[i,j].data <784):
            maskpvk[i,j] = 1

peakpvk = peakpvk * maskpvk.T

plt.imshow(peakpvk, vmin = 660, vmax = 780)
plt.show()
plt.colorbar()

#get masked average spectrum
lamella = np.zeros((506))
count = 0

for i in range(0,25):
    for j in range(0,45):
        if(heightpvk.isig[i,j].data >20 and peakpvk.isig[i,j].data <784):
            lamella = lamella + cl_sem.inav[i,j].data
            count = count + 1

lamella = lamella / count

```